

# Dynamic life of a microtubule

From birth, growth and stabilization to  
damage and destruction



Dipti Rai

Microtubule  
2017-2023

R.I.P.



# **Dynamic life of a microtubule:**

From birth, growth and stabilization to  
damage and destruction

Dipti Rai

ISBN: 978-94-6483-016-3

DOI: <https://doi.org/10.33540/1687>

The studies described in this thesis were performed at the division of Cell Biology, Neurobiology and Biophysics at the Faculty of Science of Utrecht University in Utrecht, The Netherlands.

Cover and Layout: Dipti Rai

Printed by: Ridderprint | [www.ridderprint.nl](http://www.ridderprint.nl)

Copyright © Dipti Rai, 2023  
All rights reserved.

# **Dynamic life of a microtubule**

**From birth, growth and stabilization to damage and destruction**

## **Het dynamische leven van een microtubulus**

**Van geboorte, groei en stabilisatie tot beschadiging en destructie**

(met een samenvatting in het Nederlands)

### **Proefschrift**

ter verkrijging van de graad van doctor aan de  
Universiteit Utrecht  
op gezag van de  
rector magnificus, prof.dr. H.R.B.M. Kummeling,  
ingevolge het besluit van het college voor promoties  
in het openbaar te verdedigen op

woensdag 5 april 2023 des middags te 2.15 uur

door

**Dipti Rai**

geboren op 25 september 1990  
te Mau, India

**Promotor:**

Prof. dr. A.S. Akhmanova

**Beoordelingscommissie:**

Prof. dr. M. Dogterom

Prof. dr. E.M. Hol

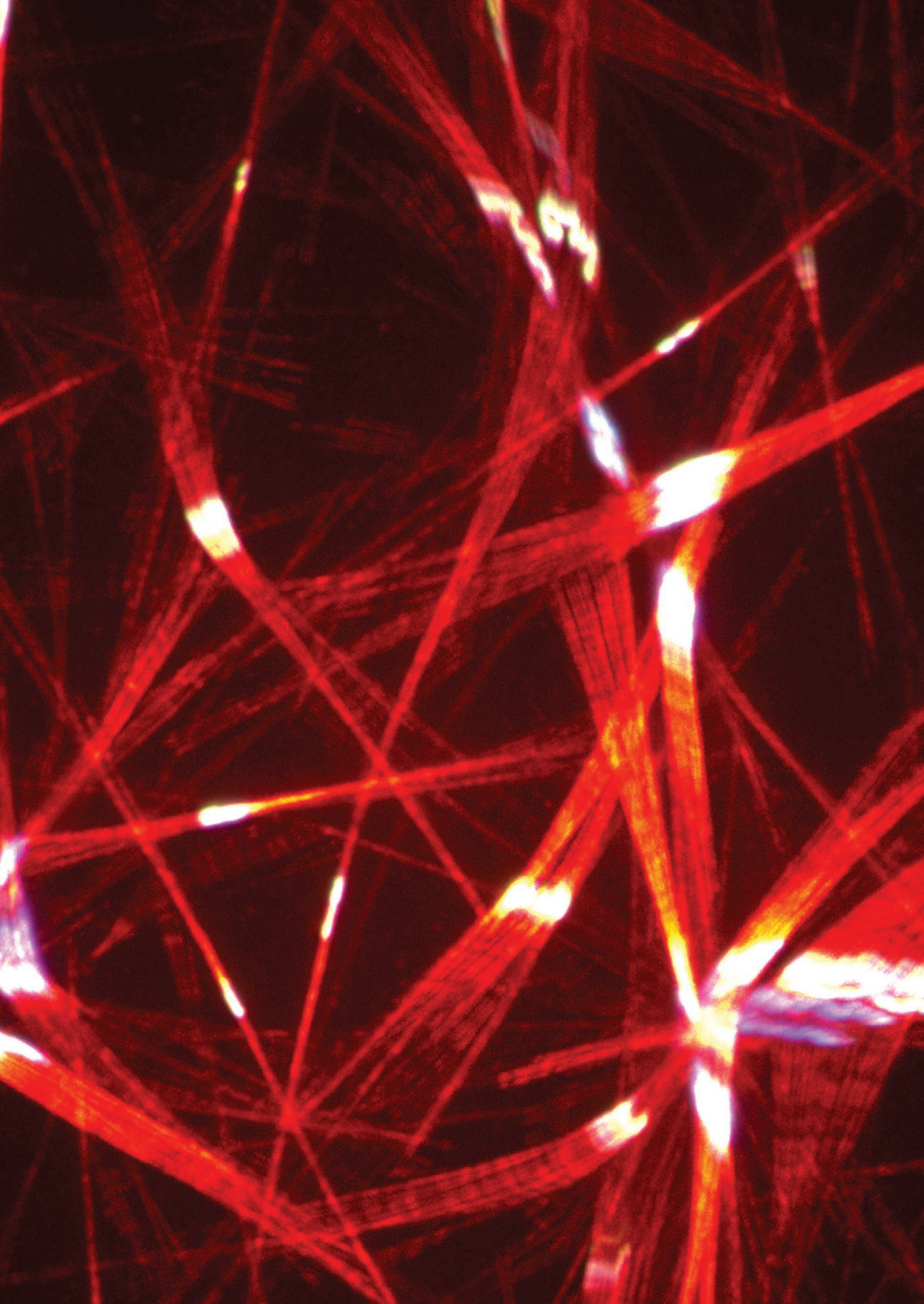
Prof. dr. S.M.A. Lens

Prof. dr. S.J.L. van den Heuvel

Prof. dr. F.G. Förster

# Table of Contents

|   |     |
|---|-----|
| <b><u>Chapter 1</u></b>   | 5   |
| General Introduction  |     |
| <b><u>Chapter 2</u></b>   | 53  |
| CAMSAP-driven microtubule release from $\gamma$ -TuRC and its regulation<br>by nucleation-promoting factors                 |     |
| <b><u>Chapter 3</u></b>   | 97  |
| Feedback-driven assembly of the axon initial segment  |     |
| <b><u>Chapter 4</u></b>   | 155 |
| CLASP mediates microtubule repair by restricting lattice damage<br>and regulating tubulin incorporation                     |     |
| <b><u>Chapter 5</u></b>   | 191 |
| In vitro reconstitution of the interplay between CAMSAPs, katanin and WDR47<br>in regulating microtubule minus-end dynamics |     |
| <b><u>Chapter 6</u></b>   | 225 |
| General Discussion  |     |
| <b>Addendum</b>   |     |
| <u>Summary</u>  | 256 |
| <u>Nederlandse samenvatting</u>   | 258 |
| <u>Curriculum Vitae</u>   | 260 |
| <u>List of publications</u>   | 261 |
| <u>Acknowledgments</u>  | 262 |





# 1

## General Introduction

Dipti Rai

Microtubules are one of the three major cytoskeletal components. They are ~25 nm-wide tubes built of protein subunits. They are essential for controlling cell shape, cell polarity, organelle positioning, intracellular transport, cell division and cell migration. The density and organization of microtubule filaments in cells control different aspects of cell mechanics. In this chapter, we will discuss the dynamic life of microtubules and the factors that regulate it. We will cover topics ranging from microtubule birth, growth, stabilization or damage and destruction to repair and amplification.

### **Saga in short**

Microtubules are long, but dynamic polymers that are composed of tubulin heterodimers, which consist of alpha- and beta-tubulin subunits.  $\alpha\beta$ -tubulin dimers associate longitudinally in a head-to-tail fashion to form protofilaments, which associate laterally to assemble the canonical 13-protofilament hollow and cylindrical microtubules (Chaaban and Brouhard, 2017). In the neighboring protofilaments, the lateral contacts are typically formed between  $\alpha$ - $\alpha$  and  $\beta$ - $\beta$  tubulins (B-lattice configuration), except at the microtubule seam, where heterotypic  $\alpha$ - $\beta$  and  $\beta$ - $\alpha$  interactions occur (A-lattice configuration) (Kikkawa et al., 1994; McIntosh et al., 2009). Thus, in a typical microtubule would be a three-start helix of tubulin subunits in a B-lattice configuration with one single seam. However, heterogeneity in protofilament number and lattice configuration can also be observed in cells (Chaaban and Brouhard, 2017; Atherton et al., 2018; Guyomar et al., 2022).

Independent of protofilament number or lattice configuration, the addition of GTP-bound tubulin dimers is faster at the  $\beta$ -tubulin side and slower at the  $\alpha$ -tubulin side, generating a rapidly growing plus end and a slow growing minus end (**Fig. 1**) (Desai and Mitchison, 1997). Therefore, microtubules are intrinsically polar. Once the longitudinal contacts are formed between the curved GTP-tubulin dimer and the terminal  $\beta$ -tubulin at the plus end, the lateral contacts are also established with the dimers of the neighboring protofilaments (Brouhard and Rice, 2018). This leads to the straightening of the dimer in the protofilament and gives rise to a strained conformation. The GTP molecule bound to the exchangeable site (E-site) of  $\beta$ -tubulin, but not the non-exchangeable GTP bound to  $\alpha$ -tubulin, undergoes hydrolysis when the incoming  $\alpha$ -tubulin contacts the E-site GTP of the terminal  $\beta$ -tubulin and completes the GTP pocket (Nogales et al., 1999). This hydrolysis occurs with a delay after incorporation, thereby producing a stable GTP-cap and a GDP-lattice, if the rate of tubulin addition outcompetes the hydrolysis rate (Brouhard, 2015). However, due to the stochastic binding of new tubulin dimers and GTP hydrolysis to GDP, a microtubule can lose its GTP-cap. The loss of GTP-cap exposes

the unstable GDP-lattice, causing the release of tubulin dimers, and the microtubule undergoes rapid depolymerization. Microtubules can also spontaneously switch from the shrinking state to a growing state. Therefore, growing microtubule ends are very dynamic and can quickly alternate between phases of growth and shrinkage, a behavior known as dynamic instability (**Fig. 1**) (Mitchison and Kirschner, 1984; Brouhard, 2015). Many structural studies have given insights into the mechanism of this behavior by linking the nucleotide state of tubulin dimers to the strength of lateral and longitudinal contacts. It has been shown that GTP-hydrolysis leads to a compaction along the longitudinal interface between the dimers by inducing a conformational change in  $\alpha$ -tubulin that makes the microtubule lattice less stable (Zhang et al., 2018; Manka and Moores, 2018). This conformational change caused by the uneven compression of  $\alpha$ -tubulin strengthens the longitudinal contacts, but weakens the lateral contacts to a level that they cannot withstand the strain stored in the straightened tubulin dimers (Manka and Moores, 2018; Richard McIntosh et al., 2018; Brouhard and Rice, 2018; Gudimchuk et al., 2020). This leads to the peeling of protofilaments owing to the intrinsic curvature of the GTP- and GDP-tubulin dimers.

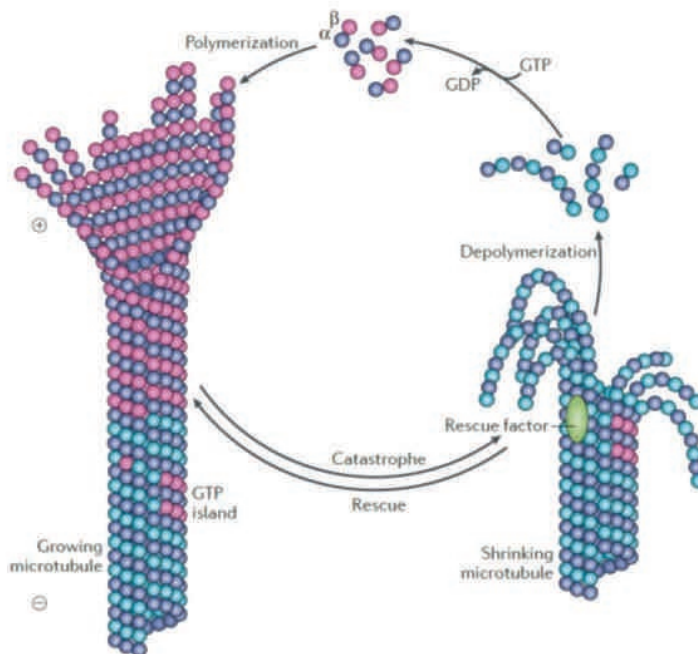


**Figure 1. Microtubule dynamic instability.** Reproduced from Akhmanova and Steinmetz, 2015, *Nature Reviews Molecular Cell Biology*.

In vitro, microtubule minus ends are more stable and switch between growth and shrinkage less frequently than the plus ends, while in cells, the minus ends are usually anchored to microtubule-organizing centers (MTOCs) or, if free, grow very slowly and persistently (Erickson and O'Brien, 1992; Dammermann et al., 2003; Sanchez and Feldman, 2017; Wu and Akhmanova, 2017a; Akhmanova and Steinmetz, 2019; Vineethakumari and Lüders, 2022). At the MTOCs, namely the centrosome, the Golgi apparatus, cell cortex, nucleus etc., microtubules are nucleated *de novo* from a nucleation template called  $\gamma$ -tubulin ring complex ( $\gamma$ -TuRC), which caps the minus ends (Wiese and Zheng, 2000; Kollman et al., 2011; Teixidó-Travesa et al., 2012). Microtubules can also be generated by cutting of pre-existing microtubules by severing enzymes (AAA-type ATPases) and subsequent stabilization of their minus ends by factors like Calmodulin-regulated spectrin-associated proteins (CAMSAPs), or their counterpart in invertebrates, Patronin (Keating et al., 1997; Abal et al., 2002; Hendershott and Vale, 2014; Jiang et al., 2014; Dong et al., 2017; Gillard et al., 2021; Kuo and Howard, 2021). Depending upon the cell type and cellular context, these free microtubules can be recruited to different MTOCs by anchoring of their minus ends via numerous microtubule and  $\gamma$ -TuRC tethering factors (Teixidó-Travesa et al., 2012; Vineethakumari and Lüders, 2022; Akhmanova and Kapitein, 2022).

Contrary to the minus ends, microtubule plus ends are very dynamic and can quickly switch between phases of growth and shrinkage (Horio and Hotani, 1986; Walker et al., 1988; Erickson and O'Brien, 1992). The transition from growth to shrinkage, termed catastrophe, or from shrinkage to growth, termed rescue, is stochastic, but can be highly regulated by microtubule associated proteins (MAPs), tubulin concentration and post-translational modifications (PTMs) (Verhey and Gaertig, 2007; Akhmanova and Steinmetz, 2015; Goodson and Jonasson; Janke and Magiera, 2020). These factors cooperate at microtubule plus ends to produce most of the polymer mass. The dynamic instability of microtubules is essential for many processes- generating microtubule arrays with different geometry and density to control the positioning of cellular structures and maintain cell architecture, complete remodeling of microtubule network during cell polarization, cell migration, making neuronal protrusions and chromosome separation during cell division. All these processes involve rapid alteration between microtubule growth and shrinkage. Therefore, dynamic instability is tightly regulated by MAPs.

Microtubule regulatory proteins can stabilize or destabilize both microtubule ends as well as microtubule lattice (Akhmanova and Steinmetz, 2015; Goodson and Jonasson, 2018; Akhmanova and Kapitein, 2022). Moreover, they can also crosslink microtubules to form

microtubule bundles, and in this way provide extra stability to generate long-lived microtubules and dense microtubule networks. Microtubule bundles are necessary for efficient motor protein-based long-range cargo transport in neurons, establishment and maintenance of bipolar mitotic spindle for proper chromosome segregation in dividing cells and assembly of perinuclear microtubule bundles required for Golgi ribbon formation (Bieling et al., 2010b; Subramanian et al., 2010; Sato et al., 2014; Satake et al., 2017; Fréal et al., 2019; Harterink et al., 2019).

Another interesting mechanism to stabilize microtubule shafts and generate long-lived microtubule segments is tubulin exchange along the microtubule lattice (Théry and Blanchoin, 2021). In recent years, increasing evidence has established that the tubulin turnover not only occurs at the growing ends, but can also take place along the GDP-lattice at “specific sites”. These sites have been associated with microtubule rescues due to their GTP-content and proposed to be the sites of lattice defects and damages (Dimitrov et al., 2008b; Schaedel et al., 2015; Aumeier et al., 2016). Microtubule lattice defects occur in vitro as well as in cells and can arise due to the structural heterogeneity within an individual microtubule. This heterogeneity can be caused by a change in the protofilament or helix start number, as well as by occurrence of multiple seams and transitions between microtubule lattice configurations (Chretien et al., 1992; Atherton et al., 2018; Schaedel et al., 2019; Guyomar et al., 2022). Structural work identified these sites as “gaps” or “holes” along the microtubule lattice with missing tubulin dimers. Furthermore, lattice damages can be induced by microtubule crossings or bending, mechanical stress, compressive forces, microtubule stabilizing agents (MSAs), stepping of molecular motors or activity of microtubule severing enzymes (Schaedel et al., 2015; Aumeier et al., 2016; Vemu et al., 2018; Rai et al., 2019, 2021; Triclin et al., 2021; Théry and Blanchoin, 2021; Budaitis et al., 2022). Strikingly, these damaged sites undergo self-repair by incorporation of free tubulin dimers and serve as microtubule rescue sites that would generate stable and long-lived microtubule segments (Schaedel et al., 2015; Aumeier et al., 2016; Schaedel et al., 2019; Budaitis et al., 2022; Andreu-Carbó et al., 2022). Several MAPs have been shown to promote repair of damaged microtubule lattices by facilitating tubulin exchange at the defect sites, restricting lattice damage, promoting and/or stabilizing tubulin incorporation (Aher et al., 2020; Vemu et al., 2018; Lawrence et al., 2021; Berg et al., 2022). Although the extent of damage and repair controls whether the lattice will be fully repaired or fragmented, the outcome is highly dependent on the local tubulin concentration and microtubule growth regimes (Triclin et al., 2021; Kuo and Howard, 2021; Budaitis et al., 2022). Microtubule severases can create nanoscale damages, which upon incorporation of new tubulin

dimers would serve as rescue sites after repair (Vemu et al., 2018). If the damage is too big or cannot be repaired, it could lead to microtubule breakage creating fragments. If the microtubule fragments are stabilized by MAPs, this would lead to microtubule amplification, but if the fragments are destabilized, this would induce microtubule destruction (Kuo and Howard, 2021). Excessive walking of molecular motors or excessive activity of microtubule severing enzymes, instead of repair and amplification, can lead to destruction of microtubules (McNally and Vale, 1993; Zhang et al., 2007; Triclin et al., 2021; Budaitis et al., 2022; Lawrence et al., 2021; Kuo and Howard, 2021).

Below, we will discuss this saga of dynamic life of microtubules in more detail.

### **Microtubule organization and MTOCs**

The organization of microtubules in cells is key to any of its cellular function. The organization varies drastically in different cell types and cell cycle stages and highly depends on the localization of microtubule nucleation sites and anchoring factors (Muroyama and Lechler, 2017; Sanchez and Feldman, 2017; Tovey and Conduit, 2018; Burute and Kapitein, 2019; Akhmanova and Kapitein, 2022). Centrosomes have been established as a major MTOC in various cell types. However, depending on the cellular context, the Golgi complex, nuclear envelope, cell cortex, mitochondria and/or pre-existing microtubules can take over as the major MTOC (s) (**Fig. 2**). While cycling animal cells mainly depend on their radial centrosomal microtubule arrays, fungi, such as *S. pombe*, differentiated plant and animal cells or mitotic spindles have been shown to rely on the non-centrosomal arrays that can be organized as asters, linear bundles or two-dimensional sheets (Bartolini and Gundersen, 2006). In each case, microtubule minus ends are mainly anchored at an MTOC, whereas plus end grow distally either freely or become tethered to, for example, the cell cortex (Martin and Akhmanova, 2018; Akhmanova and Steinmetz, 2019; Akhmanova and Kapitein, 2022).

Whereas centrosomal microtubules are mainly nucleated *de novo* from the microtubule nucleator  $\gamma$ -TuRC, non-centrosomal microtubules can be generated and organized via different mechanisms, such as, microtubule nucleation at non-centrosomal sites, microtubule severing or breakage, microtubule anchoring by recruitment factors or cytoplasmic assembly (Keating and Borisy, 1999; Kollman et al., 2011; Teixidó-Travesa et al., 2012; Liu et al., 2021; Vineethakumari and Lüders, 2022). Since a pool of common nucleation factors like  $\gamma$ -TuRC, chTOG/XMAP215/Stu2, CDK5RAP2, CLASPs, etc., overlap between different MTOCs, microtubule nucleation can also occur *de novo* at non-centrosomal sites (Wu and Akhmanova, 2017b; Roostalu and Surrey, 2017; Tovey and Conduit, 2018). Moreover, live cell studies

together with *in vitro* reconstitutions have shown how concerted action of TPX2, augmin and  $\gamma$ -TuRC nucleates branched microtubules from pre-existing microtubules in the mitotic spindle (Goshima et al., 2008; Verma and Maresca, 2019; Thawani et al., 2019; Alfaro-Aco et al., 2020; Tariq et al., 2020).

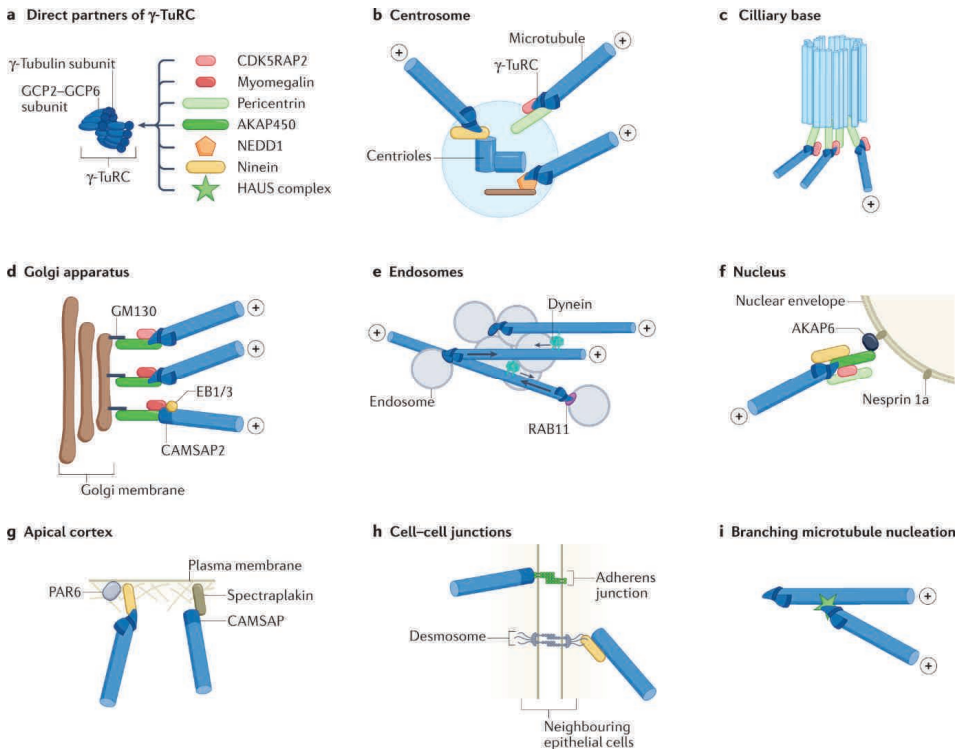


**Figure 2. Microtubule organizing centers (MTOCs).** Reproduced from Akhmanova and Kapitein, 2022, *Nature Reviews Molecular Cell Biology*.

Alternatively, microtubules can also be detached from the centrosome by severing enzymes and then recruited to other MTOCs to generate non-centrosomal arrays with the help of motor proteins or stabilizing and recruitment factors (Keating et al., 1997; Ahmad et al., 1999; Abal et al., 2002; Hendershott and Vale, 2014; Jiang et al., 2014; Dong et al., 2017; Gillard et al., 2021; Kuo and Howard, 2021; Vineethakumari and Lüders, 2022). For example, in DLD1 epithelial cells, microtubules upon severing by katanin and release from centrosome are stabilized by minus-end stabilizing protein, CAMSAP3, and get recruited to the apical membrane (Dong et al., 2017). This results into complete remodeling of the centrosomal

microtubule network into an apico-basally polarized array upon the establishment of cell-cell junctions. CAMSAPs have also been shown to stabilize non-centrosomal microtubules in an intestinal epithelial cell model, Caco2 cells (Tanaka et al., 2012). In fly placodal cells, katanin and Patronin has been shown to cooperate for microtubule release and anchoring to generate longitudinal non-centrosomal arrays that are important for apical constriction and epithelial tube formation (Gillard et al., 2021). Furthermore, in neurons, developing axons lack a clear single MTOC, therefore, they employ both microtubule-dependent microtubule nucleation and microtubule severing by katanin and spastin to generate the typical densely arranged parallel plus-end-out microtubule bundles (Conde and Cáceres, 2009; Leterrier, 2018). In rat sympathetic neurons, cytoplasmic dynein has been shown to contribute to the transport of microtubules into the axon upon their release from the centrosome to produce non-centrosomal microtubules (Ahmad et al., 1999).

### Microtubule nucleation

Independent of where the nucleation sites are distributed,  $\gamma$ -TuRC has been established as the major microtubule nucleating factor in cells (Kollman et al., 2011; Teixidó-Travesa et al., 2012; Oakley et al., 2015; Tovey and Conduit, 2018; Liu et al., 2021; Thawani and Petry, 2021; Zupa et al., 2021). Purified  $\gamma$ -TuRC has been shown to nucleate microtubules from soluble tubulin dimers in vitro (Zheng et al., 1995; Oegema et al., 1999). In vitro studies and structural work have further shown that  $\gamma$ -TuRC also acts as a cap for the minus-ends of microtubules (**Fig. 3**) (Wiese and Zheng, 2000; Würtz et al., 2021). This explains why minus ends usually do not grow in cells.

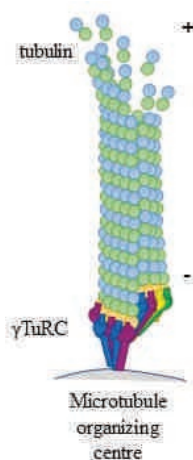


**Figure 3. Microtubule nucleation and minus-end capping by  $\gamma$ -TuRC.**



While microtubule nucleation can occur spontaneously *in vitro* in solutions of pure tubulin, in order to form oligomers, tubulin dimers must overcome a high energy barrier (Roostalu and Surrey, 2017). Initially, small tubulin intermediates are assembled, and their disassembly is energetically favored over assembly, owing to the GTP-hydrolysis, resulting in very slow initial growth (Rice et al., 2008). Once oligomers of sufficient size form, microtubule growth crosses the energy barrier for nucleation and elongation is initiated. Therefore, in cells, microtubules are mainly nucleated from a template. In line with this view, it was shown that  $\gamma$ -TuRC nucleates microtubule more efficiently than spontaneous microtubule nucleation (Thawani et al., 2020). While nucleation of a microtubule from  $\gamma$ -TuRC requires 4 tubulin dimers, the critical nucleus size for spontaneous microtubule assembly is 8 tubulin dimers. However, nucleation was even more efficient from stabilized microtubule seeds, where only a single dimer is sufficient to initiate microtubule elongation. This also explains why the critical tubulin concentration for microtubule nucleation is 15  $\mu\text{M}$  for spontaneous nucleation, 7.5  $\mu\text{M}$  for  $\gamma$ -TuRC-dependent nucleation and 2  $\mu\text{M}$  for templated nucleation from preassembled microtubules (Roostalu and Surrey, 2017; Consolati et al., 2020).

#### *Gamma-tubulin ring complex ( $\gamma$ -TuRC)*

$\gamma$ -TuRC is a ~2.2 MDa macromolecular assembly that is composed of seven 300 kDa  $\gamma$ -tubulin small complexes ( $\gamma$ -TuSCs) (Kollman et al., 2011).  $\gamma$ -TuSC is a Y-shaped subcomplex, composed of 2  $\gamma$ -tubulin subunits, each bound to a gamma-tubulin complex protein (GCP), namely GCP2 and GCP3, forming a heterotetramer. In budding yeast, seven of these  $\gamma$ -TuSCs arrange in a helical manner to assemble a complete  $\gamma$ -TuRC ring that partly resembles a microtubule geometry, albeit with a mismatch compared to microtubule helical pitch and diameter (Kollman et al., 2015). This arrangement presents 14  $\gamma$ -tubulins exposed at the surface to allow binding of 14  $\alpha\beta$ -tubulin dimers via  $\alpha$ -tubulin and  $\gamma$ -tubulin interactions.  $\gamma$ -tubulin, GCP2 and GCP3 are conserved in all eukaryotes, while fission yeast and higher organisms have also evolved additional GCP proteins, namely GCP4, GCP5 and GCP6, which replace some of the GCP2/3 subunits within  $\gamma$ -TuRC (Tovey and Conduit, 2018). These additional GCPs show structural similarity to GCP2/3. They all have a conserved gamma ring protein 1 (GRIP1) domain at N-terminus and a GRIP2 domain at C-terminus. Through GRIP1 domains, GCPs associate with each other, while GRIP2 is required to bind  $\gamma$ -tubulin (Kollman et al., 2011; Tovey and Conduit, 2018). GCP6 specifically has been shown to contain N-terminal

sequence extensions and insertions between GRIP1 and GRIP2 domains, and their role has been recently described (see Discussion).

Recent structural work has provided beautiful insights into the structure, composition and stoichiometry of the native *Xenopus* and native and recombinant human  $\gamma$ -TuRCs (Liu et al., 2019; Wieczorek et al., 2020b; Consolati et al., 2020; Zimmermann et al., 2020; Wieczorek et al., 2020a, 2021; Würtz et al., 2021, 2022). All these high resolution ( $\sim 4$  Å) cryo-EM reconstructions clearly depicted a 30 nm wide and 20 nm high 14-spoke left-handed helical arrangement of GCP- $\gamma$ -tubulin subunits, which, similar to the yeast  $\gamma$ -TuRC, partly matched microtubule geometry. The ring was composed of 5  $\gamma$ -TuSC units and 2  $\gamma$ -TuSC-like units, where GCP2 was replaced with GCP4 and GCP3 was replaced with GCP5 or GCP6 (Fig. 4).

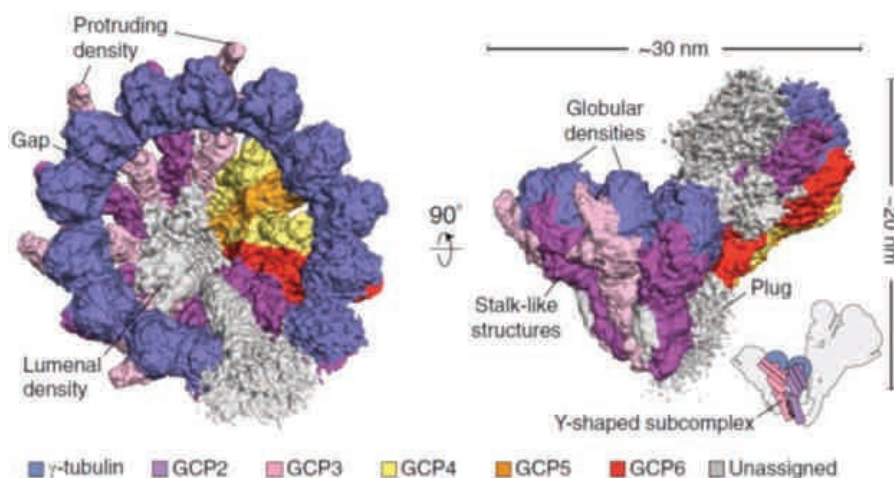


**Figure 4. Cryo-EM reconstructions of purified human  $\gamma$ -TuRC.** Reproduced from Wieczorek et al., 2020, *Cell*.

However, one striking feature of these cryo-EM density maps was the asymmetry in the ring (Fig. 5a). While one half of the ring composed of  $\gamma$ -TuSC core showed a more compact interface that matched microtubule geometry, the other half composed of GCP4/5/6 and a terminal  $\gamma$ -TuSC showed a loose and more variable interface that deviated from the microtubule geometry (Fig. 5b). It was proposed that due to this asymmetry, purified  $\gamma$ -TuRCs are mainly inactive and have very low nucleation efficiency (only  $< 1\%$   $\gamma$ -TuRCs could nucleate a microtubule) and, therefore, they require an activator (Brilot et al., 2021). In line with this idea, an activation mechanism has been previously shown for yeast  $\gamma$ -TuRC that leads to the ring

closure to ultimately match microtubule geometry, and therefore, enhanced microtubule nucleation (Kollman et al., 2015).

Nevertheless, these recent cryo-EM density maps, discussed above, shed further insights into the other core components of  $\gamma$ -TuRC. In all these structures, a monomeric actin was discovered as a part of a luminal bridge at the base of the ring, which connects the symmetric half of the ring to the asymmetric half. Whereas two copies of Mozart1 was found to be part of the luminal bridge in association with N-terminal  $\alpha$ -helical domains of GCP3 or GCP6 (GCP-NHDs), one Mozart2 and GCP2-NHD module was identified at the overlap region between first and terminal  $\gamma$ -TuSC (Wieczorek et al., 2020a). Interestingly, partial  $\gamma$ -TuRCs containing 4-5  $\gamma$ -TuSCs lacking the luminal bridge could also nucleate microtubules with the same efficiency as full  $\gamma$ -TuRCs (Wieczorek et al., 2021; Consolati et al., 2020; Thawani et al., 2020). Therefore, the luminal bridge likely has a regulatory role in cells in cooperation with other factors. A role has been proposed for the monomeric actin in determining the  $\gamma$ -TuRC geometry, but not assembly or structural integrity, via its interaction with two N-terminal helices of GCP6 (Würtz et al., 2022). Actin incorporation was shown to be required for efficient microtubule nucleation. Furthermore, this study also delineated the stepwise assembly of  $\gamma$ -TuRC, which requires expansion of the GCP6-stabilized subcomplex, consisting of GCP2-3-4-5-4-6, by stepwise incorporation of four pre-formed  $\gamma$ -TuSC. The formation of luminal bridge allows incorporation of the terminal  $\gamma$ -TuSC. The stable core of GCP4-5-4-6 was found to exist as a salt-resistant subcomplex which can be observed during  $\gamma$ -TuRC purification (Haren et al., 2020).

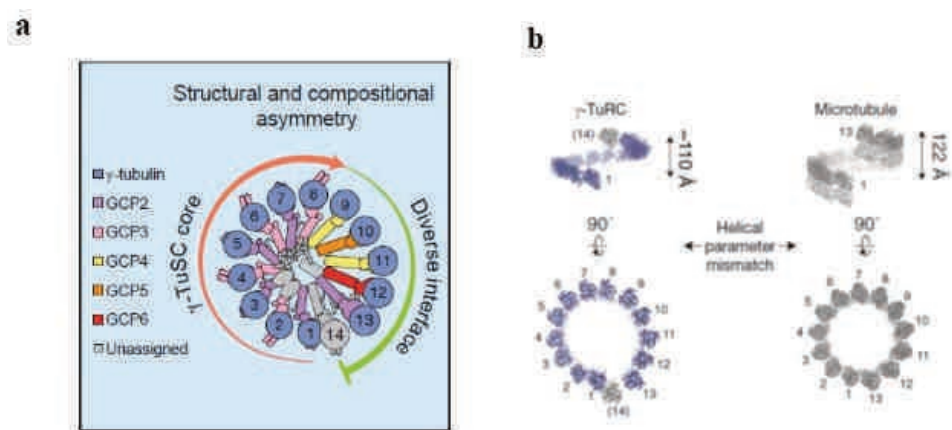


**Figure 5. Structural asymmetry in  $\gamma$ -TuRC and a mismatch with microtubule geometry.**

Reproduced from Wieczorek et al., 2020, *Cell*.

**Microtubule Associated Proteins (MAPs)**

Whereas microtubule minus ends remain capped by  $\gamma$ -TuRC after nucleation, the plus ends continue to grow and shrink, producing most of the polymer mass in cells. Regulation of the microtubule polymer is crucial to generate an organized microtubule array according to the cellular needs. Many microtubule- and  $\gamma$ -TuRC associated-proteins that control the dynamicity of the microtubule network have been discovered so far (Gupta et al., 2014; Akhmanova and Steinmetz, 2015; Goodson and Jonasson, 2018; Tovey and Conduit, 2018; Thawani and Petry, 2021). MAPs that directly regulate microtubules can be classified into several categories depending on their site and mode of action: microtubule plus-end tracking proteins (+TIPs) (Akhmanova and Steinmetz, 2015), microtubule minus-end targeting proteins (-TIPs) (Akhmanova and Steinmetz, 2019); motile MAPs, such as molecular motor proteins (Reck-Peterson et al., 2018; Hirokawa et al., 2009); microtubule nucleators (Liu et al., 2021); microtubule severing enzymes (Kuo and Howard, 2021); structural MAPs that bind to microtubule lattice, such as tau, MAP2, MAP4, and microtubule bundling proteins like TRIM46 and PRC1 (Walczak and Shaw, 2010; Bodakuntla et al., 2019). +TIPs have been subcategorized further according to their microtubule interacting domains and include proteins such as end-binding proteins (EBs), cytoplasmic linker proteins (CLIPs), CLIP-associated proteins (CLASPs), microtubule assembly protein 215 kDa (XMAP215), microtubule-actin crosslinking factor (MACF) (Akhmanova and Steinmetz, 2010). Several MAPs will be discussed in more detail in the sections below.

**Microtubule nucleation factors**

Numerous factors that promote microtubule nucleation have been identified, such as CDK5RAP2, XMAP215/chTOG, CLASPs, TPX2 (Liu et al., 2021; Thawani and Petry, 2021). However, their mechanisms of action might differ. They can either regulate the activity of  $\gamma$ -TuRC or the microtubule assembly itself by facilitating tubulin polymerization. In human colon cancer cells, CLASP1, chTOG and CAMSAPs have been shown to generate microtubules in a  $\gamma$ -TuRC-independent manner during interphase (Tsuchiya and Goshima, 2021). Therefore, a few of these interesting candidates are discussed here.

*CDK5RAP2*

The centrosomal scaffold protein CDK5RAP2 (CDK5 regulatory subunit-associated protein 2), also known as CEP215, is a human microcephaly associated pericentriolar material (PCM) protein that is involved in the recruitment of  $\gamma$ -TuRC to centrosomes and Golgi membranes (Bond et al., 2005; Fong et al., 2008; Wu et al., 2016). Its *D. melanogaster* homolog, centrosomin, or yeast Spc110/Mto1/Mto2, or *C. elegans* SPD5, all have been shown to stimulate microtubule nucleation from  $\gamma$ -TuRC (Choi et al., 2010; Woodruff et al., 2017; Tovey et al., 2021; Brilot et al., 2021; Rale et al., 2022). They all consist of a conserved centrosomin motif 1 (CM1) domain at the N-terminus, which binds to  $\gamma$ -TuRC, and another conserved motif, CM2, at the C-terminus, which localizes the protein to the centrosome or the Golgi complex by binding to its interacting partners like pericentrin or AKAP9 (also known as AKAP450) (**Fig. 6**) (Choi et al., 2010; Wang et al., 2010; Wu and Akhmanova, 2017b; Watanabe et al., 2020; Tovey et al., 2021). A minimal domain of CDK5RAP2/centrosomin containing just the CM1 region, referred as  $\gamma$ -TuRC nucleation activator ( $\gamma$ -TuNA), was sufficient to stimulate microtubule nucleation from  $\gamma$ -TuRC, both in vivo and in vitro (Choi et al., 2010; Tovey et al., 2021; Rale et al., 2022). Recently, structural work has shown that a  $\gamma$ -TuNA dimer forms a coiled-coil and binds to the MZT2/GCP2-NHD module at position 13 and docks on the outer surface of  $\gamma$ -TuRC, similar to its yeast counterpart (Brilot et al., 2021; Wieczorek et al., 2020a).

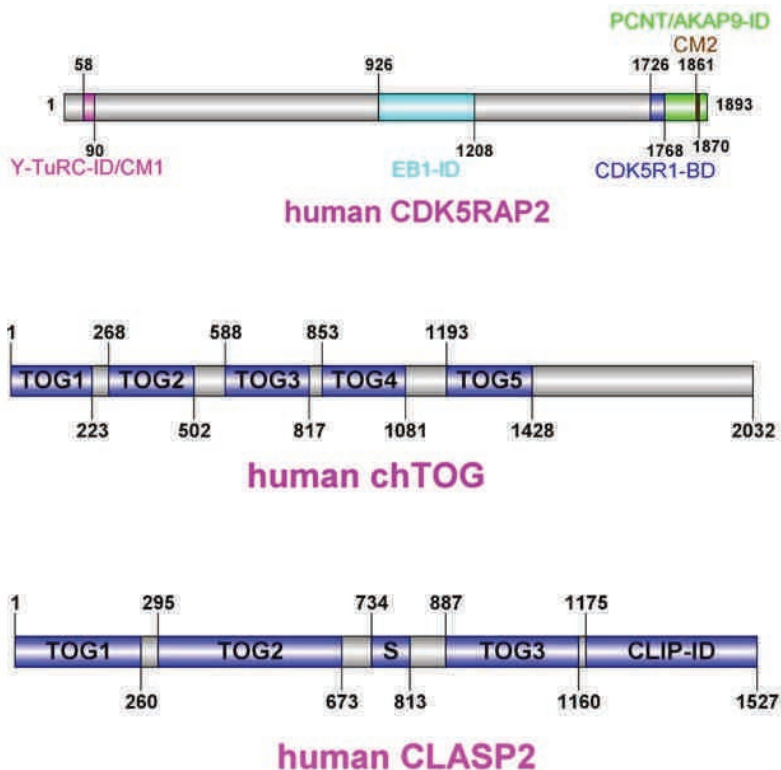


**Figure 6. Domain organization of human CDK5RAP2, chTOG and CLASP2.**

#### *chTOG/XMAP215/Stu2*

chTOG (colonic and hepatic tumour overexpressed gene) or its *Xenopus* homolog XMAP215 or *Drosophila* MiniSpindles (MSPS) or the yeast homolog Stu2 are well characterized microtubule polymerases that promote microtubule assembly by catalyzing tubulin addition to the plus end and increasing microtubule plus-end growth rate by several fold, both in vitro and in vivo (Brouhard et al., 2008; Al-Bassam and Chang, 2011). The human, *Xenopus* and fly orthologs consist of five copies of canonical TOG-domains at the N-terminus, each of which can bind to soluble  $\alpha\beta$ -tubulin dimers, and a C-terminal microtubule-binding domain (**Fig. 6**) (Al-Bassam and Chang, 2011). TOG-domains are paddle-like structures containing six HEAT-repeats composed of  $\alpha$ -helices separated by loops that recognize the curved tubulin dimers in solution (Al-Bassam et al., 2007). Therefore, all these orthologs can bind to tubulin dimers and microtubule plus ends simultaneously and can promote rapid incorporation of tubulin dimers

into the microtubule lattice. XMAP215 has been shown to have a synergistic effect with EBs, and together, they can accelerate the microtubule growth rate in vitro to match the microtubule growth rates observed in cells (Zanic et al., 2013). XMAP215 also functions synergistically with  $\gamma$ -TuRC in *Xenopus* egg extracts to stimulate microtubule nucleation (Thawani et al., 2018). Similarly, human chTOG has been shown to cooperate with TPX2, an importin binding protein that stabilizes growing plus ends by suppressing catastrophes, for efficient microtubule nucleation in vitro (Roostalu et al., 2015). chTOG also increases microtubule nucleation efficiency of  $\gamma$ -TuRC (Consolati et al., 2020). Interestingly, chTOG also increases catastrophe frequency by causing growth rate fluctuations and tapering of the plus ends (Farmer et al., 2021).

### CLASPs

CLASPs are well-studied regulators of microtubule dynamics and organization in cells during interphase as well as in mitosis (Lawrence et al., 2020). They had been discovered as binding partners of CLIP-115 and CLIP-170 (Akhmanova et al., 2001). CLIP-170, the first described member of the +TIP group of proteins, contains CAP-Gly domains that can bind EBs and the C-terminal tails of  $\alpha$ -tubulin, and these two interactions mediate its ability to track growing microtubule ends (Pierre et al., 1992a; Perez et al., 1999; Dixit et al., 2009). CLASPs are highly conserved from yeast to mammals and localize to the microtubule plus ends by binding to CLIPs or EBs through their CLIP-interacting domain and SxIP motifs, respectively (**Fig. 6**, depicted as “S” and “CLIP-ID” domain in human CLASP2) (Akhmanova et al., 2001; Mimori-Kiyosue et al., 2005; Honnappa et al., 2009). Depletion of both mammalian CLASP paralogs, CLASP1 and CLASP2, or the single *Drosophila* ortholog, MAST/Orbit, results in a strong reduction in microtubule density in cells during interphase and also leads to mitotic defects and aberrant chromosome segregation (Mimori-Kiyosue et al., 2005; Maiato et al., 2002, 2003, 2005; Pereira et al., 2006). Moreover, CLASPs are also involved in microtubule nucleation and stabilization at the Golgi apparatus, where they get recruited by binding to GCC185 (Efimov et al., 2007; Miller et al., 2009). Additionally, CLASP2 also promotes microtubule outgrowth from stabilized microtubule seeds (Aher et al., 2018). CLASP2 was also recently shown to stabilize kinetochore-microtubule attachments and promote poleward spindle flux during metaphase (Girão et al., 2019). Furthermore, CLASPs are also required for the attachment of microtubule plus ends to the cell cortex by binding to LL5 $\beta$  and ELKS (Lansbergen et al., 2006). Structurally, CLASPs, similarly to chTOG/XMAP215, contain TOG-like domains (**Fig. 6**), which however function differently from the canonical TOG-domains of microtubule

polymerases. Human CLASPs contain 3 TOG-like domains, TOG1, TOG2 and TOG3. Crystal structures and biochemical assays with human TOG1 and TOG2 and mouse TOG3 domains suggest that they are deficient in tubulin binding, however, TOG2 and TOG3 can bind to the distinct curved protofilament structures at the microtubule plus ends (Leano et al., 2013; Grimaldi et al., 2014; Aher et al., 2018; Leano and Id, 2019). While TOG1 domain has an auto-inhibitory role, the TOG2 domain is sufficient to completely suppress microtubule catastrophes and TOG3 domain is a potent rescue factor (Aher et al., 2018; Lawrence et al., 2018). Stu1 and Cls1p, the budding yeast and fission yeast CLASP orthologs, also promoted rescues and suppressed catastrophes (Majumdar et al., 2018; Al-Bassam et al., 2010).

### **Microtubule plus-end regulation**

MAPs have been also extensively studied for their regulation of microtubule dynamics at the plus ends. The best studied +TIPs are EBs. This family of proteins tracks the growing ends autonomously by dynamically recognizing the GTP-cap, an extended region at growing microtubule ends (Bieling et al., 2008; Komarova et al., 2009; Maurer et al., 2012; Zhang et al., 2015; Roth et al., 2019; Roostalu et al., 2020). Upon binding, they can also induce lattice compaction (Zhang et al., 2018), thereby regulating the microtubule conformation at the plus ends. EB proteins contain a highly conserved calponin homology (CH) domain at the N-terminus, which is responsible for microtubule binding and is sufficient for plus-end tracking (Komarova et al., 2009; Skube et al., 2010). EBs also contain a unique EB homology (EBH) domain and an acidic tail encompassing a C-terminal EEY/F motif, that is also found in CLIP-170. EBs recruit an array of +TIPs to microtubule ends using these two domains (Komarova et al., 2005; Miller et al., 2006; Weisbrich et al., 2007).

Another +TIP, CLIP-170 can dynamically track plus ends, by binding to EBs, and promote microtubule rescue and growth, both in cells and in vitro (Pierre et al., 1992b; Perez et al., 1999; Arnal et al., 2004; Bieling et al., 2008; Komarova et al., 2002). CLIP-170 can also self-associate or associate with other +TIPs, specifically EBs, to build a +TIP network that can phase separate to form condensates and regulate microtubule dynamics (Gupta et al., 2014; Wu et al., 2021; Miesch et al., 2022). These liquid droplets can then recruit other +TIPs and condensate tubulin to promote microtubule growth by constraining structural fluctuations at the growing tips, and therefore, act as a polymerization chaperone.

Another interesting class of +TIPs that regulate microtubule plus-end dynamics are motor proteins, especially the members of kinesin-superfamily, as they are mostly plus-end directed motors (Endow et al., 2010; Wang et al., 2015b; Akhmanova and Steinmetz, 2015). They can



either stabilize or destabilize microtubule plus ends. One such interesting candidate is kinesin-5, also known as Eg5 or KIF11, which is essential for bipolar spindle assembly and regulation of spindle elongation (Saunders et al., 2007; Brust-Mascher et al., 2009; She et al., 2020; Pandey et al., 2021). It is a homotetrameric motor protein that can crosslink microtubules and slide them against each other by walking in both directions (Kapitein et al., 2005; Scholey et al., 2014). Kinesin-5 is a tip-tracking microtubule polymerase that increases growth rate and suppresses catastrophes (Chen and Hancock, 2015). It was proposed to straighten tubulin dimers at the plus ends and promote lateral tubulin interactions, thereby promoting microtubule polymerization (Chen et al., 2019).

In addition to the positive regulators of microtubule assembly, there are different microtubule destabilizers that include motor proteins and microtubule severing enzymes. Destabilizing motor proteins can be either motile, such as kinesin-8 family, or non-motile, such as kinesin-13 family members (Akhmanova and Steinmetz, 2015). Motile motor proteins from the Kinesin-8 family can walk on microtubules in a processive, ATP-dependent manner and accumulate at the plus ends, where they can induce microtubule depolymerization by increasing the off rate of tubulin dimers (Lin et al., 2020). Members of kinesin-13 family, which contain the motor domain in the middle, however, cannot walk (Friel and Welburn, 2018). In mammals, this family consists of KIF2A, KIF2B, KIF2C and KIF24. KIF2C/MCAK (mitotic centromere-associated kinesin) is the most well-studied member and has been shown to bind to EBs via its SXIP-motif, which mediates MCAK enrichment at the growing ends (Honnappa et al., 2009; Lee et al., 2008; Montenegro Gouveia et al., 2010; Tanenbaum et al., 2011). MCAK has been shown to promote a curved conformation of tubulin dimers at microtubule ends in an ATP-dependent manner to induce microtubule catastrophes (Hunter et al., 2003; Helenius et al., 2006; Wang et al., 2017; Benoit et al., 2018).

### **Microtubule minus-end regulation**

Similar to microtubule plus ends, microtubule minus ends are also highly regulated and are frequently stabilized and anchored in cells. Several minus end regulators have been well-described for their role in minus-end stabilization and anchoring at MTOCs. Here, regulators other than  $\gamma$ -TuRC will be discussed. One such regulator is ninein. Ninein is a coiled-coil centrosomal protein that localizes to the subdistal appendages of the mother centriole in interphase cells (Piel et al., 2000). It has later emerged as a microtubule anchoring protein at both centrosomal as well as non-centrosomal MTOCs, such as apical membrane or desmosomes, in different cell types and organisms (Mogensen et al., 2000; Abal et al., 2002;

Delgehyr et al., 2005; Lechler and Fuchs, 2007; Wang et al., 2015a; Goldspink et al., 2017). While ninein anchors microtubules nucleated from  $\gamma$ -TuRC, it has been shown to work redundantly with CAMSAPs/Patronin family proteins (Wang et al., 2015a; Zheng et al., 2020). Both ninein and CAMSAPs, or their ortholog Patronin, have been implicated in the capture of microtubules released from centrosomes and their subsequent anchoring at MTOCs (Ahmad et al., 1999; Abal et al., 2002; Dong et al., 2017; Gillard et al., 2021). Components of the centrosomal Pericentriolar Material (PCM), such as Pericentrin, CDK5RAP2, NEDD1, CEP192, or Golgi-associated proteins, such as GM130, AKAP9/450, CDK5RAP2, Myomegalin, or the Augmin/HAUS complex responsible from branching microtubule nucleation, or minus-end directed-motor proteins, such as members of the kinesin-14 family and cytoplasmic dynein, have been shown to tether either  $\gamma$ -TuRC-nucleated microtubules or CAMSAP-stabilized microtubules to MTOCs (She and Yang, 2017; Tan et al., 2018; Thawani and Petry, 2021; Vineethakumari and Lüders, 2022; Akhmanova and Kapitein, 2022).

Kinesins, such as MCAK and kinesin-14 family member HSET/KIFC1, has been shown to be important for regulating the microtubule minus-end dynamics in mitotic spindles. MCAK, that has been discussed above as a +TIP, can also induce depolymerization of microtubule minus ends as it recognizes all growing microtubule ends and has no specificity for either plus or minus ends (Hunter et al., 2003; Helenius et al., 2006). However, HSET/KIFC1, a minus-end directed-motor, shows specificity for the minus ends and reduces tubulin off-rate to suppress catastrophes, thereby stabilizing the microtubule minus ends (Strothman et al., 2019). In the same study, it was shown that HSET can protect microtubule minus ends from MCAK-mediated depolymerization by inhibiting MCAK localization to the minus ends. Another mitotic microtubule minus-end binding protein is ASPM (abnormal spindle-like microcephaly-associated protein), also known as Asp in flies; it autonomously tracks growing minus ends and inhibits their polymerization (Jiang et al., 2017). ASPM also forms a complex with the microtubule-severing enzyme katanin and recruits it to microtubules to increase the efficiency of microtubule severing. In cells, both ASPM and katanin colocalize at the spindle poles (Jiang et al., 2017).

### *CAMSAPs*

CAMSAP/Patronin family proteins comprise the class of microtubule minus-end targeting proteins (-TIPs) (Akhmanova and Hoogenraad, 2015). They bind to free microtubule minus ends without capping them. CAMSAP3/Nezha was first identified as a microtubule minus-end

binding protein that anchored microtubules at the cadherin-based adherens junctions by binding to PLEKHA7, an adherens junction component, in epithelial cells (Meng et al., 2008). In mammals, the CAMSAP family consists of three homologues, one of which, CAMSAP1, was shown to bind microtubules and interact with spectrin and calmodulin (Baines et al., 2009). Patronin, the only homolog of CAMSAPs in invertebrates, was shown to protect microtubule minus ends against kinesin-13-induced depolymerization, both in vitro as well as in *Drosophila* S2 cells, and is required for spindle elongation during anaphase B (Goodwin and Vale, 2010; Wang et al., 2013). CAMSAP2 and CAMSAP3 were shown to cooperate in epithelial cells to maintain non-centrosomal microtubule arrays (Tanaka et al., 2012). In two concurrent studies, all three mammalian CAMSAPs, CAMSAP1, CAMSAP2 and CAMSAP3, showed microtubule minus-end binding in vitro as well as in cells (Hendershott and Vale, 2014; Jiang et al., 2014). Whereas CAMSAP1 dynamically tracked the growing microtubule minus ends, CAMSAP2 and CAMSAP3 were deposited along the minus-end grown microtubule lattice, slowed down its growth and stabilized it against depolymerization (**Fig. 7**). Domain mapping showed that all three CAMSAPs recognized the minus ends through a conserved globular CCK domain at the C-terminus. Structural studies showed that CCK domain binds to an intradimer site between protofilaments at the minus ends (**Fig. 7**) (Atherton et al., 2017). It preferentially associates with the transition zone between curved protofilaments and the regular microtubule lattice.

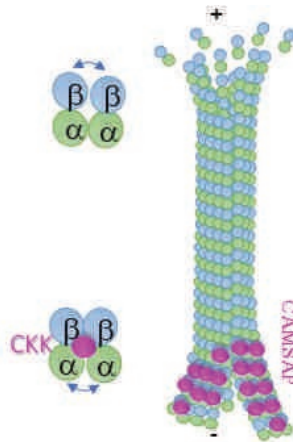


**Figure 7. Illustration of CAMSAP2/3 decoration on microtubule minus ends and the binding site of the CCK domain.**

Upon binding, the CKK domain induces a tilt of whole protofilaments that leads to a protofilament skew relative to the helical axis causing the contraction of microtubule diameter (Atherton et al., 2019). A recent preprint has shown that CAMSAPs prefer expanded lattices, such as GMPCPP-polymerized, taxol-stabilized and kinesin-pretreated microtubules over compact GDP-lattices (Liu and Shima, 2022). This effect was mediated by a helical region of CAMSAP3 next to the CKK, termed D2, which is only present in CAMSAP3. Furthermore, the binding of the CAMSAP3 D2 domain expanded GDP-lattice and stabilized it against depolymerization. CAMSAP2 and CAMSAP3 also contain a microtubule binding domain (MBD) that prefers expanded GMPCPP-polymerized lattice (Jiang et al., 2014). Additionally, CAMSAP2 and CAMSAP3 interact with the microtubule severing protein katanin through a short katanin-binding helix (KBH), and thereby recruit katanin to the minus ends they decorate (Jiang et al., 2018). However, CAMSAP1 lacks all these three additional domains, namely-D2, MBD, and KBH, and does not interact with katanin or display stable microtubule decoration. Interestingly, all three CAMSAPs also interact with the neuronally enriched protein called WDR47 (WD40 repeat-containing protein) (Buijs et al., 2021; Chen et al., 2020). WDR47 plays an essential role in axonal and dendritic development in neurons, where it colocalizes with CAMSAP3 and CAMSAP2-decorated microtubules (Buijs et al., 2021; Chen et al., 2020; Kannan et al., 2017). CAMSAP2 and CAMSAP3 interact with WDR47 through the same region that contains the katanin binding domain (Buijs et al., 2021; Jiang et al., 2018). An interesting study has shown that CAMSAP2 can phase separate at high concentrations (>250 nM) and can condensate tubulin to promote *de novo* microtubule nucleation (Imasaki et al., 2022). However, since such high CAMSAP concentrations are unlikely to be reached in cells, the physiological relevance of these observations is unclear.

### **Microtubule bundling**

Microtubule ends are not the only regions accountable for microtubule stability and turnover of polymer mass. Microtubule lattice located between the two ends can also be an ideal substrate for microtubule regulatory proteins. These proteins include so-called structural MAPs, such as tau, MAP2, MAP4 (Bodakuntla et al., 2019). Overexpression of multiple MAPs, such as tau and Cep169, induces microtubule bundling in cells, however, there are few MAPs, whose essential role is microtubule bundling, such as TRIM46 (tripartite motif containing 46), PRC1 (Protein Regulator Of Cytokinesis 1) and MTCL1 (Kanai et al., 1989; Walczak and Shaw, 2010; Sato et al., 2014; Mori et al., 2015a). A dimerization domain and a microtubule-binding domain are a typical feature of these bundling proteins. They can

physically crosslink two neighboring microtubules and control precise spacing between them (Kellogg et al., 2016; Harterink et al., 2019).

Conventionally, the so-called structural MAPs and microtubule-bundling proteins stabilize microtubule lattices from disassembly and might also protect them against the action of microtubule severing enzymes (Qiang et al., 2006; Lee et al., 2015; Siahaan et al., 2019; Burkart and Dixit, 2019). Depending on their structural organization, microtubule bundlers can form parallel or anti-parallel bundles. For example, PRC1/MAP65/Ase1 family proteins bundle microtubules emanating from opposite spindle poles specifically in an anti-parallel manner at the spindle midzone and are required for the organization of the central spindle and cytokinesis (Loiodice et al., 2005; Bieling et al., 2010a; Subramanian et al., 2010; Roostalu et al., 2010; Lee et al., 2015). In neurons, TRIM46 bundles microtubules in a parallel orientation in the axon initial segment with plus-ends out (van Beuningen et al., 2015). TRIM46 is the member of C-I TRIM subfamily of the N-terminal RING finger/B-box/coiled-coil (RBCC)/TRIM superfamily (Short and Cox, 2006). It encompasses a unique C-terminal subgroup one signature (COS) box and a C-terminal FN3 and B30.2-like domain. TRIM46 localizes to the proximal axon through the interactions mediated by the RING finger and the COS box domains (van Beuningen et al., 2015). The correct localization of TRIM46 is essential for neuronal polarity and axon specification.

Another MAP, Cep169, is a plus-end tracking centrosomal protein and CDK5RAP2 binding partner, which accumulates at the distal ends of microtubules and centrosomes (Mori et al., 2015a). Overexpressed Cep169 bundles microtubules by forming homodimers through its N-terminus and binds to microtubules through the C-terminus. The bundling activity of Cep169 is independent of its plus-end tracking and EB-binding activity (Mori et al., 2015b).

### **Microtubule damage and repair**

Structural work has shown that heterogeneity in protofilament number or occurrence of multiple seams and transitions between microtubule lattice configuration within the same microtubule can be observed in cultured neurons and *Xenopus* egg extracts (**Fig. 8, top panel**) (Chretien et al., 1992; Atherton et al., 2018; Guyomar et al., 2022). Moreover, structural heterogeneities like tubulin dislocations, switch in protofilament number or microtubule tube closure defects can also be induced by increasing the speed of microtubule polymerization or by binding of microtubule stabilizing agents (MSAs), such as taxanes, respectively (Schaedel et al., 2019; Rai et al., 2019, 2021). These lattice defects in a crowded cellular environment with a dense microtubule array can be created or further amplified due to microtubule bending

and crossing, because of retrograde actin flow during cell migration, by stepping of molecular motors or due to nanoscale damages induced by microtubule severing enzymes (**Fig. 8, bottom panel**) (Waterman-Storer and Salmon, 1997; Kalil and Szebenyi, 2000; Eaton et al., 2002; Schaedel et al., 2015; Aumeier et al., 2016; Vemu et al., 2018; Triclin et al., 2021; Théry and Blanchoin, 2021; Budaitis et al., 2022; Andreu-Carbó et al., 2022). This could either result in microtubule breakage and fragmentation or induction of self-repair by the incorporation of tubulin dimers at the damage sites (**Fig. 8, middle panel**) (Waterman-Storer and Salmon, 1997; Kalil and Szebenyi, 2000; Aumeier et al., 2016; Triclin et al., 2021; Théry and Blanchoin, 2021; Budaitis et al., 2022; Gazzola et al., 2022).

Recent *in vitro* work has shown that walking of mammalian kinesin-1 (KIF5B), yeast kinesin-8 motor (Klp3) and yeast cytoplasmic dynein can cause microtubule destruction by microtubule fragmentation and subsequent depolymerization (Triclin et al., 2021). This study also showed that the presence of free tubulin can induce lattice repair and protect microtubule from destruction. Another interesting study has shown that a kinesin-1 KIF5C mutant, that has an increased tendency to create damage sites, can cause microtubule breakage and fragmentation in cells, as this damage cannot be sufficiently repaired by free tubulin (Budaitis et al., 2022). Therefore, a balance between microtubule damage and repair can determine microtubule stability. Self-repair can generate sites with GTP-bound tubulin dimers along the lattice, which would then serve as rescue sites (Dimitrov et al., 2008a; de Forges et al., 2016; Aumeier et al., 2016; Gazzola et al., 2022; Andreu-Carbó et al., 2022). Rescues would increase the lifetime of the microtubules, and thereby, stabilize the microtubule shafts.

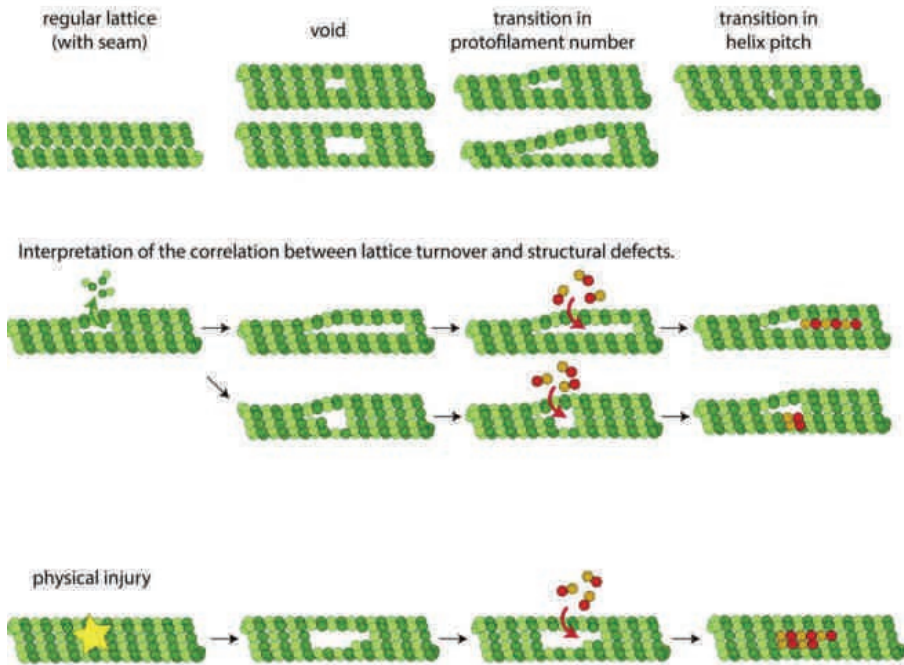


**Figure 8. Microtubule lattice defects, damage and self-repair.** Reproduced from Théry and Blanchoin, 2021, *Current Opinion in Cell Biology*.

Several MAPs can prevent depolymerization of microtubule lattice and restrict lattice damage (Lawrence et al., 2021; Berg et al., 2022). One such MAP is Centrosome/spindle pole associated protein 1 (CSPP1). CSPP1 is a centrosome and cilia-associated protein, which was shown to recognize and bind microtubule ends that are in pre-catastrophe state with perturbed growth, a behavior observed for taxanes (Berg et al., 2022; Rai et al., 2019). CSPP1 binds to the microtubule lumen and also recognizes damaged lattices, where it prevents microtubule disassembly, promotes tubulin incorporation and triggers the formation of stable rescue sites that can cause repeated rescue as observed previously with taxanes (Berg et al., 2022; Rai et al., 2021). A different study identified a MAP, Sjögren's syndrome nuclear autoantigen-1 (SSNA1/NA14), as a sensor for microtubule damage (Lawrence et al., 2021). SSNA1 also protected taxol-stabilized microtubules against spastin-mediated severing.

**Microtubule severing**

A microtubule can be used as a substrate by microtubule severing enzymes that can cut this microtubule to either generate new microtubules, regulate microtubule length, destroy the microtubule or promote its repair (Sharp and Ross, 2012; McNally and Roll-Mecak, 2018; Kuo and Howard, 2021). Microtubule severing enzymes are ATPases of AAA-type protein family. There are three well known classes of microtubule severing proteins: spastin, katanin and fidgetin. Together with the vacuolar protein 4 (VPS4), which disassembles ESCRTIII polymers, these nanomachines constitute the meiotic subfamily of AAA ATPases that disrupt noncovalent bonds within large polymers (Monroe and Hill, 2016). Severing enzymes were first discovered in frog and sea urchin egg extracts, which contained a mitotically activated protein, later termed katanin, that could disassemble taxol-stabilized microtubules into tubulin dimers (Vale, 1991; McNally and Vale, 1993).

A few years later, another katanin-related AAA ATPase was discovered and named Spastin (Hazan et al., 1999). Mutations in the gene encoding this protein are associated with a group of neurological disorders, hereditary spastic paraplegias. The *Drosophila* homolog, D-spastin, was shown to sever and disassemble microtubules in S2 cells, as well as in vitro, in assays with purified components (Roll-Mecak and Vale, 2005). In neurons, it was shown that polyglutamylation of  $\alpha/\beta$ -tubulin tails increased the binding affinity of spastin for microtubules, while its severing activity was highly dependent on the  $\beta$ -tubulin tail (Valenstein and Roll-Mecak, 2016). Interestingly, spastin-mediated severing amplified the number and mass of microtubules by promoting rescues at the newly generated severed plus ends (Kuo et al., 2019). It was further observed that spastin tracks shrinking plus ends and triggers their rescue. Both katanin and spastin assemble into a hexameric ring and have a similar mechanism for severing of microtubules (see katanin section below) (Roll-Mecak and Vale, 2008; McNally and Roll-Mecak, 2018).

In *Drosophila* S2 cells, overexpression of any of the three severing enzymes resulted in the destruction of microtubules during interphase (Zhang et al., 2007). It was also found that katanin, spastin and fidgetin were important for maintaining poleward flux in spindles. Whereas spastin and fidgetin were shown to catalyze microtubule minus-end depolymerization at spindle poles, katanin caused the depolymerization of plus ends attached to the chromosomes (Zhang et al., 2007). Later, human fidgetin was also reported to possess microtubule severing and depolymerizing activity in vitro (Mukherjee et al., 2012). In the same study, fidgetin was found to be crucial for regulating mitotic spindle architecture, promoting poleward tubulin flux in anaphase A and suppressing microtubule attachment to the spindle poles. In zebrafish,



fidgetin family members were shown to contribute to endothelial and neuronal branching during development (Dong et al., 2021).

### *Katanin*

Katanin is a heterodimeric microtubule severing protein composed of two subunits: the ATPase-containing catalytic subunit p60 (KATNA1) and the regulatory subunit p80 (KATNB1), bearing a WD40-repeat domain at N-terminus, that was involved in localization of katanin at spindle poles (Hartman et al., 1998). There are three additional katanin subunits known in mammalian cells, which are the A-like subunits (KATNAL1 and KATNAL2) or the B-like subunit (KATNBL1) (Cheung et al., 2016). Katanin heterodimerization involves the N-terminal microtubule-interacting and -trafficking (MIT) domain of p60 and the C-terminal domain of p80 that together form a large  $\alpha$ -helix bundle, to which CAMSAP and ASPM bind (Jiang et al., 2017, 2018). The p60 subunit alone is sufficient for microtubule severing, but the interaction of p60 and p80 was shown to promote microtubule affinity and enhance microtubule-disassembly activity in vitro and in cells (McNally et al., 2000; Jiang et al., 2017). Katanin p60 assembles into a hexamer, in the presence of ATP, with a spiral arrangement of its C-terminal AAA-domains (P1-P6) forming a central pore and the MIT-domains radiating outwards (**Fig. 9, top panel**) (McNally and Roll-Mecak, 2018; Díaz-Valencia et al., 2011).

A study using *C. elegans* katanin (Mei1/Mei2) and *D. melanogaster* spastin has shown that despite the destructive severing activity of these proteins, they both can amplify microtubule number and mass by creating nanoscale damages (Vemu et al., 2018). Microtubule lattice can then incorporate GTP-tubulin dimers at these nanoscale damages and form a rescue site. Rescues together with the newly generated GTP-caps at the plus ends can stabilize microtubules from complete depolymerization and promote their growth. Cryo-EM structures revealed that katanin binds the glutamylated  $\beta$ -tubulin tail through a double spiral, formed by the 2 conserved loops of p60 subunits lining its central pore, and induces tubulin extraction from the polymer in an ATP-hydrolysis dependent manner (**Fig. 9, bottom panel**) (Zehr et al., 2020). Katanin can also recognize microtubule lattice defects and cause breakage of microtubules at those sites (Davis et al., 2002). The microtubule binding and severing activity of katanin is inhibited by free tubulin, because the C-terminal tails of tubulin, especially that of  $\beta$ -tubulin, can bind to katanin and sequester it (Bailey et al., 2015).

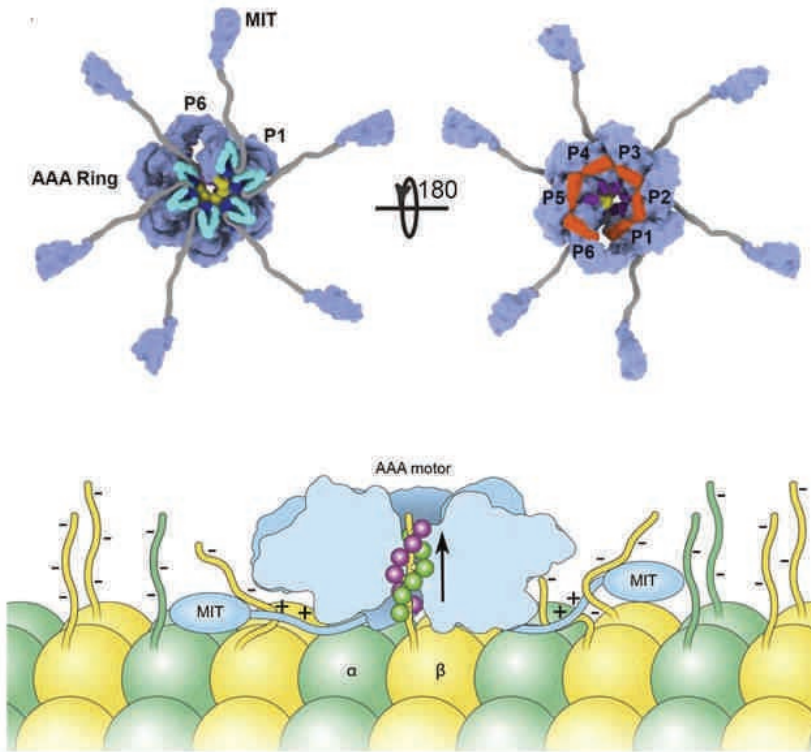


**Figure 9.** The assembly of a katanin p60 hexamer and its severing action on a microtubule. Reproduced from McNally and Roll-Mecak, 2018, *JCB* and Zehr et al., 2020, *Developmental Cell*.

Katanin amplifies microtubule number at the initial stages of the assembly of *C. elegans* meiotic spindle, while it promotes shortening of the meiotic spindle at later stages by reducing microtubule number and length at the spindle poles (McNally et al., 2006; Srayko et al., 2006). It was also reported that katanin promoted shortening of the mitotic spindle in nocodazole-treated mammalian cells (McNally et al., 2006). Katanin was shown to be involved in microtubule release from the centrosome in neurons and epithelial cells (Ahmad et al., 1999; Dong et al., 2017; Gillard et al., 2021). In plants, katanin was shown to be recruited at specific sites like cortical microtubule crossings, nucleation sites on pre-existing microtubules or distal zones of phragmoplasts during cytokinesis (Nakamura et al., 2022). Katanin plays an important role in organizing non-centrosomal microtubule arrays in different cell types, such as epithelial

cells and neurons, and therefore, it is highly important throughout the development (Conde and Cáceres, 2009; Lynn et al., 2021).

### **In vitro reconstitution assays for studying microtubule dynamics**

In this thesis, we take advantage of the in vitro assays with purified proteins to investigate fundamental mechanisms controlling different aspects of microtubule formation, dynamics and disassembly by various factors in order to understand how they regulate cellular functions. The design of the biochemical reconstitutions varies according to the specific question, but they share some similarities. For the simplest reconstitution of microtubule dynamics, microtubule templates are attached to the glass surface, via NeutrAvidin-Biotin links, and then incubated with a reaction mixture containing a known concentration of soluble tubulin, GTP and proteins of interest to allow microtubule assembly (Bieling et al., 2007; Komarova et al., 2009). The reconstitutions are then monitored in real-time under Total Internal Reflection (TIRF) microscopy. The specific biochemical reconstitutions have been discussed in the respective chapters.

### **Scope of this thesis**

In this thesis, we shed light on the individual stages of the dynamic life of microtubules and the factors that regulate it. The different behaviors shown by microtubules and the outcomes facilitated by microtubule regulatory factors further deepen our understanding about how microtubule polymer mass is produced in cells and how it is maintained. Also, this thesis accentuates the power of biochemical in vitro reconstitution assays in providing a mechanistic link between individual molecular interactions and the global impact of those interactions in a broader cellular context.

**In Chapter 2, we investigate a mechanism associated with microtubule birth.** We reveal a novel mechanism for generation of stable microtubule minus ends. At a resolution of single microtubules, we show that CAMSAPs can displace  $\gamma$ -TuRC from the minus end of the microtubule it nucleated to generate free microtubules with CAMSAP-stabilized minus ends. We also show that a very well-studied  $\gamma$ -TuRC activator, CDK5RAP2, inhibits  $\gamma$ -TuRC dissociation from the minus ends by improving the fit between  $\gamma$ -TuRC and a 13-protofilament microtubule. We also propose that CAMSAPs can serve as a readout for imperfect attachment between  $\gamma$ -TuRC and microtubule minus ends.

**In Chapter 3, we study how microtubules are stabilized.** We uncover the molecular mechanisms underlying axon initial segment assembly (AIS). We show that Ankyrin-G acts as a scaffold between End-Binding proteins and axonal membrane protein Neurofascin-186 to recruit TRIM46 decorated microtubule-bundles to the axonal membrane. Through our in vitro reconstitution assays, we also show that TRIM46 forms and stabilizes parallel microtubule bundles by acting as a rescue factor and provides stable microtubule tracks for the feedback-driven assembly of AIS.

**In Chapter 4, we focus on microtubule maintenance by investigating microtubule repair.** We discovered a new role of CLASP2 as a microtubule repair factor. We show that CLASP2 can accumulate at induced damage sites on the microtubule lattice and facilitate self-repair of microtubules by promoting stable tubulin incorporation and restricting lattice damage.

**In Chapter 5, we address microtubule destruction and amplification.** We exploit the power of in vitro reconstitution assays to show that a three-protein module composed of CAMSAP, katanin and WDR47 can regulate the elongation and the number of microtubule minus ends. We show that WDR47 binds to the minus ends decorated by CAMSAPs and protects them from katanin-mediated severing by inhibiting katanin binding to these minus ends.

**In Chapter 6,** we discuss our findings in a general context of the updated scientific literature and a prospective outlook on this research.

---

**References**

- Abal, M., M. Piel, V. Bouckson-Castaing, M. Mogensen, J.B. Sibarita, and M. Bornens. 2002. Microtubule release from the centrosome in migrating cells. *J. Cell Biol.* 159:731–737. doi:10.1083/jcb.200207076.
- Aher, A., M. Kok, A. Sharma, A. Rai, N. Olieric, R. Rodriguez-Garcia, E.A. Katrukha, T. Weinert, V. Olieric, L.C. Kapitein, M.O. Steinmetz, M. Dogterom, and A. Akhmanova. 2018. CLASP Suppresses Microtubule Catastrophes through a Single TOG Domain. *Dev. Cell.* 46:40–58.e8. doi:10.1016/j.devcel.2018.05.032.
- Aher, A., D. Rai, L. Schaedel, J. Gaillard, K. John, Q. Liu, M. Altelaar, L. Blanchoin, M. Thery, and A. Akhmanova. 2020. CLASP Mediates Microtubule Repair by Restricting Lattice Damage and Regulating Tubulin Incorporation. *Curr. Biol.* 30:2175–2183.e6. doi:10.1016/j.cub.2020.03.070.
- Ahmad, F.J., W. Yu, F.J. McNally, and P.W. Baas. 1999. An Essential Role for Katanin in Severing Microtubules in the Neuron. *J. Cell Biol.* 145:305–315. doi:10.1083/JCB.145.2.305.
- Akhmanova, A., and C.C. Hoogenraad. 2015. Microtubule minus-end-targeting proteins. *Curr. Biol.* 25:R162–R171. doi:10.1016/j.cub.2014.12.027.
- Akhmanova, A., C.C. Hoogenraad, K. Drabek, T. Stepanova, B. Dortland, T. Verkerk, W. Vermeulen, B.M. Burgering, C.I. De Zeeuw, F. Grosveld, and N. Galjart. 2001. CLASPs are CLIP-115 and -170 associating proteins involved in the regional regulation of microtubule dynamics in motile fibroblasts. *Cell.* 104:923–935. doi:10.1016/S0092-8674(01)00288-4.
- Akhmanova, A., and L.C. Kapitein. 2022. Mechanisms of microtubule organization in differentiated animal cells. *Nat. Rev. Mol. Cell Biol.* 23:541–558. doi:10.1038/s41580-022-00473-y.
- Akhmanova, A., and M.O. Steinmetz. 2010. Microtubule +TIPs at a glance. *J. Cell Sci.* 123:3415–3419. doi:10.1242/jcs.062414.
- Akhmanova, A., and M.O. Steinmetz. 2015. Control of microtubule organization and dynamics: two ends in the limelight. *Nat. Rev. Mol. Cell Biol.* 16:711–726. doi:10.1038/nrm4084.
- Akhmanova, A., and M.O. Steinmetz. 2019. Microtubule minus-end regulation at a glance. *J. Cell Sci.* 132:1–7. doi:10.1242/JCS.227850.
- Al-Bassam, J., and F. Chang. 2011. Regulation of microtubule dynamics by TOG-domain proteins XMAP215/Dis1 and CLASP. *Trends Cell Biol.* 21:604–614. doi:10.1016/j.tcb.2011.06.007.
- Al-Bassam, J., H. Kim, G. Brouhard, A. van Oijen, S.C. Harrison, and F. Chang. 2010. CLASP promotes microtubule rescue by recruiting tubulin dimers to the microtubule. *Dev. Cell.* 19:245–258. doi:10.1016/j.devcel.2010.07.016.
- Al-Bassam, J., N.A. Larsen, A.A. Hyman, and S.C. Harrison. 2007. Crystal Structure of a TOG Domain: Conserved Features of XMAP215/Dis1-Family TOG Domains and Implications for Tubulin Binding. *Structure.* 15:355–362. doi:10.1016/J.STR.2007.01.012.

- Alfaro-Aco, R., A. Thawani, and S. Petry. 2020. Biochemical reconstitution of branching microtubule nucleation. *Elife*. 9:1–16. doi:10.7554/eLife.49797.
- Andreu-Carbó, M., S. Fernandes, M.C. Velluz, K. Kruse, and C. Aumeier. 2022. Motor usage imprints microtubule stability along the shaft. *Dev. Cell*. 57:5-18.e8. doi:10.1016/J.DEVCEL.2021.11.019.
- Arnal, I., C. Heichette, G.S. Diamantopoulos, and D. Chrétien. 2004. CLIP-170/tubulin-curved oligomers coassemble at microtubule ends and promote rescues. *Curr. Biol*. 14:2086–2095. doi:10.1016/J.CUB.2004.11.055.
- Atherton, J., K. Jiang, M.M. Stangier, Y. Luo, S. Hua, K. Houben, J.J.E. Van Hooff, A.P. Joseph, G. Scarabelli, B.J. Grant, A.J. Roberts, M. Topf, M.O. Steinmetz, M. Baldus, C.A. Moores, and A. Akhmanova. 2017. A structural model for microtubule minus-end recognition and protection by CAMSAP proteins. *Nat. Struct. Mol. Biol*. 24:931–943. doi:10.1038/nsmb.3483.
- Atherton, J., Y. Luo, S. Xiang, C. Yang, A. Rai, K. Jiang, M. Stangier, A. Vemu, A.D. Cook, S. Wang, A. Roll-Mecak, M.O. Steinmetz, A. Akhmanova, M. Baldus, and C.A. Moores. 2019. Structural determinants of microtubule minus end preference in CAMSAP CKK domains. *Nat. Commun*. 10:1–16. doi:10.1038/s41467-019-13247-6.
- Atherton, J., M. Stouffer, F. Francis, and C.A. Moores. 2018. Microtubule architecture in vitro and in cells revealed by cryo-electron tomography research papers. 572–584. doi:10.1107/S2059798318001948.
- Aumeier, C., L. Schaedel, J. Gaillard, K. John, L. Blanchoin, and M. Théry. 2016. Self-repair promotes microtubule rescue. *Nat. Cell Biol*. 18:1054–1064. doi:10.1038/ncb3406.
- Bailey, M.E., D.L. Sackett, and J.L. Ross. 2015. Article Katanin Severing and Binding Microtubules Are Inhibited by Tubulin Carboxy Tails. *Biophysj*. 109:2546–2561. doi:10.1016/j.bpj.2015.11.011.
- Baines, A.J., P.A. Bignone, M.D.A. King, A.M. Maggs, P.M. Bennett, J.C. Pinder, and G.W. Phillips. 2009. The CKK domain (DUF1781) binds microtubules and defines the CAMSAP/ssp4 family of animal proteins. *Mol. Biol. Evol*. 26:2005–2014. doi:10.1093/molbev/msp115.
- Bartolini, F., and G.G. Gundersen. 2006. Generation of noncentrosomal microtubule arrays. *J. Cell Sci*. 119:4155–4163. doi:10.1242/jcs.03227.
- Benoit, M.P.M.H., A.B. Asenjo, and H. Sosa. 2018. Cryo-EM reveals the structural basis of microtubule depolymerization by kinesin-13s. *Nat. Commun*. 9. doi:10.1038/S41467-018-04044-8.
- Berg, C.M. van den, V.A. Volkov, S. Schnorrenberg, Z. Huang, K.E. Stecker, I. Grigoriev, S. Patzke, T. Zimmermann, M. Dogterom, and A. Akhmanova. 2022. CSPP1 stabilizes growing microtubule ends and damaged lattices from the luminal side. *bioRxiv*. 2022.06.23.497320.
- van Beuningen, S.F.B., L. Will, M. Harterink, A. Chazeau, E.Y. Van Battum, C.P. Frias, M.A.M. Franker, E.A. Katrukha, R. Stucchi, K. Vocking, A.T. Antunes, L. Slenders, S. Doukeridou, P. Sillevs Smitt, A.F.M. Altelaar, J.A. Post, A. Akhmanova, R.J. Pasterkamp, L.C. Kapitein, E. de Graaff, and C.C. Hoogenraad. 2015. TRIM46 Controls Neuronal Polarity and Axon Specification by Driving the Formation of Parallel

- Microtubule Arrays. *Neuron*. 88:1208–1226. doi:10.1016/j.neuron.2015.11.012.
- Bieling, P., S. Kandels-Lewis, I.A. Telley, J. Van Dijk, C. Janke, and T. Surrey. 2008. CLIP-170 tracks growing microtubule ends by dynamically recognizing composite EB1/tubulin-binding sites. *J. Cell Biol.* 183:1223. doi:10.1083/JCB.200809190.
- Bieling, P., L. Laan, H. Schek, E.L. Munteanu, L. Sandblad, M. Dogterom, D. Brunner, and T. Surrey. 2007. Reconstitution of a microtubule plus-end tracking system in vitro. *Nature*. 450:1100–1105. doi:10.1038/nature06386.
- Bieling, P., I.A. Telley, and T. Surrey. 2010a. A minimal midzone protein module controls formation and length of antiparallel microtubule overlaps. *Cell*. 142:420–432. doi:10.1016/j.cell.2010.06.033.
- Bieling, P., I.A. Telley, and T. Surrey. 2010b. A minimal midzone protein module controls formation and length of antiparallel microtubule overlaps. *Cell*. 142:420–32. doi:10.1016/j.cell.2010.06.033.
- Bodakuntla, S., A.S. Jijumon, C. Villablanca, C. Gonzalez-Billault, and C. Janke. 2019. Microtubule-Associated Proteins: Structuring the Cytoskeleton. *Trends Cell Biol.* 29:804–819. doi:10.1016/j.tcb.2019.07.004.
- Bond, J., E. Roberts, K. Springell, S. Lizarraga, S. Scott, J. Higgins, D.J. Hampshire, E.E. Morrison, G.F. Leal, E.O. Silva, S.M.R. Costa, D. Baralle, M. Raponi, G. Karbani, Y. Rashid, H. Jafri, C. Bennett, P. Corry, C.A. Walsh, and C.G. Woods. 2005. A centrosomal mechanism involving CDK5RAP2 and CENPJ controls brain size. *Nat. Genet.* 37:353–355. doi:10.1038/NG1539.
- Brilot, A.F., A.S. Lyon, A. Zelter, S. Viswanath, A. Maxwell, M.J. Maccoss, E.G. Muller, A. Sali, T.N. Davis, and D.A. Agard. 2021. Cm1-driven assembly and activation of yeast g-tubulin small complex underlies microtubule nucleation. *Elife*. 10. doi:10.7554/eLife.65168.
- Brouhard, G.J. 2015. Dynamic instability 30 years later : complexities in microtubule growth and catastrophe. 26:1207–1210. doi:10.1091/mbc.E13-10-0594.
- Brouhard, G.J., and L.M. Rice. 2018. Microtubule dynamics: An interplay of biochemistry and mechanics. *Nat. Rev. Mol. Cell Biol.* 19:451–463. doi:10.1038/s41580-018-0009-y.
- Brouhard, G.J., J.H. Stear, T.L. Noetzel, J. Al-Bassam, K. Kinoshita, S.C. Harrison, J. Howard, and A.A. Hyman. 2008. XMAP215 Is a Processive Microtubule Polymerase. *Cell*. 132:79–88. doi:10.1016/j.cell.2007.11.043.
- Brust-Mascher, I., P. Sommi, D.K. Cheerambathur, and J.M. Scholey. 2009. Kinesin-5-dependent poleward flux and spindle length control in *Drosophila* embryo mitosis. *Mol. Biol. Cell*. 20:1749–1762. doi:10.1091/MBC.E08-10-1033.
- Budaitis, B.G., S. Badiyan, Y. Yue, T.L. Blasius, D.N. Reinemann, M.J. Lang, M.A. Cianfrocco, and K.J. Verhey. 2022. A kinesin-1 variant reveals motor-induced microtubule damage in cells. *Curr. Biol.* 32:2416-2429.e6. doi:10.1016/j.cub.2022.04.020.
- Buijs, R.R., J.J.A. Hummel, M. Burute, X. Pan, Y. Cao, R. Stucchi, M. Altelaar, A. Akhmanova, L.C. Kapitein, and C.C. Hoogenraad. 2021. WDR47 protects neuronal microtubule minus ends from katanin-mediated severing. *Cell Rep.* 36:109371. doi:10.1016/j.celrep.2021.109371.

- Burkart, G.M., and R. Dixit. 2019. Microtubule bundling by MAP65-1 protects against severing by inhibiting the binding of katanin. *Mol. Biol. Cell.* 30:1587–1597. doi:10.1091/MBC.E18-12-0776/MC-E18-12-0776-S03.MOV.
- Burute, M., and L.C. Kapitein. 2019. Cellular Logistics : Unraveling the Interplay Between Microtubule Organization and Intracellular Transport.
- Chaaban, S., and G.J. Brouhard. 2017. A microtubule bestiary: structural diversity in tubulin polymers. *Mol. Biol. Cell.* 28:2924–2931. doi:10.1091/mbc.e16-05-0271.
- Chen, G.Y., J.M. Cleary, A.B. Asenjo, Y. Chen, J.A. Mascaro, D.F.J. Argenteanu, H. Sosa, and W.O. Hancock. 2019. Kinesin-5 Promotes Microtubule Nucleation and Assembly by Stabilizing a Lattice-Competent Conformation of Tubulin. *Curr. Biol.* 29:2259–2269.e4. doi:10.1016/J.CUB.2019.05.075.
- Chen, Y., and W.O. Hancock. 2015. Kinesin-5 is a microtubule polymerase. *Nat. Commun.* 6. doi:10.1038/ncomms9160.
- Chen, Y., J. Zheng, X. Li, L. Zhu, Z. Shao, X. Yan, and X. Zhu. 2020. Wdr47 Controls Neuronal Polarization through the Camsap Family Microtubule Minus-End-Binding Proteins. *Cell Rep.* 31. doi:10.1016/j.celrep.2020.107526.
- Cheung, K., S. Senese, J. Kuang, N. Bui, C. Ongpipattanakul, A. Gholkar, W. Cohn, J. Capri, J.P. Whitelegge, and J.Z. Torres. 2016. Proteomic analysis of the mammalian katanin family of microtubule-severing enzymes defines Katanin p80 subunit B-like 1 (KATNBL1) as a regulator of mammalian Katanin microtubule-severing. *Mol. Cell. Proteomics.* 15:1658–1669. doi:10.1074/mcp.M115.056465.
- Choi, Y.K., P. Liu, S.K. Sze, C. Dai, and R.Z. Qi. 2010. CDK5RAP2 stimulates microtubule nucleation by the  $\gamma$ -tubulin ring complex. *J. Cell Biol.* 191:1089–1095. doi:10.1083/JCB.201007030.
- Chretien, D., F. Metoz, F. Verde, E. Karsenti, and R.H. Wade. 1992. Lattice defects in microtubules: Protofilament numbers vary within individual microtubules. *J. Cell Biol.* 117:1031–1040. doi:10.1083/jcb.117.5.1031.
- Conde, C., and A. Cáceres. 2009. Microtubule assembly, organization and dynamics in axons and dendrites. *Nat. Rev. Neurosci.* 10:319–332. doi:10.1038/nrn2631.
- Consolati, T., J. Locke, J. Roostalu, Z.A. Chen, J. Gannon, J. Asthana, W.M. Lim, F. Martino, M.A. Cvetkovic, J. Rappsilber, A. Costa, and T. Surrey. 2020. Microtubule Nucleation Properties of Single Human  $\gamma$ TuRCs Explained by Their Cryo-EM Structure. *Dev. Cell.* 53:603–617.e8. doi:10.1016/j.devcel.2020.04.019.
- Dammermann, A., A. Desai, and K. Oegema. 2003. The minus end in sight. *Curr. Biol.* 13:614–624. doi:10.1016/S0960-9822(03)00530-X.
- Davis, L.J., D.J. Odde, S.M. Block, and S.P. Gross. 2002. The importance of lattice defects in katanin-mediated microtubule severing in vitro. *Biophys. J.* 82:2916–2927. doi:10.1016/S0006-3495(02)75632-4.
- Delgehyr, N., J. Sillibourne, and M. Bornens. 2005. Microtubule nucleation and anchoring at the centrosome are independent processes linked by ninein function. 2. doi:10.1242/jcs.02302.
- Desai, A., and T.J. Mitchison. 1997. Microtubule Polymerization Dynamics. *Annu. Rev. Cell*



- Dev. Biol.* 13:83–117. doi:10.1146/annurev.cellbio.13.1.83.
- Díaz-Valencia, J.D., M.M. Morelli, M. Bailey, D. Zhang, D.J. Sharp, and J.L. Ross. 2011. Drosophila katanin-60 depolymerizes and severs at microtubule defects. *Biophys. J.* 100:2440–2449. doi:10.1016/J.BPJ.2011.03.062.
- Dimitrov, A., S. Moutel, I. Cantaloube, and F. Perez. 2008a. Detection of GTP-Tubulin conformation in vivo reveals a role for GTP remnants - Supp data. *Science (80-. )*. 4:1353–1357. doi:10.1126/science.
- Dimitrov, A., M. Quesnoit, S. Moutel, I. Cantaloube, C. Poüs, and F. Perez. 2008b. Detection of GTP-tubulin conformation in vivo reveals a role for GTP remnants in microtubule rescues. *Science (80-. )*. 322:1353–1356. doi:10.1126/science.1165401.
- Dixit, R., B. Barnett, J.E. Lazarus, M. Tokito, Y.E. Goldman, and E.L.F. Holzbaur. 2009. Microtubule plus-end tracking by CLIP-170 requires EB1. *Proc. Natl. Acad. Sci.* 106:492–497. doi:10.1073/pnas.0807614106.
- Dong, C., H. Xu, R. Zhang, N. Tanaka, M. Takeichi, and W. Meng. 2017. CAMSAP3 accumulates in the pericentrosomal area and accompanies microtubule release from the centrosome via katanin. *J. Cell Sci.* 130:1709–1715. doi:10.1242/jcs.198010.
- Dong, Z., X. Chen, Y. Li, R. Zhuo, X. Lai, and M. Liu. 2021. Microtubule Severing Protein Figl2 Contributes to Endothelial and Neuronal Branching in Zebrafish Development. *Front. Cell Dev. Biol.* 8:1833. doi:10.3389/FCELL.2020.593234/BIBTEX.
- Eaton, B.A., R.D. Fetter, and G.W. Davis. 2002. Dynactin is necessary for synapse stabilization. *Neuron.* 34:729–741. doi:10.1016/S0896-6273(02)00721-3.
- Efimov, A., A. Kharitonov, N. Efimova, J. Loncarek, P.M. Miller, N. Andreyeva, P. Gleeson, N. Galjart, A.R.R. Maia, I.X. McLeod, J.R. Yates, H. Maiato, A. Khodjakov, A. Akhmanova, and I. Kaverina. 2007. Asymmetric CLASP-Dependent Nucleation of Noncentrosomal Microtubules at the trans-Golgi Network. *Dev. Cell.* 12:917–930. doi:10.1016/j.devcel.2007.04.002.
- Endow, S.A., F.J. Kull, and H. Liu. 2010. Kinesins at a glance. *J. Cell Sci.* 123:3420–3424. doi:10.1242/jcs.064113.
- Erickson, H.P., and E.T. O'Brien. 1992. Microtubule dynamic instability and GTP hydrolysis. *Annu. Rev. Biophys. Biomol. Struct.* 21:145–166. doi:10.1146/annurev.bb.21.060192.001045.
- Farmer, V., G. Arpağ, S.L. Hall, and M. Zanic. 2021. Xmap215 promotes microtubule catastrophe by disrupting the growing microtubule end. *J. Cell Biol.* 220:1–13. doi:10.1083/jcb.202012144.
- Fong, K., Y. Choi, J.B. Rattner, and R.Z. Qi. 2008. CDK5RAP2 Is a Pericentriolar Protein That Functions in Centrosomal Attachment of the  $\gamma$ -Tubulin Ring Complex. *J. Cell Biol.* 19:115–125. doi:10.1091/mbc.E07.
- de Forges, H., A. Pilon, I. Cantaloube, A. Pallandre, A.M. Haghiri-Gosnet, F. Perez, and C. Poüs. 2016. Localized Mechanical Stress Promotes Microtubule Rescue. *Curr. Biol.* 26:3399–3406. doi:10.1016/j.cub.2016.10.048.
- Fréal, A., D. Rai, R.P. Tas, X. Pan, E.A. Katrukha, D. van de Willige, R. Stucchi, A. Aher, C. Yang, A.F.M. Altelaar, K. Vocking, J.A. Post, M. Harterink, L.C. Kapitein, A.

- Akhmanova, and C.C. Hoogenraad. 2019. Feedback-Driven Assembly of the Axon Initial Segment. *Neuron*. 104:305-321.e8. doi:10.1016/j.neuron.2019.07.029.
- Friel, C.T., and J.P. Welburn. 2018. Parts list for a microtubule depolymerising kinesin. *Biochem. Soc. Trans.* 46:1665–1672. doi:10.1042/BST20180350.
- Gazzola, M., A. Schaeffer, B. Vianay, and J. Gaillard. 2022. Microtubules self-repair in living cells.
- Gillard, G., G. Girdler, and K. Röper. 2021. A release-and-capture mechanism generates an essential non-centrosomal microtubule array during tube budding. *Nat. Commun.* 12. doi:10.1038/s41467-021-24332-0.
- Girão, H., N. Okada, T.A. Rodrigues, A.O. Silva, A.C. Figueiredo, Z. Garcia, and T. Moutinho-santos. 2019. CLASP2 binding to curved microtubule tips promotes flux and stabilizes kinetochore attachments.
- Goldspink, D.A., C. Rookyard, B.J. Tyrrell, J. Gadsby, J. Perkins, E.K. Lund, N. Galjart, P. Thomas, T. Wileman, and M.M. Mogensen. 2017. Ninein is essential for apico-basal microtubule formation and CLIP-170 facilitates its redeployment to non-centrosomal microtubule organizing centres. *Open Biol.* 7. doi:10.1098/RSOB.160274.
- Goodson, H. V., and E.M. Jonasson. 2018. Microtubules and Microtubule-Associated Proteins. *Cold Spring Harb. Perspect. Biol.* 10:a022608. doi:10.1101/CSHPERSPECT.A022608.
- Goodson, H. V., and E.M. Jonasson. Microtubules and Microtubule-Associated Proteins.
- Goodwin, S.S., and R.D. Vale. 2010. Patronin Regulates the Microtubule Network by Protecting Microtubule Minus Ends. *Cell*. 143:263–274. doi:10.1016/j.cell.2010.09.022.
- Goshima, G., M. Mayer, N. Zhang, N. Stuurman, and R.D. Vale. 2008. Augmin: A protein complex required for centrosome-independent microtubule generation within the spindle. *J. Cell Biol.* 181:421–429. doi:10.1083/JCB.200711053/VIDEO-7.
- Grimaldi, A.D., T. Maki, B.P. Fitton, D. Roth, D. Yampolsky, M.W. Davidson, T. Svitkina, A. Straube, I. Hayashi, and I. Kaverina. 2014. CLASPs are required for proper microtubule localization of end-binding proteins. *Dev. Cell*. 30:343–352. doi:10.1016/j.devcel.2014.06.026.
- Gudimchuk, N.B., E. V. Ulyanov, E. O’Toole, C.L. Page, D.S. Vinogradov, G. Morgan, G. Li, J.K. Moore, E. Szczesna, A. Roll-Mecak, F.I. Ataullakhanov, and J. Richard McIntosh. 2020. Mechanisms of microtubule dynamics and force generation examined with computational modeling and electron cryotomography. *Nat. Commun.* 11:1–15. doi:10.1038/s41467-020-17553-2.
- Gupta, K.K., E.O. Alberico, I.S. Näthke, and H. V. Goodson. 2014. Promoting microtubule assembly: A hypothesis for the functional significance of the +TIP network. *BioEssays*. 36:818–826. doi:10.1002/bies.201400029.
- Guyomar, C., C. Bousquet, S. Ku, J. Heumann, and G. Guilloux. 2022. Changes in seam number and location induce holes within microtubules assembled from porcine brain tubulin and in *Xenopus* egg cytoplasmic.
- Haren, L., D. Farache, L. Emorine, and A. Merdes. 2020. A stable sub-complex between GCP4, GCP5 and GCP6 promotes the assembly of tubulin ring complexes. *J. Cell Sci.*

133. doi:10.1242/jcs.244368.

- Harterink, M., K. Vocking, X. Pan, E.M. Soriano Jerez, L. Slenders, A. Fréal, R.P. Tas, W.J. Van De Wetering, K. Timmer, J. Motshagen, S.F.B. Van Beuningen, L.C. Kapitein, W.J.C. Geerts, J.A. Post, and C.C. Hoogenraad. 2019. Trim46 organizes microtubule fasciculation in the axon initial segment. *J. Neurosci.* 39:4864–4873. doi:10.1523/JNEUROSCI.3105-18.2019.
- Hartman, J.J., J. Mahr, K. McNally, K. Okawa, A. Iwamatsu, S. Thomas, S. Cheesman, J. Heuser, R.D. Vale, and F.J. McNally. 1998. Katanin, a microtubule-severing protein, is a novel AAA ATPase that targets to the centrosome using a WD40-containing subunit. *Cell.* 93:277–287. doi:10.1016/S0092-8674(00)81578-0.
- Hazan, J., N. Fonknechten, D. Mavel, C. Paternotte, D. Samson, F. Artiguenave, C.S. Davoine, C. Cruaud, A. Dürr, P. Wincker, P. Brottier, L. Cattolico, V. Barbe, J.M. Burgunder, J.F. Prud'homme, A. Brice, B. Fontaine, R. Heilig, and J. Weissenbach. 1999. Spastin, a new AAA protein, is altered in the most frequent form of autosomal dominant spastic paraplegia. *Nat. Genet.* 23:296–303. doi:10.1038/15472.
- Helenius, J., G. Brouhard, Y. Kalaidzidis, S. Diez, and J. Howard. 2006. The depolymerizing kinesin MCAK uses lattice diffusion to rapidly target microtubule ends. *Nature.* 441:115–119. doi:10.1038/nature04736.
- Hendershott, M.C., and R.D. Vale. 2014. Regulation of microtubule minus-end dynamics by CAMSAPs and Patronin. *Proc. Natl. Acad. Sci.* 111:5860–5865. doi:10.1073/pnas.1404133111.
- Hirokawa, N., Y. Noda, Y. Tanaka, and S. Niwa. 2009. Kinesin superfamily motor proteins and intracellular transport. *Nat. Rev. Mol. Cell Biol.* 10:682–696. doi:10.1038/nrm2774.
- Honnappa, S., S.M. Gouveia, A. Weisbrich, F.F. Damberger, N.S. Bhavesh, H. Jawhari, I. Grigoriev, F.J.A. van Rijssel, R.M. Buey, A. Lawera, I. Jelesarov, F.K. Winkler, K. Wüthrich, A. Akhmanova, and M.O. Steinmetz. 2009. An EB1-Binding Motif Acts as a Microtubule Tip Localization Signal. *Cell.* 138:366–376. doi:10.1016/j.cell.2009.04.065.
- Horio, T., and H. Hotani. 1986. Visualization of the dynamic instability of individual microtubules by dark-field microscopy. *Nature.* 321:605–607. doi:10.1038/321605a0.
- Hunter, A.W., M. Caplow, D.L. Coy, W.O. Hancock, S. Diez, L. Wordeman, and J. Howard. 2003. The kinesin-related protein MCAK is a microtubule depolymerase that forms an ATP-hydrolyzing complex at microtubule ends. *Mol. Cell.* 11:445–457. doi:10.1016/S1097-2765(03)00049-2.
- Imasaki, T., S. Kikkawa, S. Niwa, Y. Saijo-Hamano, H. Shigematsu, K. Aoyama, K. Mitsuoka, T. Shimizu, M. Aoki, A. Sakamoto, Y. Tomabechei, N. Sakai, M. Shirouzu, S. Taguchi, Y. Yamagishi, T. Setsu, Y. Sakihama, E. Nitta, M. Takeichi, and R. Nitta. 2022. CAMSAP2 organizes a  $\gamma$ -tubulin-independent microtubule nucleation centre through phase separation. *Elife.* 11:1–28. doi:10.7554/eLife.77365.
- Janke, C., and M.M. Magiera. 2020. The tubulin code and its role in controlling microtubule properties and functions. *Nat. Rev. Mol. Cell Biol.* 21:307–326. doi:10.1038/s41580-020-0214-3.
- Jiang, K., L. Faltova, S. Hua, G. Capitani, A.E. Prota, C. Landgraf, R. Volkmer, R.A.

- Kammerer, M.O. Steinmetz, and A. Akhmanova. 2018. Structural Basis of Formation of the Microtubule Minus-End-Regulating CAMSAP-Katanin Complex. *Structure*. 26:375-382.e4. doi:10.1016/j.str.2017.12.017.
- Jiang, K., S. Hua, R. Mohan, I. Grigoriev, K.W. Yau, Q. Liu, E.A. Katrukha, A.F.M. Altelaar, A.J.R. Heck, C.C. Hoogenraad, and A. Akhmanova. 2014. Microtubule Minus-End Stabilization by Polymerization-Driven CAMSAP Deposition. *Dev. Cell*. 28:295–309. doi:10.1016/j.devcel.2014.01.001.
- Jiang, K., L. Rezabkova, S. Hua, Q. Liu, G. Capitani, A.F.M. Altelaar, A.J.R. Heck, R.A. Kammerer, M.O. Steinmetz, and A. Akhmanova. 2017. Microtubule minus-end regulation at spindle poles by an ASPM – katanin complex. 19. doi:10.1038/ncb3511.
- Kalil, K., and G. Szebenyi. 2000. Common mechanisms underlying growth cone guidance and axon branching. *J. Neurobiol.* 44:145–158. doi:10.1002/1097-4695(200008)44:2<145::AID-NEU5>3.0.CO;2-X.
- Kanai, Y., R. Takemura, T. Oshima, H. Mori, Y. Ihara, M. Yanagisawa, T. Masaki, and N. Hirokawa. 1989. Expression of multiple tau isoforms and microtubule bundle formation in fibroblasts transfected with a single tau cDNA. *J. Cell Biol.* 109:1173–1184. doi:10.1083/JCB.109.3.1173.
- Kannan, M., E. Bayam, C. Wagner, B. Rinaldi, P.F. Kretz, P. Tilly, M. Roos, L. McGillewie, S. Bär, S. Minocha, C. Chevalier, C. Po, V.E. Vancollie, L.F.E. Anthony, S.A. Maguire, D. Lafont, S.A. Pearson, A.S. Gates, M. Sanderson, C. Shannon, M.T. Sumowski, R.S.B. McLaren-Jones, A. Swiatkowska, C.M. Isherwood, E.L. Cambridge, H.M. Wilson, S.S. Caetano, A.K.B. Maguire, A. Galli, A.O. Speak, J. Dench, E. Tuck, J. Estabel, A. Green, C. Tudor, E. Siragher, M. Dabrowska, C.I. Mazzeo, Y. Hooks, F. Kussy, M. Griffiths, D. Gannon, B. Doe, K. Boroviak, H. Wardle-Jones, N. Griggs, J. Bottomley, E. Ryder, D. Gleeson, J.K. White, R. Ramirez-Solis, C.J. Lelliott, J. Chelly, J.L. Mandel, R. Borgatti, A. Piton, C. Kinnear, B. Loos, D.J. Adams, Y. Hérault, S.C. Collins, S. Friant, J.D. Godin, and B. Yalcin. 2017. WD40-repeat 47, a microtubule-associated protein, is essential for brain development and autophagy. *Proc. Natl. Acad. Sci. U. S. A.* 114:E9308–E9317. doi:10.1073/pnas.1713625114.
- Kapitein, L.C., E.J.G. Peterman, B.H. Kwok, J.H. Kim, T.M. Kapoor, and C.F. Schmidt. 2005. The bipolar mitotic kinesin Eg5 moves on both microtubules that it crosslinks. *Nature*. 435:114–118. doi:10.1038/NATURE03503.
- Keating, T.J., and G.G. Borisy. 1999. Centrosomal and non-centrosomal microtubules. *Biol. Cell*. 91:321–329. doi:10.1111/j.1768-322X.1999.tb01090.x.
- Keating, T.J., J.G. Peloquin, V.I. Rodionov, D. Momcilovic, and G.G. Borisy. 1997. Microtubule release from the centrosome. *Proc. Natl. Acad. Sci. U. S. A.* 94:5078–5083. doi:10.1073/pnas.94.10.5078.
- Kellogg, E.H., S. Howes, S.-C. Ti, E. Ramírez-Aportela, T.M. Kapoor, P. Chacón, and E. Nogales. 2016. Near-atomic cryo-EM structure of PRC1 bound to the microtubule. *Proc. Natl. Acad. Sci.* 113:9430–9439. doi:10.1073/pnas.1609903113.
- Kikkawa, M., T. Ishikawa, T. Nakata, T. Wakabayashi, and N. Hirokawa. 1994. Direct visualization of the microtubule lattice seam both in vitro and in vivo. *J. Cell Biol.* 127:1965–1971. doi:10.1083/jcb.127.6.1965.
- Kollman, J.M., C.H. Greenberg, S. Li, M. Moritz, A. Zelter, K.K. Fong, J.J. Fernandez, A.

- Sali, J. Kilmartin, T.N. Davis, and D.A. Agard. 2015. Ring closure activates yeast  $\gamma$ TuRC for species-specific microtubule nucleation. *Nat. Struct. Mol. Biol.* 22:132–137. doi:10.1038/nsmb.2953.
- Kollman, J.M., A. Merdes, L. Mourey, and D.A. Agard. 2011. Microtubule nucleation by  $\gamma$ -tubulin complexes. *Nat. Rev. Mol. Cell Biol.* 12:709–721. doi:10.1038/NRM3209.
- Komarova, Y., C.O. De Groot, I. Grigoriev, S.M. Gouveia, E.L. Munteanu, J.M. Schober, S. Honnappa, R.M. Buey, C.C. Hoogenraad, M. Dogterom, G.G. Borisy, M.O. Steinmetz, and A. Akhmanova. 2009. Mammalian end binding proteins control persistent microtubule growth. *J. Cell Biol.* 184:691–706. doi:10.1083/jcb.200807179.
- Komarova, Y., G. Lansbergen, N. Galjart, F. Grosveld, G.G. Borisy, and A. Akhmanova. 2005. EB1 and EB3 control CLIP dissociation from the ends of growing microtubules. *Mol. Biol. Cell.* 16:5334–5345. doi:10.1091/MBE.E05-07-0614.
- Komarova, Y.A., A.S. Akhmanova, S.I. Kojima, N. Galjart, and G.G. Borisy. 2002. Cytoplasmic linker proteins promote microtubule rescue in vivo. *J. Cell Biol.* 159:589–599. doi:10.1083/jcb.200208058.
- Kuo, Y.W., and J. Howard. 2021. Cutting, Amplifying, and Aligning Microtubules with Severing Enzymes. *Trends Cell Biol.* 31:50–61. doi:10.1016/j.tcb.2020.10.004.
- Kuo, Y.W., O. Trottier, M. Mahamdeh, and J. Howard. 2019. Spastin is a dual-function enzyme that severs microtubules and promotes their regrowth to increase the number and mass of microtubules. *Proc. Natl. Acad. Sci. U. S. A.* 116:5533–5541. doi:10.1073/PNAS.1818824116.
- Lansbergen, G., I. Grigoriev, Y. Mimori-Kiyosue, T. Ohtsuka, S. Higa, I. Kitajima, J. Demmers, N. Galjart, A.B. Houtsmuller, F. Grosveld, and A. Akhmanova. 2006. CLASPs attach microtubule plus ends to the cell cortex through a complex with LL5beta. *Dev. Cell.* 11:21–32. doi:10.1016/j.devcel.2006.05.012.
- Lawrence, E.J., G. Arpag, S.R. Norris, and M. Zanic. 2018. Human CLASP2 specifically regulates microtubule catastrophe and rescue. *Mol. Biol. Cell.* 29:1168–1177. doi:10.1091/mbc.E18-01-0016.
- Lawrence, E.J., G. Arpag, C. Arnaiz, and M. Zanic. 2021. Ssn1 stabilizes dynamic microtubules and detects microtubule damage. *Elife.* 10. doi:10.7554/ELIFE.67282.
- Lawrence, E.J., M. Zanic, and L.M. Rice. 2020. CLASPs at a glance. *J. Cell Sci.* 133:1–7. doi:10.1242/jcs.243097.
- Leano, J.B., and K.C.S. Id. 2019. Structures of TOG1 and TOG2 from the human microtubule dynamics regulator. 1–25.
- Leano, J.B., S.L. Rogers, and K.C. Slep. 2013. A cryptic TOG domain with a distinct architecture underlies CLASP-dependent bipolar spindle formation. *Structure.* 21:939–950. doi:10.1016/j.str.2013.04.018.
- Lechler, T., and E. Fuchs. 2007. Desmoplakin: An unexpected regulator of microtubule organization in the epidermis. *J. Cell Biol.* 176:147–154. doi:10.1083/JCB.200609109/VIDEO-6.
- Lee, K.Y., B. Esmaeili, B. Zealley, and M. Mishima. 2015. Direct interaction between centralspindlin and PRC1 reinforces mechanical resilience of the central spindle. *Nat.*

- Commun.* 2015 61. 6:1–10. doi:10.1038/ncomms8290.
- Lee, T., K.J. Langford, J.M. Askham, A. Brüning-Richardson, and E.E. Morrison. 2008. MCAK associates with EB1. *Oncogene*. 27:2494–2500. doi:10.1038/SJ.ONC.1210867.
- Leterrier, C. 2018. The axon initial segment: an updated viewpoint. *J. Neurosci.* 38:1922–17. doi:10.1523/JNEUROSCI.1922-17.2018.
- Lin, Y., Y.L. Wei, and Z.Y. She. 2020. Kinesin-8 motors: regulation of microtubule dynamics and chromosome movements. *Chromosoma*. 129:99–110. doi:10.1007/S00412-020-00736-7.
- Liu, H., and T. Shima. 2022. Preference of CAMSAP3 for microtubules with expanded lattice contributes to stabilization of the minus end. *bioRxiv*. 2022.08.21.504720. doi:10.1101/2022.08.21.504720.
- Liu, P., M. Würtz, E. Zupa, S. Pfeffer, and E. Schiebel. 2021. Microtubule nucleation: The waltz between  $\gamma$ -tubulin ring complex and associated proteins. *Curr. Opin. Cell Biol.* 68:124–131. doi:10.1016/j.ceb.2020.10.004.
- Liu, P., E. Zupa, A. Neuner, A. Böhrer, J. Loerke, D. Flemming, T. Ruppert, T. Rudack, C. Peter, C. Spahn, O.J. Gruss, S. Pfeffer, and E. Schiebel. 2019. Insights into the assembly and activation of the microtubule nucleator  $\gamma$ -TuRC. doi:10.1038/s41586-019-1896-6.
- Loïdouce, I., J. Staub, T.G. Setty, N.P.T. Nguyen, A. Paoletti, and P.T. Tran. 2005. Ase1p Organizes Antiparallel Microtubule Arrays during Interphase and Mitosis in Fission Yeast. *Mol. Biol. Cell*. 16:1756. doi:10.1091/MBC.E04-10-0899.
- Lynn, N.A., E. Martinez, H. Nguyen, and J.Z. Torres. 2021. The Mammalian Family of Katanin Microtubule-Severing Enzymes. *Front. Cell Dev. Biol.* 9:1–18. doi:10.3389/fcell.2021.692040.
- Maiato, H., E.A.L. Fairley, C.L. Rieder, J.R. Swedlow, C.E. Sunkel, and W.C. Earnshaw. 2003. Human CLASP1 is an outer kinetochore component that regulates spindle microtubule dynamics. *Cell*. 113:891–904. doi:10.1016/S0092-8674(03)00465-3.
- Maiato, H., A. Khodjakov, and C.L. Rieder. 2005. Drosophila CLASP is required for the incorporation of microtubule subunits into fluxing kinetochore fibres. *Nat. Cell Biol.* 7:42–47. doi:10.1038/ncb1207.
- Maiato, H., P. Sampaio, C.L. Lemos, J. Findlay, M. Carmena, W.C. Earnshaw, and C.E. Sunkel. 2002. MAST/Orbit has a role in microtubule-kinetochore attachment and is essential for chromosome alignment and maintenance of spindle bipolarity. *J. Cell Biol.* 157:749–760. doi:10.1083/jcb.200201101.
- Majumdar, S., T. Kim, Z. Chen, S. Munyoki, S.-C. Tso, C.A. Brautigam, and L.M. Rice. 2018. An isolated CLASP TOG domain suppresses microtubule catastrophe and promotes rescue. *Mol. Biol. Cell*. 29:1359–1375. doi:10.1091/mbc.E17-12-0748.
- Manka, S.W., and C.A. Moores. 2018. mechanism of microtubule dynamic instability. 25. doi:10.1038/s41594-018-0087-8.
- Martin, M., and A. Akhmanova. 2018. Coming into Focus: Mechanisms of Microtubule Minus-End Organization. *Trends Cell Biol.* 28:574–588. doi:10.1016/j.tcb.2018.02.011.
- Maurer, S.P., F.J. Fourniol, G. Böhner, C.A. Moores, and T. Surrey. 2012. EBs recognize a

- nucleotide-dependent structural cap at growing microtubule ends. *Cell*. 149:371–382. doi:10.1016/j.cell.2012.02.049.
- McIntosh, J.R., M.K. Morphew, P.M. Grissom, S.P. Gilbert, and A. Hoenger. 2009. Lattice Structure of Cytoplasmic Microtubules in a Cultured Mammalian Cell. *J. Mol. Biol.* 394:177–182. doi:10.1016/j.jmb.2009.09.033.
- McNally, F.J., and A. Roll-Mecak. 2018. Microtubule-severing enzymes: From cellular functions to molecular mechanism. *J. Cell Biol.* 217:4057–4069. doi:10.1083/JCB.201612104.
- McNally, F.J., and R.D. Vale. 1993. Identification of katanin, an ATPase that severs and disassembles stable microtubules. *Cell*. 75:419–429. doi:10.1016/0092-8674(93)90377-3.
- McNally, K., A. Audhya, K. Oegema, and F.J. McNally. 2006. Katanin controls mitotic and meiotic spindle length. *J. Cell Biol.* 175:881–891. doi:10.1083/jcb.200608117.
- McNally, K.P., O.A. Bazirgan, and F.J. McNally. 2000. Two domains of p80 katanin regulate microtubule severing and spindle pole targeting by p60 katanin. *J. Cell Sci.* 113:1623–1633. doi:10.1242/jcs.113.9.1623.
- Meng, W., Y. Mushika, T. Ichii, and M. Takeichi. 2008. Anchorage of Microtubule Minus Ends to Adherens Junctions Regulates Epithelial Cell-Cell Contacts. *Cell*. 135:948–959. doi:10.1016/j.cell.2008.09.040.
- Miesch, J., R.T. Wimbish, M.-C. Velluz, and C. Aumeier. 2022. Phase separation of +TIP-networks regulates microtubule dynamics. *bioRxiv*. 2021.09.13.459419. doi:10.1101/2021.09.13.459419.
- Miller, P.M., A.W. Folkmann, A.R.R. Maia, N. Efimova, A. Efimov, and I. Kaverina. 2009. Golgi-derived CLASP-dependent microtubules control Golgi organization and polarized trafficking in motile cells. *Nat. Cell Biol.* 11:1069–1080. doi:10.1038/ncb1920.
- Miller, R.K., S. D’Silva, J.K. Moore, and H. V. Goodson. 2006. The CLIP-170 Orthologue Bik1p and Positioning the Mitotic Spindle in Yeast. *Curr. Top. Dev. Biol.* 76:49–87. doi:10.1016/S0070-2153(06)76002-1.
- Mimori-Kiyosue, Y., I. Grigoriev, G. Lansbergen, H. Sasaki, C. Matsui, F. Severin, N. Galjart, F. Grosveld, I. Vorobjev, S. Tsukita, and A. Akhmanova. 2005. CLASP1 and CLASP2 bind to EB1 and regulate microtubule plus-end dynamics at the cell cortex. *J. Cell Biol.* 168:141–153. doi:10.1083/jcb.200405094.
- Mitchison, T., and M. Kirschner. 1984. Dynamic instability of microtubule growth. *Nature*. 312:237–242. doi:10.1038/312237A0.
- Mogensen, M.M., A. Malik, M. Piel, V. Bouckson-castaing, and M. Bornens. 2000. Microtubule minus-end anchorage at centrosomal and non-centrosomal sites : the role of ninein. 3023:3013–3023.
- Monroe, N., and C.P. Hill. 2016. Meiotic Clade AAA ATPases: Protein Polymer Disassembly Machines. *J. Mol. Biol.* 428:1897–1911. doi:10.1016/J.JMB.2015.11.004.
- Montenegro Gouveia, S., K. Leslie, L.C. Kapitein, R.M. Buey, I. Grigoriev, M. Wagenbach, I. Smal, E. Meijering, C.C. Hoogenraad, L. Wordeman, M.O. Steinmetz, and A. Akhmanova. 2010. In vitro reconstitution of the functional interplay between MCAK

- and EB3 at microtubule plus ends. *Curr. Biol.* 20:1717–22. doi:10.1016/j.cub.2010.08.020.
- Mori, Y., Y. Inoue, S. Tanaka, S. Doda, S. Yamanaka, and H. Fukuchi. 2015a. Cep169, a Novel Microtubule Plus-End- Tracking Centrosomal Protein, Binds to CDK5RAP2 and Regulates Microtubule Stability. 1:1–13. doi:10.1371/journal.pone.0140968.
- Mori, Y., Y. Taniyama, S. Tanaka, H. Fukuchi, and Y. Terada. 2015b. Microtubule-bundling activity of the centrosomal protein, Cep169, and its binding to microtubules. *Biochem. Biophys. Res. Commun.* 467:754–759. doi:10.1016/J.BBRC.2015.10.069.
- Mukherjee, S., J.D. Diaz Valencia, S. Stewman, J. Metz, S. Monnier, U. Rath, A.B. Asenjo, R.A. Charafeddine, H.J. Sosa, J.L. Ross, A. Ma, and D.J. Sharp. 2012. Human Fidgetin is a microtubule severing the enzyme and minus-end depolymerase that regulates mitosis. *Cell Cycle.* 11:2359. doi:10.4161/CC.20849.
- Muroyama, A., and T. Lechler. 2017. Microtubule organization, dynamics and functions in differentiated cells. *Dev.* 144:3012–3021. doi:10.1242/dev.153171.
- Nakamura, M., N. Yagi, and T. Hashimoto. 2022. Finding a right place to cut: How katanin is targeted to cellular severing sites. *Quant. Plant Biol.* 3:1–7. doi:10.1017/qpb.2022.2.
- Nogales, E., M. Whittaker, R.A. Milligan, and K.H. Downing. 1999. High-resolution model of the microtubule. *Cell.* 96:79–88. doi:10.1016/S0092-8674(00)80961-7.
- Oakley, B.R., V. Paolillo, Y. Zheng, and D.G. Drubin. 2015.  $\gamma$ -Tubulin complexes in microtubule nucleation and beyond. 26:2957–2962. doi:10.1091/mbc.E14-11-1514.
- Oegema, K., C. Wiese, O.C. Martin, R.A. Milligan, A. Iwamatsu, T.J. Mitchison, and Y. Zheng. 1999. Characterization of two related Drosophila  $\gamma$ -tubulin complexes that differ in their ability to nucleate microtubules. *J. Cell Biol.* 144:721–733. doi:10.1083/JCB.144.4.721.
- Pandey, H., M. Popov, A. Goldstein-levitin, and L. Gheber. 2021. Mechanisms by Which Kinesin-5 Motors Perform Their Multiple Intracellular Functions. *Int. J. Mol. Sci.* 22. doi:10.3390/IJMS22126420.
- Pereira, A.L., J. Pereira, A.R.R. Maia, K. Drabek, C.L. Sayas, P.J. Hergert, M. Lince-faria, I. Matos, C. Duque, T. Stepanova, C.L. Rieder, W.C. Earnshaw, N. Galjart, and H. Maiato. 2006. Mammalian CLASP1 and CLASP2 Cooperate to Ensure Mitotic Fidelity by Regulating Spindle and Kinetochore Function. 17:4526–4542. doi:10.1091/mbc.E06.
- Perez, F., G.S. Diamantopoulos, R. Stalder, and T.E. Kreis. 1999. CLIP-170 highlights growing microtubule ends in vivo. *Cell.* 96:517–527. doi:10.1016/S0092-8674(00)80656-X.
- Piel, M., P. Meyer, A. Khodjakov, C.L. Rieder, and M. Bornens. 2000. The Respective Contributions of the Mother and Daughter Centrioles to Centrosome Activity and Behavior in Vertebrate Cells. *J. Cell Biol.* 149:317–330. doi:10.1083/JCB.149.2.317.
- Pierre, P., J. Scheel, J.E. Rickard, and T.E. Kreis. 1992a. CLIP-170 links endocytic vesicles to microtubules. *Cell.* 70:887–900. doi:10.1016/0092-8674(92)90240-D.
- Pierre, P., J. Scheel, J.E. Rickard, and T.E. Kreis. 1992b. CLIP-170 links endocytic vesicles to microtubules. *Cell.* 70:887–900. doi:10.1016/0092-8674(92)90240-D.



- Qiang, L., W. Yu, A. Andreadis, M. Luo, and P.W. Baas. 2006. Tau Protects Microtubules in the Axon from Severing by Katanin. *J. Neurosci.* 26:3120–3129. doi:10.1523/JNEUROSCI.5392-05.2006.
- Rai, A., T. Liu, S. Glauser, E.A. Katrukha, J. Estévez-Gallego, R. Rodríguez-García, W.S. Fang, J.F. Díaz, M.O. Steinmetz, K.H. Altmann, L.C. Kapitein, C.A. Moores, and A. Akhmanova. 2019. Taxanes convert regions of perturbed microtubule growth into rescue sites. *Nat. Mater.* doi:10.1038/s41563-019-0546-6.
- Rai, A., T. Liu, E.A. Katrukha, J. Estevez-Gallego, S.W. Manka, I. Paterson, J. Fernando Diaz, L.C. Kapitein, C.A. Moores, and A. Akhmanova. 2021. Lattice defects induced by microtubule-stabilizing agents exert a long-range effect on microtubule growth by promoting catastrophes. *Proc. Natl. Acad. Sci. U. S. A.* 118. doi:10.1073/pnas.2112261118.
- Rale, M., B. Romer, B.P. Mahon, S.M. Travis, and S. Petry. 2022. The conserved centrosomal motif,  $\gamma$ TuNA, forms a dimer that directly activates microtubule nucleation by the  $\gamma$ -tubulin ring complex ( $\gamma$ TuRC). 2. 1–47.
- Reck-Peterson, S.L., W.B. Redwine, R.D. Vale, and A.P. Carter. 2018. The cytoplasmic dynein transport machinery and its many cargoes. *Nat. Rev. Mol. Cell Biol.* 2018 196. 19:382–398. doi:10.1038/s41580-018-0004-3.
- Rice, L.M., E.A. Montabana, and D.A. Agard. 2008. The lattice as allosteric effector: Structural studies of  $\alpha\beta$ - and  $\gamma$ -tubulin clarify the role of GTP in microtubule assembly. *Proc. Natl. Acad. Sci. U. S. A.* 105:5378–5383. doi:10.1073/PNAS.0801155105/SUPPL\_FILE/0801155105SI.PDF.
- Richard McIntosh, J., E. O’Toole, G. Morgan, J. Austin, E. Ulyanov, F. Ataullakhanov, and N. Gudimchuk. 2018. Microtubules grow by the addition of bent guanosine triphosphate tubulin to the tips of curved protofilaments. *J. Cell Biol.* 217:2691–2708. doi:10.1083/jcb.201802138.
- Roll-Mecak, A., and R.D. Vale. 2005. The Drosophila Homologue of the Hereditary Spastic Paraplegia Protein, Spastin, Severs and Disassembles Microtubules. *Curr. Biol.* 15:650–655. doi:10.1016/J.CUB.2005.02.029.
- Roll-Mecak, A., and R.D. Vale. 2008. Structural basis of microtubule severing by the hereditary spastic paraplegia protein spastin. *Nature.* 451:363–367. doi:10.1038/NATURE06482.
- Roostalu, J., N.I. Cade, and T. Surrey. 2015. Complementary activities of TPX2 and chTOG constitute an efficient importin-regulated microtubule nucleation module. 17. doi:10.1038/ncb3241.
- Roostalu, J., E. Schiebel, and A. Khmelinskii. 2010. Cell cycle control of spindle elongation. *Cell Cycle.* 9:1084–1090. doi:10.4161/cc.9.6.11017.
- Roostalu, J., and T. Surrey. 2017. Microtubule nucleation: Beyond the template. *Nat. Rev. Mol. Cell Biol.* 18:702–710. doi:10.1038/NRM.2017.75.
- Roostalu, J., C. Thomas, N.I. Cade, S. Kunzelmann, I.A. Taylor, and T. Surrey. 2020. The speed of GTP hydrolysis determines GTP cap size and controls microtubule stability. 1–22.
- Roth, D., B.P. Fitton, N.P. Chmel, N. Wasiluk, and A. Straube. 2019. Spatial positioning of

- EB family proteins at microtubule tips involves distinct nucleotide-dependent binding properties. doi:10.1242/jcs.219550.
- Sanchez, A.D., and J.L. Feldman. 2017. Microtubule-organizing centers: from the centrosome to non-centrosomal sites. *Curr. Opin. Cell Biol.* 44:93–101. doi:10.1016/j.ceb.2016.09.003.
- Satake, T., K. Yamashita, K. Hayashi, S. Miyatake, M. Tamura-Nakano, H. Doi, Y. Furuta, G. Shioi, E. Miura, Y.H. Takeo, K. Yoshida, H. Yahikozawa, N. Matsumoto, M. Yuzaki, and A. Suzuki. 2017. MTCL1 plays an essential role in maintaining Purkinje neuron axon initial segment. *EMBO J.* 36:1227–1242. doi:10.15252/embj.201695630.
- Sato, Y., K. Hayashi, Y. Amano, M. Takahashi, S. Yonemura, I. Hayashi, H. Hirose, S. Ohno, and A. Suzuki. 2014. MTCL1 crosslinks and stabilizes non-centrosomal microtubules on the Golgi membrane. *Nat. Commun.* 5:1–14. doi:10.1038/ncomms6266.
- Saunders, A.M., J. Powers, S. Strome, and W.M. Saxton. 2007. Kinesin-5 acts as a brake in anaphase spindle elongation. *Curr. Biol.* 17:1–5. doi:10.1016/j.cub.2007.05.001.
- Schaedel, L., K. John, J. Gaillard, M. V. Nachury, L. Blanchoin, and M. Thery. 2015. Microtubules self-repair in response to mechanical stress. *Nat. Mater.* 14:1156–1163. doi:10.1038/nmat4396.
- Schaedel, L., S. Triclin, D. Chrétien, A. Abrieu, C. Aumeier, J. Gaillard, L. Blanchoin, M. Théry, and K. John. 2019. Lattice defects induce microtubule self-renewal. *Nat. Phys.* doi:10.1038/s41567-019-0542-4.
- Scholey, J.E., S. Nithianantham, J.M. Scholey, and J. Al-Bassam. 2014. Structural basis for the assembly of the mitotic motor kinesin-5 into bipolar tetramers. *Elife.* 2014. doi:10.7554/ELIFE.02217.
- Sharp, D.J., and J.L. Ross. 2012. Microtubule-severing enzymes at the cutting edge. *J. Cell Sci.* 125:2561–2569. doi:10.1242/jcs.101139.
- She, Z.-Y., and W.-X. Yang. 2017. Molecular mechanisms of kinesin-14 motors in spindle assembly and chromosome segregation. *J. Cell Sci.* 130:2097–2110. doi:10.1242/jcs.200261.
- She, Z.Y., N. Zhong, K.W. Yu, Y. Xiao, Y.L. Wei, Y. Lin, Y.L. Li, and M.H. Lu. 2020. Kinesin-5 Eg5 is essential for spindle assembly and chromosome alignment of mouse spermatocytes. *Cell Div.* 15:1–18. doi:10.1186/S13008-020-00063-4/FIGURES/7.
- Short, K.M., and T.C. Cox. 2006. Subclassification of the RBCC/TRIM superfamily reveals a novel motif necessary for microtubule binding. *J. Biol. Chem.* 281:8970–8980. doi:10.1074/jbc.M512755200.
- Siahaan, V., J. Krattenmacher, A.A. Hyman, S. Diez, A. Hernández-Vega, Z. Lansky, and M. Braun. 2019. Kinetically distinct phases of tau on microtubules regulate kinesin motors and severing enzymes. *Nat. Cell Biol.* 21:1086–1092. doi:10.1038/S41556-019-0374-6.
- Skube, S.B., J.M. Chaverri, and H. V. Goodson. 2010. Effect of GFP tags on the localization of EB1 and EB1 fragments in vivo. *Cytoskeleton.* 67:1–12. doi:10.1002/cm.20409.
- Srayko, M., E.T. O’Toole, A.A. Hyman, and T. Müller-Reichert. 2006. Katanin disrupts the microtubule lattice and increases polymer number in *C. elegans* meiosis. *Curr. Biol.* 16:1944–1949. doi:10.1016/J.CUB.2006.08.029.

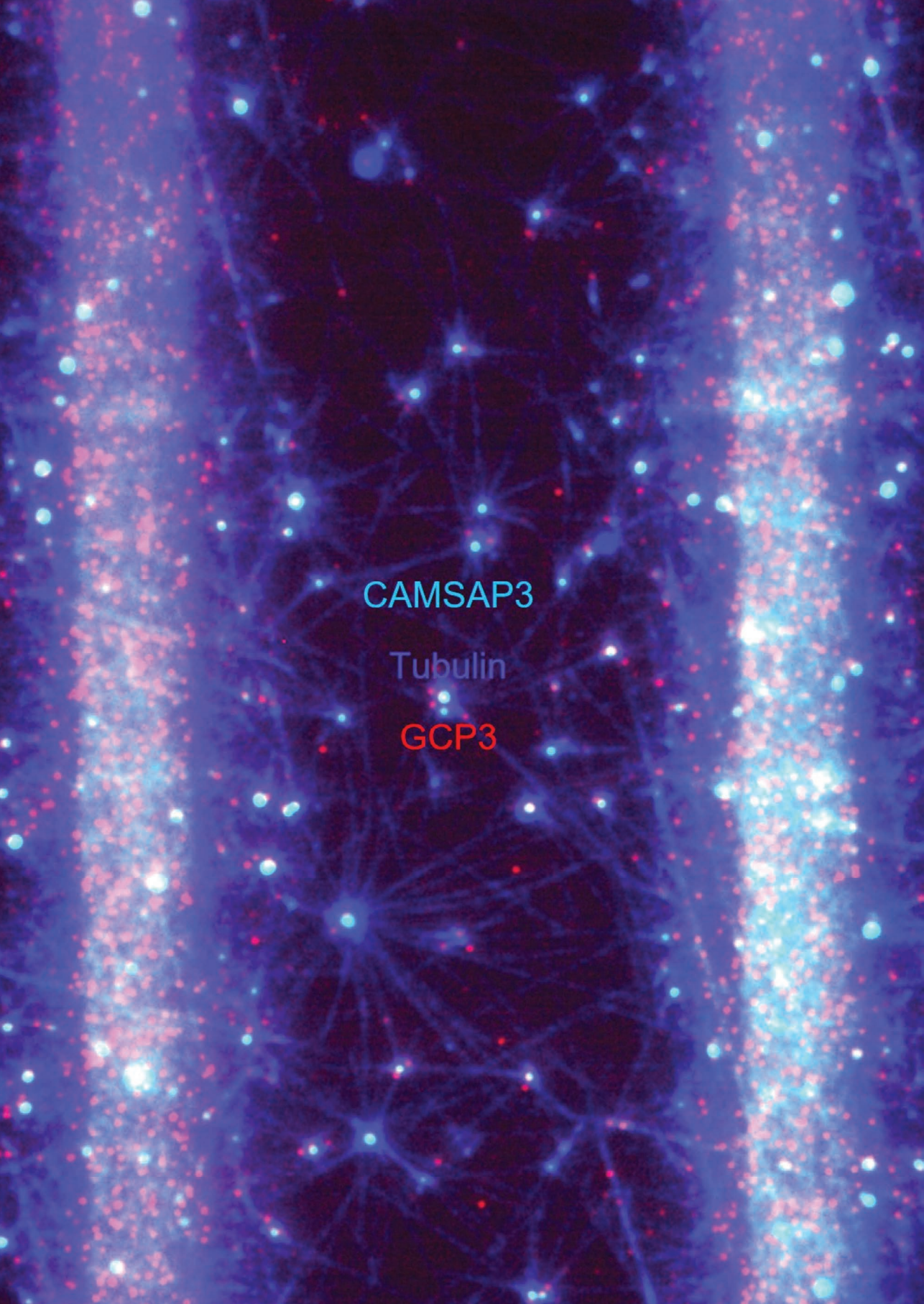
- Strothman, C., V. Farmer, G. Arpag, N. Rodgers, M. Podolski, S. Norris, R. Ohi, and M. Zanic. 2019. Microtubule minus-end stability is dictated by the tubulin off-rate. *J. Cell Biol.* 218:2841–2853. doi:10.1083/JCB.201905019.
- Subramanian, R., E.M. Wilson-Kubalek, C.P. Arthur, M.J. Bick, E.A. Campbell, S.A. Darst, R.A. Milligan, and T.M. Kapoor. 2010. Insights into antiparallel microtubule crosslinking by PRC1, a conserved nonmotor microtubule binding protein. *Cell.* 142:433–443. doi:10.1016/j.cell.2010.07.012.
- Tan, R., P.J. Foster, D.J. Needleman, and R.J. McKenney. 2018. Cooperative Accumulation of Dynein-Dynactin at Microtubule Minus-Ends Drives Microtubule Network Reorganization. *Dev. Cell.* 44:233–247.e4. doi:10.1016/J.DEVCEL.2017.12.023/ATTACHMENT/8774BBEC-BB2E-45E9-BD5C-64816F9761AF/MMC8.MP4.
- Tanaka, N., W. Meng, S. Nagae, and M. Takeichi. 2012. Nezha / CAMSAP3 and CAMSAP2 cooperate in epithelial-specific organization of noncentrosomal microtubules. 109:20029–20034. doi:10.1073/pnas.1218017109.
- Tanenbaum, M.E., R.H. Medema, and A. Akhmanova. 2011. Regulation of localization and activity of the microtubule depolymerase MCAK. *Bioarchitecture.* 1:80–87. doi:10.4161/bioa.1.2.15807.
- Tariq, A., L. Green, J.C.G. Jeynes, C. Soeller, and J.G. Wakefield. 2020. In vitro reconstitution of branching microtubule nucleation. *Elife.* 9. doi:10.7554/ELIFE.49769.
- Teixidó-Travesa, N., J. Roig, and J. Lüders. 2012. The where, when and how of microtubule nucleation - one ring to rule them all. *J. Cell Sci.* 125:4445–4456. doi:10.1242/jcs.106971.
- Thawani, A., R.S. Kadzik, and S. Petry. 2018. XMAP215 is a microtubule nucleation factor that functions synergistically with the  $\gamma$ -tubulin ring complex. *Nat. Cell Biol.* 20:575–585. doi:10.1038/S41556-018-0091-6.
- Thawani, A., and S. Petry. 2021. Molecular insight into how  $\gamma$ -TuRC makes microtubules. *J. Cell Sci.* 134. doi:10.1242/JCS.245464.
- Thawani, A., M.J. Rale, N. Coudray, G. Bhabha, H.A. Stone, J.W. Shaevitz, and S. Petry. 2020. The transition state and regulation of  $\gamma$ -TuRC-mediated microtubule nucleation revealed by single molecule microscopy. *Elife.* 9:1–34. doi:10.7554/ELIFE.54253.
- Thawani, A., H.A. Stone, J.W. Shaevitz, and S. Petry. 2019. Spatiotemporal organization of branched microtubule networks. *Elife.* 8. doi:10.7554/ELIFE.43890.
- Théry, M., and L. Blanchoin. 2021. Microtubule self-repair. *Curr. Opin. Cell Biol.* 68:144–154. doi:10.1016/j.ceb.2020.10.012.
- Tovey, C.A., and P.T. Conduit. 2018. Microtubule nucleation by  $\gamma$ -tubulin complexes and beyond. *Essays Biochem.* 62:765–780. doi:10.1042/EBC20180028.
- Tovey, C.A., C. Tsuji, A. Egerton, F. Bernard, A. Guichet, M. De La Roche, and P.T. Conduit. 2021. Autoinhibition of  $\gamma$ -tubulin binding to  $\gamma$ -turcs prevents ectopic microtubule nucleation and cell division defects. *J. Cell Biol.* 220. doi:10.1083/jcb.202010020.
- Triclin, S., D. Inoue, J. Gaillard, Z.M. Htet, M.E. DeSantis, D. Portran, E. Derivery, C. Aumeier, L. Schaedel, K. John, C. Leterrier, S.L. Reck-Peterson, L. Blanchoin, and M.

- Théry. 2021. Self-repair protects microtubules from destruction by molecular motors. *Nat. Mater.* 20:883–891. doi:10.1038/s41563-020-00905-0.
- Tsuchiya, K., and G. Goshima. 2021. Microtubule-associated proteins promote microtubule generation in the absence of  $\gamma$ -tubulin in human colon cancer cells. *J. Cell Biol.* 220. doi:10.1083/JCB.202104114.
- Vale, R.D. 1991. Severing of stable microtubules by a mitotically activated protein in *Xenopus* egg extracts. *Cell.* 64:827–839. doi:10.1016/0092-8674(91)90511-V.
- Valenstein, M.L., and A. Roll-Mecak. 2016. Graded Control of Microtubule Severing by Tubulin Glutamylation. *Cell.* 164:911–921. doi:10.1016/j.cell.2016.01.019.
- Vemu, A., E. Szczesna, E.A. Zehr, J.O. Spector, N. Grigorieff, A.M. Deaconescu, and A. Roll-Mecak. 2018. Severing enzymes amplify microtubule arrays through lattice GTP-tubulin incorporation. *Science (80-. ).* 361. doi:10.1126/science.aau1504.
- Verhey, K.J., and J. Gaertig. 2007. The tubulin code. *Cell Cycle.* 6:2152–2160. doi:10.4161/cc.6.17.4633.
- Verma, V., and T.J. Maresca. 2019. Direct observation of branching MT nucleation in living animal cells. *J. Cell Biol.* 218:2829–2840. doi:10.1083/JCB.201904114.
- Vineethakumari, C., and J. Lüders. 2022. Microtubule Anchoring: Attaching Dynamic Polymers to Cellular Structures. *Front. Cell Dev. Biol.* 10:1–11. doi:10.3389/fcell.2022.867870.
- Walczak, C.E., and S.L. Shaw. 2010. A MAP for bundling microtubules. *Cell.* 142:364–367. doi:10.1016/j.cell.2010.07.023.
- Walker, R.A., E.T. O'Brien, N.K. Pryer, M.F. Soboeiro, W.A. Voter, H.P. Erickson, and E.D. Salmon. 1988. Dynamic instability of individual microtubules analyzed by video light microscopy: rate constants and transition frequencies. *J. Cell Biol.* 107:1437–1448. doi:10.1083/jcb.107.4.1437.
- Wang, H., I. Brust-Mascher, G. Civelekoglu-Scholey, and J.M. Scholey. 2013. Patronin mediates a switch from kinesin-13-dependent poleward flux to anaphase b spindle elongation. *J. Cell Biol.* 203:35–46. doi:10.1083/jcb.201306001.
- Wang, S., D. Wu, S. Quintin, R.A. Green, D.K. Cheerambathur, S.D. Ochoa, A. Desai, and K. Oegema. 2015a. NOCA-1 functions with  $\gamma$ -tubulin and in parallel to Patronin to assemble non-centrosomal microtubule arrays in *C. elegans*. *Elife.* 4:1–34. doi:10.7554/eLife.08649.
- Wang, W., S. Cantos-Fernandes, Y. Lv, H. Kuerban, S. Ahmad, C. Wang, and B. Gigant. 2017. Insight into microtubule disassembly by kinesin-13s from the structure of Kif2C bound to tubulin. *Nat. Commun.* 2017 81. 8:1–11. doi:10.1038/s41467-017-00091-9.
- Wang, W., L. Cao, C. Wang, B. Gigant, and M. Knossow. 2015b. Kinesin, 30 years later: Recent insights from structural studies. *Protein Sci.* 24:1047–1056. doi:10.1002/PRO.2697.
- Wang, Z., T. Wu, L. Shi, L. Zhang, W. Zheng, J.Y. Qu, R. Niu, and R.Z. Qi. 2010. Conserved Motif of CDK5RAP2 Mediates Its Localization to Centrosomes and the Golgi Complex \*. 285:22658–22665. doi:10.1074/jbc.M110.105965.

- Watanabe, S., F. Meitinger, A.K. Shiau, K. Oegema, and A. Desai. 2020. Centriole-independent mitotic spindle assembly relies on the PCNT–CDK5RAP2 pericentriolar matrix. *J. Cell Biol.* 219. doi:10.1083/jcb.202006010.
- Waterman-Storer, C.M., and E.D. Salmon. 1997. Actomyosin-based retrograde flow of microtubules in the lamella of migrating epithelial cells influences microtubule dynamic instability and turnover and is associated with microtubule breakage and treadmilling. *J. Cell Biol.* 139:417–434. doi:10.1083/JCB.139.2.417.
- Weisbrich, A., S. Honnappa, R. Jaussi, O. Okhrimenko, D. Frey, I. Jelesarov, A. Akhmanova, and M.O. Steinmetz. 2007. Structure–function relationship of CAP–Gly domains. *Nat. Struct. Mol. Biol.* 14:959–967. doi:10.1038/NSMB1291.
- Wieczorek, M., T.L. Huang, L. Urnavicius, K.C. Hsia, and T.M. Kapoor. 2020a. MZT Proteins Form Multi-Faceted Structural Modules in the  $\gamma$ -Tubulin Ring Complex. *Cell Rep.* 31:107791. doi:10.1016/j.celrep.2020.107791.
- Wieczorek, M., S.C. Ti, L. Urnavicius, K.R. Molloy, A. Aher, B.T. Chait, and T.M. Kapoor. 2021. Biochemical reconstitutions reveal principles of human  $\gamma$ -TuRC assembly and function. *J. Cell Biol.* 220. doi:10.1083/JCB.202009146.
- Wieczorek, M., L. Urnavicius, S.C. Ti, K.R. Molloy, B.T. Chait, and T.M. Kapoor. 2020b. Asymmetric Molecular Architecture of the Human  $\gamma$ -Tubulin Ring Complex. *Cell.* 180:165–175.e16. doi:10.1016/j.cell.2019.12.007.
- Wiese, C., and Y. Zheng. 2000. A new function for the  $\gamma$ -tubulin ring complex as a microtubule minus-end cap. *Nat. Cell Biol.* 2:358–364. doi:10.1038/35014051.
- Woodruff, J.B., B.F. Gomes, P.O. Widlund, J. Mahamid, A. Honigmann, A.A. Hyman, J.B. Woodruff, B.F. Gomes, P.O. Widlund, J. Mahamid, and A. Honigmann. 2017. The Centrosome Is a Selective Condensate that Nucleates Microtubules by Concentrating Tubulin Article The Centrosome Is a Selective Condensate that Nucleates Microtubules by Concentrating Tubulin. *Cell.* 169:1066–1071.e10. doi:10.1016/j.cell.2017.05.028.
- Wu, J., and A. Akhmanova. 2017a. Microtubule-Organizing Centers.
- Wu, J., and A. Akhmanova. 2017b. Microtubule-Organizing Centers. <https://doi.org/10.1146/annurev-cellbio-100616-060615>. 33:51–75. doi:10.1146/ANNUREV-CELLBIO-100616-060615.
- Wu, J., C. de Heus, Q. Liu, B.P. Bouchet, I. Noordstra, K. Jiang, S. Hua, M. Martin, C. Yang, I. Grigoriev, E.A. Katrukha, A.F.M. Altelaar, C.C. Hoogenraad, R.Z. Qi, J. Klumperman, and A. Akhmanova. 2016. Molecular Pathway of Microtubule Organization at the Golgi Apparatus. *Dev. Cell.* 39:44–60. doi:10.1016/j.devcel.2016.08.009.
- Wu, Y.F.O., A.T. Bryant, N.T. Nelson, A.G. Madey, G.F. Fernandes, and H. V. Goodson. 2021. Overexpression of the microtubule-binding protein CLIP-170 induces a +TIP network superstructure consistent with a biomolecular condensate. 16. 1–31 pp.
- Würtz, M., A. Böhler, A. Neuner, E. Zupa, L. Rohland, P. Liu, B.J.A. Vermeulen, S. Pfeffer, S. Eustermann, and E. Schiebel. 2021. Reconstitution of the recombinant human  $\gamma$ -tubulin ring complex. *Open Biol.* 11. doi:10.1098/rsob.200325.
- Würtz, M., E. Zupa, E.S. Atorino, A. Neuner, A. Böhler, A.S. Rahadian, B.J.A. Vermeulen, G. Tonon, S. Eustermann, E. Schiebel, and S. Pfeffer. 2022. Modular assembly of the

- principal microtubule nucleator  $\gamma$ -TuRC. *Nat. Commun.* 13. doi:10.1038/s41467-022-28079-0.
- Zanic, M., P.O. Widlund, A.A. Hyman, and J. Howard. 2013. Synergy between XMAP215 and EB1 increases microtubule growth rates to physiological levels. *Nat. Cell Biol.* 15:688–693. doi:10.1038/ncb2744.
- Zehr, E.A., A. Szyk, E. Szczesna, and A. Roll-Mecak. 2020. Katanin Grips the  $\beta$ -Tubulin Tail through an Electropositive Double Spiral to Sever Microtubules. *Dev. Cell.* 52:118–131.e6. doi:10.1016/j.devcel.2019.10.010.
- Zhang, D., G.C. Rogers, D.W. Buster, and D.J. Sharp. 2007. Three microtubule severing enzymes contribute to the “Pacman- flux” machinery that moves chromosomes. *J. Cell Biol.* 177:231–242. doi:10.1083/jcb.200612011.
- Zhang, R., G.M. Alushin, A. Brown, and E. Nogales. 2015. Mechanistic origin of microtubule dynamic instability and its modulation by EB proteins. *Cell.* 162:849–859. doi:10.1016/j.cell.2015.07.012.
- Zhang, R., B. LaFrance, and E. Nogales. 2018. Separating the effects of nucleotide and EB binding on microtubule structure. *Proc. Natl. Acad. Sci. U. S. A.* 115:E6191–E6200. doi:10.1073/pnas.1802637115.
- Zheng, Y., R.A. Buchwalter, C. Zheng, E.M. Wight, J. V. Chen, and T.L. Megraw. 2020. A perinuclear microtubule-organizing centre controls nuclear positioning and basement membrane secretion. *Nat. Cell Biol.* 22:297–309. doi:10.1038/s41556-020-0470-7.
- Zheng, Y., M.L. Wong, B. Alberts, and T. Mitchison. 1995. Nucleation of microtubule assembly by a  $\gamma$ -tubulin-containing ring complex. *Nat.* 1995 3786557. 378:578–583. doi:10.1038/378578a0.
- Zimmermann, F., M. Serna, A. Ezquerro, R. Fernandez-Leiro, O. Llorca, and J. Luders. 2020. Assembly of the asymmetric human  $\gamma$ -tubulin ring complex by RUVBL1-RUVBL2 AAA ATPase. *Sci. Adv.* 6:1–20. doi:10.1126/SCIADV.ABE0894.
- Zupa, E., P. Liu, M. Würtz, E. Schiebel, and S. Pfeffer. 2021. The structure of the  $\gamma$ -TuRC: a 25-years-old molecular puzzle. *Curr. Opin. Struct. Biol.* 66:15–21. doi:10.1016/J.SBI.2020.08.008.





CAMSAP3

Tubulin

GCP3



# 2

## **CAMSAP-driven microtubule release from $\gamma$ -TuRC and its regulation by nucleation-promoting factors**

Dipti Rai<sup>1</sup>, Shasha Hua<sup>1,2,3</sup>, Joeske L. Monster<sup>1,4</sup>, Riccardo Stucchi<sup>1,5</sup>, Kelly Stecker<sup>5</sup>, Yaqian Zhang<sup>2,3</sup>, Eugene A. Katrukha<sup>1</sup>, Maarten Altelaar<sup>5</sup>, Michal Wieczorek<sup>6</sup>, Kai Jiang<sup>1,2,3#</sup> and Anna Akhmanova<sup>1#</sup>

<sup>1</sup> Cell Biology, Department of Biology, Faculty of Science, Utrecht University, Padualaan 8, 3584 CH Utrecht, the Netherlands

<sup>2</sup> The State Key Laboratory Breeding Base of Basic Science of Stomatology (Hubei-MOST) & Key Laboratory of Oral Biomedicine Ministry of Education, School & Hospital of Stomatology, Wuhan University, Wuhan 430071, China

<sup>3</sup> Medical Research Institute, Wuhan University, Wuhan 430071, China

<sup>4</sup> Center for Molecular Medicine, University Medical Center Utrecht, Utrecht, 3584 CX, The Netherlands

<sup>5</sup> Mass Spectrometry and Proteomics, Bijvoet Center for Biomolecular Research, Utrecht Institute for Pharmaceutical Sciences and the Netherlands Proteomics Center, Utrecht University, Padualaan 8, 3584 CH Utrecht, the Netherlands

<sup>6</sup> Department of Biology, ETH Zürich, Otto-Stern-Weg 5, 8093 Zürich, Switzerland

# Corresponding authors: jiangkai@whu.edu.cn; a.akhmanova@uu.nl

**bioRxiv 2022.08.03.502613**; doi: <https://doi.org/10.1101/2022.08.03.502613>

**Abstract**

$\gamma$ -tubulin ring complex ( $\gamma$ -TuRC) is the major microtubule-nucleating factor. After nucleation, microtubules can be released from  $\gamma$ -TuRC and stabilized by other proteins, such as CAMSAPs, but the biochemical cross-talk between minus-end regulation pathways is poorly understood. Here, we reconstituted this process *in vitro* using purified components. We found that all CAMSAP proteins could bind to the minus-ends of  $\gamma$ -TuRC-attached microtubules. CAMSAP2 and CAMSAP3, which decorate and stabilize growing minus ends, but not the minus-end tracking protein CAMSAP1 induced microtubule release from  $\gamma$ -TuRC. CDK5RAP2, a  $\gamma$ -TuRC-interactor, and CLASP2, a regulator of microtubule growth, stimulated  $\gamma$ -TuRC-dependent microtubule nucleation, but only CDK5RAP2 inhibited CAMSAP-driven microtubule detachment by suppressing CAMSAP binding to  $\gamma$ -TuRC-anchored minus ends. CDK5RAP2 also improved  $\gamma$ -TuRC selectivity for 13- rather than 14- protofilament microtubules in microtubule-capping assays. Our results support a model whereby CAMSAPs exploit an imperfect attachment between  $\gamma$ -TuRC and the nucleated microtubule to promote minus-end elongation and release, whereas CDK5RAP2 improves the fit between  $\gamma$ -TuRC and 13-protofilament microtubules and enhances nucleation.

**Introduction**

Microtubule organization in animal cells is a major determinant of cell architecture and polarity<sup>1</sup>. This organization critically depends on the activity of microtubule-organizing centers (MTOCs) – structures that can nucleate microtubules and stabilize and anchor their minus ends<sup>2-4</sup>. The major microtubule-nucleating factor in cells is the  $\gamma$ -tubulin ring complex ( $\gamma$ -TuRC) – a cone-shaped macromolecular assembly that is required for the kinetically dominant pathway of generating new microtubules from tubulin dimers<sup>5, 6</sup>.  $\gamma$ -TuRC localization and activity are controlled by a variety of tethering and nucleation-promoting factors, such as augmin, pericentrin, CDK5RAP2 and chTOG<sup>6, 7</sup>.  $\gamma$ -TuRC can also cap microtubule minus ends<sup>8</sup> and participate in their anchoring, possibly with the aid of additional MTOC components<sup>9</sup>. An alternative well-studied pathway of minus-end stabilization and anchoring depends on the members of CAMSAP/Patronin family<sup>10-13</sup>. These proteins specifically recognize free, uncapped microtubule minus ends because their signature domain, CKK, binds to a minus-end-specific site between flared protofilaments<sup>14</sup>. Recently, a role of CAMSAP2 in  $\gamma$ -tubulin-independent microtubule nucleation has also been proposed<sup>15</sup>.

Importantly, since in  $\gamma$ -TuRC-capped microtubules protofilaments at the minus ends are straight<sup>16, 17</sup>, they should not be able to bind to CAMSAPs. However, recent structural work

revealed that purified  $\gamma$ -TuRCs are strikingly asymmetric, and their structure does not fully match with that of a complete 13-protofilament microtubule<sup>18-21</sup>. This finding raises the possibility that  $\gamma$ -TuRC-nucleated microtubules may not be fully attached to their template, and some protofilaments might have a flared conformation that would permit CAMSAP binding. Furthermore, since the microtubule-nucleating activity of purified  $\gamma$ -TuRC turned out to be quite low<sup>18, 22</sup>, a potential mechanism of stimulating nucleation would be to alter  $\gamma$ -TuRC conformation to make it more similar to the microtubule structure<sup>6, 7, 23, 24</sup>. To explore these possibilities, we have set up in vitro reconstitution assays and confirmed that purified  $\gamma$ -TuRC has by itself a rather low activity that can be enhanced by nucleation-promoting factors, microtubule polymerase chTOG, and  $\gamma$ -TuRC associated protein CDK5RAP2<sup>25-27</sup>. We further established that the microtubule-nucleation activity of  $\gamma$ -TuRC can also be stimulated by CLASP2, a protein known to strongly enhance microtubule outgrowth from stabilized microtubule seeds<sup>28</sup>.

We then set up assays where the activities of  $\gamma$ -TuRC, CAMSAPs and CDK5RAP2 or CLASP2 could be observed simultaneously. We found that while microtubules almost never detached from  $\gamma$ -TuRC when it was present alone or together with CDK5RAP2 or CLASP2, CAMSAPs could bind to a subset of  $\gamma$ -TuRC-anchored minus ends and trigger their detachment. While minus-end binding was observed with all three CAMSAPs, microtubule release from  $\gamma$ -TuRC was only induced by CAMSAP2 and 3, which decorate and stabilize growing microtubule minus ends, but not by CAMSAP1, which tracks growing minus ends without decorating them<sup>29</sup>. We also found that CDK5RAP2, but not CLASP2 suppressed CAMSAP binding and subsequent microtubule release. We reasoned that this could be due to the ability of CDK5RAP2 to alter  $\gamma$ -TuRC conformation so that it would fit the regular microtubule structure better. We found support for this idea in microtubule-capping assays, where CDK5RAP2 made  $\gamma$ -TuRC more selective for 13-protofilament microtubules. Together, our results indicate that CAMSAPs can bind to a subpopulation of microtubule minus ends anchored at  $\gamma$ -TuRC, likely because they are only partially attached to their template. By decorating and stabilizing the growing microtubule minus ends, CAMSAP2 and 3 help to generate the force required to push the  $\gamma$ -TuRC cap away. This process can be counteracted by the  $\gamma$ -TuRC-binding factor CDK5RAP2, possibly because it improves the fit between the  $\gamma$ -TuRC and a microtubule.

## Results

### *Human CDK5RAP2, CLASP2 and chTOG promote microtubule nucleation by purified $\gamma$ -TuRC*

To obtain purified  $\gamma$ -TuRC, we have used CRISPR-Cas9-mediated gene editing to generate a homozygous knock-in HEK293T cell line where the GCP3-encoding gene was modified by a C-terminal insertion of the GFP and a Twin-Strep-tag (two Strep-tag II in tandem, abbreviated as GFP-SII, Extended data Fig. 1a,b). Western blotting of this cell line showed that the whole GCP3 pool was shifted up by ~30 kDa (Extended data Fig. 1c), and fluorescence microscopy revealed GFP signal was present diffusely in the cytoplasm and concentrated at the centrosome, as expected for a  $\gamma$ -TuRC component (Extended data Fig. 1d). Twin-Strep-tag based purification (Extended data Fig. 1e) yielded protein complexes, which, based on Western blotting and mass spectrometry, contained all expected  $\gamma$ -TuRC components (Extended data Fig. 1f, g and Supplementary Table 1). In these  $\gamma$ -TuRC preparations, we detected two proteins known to co-purify with  $\gamma$ -TuRC, NEDD1 (Neural precursor cell expressed developmentally down-regulated protein 1) and NME7 (Nucleoside diphosphate kinase 7)<sup>18-20, 26, 30, 31</sup> (Extended data Fig. 1g), but no other known  $\gamma$ -TuRC binding partners or microtubule nucleation-promoting factors. 3D reconstruction of negative stain transmission EM micrographs of purified  $\gamma$ -TuRCs showed a cone-like complex (Fig. 1a and see below), matching the recently published  $\gamma$ -TuRC structures<sup>17-21</sup>. We also characterized the fluorescence intensity of purified  $\gamma$ -TuRC and compared it to that of single GFP molecules and GFP-EB3, which is known to be a dimer<sup>32</sup>. In these measurements, GFP-EB3 looked brighter than GFP, as expected, and GCP3-GFP-containing  $\gamma$ -TuRC showed a rather broad distribution (Fig. 1b). We build the expected intensity distributions of GFP oligomers using single GFP intensity distribution as a starting point and fitted the GCP3-GFP distribution as a sum of these "basis" distributions. This fit showed two clearly visible peaks, the first coinciding with single GFP-intensity and the second peak lying in the range of 4-5 GFP-molecules. This fits with the fact that  $\gamma$ -TuRCs derived from cells where all GCP3 subunits bear a GFP tag would be expected to contain five GCP3-GFP subunits<sup>18-21, 24</sup>.

We next immobilized purified GFP-tagged  $\gamma$ -TuRCs on coverslips using a biotinylated GFP nanobody, observed microtubule nucleation in the presence of Rhodamine-labeled tubulin by Total Internal Reflection Fluorescence (TIRF) microscopy (Extended data Fig. 1h) and counted the percentage of  $\gamma$ -TuRCs nucleating microtubules within three consecutive 10 min periods.

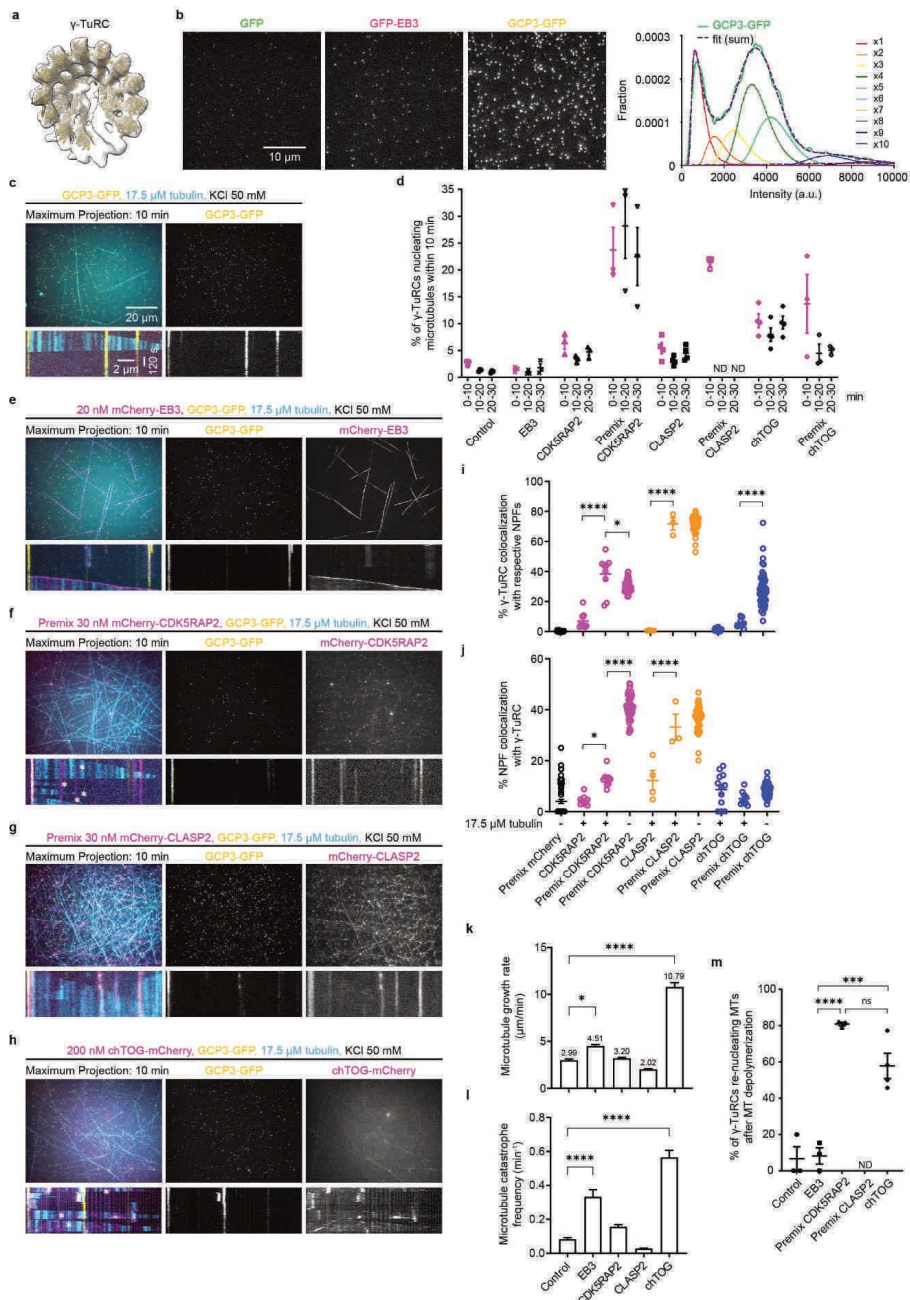


**Figure 1 | Human CDK5RAP2, CLASP2 and chTOG promote microtubule nucleation by purified  $\gamma$ -TuRC.**

**a**, A 3D reconstruction of the  $\gamma$ -TuRC from negative-stain EM data and rigid body fit of repeating  $\gamma$ -tubulin/GCP2 subcomplexes (from PDB ID: 6V6S<sup>20</sup>) individually docked into the  $\gamma$ -TuRC density

map. Fits for two subcomplexes at the  $\gamma$ -TuRC “seam” were not reliable and are therefore omitted for clarity. 3D reconstruction was generated from 12,851 particles (Also see **Extended data Fig. 4i** for details).

**b**, Left: representative images of single molecules of the indicated purified proteins (GFP, dimeric control GFP-EB3, GCP3-GFP) attached to coverslips. Right: The probability density of GCP3-GFP intensities (thick green line) fitted to a weighted sum of  $N$ -mers of GFP (thick dashed magenta line) and shown for one experiment. The weighted probability densities of individual GFP  $N$ -mers intensities are plotted as thin lines. Number of replicates=3;  $n=21,349$  for GFP and  $n=24,216$  for GCP3-GFP, where  $n$  is the number of molecules analyzed.

**c, e-h**, Top: maximum intensity projections of 10 min time-lapse videos, acquired after 20 min of incubation, showing microtubules (cyan) nucleated from  $\gamma$ -TuRC (GCP3-GFP, yellow) in the presence of either 17.5  $\mu$ M tubulin (17  $\mu$ M unlabeled porcine tubulin and 0.5  $\mu$ M HiLyte647-tubulin) and 50 mM KCl only (**c**), or together with the indicated proteins shown in magenta (**e-h**). For **f** and **g**,  $\gamma$ -TuRC was also preincubated with the same concentration of indicated proteins before immobilization on the coverslips. Bottom: representative kymographs illustrating dynamics of microtubules nucleated from  $\gamma$ -TuRC and microtubule re-nucleation events (asterisks) from experiments shown in top panels.

**d**, Quantification of average microtubule nucleation efficiency of  $\gamma$ -TuRC in the presence of either 17.5  $\mu$ M tubulin alone ( $n=3$ ), or together with 20 nM mCherry-EB3 ( $n=3$ ); 30 nM mCherry-CDK5RAP2 ( $n=3$ ); 30 nM mCherry-CDK5RAP2, also preincubated with  $\gamma$ -TuRC ( $n=3$ ); 30 nM mCherry-CLASP2 ( $n=4$ ); 30 nM mCherry-CLASP2, also preincubated with  $\gamma$ -TuRC ( $n=3$ ); 200 nM chTOG-mCherry ( $n=4$ ); 200 nM chTOG-mCherry, also preincubated with  $\gamma$ -TuRC ( $n=3$ ), where  $n$  is the number of independent experiments. Representative images are shown in **c, e-h** (top panels), and **Extended data Fig. 2c, e**. The plot presents mean  $\pm$  s.e.m., and each data point represents a single field of view from which % of  $\gamma$ -TuRCs nucleating microtubules were quantified for the given time point from an individual experiment. Data points in magenta (0-10 min) were acquired from a smaller field of view and are not directly comparable to the data points in black (10-20 min and 20-30 min) acquired from a bigger field of view shown in top panels of **c, e-h**.

**i, j**, Quantification of colocalization of  $\gamma$ -TuRC with indicated nucleation-promoting factors (NPFs)(**i**) or colocalization of indicated NPFs with  $\gamma$ -TuRC (**j**) under experimental conditions shown in **c, e-h**, and **Extended data Fig. 2d**. The plots show data for  $\gamma$ -TuRC premixed with mCherry without tubulin ( $n=63$ ,  $N=3$ );  $\gamma$ -TuRC with mCherry-CDK5RAP2 and 17.5  $\mu$ M tubulin ( $n=9$ ,  $N=3$ );  $\gamma$ -TuRC premixed with mCherry-CDK5RAP2 with ( $n=9$ ,  $N=3$ ) and without 17.5  $\mu$ M tubulin ( $n=47$ ,  $N=3$ );  $\gamma$ -TuRC with mCherry-CLASP2 and 17.5  $\mu$ M tubulin ( $n=4$ ,  $N=4$ );  $\gamma$ -TuRC premixed with mCherry-CLASP2 with ( $n=3$ ,  $N=3$ ) and without 17.5  $\mu$ M tubulin ( $n=48$ ,  $N=3$ );  $\gamma$ -TuRC with chTOG-mCherry and 17.5  $\mu$ M tubulin ( $n=12$ ,  $N=4$ );  $\gamma$ -TuRC premixed with chTOG-mCherry with ( $n=9$ ,  $N=3$ ) and without 17.5  $\mu$ M tubulin ( $n=51$ ,  $N=3$ ), where  $n$  is the number of fields of view analyzed and  $N$  is the number of independent experiments. The plots present mean  $\pm$  s.e.m., and individual data points represent % of  $\gamma$ -TuRC molecules colocalizing with the indicated protein or vice versa in a single field of view. One-way ANOVA with Tukey's multiple comparisons test was used to compare the means with each other (**i**:  $*p=0.0199$ ;  $***p < 0.0001$ , **j**:  $*p=0.0246$ ;  $***p < 0.0001$ ).

**k, l**, Quantification of average plus-end growth rate (**k**) and catastrophe frequency (**l**) of microtubules nucleated from  $\gamma$ -TuRC in the presence of either 17.5  $\mu$ M tubulin alone ( $n=25$ ), or together with mCherry-EB3 ( $n=36$ ); mCherry-CDK5RAP2 ( $n=52$ ); mCherry-CLASP2 ( $n=60$ ); chTOG-mCherry ( $n=78$ ), where  $n$  is the number of growth events analyzed. The bar plots present mean  $\pm$  s.e.m. from three independent experiments. Representative kymographs are shown in **c, e, h** (bottom panels) and **Extended data Fig. 2c, e**. One-way ANOVA with Dunnett's multiple comparisons test was used to compare the means with control (**k**:  $*p=0.0444$ ;  $***p < 0.0001$ , **l**:  $***p < 0.0001$ ).

**m**, Quantification of microtubule re-nucleation efficiency of  $\gamma$ -TuRCs analyzed from experiments shown in **c, e-h**. The plot shows data for  $\gamma$ -TuRC with 17.5  $\mu$ M tubulin only ( $n=3$ ,  $m=10$ ); together with mCherry-EB3 ( $n=3$ ,  $m=26$ ); premixed mCherry-CDK5RAP2 ( $n=3$ ,  $m=107$ ); premixed mCherry-CLASP2 ( $n=3$ ,  $m=0$ ) and chTOG-mCherry ( $n=4$ ,  $m=178$ ), where  $n$  is the number of independent experiments analyzed and  $m$  is the number of  $\gamma$ -TuRCs which nucleated microtubules that underwent depolymerization, pooled from three 10 min videos of a single experiment. The plot presents mean  $\pm$  s.e.m., and individual data points represent % of  $\gamma$ -TuRCs re-nucleating

---

*microtubules in a single experiment. One-way ANOVA with Tukey's multiple comparisons test was used to compare the means with each other (ns, not significant,  $p=0.0704$ ; \*\*\* $p=0.0007$ ; \*\*\*\* $p<0.0001$ ). ND, could not be determined.*

---

In the presence of  $17.5 \mu\text{M}$  tubulin, only  $\sim 1\text{-}3\%$  of  $\gamma$ -TuRC could nucleate microtubules per 10 minutes of observation (Fig. 1c,d), which is similar to previous studies using purified  $\gamma$ -TuRCs obtained from other cell types using different tagging and purification approaches<sup>18,22</sup>. We then set out to investigate the impact of several microtubule- or  $\gamma$ -TuRC-binding proteins on  $\gamma$ -TuRC-mediated microtubule nucleation (Fig. 1d-j). The addition of mCherry-EB3 did not affect the nucleation efficiency although it increased both microtubule growth rate and catastrophe frequency (Fig. 1d,e,k,l and Extended data Fig. 2a). In contrast, three nucleation-promoting factors, CDK5RAP2, chTOG and CLASP2, could potentiate microtubule nucleation, both when added to  $\gamma$ -TuRC immobilized on coverslips or when additionally preincubated with  $\gamma$ -TuRC in solution ("Premix") before immobilization (Fig. 1d, f-h, Extended data Fig. 2b,c,e,f, and see Supplementary Tables 2-4 for mass spectrometry-based characterization of the purified proteins).

Full-length mCherry-CDK5RAP2 increased microtubule nucleation  $\sim 3$  fold when added to immobilized  $\gamma$ -TuRCs and more than 20-fold (up to  $\sim 35\%$  nucleation efficiency) when additionally preincubated with  $\gamma$ -TuRC (Fig. 1d,f and Extended data Fig. 2b,c). This was likely because preincubation greatly increased the percentage of  $\gamma$ -TuRCs colocalizing with CDK5RAP2 (4-6 fold), which in preincubated samples could reach 30-40%, both in the presence and absence of free tubulin (Fig. 1f,i,j and Extended data Fig. 2c,d). These data confirm that CDK5RAP2 directly interacts with  $\gamma$ -TuRC<sup>26</sup> and suggest that in our assays, it can activate the majority of  $\gamma$ -TuRCs to which it binds. The percentage of CDK5RAP2-positive dots colocalizing with  $\gamma$ -TuRCs was rather low in these experiments ( $\sim 13\%$  with tubulin,  $\sim 41\%$  without tubulin), likely because CDK5RAP2 was present in excess, or due to the autoinhibitory regulation of CDK5RAP2 that is controlled by its phosphorylation state<sup>33,34</sup>. Compared to the samples with tubulin alone or with mCherry-EB3, mCherry-CDK5RAP2 had no significant effect on microtubule growth rate or catastrophe frequency, but strongly increased the frequency of microtubule re-nucleation after depolymerization, indicating that CDK5RAP2 can maintain  $\gamma$ -TuRC in an active state (Fig. 1k-m).

We also observed a strong increase in microtubule nucleation efficiency with mCherry-CLASP2 (Fig. 1d,g and Extended data Fig. 2b), a protein previously shown to promote microtubule outgrowth from stabilized seeds<sup>28</sup>, but never tested for interaction with  $\gamma$ -TuRC.

The activating effect of mCherry-CLASP2 was similar in magnitude to that of CDK5RAP2 and was again stronger after preincubation (Fig. 1d,g and Extended data Fig. 2e). mCherry-CLASP2 also strongly colocalized with  $\gamma$ -TuRC, even in the absence of free tubulin, suggesting that it might bind to  $\gamma$ -TuRC directly (Fig. 1i,j and Extended data Fig. 2d). It should be noted that since CLASP2 strongly suppresses catastrophes, and therefore microtubules become very long<sup>28</sup> (Fig. 1g,l), it was not possible to examine microtubule re-nucleation from the same  $\gamma$ -TuRC or analyze premixed CLASP2- $\gamma$ -TuRC samples that were incubated longer than 10 minutes due to very high microtubule density.

Finally, we also examined the effect of chTOG, because it can weakly promote microtubule nucleation from free tubulin<sup>35</sup> and strongly promote  $\gamma$ -TuRC-dependent microtubule nucleation<sup>18</sup>, and its *Xenopus* homolog XMAP215 can synergize with  $\gamma$ -TuRC<sup>25</sup> and promote outgrowth from seeds<sup>36</sup>. We confirmed that chTOG enhanced  $\gamma$ -TuRC-dependent microtubule nucleation, although unlike CDK5RAP2 and CLASP2, the effect was similar with and without preincubation (Fig. 1d,h and Extended data Fig. 2b) and not as strong as previously published<sup>18</sup>. This could be due to the differences in experimental conditions, but was unlikely to be due to the low activity of chTOG, as it strongly increased the growth rate and catastrophe frequency in our assays (Fig. 1k,l), in line with the published data<sup>37,38</sup>. Colocalization of chTOG-positive dots with  $\gamma$ -TuRC was lower than that of CDK5RAP2 or CLASP2, but increased in the absence of free tubulin (Fig. 1i,j), with which chTOG interacts through its TOG domains<sup>39</sup>. It should be noted that when chTOG was preincubated with  $\gamma$ -TuRC, it formed clusters that sequestered  $\gamma$ -TuRC (Extended data Fig. 2d), and therefore we did not premix chTOG and  $\gamma$ -TuRC in the experiments described from here onwards. Interestingly, similar to CDK5RAP2, chTOG potentiated repeated microtubule nucleation from the same  $\gamma$ -TuRC (Fig. 1m).

For all these proteins, we also tested whether increasing their concentration in conditions without premixing would boost nucleation efficiency but found this not to be the case (Extended data Fig. 2a,c,e,f). This indicates that in the conditions tested, nucleation is limited by the activity and/or surface interactions of  $\gamma$ -TuRCs rather than the availability of nucleation-promoting factors. We conclude that purified  $\gamma$ -TuRC can nucleate microtubules *in vitro* in a manner dependent on various interactors.

### ***CAMSAP3 triggers microtubule release from $\gamma$ -TuRC***

In the assays described above, microtubule minus ends did not grow because they were stably capped and almost never released from  $\gamma$ -TuRCs that nucleated them, though the frequency of release events was slightly increased by chTOG (from ~1 to ~2.5-3%) (Extended data Fig. 3a-



c). We then set out to examine whether  $\gamma$ -TuRC prevents CAMSAPs from binding to microtubule minus ends, initially by using CAMSAP3, which among the CAMSAP family members has been suggested to have the highest minus-end affinity *in vitro*<sup>29</sup>. To recapitulate *in vitro* CAMSAP3 specificity for growing microtubule minus ends, the ionic strength of the buffer needs to be sufficiently high (MRB80 buffer supplemented with 80 mM KCl, as opposed

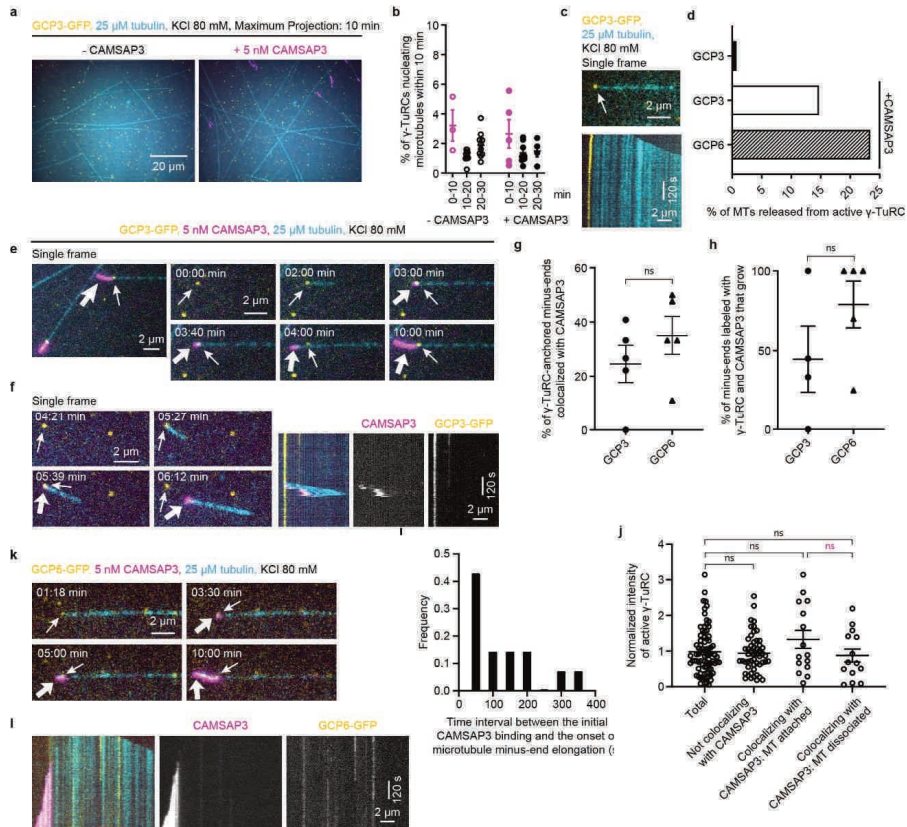


**Figure 2 | CAMSAP3 triggers microtubule release from  $\gamma$ -TuRC.**

**a**, Maximum intensity projections of 10 min time-lapse videos, acquired after 10 min of incubation, showing microtubules (cyan) nucleated from  $\gamma$ -TuRC (GCP3-GFP, yellow) in the presence of either 25  $\mu$ M tubulin (24.5  $\mu$ M unlabeled porcine tubulin and 0.5  $\mu$ M rhodamine-tubulin) and 80 mM KCl only (left), or together with 5 nM SNAP-AF647-CAMSAP3 (magenta) (right).

**b**, Quantification of average microtubule nucleation efficiency of  $\gamma$ -TuRC in the presence of either 25  $\mu$ M tubulin alone (for 0-10 min,  $n=3$ ; for 10-20 min,  $n=10$ ; for 20-30 min,  $n=10$ , analyzed from three independent experiments) or together with SNAP-AF647-CAMSAP3 (for 0-10 min,  $n=5$ ; for 10-20 min,  $n=8$ ; for 20-30 min,  $n=4$ , analyzed from five independent experiments), where  $n$  is the number of fields of view analyzed. Representative images are shown in **a**. The plot presents mean  $\pm$  s.e.m., and each data point represents a single field of view from which % of  $\gamma$ -TuRCs nucleating microtubules were quantified for the given time point from an individual experiment. Data points in magenta (0-10 min) were acquired from a smaller field of view and are not directly comparable to the data points in black (10-20 min and 20-30 min) acquired from a bigger field of view shown in **a**.

**c**, Single frame (top, arrow points to a  $\gamma$ -TuRC-anchored microtubule) and representative kymograph (bottom) from the experiment shown in **a** without CAMSAP3.

**d**, Plot showing frequency of microtubule release from active  $\gamma$ -TuRC in the absence ( $n=136$  for  $\gamma$ -TuRC purified using GCP3-GFP-SII, pooled from three independent experiments) or presence of SNAP-AF647-CAMSAP3 ( $n=102$  for  $\gamma$ -TuRC purified using GCP3-GFP-SII, pooled from five independent experiments; and  $n=47$  for  $\gamma$ -TuRC purified using GCP6-GFP-SII, pooled from five independent experiments), where  $n$  is the number of active  $\gamma$ -TuRCs analyzed. Representative images are shown in **c,e,k**.

**e**, Single frame and cropped images, at indicated time points in min, from a 10 min time-lapse video showing microtubule (cyan) nucleation from  $\gamma$ -TuRC (GCP3-GFP, yellow), CAMSAP3 colocalization (magenta) with  $\gamma$ -TuRC-anchored microtubule minus-end and subsequent microtubule release from  $\gamma$ -TuRC in conditions described in **a** with CAMSAP3. Thin arrows indicate  $\gamma$ -TuRC, while thick arrows indicate CAMSAP3.

**f**, Still frames at indicated time points in min (left) and kymographs (right) of a 10 min time-lapse video showing microtubule nucleation and rapid microtubule release from  $\gamma$ -TuRC under conditions shown in **e**.

**g,h**, Colocalization frequency of  $\gamma$ -TuRC-anchored microtubule minus-ends with CAMSAP3, from experiments shown in **e** ( $n=5$ ,  $m=18$ ,  $l=102$  for GCP3-GFP) and **k** ( $n=5$ ,  $m=16$ ,  $l=47$  for GCP6-GFP) (**g**). Individual data points represent single experiments from which % of  $\gamma$ -TuRC-anchored microtubule minus-ends colocalizing with CAMSAP3 were quantified,  $p=0.3157$ . **h**, Quantification of % of microtubules released from  $\gamma$ -TuRC colocalizing with CAMSAP3, as shown in **g**.  $n=4$ ,  $m=18$ ,  $l=32$  for GCP3-GFP and  $n=5$ ,  $m=16$ ,  $l=17$  for GCP6-GFP. Individual data points represent single experiments from which % of growing microtubule minus-ends that were labeled with  $\gamma$ -TuRC and CAMSAP3 were quantified,  $p=0.2065$ . In **g** and **h**,  $n$  is the number of independent experiments,  $m$  is the number of fields of view and  $l$  is the total number of active  $\gamma$ -TuRCs in **g** and number of active  $\gamma$ -TuRCs colocalizing with CAMSAP3 in **h**, analyzed over 10 min duration. The plots present mean  $\pm$  s.e.m. Two-tailed unpaired  $t$ -tests were used to test for significance. ns, not significant.

**i**, Histogram showing frequency distribution of  $\gamma$ -TuRC dissociation times quantified as time interval between the initial CAMSAP3 binding and the onset of microtubule minus-end elongation.  $n=14$   $\gamma$ -TuRC dissociation events from experiments shown in **e** and pooled from three independent experiments.

**j**, Comparison of fluorescence intensities of total active GCP3-GFP molecules nucleating microtubules ( $n=80$ ); active GCP3-GFP molecules that did not recruit CAMSAP3 ( $n=52$ , ns,  $p=0.9846$ ); active GCP3-GFP molecules that recruited CAMSAP3 and remained attached to the microtubule ( $n=15$ , ns,  $p=0.2382$ ); and active GCP3-GFP molecules that recruited CAMSAP3 and subsequently released microtubule ( $n=14$ , ns,  $p=0.9427$ ). Data was analyzed from experiments shown in **e** and pooled from four independent experiments. One-way ANOVA with Tukey's multiple comparisons test was used to compare the means with each other. ns,  $p$  (magenta)=0.2463.

**k,l**, Still frames (at indicated time points in min) (**k**) and representative kymographs (**l**) from a 10 min time-lapse video showing CAMSAP3 colocalization (magenta) with  $\gamma$ -TuRC-anchored microtubule minus-end and subsequent microtubule (cyan) release from  $\gamma$ -TuRC (GCP3-GFP, yellow) in the same conditions as in **a**. Thin arrows indicate  $\gamma$ -TuRC signal, while thick arrows indicate CAMSAP3 signal.

to 50 mM KCl used above). Since high ionic strength suppresses microtubule assembly<sup>40</sup>, we increased tubulin concentration to 25  $\mu$ M and obtained ~1.5-3% nucleation efficiency with and without SNAP-AF647-CAMSAP3 (Fig. 2a,b and Extended data Fig. 3d). Also in these buffer conditions, very little microtubule release from  $\gamma$ -TuRC was detected in the absence of CAMSAP3 (Fig. 2c,d). Strikingly, when SNAP-AF647-CAMSAP3 was added, microtubule nucleation events were frequently followed by specific binding of SNAP-AF647-CAMSAP3

to the  $\gamma$ -TuRC-associated microtubule minus end and its subsequent elongation (Fig. 2e,f). In some cases, the microtubule remained attached to the glass surface in the vicinity of  $\gamma$ -TuRC that nucleated it (e.g. Fig. 2e and Supplementary Video 1), while in other cases the minus end detached from the surface and the microtubule floated away from the  $\gamma$ -TuRC (Fig. 2f and Supplementary Video 1). Approximately 25% of all  $\gamma$ -TuRC-nucleated microtubules acquired a CAMSAP3 signal at their minus end (Fig. 2g and Extended data Fig. 3e), and approximately half of these microtubules initiated minus-end growth (Fig. 2h). As a result, the percentage of microtubules released from  $\gamma$ -TuRC increased more than 10-fold, to 15% (Fig. 2d). The time interval between the initial CAMSAP3 binding and the onset of microtubule minus end elongation varied between 50-350s (Fig. 2i). After microtubule release, the same  $\gamma$ -TuRC could sometimes initiate growth of a new microtubule (Extended data Fig. 3f).

Recent work has shown that also partial/incomplete  $\gamma$ -TuRCs can nucleate microtubules<sup>22</sup>. To test whether CAMSAP3 preferentially binds to minus ends anchored by incomplete  $\gamma$ -TuRCs and triggers their detachment, we have measured fluorescence intensity of  $\gamma$ -TuRCs in the GFP channel, because it should directly reflect the number of GCP3-GFP molecules. We found the fluorescence intensity of the total active  $\gamma$ -TuRC population was similar to that of  $\gamma$ -TuRCs that nucleated microtubules and did not recruit CAMSAP3 and was not different from those that subsequently recruited CAMSAP3 and either stayed attached or got released (Fig. 2j). To further validate our result, we also generated  $\gamma$ -TuRC that were purified using a homozygous knock-in HEK293T cell line where the GCP6 subunit of  $\gamma$ -TuRC was C-terminally tagged with GFP and Twin-Strep-tag (Extended data Fig. 3g,h). Mass spectrometry showed that  $\gamma$ -TuRC purified from this cell line was similar in terms of components and associated proteins to that purified using GCP3-GFP-SII (Extended data Fig. 3i and Supplementary Table 5). It was shown previously that a subcomplex containing GCP4, 5 and 6 is by itself nucleation-incompetent and needs to be supplemented with cell extracts containing GCP2 and 3 to nucleate microtubules<sup>41</sup>. Therefore, GCP6-containing  $\gamma$ -TuRCs that can nucleate microtubules are likely to be complete rings. In our reconstitutions, we observed that GCP6-GFP-SII-containing  $\gamma$ -TuRCs could nucleate microtubules, which then could recruit CAMSAP3 to their minus ends, initiate minus-end growth and detach from  $\gamma$ -TuRC, and the frequency of CAMSAP3 binding and minus end growth was even slightly higher than for  $\gamma$ -TuRCs purified using GCP3-GFP-SII (Fig. 2g,h,k,l and Supplementary Video 1, right panel). We conclude that CAMSAP3 can bind to the minus ends of a subset of microtubules nucleated and anchored by  $\gamma$ -TuRC, promote minus end polymerization and trigger their release.

***CDK5RAP2 inhibits CAMSAP binding to the minus ends of  $\gamma$ -TuRC-anchored microtubules***

To test whether nucleation-promoting factors affect CAMSAP3 binding and microtubule release from  $\gamma$ -TuRC, we first examined whether they were active in the same assay conditions. We found that whereas CDK5RAP2 and CLASP2 could still potentiate  $\gamma$ -TuRC-dependent microtubule nucleation up to ~20% and ~9% respectively in the presence of 80 mM KCl and 25  $\mu$ M tubulin, this was not the case for chTOG (Fig. 3a,b). CAMSAP3 binding to  $\gamma$ -TuRC-anchored minus ends and microtubule release were observed in the presence of either of the three proteins (Fig. 3c-e and Supplementary Video 2). Interestingly, CDK5RAP2, but not CLASP2 or chTOG, strongly suppressed CAMSAP3 binding to the minus ends of  $\gamma$ -TuRC-nucleated microtubules (Fig. 3f). Microtubule minus ends that did recruit CAMSAP3 started to grow and detached from  $\gamma$ -TuRC with a comparable frequency in all conditions (Fig. 3g), though the data for chTOG were less reliable because the combination of high ionic strength and chTOG made microtubule growth events very short-lived and thus limited the time when microtubule release could be observed. Altogether, CDK5RAP2 strongly suppressed CAMSAP3-driven microtubule detachment from  $\gamma$ -TuRC, while this was not the case for CLASP2, and no strong conclusions could be made for chTOG (Fig. 3h).

We next hypothesized that CDK5RAP2 exerts its effect by altering  $\gamma$ -TuRC geometry so that it would be more similar to a 13-protofilament microtubule, which would be beneficial for microtubule nucleation and at the same time inhibit CAMSAP3 binding. We first tested this possibility by performing negative stain transmission EM of  $\gamma$ -TuRC, either alone or incubated in the presence of 120 nM CDK5RAP2 but found no support for this idea (Extended data Fig. 4).  $\gamma$ -TuRC alone in negatively stained micrographs and 3D reconstructions of density maps looked similar to previously reported work and fitted well into the density map of a published model (from PDB ID: 6V6S<sup>20</sup>) (Extended data Fig. 4a-c,i). However, we could not detect any noticeable differences in the  $\gamma$ -TuRC structure in the presence (Extended data Fig. 4d-f,j) and absence of CDK5RAP2 (Extended data Fig. 4g). Both reconstructions deviated significantly from the closed conformation of  $\gamma$ -tubulin small complex ( $\gamma$ -TuSC) oligomers (from PDB ID: 5FLZ<sup>42</sup>), and did not match the microtubule geometry (from PDB ID: 2HXF<sup>43</sup> and EMD-5193<sup>44</sup>) (Extended data Fig. 4h). It should be noted that the densities of terminal  $\gamma$ -TuSC at the  $\gamma$ -TuRC seam and in the luminal bridge were not clearly resolved in our  $\gamma$ -TuRC reconstructions. Therefore, we cannot make conclusions about potential conformational changes that could occur at these sites.

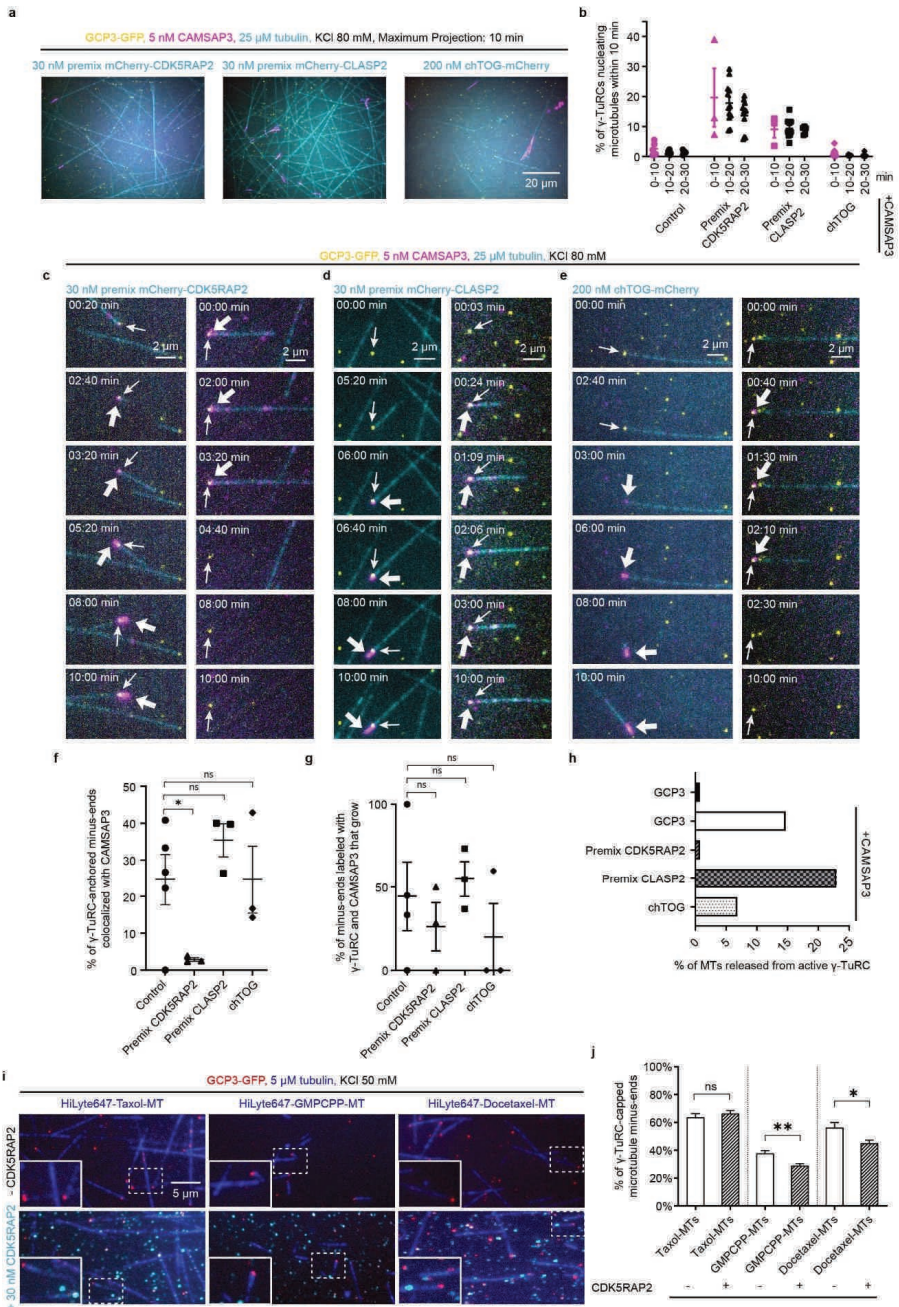


**Figure 3 | CDK5RAP2 inhibits CAMSAP3 binding to the minus ends of  $\gamma$ -TuRC-anchored microtubules.**

**a**, Maximum intensity projections of 10 min time-lapse videos, acquired after 10 min of incubation, showing microtubules (cyan) nucleated from  $\gamma$ -TuRC (GCP3-GFP, yellow) in the presence of 25  $\mu$ M

tubulin (24.5  $\mu\text{M}$  unlabeled porcine tubulin and 0.5  $\mu\text{M}$  rhodamine-tubulin), 80 mM KCl and 5 nM SNAP-AF647-CAMSAP3 (magenta) supplemented with either mCherry-CDK5RAP2 (cyan) (preincubated with  $\gamma$ -TuRC); or mCherry-CLASP2 (cyan) (preincubated with  $\gamma$ -TuRC); or 200 nM chTOG-mCherry (cyan).

**b**, Plot showing average microtubule nucleation efficiency of  $\gamma$ -TuRC quantified from experiments shown in **a**. For premix CDK5RAP2:  $n=3$  for 0-10 min;  $n=12$  for 10-20 min;  $n=11$  for 20-30 min; analyzed from three independent experiments. For premix CLASP2:  $n=3$  for 0-10 min;  $n=10$  for 10-20 min;  $n=5$  for 20-30 min; analyzed from three independent experiments. For chTOG:  $n=7$  for 0-10 min;  $n=6$  for 10-20 min;  $n=6$  for 20-30 min; analyzed from three independent experiments.  $n$  is the number of fields of view analyzed. Control data have been taken from **Fig. 2b** and replotted here for direct comparison. The plot presents mean  $\pm$  s.e.m., and each data point represents a single field of view from which % of  $\gamma$ -TuRCs nucleating microtubules were quantified for the given time point from an individual experiment. Data points in magenta (0-10 min) were acquired from a smaller field of view and are not directly comparable to the data points in black (10-20 min and 20-30 min) acquired from a bigger field of view shown in **a**.

**c-e**, Still frames (at indicated time points in min) from 10 min time-lapse videos showing two different examples (left and right) of  $\gamma$ -TuRC-CAMSAP3 interplay at the  $\gamma$ -TuRC-anchored microtubule minus-ends under indicated experimental conditions, also shown in **a**. Example on the left illustrates microtubule (cyan) release from  $\gamma$ -TuRC (yellow, thin arrows) colocalizing with CAMSAP3 (magenta, thick arrows) in the presence of indicated proteins (cyan). Example 2 on the right illustrates occasions when CAMSAP3 binds, but does not displace  $\gamma$ -TuRC from the microtubule minus-end.

**f,g**, Colocalization frequency of  $\gamma$ -TuRC-anchored microtubule minus-ends with CAMSAP3, from experiments shown in **a,c-e** (**f**).  $n=3$ ,  $m=26$ ,  $l=393$  for premix mCherry-CDK5RAP2,  $*p=0.0394$ ;  $n=3$ ,  $m=13$ ,  $l=310$  for premix mCherry-CLASP2, ns, not significant,  $p=0.2678$ ; and  $n=3$ ,  $m=23$ ,  $l=44$  for chTOG-mCherry, ns,  $p=0.9996$ . Individual data points represent single experiments from which % of  $\gamma$ -TuRC-anchored microtubule minus-ends colocalizing with CAMSAP3 were quantified.

**g**, Quantification of % of microtubules released from the CAMSAP3 colocalized population of  $\gamma$ -TuRC shown in **f**.  $n=3$ ,  $m=26$ ,  $l=12$  for premix mCherry-CDK5RAP2, ns, not significant,  $p=0.4778$ ;  $n=3$ ,  $m=13$ ,  $l=114$  for premix mCherry-CLASP2, ns,  $p=0.6836$ ; and  $n=3$ ,  $m=23$ ,  $l=9$  for chTOG-mCherry, ns,  $p=0.3480$ . Individual data points represent single experiments from which % of growing microtubule minus-ends that were labeled with  $\gamma$ -TuRC and CAMSAP3 were quantified. In **f** and **g**,  $n$  is the number of independent experiments,  $m$  is the number of fields of view and  $l$  is the total number of active  $\gamma$ -TuRCs in **f** and number of active  $\gamma$ -TuRCs colocalized with CAMSAP3 in **g**, analyzed over 10 min duration. Control data has been taken from **Fig. 2g** for **f** and from **Fig. 2h** for **g** (GCP3 values) and replotted here for direct comparison. The plots present mean  $\pm$  s.e.m. One-way ANOVA with uncorrected Fisher's LSD tests were used to compare the means with control.

**h**, Plot showing frequency of microtubule release from active  $\gamma$ -TuRC in the presence of 5 nM SNAP-AF647-CAMSAP3 under the experimental conditions shown in **a,c-e**.  $n=393$  for premix mCherry-CDK5RAP2, pooled from three independent experiments;  $n=310$  for premix mCherry-CLASP2, pooled from three independent experiments; and  $n=44$  for chTOG-mCherry, pooled from three independent experiments; where  $n$  is the number of active  $\gamma$ -TuRCs analyzed. The two control data values (GCP3 with or without CAMSAP3) have been taken from **Fig. 2d** (GCP3 values with or without CAMSAP3) and replotted here for direct comparison.

**i**, Maximum intensity projections of 5 min time-lapse videos showing  $\gamma$ -TuRC-capped minus ends of stabilized microtubules (blue), as indicated, that contain different protofilament number: rhodamine-labeled Taxol-stabilized microtubules with 12 or 13 protofilaments (left) and rhodamine-labeled GMPCPP- and Docetaxel-stabilized microtubules with predominantly 14 protofilaments (middle and right respectively) were incubated with  $\gamma$ -TuRC (20 nM GCP3-GFP, red) in the presence of 5  $\mu\text{M}$  tubulin (4.5  $\mu\text{M}$  unlabeled porcine tubulin and 0.5  $\mu\text{M}$  rhodamine-tubulin) and 50 mM KCl with (bottom) or without (top) 30 nM SNAP-AF647-CDK5RAP2 (cyan). Insets show enlarged view of the ROI marked with dashed white line.

**j**, Plot generated from experiments shown in **i**, comparing minus-end capping efficiency of  $\gamma$ -TuRC for stabilized microtubules with different protofilament numbers in the absence or presence of 30 nM SNAP-AF647-CDK5RAP2.  $n=18$ ,  $m=1075$ ,  $N=3$  for Taxol-stabilized microtubules without

---

*CDK5RAP2; n=11, m=1420, N=3 for Taxol-stabilized microtubules with CDK5RAP2; n=29, m=3032, N=3 for GMPCPP-stabilized microtubules without CDK5RAP2; n=26, m=2454, N=3 for GMPCPP-stabilized microtubules with CDK5RAP2; n=11, m=1253, N=3 for Docetaxel-stabilized microtubules without CDK5RAP2; n=15, m=1171, N=3 for Docetaxel-stabilized microtubules with CDK5RAP2; where n is the number of fields of view analyzed, m is the number of microtubule minus-ends analyzed and N is the number of independent experiments. The bar plot presents mean  $\pm$  s.e.m., and individual data points represent single fields of view from which % of minus-ends capped by  $\gamma$ -TuRC were quantified. One-way ANOVA with Šidák's multiple comparisons test was used to compare the pre-selected pair of means. ns, not significant,  $p=0.8573$ ; \* $p=0.0187$ ; \*\* $p=0.0050$ .*

---

As an alternative approach, we used a microtubule-capping assay, whereby  $\gamma$ -TuRCs bind to the ends of preformed microtubules. We have compared Taxol-stabilized microtubules, which in our hands have 12 or 13 protofilaments to GMPCPP- and Docetaxel-stabilized microtubule preparations, which predominantly have 14 protofilament microtubules<sup>45</sup>. As expected, Taxol-stabilized microtubules were capped by  $\gamma$ -TuRC more efficiently than Docetaxel-stabilized ones, and GMPCPP-stabilized were capped even less well, possibly because they have more curved terminal protofilaments than the taxane-stabilized ones<sup>46, 47</sup> (Fig. 3i,j). Interestingly, the addition of CDK5RAP2 significantly inhibited capping of both types of 14-protofilament microtubules, without affecting the capping efficiency of Taxol-bound microtubules (Fig. 3i, j). These data are in line with the idea that in the presence of microtubules, CDK5RAP2 promotes a conformational change or conformational flexibility in  $\gamma$ -TuRC that would allow a better match with the 13-protofilament microtubule geometry.

### ***CAMSAPs cause $\gamma$ -TuRC detachment by stabilizing growing microtubule minus ends***

Since in our assays microtubules rarely dissociated from  $\gamma$ -TuRC spontaneously, their CAMSAP3-induced detachment must be an active process. To get more insight into this process, we compared the effects of CAMSAP2 and CAMSAP3, which decorate and stabilize growing microtubule minus ends, and CAMSAP1, which labels free minus ends but does not decorate or stabilize them<sup>29</sup>. All three CAMSAPs could bind to  $\gamma$ -TuRC-anchored minus ends, with CAMSAP2 being slightly less efficient (Fig. 4a-c and Extended data Fig. 3d). However, although CAMSAP1 and CAMSAP3 bound to the minus ends equally well, CAMSAP1 had little effect on microtubule release from  $\gamma$ -TuRC (Fig. 4d,e and Supplementary Video 3). These data support the view that  $\gamma$ -TuRC is displaced from the minus ends due to their elongation, which is made more robust by CAMSAP2 and CAMSAP3 that stably decorate the newly formed microtubule lattice and may also alter its conformation.

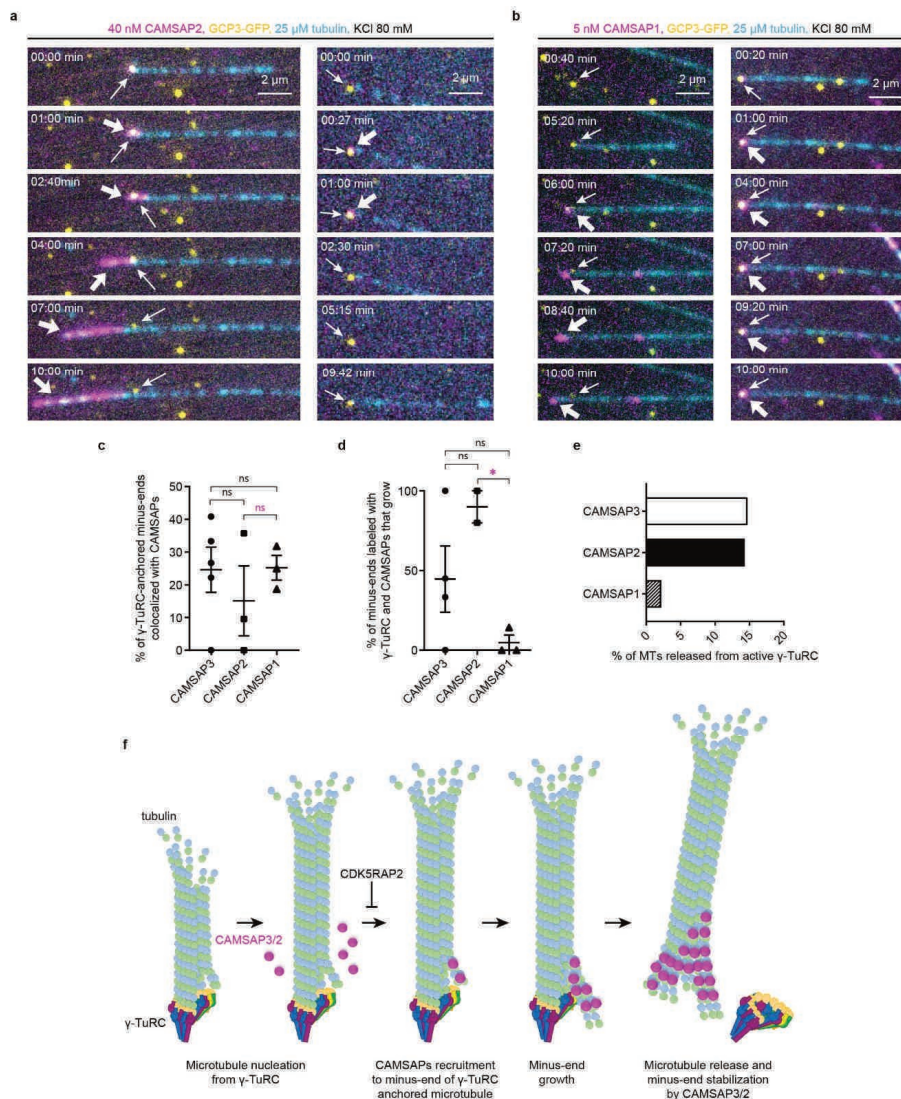


**Figure 4 | CAMSAPs cause  $\gamma$ -TuRC detachment by stabilizing growing microtubule minus ends.**

**a, b**, Still frames (at indicated time points in min) from 10 min time-lapse video showing two different examples (left and right) of  $\gamma$ -TuRC interplay with CAMSAP2 (**a**) or CAMSAP1 (**b**) in the indicated conditions in the presence of 25  $\mu$ M tubulin (24.5  $\mu$ M unlabeled porcine tubulin and 0.5  $\mu$ M rhodamine-tubulin). Example on left illustrates microtubule release; example on right illustrates occasions when CAMSAP2 (**a**) or CAMSAP1 (**b**) does not displace  $\gamma$ -TuRC from microtubule minus-ends.

**c, d**, Colocalization frequency of  $\gamma$ -TuRC-anchored microtubule minus-ends with CAMSAPs, from experiments shown in **a, b** (**c**).  $n=3$ ,  $m=15$ ,  $l=42$  for CAMSAP2, ns, not significant,  $p=0.4000$ ; and  $n=3$ ,  $m=18$ ,  $l=46$  for CAMSAP1, ns,  $p=0.9581$ . ns,  $p$  (magenta)=0.4234. Individual data points represent single experiments from which % of  $\gamma$ -TuRC-anchored microtubule minus-ends colocalized with CAMSAPs were quantified. **d**, Quantification of % of microtubules released from  $\gamma$ -TuRCs



colocalizing with CAMSAPs, as shown in **a,b**.  $n=3$ ,  $m=15$ ,  $l=7$  for CAMSAP2,  $ns$ ,  $p=0.1346$ ; and  $n=3$ ,  $m=18$ ,  $l=12$  for CAMSAP1,  $ns$ ,  $p=0.1365$ . \* $p$  (magenta)=0.0217. Individual data points represent single experiments from which % of growing microtubule minus-ends that were labeled with  $\gamma$ -TuRC and CAMSAPs were quantified. In **c** and **d**,  $n$  is the number of independent experiments,  $m$  is the number of fields of view and  $l$  is the total number of active  $\gamma$ -TuRCs in **c** and number of active  $\gamma$ -TuRCs colocalized with CAMSAPs in **d**, analyzed over 10 min duration. Control data (CAMSAP3 values) have been taken from **Fig. 2g** for **c** and from **Fig. 2h** for **d** (GCP3 values) and replotted here for direct comparison. The plots present mean  $\pm$  s.e.m. One-way ANOVA with uncorrected Fisher's LSD tests were used to compare the means with each other.

**e**, Plot showing frequency of microtubule release from active  $\gamma$ -TuRC in the presence of CAMSAPs under the experimental conditions shown in **a,b**.  $n=42$  for CAMSAP2, pooled from three independent experiments;  $n=46$  for CAMSAP1, pooled from three independent experiments; where  $n$  is the number of active  $\gamma$ -TuRCs analyzed. Control data (CAMSAP3) has been taken from **Fig. 2d** (GCP3 values with CAMSAP3) and replotted here for direct comparison.

**f**, Model: A microtubule is first nucleated by  $\gamma$ -TuRC with some protofilaments that are not attached to the  $\gamma$ -tubulin subunits, allowing them to attain a conformation permissive for CAMSAP binding. CAMSAP2 or 3 binds to the minus-end of the  $\gamma$ -TuRC-capped microtubule at an intradimer site between two protofilaments<sup>14</sup>, promotes minus-end polymerization and stabilizes the growing minus-end lattice. Growing minus-end pushes away  $\gamma$ -TuRC, and the microtubule is released. CDK5RAP2 inhibits microtubule release, possibly by altering  $\gamma$ -TuRC conformation to fit the geometry of a 13-protofilament microtubule and therefore, suppresses CAMSAP binding.

## Discussion

In this study, we have uncovered a new mechanism of generation of stable microtubule minus ends – displacement of  $\gamma$ -TuRC from a newly nucleated microtubule by a polymerizing minus end, which is promoted by CAMSAP2 and CAMSAP3.  $\gamma$ -TuRC is the major microtubule-nucleating factor in most cell types, but particularly in cells with dense microtubule arrays, many microtubule minus ends depend for their stabilization and anchoring on CAMSAP family members. How CAMSAP-stabilized microtubules are generated is currently unclear. CAMSAPs are diffusely distributed in mammalian cells where microtubules are depolymerized<sup>29</sup>, but can bind to microtubule minus ends released from nucleation centers such as the centrosome or the Golgi<sup>29,48</sup>. While such release can in principle be induced by severing enzymes or motor proteins pulling on microtubules<sup>49</sup>, here we show that CAMSAPs themselves can be sufficient to mediate this process. The microtubule minus-end binding domain of CAMSAPs, CKK, recognizes the minus ends by binding to an interface between two curved protofilaments<sup>14</sup>. Such protofilament arrangement would not occur at microtubule minus ends fully attached to a  $\gamma$ -TuRC<sup>16,17</sup>. However, given the asymmetric  $\gamma$ -TuRC structure<sup>18-21</sup> and the fact that not all  $\gamma$ -tubulin subunits within  $\gamma$ -TuRC are essential for microtubule nucleation<sup>22</sup>, it is possible that some protofilaments at the  $\gamma$ -TuRC-capped minus end will be unattached and acquire a flared conformation permissive for CAMSAP binding (Fig. 4f). Having bound to some sites at the interface between the microtubule minus end and  $\gamma$ -TuRC, CAMSAPs could

stabilize free protofilaments and promote their elongation. Furthermore, CAMSAPs could potentially trigger detachment of neighboring protofilaments from  $\gamma$ -TuRC by inducing protofilament skew<sup>14</sup>. Protofilaments elongating from the minus end would be expected to generate a pushing force, similar to growing microtubule plus ends<sup>50</sup>, that would contribute to microtubule release from  $\gamma$ -TuRC. In accordance with this model, stable decoration of minus-end-grown lattice, a property common for CAMSAP2 and CAMSAP3 but not CAMSAP1<sup>29</sup> is required for release. Repeated activity of  $\gamma$ -TuRC in the presence of CAMSAP2 or CAMSAP3 thus can lead to generation of a pool of stable microtubule minus ends that are not directly attached to their nucleation sites. Such a “handover” mechanism can help to increase microtubule density in different settings. For example, it can generate free, stable non-centrosomal minus ends in cells such as fibroblasts or cancer cells, or amplify microtubules at non-centrosomal MTOCs such as the Golgi apparatus or the apical cortex of epithelial cells, where  $\gamma$ -TuRC and CAMSAPs operate in parallel<sup>1</sup>. Moreover, a pool of CAMSAP-stabilized minus ends could recruit katanin for severing and further amplification of non-centrosomal microtubules<sup>29, 49</sup>.

Similar to microtubule nucleation, microtubule release from  $\gamma$ -TuRC is expected to be tightly regulated in order to control the abundance and positioning of microtubule minus ends. Our data suggest that the factors promoting microtubule nucleation can play a role in this process. In this study, we focused on three such factors, chTOG, CLASP2 and CDK5RAP2. While we were able to confirm that chTOG potently promotes  $\gamma$ -TuRC-dependent microtubule nucleation, the incompatibility in experimental conditions did not allow us to reach firm conclusions about its interplay with CAMSAPs. However, we were successful in examining the effect of CDK5RAP2. This protein is well-known for its ability to bind  $\gamma$ -TuRC through the domain called  $\gamma$ -TuNA ( $\gamma$ -TuRC nucleation activator), but there was some conflicting evidence about its ability to activate  $\gamma$ -TuRC in vitro<sup>19, 26, 27, 34, 51</sup>. Two studies showed a stimulatory effect of nanomolar  $\gamma$ -TuNA concentrations on microtubule nucleation by  $\gamma$ -TuRC purified from mammalian cells using its affinity for  $\gamma$ -TuNA<sup>26,27</sup>, whereas, more recently, two other groups found no to little effect of even micromolar  $\gamma$ -TuNA concentrations on *Xenopus*  $\gamma$ -TuRC when purified using a  $\gamma$ -tubulin antibody<sup>19, 51</sup>. A recent study attributed these differences to the presence of bulkier N-terminal tags on  $\gamma$ -TuNA and purification methods involving different affinity tags<sup>34</sup>.

Here, we show that full-length CDK5RAP2 can stimulate  $\gamma$ -TuRC-dependent microtubule nucleation already at 30 nM concentration, which is consistent with previously published data<sup>26</sup>. Interestingly, CDK5RAP2 also suppressed CAMSAP binding to  $\gamma$ -TuRC-anchored

minus ends and as well as capping of 14- but not 13-protofilament microtubules. All these data can be best explained by the ability of CDK5RAP2 to trigger a conformational change that would make  $\gamma$ -TuRC match better with the 13-protofilament microtubule geometry. However, we could find no structural support for this idea. Since the densities of terminal  $\gamma$ -TuSC (GCP2<sub>13</sub> and GCP3<sub>14</sub>) and the luminal bridge were not clearly resolved in our reconstructions, so we cannot exclude the possibility of CDK5RAP2-induced conformational changes occurring at these sites. Notably, the terminal  $\gamma$ -TuSC constitutes the binding site for a dimeric  $\gamma$ -TuNA<sup>52</sup>. In a recent comparative study,  $\gamma$ -TuNA-bound human  $\gamma$ -TuRC showed a structural difference at the interface of GCP6 and neighboring GCP2 when compared to that of  $\gamma$ -TuNA-unbound *Xenopus*  $\gamma$ -TuRC<sup>23</sup>. Furthermore, it is also possible that CDK5RAP2 might only contribute to a local conformational change in the terminal  $\gamma$ -TuSC<sup>23</sup>, and this small change would synergize with other  $\gamma$ -TuRC activation mechanisms such as binding of tubulin dimers or activators<sup>6, 7, 51</sup>. Further study would be needed to find out whether the lack of detectable CDK5RAP2-induced structural change in our reconstructions was due to technical reasons or because this alteration is manifested as increased flexibility, is transient and/or requires binding to a microtubule.

We also discovered that  $\gamma$ -TuRC-dependent microtubule nucleation can be strongly enhanced by CLASP2, a positive regulator of microtubule density and growth<sup>53</sup>. Given the abundant colocalization between CLASP2 and  $\gamma$ -TuRC even in the absence of free tubulin, they might bind to each other directly. Previous work has shown that CLASP2 potently promotes formation of complete tubes from incomplete tubulin assemblies and microtubule outgrowth from seeds at low tubulin concentration<sup>28, 54</sup>. The mechanism underlying these activities needs further study, but since CLASP2 did not inhibit CAMSAP binding to  $\gamma$ -TuRC-anchored minus ends and their release, it is unlikely to affect  $\gamma$ -TuRC geometry but more likely acts by affecting microtubule polymerization intermediates. Altogether, our work shows that mechanisms controlling microtubule nucleation and the players involved in this process can also affect the destiny of the generated microtubule minus-ends.

## Materials and Methods

### DNA constructs

We used previously described SII-mCherry-CLASP2 construct<sup>28</sup>. chTOG construct was a gift of S. Royle (University of Warwick, UK). chTOG-mCherry-SII was made by cloning the full length construct in a modified pTT5 expression vector (Addgene no. 44006) with a C-terminus

mCherry-Twin-Strep-tag. GFP-CDK5RAP2 was a gift from Robert Z. Qi (The Hong Kong University of Science and Technology, China). SII-mCherry-CDK5RAP2, SII-SNAP-CAMSAP3, Bio-Tev-mCherry-CAMSAP2 and SII-SNAP-CAMSAP1 were made by cloning the full length previously described constructs<sup>29</sup> in modified C1 vectors with either a Twin-Strep-mCherry, or Twin-Strep-SNAP, or Bio-Tev-mCherry tag at the N-terminus.

### **Cell lines and cell culture**

HEK293T cells (from ATCC) were cultured in Dulbecco's Modified Eagle's Medium DMEM/Ham's F10 media (1:1) supplemented with 10% fetal calf serum (FCS) and 1% antibiotics (penicillin and streptomycin). The cell line used here was not found in the commonly misidentified cell lines database maintained by the Immunization Coalition of Los Angeles County. No further cell line authentication was performed. The cell lines were routinely checked for mycoplasma contamination using LT07-518 Mycoalert assay. Polyethylenimine (PEI, Polysciences) was used to transfect HEK293T cells with plasmids for StrepTactin- and Streptavidin-based protein purification at 3:1 ratio of PEI:plasmid.

### **Generation of homozygous HEK93T knock-in cell lines endogenously tagged with a GFP-SII for GCP3 and GCP6**

GCP3-GFP-SII and GCP6-GFP-SII knock-in cell lines were generated using CRISPR-Cas9 technology<sup>55</sup>. To generate knock-in cell lines, CRISPR guide RNAs were designed using the web tool from MIT: <http://crispr.mit.edu/>. The guide RNAs were designed to overlap with the stop-codon to disrupt the recognition site after insertion of the tag avoiding any further cleavage. Annealed oligo's were inserted into pSpCas9(BB)-2A-Puro (px459, Addgene #62988) using BbsI. Donor plasmids were designed by selecting 800-1000 bp of homology flanking both sides of the stop codon of the targeted gene. The two homology arms were obtained by genomic DNA PCR from HeLa cells. GFP-SII tag was amplified by PCR using primers with complementary domains for the homology arms. Using Gibson assembly, the two homology arms and GFP-SII were cloned into the donor plasmid. FuGENE6 (Roche) was used to cotransfect cells with px459 containing humanized Cas9, guide RNA followed by tracrRNA and a puromycin resistance marker together with a donor construct. 24 hours post-transfection, cells were selected for two days using 2 µg/mL Puromycin and subsequently subcloned to a single cell dilution. Positive clones were confirmed using immunofluorescence, genomic DNA-PCR genotyping and Western blotting. Following are the guide RNA sequences and primers used: for GCP3, gRNA, 5'-GGACCGCGAGCTTCACGTGT-3'; 5'-homology arm,

5'-TCAACACAGCAGAGCCTGTGC-3' and 5'-CGTGTGGGAGCTGCGCCGCC-3'; 3'-homology arm, 5'-AGCTCGCGTCCTCCCAGGG-3' and 5'-CGAATGCATCTGAAAGATAATTGC-3'; genotyping, 5'-GGAAGGAAAAACAGACCCAACC-3' and 5'-CGAATGCATCTGAAAGATAATTGC-3'. For GCP6, gRNA, 5'-CAGAGCAGCTCAGGCGTCC-3'; 5'-homology arm, 5'-TTTCTGCCTAGCTTGGAGCTG-3' and 5'-GGCGTCCTGGTAGTAGTTGTTGAAGTTG-3'; 3'-homology arm, 5'-GGCTGCTCTGCGGGGGAC-3' and 5'-CTACAGGCGTACAGGTGAGC-3'.

### Immunofluorescence and Western blotting

HEK293T GCP3- and GCP6-GFP-SII knock-in cells, seeded on coverslips, were fixed with prechilled methanol at -20°C for 10 min followed by three washes with PBS and mounting on glass slides in Vectashield mounting medium containing DAPI (Vector laboratories).

For Western blotting of GCP3- and GCP6-GFP-SII HEK293T cell lysates, cells grown in 6-well plates were harvested and lysed in lysis buffer containing 20 mM Tris-Cl pH 7.5, 100 mM NaCl, 1% Triton-X-100 supplemented with 10% glycerol and complete protease inhibitor cocktail (Roche). Lysates were cleared by centrifugation at 21,000xg for 20 min at 4 °C. 20  $\mu$ g supernatants from the above step or 35  $\mu$ g purified  $\gamma$ -TuRC were loaded on 8% SDS-PAGE gels, then transferred onto a nitrocellulose membrane (Sigma-Aldrich). Membranes were blocked in 2% BSA in 0.02% Tween-20 in PBS for 30 min at room temperature followed by overnight incubation with primary antibodies (rabbit polyclonal anti-GFP (1:4000, Abcam, ab290); mouse anti-GCP3 (1:1000, Santa Cruz, sc-373758); mouse monoclonal anti-GCP6 (1:500, Santa Cruz, sc-374063); mouse monoclonal anti-GCP5 (1:500, Santa Cruz, sc-365837); mouse monoclonal anti-GCP2 (1:500, Santa Cruz, sc-377117); rabbit polyclonal anti-GCP4 (1:1000, ThermoFisher, PA5-30557) and mouse monoclonal anti- $\gamma$ -tubulin (1:10000, Sigma, T6557)) at 4°C, three washes with 0.02% Tween-20 in PBS, 1 hour incubation with secondary antibodies (1:15000, goat anti-rabbit IRDye-800CW and goat anti-mouse IRDye-680LT from Li-Cor Biosciences, Lincoln, LE) at room temperature and final three washes. Membranes were imaged using Odyssey CLx infrared imaging system (Li-Cor Biosciences).

### Purification of $\gamma$ -TuRC from HEK293T GCP3- and GCP6-GFP-SII knock-in cells

Human  $\gamma$ -TuRCs used in the in vitro reconstitution assays were purified using Twin-Strep-tag and Strep-Tactin affinity purification method as described previously<sup>56</sup>. Homozygous HEK293T GCP3- and GCP6-GFP-SII knock-in cells, cultured in dark, were harvested from

eight 15 cm dishes each and resuspended and lysed in lysis buffer (50 mM HEPES, 150 mM NaCl, 0.5% Triton-X-100, 1 mM MgCl<sub>2</sub>, 1 mM EGTA, 0.1mM GTP and 1 mM DTT, pH 7.4) supplemented with EDTA-free protease inhibitor cocktail (Roche). Cell lysates were subjected to centrifugation at 21,000xg for 20 min at 4°C. The supernatants obtained from the previous step were incubated with equilibrated Strep-Tactin Sepharose beads (28-9355-99, GE Healthcare) for 45 min at 4 °C. Following incubation, beads were washed three times with the wash buffer (50 mM HEPES, 150 mM NaCl and 0.1% Triton-X-100, 1 mM MgCl<sub>2</sub>, 1 mM EGTA, 0.1mM GTP and 1 mM DTT, pH 7.4) and  $\gamma$ -TuRC was eluted for 15 min at 4 °C in elution buffer (50 mM HEPES, 150 mM NaCl (300 mM NaCl for GCP6-GFP-SII), 0.05% Triton-X-100, 1 mM MgCl<sub>2</sub>, 1 mM EGTA, 0.1mM GTP, 1 mM DTT and 2.5 mM d-Desthiobiotin, pH 7.4). GCP6-tagged purified  $\gamma$ -TuRC was then subjected to buffer exchange using Vivaspin 500 centrifugal concentrator (10 kDa MWCO, Sartorius VS0102) for a final NaCl concentration of 150 mM in eluate. Purified  $\gamma$ -TuRCs were immediately aliquoted, snap-frozen in liquid N<sub>2</sub> and stored at -80 °C. Throughout the purification process, tubes were covered with aluminium foil wherever possible. The purity and composition of purified  $\gamma$ -TuRCs were analyzed by western blot and mass spectrometry.

### **Purification of recombinant proteins from HEK293T cells for in vitro reconstitution assays**

Human mCherry-CDK5RAP2, mCherry-CLASP2, chTOG-mCherry and SNAP-AF647-CAMSAP1 and mouse SNAP-AF647-CAMSAP3 used in the in vitro reconstitution assays were purified using same Twin-Strep-tag and Strep-Tactin affinity purification method as described above for  $\gamma$ -TuRC, but with modified buffers and steps. In brief, HEK293T cells transfected with 50  $\mu$ g of respective constructs per 15 cm dish were harvested 36 hours post-transfection from four 15 cm dishes each and resuspended and lysed in lysis buffer (50 mM HEPES, 300 mM NaCl, 0.5% Triton-X-100, 1 mM MgCl<sub>2</sub> and 1 mM EGTA, pH 7.4) supplemented with EDTA-free protease inhibitor cocktail (Roche). Cell lysates were clarified and the supernatants obtained were incubated with equilibrated Strep-Tactin Sepharose beads. Following incubation of mCherry-CDK5RAP2, mCherry-CLASP2 and chTOG-mCherry preparations, beads were additionally washed five times using high salt (1 M NaCl) containing wash buffer (50 mM HEPES, 0.1% Triton-X-100, 1 mM MgCl<sub>2</sub> and 1 mM EGTA, pH 7.4) before washing three times with 300 mM NaCl containing wash buffer. For SNAP-tag labeling of CAMSAP3 and CAMSAP1 with Alexa Fluor 647 dye, washed beads were incubated with labeling mix (50  $\mu$ M Alexa Fluor 647 dye in 50 mM HEPES, 150 mM NaCl and 0.1% Triton-

X-100, 1 mM MgCl<sub>2</sub>, 1 mM EGTA and 1 mM DTT, pH 7.4) for 1 hour. Following this incubation, beads were washed five times with wash buffer containing 300 mM NaCl to remove excess dye. Proteins were then eluted in elution buffer containing 50 mM HEPES, 150 mM NaCl, 0.05% Triton-X-100, 1 mM MgCl<sub>2</sub>, 1 mM EGTA, 1 mM DTT and 2.5 mM d-Desthiobiotin, pH 7.4.

For purification of human mCherry-CAMSAP2, HEK293T cells were transfected with 25  $\mu$ g of Bio-Tev-mCherry-CAMSAP2 and 25  $\mu$ g of BirA per 15 cm dish. Cells were harvested 36 hours post-transfection from four 15 cm dishes and resuspended in lysis buffer (50 mM HEPES, 300 mM NaCl, 0.5% Triton-X-100, 1 mM MgCl<sub>2</sub>, 1 mM EGTA and 1 mM DTT, pH 7.4) supplemented with EDTA-free protease inhibitor cocktail (Roche). Cell lysate was incubated with Dynabeads M-280 streptavidin (Invitrogen-11206D) for 1 hour. Beads were washed thrice with lysis buffer without protease inhibitors and thrice with the TEV cleavage buffer (50 mM HEPES, 150 mM NaCl, 0.05% Triton-X-100, 1 mM MgCl<sub>2</sub>, 1 mM EGTA and 1 mM DTT). mCherry-CAMSAP2 was eluted in 50  $\mu$ l TEV cleavage buffer containing 0.5  $\mu$ g of glutathione S-transferase-6x-histidine Tobacco etch virus protease site (Sigma-Aldrich) for 2 hr at 4 °C.

Purified proteins were immediately aliquoted, snap-frozen in liquid N<sub>2</sub> and stored at -80 °C. Bacterially expressed mCherry-EB3 was a gift of Dr. M.O. Steinmetz (Paul Scherrer Institut, Switzerland); they were produced as described previously<sup>57</sup>. Purity of the samples was analyzed by Coomassie-staining of SDS-PAGE gels and mass spectrometry.

### Mass spectrometry

Purified  $\gamma$ -TuRC preparations (GCP3- and GCP6-tagged) were resuspended in 20  $\mu$ l of Laemmli Sample buffer (Biorad) and were loaded on a 4%–12% gradient Criterion XT Bis-Tris precast gel (Biorad). Gel was fixed with 40% methanol/10% acetic acid and then stained with colloidal Coomassie dye G-250 (Gel Code Blue Stain Reagent, Thermo Scientific) for 1 hour. Samples were resuspended in 10% formic acid (FA)/5% DMSO post in-gel digestion, and analyzed with an Agilent 1290 Infinity (Agilent Technologies, CA) LC, operating in reverse-phase (C18) mode, coupled to an Orbitrap Q-Exactive mass spectrometer (Thermo Fisher Scientific, Bremen, Germany). Onto a trap column (Reprosil C18, 3  $\mu$ m, 2 cm x 100  $\mu$ m; Dr. Maisch) with solvent A (0.1% formic acid in water), peptides were loaded at a maximum pressure of 800 bar and chromatographically separated over the analytical column (Zorbax SB-C18, 1.8  $\mu$ m, 40 cm x 50  $\mu$ m; Agilent) using 90 min linear gradient from 7%–30% solvent B (0.1% formic acid in acetonitrile) at a flow rate of 150 nL/min. The mass

spectrometer automatically switched between MS and MS/MS in a data-dependent acquisition (DDA) mode. The 10 most abundant peptides were subjected to HCD fragmentation after a survey scan from 350-1500 m/z. MS spectra in high-resolution mode ( $R > 30,000$ ) were acquired, whereas MS2 was in high-sensitivity mode ( $R > 15,000$ ). Raw data were processed using Proteome Discoverer 1.4 (version 1.4.0.288, Thermo Scientific, Bremen, Germany) and a database search was performed using Mascot (version 2.4.1, Matrix Science, UK) against a Swiss-Prot database (taxonomy human). Whereas oxidation of methionine was set as a variable modification, carbamidomethylation of cysteines was set as a fixed modification. Up to two missed cleavages were allowed by Trypsin. Data filtering performed using percolator resulted in 1% false discovery rate (FDR). Additional filters set were search engine rank 1 and mascot ion score  $>20$ .

To assess the quality of purified recombinant proteins (mCherry-CDK5RAP2, mCherry-CLASP2 and chTOG-mCherry), samples were digested using S-TRAP micro filters (ProtiFi) according to the manufacturer's protocol. In brief, 4  $\mu\text{g}$  of protein samples were denatured using 5% SDS buffer and reduced and alkylated using DTT (20 mM, 10 min, 95 °C) and iodoacetamide (IAA, 40 mM, 30 min), followed by acidification and precipitation using a methanol triethylammonium bicarbonate (TEAB) buffer before finally loading on a S-TRAP column. Trapped proteins were washed four times with methanol TEAB buffer followed by overnight Trypsin (1  $\mu\text{g}$ , Promega) digestion at 37 °C. Before LC-MS analysis, digested peptides were eluted and dried in a vacuum centrifuge.

Samples were analyzed by reversed phase nLC-MS/MS using an Ultimate 3000 UHPLC coupled to an Orbitrap Q Exactive HF-X mass spectrometer (Thermo Scientific). Digested peptides were separated over a 50 cm reversed phase column, packed in-house, (Agilent Poroshell EC-C18, 2.7  $\mu\text{m}$ , 50 cm x 75  $\mu\text{m}$ ) using a linear gradient with buffer A (0.1% FA) and buffer B (80% acetonitrile, 0.1% FA) ranging from 13-44% B over 38 min at a flow rate of 300 nL/min, followed by a column wash and re-equilibration step. MS data was acquired using a DDA method with the set MS1 scan parameters in profile mode: 60,000 resolution, automatic gain control (AGC) target equal to 3E6, scan range of 375-1600 m/z, maximum injection time of 20 ms. The MS2 scan parameters were set at 15,000 resolution, with an AGC target set to standard, an automatic maximum injection time and an isolation window of 1.4 m/z. Scans were acquired using a fixed first mass of 120 m/z and a mass range of 200-2000 and a normalized collision energy (NCE) of 28. Precursor ions were selected for fragmentation



using a 1 second scan cycle, a 10 s dynamic exclusion time and a precursor charge selection filter for ion possessing +2 to +6 charges. The total data acquisition time was 55 min.

Raw files were processed using Proteome Discoverer (PD) (version 2.4, Thermo Scientific). A database search was performed for MS/MS fragment spectra using Sequest HT against a human database (UniProt, year 2020) that was modified to include protein sequences from our cloned constructs and a common contaminants database. A precursor mass tolerance of 20 ppm and a fragment mass tolerance of 0.06 Da was set for the search parameters. Up to two missed cleavages were allowed by Trypsin digestion. Carbamidomethylation was set as fixed modification and methionine oxidation and protein N-term acetylation was set as variable modifications. Data filtering performed using percolator resulted in 1% FDR for peptide spectrum match (PSM) and a 1% FDR was applied to peptide and protein assemblies. An additional filter with a minimum Sequest score of 2.0 was set for PSM inclusion. MS1 based quantification was performed using the Precursor Ion Quantifier node with default settings and precursor ion feature matching was enabled using the Feature Mapper node. Common protein contaminants were filtered out from the results table.

### **Negative-stain EM and data processing**

Purified  $\gamma$ -TuRC was thawed and incubated in the presence or absence of 120 nM CDK5RAP2 on ice for 20 min. 2-3  $\mu$ l of protein was applied to glow-discharged carbon-coated copper grids (EMS; CF-400-Cu) and incubated for 45 s at room temperature. Protein solution was removed by manual blotting with Whatman No. 1 filter paper. Then 2-3  $\mu$ l of protein solution was applied again to improve particle density. The protein solution was manually blotted from one side of the grid while freshly filtered 1% uranyl acetate (wt/vol) was simultaneously pipetted from the opposite side to exchange the solution. Grids were incubated in uranyl acetate for a further 45 s. Stain was removed by manual blotting, and grids were air-dried for >24–48 h in a sealed container containing desiccant before imaging. Grids were initially screened on a TFS Tecnai F20 located at ETH Zurich's ScopeM facility, and final datasets on suitable grids were collected on an FEI Talos 120 at the University of Zurich's Center for Microscopy and Image Analysis.

For each condition, several thousand micrographs were recorded via the MAPS automated acquisition software at a magnification of 57,000 X (2.4  $\text{\AA}$ /pixel) on a BM-Ceta CMOS camera. Contrast transfer function (CTF) parameters were estimated using CTFFIND4<sup>58</sup>. All subsequent processing was done in RELION version 3.1 and UCSF Chimera and ChimeraX<sup>59-61</sup>.

The main 3D reconstruction workflow steps are outlined in Extended data Fig. 4i,j. Generally, micrographs were imported, and a small set of <1,000 particles was manually picked and subjected to reference-free 2D classification. The resulting set of averages was used as an initial template for RELION's built-in auto-picking implementation. One or two rounds of auto-picking were performed to yield the best templates for optimal picking. Auto-picked particles were binned by four and subjected to reference-free 2D classification to remove particles likely corresponding to dirt and other contaminants. A random subset of the cleaned, binned particles was used to generate an ab initio model. Then, all cleaned, binned particles were subjected to an intermediate 3D auto-refinement step using the ab initio model as a reference, re-extracted using the refined coordinates, and subjected to 3D classification. Particles that generated 3D classes containing the highest level of detail were re-extracted from micrographs at either bin-2 pixel size (4.8 Å) and subjected to a final round of 3D auto-refinement using one of the classes as a new reference model.

A published model for  $\gamma$ -tubulin bound to GCP2 (PDB ID: 6V6S<sup>20</sup>) was individually docked into each radial "spoke" density of the resulting EM density maps using UCSF Chimera's "Fit in map" function. Only resulting fits for which i) the number of atoms outside the contour was <20% of the total number of atoms fitted and ii) the resulting fit did not form domain clashes with neighbouring  $\gamma$ -tubulin/GCP2 subunits were kept for further analysis. This procedure led to 12 out of possible 14  $\gamma$ -tubulin/GCP2 subcomplexes to be reliably fitted into both density maps (Extended data Fig. 4b,c,e,f).

A model for twelve laterally-associated  $\beta$ -tubulin subunits was constructed using PDB ID: 2HXF<sup>43</sup> and EMD-5193<sup>44</sup>. The ring was aligned to each  $\gamma$ -tubulin ring using the align command in Pymol; the 6th  $\gamma$ -tubulin subunit was used as an alignment anchor. The center of mass of each  $\beta$ - or  $\gamma$ -tubulin subunit was then calculated based on its C $\alpha$  coordinates and the radial or axial displacement relative to the helical axis of the  $\beta$ -tubulin ring (i.e., the microtubule) was determined using a custom MATLAB script. A similar analysis was performed using the  $\gamma$ -tubulin ring from the  $\gamma$ -TuSC oligomer in the "closed" conformation (blue; PDB ID: 5FLZ<sup>42</sup>). The results are plotted in Extended data Fig. 4h; values close to zero indicate a closer fit to the 13-protofilament microtubule.

## **In vitro reconstitution assays**

### *Stabilized microtubule preparations*

Taxol- and Docetaxel-stabilized and double-cycled GMPCPP-stabilized microtubules used for in vitro  $\gamma$ -TuRC capping assays were prepared as described previously<sup>45,62</sup>. In brief, GMPCPP-stabilized microtubules seeds were prepared in the presence of GMPCPP (Guanylyl-(a,b)-methylene-diphosphonate (Jena Biosciences)) by two rounds of polymerization and a depolymerization cycle. First, a 20  $\mu$ M porcine brain tubulin (Cytoskeleton) mix composed of 70% porcine unlabeled tubulin, 18% biotin tubulin and 12% HiLyte647-tubulin was incubated with 1 mM GMPCPP in MRB80 buffer (pH 6.8, 80 mM K-PIPES, 1 mM EGTA and 4 mM MgCl<sub>2</sub>) at 37°C for 30 minutes. Polymerization mix was then pelleted by centrifugation in an Airfuge for 5 min at 119,000xg followed by resuspension and depolymerization in MRB80 buffer on ice for 20 min and subsequent polymerization for 30 min in presence of fresh 1 mM GMPCPP at 37°C. GMPCPP-stabilized microtubule seeds were pelleted, resuspended in MRB80 buffer containing 10% glycerol, aliquoted, snap-frozen in liquid N<sub>2</sub> and stored at -80 °C.

Taxol- and Docetaxel-stabilized microtubules were prepared 24 hours in advance by polymerizing a 29  $\mu$ M porcine brain tubulin mix (86% porcine unlabeled tubulin, 10% biotin tubulin and 4% HiLyte647-tubulin) in the presence of 2.5 mM GTP (Sigma-Aldrich) and 20  $\mu$ M Taxol (Sigma-Aldrich) or Docetaxel (Sanofi-Aventis) in MRB80 buffer (pH 6.8, 80 mM K-PIPES, 1 mM EGTA and 4 mM MgCl<sub>2</sub>) at 37°C for 30 minutes. After polymerization, GTP-tubulin-Taxol mix was diluted 5 times with prewarmed 20  $\mu$ M Taxol or Docetaxel made in MRB80 buffer and centrifuged at 16200xg for 15 min at room temperature. The microtubule pellet was resuspended in prewarmed 20  $\mu$ M Taxol solution in MRB80 buffer and stored at room temperature in the dark covered with aluminium foil.

#### *In vitro reconstitution of microtubule nucleation*

Flow chamber was assembled using plasma-cleaned glass coverslip and microscopic slide attached together using double-sided tape. These chambers were then functionalized by 5 min incubation with 0.2 mg/ml PLL-PEG-biotin (Susos AG, Switzerland) followed by 5 min incubation with 1 mg/ml NeutrAvidin (Invitrogen) in MRB80 buffer. Next, biotinylated-anti-GFP nanobody was attached to the coverslip through biotin-NeutrAvidin links by incubating the chamber for 5 min. During this incubation,  $\gamma$ -TuRC-GFP was diluted 10 times and either preincubated with nucleation-promoting factors or MRB80 buffer for 3 min and then immobilized on the GFP-nanobody coated coverslips by incubating it with flow chamber by 3 min. Non-immobilized  $\gamma$ -TuRC was washed away with MRB80 buffer and flow chambers were further incubated with 0.8 mg/ml k-casein to prevent non-specific protein binding. The

nucleation mix with or without proteins (MRB80 buffer supplemented with 17.5  $\mu$ M or 25  $\mu$ M porcine brain tubulin, 50 mM or 80 mM (for CAMSAP assays) KCl, 1mM GTP, 0.5 mg/ml k-casein, 0.1% methylcellulose, and oxygen scavenger mix (50 mM glucose, 400 mg/ml glucose-oxidase, 200 mg/ml catalase, and 4 mM DTT)) were added to the flow chambers after centrifugation in an ultracentrifuge (Beckman Airfuge) at 119,000xg for 5 minutes. Concentrations of the proteins and composition of the nucleation mix have been indicated in either figure or figure legends. The flow chambers were then sealed with high-vacuum silicone grease (Dow Corning), and three consecutive 10 min time-lapse videos were acquired after 2 min incubation (time, t=0) of the flow chambers with the nucleation reactions on total internal reflection fluorescence microscope stage at 30 °C. All tubulin products were from Cytoskeleton.

#### *Capping assays*

For capping assays, 2 parallel flow chambers on the same coverslip were functionalized as mentioned above and then incubated with GMPCPP- and Taxol- or GMPCPP- and Docetaxel-stabilized microtubules for 2 min for their attachment to the coverslips through biotin-neutravidin links. Flow chambers were then incubated with 0.8 mg/ml k-casein to prevent non-specific protein binding and a master mix of reaction mix (5  $\mu$ M tubulin, 50 mM KCl, 1mM GTP, 0.5 mg/ml k-casein, 0.1% methylcellulose, and oxygen scavenger mix (50 mM glucose, 400 mg/ml glucose-oxidase, 200 mg/ml catalase, and 4 mM DTT) in MRB80 buffer centrifuged in an Airfuge for 5 min at 119,000xg) supplemented with  $\gamma$ -TuRC (GCP3-GFP) and with or without 30 nM mCherry-CDK5RAP2 was prepared and divided into 2 for adding it to the parallel chambers. The flow chambers were then sealed with high-vacuum silicone grease and three 5 min time-lapse videos were acquired from both the parallel chambers alternatively after 2 min incubation (time, t=0) on TIRF microscope stage at 30 °C. Time interval was kept 20 s.

### **Image acquisition, processing and data analysis**

#### *Widefield microscopy*

Fixed HEK293T cells were imaged on a Nikon Eclipse Ni upright widefield fluorescence microscope equipped with a Nikon DS-Qi2 camera (Nikon), an Intensilight CHGFI precentered fiber illuminator (Nikon), ET-DAPI and ET-EGFP filters (Chroma), controlled by

Nikon NIS Br software. Slides were imaged using a Plan Apo Lambda 60x NA 1.4 oil objective (Nikon).

### *TIRF microscopy*

In vitro assays were imaged on an iLas2 TIRF microscope setup as described previously<sup>56</sup>. Briefly, iLas2 system (Roper Scientific, Evry, France) is a dual laser illuminator for azimuthal spinning TIRF illumination and powered with a custom modification for targeted photomanipulation. This system was installed on the Nikon Eclipse Ti-E inverted microscope with the perfect focus system. This microscope was equipped with Nikon Apo TIRF 100x 1.49 N.A. oil objective (Nikon), CCD camera CoolSNAP MYO M- USB-14-AC (Roper Scientific), EMCCD Evolve mono FW DELTA 512x512 camera (Roper Scientific) with the intermediate lens 2.5X (Nikon C mount adaptor 2.5X), 150 mW 488 nm laser, 100 mW 561 nm laser and 49002 and 49008 Chroma filter sets and controlled with MetaMorph 7.10.2.240 software (Molecular Devices). The final magnification using Evolve EMCCD camera was 0.064  $\mu\text{m}/\text{pixel}$  and for CoolSNAP Myo CCD camera it was 0.045  $\mu\text{m}/\text{pixel}$ . Temperature was maintained at 30 °C to image the in vitro assays using a stage top incubator model INUBG2E-ZILCS (Tokai Hit). Time-lapse movies were acquired using a CoolSNAP Myo CCD camera (Roper Scientific) at either 5 s (for nucleation assays without CAMSAPs) or 20 s (for assays with CAMSAPs) time interval with 200 ms, 300 ms and 500 ms exposure time for 642 nm, 561 nm and 488 nm illumination respectively for 10 minutes, while time-lapse images acquired on more sensitive Photometrics Evolve 512 EMCCD camera (Roper Scientific) were taken at 3 s time interval with 100 ms exposure time for 10 minutes.

### *$\gamma$ -TuRC nucleation efficiency*

For each independent nucleation assay,  $\gamma$ -TuRCs that nucleated microtubules or were anchored to an already nucleated microtubule within 10 min of a time-lapse movie were manually counted. Also, all the  $\gamma$ -TuRC (GCP3-GFP or GCP6-GFP) particles were detected and counted from the first or second frame of that time-lapse movie using an open-source ImageJ plugin ComDet v.0.5.4 <https://github.com/ekatruxha/ComDet> and the percentage of active ones out of the total was calculated and plotted for nucleation efficiency. From each independent assay, nucleation efficiency was calculated for three consecutive 10 min time-lapse movies from three different fields of view and plotted as 0-10, 10-20 and 20-30 min.

### *Microtubule growth dynamics analysis*

Images and movies were processed using Fiji (<https://imagej.net/Fiji>). Kymographs from the in vitro reconstitution assays were generated using the ImageJ plugin KymoResliceWide v.0.4 <https://github.com/ekatruxha/KymoResliceWide>. Microtubule dynamics parameters viz. plus-end growth rate and catastrophe frequency were determined from kymographs using an optimized version of the custom made JAVA plugin for ImageJ as described previously<sup>57, 62</sup>. The relative standard error for catastrophe frequency was calculated as described in<sup>56</sup>.

#### *Single-molecule intensity analysis of surface attached $\gamma$ -TuRC*

To estimate the number of GCP3-GFP molecules in  $\gamma$ -TuRC, three parallel flow chambers were assembled on the same plasma-cleaned glass coverslip. The three chambers were incubated with the dilutions of GFP protein (monomeric), GFP-EB3 (dimeric) and GCP3-GFP (test) strongly diluted to single molecules level. Flow chambers were then washed with MRB80 buffer, sealed with vacuum grease and immediately imaged using TIRF microscope. Samples were focussed first in one area and 15-20 images of unexposed coverslip regions were acquired with 100 ms exposure time. Acquisition settings were kept constant for the three parallel chambers. Single molecule fluorescence puncta were detected, measured and fitted with 2D Gaussian function using custom written ImageJ plugin DoM\_Utrecht v.1.1.6 ([https://github.com/ekatruxha/DoM\\_Utrecht](https://github.com/ekatruxha/DoM_Utrecht)). Using single GFP distribution as a starting point, we were able to build expected intensity distributions of 2x,3x,4x, and so on GFP molecules by using the convolution of its probability density function. The intensity distributions of GFP N-mers, where N corresponds to the oligomers with increasing number of GFP molecules, formed the "basis" distributions. Then, we fitted GCP3-GFP intensity distribution as a sum of these "basis" distributions with different weights, serving as the fit parameters (see Noordstra et al., 2022 for details).

#### *Single-molecule intensity analysis of $\gamma$ -TuRC from CAMSAP3 assays*

All the  $\gamma$ -TuRC (GCP3-GFP) particles immobilized on coverslip using biotinylated-GFP-nanobody within a field of view were detected from the first frame or second frame of a 10 min time-lapse movie using above mentioned ImageJ plugin ComDet. Integrated intensity values for individual active  $\gamma$ -TuRCs that nucleated microtubules and either colocalized or not colocalized with CAMSAP3 or dissociated from microtubules after CAMSAP3 recruitment were manually extracted and normalized to the average integrated intensity of total active  $\gamma$ -TuRCs that nucleated microtubules within that field of view.

### *Colocalization frequency of $\gamma$ -TuRC and nucleation-promoting factors*

All the  $\gamma$ -TuRC (GCP3-GFP) particles immobilized on coverslip within a field of view were detected from the first frame or second frame of 10 min time-lapse movies or single images (for assays without tubulin) using above mentioned ImageJ plugin ComDet and their colocalization percentage with the respective nucleation-promoting factor was calculated using the colocalization function of this ComDet plugin.

### *Analysis of $\gamma$ -TuRC-CAMSAPs colocalization and microtubule release frequency*

All the active  $\gamma$ -TuRCs that nucleated or anchored a microtubule were counted manually. Each of these  $\gamma$ -TuRC-anchored microtubule minus-ends were monitored for any binding of CAMSAPs within 10 min of a time-lapse movie and were scored manually if recruited CAMSAPs and plotted. Out of these CAMSAP-colocalized  $\gamma$ -TuRC-anchored minus-ends, the minus ends that started growing during this 10 min duration were quantified as released microtubules. For quantification of % of microtubules released from active  $\gamma$ -TuRC, all the  $\gamma$ -TuRC-anchored minus ends that started growing within 10 min were counted as released microtubules.

### *$\gamma$ -TuRC capping efficiency*

For quantification of  $\gamma$ -TuRC capping efficiency, stabilized microtubules were monitored for 5 min during a time-lapse movie and if one of the ends of a microtubule was stably bound to  $\gamma$ -TuRC for at least 2 min, that microtubule was scored as  $\gamma$ -TuRC-capped microtubule.

## **Statistical analysis**

All statistical details of experiments including the definitions, exact values of number of measurements, precision measures and statistical tests performed are mentioned in the figure legends. All experiments were repeated at least three times. Data processing and statistical analysis were done in Excel and GraphPad Prism 9 (GraphPad Software). Significance was defined as: ns =not significant, \* $p < 0.05$ , \*\* $p < 0.01$ , \*\*\* $p < 0.001$  and \*\*\*\* $p < 0.0001$ .

## **Data availability**

All data that support the conclusions are either available in the manuscript itself or available from the authors on request.

## **Code availability**

MATLAB script used for analysis of structural data is available from the authors on request. ImageJ macros used in this study are either available online at <https://github.com/ekatrukha/KymoResliceWide>, <https://github.com/ekatrukha/ComDet>, [https://github.com/ekatrukha/DoM\\_Utrecht](https://github.com/ekatrukha/DoM_Utrecht), or from the corresponding authors on request.

### **Author Contributions**

D.R. designed and performed protein purifications and in vitro reconstitution experiments, analyzed data and wrote the paper; S.H., J.L.M. and Y.Z. have generated and characterized essential reagents; R.S., K.E.S. and A.F. M.A. performed, analyzed and supervised mass spectrometry experiments; E.A.K. facilitated and performed data analysis; M.W. generated and analyzed transmission EM data; K.J. generated reagents, performed experiments, supervised the project and wrote the paper; A.A. coordinated the project and wrote the paper.

### **Acknowledgements**

Negative stain EM grid screening was performed with support of the ScopeM imaging center, ETH Zurich. Negative stain EM data collection was performed with support of the Center for Microscopy and Image Analysis, University of Zurich. The authors gratefully acknowledge Lina Carlini for her help in developing the MATLAB analysis scripts used to compare  $\gamma$ -TuRC structural data. This work was supported by the European Research Council Synergy grant 609822 and the ZonMW TOP 91216006 program to A.A and grants from National Natural Science Foundation of China (31871356, 32070705) to K.J.

### **Competing financial interests**

The authors declare no competing financial interests.

### **Supplemental Information**

Supplemental Information can be found online at <https://doi.org/10.1101/2022.08.03.502613>



## References

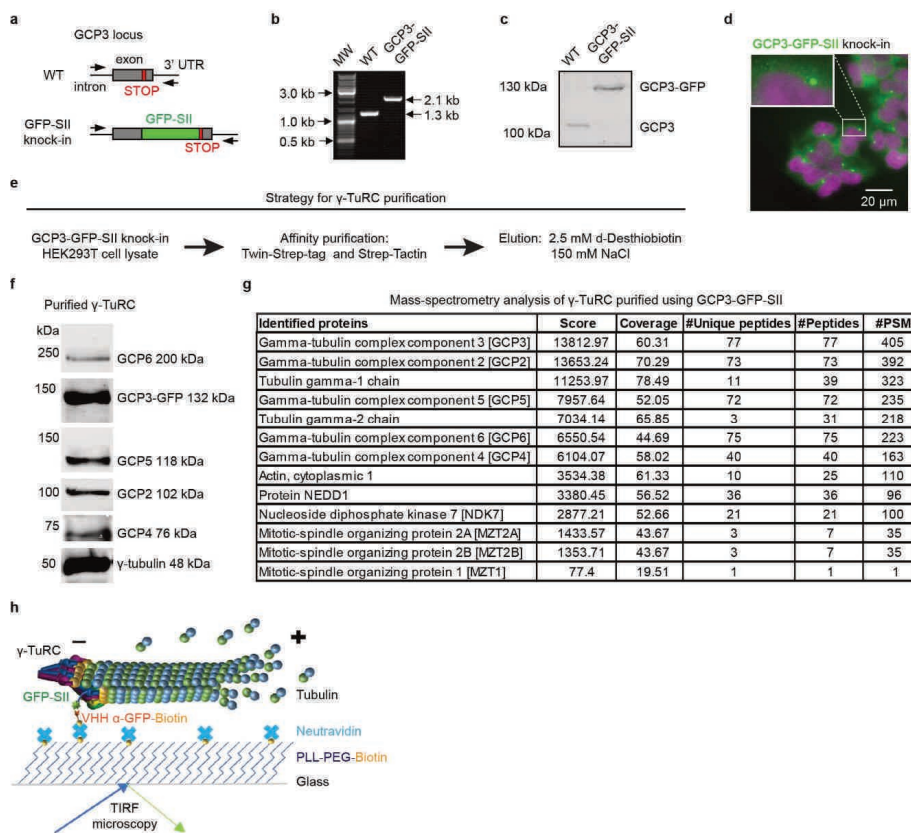
1. Akhmanova, A. & Kapitein, L.C. Mechanisms of microtubule organization in differentiated animal cells. *Nat Rev Mol Cell Biol* **23**, 541-558 (2022).
2. Sanchez, A.D. & Feldman, J.L. Microtubule-organizing centers: from the centrosome to non-centrosomal sites. *Curr Opin Cell Biol* **44**, 93-101 (2017).
3. Muroyama, A. & Lechler, T. Microtubule organization, dynamics and functions in differentiated cells. *Development* **144**, 3012-3021 (2017).
4. Martin, M. & Akhmanova, A. Coming into Focus: Mechanisms of Microtubule Minus-End Organization. *Trends Cell Biol* **28**, 574-588 (2018).
5. Roostalu, J. & Surrey, T. Microtubule nucleation: beyond the template. *Nat Rev Mol Cell Biol* **18**, 702-710 (2017).
6. Liu, P., Wurtz, M., Zupa, E., Pfeffer, S. & Schiebel, E. Microtubule nucleation: The waltz between gamma-tubulin ring complex and associated proteins. *Curr Opin Cell Biol* **68**, 124-131 (2021).
7. Thawani, A. & Petry, S. Molecular insight into how gamma-TuRC makes microtubules. *J Cell Sci* **134** (2021).
8. Wiese, C. & Zheng, Y. A new function for the gamma-tubulin ring complex as a microtubule minus-end cap. *Nat Cell Biol* **2**, 358-364 (2000).
9. Vineethakumari, C. & Luders, J. Microtubule Anchoring: Attaching Dynamic Polymers to Cellular Structures. *Front Cell Dev Biol* **10**, 867870 (2022).
10. Meng, W., Mushika, Y., Ichii, T. & Takeichi, M. Anchorage of microtubule minus ends to adherens junctions regulates epithelial cell-cell contacts. *Cell* **135**, 948-959 (2008).
11. Goodwin, S.S. & Vale, R.D. Patronin regulates the microtubule network by protecting microtubule minus ends. *Cell* **143**, 263-274 (2010).
12. Akhmanova, A. & Hoogenraad, C.C. Microtubule Minus-End-Targeting Proteins. *Curr. Biol.* **25**, R162-R171 (2015).
13. Zheng, Y., Buchwalter, R.A., Zheng, C., Wight, E.M., Chen, J.V. & Megraw, T.L. A perinuclear microtubule-organizing centre controls nuclear positioning and basement membrane secretion. *Nat Cell Biol* **22**, 297-309 (2020).
14. Atherton, J., Jiang, K., Stangier, M.M., Luo, Y., Hua, S., Houben, K., van Hooff, J.J.E., Joseph, A.P., Scarabelli, G., Grant, B.J., Roberts, A.J., Topf, M., Steinmetz, M.O., Baldus, M., Moores, C.A. & Akhmanova, A. A structural model for microtubule minus-end recognition and protection by CAMSAP proteins. *Nat Struct Mol Biol* **24**, 931-943 (2017).
15. Imasaki, T., Kikkawa, S., Niwa, S., Saijo-Hamano, Y., Shigematsu, H., Aoyama, K., Mitsuoka, K., Shimizu, T., Aoki, M., Sakamoto, A., Tomabechi, Y., Sakai, N., Shirouzu, M., Taguchi, S., Yamagishi, Y., Setsu, T., Sakihama, Y., Nitta, E., Takeichi, M. & Nitta, R. CAMSAP2 organizes a gamma-tubulin-independent microtubule nucleation centre through phase separation. *Elife* **11**, e77365 (2022).
16. Moritz, M., Braunfeld, M.B., Guenebaut, V., Heuser, J. & Agard, D.A. Structure of the gamma-tubulin ring complex: a template for microtubule nucleation. *Nat Cell Biol* **2**, 365-370 (2000).
17. Wurtz, M., Bohler, A., Neuner, A., Zupa, E., Rohland, L., Liu, P., Vermeulen, B.J.A., Pfeffer, S., Eustermann, S. & Schiebel, E. Reconstitution of the recombinant human gamma-tubulin ring complex. *Open Biol* **11**, 200325 (2021).
18. Consolati, T., Locke, J., Roostalu, J., Chen, Z.A., Gannon, J., Asthana, J., Lim, W.M., Martino, F., Cvetkovic, M.A., Rappsilber, J., Costa, A. & Surrey, T. Microtubule Nucleation Properties of Single Human gammaTuRCs Explained by Their Cryo-EM Structure. *Dev Cell* **53**, 603-617 (2020).

19. Liu, P., Zupa, E., Neuner, A., Bohler, A., Loerke, J., Flemming, D., Ruppert, T., Rudack, T., Peter, C., Spahn, C., Gruss, O.J., Pfeffer, S. & Schiebel, E. Insights into the assembly and activation of the microtubule nucleator gamma-TuRC. *Nature* **578**, 467-471 (2020).
20. Wieczorek, M., Urnavicius, L., Ti, S.C., Molloy, K.R., Chait, B.T. & Kapoor, T.M. Asymmetric Molecular Architecture of the Human gamma-Tubulin Ring Complex. *Cell* **180**, 165-175 (2020).
21. Zimmermann, F., Serna, M., Ezquerra, A., Fernandez-Leiro, R., Llorca, O. & Luders, J. Assembly of the asymmetric human gamma-tubulin ring complex by RUVBL1-RUVBL2 AAA ATPase. *Sci Adv* **6**, eabe0894 (2020).
22. Wieczorek, M., Ti, S.C., Urnavicius, L., Molloy, K.R., Aher, A., Chait, B.T. & Kapoor, T.M. Biochemical reconstitutions reveal principles of human gamma-TuRC assembly and function. *J Cell Biol* **220**, e202009146 (2021).
23. Brilot, A.F., Lyon, A.S., Zelter, A., Viswanath, S., Maxwell, A., MacCoss, M.J., Muller, E.G., Sali, A., Davis, T.N. & Agard, D.A. CM1-driven assembly and activation of yeast gamma-tubulin small complex underlies microtubule nucleation. *Elife* **10**, e65168 (2021).
24. Wurtz, M., Zupa, E., Atorino, E.S., Neuner, A., Bohler, A., Rahadian, A.S., Vermeulen, B.J.A., Tonon, G., Eustermann, S., Schiebel, E. & Pfeffer, S. Modular assembly of the principal microtubule nucleator gamma-TuRC. *Nat Commun* **13**, 473 (2022).
25. Thawani, A., Kadzik, R.S. & Petry, S. XMAP215 is a microtubule nucleation factor that functions synergistically with the gamma-tubulin ring complex. *Nat Cell Biol* **20**, 575-585 (2018).
26. Choi, Y.K., Liu, P., Sze, S.K., Dai, C. & Qi, R.Z. CDK5RAP2 stimulates microtubule nucleation by the gamma-tubulin ring complex. *J Cell Biol* **191**, 1089-1095 (2010).
27. Muroyama, A., Seldin, L. & Lechler, T. Divergent regulation of functionally distinct gamma-tubulin complexes during differentiation. *J Cell Biol* **213**, 679-692 (2016).
28. Aher, A., Kok, M., Sharma, A., Rai, A., Olieric, N., Rodriguez-Garcia, R., Katrukha, E.A., Weinert, T., Olieric, V., Kapitein, L.C., Steinmetz, M.O., Dogterom, M. & Akhmanova, A. CLASP Suppresses Microtubule Catastrophes through a Single TOG Domain. *Dev Cell* **46**, 40-58 (2018).
29. Jiang, K., Hua, S., Mohan, R., Grigoriev, I., Yau, K.W., Liu, Q., Katrukha, E.A., Altelaar, A.F., Heck, A.J., Hoogenraad, C.C. & Akhmanova, A. Microtubule minus-end stabilization by polymerization-driven CAMSAP deposition. *Dev Cell* **28**, 295-309 (2014).
30. Liu, P., Choi, Y.K. & Qi, R.Z. NME7 is a functional component of the gamma-tubulin ring complex. *Mol Biol Cell* **25**, 2017-2025 (2014).
31. Luders, J., Patel, U.K. & Stearns, T. GCP-WD is a gamma-tubulin targeting factor required for centrosomal and chromatin-mediated microtubule nucleation. *Nat Cell Biol* **8**, 137-147 (2006).
32. Sen, I., Veprintsev, D., Akhmanova, A. & Steinmetz, M.O. End binding proteins are obligatory dimers. *PLoS One* **8**, e74448 (2013).
33. Tovey, C.A. & Conduit, P.T. Microtubule nucleation by gamma-tubulin complexes and beyond. *Essays Biochem* **62**, 765-780 (2018).
34. Rale, M., Romer, B., Mahon, B.P., Travis, S.M. & Petry, S. The conserved centrosomal motif,  $\gamma$ TuNA, forms a dimer that directly activates microtubule nucleation by the  $\gamma$ -tubulin ring complex ( $\gamma$ TuRC). *bioRxiv*, 2022.2004.2011.487887 (2022).

35. Roostalu, J., Cade, N.I. & Surrey, T. Complementary activities of TPX2 and chTOG constitute an efficient importin-regulated microtubule nucleation module. *Nat Cell Biol* **17**, 1422-1434 (2015).
36. Wieczorek, M., Bechstedt, S., Chaaban, S. & Brouhard, G.J. Microtubule-associated proteins control the kinetics of microtubule nucleation. *Nat Cell Biol* **17**, 907-916 (2015).
37. Brouhard, G.J., Stear, J.H., Noetzel, T.L., Al-Bassam, J., Kinoshita, K., Harrison, S.C., Howard, J. & Hyman, A.A. XMAP215 is a processive microtubule polymerase. *Cell* **132**, 79-88 (2008).
38. Farmer, V., Arpag, G., Hall, S.L. & Zanic, M. XMAP215 promotes microtubule catastrophe by disrupting the growing microtubule end. *J Cell Biol* **220**, e202012144 (2021).
39. Widlund, P.O., Stear, J.H., Pozniakovsky, A., Zanic, M., Reber, S., Brouhard, G.J., Hyman, A.A. & Howard, J. XMAP215 polymerase activity is built by combining multiple tubulin-binding TOG domains and a basic lattice-binding region. *Proc Natl Acad Sci U S A* **108**, 2741-2746 (2011).
40. Olmsted, J.B. & Borisy, G.G. Characterization of microtubule assembly in porcine brain extracts by viscometry. *Biochemistry* **12**, 4282-4289 (1973).
41. Haren, L., Farache, D., Emorine, L. & Merdes, A. A stable sub-complex between GCP4, GCP5 and GCP6 promotes the assembly of gamma-tubulin ring complexes. *J Cell Sci* **133**, jcs244368 (2020).
42. Greenberg, C.H., Kollman, J., Zelter, A., Johnson, R., MacCoss, M.J., Davis, T.N., Agard, D.A. & Sali, A. Structure of gamma-tubulin small complex based on a cryo-EM map, chemical cross-links, and a remotely related structure. *J Struct Biol* **194**, 303-310 (2016).
43. Kikkawa, M. & Hirokawa, N. High-resolution cryo-EM maps show the nucleotide binding pocket of KIF1A in open and closed conformations. *EMBO J* **25**, 4187-4194 (2006).
44. Sui, H. & Downing, K.H. Structural basis of interprotofilament interaction and lateral deformation of microtubules. *Structure* **18**, 1022-1031 (2010).
45. Rai, A., Liu, T., Katrukha, E.A., Estevez-Gallego, J., Manka, S.W., Paterson, I., Diaz, J.F., Kapitein, L.C., Moores, C.A. & Akhmanova, A. Lattice defects induced by microtubule-stabilizing agents exert a long-range effect on microtubule growth by promoting catastrophes. *Proc Natl Acad Sci U S A* **118**, e2112261118 (2021).
46. Gudimchuk, N.B., Ulyanov, E.V., O'Toole, E., Page, C.L., Vinogradov, D.S., Morgan, G., Li, G., Moore, J.K., Szczesna, E., Roll-Mecak, A., Ataulakhanov, F.I. & Richard McIntosh, J. Mechanisms of microtubule dynamics and force generation examined with computational modeling and electron cryotomography. *Nat Commun* **11**, 3765 (2020).
47. Elie-Caille, C., Severin, F., Helenius, J., Howard, J., Muller, D.J. & Hyman, A.A. Straight GDP-tubulin protofilaments form in the presence of taxol. *Curr Biol* **17**, 1765-1770 (2007).
48. Wu, J., de Heus, C., Liu, Q., Bouchet, B.P., Noordstra, I., Jiang, K., Hua, S., Martin, M., Yang, C., Grigoriev, I., Katrukha, E.A., Altelaar, A.F., Hoogenraad, C.C., Qi, R.Z., Klumperman, J. & Akhmanova, A. Molecular Pathway of Microtubule Organization at the Golgi Apparatus. *Dev Cell* **39**, 44-60 (2016).
49. Dong, C., Xu, H., Zhang, R., Tanaka, N., Takeichi, M. & Meng, W. CAMSAP3 accumulates in the pericentrosomal area and accompanies microtubule release from the centrosome via katanin. *J Cell Sci* **130**, 1709-1715 (2017).

50. Dogterom, M., Kerssemakers, J.W., Romet-Lemonne, G. & Janson, M.E. Force generation by dynamic microtubules. *Curr Opin Cell Biol* **17**, 67-74 (2005).
51. Thawani, A., Rale, M.J., Coudray, N., Bhabha, G., Stone, H.A., Shaevitz, J.W. & Petry, S. The transition state and regulation of gamma-TuRC-mediated microtubule nucleation revealed by single molecule microscopy. *Elife* **9**, e54253 (2020).
52. Wieczorek, M., Huang, T.L., Urnavicius, L., Hsia, K.C. & Kapoor, T.M. MZT Proteins Form Multi-Faceted Structural Modules in the gamma-Tubulin Ring Complex. *Cell Rep* **31**, 107791 (2020).
53. Lawrence, E.J., Zanic, M. & Rice, L.M. CLASPs at a glance. *J Cell Sci* **133**, jcs243097 (2020).
54. Aher, A., Rai, D., Schaedel, L., Gaillard, J., John, K., Liu, Q., Altelaar, M., Blanchoin, L., Thery, M. & Akhmanova, A. CLASP Mediates Microtubule Repair by Restricting Lattice Damage and Regulating Tubulin Incorporation. *Curr Biol* **30**, 2175-2183 (2020).
55. Ran, F.A., Hsu, P.D., Wright, J., Agarwala, V., Scott, D.A. & Zhang, F. Genome engineering using the CRISPR-Cas9 system. *Nat Protoc* **8**, 2281-2308 (2013).
56. Sharma, A., Aher, A., Dynes, N.J., Frey, D., Katrukha, E.A., Jaussi, R., Grigoriev, I., Croisier, M., Kammerer, R.A., Akhmanova, A., Gonczy, P. & Steinmetz, M.O. Centriolar CPAP/SAS-4 Imparts Slow Processive Microtubule Growth. *Dev Cell* **37**, 362-376 (2016).
57. Montenegro Gouveia, S., Leslie, K., Kapitein, L.C., Buey, R.M., Grigoriev, I., Wagenbach, M., Smal, I., Meijering, E., Hoogenraad, C.C., Wordeman, L., Steinmetz, M.O. & Akhmanova, A. In Vitro Reconstitution of the Functional Interplay between MCAK and EB3 at Microtubule Plus Ends. *Curr Biol* **20**, 1717-1722 (2010).
58. Rohou, A. & Grigorieff, N. CTFIND4: Fast and accurate defocus estimation from electron micrographs. *J Struct Biol* **192**, 216-221 (2015).
59. Zivanov, J., Nakane, T., Forsberg, B.O., Kimanius, D., Hagen, W.J., Lindahl, E. & Scheres, S.H. New tools for automated high-resolution cryo-EM structure determination in RELION-3. *Elife* **7**, e42166 (2018).
60. Pettersen, E.F., Goddard, T.D., Huang, C.C., Couch, G.S., Greenblatt, D.M., Meng, E.C. & Ferrin, T.E. UCSF Chimera--a visualization system for exploratory research and analysis. *J Comput Chem* **25**, 1605-1612 (2004).
61. Pettersen, E.F., Goddard, T.D., Huang, C.C., Meng, E.C., Couch, G.S., Croll, T.I., Morris, J.H. & Ferrin, T.E. UCSF ChimeraX: Structure visualization for researchers, educators, and developers. *Protein Sci* **30**, 70-82 (2021).
62. Mohan, R., Katrukha, E.A., Doodhi, H., Smal, I., Meijering, E., Kapitein, L.C., Steinmetz, M.O. & Akhmanova, A. End-binding proteins sensitize microtubules to the action of microtubule-targeting agents. *Proc Natl Acad Sci U S A* **110**, 8900-8905 (2013).
63. Noordstra I, van den Berg CM, Boot FWJ, Katrukha EA, Yu KL, Tas RP, Portegies S, Viergever BJ, de Graaff E, Hoogenraad CC, de Koning EJP, Carlotti F, Kapitein LC, Akhmanova A. Organization and dynamics of the cortical complexes controlling insulin secretion in  $\beta$ -cells. *J Cell Sci*. 2022 Feb 1;135(3):jcs259430. doi: 10.1242/jcs.259430.

## Supplementary Figures



**Extended data Figure 1, related to Figure 1 | Characterization of HEK293T GCP3-GFP-SII homozygous knock-in cell line and  $\gamma$ -TuRC purified using GCP3-GFP-SII.**

**a**, Schematic showing GCP3 gene locus and knock-in strategy.

**b**, 1% Agarose gel showing genomic-DNA PCR products for wild type HEK293T cells and GCP3-GFP-SII knock-in cells. MW, molecular weight DNA ladder; WT, wild type.

**c**, Western blot for wild type and GCP3-GFP-SII knock-in HEK293T cell lysate, blotted using mouse anti-GCP3 antibody.

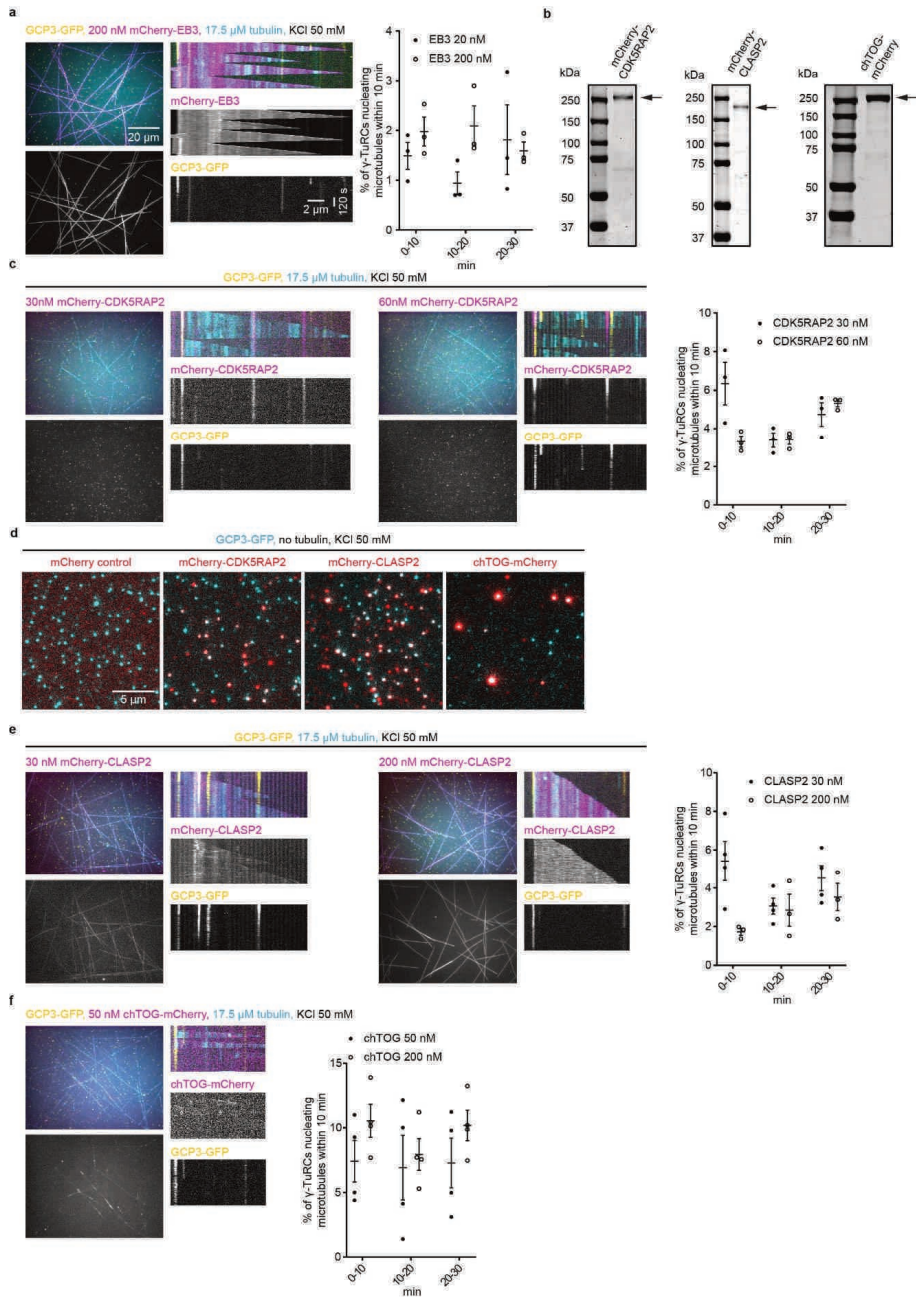
**d**, Widefield fluorescent image of fixed HEK293T GCP3-GFP-SII homozygous knock-in cells showing GFP fluorescence (green). Nuclei (magenta) were stained with DAPI.

**e**, Strategy for  $\gamma$ -TuRC purification.

**f**, Western blot results showing the presence of all the core components in our  $\gamma$ -TuRC purified using GCP3-GFP-SII using antibodies against GCP6, GFP, GCP5, GCP2, GCP4 and  $\gamma$ -tubulin.

**g**, Mass spectrometry results showing the presence of all the core components in  $\gamma$ -TuRC purified using GCP3-GFP-SII.

**h**, Schematic showing experimental TIRF microscopy setup for in vitro reconstitution of microtubule nucleation from  $\gamma$ -TuRC.

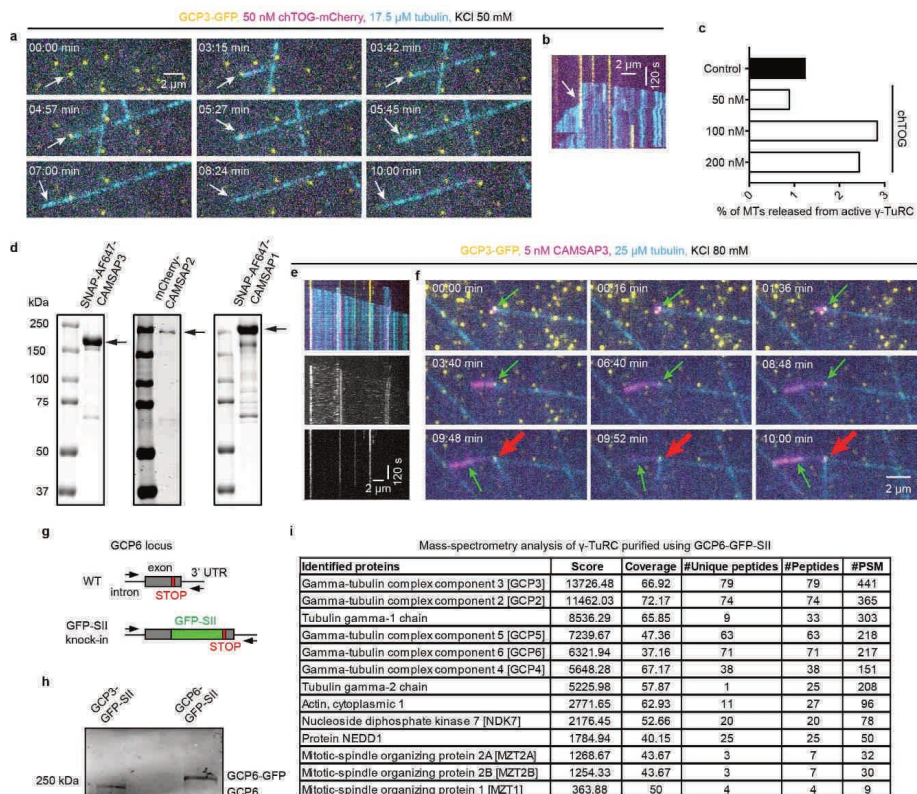


**Extended data Figure 2, related to Figure 1 | Characterization of effective concentrations of nucleation-promoting factors.** *a,c,e,f*, Left: maximum intensity projections and representative kymographs illustrating microtubule dynamics in 10 min time-lapse videos, acquired after 20 min of incubation, showing microtubules (cyan) nucleated from  $\gamma$ -TuRC (GCP3-GFP, yellow) in the

presence of either 17.5  $\mu$ M tubulin (17  $\mu$ M unlabeled porcine tubulin and 0.5  $\mu$ M HiLyte647-tubulin), 50 mM KCl and together with indicated concentrations of indicated proteins (magenta) and without any preincubation: 200 nM mCherry-EB3 (a); or 30 nM and 60 nM mCherry-CDK5RAP2 (c); or 30 nM and 200 nM mCherry-CLASP2 (e); or 50 nM chTOG-mCherry (f). Right: Quantification of average microtubule nucleation efficiency of  $\gamma$ -TuRC as indicated: 200 nM mCherry-EB3 (n=3); 30 nM (n=3) or 60 nM (n=3) mCherry-CDK5RAP2; 30 nM (n=4) or 200 nM mCherry-CLASP2 (n=3); 50 nM (n=4) or 200 nM chTOG-mCherry (n=4); where n is the number of independent experiments analyzed, also see Fig. 1c-h. The plots present mean  $\pm$  s.e.m., and each data point represents a single field of view from which % of  $\gamma$ -TuRCs nucleating microtubules were quantified for the given time point from an individual experiment. Data points at 0-10 min were acquired from a smaller field of view and cannot be directly compared to the data points at 10-20 min and 20-30 min acquired from a bigger field of view (shown in the panels on the left). Data points for concentrations already shown in Fig. 1c,e-h, have been taken from Fig. 1d and replotted here for direct comparison.

b, Coomassie-stained SDS-PAGE gels loaded with purified mCherry-CDK5RAP2 or mCherry-CLASP2 or chTOG-mCherry.

d, Representative images showing colocalization of  $\gamma$ -TuRC (cyan, GCP3-GFP) with indicated proteins (red) in the presence of 50 mM KCl and no soluble tubulin.



Extended data Figure 3, related to Figure 2 | Characterization of purified CAMSAPs and GCP6-tagged  $\gamma$ -TuRC and microtubule release from  $\gamma$ -TuRC.

**a,b**, Still frames (at indicated time points in min) (**a**) and representative kymograph (**b**) from a 10 min time-lapse video showing microtubule (cyan) nucleation (magenta) and subsequent microtubule release from  $\gamma$ -TuRC (GCP3-GFP, yellow) in the presence of 50 nM mCherry-chTOG (magenta), 17.5  $\mu$ M tubulin (17  $\mu$ M unlabeled porcine tubulin and 0.5  $\mu$ M HiLyte647-tubulin). Thin arrows indicate microtubule minus-end.

**c**, Plot showing frequency of microtubule release from active  $\gamma$ -TuRC over 10 min duration in the presence of either 17.5  $\mu$ M tubulin alone (control,  $n=52$ , pooled from eight independent experiments); or together with 50 nM ( $n=280$ , pooled from four independent experiments); or 100 nM ( $n=183$ , pooled from four independent experiments); or 200 nM mCherry-chTOG ( $n=301$ , pooled from four independent experiments); where  $n$  is the number of active  $\gamma$ -TuRCs analyzed. Representative images are shown in **a**.

**d**, Coomassie-stained SDS-PAGE gels loaded with purified SNAP-AF647-CAMSAP3, mCherry-CAMSAP2 or SNAP-AF647-CAMSAP1.

**e,f**, Two different examples: kymographs (**e**) and still frames (at indicated time points in min) from a 10 min time-lapse video showing  $\gamma$ -TuRC-CAMSAP3 interplay at the  $\gamma$ -TuRC-anchored microtubule minus-ends under indicated experimental conditions. Example 1 (kymographs) illustrates occasions when CAMSAP3 (magenta) fails to displace  $\gamma$ -TuRC (GCP3-GFP, yellow) from  $\gamma$ -TuRC-anchored microtubule (cyan) minus-end that recruited CAMSAP3. Example 2 (still frames) illustrates microtubule re-nucleation (thick red arrows) from the same  $\gamma$ -TuRC that released previously nucleated microtubule (thin green arrows) upon CAMSAP3 binding and minus-end growth. Experimental conditions are same as shown in **Fig. 2e**, i.e., 25  $\mu$ M tubulin (24.5  $\mu$ M unlabeled porcine tubulin and 0.5  $\mu$ M rhodamine-tubulin), 80 mM KCl and 5 nM SNAP-AF647-CAMSAP3.

**g**, Schematic showing GCP6 gene locus and knock-in strategy.

**h**, Western blot for GCP3-GFP-SII and GCP6-GFP-SII knock-in HEK293T cell lysate, blotted using mouse anti-GCP6 antibody.

**i**, Mass-spectrometry results showing the presence of all the core components in our  $\gamma$ -TuRC purified using GCP6-GFP-SII.

**Extended data Figure 4, related to Figure 3 | EM-based characterization of  $\gamma$ -TuRC in the absence or presence of CDK5RAP2.**

**a**, Transmission EM (TEM) micrograph of negatively stained  $\gamma$ -TuRC. Inset shows a 4X magnified view of a single  $\gamma$ -TuRC.

**b**, Two views of a 3D reconstruction of the  $\gamma$ -TuRC from negative-stain EM data.

**c**, Rigid body fit of repeating  $\gamma$ -tubulin/GCP2 subcomplexes (from PDB ID: 6V6S<sup>20</sup>) individually docked into the  $\gamma$ -TuRC density map. Fits for two subcomplexes at the  $\gamma$ -TuRC “seam” were not reliable; and are therefore, omitted for clarity.

**d**, Transmission EM (TEM) micrograph of negatively stained  $\gamma$ -TuRC prepared in complex with 120 nM CDK5RAP2. Inset shows a 4X magnified view of a single  $\gamma$ -TuRC.

**e**, Two views of a 3D reconstruction of the  $\gamma$ -TuRC + CDK5RAP2 preparation from negative-stain EM data.

**f**, Rigid body fit of repeating  $\gamma$ -tubulin/GCP2 subcomplexes (from PDB ID: 6V6S<sup>20</sup>) individually docked into the  $\gamma$ -TuRC + CDK5RAP2 density map. As in **c**, fits for two subcomplexes at the  $\gamma$ -TuRC “seam” were not reliable; and are therefore, omitted for clarity.

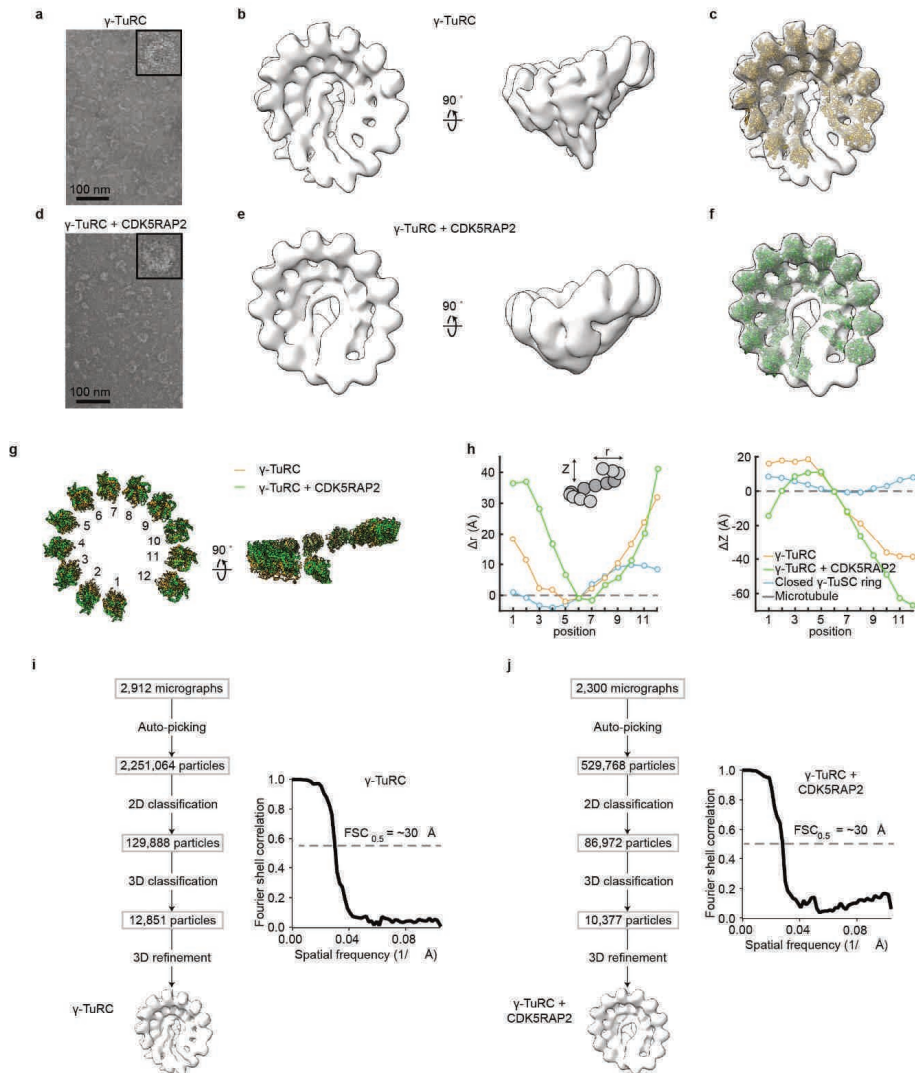
**g**, Two views of the  $\gamma$ -tubulin rings from rigid body fitted models in **c** ( $\gamma$ -TuRC) and **f** ( $\gamma$ -TuRC + CDK5RAP2).

**h**, Plots of the change in helical radius ( $r$ ) and helical pitch ( $Z$ ) relative to  $\beta$ -tubulin in the 13-protofilament microtubule lattice (grey dashed line; PDB ID: 2HXF<sup>43</sup> and EMD-5193<sup>44</sup>) calculated for  $\gamma$ -tubulin rings from  $\gamma$ -TuRC alone (orange),  $\gamma$ -TuRC + 120 nM CDK5RAP2 (green), and the  $\gamma$ -TuSC oligomer in the “closed” state (blue; PDB ID: 5FLZ<sup>42</sup>). See Methods for analysis details.

**i**, Left: Processing workflow for generating a negative-stain EM 3D reconstruction of  $\gamma$ -TuRC. Right: Unmasked FSC curve for the  $\gamma$ -TuRC reconstruction. FSC = 0.5 is indicated by a dashed gray line, and an estimate of the corresponding resolution is indicated.



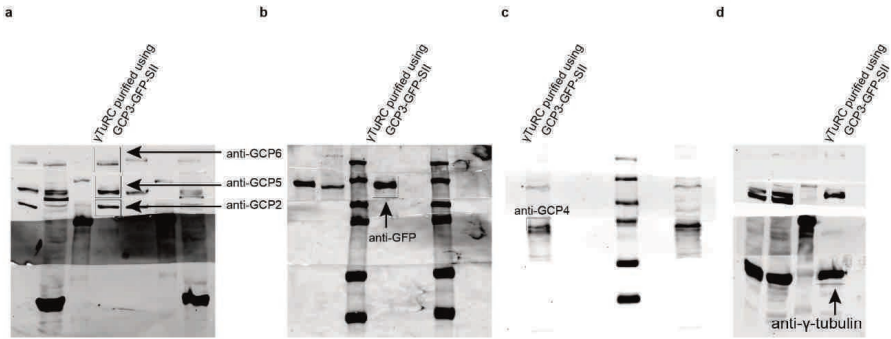
**j**, Left: Processing workflow for generating a negative-stain EM 3D reconstruction of  $\gamma$ -TuRC in the presence of 120 nM CDK5RAP2. Right: Unmasked FSC curve for the  $\gamma$ -TuRC + CDK5RAP2 reconstruction. FSC=0.5 is indicated by a dashed gray line, and an estimate of the corresponding resolution is indicated.



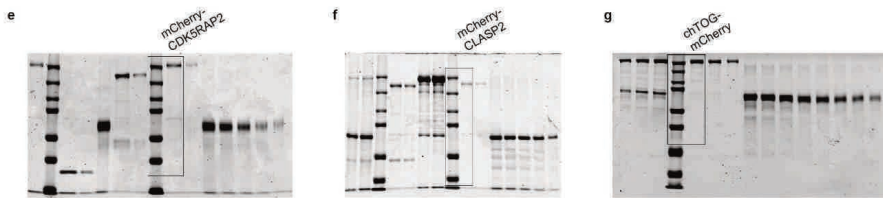
2

## Source data 1

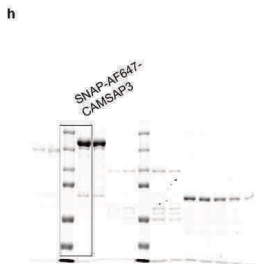
Extended data Fig. 1f (uncropped western blots)



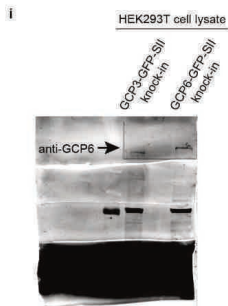
Extended data Fig. 2b (uncropped Coomassie-stained gels)



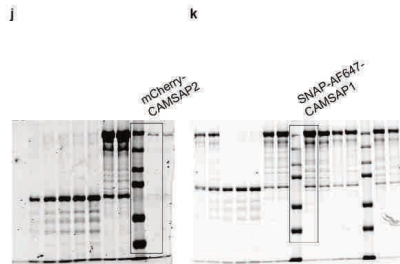
Extended data Fig. 3d  
(uncropped Coomassie-stained gel)



Extended data Fig. 3h  
(uncropped western blot)



Extended data Fig. 4a  
(uncropped Coomassie-stained gels)



## Information for supplementary materials available online

### Supplementary Video Legends

**Supplementary Video 1. CAMSAP3 mediated microtubule release from  $\gamma$ -TuRC.** 10 min time-lapse videos illustrating CAMSAP3 binding to  $\gamma$ -TuRC-anchored (left & middle: GCP3-GFP; right: GCP6-GFP) minus ends and subsequent elongation of the CAMSAP3-stabilized minus ends in the presence of 25  $\mu$ M tubulin (24.5  $\mu$ M unlabeled porcine tubulin and 0.5  $\mu$ M rhodamine-tubulin), 80 mM KCl and 5 nM SNAP-AF647-CAMSAP3. Time-lapse images were acquired using TIRF microscope at 20 s (left, constituting 31 frames) and 3 s (middle and right, constituting 201 frames) time intervals.

**Supplementary Video 2.  $\gamma$ -TuRC displacement from microtubule minus ends by CAMSAP3 in the presence of nucleation-promoting factors.** 10 min time-lapse videos illustrating CAMSAP3 binding to  $\gamma$ -TuRC-anchored minus ends and subsequent elongation of the CAMSAP3-stabilized minus ends in the presence of 25  $\mu$ M tubulin (24.5  $\mu$ M unlabeled porcine tubulin and 0.5  $\mu$ M rhodamine-tubulin), 80 mM KCl, 5 nM SNAP-AF647-CAMSAP3 and indicated nucleation- promoting factors (30 nM mCherry-CDK5RAP2 or 30 nM mCherry-CLASP2 or 200 nM chTOG-mCherry). Time-lapse images were acquired using TIRF microscope at 20 s time interval constituting 31 frames.

**Supplementary Video 3.  $\gamma$ -TuRC detachment from microtubule minus ends by CAMSAP2 or CAMSAP1.** 10 min time-lapse videos illustrating CAMSAPs binding to  $\gamma$ -TuRC-anchored minus ends and subsequent elongation of the CAMSAPs-stabilized minus ends in the presence of 25  $\mu$ M tubulin (~2% labeling), 80 mM KCl and 40 nM mCherry-CAMSAP2 or 5 nM SNAP-AF647-CAMSAP1. Time-lapse images were acquired using TIRF microscope at 20 s time interval constituting 31 frames.

### Supplementary Table Legends

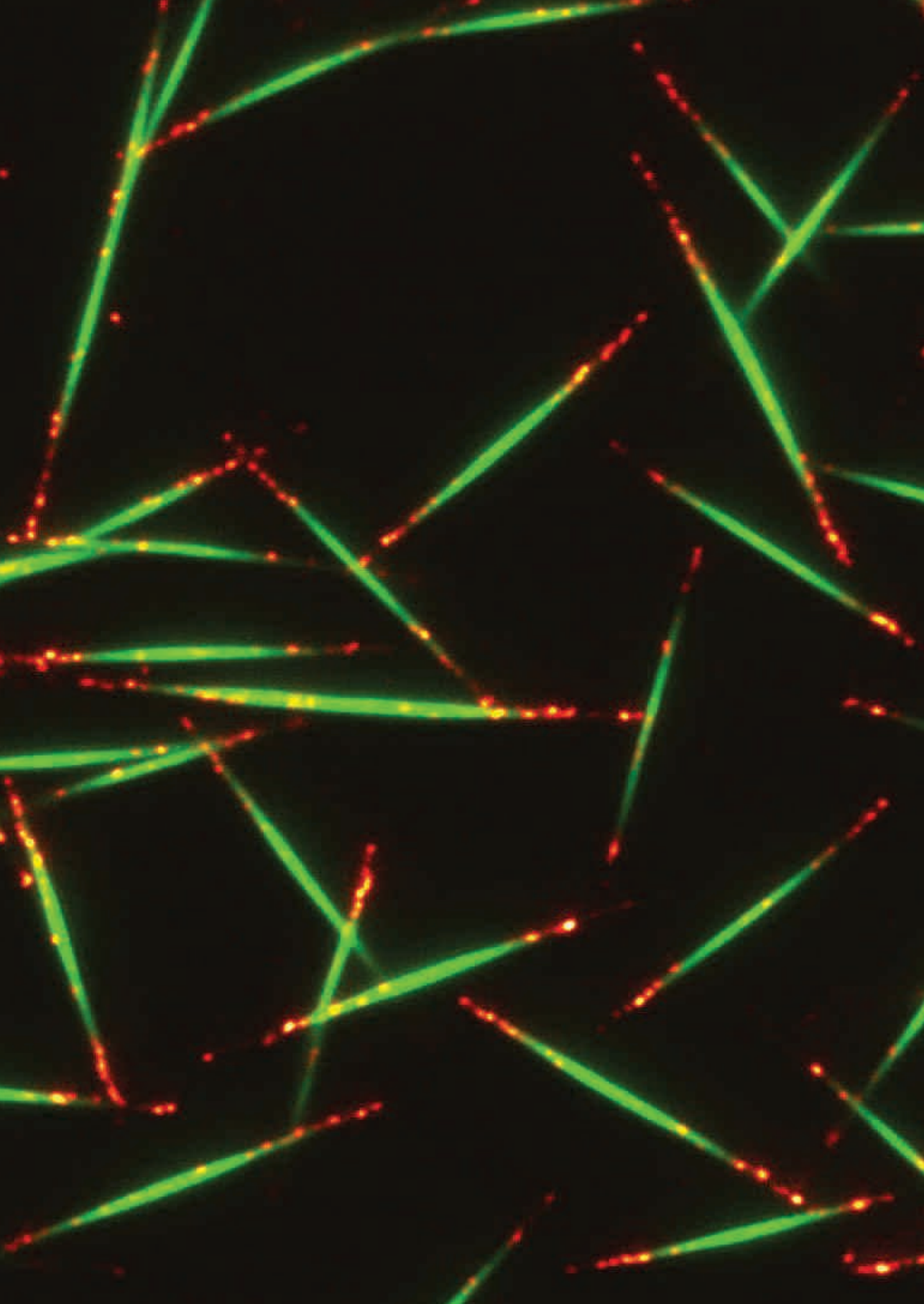
**Supplementary Table 1. Mass-spectrometry results of purified GCP3-GFP-SII.** List of proteins that were co-purified with endogenously tagged GCP3-GFP-SII contains all the core components of  $\gamma$ -TuRC, identified by mass spectrometry.

**Supplementary Table 2. Mass-spectrometry results of purified CDK5RAP2.** List of proteins identified by mass spectrometry that were co-purified with SII-mCherry-CDK5RAP2.

**Supplementary Table 3. Mass-spectrometry results of purified CLASP2.** List of proteins identified by mass spectrometry that were co-purified with SII-mCherry-CLASP2.

**Supplementary Table 4. Mass-spectrometry results of purified chTOG.** List of proteins identified by mass spectrometry that were co-purified with chTOG-mCherry-SII.

**Supplementary Table 5. Mass-spectrometry results of purified GCP6-GFP-SII.** List of proteins that were co-purified with endogenously tagged GCP6-GFP-SII contains all the core components of  $\gamma$ -TuRC, identified by mass spectrometry.



# 3

## Feedback-Driven Assembly of the Axon Initial Segment

Amélie Fréal<sup>1,2</sup>, Dipti Rai<sup>1#</sup>, Roderick P Tas<sup>1</sup>, Xingxiu Pan<sup>1</sup>, Eugene A. Katrukha<sup>1</sup>, Dieudonné van de Willige<sup>1</sup>, Riccardo Stucchi<sup>1,3</sup>, Amol Aher<sup>1</sup>, Chao Yang<sup>1</sup>, A F Maarten Altelaar<sup>3</sup>, Karin Vocking<sup>1</sup>, Jan Andries Post<sup>1</sup>, Martin Harterink<sup>1</sup>, Lukas C. Kapitein<sup>1</sup>, Anna Akhmanova<sup>1\*</sup>, Casper C. Hoogenraad<sup>1,4,5,\*</sup>

<sup>1</sup> Cell Biology, Department of Biology, Faculty of Science, Utrecht University, Padualaan 8, 3584 CH Utrecht, the Netherlands

<sup>2</sup> Department of Axonal Signaling, Netherlands Institute for Neuroscience, Royal Netherlands Academy of Arts and Sciences, Meibergdreef 47, 1105 BA Amsterdam, the Netherlands

<sup>3</sup> Biomolecular Mass Spectrometry and Proteomics, Bijvoet Center for Biomolecular Research, Utrecht Institute for Pharmaceutical Sciences and the Netherlands Proteomics Center, Utrecht University, Padualaan 8, 3584 CH Utrecht, the Netherlands

<sup>4</sup> Department of Neuroscience, Genentech, Inc., South San Francisco, CA 94080, USA

<sup>5</sup> Lead Contact

# This author has performed the biochemical in vitro reconstitutions of microtubules with TRIM46 and AnkG, and produced related data and figures.

\* Correspondence: a.akhmanova@uu.nl (A.A.), c.hoogenraad@uu.nl (C.C.H.)

**Neuron. 2019 Oct 23;104(2):305-321.e8.;** doi: 10.1016/j.neuron.2019.07.029

### Summary

The axon initial segment (AIS) is a unique neuronal compartment that plays a crucial role in the generation of action potential and neuronal polarity. The assembly of the AIS requires membrane, scaffolding, and cytoskeletal proteins, including Ankyrin-G and TRIM46. How these components cooperate in AIS formation is currently poorly understood. Here, we show that Ankyrin-G acts as a scaffold interacting with End-Binding (EB) proteins and membrane proteins such as Neurofascin-186 to recruit TRIM46-positive microtubules to the plasma membrane. Using *in vitro* reconstitution and cellular assays, we demonstrate that TRIM46 forms parallel microtubule bundles and stabilizes them by acting as a rescue factor. TRIM46-labeled microtubules drive retrograde transport of Neurofascin-186 to the proximal axon, where Ankyrin-G prevents its endocytosis, resulting in stable accumulation of Neurofascin-186 at the AIS. Neurofascin-186 enrichment in turn reinforces membrane anchoring of Ankyrin-G and subsequent recruitment of TRIM46-decorated microtubules. Our study reveals feedback-based mechanisms driving AIS assembly.

### Introduction

The axon initial segment (AIS) is a specialized membrane-associated structure at the base of the axon that generates and shapes the action potential before it is propagated along the axon (Kole and Stuart, 2008). The AIS also functions as a boundary between the somatodendritic and axonal compartments to help maintain neuron polarity (Rasband, 2010). AIS components form a diffusion barrier segregating the somatodendritic and axonal membrane proteins and act as a cytoplasmic filter regulating cargo transport into the proximal axon (Letierrier, 2018). The AIS contains a concentration of voltage-gated ion channels and cell adhesion molecules that are anchored by a submembranous layer of scaffolds, extending from the plasma membrane to the underlying microtubule (MT) cytoskeleton. However, how the AIS is formed and maintained is still poorly understood.

In electron microscopy (EM) studies, the AIS is characterized by an ~50-nm-thick submembranous undercoat lining the axonal plasma membrane and closely spaced bundles of 3–10 MTs also referred to as MT fascicles (Palay et al., 1968, Peters et al., 1968). The central component of the AIS submembrane complex is Ankyrin-G (ANK3), with a long isoform of 480 kDa (480AnkG) (Fréal et al., 2016, Jenkins et al., 2015b). Most of the AIS membrane proteins are directly recruited and concentrated by AnkG, including voltage-gated sodium (Nav) and potassium (Kv) channels and adhesion molecules, such as the 186-kDa isoform of Neurofascin (NF186) (Letierrier, 2018). The submembrane localization of AnkG depends on

the association with AIS membrane proteins and palmitoylation of its amino-terminal domain (He et al., 2012, Le Bras et al., 2014, Leterrier et al., 2015, Leterrier et al., 2017). Depletion of 480AnkG not only prevents the accumulation of membrane proteins in the AIS but also impairs MT organization in the proximal axon (Fréal et al., 2016, Hedstrom et al., 2008, Sobotzik et al., 2009). The 480AnkG carboxy-terminal domain extends ~35 nm into the cytoplasm and contains numerous SxIP motifs able to bind MTs via End-Binding (EB) proteins (Fréal et al., 2016, Leterrier et al., 2015). The interaction between EBs and AnkG is necessary for both AIS formation and maintenance (Fréal et al., 2016, Leterrier et al., 2011). These data highlight the importance of the association between the AIS submembrane complex and the underlying MT cytoskeleton. Still, the molecular mechanisms connecting axonal MT organization and AIS formation are incompletely understood.

Axon development depends on local MT stabilization and the formation of uniform MT bundles. The MT network at the AIS has specific properties compared to MTs in the rest of the neuron. AIS MTs were shown to be enriched in GTP-like tubulin (Nakata et al., 2011), and overall the AIS cytoskeleton and associated proteins are very stable, as shown by their high resistance to detergent extraction (Garrido et al., 2003, Sánchez-Ponce et al., 2012). The unique properties of AIS MTs are conferred by the presence of several MT-associated proteins (MAPs) that have been recently identified in the proximal axon, such as EB proteins (Nakata and Hirokawa, 2003), CAMSAP2 (Yau et al., 2014), MAP6 (Tortosa et al., 2017), MTCL-1 (Satake et al., 2017), MAP2 (Gumy et al., 2017), and TRIM46 (van Beuningen et al., 2015). TRIM46 belongs to the tripartite motif containing (TRIM) protein family of ubiquitin E3 ligases, but neither ubiquitin ligase activity nor substrates for TRIM46 have been reported (Meroni and Diez-Roux, 2005). Instead, TRIM46 associates with MTs in the proximal axon, where it forms plus-end-out MT bundles. TRIM46 is required for neuronal polarity and axon specification *in vitro* and *in vivo* (van Beuningen et al., 2015). TRIM46 is an early axonal marker because it localizes to the future axon before neuronal polarization and AIS assembly. Interestingly, expression of TRIM46 in heterologous cells induces the formation of bundles of closely spaced MTs linked by electron-dense cross-bridges, which closely resemble the axon-specific MT fascicles (Harterink et al., 2019, van Beuningen and Hoogenraad, 2016, van Beuningen et al., 2015). Defining the interplay between AnkG and TRIM46-induced MT fascicles may thus provide a molecular pathway for AIS assembly.

In this study, we used live-cell imaging in combination with biochemical and cell biological assays, as well as microscopy-based *in vitro* reconstitution assays to determine the mechanisms underlying AIS assembly. We show that plasma membrane-attached 480AnkG actively

recruits and anchors MT bundles to the plasma membrane. TRIM46 generates uniform MT fascicles by selectively promoting growth of parallel-oriented MTs. Subsequently, TRIM46-decorated MT bundles locally concentrate AnkG and its associated protein NF186. The uniform MT organization drives efficient transport of NF186 to the AIS, where it interacts with AnkG to stably accumulate at the AIS. Our study reveals a feedback-driven mechanism for the assembly of the AIS.

## Results

### *480AnkG Recruits MTs to the Plasma Membrane*

Our previous study showed that 480AnkG possesses numerous SxIP motifs (Figure S1A), which allow it to track MT plus-ends in an EB-dependent manner. Indeed, expression of 480AnkG-GFP in COS-7 cells revealed a comet-like distribution, which colocalized with EB1 (Figures 1A and 1B), and live imaging showed a robust MT plus-end tracking behavior (Figures 1D and S1B; Video S1). However, co-expression of 480AnkG-GFP together with one of its known AIS interacting membrane proteins, either NF186-RFP (Figures 1C, 1E, 1G, S1C, and S1D) or myc-Kv2.1-Nav1.2 (KvNav) (Bréchet et al., 2008) (Figures 1F and S1E), induced membrane recruitment of 480AnkG. When targeted to the plasma membrane by AIS membrane proteins, 480AnkG-GFP formed long linear stretches that stained positive for tubulin (Figure 1G). Live imaging revealed that membrane-attached 480AnkG-GFP no longer tracked MT-plus ends but was distributed along the MT lattice (Figures 1E and 1F), indicating that 480AnkG recruited MTs to the plasma membrane.

The ability of 480AnkG to organize MT structures at the plasma membrane relies on the interaction with both MTs and AIS membrane proteins. The 480AnkG tail construct that interacts with EBs but does not bind to AIS membrane proteins (Fréal et al., 2016) behaved as a +TIP when co-expressed with NF186 (Figure S1F). Similarly, when 480AnkG-GFP was co-expressed with NF186 mutated in its AnkG-binding motif (FIGQY→FIGQD) (Boiko et al., 2007, Zhang et al., 1998), 480AnkG-GFP still tracked MT-plus ends and did not redistribute along MT lattice (Figures S1G and S1H). Mutation of the 480AnkG palmitoylation residue (He et al., 2012) did not change the NF186-dependent membrane recruitment of 480AnkG in COS-7 cells (Figure S1I), nor its membrane association in days in vitro (DIV)3 neurons (Figure S1J). AnkG mutants that do not interact with EBs, such as 480AnkG-NN (in which 10 SxIP motifs are changed into SxNN, Figure S1A) or 270AnkG (Fréal et al., 2016), showed a diffuse cytoplasmic staining and did not recruit MTs to the plasma membrane in the presence of



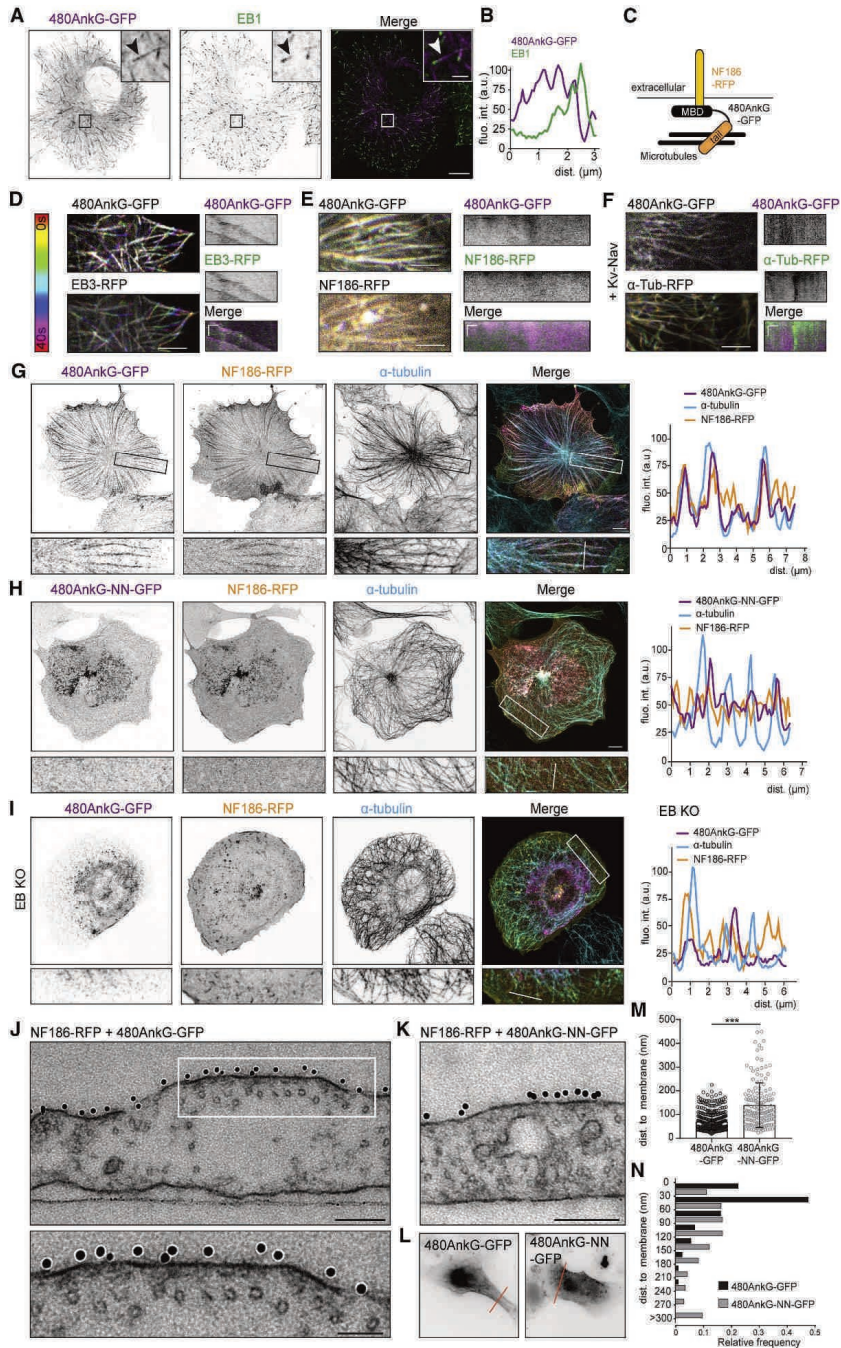


**Figure 1. 480AnkG Organizes MTs at the Plasma Membrane in an EB-Dependent Manner**  
 (A and B) COS-7 cell expressing 480AnkG-GFP, stained for GFP and EB1 (A). (B) shows fluorescence intensities along the comet pointed in the zoom.

---

(C) Scheme showing 480AnkG-GFP targeted to the plasma membrane by NF186-RFP via its membrane-binding domain (MBD), while its tail domain anchors MTs.

(D–F) Temporal-coded maximum projections from time-lapse imaging of COS-7 cells expressing 480AnkG-GFP with EB3-RFP (D), NF186-RFP (E),  $\alpha$ -Tub-RFP (F). Representative kymographs and color-coded timescale is shown.

(G and H) COS-7 cells co-expressing NF186-RFP together with 480AnkG-GFP (G) or 480AnkG-NN-GFP (H) and stained for  $\alpha$ -tubulin.

(I) EB1/2/3 KO U2OS cell co-expressing NF186-RFP and 480AnkG-GFP and stained for  $\alpha$ -tubulin.

(J–L) EM pictures of COS-7 cells co-expressing NF186-RFP with 480AnkG-GFP (J) or 480AnkG-NN-GFP (K) and immunogold labeled for extracellular NFasc. Fluorescent pictures of corresponding cells are shown in (L), and cutting sites are indicated with a line.

(M and N) Distance between MTs and the plasma membrane (M) and corresponding frequency plot (N). Mann-Whitney test,  $p = 3.26 \times 10^{-9}$ ,  $n = 123$  MTs for AnkG-GFP in  $N = 3$  cells,  $n = 102$  MTs for 480AnkG-NN-GFP in  $N = 2$  cells.

In (A) and (G–I), scale bars are  $10 \mu\text{m}$  and  $2 \mu\text{m}$  in the zoom. In (D–F), scale bars are  $5 \mu\text{m}$  and on the corresponding kymographs:  $1 \mu\text{m}$  (horizontal) and  $15 \text{s}$  (vertical). For (J) and (K), scale bars are  $200$  and  $100 \text{nm}$  in the zoom. See also Figure S1.

---

NF186-RFP (Figures 1H and S1K). Moreover, in U2OS cells in which EB1, EB2, and EB3 were stably knocked out (Yang et al., 2017) (Figures S2A and S2F), 480AnkG-GFP showed no accumulation at MT plus-ends (Figure S2A) and did not anchor MTs to the plasma membrane when co-expressed with NF186-RFP (Figures 1I versus S2B). The expression of EB3-RFP in these KO cells could rescue the MT plus-end localization of 480AnkG and its ability to anchor MTs at the membrane when co-expressed with KvNav (Figures S2C–S2E). These data suggest that the interaction with EBs is critical for the 480AnkG-dependent recruitment of MTs to the plasma membrane.

To further study 480AnkG's ability to recruit MTs to the plasma membrane, we examined COS-7 cells co-expressing NF186-RFP together with either 480AnkG-GFP or 480AnkG-NN-GFP (Figures 1J–1L) by EM. Pre-embedding immunogold labeling of NF186 allowed us to resolve the position of the AIS membrane proteins at the plasma membrane (Figure S2J). Quantifications revealed that 480AnkG organizes MTs in close proximity to the plasma membrane (30–60 nm), whereas 480AnkG-NN did not induce any significant clustering of MTs (Figures 1M, 1N, and S2I). We also observed a dark membrane undercoating where NF186 was concentrated, as noticed in previous EM studies of the AIS (Palay et al., 1968). We then used gated stimulated emission depletion (gSTED) microscopy to observe MT position with respect to the cell cortex in COS-7 cells expressing various constructs and stained with phalloidin (Figures S2G and S2H). In agreement with the EM data, 480AnkG-GFP, but not 480AnkG-NN-GFP, induced a clear recruitment of MTs to the cortex in the presence of a membrane binding partner (Figures S2G and S2H, lower panels). Interestingly, neither

480AnkG-GFP, which can bind to MT plus ends, nor the diffuse 480AnkG-NN-GFP could induce such a MT organization on their own (Figures S2G and S2H, upper panels).

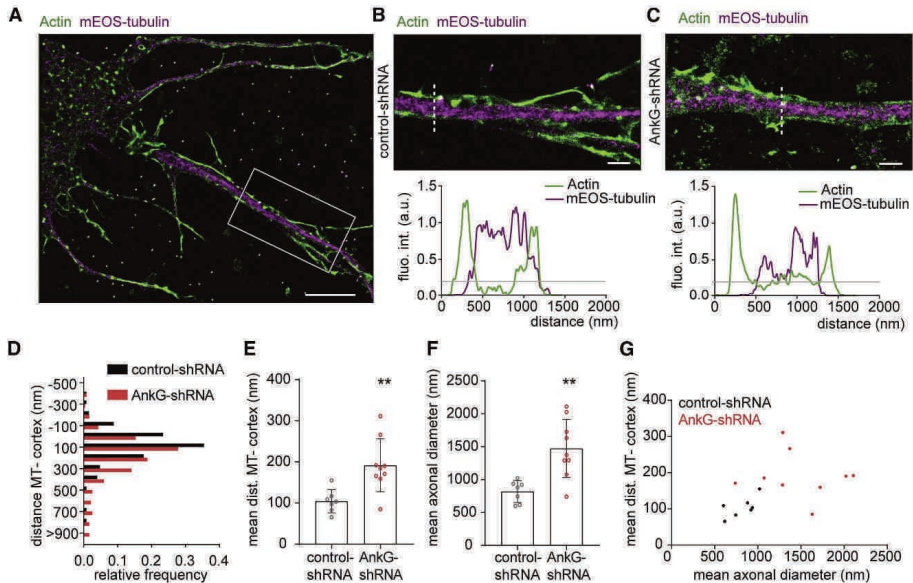


### Figure 2. AnkG Anchors MTs Close to the Axonal Membrane

(A–C) Single-molecule localization microscopy reconstructions of DIV4 hippocampal neurons transfected at DIV0 with mEOS-tubulin and a control- (A and B) or AnkG-shRNA (C). Intensity profiles along the indicated lines are shown.

(D) Distribution of the MT-cell cortex distances along the proximal axons of control neurons or neurons lacking AnkG. Control: 124 measures from 7 neurons, AnkG-shRNA: 234 measures,  $N = 2$ ,  $n = 9$  neurons.

(E–G) Mean MT-cell cortex distance (E), axonal diameter (F), and mean axonal diameter as a function of MT-cell cortex distance (G) of neurons transfected with a control-shRNA or AnkG-shRNA. Unpaired  $t$  tests,  $p = 0.058$  in (E),  $p = 0.026$  in (F) and in (G); Pearson's correlation coefficients are  $p = 0.10$  (control) and  $p = 0.72$  (AnkG-shRNA).

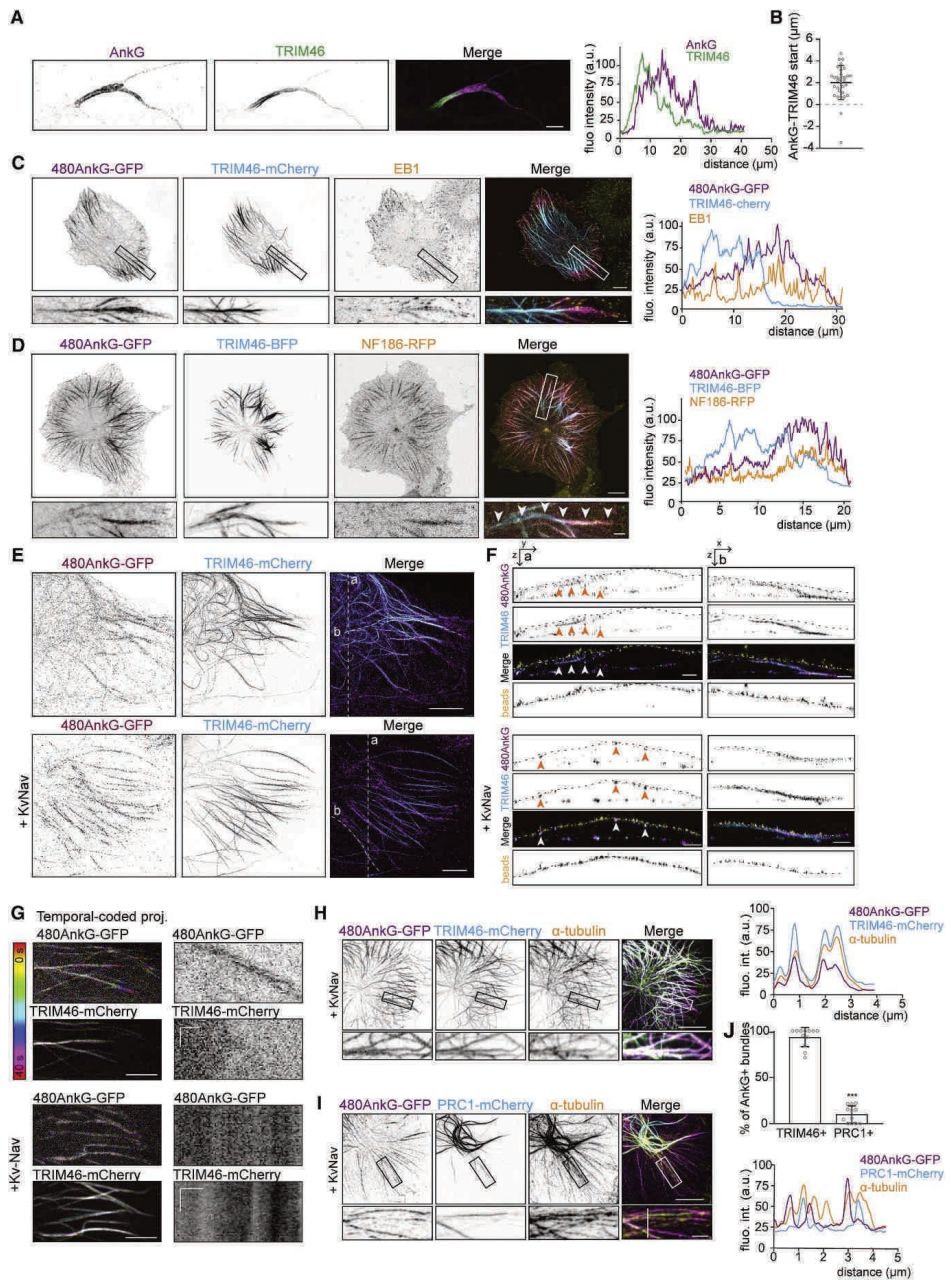
Scale bars are  $5 \mu\text{m}$  in (A) and  $1 \mu\text{m}$  in (B) and (C).

To assess whether AnkG is also capable of targeting MTs to the membrane vicinity in axons, we used single-molecule localization microscopy (SMLM) to resolve the distance between MTs and the plasma membrane in control neurons (Figures 2A and 2B) or neurons lacking AnkG (Figure 2C). As most of the AIS membrane proteins are lost upon depletion of AnkG, we imaged actin to determine the position of the cell cortex (Kiuchi et al., 2015, Schatzle et al., 2018). We observed that, in neurons lacking AnkG, the MT-cortex distances were shifted to higher values (Figure 2D) and the mean MT-cortex distance significantly increased

(Figure 2E). As previously reported (Hedstrom et al., 2008), neurons transfected with AnkG-short hairpin RNA (shRNA) had a larger axonal diameter (Figure 2F). However, this was unlikely to be the cause of the increased MT-cortex distance, because the mean axonal diameter and the mean MT-cortex distance did not correlate (Figure 2G). Together, our data indicate that AnkG recruits MTs to the plasma membrane at the AIS.

#### ***480AnkG Recruits TRIM46-Decorated Parallel MT Bundles to the Plasma Membrane***

In cultured primary neurons, TRIM46-labeled MT bundles located at the beginning of the axon as previously described (van Beuningen et al., 2015) and overlapped with AnkG, which localized to the axonal sub-membrane region (Figures 3A–3C and S3A). Depletion of TRIM46 led to a significant reduction in AnkG intensity at the AIS, whereas specific accumulation of TRIM46 in the proximal axon strongly relied on AnkG (van Beuningen et al., 2015) (Figures S3B–S3D). In COS-7 cells, when co-expressed with TRIM46-mCherry in the absence of membrane partners, 480AnkG-GFP was no longer observed at MT plus-ends only but instead coincided with TRIM46 along the MT lattice (Figure 3C). Interestingly, while 480AnkG-GFP and TRIM46-mCherry signals overlapped, they showed a spatial organization similar to that of the AIS, with TRIM46 being accumulated proximally along the MT bundle, while 480AnkG was enriched more distally toward the MT plus-ends (Figure 3C). Expression of other MAPs, such as anti-parallel MT bundler, PRC1-mCherry (Loïodice et al., 2005), or parallel MT bundler TRIM36-mCherry, a close homolog of TRIM46 that does not accumulate at the AIS (van Beuningen et al., 2015), did not recruit 480AnkG to MT bundles (Figures S3E and S3F), suggesting that 480AnkG selectively interacts with TRIM46-decorated MT bundles. Therefore, we tested whether 480AnkG specifically recruits TRIM46-labeled MTs to the plasma membrane. Co-expression of 480AnkG-GFP, NF186-RFP, and TRIM46-BFP in COS-7 cells revealed that MT bundles recruited by 480AnkG are labeled with TRIM46 (Figure 3D), suggesting that 480AnkG targets TRIM46-decorated parallel MT bundles to the plasma membrane. We used expansion microscopy (Chen et al., 2015, Tillberg et al., 2016) and gSTED microscopy to resolve the position of TRIM46-bundles in COS-7 cells expressing TRIM46-mCherry together with 480AnkG-GFP with or without KvNav (Figures 3E, 3F, and S3G–S3I). We observed that TRIM46 co-expressed with 480AnkG did not show any preferential targeting to the cell cortex (Figures 3E, 3F, upper panels, and S3G). When 480AnkG-GFP was co-expressed with its membrane partner KvNav and TRIM46-mCherry, we observed a clear cortical targeting of AnkG and TRIM46 (Figures 3E, 3F, lower panels, and S3H). TRIM46 alone, which decorates MTs in their proximal parts and localizes to



3

**Figure 3. 480AnkG Anchors TRIM46-Decorated MT Fascicles to the Plasma Membrane** (A and B) Proximal region of a DIV14 hippocampal neuron stained for TRIM46 and AnkG (A). The difference between AnkG and TRIM46 start positions was measured in (B) for 32 neurons. (C and D) COS-7 cell expressing 480AnkG-GFP with TRIM46-mCherry (C) or TRIM46-BFP and NF186-RFP (D).

---

(E and F) Expanded COS-7 cells (E) transfected with indicated constructs and stained for GFP and TRIM46. (F) shows average projections of resliced *z* stacks along transversal (left panel, a) or longitudinal (right panel, b) lines of 0.25  $\mu\text{m}$  thickness. Arrowheads point at AnkG- and TRIM46-positive bundles.

(G) Temporal-coded maximum projections from time-lapse imaging of COS-7 cells expressing indicated constructs.

(H–J) COS-7 cell expressing 480AnkG-GFP and KvNav with TRIM46-mCherry (H) or PRC1-mCherry (I) and stained for  $\alpha$ -tubulin. The percentage of positive membrane 480AnkG-GFP bundles is shown in (J).

In (A), scale bar is 5  $\mu\text{m}$ , in (C), (D), (H), and (I) scale bars are 10  $\mu\text{m}$  and 2  $\mu\text{m}$  in the zooms. In (E), scale bars are 5  $\mu\text{m}$  and 2  $\mu\text{m}$  in the *z* sections, and in the kymographs in (G) they represent 1  $\mu\text{m}$  (horizontal) and 15 s (vertical). See also Figures S2 and S3.

---

acetylated MTs (Figure S3J) did not localize close to the plasma membrane (Figure S3I). Live imaging in COS-7 cells revealed that 480AnkG-GFP, co-expressed with TRIM46-mCherry alone, was found along the MT lattice but still tracked dynamic MT plus ends (Figure 3G, upper panel). However, when targeted to the membrane by co-expressing KvNav, 480AnkG-GFP colocalized with TRIM46-mCherry bundles and was distributed along the MT lattice (Figure 3G, lower panel) confirming that in these conditions 480AnkG could recruit TRIM46-positive MT bundles to plasma membrane. Interestingly, membrane-attached 480AnkG-GFP efficiently recruited TRIM46-mCherry-positive MT bundles (Figures 3H and 3J) but was not able to target PRC1-positive bundles to the membrane (Figures 3I and 3J).

Neither 270AnkG-GFP nor 480AnkG-NN-GFP were able to localize to TRIM46-induced MT bundles (Figures S3L and S3M), suggesting that EB-binding was required for 480AnkG to be recruited to TRIM46-bound MT lattices. The 480AnkGtail construct also failed to accumulate along the TRIM46-decorated MT lattices and remained enriched at MT plus-ends (Figures S3L and S3M), suggesting that in addition to binding to EB proteins, also the 480AnkG N terminus is important for binding to MTs bundled by TRIM46. To validate this idea, we engineered a 270AnkG isoform able to track MT plus-ends, 270AnkG+TIP, by adding one SxIP motif in its C terminus. The 270AnkG+TIP efficiently accumulated at MT plus-end where it colocalized with EB1 (Figures S3L and S3N). Like 480AnkG, 270AnkG+TIP but not 270AnkG showed strong overlap with TRIM46-decorated MTs (Figures S3L and S3N). Together, these results indicate that 480AnkG specifically recruits TRIM46-bundled MTs to the plasma membrane in an EB-dependent manner.

### TRIM46 Orients and Stabilizes MTs Recruited at the Membrane by AnkG

To test the orientation of TRIM46-labeled MTs recruited to the plasma membrane, we used a laser-severing assay to record the direction of MT plus-end regrowth (Yau et al., 2014). Upon severing of MTs labeled with tubulin-GFP or 480AnkG-GFP in EB3-RFP and Kv-Nav co-expressing cells, we did not observe any preferential MT orientation (Figures 4A and 4B). However, in TRIM46-GFP-labeled MT bundles, plus-end regrowth after laser severing occurred in a single direction in ~90% of the cases. The binding of TRIM46 along MT bundles recruited at the plasma membrane by 480AnkG also conferred a uniform MT orientation (Figures 4A and 4B). This result shows that TRIM46 decoration confers a uniform orientation to MT fascicles recruited at the membrane by 480AnkG.

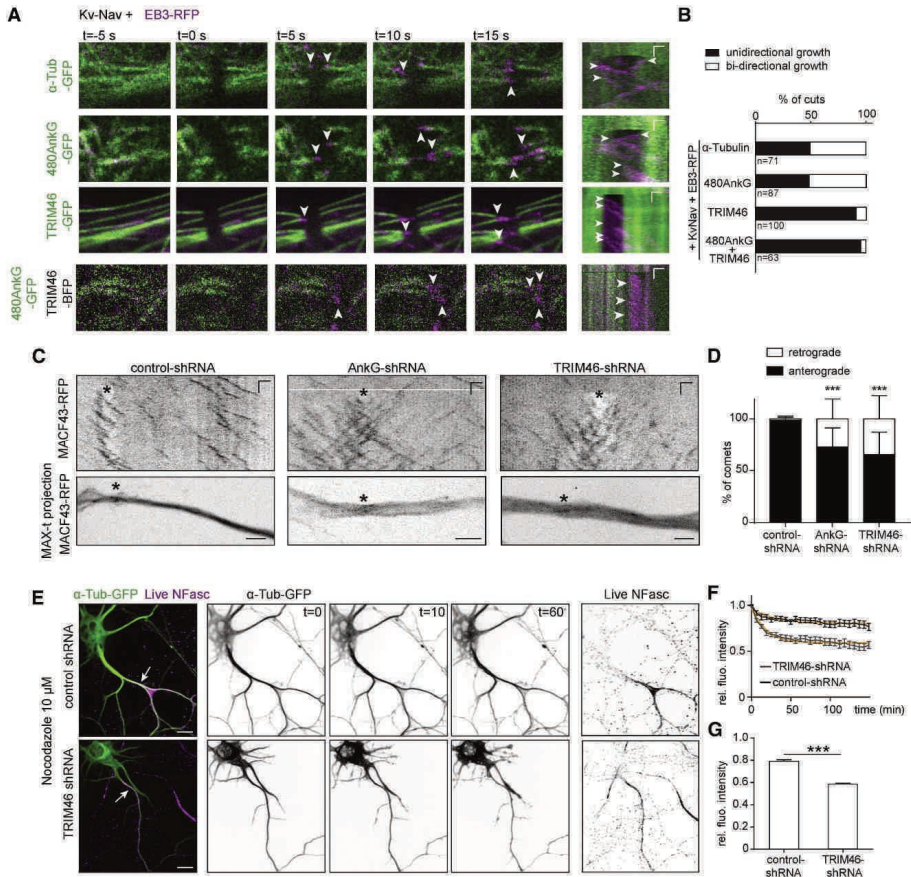


**Figure 4. TRIM46 Orients and Stabilizes MTs in the AIS**

(A and B) Photo-ablation of MTs labeled with indicated constructs in COS-7 co-expressing Kv-Nav and EB3-RFP (A). Kymographs (B) are shown on the right. Scale bars show 1 μm (horizontal) and

---

15 s (vertical). Regrowth events are indicated by arrowheads. The percentage of cuts is shown in (E).  $n$  is the number of cuts, in  $N \geq 10$  cells.

(C and D) Photo-ablation of MTs in the proximal axon of DIV8 neurons co-transfected at DIV0 with indicated constructs (C). Lower panels show the maximum-time projections of MACF43-RFP imaging. Asterisks show the ablation sites. Scales are  $1 \mu\text{m}$  (horizontal) and 15 s (vertical). The mean percentage of comets after ablation is shown in (D). 2-way ANOVA,  $p = 0.0004$  for AnkG-shRNA,  $p < 0.0001$  for TRIM46-shRNA compared to control-shRNA.  $n = 10$  neurons,  $N = 2$ .

(E–G) DIV4 hippocampal neurons transfected at DIV1 with indicated construct and imaged after addition of  $10 \mu\text{M}$  Nocodazole. (E) shows still frames at 0, 10, and 60 min. (F) Fluorescence intensity of  $\alpha$ -tub-GFP in the proximal axon of control ( $n = 20$ , black) or TRIM46 knockdown neurons ( $n = 24$ , gray) after addition of Nocodazole and normalized to the first frame. Fitted one-phase decay curves are shown in orange. (G) shows the plateau values obtained from the fits, unpaired  $t$  test,  $p < 0.0001$ .

Scale bars are  $2 \mu\text{m}$  in (C) and  $10 \mu\text{m}$  in (E). See also Figure S4.

---

TRIM46 and AnkG were shown to be important for plus-end out MT organization in axons (Van Beuningen et al., 2015; Fréal et al., 2016). In order to assess the orientation of both stable and dynamic polymerizing MTs in proximal axons, we performed laser severing experiments and monitored MT plus-end regrowth by imaging a MT plus end marker MACF43-RFP (Honnappa et al., 2009) in DIV8 neurons co-transfected at DIV0 with control- (Figure 4C, left panel), AnkG- (middle panel), or TRIM46-shRNA (right panel). Control neurons contained ~100% of plus-end out MTs, whereas AnkG- and TRIM46-depleted neurons showed a significant increase in minus-end out MTs (Figure 4D), further strengthening the importance of AnkG and TRIM46 in organizing the axonal MT network.

We next determined whether TRIM46 can protect MT bundles against nocodazole-induced depolymerization. We imaged live cells expressing NF186-RFP and 480AnkG-GFP with BFP or TRIM46-BFP and treated them with nocodazole or DMSO as a control (Figures S4A–S4C). 480AnkG and NF186 were accumulated at the plasma membrane in control cells; however, they rapidly disappeared after the addition of nocodazole. In contrast, co-expression of TRIM46-BFP preserved 480AnkG/NF186 membrane stretches in nocodazole-treated cells (Figures S4B and S4C). To determine whether the nocodazole-resistant 480AnkG/NF186 membrane structures induced by TRIM46 were associated with MTs, we fixed the cells and stained for tubulin (Figures S4E and S4F). In the absence of TRIM46, no remaining MTs were observed after the addition of the drug. Only when TRIM46-BFP was co-expressed, we detected nocodazole-resistant MTs (Figures S4E and S4F). 480AnkG-GFP, NF186-RFP, or 480AnkG-NN-GFP alone, as well as 480AnkG-GFP in combination with NF186-RFP, were not able to confer nocodazole resistance to MTs (Figure S4G). These data suggest that TRIM46-decorated MT bundles recruited to plasma membrane by 480AnkG are protected



against depolymerization. Additionally, we observed that TRIM46 bundling increased the clustering of 480AnkG/NF186 at the plasma membrane (Figures S4B and S4D). Interestingly, when 480AnkG-GFP behaved as a +TIP and as well as when it located along MT lattice upon targeting to the membrane by KvNav, it was preferentially associated with tyrosinated MTs and did not colocalize to acetylated MTs (Figure S4H). When TRIM46-BFP was co-expressed together with 480AnkG-GFP, with or without KvNav, AnkG was associated with bundles that consisted of long-lived, acetylated MTs at their proximal end and tyrosinated MTs at the distal end (Figure S4I).

To investigate whether TRIM46 also protects axonal MTs against depolymerization, we expressed  $\alpha$ -tubulin-GFP together with control- or TRIM46-shRNA and performed time-lapse imaging before and after nocodazole addition (Figures 4E–4G). Quantification revealed that the tubulin intensity in the proximal axon markedly decreased in neurons depleted of TRIM46 in the presence of nocodazole (Figures 4E–4G). These results show that TRIM46 stabilizes axonal MTs.

### ***TRIM46 Generates Long and Stable MT Bundles In Vitro by Promoting Rescues***

In order to test whether TRIM46 can autonomously confer uniform orientation and stability to 480AnkG-decorated MT bundles, we performed *in vitro* MT dynamics reconstitution assays as described previously (Bieling et al., 2007, Mohan et al., 2013, Sharma et al., 2016), using purified 480AnkG and TRIM46 (Figures S5A and S5B). Since 480AnkG interacts directly with EBs (Fréal et al., 2016), we first examined whether it regulates MT plus-end dynamics *in vitro*. We polymerized MTs from GMPCPP-stabilized seeds in the presence of EB3 alone (Figure 5A), together with 480AnkG (Figure 5B) or with 480AnkG-NN (Figure 5C) and recorded their dynamics using total internal reflection fluorescence (TIRF) microscopy. 480AnkG tracked the plus ends of growing MTs and also displayed some decoration of MT lattice (Figure 5B). The 480AnkG-NN mutant that does not bind to EBs, and the wild-type 480AnkG in the absence of EBs failed to track MT plus-ends and showed only weak MT lattice binding (Figures 5C and S5E). This was consistent with the findings reported previously in COS-7 cells and rat hippocampal neurons (Fréal et al., 2016; Figures 1E and 1F). *In vitro*, 480AnkG did not have any strong impact on MT dynamics (Figures 5D–5F): it mildly reduced MT growth rate but did not significantly affect catastrophe or rescue frequencies (Figures 5D–5F).

Next, we reconstituted MT dynamics in the presence of TRIM46 (Figure 5G). TRIM46 did not bind to single MTs on its own (Figure 5G, arrowhead and middle panel; Video S2) but got

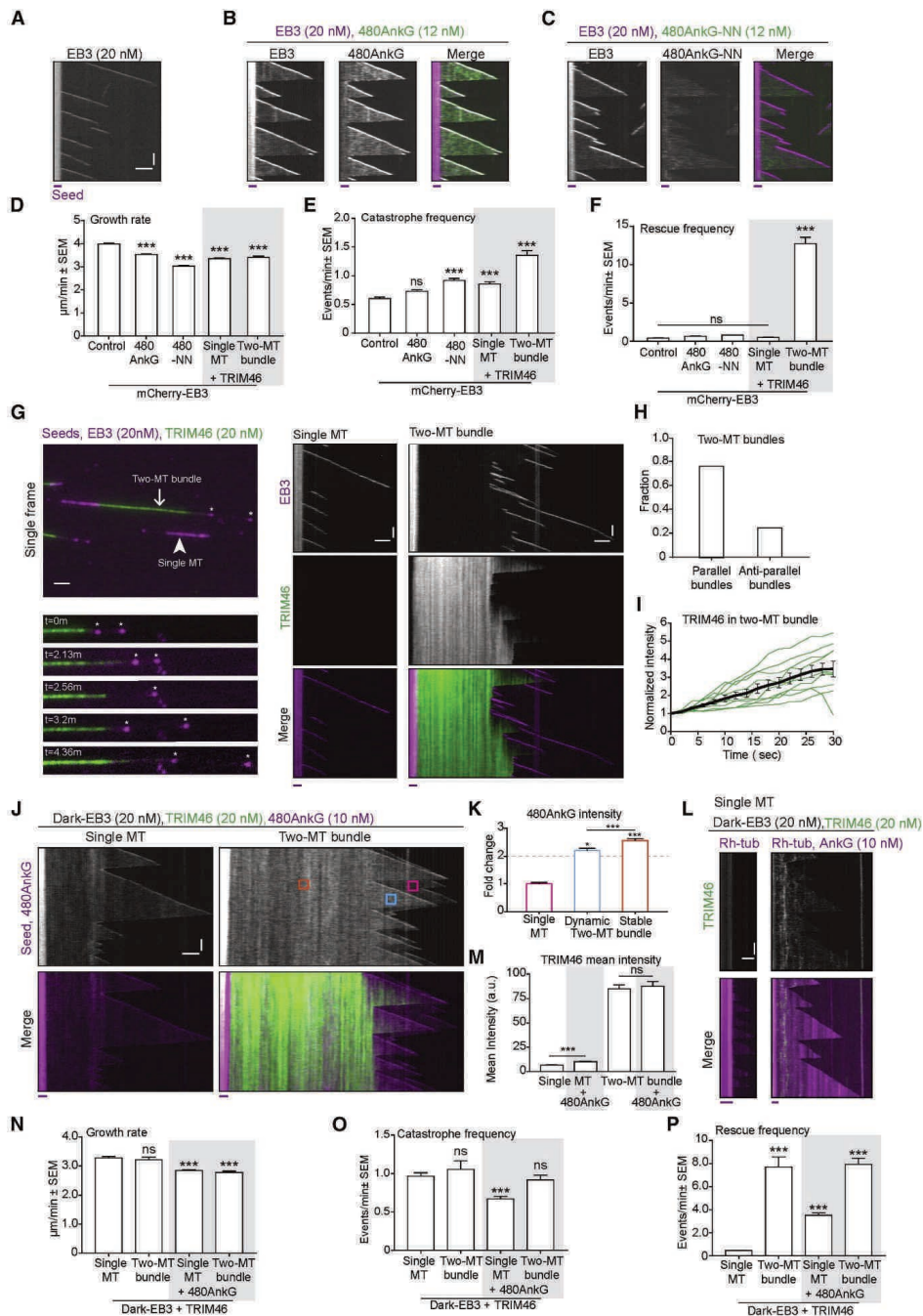


Figure 5. TRIM46 Promotes Rescues within Parallel MT Bundles and Shows Weak Interaction with 480AnkG In Vitro

(A–C) Kymographs showing MTs dynamics grown in the presence of mCherry-EB3 alone (A) or together with 480AnkG-GFP (B) or 480AnkG-NN-GFP (C).

(D–F) Quantification of MT plus-end growth rate (D), catastrophe frequency (E) and rescue frequency (F) in the presence of mCherry-EB3 ( $n = 213$ ) together with 480AnkG-GFP ( $n = 388$ ), 480AnkG-NN-GFP ( $n = 458$ ), or GFP-TRIM46 ( $n = 235$  for single MTs and  $n = 91$  for two-MT bundles), 2–3 assays per condition. One-way ANOVA with Tukey's multiple comparisons test,  $ns\ p > 0.05$ ,  $***p < 0.001$ .

(G–I) (G) Left panels: single frame (top) of a time-lapse video showing single MT (arrowhead) and two-MT bundle (arrow) growing from rhodamine-tubulin-labeled GMPCPP seeds in the presence of mCherry-EB3 and GFP-TRIM46 and still pictures (bottom) at indicated time points (in min). Corresponding kymographs are shown in the middle panel. (H) Fraction of parallel and anti-parallel TRIM46-decorated two-MT bundles ( $n = 41$  bundles). (I) Average intensity ( $\pm$ SEM, black) of GFP-TRIM46 over time in two-MT bundles, normalized to its intensity at the time when bundles form ( $n = 10$  events in green, from 7 TRIM46-positive two-MT bundles, three assays per condition).

(J and K) Kymographs (J) showing 480AnkG-mCherry dynamics of single MTs or TRIM46 MT bundles in the presence of dark-EB3. 480AnkG-mCherry mean intensity (K) on single MTs (magenta) or two-MT TRIM46-bundles (dynamic, cyan; stable, orange) normalized to average mean intensity on single MTs, from 1  $\mu$ m<sup>2</sup> 33–76 regions of interest (ROIs) of 7–15 TRIM46-decorated two-MT bundles from 6–8 assays. Error bars show 95% confidence interval. One sample *t* test was carried out to test whether fold change in AnkG intensity on TRIM46-bundles is more than 2,  $*p < 0.05$ ,  $***p < 0.001$ . One-way ANOVA was used to test whether the change in 480AnkG intensity was different in dynamic compared to stable two-MT bundle,  $**p = 0.0050$ .

(L) Kymographs illustrating GFP-TRIM46 fluorescence intensity on single MTs grown in the presence of dark-EB3, 14.5  $\mu$ M porcine tubulin, and 0.5  $\mu$ M rhodamine-tubulin without (left) or with 480AnkG-mCherry (right).

(M) Mean intensity of GFP-TRIM46 on single MTs or TRIM46-bundles with or without 480AnkG-mCherry, from 1  $\mu$ m<sup>2</sup> 80–140 ROIs from 8–14 single MTs or TRIM46 two-MT bundles, 3 assays per condition. Error bars are SEM. Two-tailed unpaired *t* test,  $ns\ p > 0.05$ ,  $***p < 0.001$ .

(N–P) Quantification of MT plus-end growth rate (N), catastrophe frequency (O), and rescue frequency (P) in the presence of dark-EB3 and GFP-TRIM46 together with 480AnkG-mCherry and 15  $\mu$ M porcine tubulin or 14.5  $\mu$ M porcine tubulin and 0.5  $\mu$ M rhodamine-tubulin.  $n = 139$  and  $n = 188$  single MTs without or with 480AnkG, respectively, and  $n = 26$  and  $n = 87$  TRIM46-decorated MT bundles without or with 480AnkG, respectively, 2–3 assays per condition. One-way ANOVA,  $ns\ p > 0.05$ ,  $***p < 0.001$ .

Scale bars in all the kymographs represent 2  $\mu$ m (horizontal) and 60 s (vertical). The red line below each kymograph represents rhodamine-labeled GMPCPP-stabilized MT seeds. See also Figure S5 and Table S1.

recruited to MT bundles (Figure 5G, arrow and right panel). Consistently with previous findings in cells (van Beuningen et al., 2015), TRIM46 preferentially bundled MTs in a parallel manner (Figure 5H). TRIM46 was abundantly present on the overlapping MTs and showed gradual enrichment on the fresh MT overlaps generated by MT growth (Figure 5I). These data indicate that TRIM46 is an autonomous parallel MT bundling factor, which requires presence of at least two closely apposed MTs for an efficient MT interaction.

Like 480AnkG, TRIM46 had little effect on the growth rate of individual MTs (Figure 5D), but, once accumulated along a MT bundle, it potently promoted rescues of MTs within the bundle (Figures 5F and 5G, bottom-left panel), thus leading to their progressive elongation and

stabilization. The ability of TRIM46 to prevent MT depolymerization within parallel bundles explains why MTs still persist in COS-7 cells, when they are treated with nocodazole, which promotes MT disassembly by sequestering soluble tubulin (Figures S4A and S4B). We also observed a mild increase in catastrophe frequency within TRIM46-decorated MT bundles (Figure 5E), and overall MT plus ends within TRIM46-decorated MT bundles remained highly dynamic. The fact that the distal part of such bundles remains dynamic and can accumulate EBs and 480AnkG might explain the partial spatial separation of TRIM46 and 480AnkG on bundled MTs (Figures 3B and 3C).

We next tested the potential interplay between 480AnkG and TRIM46. When MTs were grown in the presence of both 480AnkG and TRIM46 (Figure 5J), 480AnkG was slightly enriched along the TRIM46-decorated MT shafts in two-MT bundles (Figure 5K). This enrichment was more pronounced on the stable (orange box in Figure 5J) as compared to dynamic (blue box in Figure 5J) lattices within the bundles. Since stable MT parts had higher accumulation of TRIM46 than the freshly grown MT lattices within the bundle (Figure 5I), this suggested that 480AnkG enrichment was indeed dependent on TRIM46 and not on the presence of two closely apposed MTs. To test this idea further, we performed *in vitro* experiments with 480AnkG and another MT bundling factor, PRC1 (Loiodice et al., 2005, Mollinari et al., 2002). As previously described, we observed that PRC1 did not bind to single MTs, but decorated MT bundles (Bieling et al., 2010, Subramanian et al., 2013). In contrast to what we observed with TRIM46, we found that compared to single MTs, the intensity of 480AnkG along two-MT PRC1 bundles was exactly twice as high on freshly formed PRC1 bundles and even slightly lower on older bundles that were densely populated by PRC1 (Figures S5C and S5D). This suggested that mere bundling is not sufficient to cause enrichment of 480AnkG on MTs but rather the presence of TRIM46 is required for recruitment of 480AnkG to MT bundles. To support the specificity of 480AnkG enrichment along TRIM46-decorated MT bundles, we reconstituted MT dynamics in the presence of TRIM46 and 480AnkG or EB-binding-deficient 480AnkG-NN, without adding EBs in the assay. As expected, we observed very weak lattice binding of AnkG on single MTs in the absence of EBs (Figures S5E–S5G). However, TRIM46 still weakly but significantly recruited 480AnkG to MT bundles even in the absence of EBs and promoted a similar enrichment of the EB-binding-deficient mutant 480AnkG-NN on MT bundles (Figures S5F–S5I). Furthermore, in the presence of 480AnkG, TRIM46 was weakly bound to single MTs (Figures 5L and 5M), whereas its accumulation on two-MT bundles remained unaltered (Figure 5M). Moreover, in the presence of 480AnkG, TRIM46 was able to weakly promote rescues even on single MTs (Figure 5P), while the effects on MT growth rate and catastrophe

frequency were mild (Figures 5N and 5O). Our results show that TRIM46 is a potent rescue factor that triggers some enrichment of 480AnkG along the MT lattice. Interestingly, 480AnkG also mildly increases the affinity of TRIM46 for single MTs further supporting our findings about the weak MT-dependent cooperativity between 480AnkG and TRIM46. Taken together, our data demonstrate that TRIM46 can autonomously generate long and stable parallel MT arrays, which remain dynamic at their distal parts. These arrays concentrate EBs and Ankyrin-G, which in turn provide connections to the plasma membrane.

### ***TRIM46 Promotes Efficient Trafficking of NF186 Vesicles to the Proximal Axon***

We have shown that 480AnkG mediates the membrane recruitment of TRIM46-decorated MT bundles and that TRIM46 is a rescue factor that protects against MT depolymerization. We hypothesize that this unique membrane-MT organization may allow for efficient targeting of the AIS membrane proteins to the proximal axon. Using time-lapse imaging of DIV4 neurons expressing control shRNA, we observed mobile NF186-RFP vesicles trafficking in the axon, as well as an immobile pool of NF186 in the proximal axon (Figures 6A and 6E). NF186 vesicles colocalized with endosomal markers, such as Rab5-GFP and Rab11-GFP as well as endogenous Rab11, in fixed (Figure S6A) and live neurons (Figures S6B and S6C). In neurons depleted of TRIM46, we observed significant changes in NF186-RFP vesicle mobility in the axon and a frequent switch in the transport direction (Figures 6B–6E). In control axons (within the first ~100  $\mu\text{m}$ ), NF186-RFP vesicles were mainly transported back to the cell body (~70% retrograde, Figure 6B), whereas in the axons of TRIM46-depleted neurons, NF186 vesicles were equally transported back and forward (~50% retrograde, Figure 6B). This change in transport direction in TRIM46-depleted axons was accompanied by a strong increase in the number of reversals (~3-fold change, Figures 6C and S6D) and a decrease in the mean run time (Figures 6D and S6F). Consistently, we verified that Rab11 transport is affected in TRIM46-depleted neurons. We transfected DIV0 neurons with Rab11-GFP in combination with the control or TRIM46-shRNA (Figure 6F). We observed changes in the directionality of runs and in the number of reversals. In the axons of DIV3 control neurons, retrogradely moving Rab11 vesicles were more abundant than anterograde ones (Figure 6G). In contrast, in axons of neurons depleted of TRIM46, Rab11 vesicles moved in both directions with the same frequency, as it was the case in dendrites, and switched direction more often (Figures 6G and 6H).

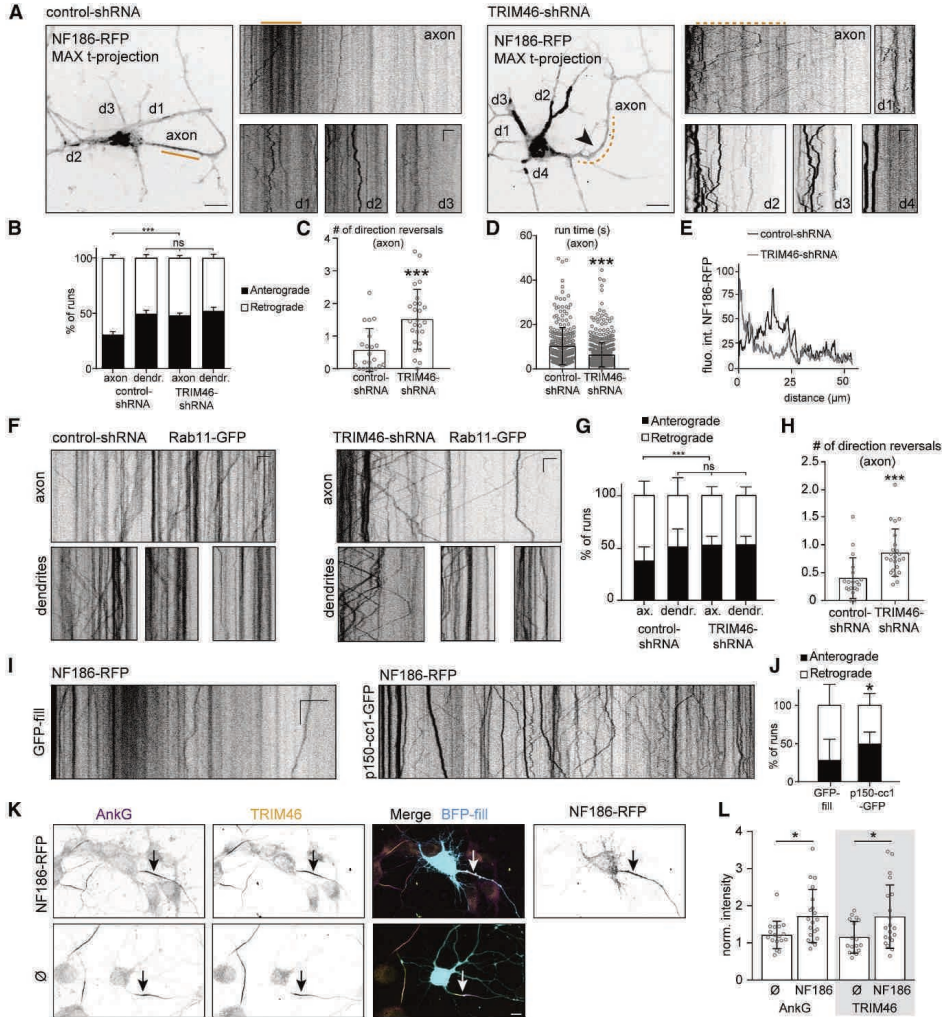


**Figure 6. TRIM46 Promotes Retrograde Transport of NF186 to the Proximal Axon**

(A) Maximum time projection from time-lapse imaging of DIV4 neurons transfected at DIV0 with indicated constructs. Kymographs of axon and dendrites are shown. Orange lines highlight the proximal axon. Scale is  $5\ \mu\text{m}$  (horizontal) and  $15\ \text{s}$  (vertical).

(B) Percentage of NF186-RFP runs in DIV4 neurons co-transfected at DIV0 with indicated constructs.  $n = 20$  neurons,  $N = 2$ , 2-way ANOVA,  $***p = 0.0002$ ,  $ns: p = 0.916$ .

(C and D) Quantification of NF186-RFP vesicle dynamics in DIV4 neurons co-transfected at DIV0 with indicated constructs. Mann-Whitney in (C),  $p = 0.0003$ ,  $n = 21\text{--}26$  axons, and in (D),  $p < 0.0001$ ,  $n = 279\text{--}645$  runs.

(E) Fluorescence intensity profiles of NF186-RFP along the axons of neurons shown in (A).

(F–H) Kymographs (F) of Rab11-GFP vesicles in DIV3 neurons co-transfected at DIV0 with indicated constructs. Scale is  $5\ \mu\text{m}$  (horizontal) and  $3\ \text{s}$  (vertical). (G) Percentage of runs. (H) Mean number of direction reversals per axon.  $n = 18$  neurons,  $N = 2$ . In (G), two-way ANOVA,  $ns\ p = 0.5$ ,  $***p < 0.001$ . In (H), Mann-Whitney test,  $***p = 0.00012$ .

---

(I and J) Kymographs (I) of NF186-RFP in the axons of DIV3 neurons co-transfected at DIV0 with indicated constructs. Scale is 10  $\mu\text{m}$  (horizontal) and 5 s (vertical). (J) Percentage of runs. Two-way ANOVA,  $*p = 0.0104$ ,  $n = 20$  neurons,  $N = 2$ .

(K and L) DIV5 hippocampal neurons (K) co-transfected at DIV1 with indicated constructs and stained for AnkG and TRIM46. (L) Intensity of AnkG and TRIM46 staining at the AIS normalized to neighboring non-transfected neurons. One-way ANOVA with Holm-Sidak's multiple comparison test,  $p = 0.037$  for AnkG,  $p = 0.020$  for TRIM46.  $n = 17$  neurons,  $N = 2$ . Scale bars are 10  $\mu\text{m}$  in (A) and (K). See also Figure S6.

---

The bias toward retrograde transport of NF186 in the axon suggested a role for the minus-end directed motor dynein. We analyzed NF186-RFP trafficking in the axons of neurons expressing GFP or p150cc1-GFP, a dominant-negative form of the dynactin adaptor p150, which is reported to perturb dynein function (Kuijpers et al., 2016). As reported for TRIM46 knockdown, perturbing dynein function induced changes in NF186 vesicles transport, with a significant increase in the fraction of anterograde runs compared to control (Figure 6J). These results indicate that TRIM46-mediated plus-end out MT orientation allows for the efficient retrograde transport of NF186 vesicles from the distal to the proximal axon via the endosomal pathway in a dynein-dependent manner.

Controlled trafficking and clustering of AIS membrane proteins, adhesion molecules, and ion channels is crucial for neuronal activity (Kole et al., 2008), and it was shown to contribute to AIS formation and maintenance by influencing AnkG accumulation in this region (Alpizar et al., 2019, Leterrier et al., 2017, Xu and Shrager, 2005, Zonta et al., 2011). We co-expressed NF186-RFP (Figure 6K) or an empty vector together with a BFP-fill in DIV1 neurons and stained for endogenous AnkG and TRIM46 at DIV5 (Figure 6K). We observed that the overexpression of both NF186 or KvNav (Figure S6G) increased the accumulation of endogenous AnkG and TRIM46 at the AIS (Figures 6L and S6H). We conclude that a membrane partner can promote clustering of both AnkG and TRIM46 at the AIS in developing neurons. Other AIS membrane proteins, such as Kv7 or NF186, as well as AnkG modifications such as palmitoylation, could possibly have an effect on AnkG/TRIM46 accumulation at the AIS.

### ***AnkG Inhibits NF186 Endocytosis Resulting In Stable Accumulation at the AIS***

We next speculated that the scaffold formed by AnkG may allow for local accumulation of the AIS membrane proteins in the proximal axon by selectively preventing their endocytosis at the AIS. To track membrane NF186 in live neurons, we performed an antibody uptake experiment

using a fluorescently labeled antibody against NF186 on DIV4 neurons expressing NF186-RFP (Figures 7A–7D).

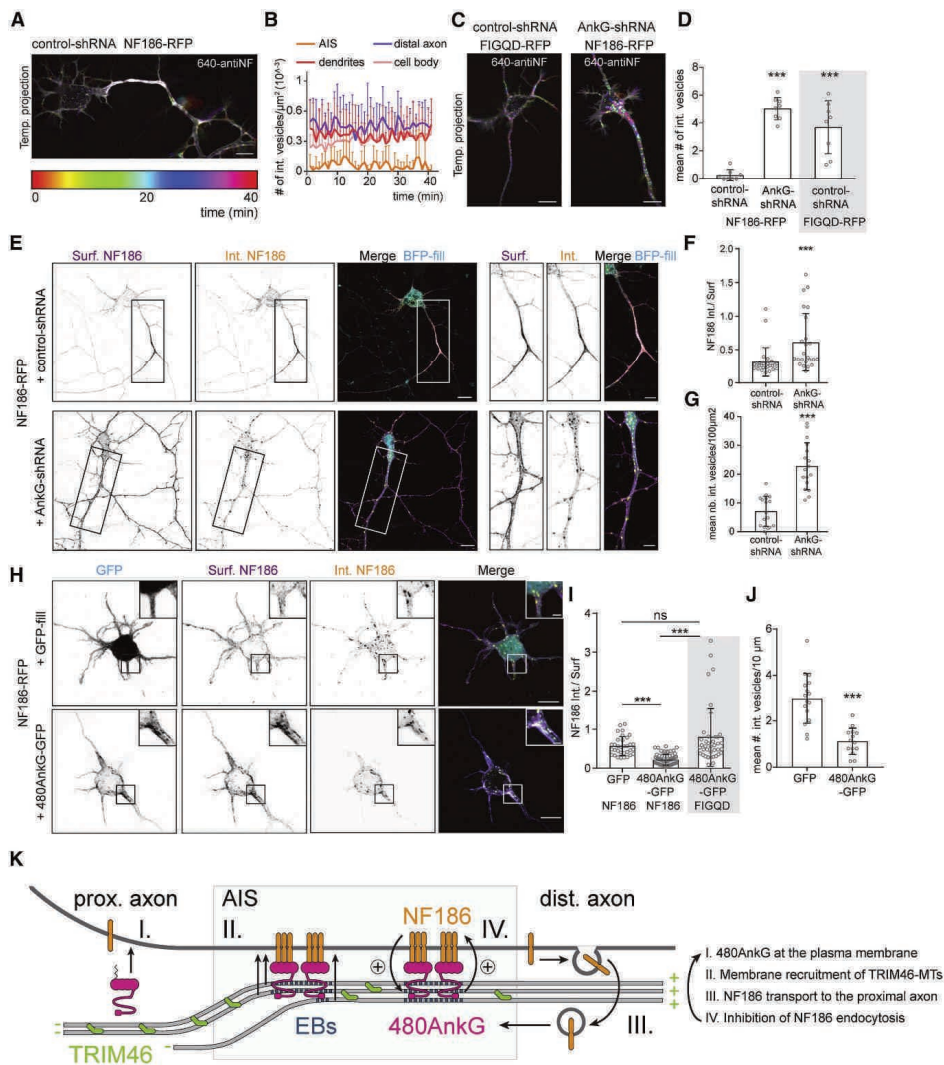


**Figure 7. AnkG Allows for the Stable Accumulation of NF186 at the AIS by Inhibiting Its Endocytosis**

(A and B) Temporal-color coded maximum projection (A) from live imaging of a DIV4 neuron co-transfected at DIV0 with indicated constructs and incubated with a fluorescently tagged anti-NF antibody (640-antiNF). (B) Number of internalized NF vesicles in indicated compartments.

(C and D) Temporal-color coded maximum projections (C) from live imaging of DIV4 neurons co-transfected at DIV0 with indicated constructs incubated with 640-antiNF. (D) Mean number of 640-antiNF vesicles during the first 5 min post incubation in the proximal axons. One-way ANOVA, \*\*\* $p < 0.0001$ ,  $n = 8$  neurons,  $N = 2$ .



(E–G) DIV4 neurons (E) co-transfected at DIV0 with indicated constructs. (F) Fluorescence intensity ratio of internalized over surface NF186 in the proximal axon. (G) Mean number of internalized NF186 vesicles per 100  $\mu\text{m}^2$  of axon. Mann-Whitney test,  $p = 1.7 \times 10^{-7}$   $n = 17$  axons.

(H–J) DIV1 neurons (H) transfected at DIV0 with indicated constructs. (I) Fluorescence intensity ratio of internalized over surface NF186 in the first 10  $\mu\text{m}$  of proximal neurites. Kruskal-Wallis test, Dunn's multiple comparison test. ns,  $p > 0.99$ ,  $***p < 0.0001$ ,  $n = 33$  ROIs. (J) Number of internalized NF186 vesicles per 10  $\mu\text{m}$ . Unpaired  $t$  test,  $***p < 0.0001$ ,  $n = 14$  neurons,  $N = 2$ .

(K) Model of the molecular pathways involved in AIS formation. See text for details.

In (A), (C), and (D), scale bars are 10  $\mu\text{m}$ ; in (E), scale bars are 10 and 2  $\mu\text{m}$  in the zooms; and in (H), scale bars are 10 and 5  $\mu\text{m}$  in the zooms. See also Figure S7.

In the first minutes after antibody incubation, high numbers of internalized NF186 vesicles were detected in dendrites, cell body, and distal axons ( $>50 \mu\text{m}$  away from the soma), whereas the AIS contained a lower number of vesicles (Figures 7A and 7B). The number of internalized-NF186 vesicles in the proximal axon increased dramatically upon depletion of AnkG (Figures 7C, left panel, and 7D) or when a NF186 mutant incapable of binding to AnkG was expressed (wt-FIGQY to mutant-FIGQD; Boiko et al., 2007, Zhang et al., 1998; Figures 7C, right panel, panel, 7D). In order to measure the endocytosis rate, we quantified the ratio of internalized-to-surface NF186 in DIV4 neurons expressing control- or AnkG-shRNA (Figures 7E–7G) and observed a robust increase in the number of NF186-positive vesicles and an enhanced endocytosis rate in neurons depleted of AnkG (Figures 7F and 7G). To question the direct role of AnkG in opposing endocytosis of NF186, we transfected DIV0 neurons, not yet expressing endogenous AnkG, with NF186-RFP together with 480AnkG-GFP or with GFP (Figures 7H–7J). In 480AnkG-GFP-expressing neurons, the surface pool of NF186 colocalized with 480AnkG-GFP along neurites (Figure 7I, lower panel and zoom), and the internalized signal was markedly decreased (Figures 7I and 7J), suggesting that 480AnkG prevents NF186 endocytosis. Next, we used the NF186-FIGQD mutant to test whether the direct interaction between AnkG and NF186 is responsible for the lower endocytosis rate. NF186-FIGQD did not accumulate in the proximal axon of DIV3 neurons and showed no colocalization with 480AnkG-GFP (Figures S7A and S7B). In DIV1 neurons, NF186-FIGQD co-expressed with 480AnkG-GFP was taken up at a rate similar to that observed for the wild-type NF186 in the absence of 480AnkG-GFP (Figures 7I and S7C). Our results indicate that AnkG, by directly interacting with NF186, is able to prevent NF186 endocytosis allowing for stable accumulation at the AIS.

## Discussion

### *Role of AnkG in MT Organization at the AIS Membrane*

The crucial role of AnkG in AIS formation and maintenance has been extensively demonstrated *in vitro* and *in vivo* (Hedstrom et al., 2008, Sobotzik et al., 2009). More recently, the 480-kDa isoform has emerged as the essential player in this process; however, the mechanisms used by this giant scaffold protein are far from being understood (Fréal et al., 2016, Jenkins et al., 2015b). Recent studies indicate that AnkG's role in AIS assembly requires both its membrane targeting and its association with MTs via EBs, but the functional pathways implicated have remained speculative (Fréal et al., 2016, He et al., 2012, Leterrier et al., 2011, Leterrier et al., 2017). We here describe novel functions for 480AnkG underpinning its pivotal role in AIS formation and maintenance (Figure 7K). First, we show that 480AnkG targets and anchors MTs in the vicinity of the plasma membrane. This newly described function of 480AnkG depends both on its membrane association and its binding to EBs, since AnkG truncations lacking one of these properties lose the ability to organize MTs. The direct control of MT organization by membrane-480AnkG was never reported and is likely to explain the axonal MT alterations described in AnkG-deficient neurons *in vitro* and *in vivo* (Fréal et al., 2016, Hedstrom et al., 2008, Leterrier et al., 2011, Sobotzik et al., 2009). Next to the direct interaction with Nav or NF186, other AIS channels such as Kv7 (Pan et al., 2006, Rasmussen et al., 2007) or the adhesion molecule NrCAM (Dzhashiashvili et al., 2007, Hedstrom et al., 2007) possibly mediate AnkG recruitment at the plasma membrane. Palmitoylation of the Cys70 residue of AnkG was reported to be crucial for its role in driving AIS assembly (He et al., 2012), and it would be interesting to test whether palmitoylation of 480AnkG isoform in neurons is required for AIS formation.

Interestingly, the membrane recruitment of MTs induced by 480AnkG in COS-7 cells is consistent with super-resolution microscopy-based observations showing that MTs in the AIS are mostly found within ~80 nm of the plasma membrane (Leterrier et al., 2015). We propose that the local membrane-MT coupling by 480AnkG could provide specific properties to this specialized axonal compartment. Since AnkG is integrated into the periodic axonal spectrin-actin rings, the localization of AnkG at the crosspoints between transversal actin rings and longitudinal MTs running under the plasma membrane may create a “grid-like” organization coupling actin and MT networks. This cytoskeleton organization may allow for cooperative control of axonal diameter and homeostatic plasticity (Berger et al., 2018, Grubb et al., 2011). Additionally, the integrated AIS-MT organization may control axonal cargo trafficking by

bringing regulatory proteins anchored at the AIS membrane within close range of the motor-cargo complexes, explaining why axonal carriers proceed and somatodendritic cargos stop and reverse. For instance, dynein regulatory protein Ndel1 localizes to the AIS by binding to AnkG and stimulates retrograde transport of somatodendritic vesicles at the AIS (Kuijpers et al., 2016).

### ***Mechanisms of Membrane Protein Accumulation in the AIS***

Although a lot of attention has recently been given to the role of the proximal axon as a transport checkpoint (Leterrier, 2018), much less is known about the transport mechanism of AIS components themselves into the proximal axon. Despite NF186's function in maintaining the AIS and recruiting specialized extracellular matrix structures (Alpizar et al., 2019, Hedstrom et al., 2007, Zonta et al., 2011), little is known about how this transmembrane protein gets targeted and retained at the AIS. Some papers suggest that clathrin-mediated endocytosis is important for NF186 surface distribution in neurons (Boiko et al., 2007, Yap et al., 2012). In this study, we show that, upon non-specific targeting of NF186 to both the axon and dendrites, NF186 gets endocytosed except at the AIS, where the interaction with AnkG locally blocks its internalization (Figure 7K). The NF186 interaction with AnkG was shown to depend on phosphorylation of its cytoplasmic FIGQY motif (Tuvia et al., 1997, Zhang et al., 1998), suggesting an additional regulatory mechanism, in which phospho-NF186 does not associate with AnkG and therefore gets internalized at the AIS. It is possible that AnkG may also inhibit the endocytosis of other transmembrane proteins such as Nav at the AIS. After a non-targeted delivery to all compartments and removal by endocytosis outside the AIS (Fache et al., 2004), Nav anchoring relies on direct interaction with AnkG, which is regulated by a phosphorylation-dependent mechanism implicating the kinase CK2 (Bréchet et al., 2008, Garrido et al., 2003, Lemailet et al., 2003). A function for AnkG in organizing membrane micro-domains by locally inhibiting endocytosis was recently reported for somatodendritic GABAergic synapses maintenance and lateral membrane assembly in MCDK cells (Cadwell et al., 2016, Jenkins et al., 2015a, Jenkins et al., 2013, Tseng et al., 2015). This newly described function of AnkG, wherein AnkG hinders the endocytosis of membrane proteins in a potentially phospho-dependent manner opens new ideas around the pathways implicated in AIS homeostasis and plasticity (Berger et al., 2018, Evans et al., 2013, Grubb et al., 2011). Once internalized by endocytosis, NF186-containing endocytic vesicles are subsequently retrieved from the distal axon and travel back to the proximal axon in a dynein-dependent manner. The polarized distribution of somatodendritic cargos such as  $\alpha 5$ -integrin or

transferrin and glutamate receptors was also shown to rely on axonal retrieval by Rab5- and Rab11-positive vesicles (Guo et al., 2016, Koseki et al., 2017). Interestingly, we observed that, in the absence of TRIM46, retrograde transport of NF186 as well as Rab11 is markedly perturbed. Impaired axonal retrieval of somatodendritic and AIS proteins could be responsible for the polarity defects observed in TRIM46-depleted neurons (van Beuningen et al., 2015). Although trafficking of the dendritic AMPA receptor subunit GluR2 was unaffected by TRIM46 depletion (van Beuningen et al., 2015), we cannot exclude that the changes in NF186 vesicles transport we report in the absence of TRIM46 could also result from the abnormal entry of somatodendritic motors into the axon. Altogether our data reveal that the formation of a stable and functional AIS relies on the cooperative coupling between directional transport and local membrane protein stabilization.

#### ***Functional Cross-talk between AnkG and TRIM46***

Our *in vitro* reconstitution assays for the first time reveal the functional relationship between the MT organizer TRIM46 and the membrane scaffold 480AnkG. Interestingly, we observed that TRIM46 does not bind to single MTs but to the lattice of at least two closely apposed parallel MTs. We propose that the 480AnkG-induced MT fascicles running along the plasma membrane facilitate TRIM46 binding along the MT lattice. This would explain the strong effects of AnkG knockdown on TRIM46, where ~90% of the neurons lacking AnkG showed altered TRIM46 accumulation in the proximal axon. We show that TRIM46 binding to parallel MTs induces their stabilization by strongly increasing rescue frequency. Importantly, the accumulation of TRIM46 on bundled MTs occurs with a time delay, and as a result MT plus ends within the bundles remain dynamic and can accumulate EBs and 480AnkG. Furthermore, 480AnkG and TRIM46 display a weak cooperativity: TRIM46 mildly stimulates recruitment of 480AnkG to the MT lattice and 480AnkG mildly increases the affinity of TRIM46 for single MTs. These weak interactions promote formation of membrane-associated MT fascicles without causing complete convergence of the TRIM46 and 480AnkG-occupied domains. Interestingly, in COS-7 cells we observed that membrane-480AnkG is able to target MTs of mixed orientation to the membrane, the uniform orientation is being caused by TRIM46 co-expression. In TRIM46 knockdown neurons, AnkG shows a reduced accumulation at the AIS but is most likely still able to recruit (some) MTs close to the membrane. Even if it is still present, this MT recruitment at the membrane by AnkG is not sufficient to prevent the transport changes of NF186 and Rab11 vesicles that we report in the axons of neurons lacking TRIM46,

revealing different but cooperative functions of TRIM46 and AnkG in the formation of the AIS.

The *in vitro* results, combined with our cellular data, highlight the molecular pathways for AIS formation. The cooperation between TRIM46-mediated MT organization and 480AnkG-mediated membrane scaffolding allows for the directional targeting and local retention of NF186 at the AIS. The stabilization of NF186 at the AIS in turn increases the submembrane concentration of AnkG in the proximal axon. Higher AnkG concentration in turn strengthens the membrane anchoring of MTs and facilitates TRIM46-lattice stabilization and preferential orientation, driving a more efficient and directed retrieval of NF186 to the proximal axon. Since the AIS was shown to be a dynamic compartment (Grubb and Burrone, 2010, Kuba et al., 2010), it would be interesting to investigate whether and how the mechanism of AIS assembly play a role in activity-induced AIS plasticity. The phosphatase calcineurin has been shown to play a role in this phenomenon (Evans et al., 2013), but the target proteins as well as the pathways implicated remain unclear. We here show that AnkG locally controls NF186 endocytosis, in a potentially phosphorylation-dependent manner, which could represent one part of the cascade regulating AIS repositioning during plasticity. Interestingly, next to the role of the scaffolding protein AnkG, interactions with the MAPs DCX and MAP1B have also been reported to participate in the regulation of NF186 and Nav1.6 endocytosis in neurons (Solé et al., 2019, Yap et al., 2012). These data further emphasize the idea of strong cooperation between membrane-associated proteins and the cytoskeleton during AIS assembly and dynamics.

## Experimental Model and Subject Details

### Animals

All experiments were approved by the DEC Dutch Animal Experiments Committee (Dier Experimenten Commissie), performed in line with institutional guidelines of University Utrecht and were conducted in agreement with Dutch law (*Wet op de Dierproeven*, 1996) and European regulations (Directive 2010/63/EU). Female pregnant Wistar rats were obtained from Janvier and were aged at least 10 weeks at the time of delivery. Upon delivery, rats were kept in a controlled 12 h light-dark cycle with a temperature of  $22 \pm 1^\circ\text{C}$  and were given unrestricted access to food and water. The animals were housed with companions in transparent Plexiglas cages with wood-chip bedding and paper tissue for nest building and cage enrichment. For hippocampal neuron culture experiments obtained from rat embryos, embryos of both gender

at E18 stage of development were used. None of the parameters analyzed in this study are reported to be affected by embryo gender. The animals, pregnant females and embryos have not been involved in previous procedures.

### **Heterologous Cell Culture and Transfection**

African Green Monkey SV40-transformed kidney fibroblast (COS-7), Human embryonic kidney 293 (HEK) and Human Bone Osteosarcoma Epithelial (U2OS) cells were from ATCC and cultured in DMEM/Ham's F10 (45%/45%) supplemented with 10% fetal calf serum and 1% penicillin/streptomycin at 37°C and 5% CO<sub>2</sub>. Cell lines were not authenticated by authors after purchase. The cell lines were routinely checked for mycoplasma contamination using LT07-518 Mycoalert assay (Lonza).

Cells were plated on 18mm glass coverslips and transfected with Fugene6 (Promega) according to manufacturer's protocol.

### **Primary Neuronal Cultures and Transfection**

Primary hippocampal neurons cultures were prepared from embryonic day 18 rat brains (both genders). Cells were plated on coverslips coated with poly-L-lysine (37.5 µg/mL) and laminin (1.25 µg/mL) at a density of 100,000/well. Neurons were cultured in Neurobasal medium (NB) supplemented with 2% B27 (GIBCO), 0.5 mM glutamine (GIBCO), 15.6 µM glutamate (Sigma), and 1% penicillin/streptomycin (GIBCO) at 37°C in 5% CO<sub>2</sub>.

Hippocampal neurons were transfected using Lipofectamine 2000 (Invitrogen). Briefly, DNA (1.8 µg/well, of a 12 wells plate) was mixed with 3.3 µL of Lipofectamine 2000 in 200 µL NB, incubated for 30 min, and then added to the neurons in NB at 37°C in 5% CO<sub>2</sub> for 45 min. Next, neurons were washed with NB and transferred to their original medium at 37°C in 5% CO<sub>2</sub>.

Alternatively, hippocampal neurons (400,000 cells) were nucleofected with 3 µg of DNA using the Amaxa Rat Neuron Nucleofector kit (Lonza) according to the manufacturer's instructions.

## **Method Details**

### **DNA and shRNA Constructs**

The following constructs were already described: TRIM46-mCherry, TRIM46-GFP, TRIM36-mCherry and PRC1-mCherry (van Beuningen et al., 2015), 480AnkG-GFP, 480AnkG-NN-GFP, 270AnkG-GFP, 480AnkGtail-GFP (Fréal et al., 2016), myc-Kv-Nav (Bréchet et al.,

2008), Rab5-GFP and Rab11-GFP (Hoogenraad et al., 2010), Rab6-GFP and NPY-GFP (Schlager et al., 2010), HA-NF186-mRFP-FKBP (Kuijpers et al., 2016), EB3-RFP (Stepanova et al., 2003) and mEOS-tubulin (Cloin et al., 2017).

TRIM46-BFP was obtained by inserting TRIM46 into pGW1-BFP (Kapitein et al., 2010) using AscI/SalI restriction sites.

HA-NF186(FIGQD)-mRFP-FKBP was obtained by overlap extension PCR. NF186(FIGQD) was amplified from HA-NF186-GFP (Kuijpers et al., 2016), and the resulting fragment was inserted in the HindIII/AgeI sites of HA-NF186-mRFP-FKBP (Kuijpers et al., 2016) to replace wt-NF186. C70A-480AnkG-GFP was created by first generating a fragment containing the C70A mutation using overlap extension PCR and using this fragment to replace the region between KpnI and AclI sites in 480AnkG-GFP.

StrepII-480AnkG-GFP and -mCherry as well as StrepII-480AnkG-NN-GFP and -mCherry were obtained by insertion of 480AnkG and 480AnkG into pTT5-EGFP-N1 or pTT5-mCherry-N1 (Atherton et al., 2017) using KpnI/AgeI restriction sites.

StrepII-GFP-TRIM46 and StrepII-GFP-PRC1 were obtained by PCR. TRIM46 and PRC1 were amplified from GFP-TRIM46 and GFP-PRC1 (van Beuningen et al., 2015) and inserted into the BglII/SalI sites of a modified StrepII-GFP-C1 vector. 270AnkG+TIP-GFP was obtained by replacing GFP from 270AnkG-GFP by MACF18-GFP (Honnappa et al., 2009) using AgeI/NotI restriction sites.  $\beta$ -tubulin-GFP was a kind gift from Dr. P. Schätzle and Dr. K. Jiang. Previously described sequences for AnkG-shRNA (Hedstrom et al., 2007) and TRIM46-shRNA (van Beuningen et al., 2015) were cloned into pSUPER (Brummelkamp et al., 2002). Empty-pSUPER was used as a control-shRNA.

### Antibodies and Reagents

Rabbit anti-TRIM46 was previously described (van Beuningen et al., 2015) as well as rabbit anti-EB3 and rat anti-EB2 (Stepanova et al., 2003).

Mouse anti-AnkG (clone N106/36 and clone N106/20) and anti-Pan-Neurofascin (clone A12/18) were from Neuromab.

Mouse anti-EB1 (clone 5/EB1), and mouse anti-Rab11 (clone 47/Rab11) were from BD Transduction Laboratories. Chicken anti-MAP2 (ab5392) and anti-GFP (ab13970), rabbit anti- $\alpha$ -tubulin (ab52866) and rat anti-tyrosinated tubulin (ab6160) were from Abcam. Rabbit anti-GFP (598) was from MBL, and mouse anti-GFP (clone 3E6, A-11120) was from Life Technologies. Mouse anti- $\alpha$ -tubulin (B-5-1-2), anti-acetylated tubulin (6-11B-1, T7451) and anti- $\beta$ -tubulin (T5201) were from Sigma-Aldrich. Corresponding secondary antibodies Alexa-

conjugated 350, 405, 488, 568, 594 or 647 goat anti-mouse, anti-rabbit or anti-chicken were used (Life Technologies). Atto 647N Phalloidin was from Atto-Tec.

### **Pharmacological Treatments**

Nocodazole (Sigma) was used at 10  $\mu$ M and DMSO (0.001%) was used as a control.

### **Immunostaining**

For immunocytochemistry, cells were fixed for 10 min with warm paraformaldehyde (4%)-sucrose (4%) or for 5 min with methanol (100%) containing 1 mM EGTA at  $-20^{\circ}\text{C}$  followed by 5 min paraformaldehyde (4%). Primary antibodies were incubated overnight at  $4^{\circ}\text{C}$  in GDB buffer (0.2% BSA, 0.8 M NaCl, 0.5% Triton X-100, 30 mM phosphate buffer, pH 7.4). After 3 washes in PBS, secondary antibodies were incubated in the same buffer for 1hr at RT. Coverslips were mounted using Vectashield (Vectorlabs).

### **Uptake Experiment**

Fixed neurons: Extracellular anti-Pan Neurofascin (1/200 in Neurobasal) was incubated with live neurons for 30 min at RT, the coverslips were then washed 2 times in warm Neurobasal, returned to original medium for 10min and fixed in warm paraformaldehyde (4%)-sucrose (4%) for 10min. Secondary anti-mouse Alexa-647 antibody diluted in 1/200 was incubated in PBS-NGS 5% for 30min at RT to stain the surface pool of NF186. Then cells were permeabilized in PBS-NGS 5%- Triton X-100 0.25% for 5min and blocked in PBS-NGS 10% for 30 min at  $37^{\circ}\text{C}$ . Secondary anti-mouse Alexa 488 or  $-405$  antibody was diluted 1/200 in PBS-NGS 5% and incubated for 30min at RT in order to stain the intracellular pool of NF186.

Live neurons: CF640R coupled (Mix-n-Stain, Biotium) extracellular anti-Pan Neurofascin antibody (1/200 in Neurobasal) was incubated with live neurons for 30 s at  $37^{\circ}\text{C}$ , the coverslips were then washed 1 time for 30 s in warm Neurobasal and original medium was added back before starting imaging.

### **Image Acquisition**

Cells were imaged using a LSM700 confocal laser-scanning microscope (Zeiss) with a Plan-Apochromat 63x NA 1.40 oil DIC, EC Plan-Neofluar 40x NA1.30 Oil DIC and a Plan-Apochromat 20x NA 0.8 objective. Each confocal image was a z stack of 2–10 images, each averaged 4 times, covering the entire region of interested from top to bottom. Maximum



projections were done from the resulting z stack. For fluorescence intensity comparison, settings were kept the same for all conditions.

*In vitro* assays were imaged on an iLas<sup>2</sup> TIRF microscope setup as described (Sharma et al., 2016). In brief, iLas<sup>2</sup> system (Roper Scientific, Evry, France) is a dual laser illuminator for azimuthal spinning TIRF illumination and with a custom modification for targeted photomanipulation. This system was installed on the Nikon Eclipse Ti-E inverted microscope with the perfect focus system, equipped with Nikon Apo TIRF 100x 1.49 N.A. oil objective (Nikon), EMCCD Evolve mono FW DELTA 512x512 camera (Roper Scientific) with the intermediate lens 2.5X (Nikon C mount adaptor 2.5X), CCD camera CoolSNAP MYO M-USB-14-AC (Roper Scientific), 150 mW 488 nm laser, 100 mW 561 nm laser and 49002 and 49008 Chroma filter sets and controlled with MetaMorph 7.8.8 software (Molecular Device). The final magnification using Evolve EMCCD camera was 0.064  $\mu\text{m}/\text{pixel}$  and for CoolSNAP Myo CCD camera it was 0.045  $\mu\text{m}/\text{pixel}$ . Temperature was maintained at 30°C to image the *in vitro* assays using a stage top incubator model INUBG2E-ZILCS (Tokai Hit). Time-lapse movies to estimate MT dynamics were acquired using a CoolSNAP Myo CCD camera (Roper Scientific), while movies for intensity analysis were acquired using a more sensitive Photometrics Evolve 512 EMCCD camera (Roper Scientific) at 2 s per frame with 100 ms exposure time for 10 minutes.

### **gSTED Microscopy**

gated STED (gSTED) imaging was performed with a Leica TCS SP8 STED 3X microscope using a HC PL APO 100  $\times$  / 1.4 oil immersion STED WHITE objective. The 488, 594 and 647 nm wavelengths of pulsed white laser (80 MHz) were used to excite the Alexa488, Alexa594 and the Atto647N secondary antibodies. Both Alexa594 and Atto647N were depleted with the 775 nm pulsed depletion laser, Alexa488 was depleted with the 592 nm pulsed depletion laser (30%–40% of maximum power), and we used an internal Leica HyD hybrid detector (set at 100% gain) with a time gate of  $0.3 \leq t_g \leq 6$  ns.

### **Expansion Microscopy**

Expansion microscopy was performed according to proExM protocol (Tillberg et al., 2016). Briefly, stained cells on an 18 mm coverslip were incubated overnight in 0.1 mg/mL Acryloyl-X (Thermo Fischer A20770) in PBS and 0.002% (solids) of 0.1  $\mu\text{m}$  yellow-green FluoroSpheres (ThermoFisher, F8803). After washing three times in PBS, cells were transferred to gelation chamber (diameter 13 mm and 120  $\mu\text{L}$  volume) made of silicone molds

(Sigma Aldrich, GBL664107) on a parafilm covered glass slide. Chamber was pre-filled with monomer solution (2 M NaCl, 8.625% (w/w) sodium acrylate, 2.5% (w/w) acrylamide, 0.15% (w/w) N,N'-methylenebisacrylamide in PBS) with added 0.4% (w/w) tetramethylethylenediamine (TEMED) accelerator and 0.2% (w/w) ammonium persulfate (APS) initiator. The gelation proceeded for one 1 h at 37°C in a humidified incubator. Gels were further immersed into 2 mL of 8 units/mL proteinase-K in digestion buffer (50 mM Tris (pH 8), 1 mM EDTA, 0.5% Triton X-100, 0.08M guanidine HCl) solution for 4 h at 37°C for digestion. Gels were transferred to 50 mL deionized water for overnight expansion with water refreshed once to ensure the expansion reached plateau. Plasma-cleaned #1.5 coverslips were incubated in 0.1% (w/v) poly-L-lysine to reduce gel's drift during acquisition. Gels on coated coverslips were mounted using custom printed imaging chambers [<https://www.tinkercad.com/things/7qqYCYgcbNU>]. Expansion factor was calculated as a ratio of a gel's diameter to the diameter of gelation chamber and was in the range of 4.2-4.4. Confocal microscopy of expanded gels was performed with a Leica TCS SP8 STED 3X microscope using a HC PL APO 63x/1.20 W CORR CS2 water immersion objective. Images were acquired with lateral pixel size in the range of 70-80 nm and axial of 180 nm using internal HyD detector. If necessary, a drift correction of Z stack was performed in Huygens Professional version 17.04 (Scientific Volume Imaging, the Netherlands) using cross-correlation between adjacent slices. All images were deconvolved in the same program, using the CMLE algorithm, with SNR:7 and 20 iterations.

### **Single Molecule Localization Microscopy**

Single Molecule Localization Microscopy was performed on a Nikon Eclipse Ti-E equipped with a 100x Apo TIRF oil immersion objective (NA 1.49) and Perfect Focus System 3. A Lighthub-6 (Omicron) with a 488nm laser (Luxx 200mW Omicron) and a 561nm laser (Coherent Obis) was used for excitation through a custom illumination pathway that allowed tuning of the incident angle. A quad-band polychroic mirror (ZT405/488/561/640rpc, Chroma), quad-band emission filter (ZET405/488/561/640 m, Chroma), and additional single-band emission filters were placed before the sCMOS camera (Hamamatsu flash 4.0v2) to separate the emission light from the excitation light. DIV4 neurons, nucleofected with mEos-tubulin and control-shRNA or AnkG-shRNA, were extracted with prewarmed 0.25% triton-X and 0.15% glutaraldehyde in MRB80 buffer for 1 minute. Subsequently, the samples were fixed with 4% paraformaldehyde in MRB80 buffer. After 3 PBS washing steps the samples were permeabilized with 0.25% triton-X in PBS for 10 minutes. After 3 more PBS washes,

fiducial markers (FluoSpheres, Thermo Fisher) were added to enable drift correction, and the cells were mounted in a Ludin chamber in PBS. Upon identification of the axon initial segment, single-molecule localization microscopy of mEos-tubulin was performed with 100 ms exposure time, 561 nm laser excitation and low intensity 405 nm laser illumination to trigger photoconversion. Subsequently, IRIS (image reconstruction by integrating exchangeable single-molecule localization) was performed using LifeAct-mNeonGreen to image actin as described previously (Kiuchi et al., 2015, Schatzle et al., 2018, Tas et al., 2018). Briefly, LifeAct-mNeonGreen-6xHis in a pET28a vector was expressed in BL21DE3, purified using Complete His-tag purification resin (Sigma) and stored in PBS supplemented with 1mM DTT and 10% Glycerol. The purified protein was added to the fixed samples at such concentrations that single-molecule binding event could be detected at 100 ms exposure times. Reconstructions of the individual channels were performed using Detection of Molecules (DoM, [https://github.com/ekatrakha/DoM\\_Utrecht](https://github.com/ekatrakha/DoM_Utrecht)).

### **Live Cell Imaging**

Live-cell imaging experiments were performed in an inverted microscope Nikon Eclipse Ti-E (Nikon), equipped with a Plan Apo VC 100x NA 1.40 oil and a Plan Apo VC 60x NA 1.40 oil objective (Nikon), a Yokogawa CSU-X1-A1 spinning disk confocal unit (Roper Scientific), a Photometrics Evolve 512 EMCCD camera (Roper Scientific) and an incubation chamber (Tokai Hit) mounted on a motorized XYZ stage (Applied Scientific Instrumentation) which were all controlled using MetaMorph (Molecular Devices) software. Coverslips were mounted in metal rings and imaged using an incubation chamber that maintains temperature and CO<sub>2</sub> optimal for the cells (37°C and 5% CO<sub>2</sub>). Neuron live imaging was performed in full conditioned medium and fresh medium was added to COS-7 before imaging.

Time-lapse live-cell imaging of EB3-RFP was performed with a time acquisition of 1 s. NF186-RFP alone was acquired at 2 frames per second. NPY-GFP, GFP-Rab6, Rab11-GFP or Rab5-GFP, alone or in combination with NF186-RFP were acquired at 10 frames per second.

For simultaneous imaging of green and red fluorescence, we used ET-mCherry/GFP filter set (59022; Chroma) together with the DualView (DV2; Roper) equipped with the dichroic filter 565dcxr (Chroma) and HQ530/30 m emission filter (Chroma).

### **MT Severing - Photoablation**

Teem Photonics 355 nm Q-switched pulsed laser was used to perform laser-induced severing and study MT orientation in COS-7 cells and neurons as describe previously (Yau et al., 2014). No signs of toxicity to cells was observed during laser-induced severing.

### **Image Processing and Data Analysis**

Movies and images were processed using Fiji (<https://imagej.net/Fiji>). Kymographs were generated using the ImageJ plugin KymoResliceWide v.0.4 <https://github.com/ekatruxha/KymoResliceWide>. Internalized NFasc vesicles were detected using the plugin ComDet (<https://github.com/ekatruxha/ComDet>). Fluorescence intensity of AIS proteins and AIS position were measured using the plugin Pro\_Feat\_Fit ([https://github.com/cleterrier/Measure\\_ROIs](https://github.com/cleterrier/Measure_ROIs)). For the in vitro reconstitution assays, MT dynamics parameters viz. MT plus-end growth rate, catastrophe frequency, and rescue frequency were determined from kymographs using an optimized version of the custom made JAVA plugin for ImageJ as described previously (Mohan et al., 2013, Montenegro Gouveia et al., 2010, Smal et al., 2009). For TRIM46-decorated MT bundles, MT dynamics were quantified from the lagging MT within bundle and only two-MT bundles were selected for analysis. The relative standard error for catastrophe frequency and the relative standard error of mean for rescue frequency was calculated as described in (Sharma et al., 2016). One-way ANOVA with Tukey's multiple comparisons test was performed to test for significance. For the quantification of parallel and anti-parallel MT-bundles fractions, polarity was determined by the velocity of MT polymerization. For intensity analysis of 480AnkG-mCherry on single MTs versus two-MT bundles, kymographs were generated with maximum intensity projection, and mean intensities on single MTs and two-MT bundles from the same TRIM46-positive MT bundles were estimated from multiple ROIs  $1 \mu\text{m}^2$  in size. For each movie, individual mean intensities for single MTs or two-MT bundles after background subtraction were normalized to average mean intensity on single MTs quantified from the same movie and fold change in 480AnkG mean intensity were plotted for single MTs and dynamic and stable lattice in TRIM46-decorated two-MT bundle. Similarly, average mean intensity of GFP-TRIM46 on single MTs or two-MT bundles with or without 480AnkG was quantified from multiple ROIs  $1 \mu\text{m}^2$  in size from assays done in two separate chambers under the same coverslip with identical acquisition settings. Pairwise mean comparisons between single MTs with and without 480AnkG and between two-MT bundles with and without 480AnkG were carried out using parametric two-tailed unpaired t test. Data are presented as mean  $\pm$  SEM unless stated differently.

To measure microtubule-cell cortex distances, 0.1  $\mu\text{m}$  large lines were traced perpendicular to the axons every 2  $\mu\text{m}$ . Distances corresponding to a fixed intensity of 0.2 were extracted from the intensity profiles of each channel.

### **Electron Microscopy**

To correlatively image COS-7 cells with fluorescence and electron microscopy we used a recently developed approach (Harterink et al., 2019). COS-7 cells were grown on needle engraved Aclar pieces (Electron Microscopy Sciences; 50426–10 (Jiménez et al., 2010)) glued in a 12-wells plate with Matrigel (Biosciences). Cells were transfected with NF186-RFP together with 480AnkG-GFP or 480AnkG-NN-GFP and extracellularly labeled with anti-NF186 (1:200; NeuroMab, A12/18). Cells were washed in culture medium and fixed with 2% paraformaldehyde + 0.2% glutaraldehyde in 0,1M PHEM buffer (pH 6.9) for 30 minutes. Free aldehyde groups were quenched with  $\text{NH}_4\text{Cl}$ , washed with PBS, incubated with a bridging secondary antibody (1:300; Dakocytomation, Z0412) in PBS, 1% BSA, washed with PBS, 0.1% BSA and incubated with both protein-A gold 15 nm (1:60; CMC Utrecht) in PBS, 1% BSA and washed in PBS. Transfected cells were fluorescently imaged and the relative position to the engravings was documented. Cells were further fixed with 3.5% glutaraldehyde and 1% paraformaldehyde in 0.1 M cacodylate buffer (pH 7.4), post-fixed with a 1% Osmium and 1.5%  $\text{KFeCN}$  solution in 0,1 M cacodylate buffer (pH 7.4), washed with water, dehydrated with ethanol and infiltrated with increasing amounts of Epon resin. After polymerization, Aclars were peeled off leaving the target cells in the Epon. Landmarks were placed around the target cell using a microdissection setup (Zeiss, PALM microbeam) (Kolotuev et al., 2009) and a 3nm gold layer was applied using a sputter coater. Excess gold was wiped off using a cotton-stab and a drop of Epon was added on top of the cells and polymerized. The Epon samples were trimmed toward the target cell using the landmarks and sectioned with a Leica Ultracut E microtome (60 nm). Sections were placed on grids (Cu 50M-H coated with Formvar film and carbon), stained with uranyl acetate and lead citrate and examined in a Tecnai10 or Tecnai12 electron microscope (FEI Company) operating at 100 kV and equipped with a SIS CCD Megaview II camera (Tecnai10) or a Tietz TVIPS TemCam F-214 (Tecnai12). Landmarks were used to identify the target cell.

### **EB1/2/3 KO Cell Line Generation**

The CRISPR/Cas9 mediated EB1, EB2 and EB3 knockout was performed as previously described (Ran et al., 2013). In brief, U2OS cells were transfected with the vectors bearing the

appropriate targeting sequences. One day after transfection, U2OS cells were subjected to selection with 2 µg/ml puromycin for 2 days. After selection, cells were allowed to recover in normal medium for ~2 days, and knockout efficiency was checked by immunofluorescence staining. Depending on the efficiency, cells were isolated and characterized by western blotting and immunostaining. U2OS EB1/2/3 knockout cells were generated by targeting EB1, EB2 and EB3-encoding genes simultaneously. The pSpCas9-2A-Puro (PX459) vector that was used for the CRISPR/Cas9 knockout was purchased from Addgene. Guide RNAs for human EB1, EB2 and EB3 (also known as MAPRE1, MAPRE2, and MAPRE3) were designed using the CRISPR design webpage tool (<http://zlab.bio/guide-design-resources>). The targeting sequences for gRNAs were as follows (coding strand sequence indicated): EB1, 5'-TGAAAAGACTATGACCCTG-3'; EB2, 5'-CCGGAAGCACACAGTGCGCG-3' and EB3, 5'-TGCACCTCAACTATAACCAAG-3'.

#### **Protein Purification for In Vitro Reconstitution Assays**

GFP-TRIM46, 480AnkG-GFP, 480AnkG-NN-GFP, 480AnkG-mCherry 480AnkG-NN-mCherry and GFP-PRC1 proteins used in the in vitro reconstitution assays were purified using Strep(II)-Strep-Tactin affinity purification as described previously (Sharma et al., 2016). HEK293T cells were transfected with the constructs using polyethylenimine (PEI) and harvested 2 days post transfection. Culture medium was refreshed next day following transfection. Cells were lysed in cell lysis buffer (50 mM HEPES, 300 mM NaCl and 0.5% Triton X-100, pH 7.4) supplemented with protease inhibitor cocktail (Roche). Cell lysate was subjected to centrifugation at 14,800 rpm for 20 minutes at 4°C. The supernatant obtained from the previous step was incubated with Strep-Tactin Sepharose beads (GE) for 45 minutes. Following incubation, beads were washed with the lysis buffer without protease inhibitors 2 times and protein was eluted in 80 µl of elution buffer (50 mM HEPES, 150 mM NaCl, 1 mM MgCl<sub>2</sub>, 1 mM EGTA, 1 mM dithiothreitol (DTT), 2.5 mM d-Desthiobiotin and 0.05% Triton X-100, pH 7.4). Purified proteins were snap-frozen and stored at -80°C. Bacterially expressed mCherry-EB3 and dark EB3 were a gift of Dr. M.O. Steinmetz (Paul Scherrer Institut, Switzerland); they were produced as described previously (Montenegro Gouveia et al., 2010). Purity of the samples was analyzed via SDS-PAGE and Coomassie staining.

#### ***In Vitro* Reconstitution Assays**

*In vitro* reconstitution of MT dynamics was performed as described previously (Mohan et al., 2013). Guanylyl-( $\alpha,\beta$ )-methylene-diphosphonate (GMPCPP) stabilized MT seeds composed of

70% porcine tubulin, 18% biotin tubulin and 12% rhodamine-tubulin were prepared. Flow chambers were assembled using plasma-cleaned glass coverslips and microscopic slides. These chambers were then functionalized by incubation with 0.2 mg/ml PLL-PEG-biotin (Susos AG, Switzerland) followed by 1 mg/ml NeutrAvidin (Invitrogen) in MRB80 buffer (80 mM piperazine-N,N[prime]-bis(2-ethanesulfonic acid), 4 mM MgCl<sub>2</sub>, and 1 mM EGTA, pH 6.8). GMPCPP stabilized biotin-labeled MT seeds were attached to the coverslips through biotin-NeutrAvidin links. Flow chambers were further incubated with 0.8 mg/ml  $\kappa$ -casein to prevent non-specific protein binding. The reaction mix with or without proteins [MRB80 buffer supplemented with 15  $\mu$ M porcine brain tubulin, 50 mM KCl, 1 mM guanosine triphosphate (GTP), 0.5 mg/ml  $\kappa$ -casein, 0.1% methylcellulose, and oxygen scavenger mix (50 mM glucose, 400  $\mu$ g/ml glucose-oxidase, 200  $\mu$ g/ml catalase, and 4 mM DTT)] were added to the flow chambers after centrifugation in an ultracentrifuge (Beckman Airfuge) at 119,000  $\times$  g for 5 minutes. All the experiments were done in the presence 20 nM of either mCherry-EB3 or dark EB3 when indicated. When added to the reaction mix, GFP-TRIM46 (20 nM), 480AnkG-GFP (12 nM), 480AnkG-NN-GFP (12nM) and 480AnkG-mCherry (10 nM) were used in the concentrations indicated in brackets. In the *in vitro* assays used for the intensity analysis of GFP-TRIM46 on the MT bundles, 0.5  $\mu$ M rhodamine-tubulin was added to the reaction mix, while 14.5  $\mu$ M porcine tubulin was used to make the final concentration of tubulin 15  $\mu$ M. The flow chambers were then sealed with high-vacuum silicone grease (Dow Corning), and movies of these reconstitutions were acquired immediately at 30°C using a TIRF microscope. All tubulin products were from Cytoskeleton.

### Mass Spectrometry

After streptavidin purification, beads were resuspended in 20  $\mu$ L of Laemmli Sample buffer (Biorad) and supernatants were loaded on a 4%–12% gradient Criterion XT Bis-Tris precast gel (Biorad). The gel was fixed with 40% methanol/10% acetic acid and then stained for 1 h using colloidal Coomassie dye G-250 (Gel Code Blue Stain Reagent, Thermo Scientific). After in-gel digestion, samples were resuspended in 10% formic acid (FA)/5% DMSO and analyzed with an Agilent 1290 Infinity (Agilent Technologies, CA) LC, operating in reverse-phase (C18) mode, coupled to an Orbitrap Q-Exactive mass spectrometer (Thermo Fisher Scientific, Bremen, Germany). Peptides were loaded onto a trap column (Reprosil C18, 3  $\mu$ m, 2 cm  $\times$  100  $\mu$ m; Dr. Maisch) with solvent A (0.1% formic acid in water) at a maximum pressure of 800 bar and chromatographically separated over the analytical column (Zorbax SB-C18, 1.8  $\mu$ m, 40 cm  $\times$  50  $\mu$ m; Agilent) using 90 min linear gradient from 7%–30% solvent B (0.1%

formic acid in acetonitrile) at a flow rate of 150 nL/min. The mass spectrometer was used in a data-dependent mode, which automatically switched between MS and MS/MS. After a survey scan from 350-1500 m/z the 10 most abundant peptides were subjected to HCD fragmentation. MS spectra were acquired in high-resolution mode ( $R > 30,000$ ), whereas MS2 was in high-sensitivity mode ( $R > 15,000$ ). Raw files were processed using Proteome Discoverer 1.4 (version 1.4.0.288, Thermo Scientific, Bremen, Germany). The database search was performed using Mascot (version 2.4.1, Matrix Science, UK) against a Swiss-Prot database (taxonomy human). Carbamidomethylation of cysteines was set as a fixed modification and oxidation of methionine was set as a variable modification. Trypsin was specified as enzyme and up to two miss cleavages were allowed. Data filtering was performed using percolator, resulting in 1% false discovery rate (FDR). Additional filters were search engine rank 1 and mascot ion score  $>20$ .

### **Quantification and Statistical Analysis**

All statistical details of experiments, including the definitions and exact values of  $n$ , and statistical tests performed, are shown in Figures and Figure Legends.  $n$  represent the number of analyzed cells, and  $N$  the number of independent experiments. Data processing and statistical analysis were done in Excel and GraphPad Prism (GraphPad Software). Significance was defined as: ns-not significant,  $*p < 0.05$ ,  $**p < 0.01$ , and  $***p < 0.001$ . Normality of the data was determined by a D'Agostino and Pearson's test and parametric two-tailed unpaired t test or non-parametric Mann Whitney test was applied. For more than one group, one or two-ways ANOVA were used followed by a Tukey's multiple comparison test.

### **Data and Code Availability**

The mass spectrometry proteomics data have been deposited to the ProteomeXchange Consortium via the PRIDE partner repository with the dataset identifier PXD013685.

### **Acknowledgments**

We thank B. Dargent for sharing the Kv-Nav construct, P. Schätzle and K. Jiang for sharing the  $\beta$ -tubulin-GFP construct, and M.O. Steinmetz for sharing purified EB3 proteins. This work was supported by the Netherlands Organization for Scientific Research (NWO-ALW-VICI, C.C.H.), the Netherlands Organization for Health Research and Development (ZonMW-TOP, C.C.H.), and the European Research Council (ERC) (ERC-consolidator to C.C.H. and ERC Synergy grant 609822 to A. Akhmanova).



**Author Contributions**

A.F. designed the project and performed experiments, analyzed data, and wrote the manuscript; D.R. and A. Aher performed *in vitro* experiments and analyzed the data; R.P.T. performed the single-molecule localization imaging experiments; X.P. and D.v.d.W. cloned constructs, performed experiments, and analyzed data; E.A.K. performed expansion microscopy experiments; R.S. performed the MS experiments; C.Y. generated the U2OS EB KO cell line; A.F.M.A. supervised the mass spectrometry experiments; K.V. performed the EM experiments; J.A.P. and M.H. supervised the EM experiments; L.C.K. supervised the single-molecule localization imaging experiments; A. Akhmanova supervised the *in vitro* experiments, gave advice, and edited the manuscript; and C.C.H. supervised the research, coordinated the study, and wrote the manuscript.

**Declaration of Interests**

C.C.H. is an employee of Genentech, Inc., a member of the Roche group. The authors declare that they have no additional conflict of interest.

**Supplemental Information**

Supplemental Information can be found online at <https://doi.org/10.1016/j.neuron.2019.07.029>.

---

**References**

Alpizar S.A., Baker A.L., Gullledge A.T., Hoppa M.B. Loss of Neurofascin-186 Disrupts Alignment of AnkyrinG Relative to Its Binding Partners in the Axon Initial Segment. *Front. Cell. Neurosci.* 2019;**13**:1. [PMCID: PMC6349729] [PubMed: 30723396]

Atherton J., Jiang K., Stangier M.M., Luo Y., Hua S., Houben K., van Hooff J.J.E., Joseph A.P., Scarabelli G., Grant B.J. A structural model for microtubule minus-end recognition and protection by CAMSAP proteins. *Nat. Struct. Mol. Biol.* 2017;**24**:931–943. [PMCID: PMC6134180] [PubMed: 28991265]

Berger S.L., Leo-Macias A., Yuen S., Khatri L., Pfennig S., Zhang Y., Agullo-Pascual E., Caillol G., Zhu M.S., Rothenberg E. Localized Myosin II Activity Regulates Assembly and Plasticity of the Axon Initial Segment. *Neuron.* 2018;**97**:555–570. [PMCID: PMC5805619] [PubMed: 29395909]

Bieling P., Laan L., Schek H., Munteanu E.L., Sandblad L., Dogterom M., Brunner D., Surrey T. Reconstitution of a microtubule plus-end tracking system in vitro. *Nature.* 2007;**450**:1100–1105. [PubMed: 18059460]

Bieling P., Telley I.A., Surrey T. A minimal midzone protein module controls formation and length of antiparallel microtubule overlaps. *Cell.* 2010;**142**:420–432. [PubMed: 20691901]

Boiko T., Vakulenko M., Ewers H., Yap C.C., Norden C., Winckler B. Ankyrin-dependent and -independent mechanisms orchestrate axonal compartmentalization of L1 family members neurofascin and L1/neuron-glia cell adhesion molecule. *J. Neurosci.* 2007;**27**:590–603. [PMCID: PMC6672792] [PubMed: 17234591]

Bréchet A., Fache M.P., Brachet A., Ferracci G., Baude A., Irondelle M., Pereira S., Leterrier C., Dargent B. Protein kinase CK2 contributes to the organization of sodium channels in axonal membranes by regulating their interactions with ankyrin G. *J. Cell Biol.* 2008;**183**:1101–1114. [PMCID: PMC2600743] [PubMed: 19064667]

Brummelkamp T.R., Bernards R., Agami R. A system for stable expression of short interfering RNAs in mammalian cells. *Science.* 2002;**296**:550–553. [PubMed: 11910072]

Cadwell C.M., Jenkins P.M., Bennett V., Kowalczyk A.P. Ankyrin-G Inhibits Endocytosis of Cadherin Dimers. *J. Biol. Chem.* 2016;**291**:691–704. [PMCID: PMC4705390] [PubMed: 26574545]

Chen F., Tillberg P.W., Boyden E.S. Optical imaging. Expansion microscopy. *Science.* 2015;**347**:543–548. [PMCID: PMC4312537] [PubMed: 25592419]

Cloin B.M.C., De Zitter E., Salas D., Gielen V., Folkers G.E., Mikhaylova M., Bergeler M., Krajnik B., Harvey J., Hoogenraad C.C. Efficient switching of mCherry fluorescence using chemical caging. *Proc. Natl. Acad. Sci. USA.* 2017;**114**:7013–7018. [PMCID: PMC5502588] [PubMed: 28630286]

Dzhashiashvili Y., Zhang Y., Galinska J., Lam I., Grumet M., Salzer J.L. Nodes of Ranvier and axon initial segments are ankyrin G-dependent domains that assemble by distinct mechanisms. *J. Cell Biol.* 2007;**177**:857–870. [PMCID: PMC2064285] [PubMed: 17548513]

- Evans M.D., Sammons R.P., Lebron S., Dumitrescu A.S., Watkins T.B., Uebele V.N., Renger J.J., Grubb M.S. Calcineurin signaling mediates activity-dependent relocation of the axon initial segment. *J. Neurosci.* 2013;**33**:6950–6963. [PMCID: PMC3743026] [PubMed: 23595753]
- Fache M.P., Moussif A., Fernandes F., Giraud P., Garrido J.J., Dargent B. Endocytotic elimination and domain-selective tethering constitute a potential mechanism of protein segregation at the axonal initial segment. *J. Cell Biol.* 2004;**166**:571–578. [PMCID: PMC2172218] [PubMed: 15302857]
- Fréal A., Fassier C., Le Bras B., Bullier E., De Gois S., Hazan J., Hoogenraad C.C., Couraud F. Cooperative Interactions between 480 kDa Ankyrin-G and EB Proteins Assemble the Axon Initial Segment. *J. Neurosci.* 2016;**36**:4421–4433. [PMCID: PMC6601828] [PubMed: 27098687]
- Garrido J.J., Giraud P., Carlier E., Fernandes F., Moussif A., Fache M.P., Debanne D., Dargent B. A targeting motif involved in sodium channel clustering at the axonal initial segment. *Science.* 2003;**300**:2091–2094. [PubMed: 12829783]
- Grubb M.S., Burrone J. Activity-dependent relocation of the axon initial segment fine-tunes neuronal excitability. *Nature.* 2010;**465**:1070–1074. [PMCID: PMC3196626] [PubMed: 20543823]
- Grubb M.S., Shu Y., Kuba H., Rasband M.N., Wimmer V.C., Bender K.J. Short- and long-term plasticity at the axon initial segment. *J. Neurosci.* 2011;**31**:16049–16055. [PMCID: PMC3232445] [PubMed: 22072655]
- Gumy L.F., Katrukha E.A., Grigoriev I., Jaarsma D., Kapitein L.C., Akhmanova A., Hoogenraad C.C. MAP2 Defines a Pre-axonal Filtering Zone to Regulate KIF1- versus KIF5-Dependent Cargo Transport in Sensory Neurons. *Neuron.* 2017;**94**:347–362. [PubMed: 28426968]
- Guo X., Farías G.G., Mattera R., Bonifacino J.S. Rab5 and its effector FHF contribute to neuronal polarity through dynein-dependent retrieval of somatodendritic proteins from the axon. *Proc. Natl. Acad. Sci. USA.* 2016;**113**:E5318–E5327. [PMCID: PMC5018783] [PubMed: 27559088]
- Harterink M., Vocking K., Pan X., Soriano Jerez E.M., Slenders L., Fréal A., Tas R.P., van de Wetering W.J., Timmer K., Motshagen J. TRIM46 organizes microtubule fasciculation in the axon initial segment. *J. Neurosci.* 2019;**39**:4864–4873. [PMCID: PMC6670255] [PubMed: 30967428]
- He M., Jenkins P., Bennett V. Cysteine 70 of ankyrin-G is S-palmitoylated and is required for function of ankyrin-G in membrane domain assembly. *J. Biol. Chem.* 2012;**287**:43995–44005. [PMCID: PMC3527982] [PubMed: 23129772]
- Hedstrom K.L., Xu X., Ogawa Y., Frischknecht R., Seidenbecher C.I., Shrager P., Rasband M.N. Neurofascin assembles a specialized extracellular matrix at the axon initial segment. *J. Cell Biol.* 2007;**178**:875–886. [PMCID: PMC2064550] [PubMed: 17709431]

Hedstrom K.L., Ogawa Y., Rasband M.N. AnkyrinG is required for maintenance of the axon initial segment and neuronal polarity. *J. Cell Biol.* 2008;**183**:635–640. [PMCID: PMC2582894] [PubMed: 19001126]

Honnappa S., Gouveia S.M., Weisbrich A., Damberger F.F., Bhavesh N.S., Jawhari H., Grigoriev I., van Rijssel F.J., Buey R.M., Lawera A. An EB1-binding motif acts as a microtubule tip localization signal. *Cell.* 2009;**138**:366–376. [PubMed: 19632184]

Hoogenraad C.C., Popa I., Futai K., Martinez-Sanchez E., Wulf P.S., van Vlijmen T., Dortland B.R., Oorschot V., Govers R., Monti M. Neuron specific Rab4 effector GRASP-1 coordinates membrane specialization and maturation of recycling endosomes. *PLoS Biol.* 2010;**8**:e1000283. [PMCID: PMC2808209] [PubMed: 20098723]

Jenkins P.M., Vasavda C., Hostettler J., Davis J.Q., Abdi K., Bennett V. E-cadherin polarity is determined by a multifunction motif mediating lateral membrane retention through ankyrin-G and apical-lateral transcytosis through clathrin. *J. Biol. Chem.* 2013;**288**:14018–14031. [PMCID: PMC3656260] [PubMed: 23530049]

Jenkins P.M., He M., Bennett V. Dynamic spectrin/ankyrin-G microdomains promote lateral membrane assembly by opposing endocytosis. *Sci. Adv.* 2015;**1**:e1500301. [PMCID: PMC4624203] [PubMed: 26523289]

Jenkins P.M., Kim N., Jones S.L., Tseng W.C., Svitkina T.M., Yin H.H., Bennett V. Giant ankyrin-G: a critical innovation in vertebrate evolution of fast and integrated neuronal signaling. *Proc. Natl. Acad. Sci. USA.* 2015;**112**:957–964. [PMCID: PMC4313853] [PubMed: 25552556]

Jiménez N., Van Donselaar E.G., De Winter D.A., Vocking K., Verkleij A.J., Post J.A. Gridded Aclar: preparation methods and use for correlative light and electron microscopy of cell monolayers, by TEM and FIB-SEM. *J. Microsc.* 2010;**237**:208–220. [PubMed: 20096051]

Kapitein L.C., Schlager M.A., Kuijpers M., Wulf P.S., van Spronsen M., MacKintosh F.C., Hoogenraad C.C. Mixed microtubules steer dynein-driven cargo transport into dendrites. *Curr. Biol.* 2010;**20**:290–299. [PubMed: 20137950]

Kiuchi T., Higuchi M., Takamura A., Maruoka M., Watanabe N. Multitarget super-resolution microscopy with high-density labeling by exchangeable probes. *Nat. Methods.* 2015;**12**:743–746. [PubMed: 26147917]

Kole M.H., Stuart G.J. Is action potential threshold lowest in the axon? *Nat. Neurosci.* 2008;**11**:1253–1255. [PubMed: 18836442]

Kole M.H., Ilschner S.U., Kampa B.M., Williams S.R., Ruben P.C., Stuart G.J. Action potential generation requires a high sodium channel density in the axon initial segment. *Nat. Neurosci.* 2008;**11**:178–186. [PubMed: 18204443]

Kolotuev I., Schwab Y., Labouesse M. A precise and rapid mapping protocol for correlative light and electron microscopy of small invertebrate organisms. *Biol. Cell.* 2009;**102**:121–132. [PubMed: 19807690]

- Koseki H., Donegá M., Lam B.Y., Petrova V., van Erp S., Yeo G.S., Kwok J.C., Ffrench-Constant C., Eva R., Fawcett J.W. Selective rab11 transport and the intrinsic regenerative ability of CNS axons. *eLife*. 2017;**6**:6. [PMCID: PMC5779230] [PubMed: 28829741]
- Kuba H., Oichi Y., Ohmori H. Presynaptic activity regulates Na(+) channel distribution at the axon initial segment. *Nature*. 2010;**465**:1075–1078. [PubMed: 20543825]
- Kuijpers M., van de Willige D., Freal A., Chazeau A., Franker M.A., Hofenk J., Rodrigues R.J., Kapitein L.C., Akhmanova A., Jaarsma D., Hoogenraad C.C. Dynein Regulator NDEL1 Controls Polarized Cargo Transport at the Axon Initial Segment. *Neuron*. 2016;**89**:461–471. [PubMed: 26844830]
- Le Bras B., Fréal A., Czarnecki A., Legendre P., Bullier E., Komada M., Brophy P.J., Davenne M., Couraud F. In vivo assembly of the axon initial segment in motor neurons. *Brain Struct. Funct.* 2014;**219**:1433–1450. [PMCID: PMC4072062] [PubMed: 23728480]
- Lemaillet G., Walker B., Lambert S. Identification of a conserved ankyrin-binding motif in the family of sodium channel alpha subunits. *J. Biol. Chem.* 2003;**278**:27333–27339. [PubMed: 12716895]
- Leterrier C. The Axon Initial Segment: An Updated Viewpoint. *J. Neurosci.* 2018;**38**:2135–2145. [PMCID: PMC6596274] [PubMed: 29378864]
- Leterrier C., Vacher H., Fache M.P., d’Ortoli S.A., Castets F., Autillo-Touati A., Dargent B. End-binding proteins EB3 and EB1 link microtubules to ankyrin G in the axon initial segment. *Proc. Natl. Acad. Sci. USA*. 2011;**108**:8826–8831. [PMCID: PMC3102358] [PubMed: 21551097]
- Leterrier C., Potier J., Caillol G., Debarnot C., Rueda Boroni F., Dargent B. Nanoscale Architecture of the Axon Initial Segment Reveals an Organized and Robust Scaffold. *Cell Rep.* 2015;**13**:2781–2793. [PubMed: 26711344]
- Leterrier C., Clerc N., Rueda-Boroni F., Montersino A., Dargent B., Castets F. Ankyrin G Membrane Partners Drive the Establishment and Maintenance of the Axon Initial Segment. *Front. Cell. Neurosci.* 2017;**11**:6. [PMCID: PMC5266712] [PubMed: 28184187]
- Loiodice I., Staub J., Setty T.G., Nguyen N.P., Paoletti A., Tran P.T. Ase1p organizes antiparallel microtubule arrays during interphase and mitosis in fission yeast. *Mol. Biol. Cell.* 2005;**16**:1756–1768. [PMCID: PMC1073658] [PubMed: 15689489]
- Meroni G., Diez-Roux G. TRIM/RBCC, a novel class of ‘single protein RING finger’ E3 ubiquitin ligases. *BioEssays*. 2005;**27**:1147–1157. [PubMed: 16237670]
- Mohan R., Katrukha E.A., Doodhi H., Smal I., Meijering E., Kapitein L.C., Steinmetz M.O., Akhmanova A. End-binding proteins sensitize microtubules to the action of microtubule-targeting agents. *Proc. Natl. Acad. Sci. USA*. 2013;**110**:8900–8905. [PMCID: PMC3670352] [PubMed: 23674690]
- Mollinari C., Kleman J.P., Jiang W., Schoehn G., Hunter T., Margolis R.L. PRC1 is a microtubule binding and bundling protein essential to maintain the mitotic spindle midzone. *J. Cell Biol.* 2002;**157**:1175–1186. [PMCID: PMC2173564] [PubMed: 12082078]

- Montenegro Gouveia S., Leslie K., Kapitein L.C., Buey R.M., Grigoriev I., Wagenbach M., Smal I., Meijering E., Hoogenraad C.C., Wordeman L. In vitro reconstitution of the functional interplay between MCAK and EB3 at microtubule plus ends. *Curr. Biol.* 2010;**20**:1717–1722. [PubMed: 20850319]
- Nakata T., Hirokawa N. Microtubules provide directional cues for polarized axonal transport through interaction with kinesin motor head. *J. Cell Biol.* 2003;**162**:1045–1055. [PMCID: PMC2172855] [PubMed: 12975348]
- Nakata T., Niwa S., Okada Y., Perez F., Hirokawa N. Preferential binding of a kinesin-1 motor to GTP-tubulin-rich microtubules underlies polarized vesicle transport. *J. Cell Biol.* 2011;**194**:245–255. [PMCID: PMC3144414] [PubMed: 21768290]
- Palay S.L., Sotelo C., Peters A., Orkand P.M. The axon hillock and the initial segment. *J. Cell Biol.* 1968;**38**:193–201. [PMCID: PMC2107452] [PubMed: 5691973]
- Pan Z., Kao T., Horvath Z., Lemos J., Sul J.Y., Cranstoun S.D., Bennett V., Scherer S.S., Cooper E.C. A common ankyrin-G-based mechanism retains KCNQ and NaV channels at electrically active domains of the axon. *J. Neurosci.* 2006;**26**:2599–2613. [PMCID: PMC6675151] [PubMed: 16525039]
- Peters A., Proskauer C.C., Kaiserman-Abramof I.R. The small pyramidal neuron of the rat cerebral cortex. The axon hillock and initial segment. *J. Cell Biol.* 1968;**39**:604–619. [PMCID: PMC2107556] [PubMed: 5699934]
- Ran F.A., Hsu P.D., Wright J., Agarwala V., Scott D.A., Zhang F. Genome engineering using the CRISPR-Cas9 system. *Nat. Protoc.* 2013;**8**:2281–2308. [PMCID: PMC3969860] [PubMed: 24157548]
- Rasband M.N. The axon initial segment and the maintenance of neuronal polarity. *Nat. Rev. Neurosci.* 2010;**11**:552–562. [PubMed: 20631711]
- Rasmussen H.B., Frøkjær-Jensen C., Jensen C.S., Jensen H.S., Jørgensen N.K., Misonou H., Trimmer J.S., Olesen S.P., Schmitt N. Requirement of subunit co-assembly and ankyrin-G for M-channel localization at the axon initial segment. *J. Cell Sci.* 2007;**120**:953–963. [PubMed: 17311847]
- Sánchez-Ponce D., Blázquez-Llorca L., DeFelipe J., Garrido J.J., Muñoz A. Colocalization of  $\alpha$ -actinin and synaptopodin in the pyramidal cell axon initial segment. *Cereb. Cortex.* 2012;**22**:1648–1661. [PubMed: 21940706]
- Satake T., Yamashita K., Hayashi K., Miyatake S., Tamura-Nakano M., Doi H., Furuta Y., Shioi G., Miura E., Takeo Y.H. MTCL1 plays an essential role in maintaining Purkinje neuron axon initial segment. *EMBO J.* 2017;**36**:1227–1242. [PMCID: PMC5412768] [PubMed: 28283581]
- Schatzle P., Esteves da Silva M., Tas R.P., Katrukha E.A., Hu H.Y., Wierenga C.J., Kapitein L.C., Hoogenraad C.C. Activity-Dependent Actin Remodeling at the Base of Dendritic Spines Promotes Microtubule Entry. *Curr. Biol.* 2018;**28**:2081–2093. [PubMed: 29910073]
- Schlager M.A., Kapitein L.C., Grigoriev I., Burzynski G.M., Wulf P.S., Keijzer N., de Graaff E., Fukuda M., Shepherd I.T., Akhmanova A., Hoogenraad C.C. Pericentrosomal targeting of

- Rab6 secretory vesicles by Bicaudal-D-related protein 1 (BICDR-1) regulates neuritogenesis. *EMBO J.* 2010;**29**:1637–1651. [PMCID: PMC2876961] [PubMed: 20360680]
- Sharma A., Aher A., Dynes N.J., Frey D., Katrukha E.A., Jaussi R., Grigoriev I., Croisier M., Kammerer R.A., Akhmanova A. Centriolar CPAP/SAS-4 Imparts Slow Processive Microtubule Growth. *Dev. Cell.* 2016;**37**:362–376. [PMCID: PMC4884677] [PubMed: 27219064]
- Smal I., Grigoriev I., Akhmanova A., Niessen W.J., Meijering E. Accurate estimation of microtubule dynamics using kymographs and variable-rate particle filters. *Conf. Proc. IEEE Eng. Med. Biol. Soc.* 2009;**2009**:1012–1015. [PubMed: 19963986]
- Sobotzik J.M., Sie J.M., Politi C., Del Turco D., Bennett V., Deller T., Schultz C. AnkyrinG is required to maintain axo-dendritic polarity in vivo. *Proc. Natl. Acad. Sci. USA.* 2009;**106**:17564–17569. [PMCID: PMC2765162] [PubMed: 19805144]
- Solé L., Wagnon J.L., Akin E.J., Meisler M.H., Tamkun M.M. The MAP1B binding domain of Nav1.6 is required for stable expression at the axon initial segment. *J. Neurosci.* 2019;**39**:4238–4251. [PMCID: PMC6538857] [PubMed: 30914445]
- Stepanova T., Slemmer J., Hoogenraad C.C., Lansbergen G., Dortland B., De Zeeuw C.I., Grosveld F., van Cappellen G., Akhmanova A., Galjart N. Visualization of microtubule growth in cultured neurons via the use of EB3-GFP (end-binding protein 3-green fluorescent protein) *J. Neurosci.* 2003;**23**:2655–2664. [PMCID: PMC6742099] [PubMed: 12684451]
- Subramanian R., Ti S.C., Tan L., Darst S.A., Kapoor T.M. Marking and measuring single microtubules by PRC1 and kinesin-4. *Cell.* 2013;**154**:377–390. [PMCID: PMC3761943] [PubMed: 23870126]
- Tas R.P., Bos T.G.A.A., Kapitein L.C. Purification and Application of a Small Actin Probe for Single-Molecule Localization Microscopy. *Methods Mol. Biol.* 2018;**1665**:155–171. [PubMed: 28940069]
- Tillberg P.W., Chen F., Piatkevich K.D., Zhao Y., Yu C.C., English B.P., Gao L., Martorell A., Suk H.J., Yoshida F. Protein-retention expansion microscopy of cells and tissues labeled using standard fluorescent proteins and antibodies. *Nat. Biotechnol.* 2016;**34**:987–992. [PMCID: PMC5068827] [PubMed: 27376584]
- Tortosa E., Adolfs Y., Fukata M., Pasterkamp R.J., Kapitein L.C., Hoogenraad C.C. Dynamic Palmitoylation Targets MAP6 to the Axon to Promote Microtubule Stabilization during Neuronal Polarization. *Neuron.* 2017;**94**:809–825. [PubMed: 28521134]
- Tseng W.C., Jenkins P.M., Tanaka M., Mooney R., Bennett V. Giant ankyrin-G stabilizes somatodendritic GABAergic synapses through opposing endocytosis of GABAA receptors. *Proc. Natl. Acad. Sci. USA.* 2015;**112**:1214–1219. [PMCID: PMC4313813] [PubMed: 25552561]
- Tuvia S., Garver T.D., Bennett V. The phosphorylation state of the FIGQY tyrosine of neurofascin determines ankyrin-binding activity and patterns of cell segregation. *Proc. Natl. Acad. Sci. USA.* 1997;**94**:12957–12962. [PMCID: PMC24245] [PubMed: 9371782]

van Beuningen S.F., Hoogenraad C.C. Neuronal polarity: remodeling microtubule organization. *Curr. Opin. Neurobiol.* 2016;**39**:1–7. [PubMed: 26945466]

van Beuningen S.F.B., Will L., Harterink M., Chazeau A., van Battum E.Y., Frias C.P., Franker M.A.M., Katrukha E.A., Stucchi R., Vocking K. TRIM46 Controls Neuronal Polarity and Axon Specification by Driving the Formation of Parallel Microtubule Arrays. *Neuron.* 2015;**88**:1208–1226. [PubMed: 26671463]

Xu X., Shrager P. Dependence of axon initial segment formation on Na<sup>+</sup> channel expression. *J. Neurosci. Res.* 2005;**79**:428–441. [PubMed: 15635682]

Yang C., Wu J., de Heus C., Grigoriev I., Liv N., Yao Y., Smal I., Meijering E., Klumperman J., Qi R.Z., Akhmanova A. EB1 and EB3 regulate microtubule minus end organization and Golgi morphology. *J. Cell Biol.* 2017;**216**:3179–3198. [PMCID: PMC5626540] [PubMed: 28814570]

Yap C.C., Vakulenko M., Kruczek K., Motamedi B., Digilio L., Liu J.S., Winckler B. Doublecortin (DCX) mediates endocytosis of neurofascin independently of microtubule binding. *J. Neurosci.* 2012;**32**:7439–7453. [PMCID: PMC3372911] [PubMed: 22649224]

Yau K.W., van Beuningen S.F., Cunha-Ferreira I., Cloin B.M., van Battum E.Y., Will L., Schätzle P., Tas R.P., van Krugten J., Katrukha E.A. Microtubule minus-end binding protein CAMSAP2 controls axon specification and dendrite development. *Neuron.* 2014;**82**:1058–1073. [PubMed: 24908486]

Zhang X., Davis J.Q., Carpenter S., Bennett V. Structural requirements for association of neurofascin with ankyrin. *J. Biol. Chem.* 1998;**273**:30785–30794. [PubMed: 9804856]

Zonta B., Desmazieres A., Rinaldi A., Tait S., Sherman D.L., Nolan M.F., Brophy P.J. A critical role for Neurofascin in regulating action potential initiation through maintenance of the axon initial segment. *Neuron.* 2011;**69**:945–956. [PMCID: PMC3057015] [PubMed: 21382554]



Supplementary Figures

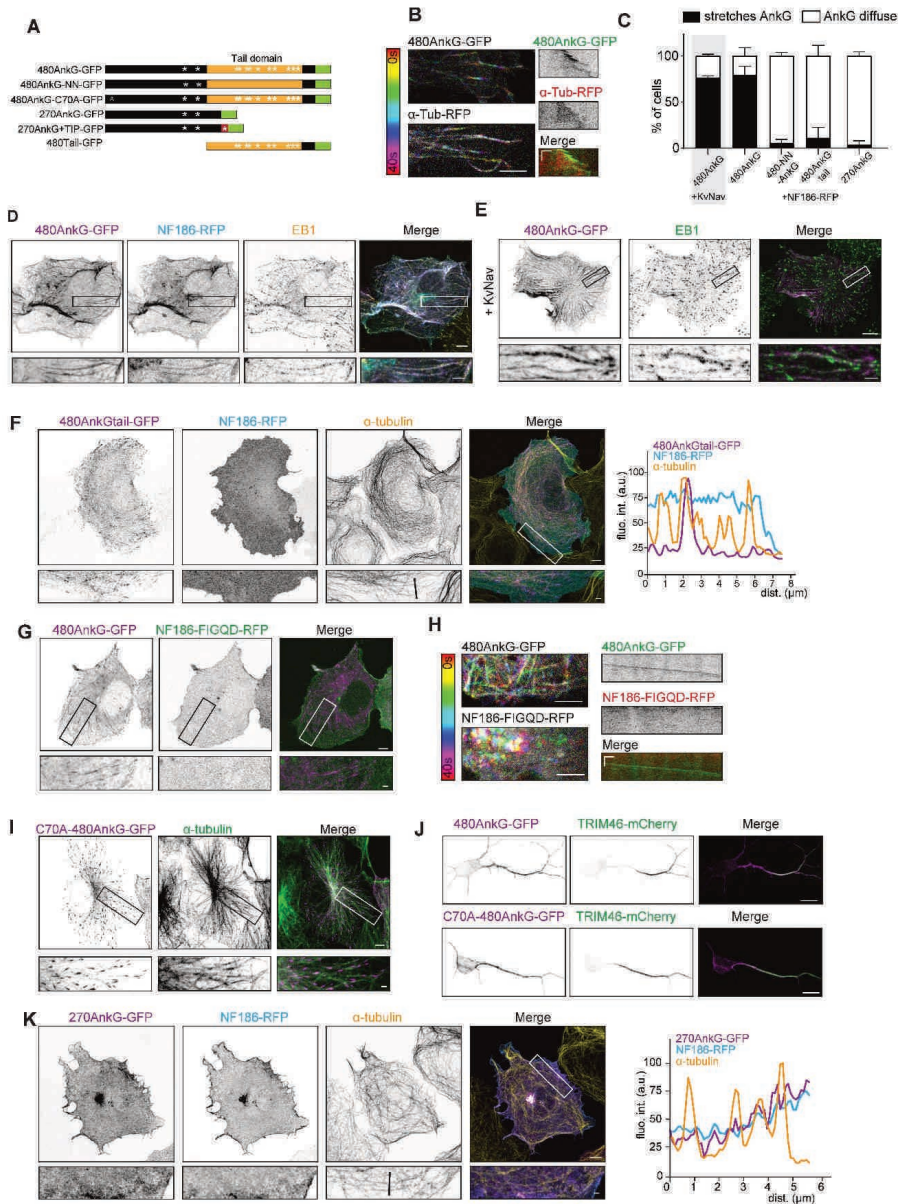


**Figure S1. Related to Figure 1: 480AnkG recruits MTs to the plasma membrane**

A. Scheme of AnkG constructs used in this study. The specific Tail of 480AnkG is shown in orange and GFP in green and asterisks show SxIP motifs.

*B. Temporal-coded maximum projections from time lapse-imaging of a COS-7 cell expressing 480AnkG-GFP with  $\alpha$ -Tub-RFP. Representative kymographs from this cell is shown on the right. Color-coded time scale is shown on the left.*

*C. Percentage of COS-7 cells transfected with indicated constructs showing AnkG as stretches (black) or diffuse (white). At least 150 cells were counted from 2 experiments for each condition.*

*D-E. COS-7 cells co-transfected with 480AnkG-GFP and either NF186-RFP (D) or Kv-Nav (E) and stained for GFP and EB1. Lower panels show zooms of the boxed areas.*

*F. COS-7 cell co-expressing NF186-RFP together with 480AnkGtail-GFP and stained for  $\alpha$ -tubulin. Lower panel shows a zoom of the boxed area. Fluorescence intensity profiles along the black bar in the zoom are shown on the right.*

*G-H. COS-7 cells transfected with 480AnkG-GFP and NF186-FIGQD-RFP and stained for GFP (G). Lower panel shows zooms of the boxed areas. (H) shows the temporal-coded maximum projections from time lapse-imaging of a COS-7 cells transfected with 480AnkG-GFP and NF186-FIGQD-RFP. Representative kymographs from this cell is shown on the right.*

*I-J. COS-7 cell (I) transfected with C70A-480AnkG-GFP and stained for GFP and  $\alpha$ -tubulin. (J) shows DIV3 hippocampal neurons transfected at DIV0 with TRIM46-mCherry and 480AnkG-GFP (upper panel) or C70A-480AnkG-GFP (lower panel) and stained for GFP.*

*K. COS-7 cell co-expressing NF186-RFP together with 270AnkG-GFP and stained for  $\alpha$ -tubulin. Lower panel shows a zoom of the boxed area. Fluorescence intensity profiles along the black bar in the zoom are shown on the right.*

*Scale bars represent 10  $\mu$ m and 2  $\mu$ m in the zooms and in the kymographs: 1  $\mu$ m (horizontal) and 15 s (vertical).*

**Figure S2. Related to Figure 3: Membrane recruitment of MTs by 480AnkG is EB-dependent**

*A. U2OS control (left panel) and EB1/2/3 KO (right panel) cells transfected with 480AnkG-GFP and stained for GFP and EB1. Zooms of the boxed areas are shown on the right of each panel.*

*B. U2OS control cell co-expressing 480AnkG-GFP and NF186-RFP, stained for  $\alpha$ -tubulin. Fluorescence intensity along the white bar is shown on the right.*

*C-E. EB KO U2OS cells transfected with 480AnkG-GFP, with or without EB3-RFP (C) or co-expressing 480AnkG-GFP and KvNav with or without EB3-RFP (D) and stained for  $\alpha$ -tubulin. Percentage of cells showing 480AnkG as stretches or as diffuse in indicated transfection conditions is shown in E.*

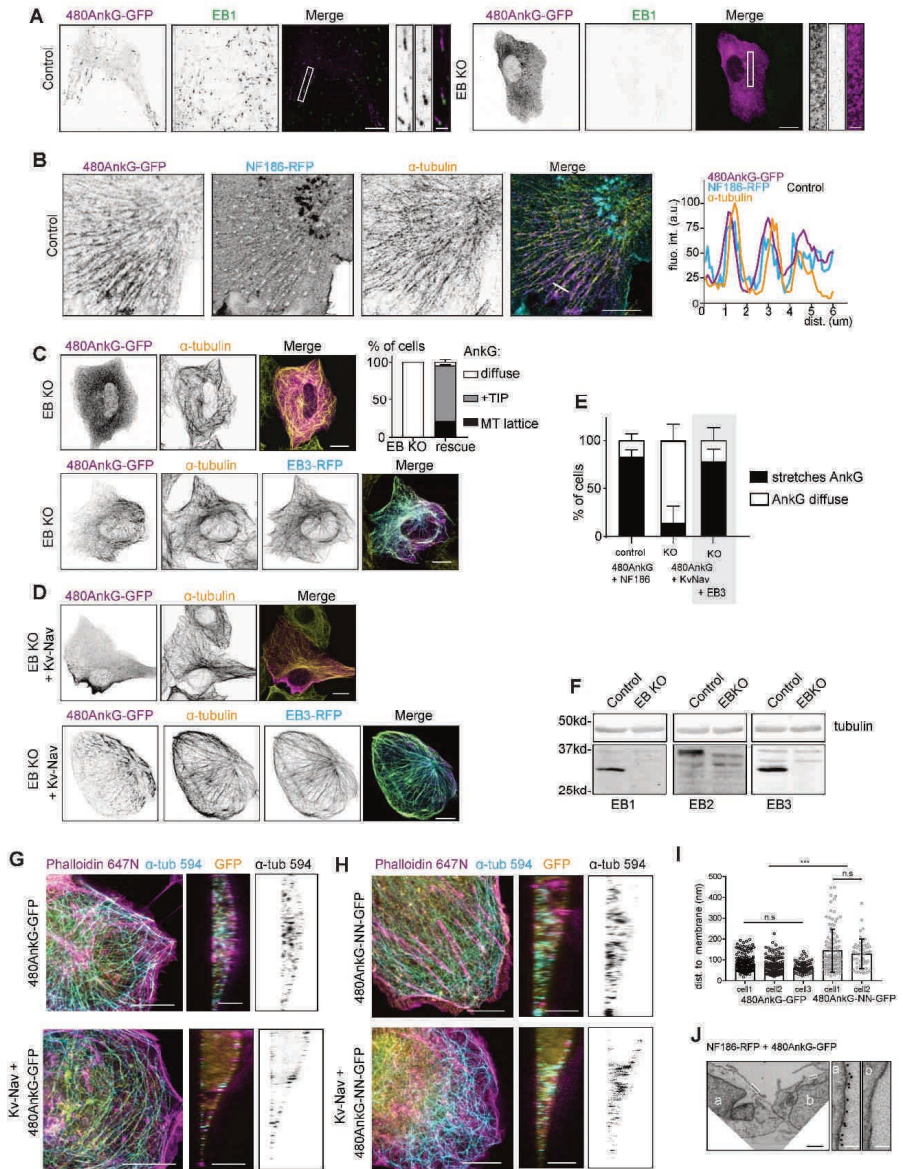
*F. Western-blot of U2OS EB KO and control cells lysates probed for EB1, EB2 and EB3. Tubulin was used as a loading control.*

*G-H. STED imaging of COS-7 co-expressing KvNav (lower panels) or not (upper panels) with 480AnkG-GFP (G) or 480AnkG-NN-GFP (H) stained for GFP,  $\alpha$ -tubulin (Alexa595) and Phalloidin (Atto 647N). Z-sections are shown on the right.*

*I. Distance between MTs and membrane in COS-7 cells co-expressing NF186-RFP together with 480AnkG-GFP (3 cells) or 480AnkG-NN-GFP (2 cells). One-way ANOVA, n.s,  $p > 0.4$ .*

*J. EM picture of COS-7 cells either co-expressing NF186-RFP and 480AnkG-GFP (left cell, a) or not transfected (right cell, b), which were immunogold labeled using an extracellular anti-NF186 antibody. No labeling could be observed on the non-transfected cell. Zooms of the indicated boxed areas are shown on the right.*

*In A-D, scale bars represent 10  $\mu$ m, 2  $\mu$ m in the zooms, in G-H, they represent 10  $\mu$ m and 5  $\mu$ m in the Z-sections. In J, scale bars represent 1  $\mu$ m and 100 nm in the zooms.*





TRIM46-depleted neurons (at least 17 neurons from 2 experiments were analysed, unpaired ttest,  $***p < 0.0001$ ). (D) Percentage of neurons showing TRIM46 immunoreactivity in the proximal axon in control conditions and upon AnkG depletion. (4 coverslips were counted for each phenotype, from 4 different cultures, unpaired t-test,  $***p < 0.0001$ ).

E-F. C. COS-7 cells transfected with 480AnkG-GFP either with PRC1-mCherry (E) or with TRIM36-mCherry (F). Lower panels are zooms of the boxed areas and corresponding fluorescence intensity profiles are shown on the right.

G-I. STED imaging of COS-7 cells transfected with 480AnkG-GFP, TRIM46-mCherry (G) and KvNav (I) and stained for GFP (Alexa488), TRIM46 (Alexa595) and Phalloidin (Atto 647N) or transfected with TRIM46-mCherry alone and stained for TRIM46 (Alexa 594) and Phalloidin (Atto 647N). Corresponding z-sections are shown on the right.

J-K. STED imaging of COS-7 cells expressing TRIM46-mCherry and stained for TRIM46 (Alexa594) and  $\alpha$ -tubulin (Alexa647, J) or acetylated tubulin (Alexa647, K).

L. Percentage of cells expressing indicated constructs, showing GFP as diffuse (white bars), +TIP (grey bars) or on the MT lattice (black bars). At least 150 cells per condition from at least 2 experiments were counted.

M. COS-7 cells co-expressing TRIM46-mCherry together with 270AnkG-GFP (first panel), 480AnkG-NN-GFP (second panel) or 480AnkGtail-GFP (third panel). Lower panels are zooms of the boxed areas and corresponding fluorescence intensity profiles are shown on the right.

N. COS-7 cells expressing 270AnkG+TIP-GFP alone and stained for endogenous EB1 (first panel) or together with TRIM46-mCherry. Lower panels are zooms of the boxed areas and corresponding fluorescence intensity profiles are shown on the right.

Scale bars are 5  $\mu$ m in B, 10  $\mu$ m in E, F, M and N, and 2  $\mu$ m in the corresponding zooms. They represent 10  $\mu$ m in G-I and 5  $\mu$ m in the Z-sections, 10  $\mu$ m in J and 30  $\mu$ m in K.

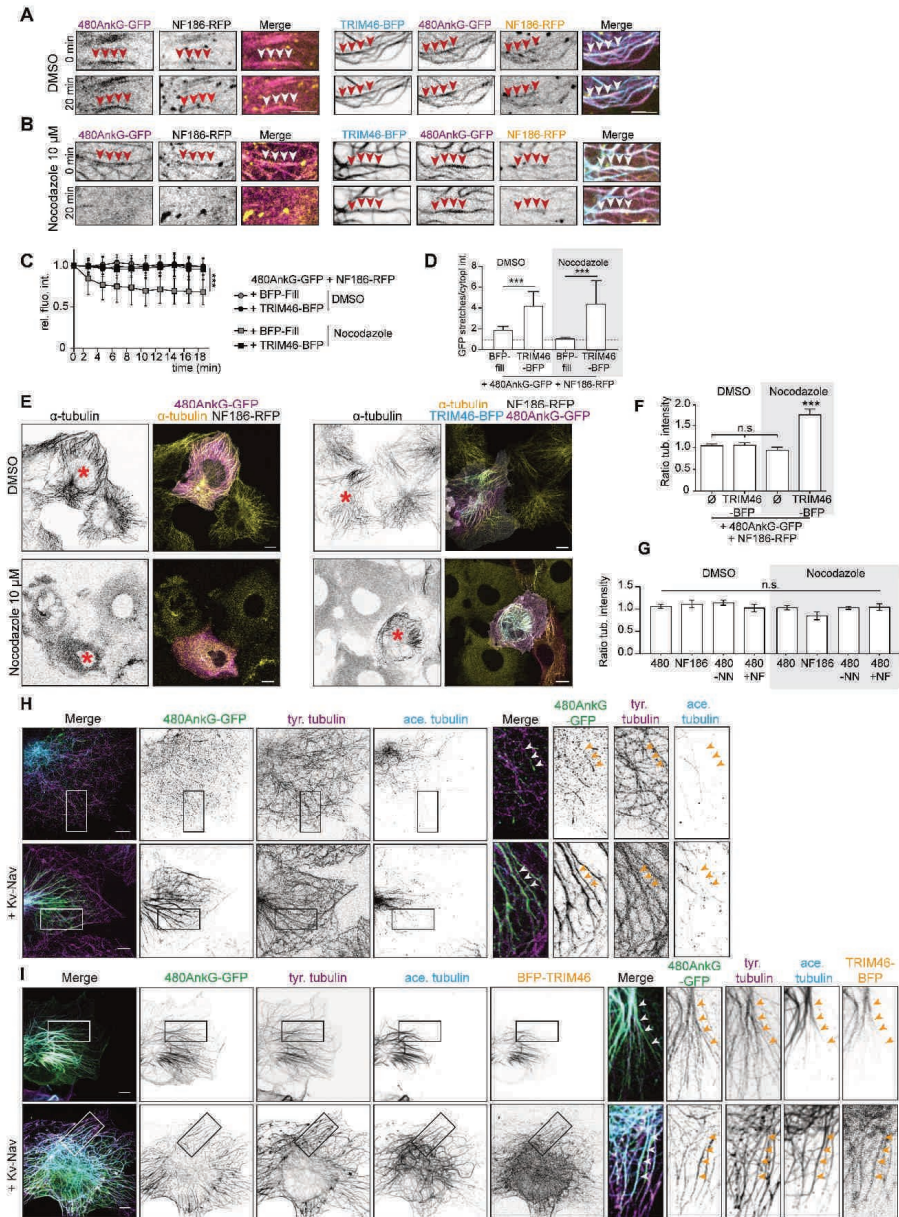
#### **Figure S4. Related to Figure 4: TRIM46 stabilizes and protects MTs from depolymerization**

A-D. Stills from time-lapse recordings of COS-7 cells expressing 480AnkG-GFP and NF186-RFP together with a BFP-fill (left) or with TRIM46-BFP (right), at 0 and 20 min after addition of DMSO (A) or Nocodazole (B, 10  $\mu$ M). Arrowheads point at stable bundles. Ratio of GFP fluorescence intensity along stretches over cytoplasm was measured over time after addition of DMSO or Nocodazole and normalized to the first frame (C) or measured after 20 min of the indicated treatment (D). Two-way ANOVA (C) and One-way ANOVA (D),  $***p < 0.0001$ , at least 19 ROIs were analyzed from at least 6 different cells.

E-G. COS-7 cells expressing NF186-RFP and 480AnkG-GFP (E, left panels) in combination with TRIM46-BFP (E, right panels) treated for 1 hr in DMSO 0.001% (upper panels) or in 10  $\mu$ M Nocodazole (lower panels) and stained for  $\alpha$ -tubulin. Asterisks indicate transfected cells. F and G show the  $\alpha$ -tubulin fluorescence intensity ratio between transfected and non-transfected neighboring cells after indicated treatment. One-way ANOVA, 18-22 cells were analyzed per condition.

H-I. gSTED imaging of COS-7 cells expressing 480AnkG-GFP (H, upper panel) in combination with KvNav (H, lower panel), or TRIM46-BFP (I, upper panel) or TRIM46-BFP and KvNav (I, lower panel) and stained for GFP (Alexa488), tyrosinated- (Alexa568) and acetylated tubulin (Alexa647) and TRIM46 (in I).

Scale bars represent 5  $\mu$ m in A and B, 10  $\mu$ m in E and 5  $\mu$ m in H and I.



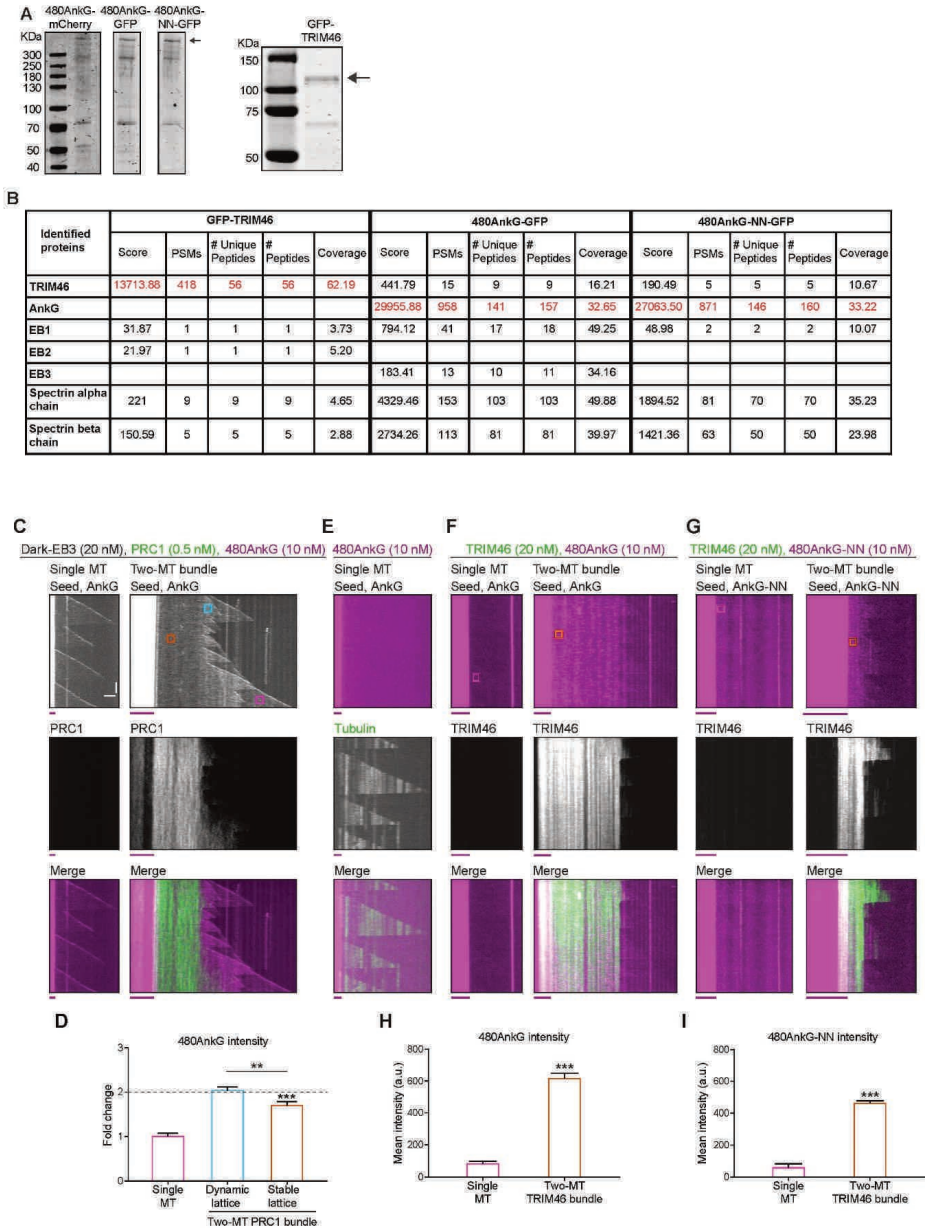


**Figure S5. Related to Figure 5: Specificity of TRIM46-mediated enrichment of 480AnkG along MT bundles using *in vitro* reconstitution assays with purified proteins**

**A.** Coomassie-blue stained gels with purified GFP-TRIM46, 480AnkG-GFP, 480AnkG-NN-GFP and 480AnkG-mCherry. Black arrows indicate isolated proteins.

**B.** Mass spectrometry analysis of purified GFP-TRIM46, 480AnkG-GFP and 480AnkG-NN-GFP. The table shows results for respective proteins and their major interacting partners, which were co-

purified. Mass spectrometry results for other interactors and common contaminants have been included in the Table S1 with a top 10% cut-off.

C. Kymographs illustrating 480AnkG-mCherry intensity and dynamics of single MTs or PRC1 MT bundles grown in vitro in the presence of 20 nM dark-EB3, 0.5 nM GFP-PRC1 and 10 nM 480AnkG-mCherry. Colored boxes depict single MT (magenta), dynamic lattice (cyan) and stable lattice (orange) in two-MT bundle where ROIs were drawn to quantify 480AnkG-mCherry mean intensity.

D. 480AnkG-mCherry mean intensity on single MT or two-MT PRC1-positive bundles normalized to average mean intensity on single MTs. This data was obtained from 65-75 ROIs of  $1 \mu\text{m}^2$  in size from 15 PRC1-decorated two-MT bundles analyzed from 2 independent assays. Error bars represent  $\pm$ SEM. One sample t-test was carried out to test if fold change in AnkG mean intensity on PRC1-positive MT bundles is more than 2,  $***p < 0.001$ . One-way ANOVA with Tukey's post-test was used to test if the change in 480AnkG intensity was different in dynamic compared to stable two-MT bundle,  $**p = 0.0032$ .

E. Kymographs illustrating 480AnkG-mCherry fluorescence intensity on single MTs grown in vitro in the presence of 10 nM 480AnkG-mCherry, 14.5  $\mu\text{M}$  unlabeled porcine tubulin and 0.5  $\mu\text{M}$  HiLyte Fluor™ 488 labeled tubulin.

F-G. Kymographs illustrating 480AnkG-mCherry intensity and dynamics of single MTs or TRIM46 MT bundles grown in vitro in the presence of 20 nM GFP-TRIM46 and 10 nM 480AnkG-mCherry (F) or 10 nM 480AnkG-NN-mCherry (G) and in the absence of EB3. Colored boxes depict single MTs (magenta), and two-MT bundles (orange) where ROIs were drawn to quantify 480AnkG-mCherry or 480AnkG-NN-mCherry mean intensity. Since MTs were not labelled and the interaction of 480AnkG or 480AnkG-NN with MTs in the absence of EBs was weak, MT lattice regions were identified by proximity to MT seeds, where MTs outgrowth initiates.

H-I. 480AnkG-mCherry (H) and 480AnkG-NN-mCherry (I) mean intensity on single MT or two-MT TRIM46-positive bundles obtained from assays represented in (F) and (G) respectively. This data was obtained from 50 ROIs (H) and 15 ROIs (I) of  $1 \mu\text{m}^2$  in size from 5-10 single MTs or TRIM46-decorated two-MT bundles, analyzed from 2 independent assays. Error bars represent  $\pm$  SEM. Pairwise mean comparisons between single MTs and two-MT bundles were carried out using two-tailed unpaired t-test,  $***p < 0.001$ .

Scale bars represent 2  $\mu\text{m}$  (horizontal) and 60 s (vertical). The red and magenta lines below each kymograph represents rhodamine labeled GMPCPP-stabilized MT seeds.

### Figure S6. Related to Figure 6: NF186 travels via the endosomal pathway

A-C. Expression of NF186-RFP together with NPY-GFP, Rab6-GFP, Rab5-GFP or Rab11-GFP or stained for endogenous Rab11 in fixed (A) or live (B-C) DIV2 neurons. In A, orange arrowheads point to overlapping vesicles, whereas grey ones show vesicles only positive for NF186-RFP. Kymographs of NF186-RFP vesicles imaged together with NPY-GFP, Rab6-GFP, Rab5-GFP or Rab11-GFP are shown in B. The percentage of NF186-RFP vesicles colocalizing with the indicated markers in fixed neurons is shown in C. At least 440 NF186-RFP vesicles from at least 7 neurons from 2 experiments were counted.

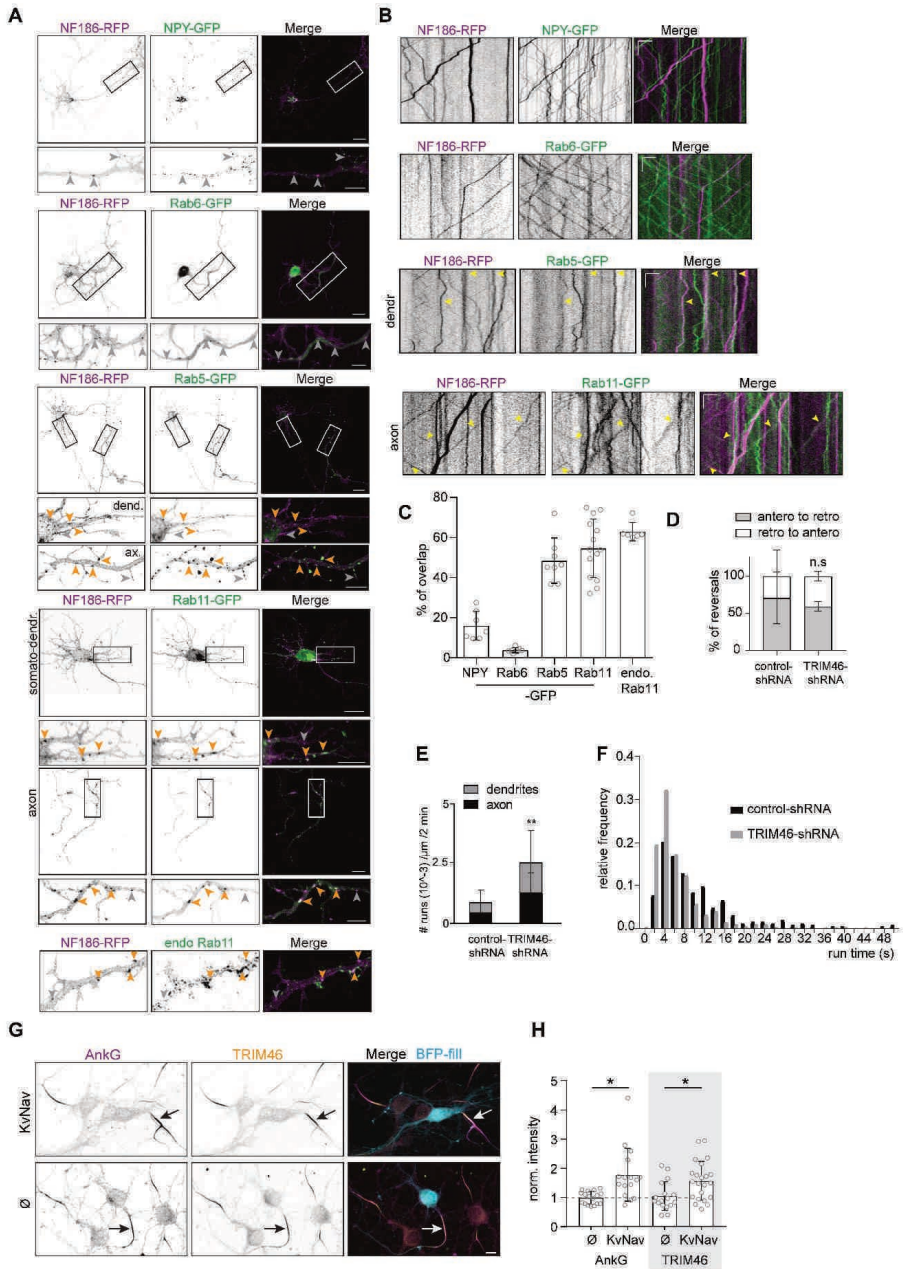
D-E. Percentage of direction reversals from anterograde to retrograde (D, grey) or retrograde to anterograde (D, white) and number of runs (E) of NF186-RFP vesicles in neurons transfected with control- or TRIM46-shRNA. In D; n.s,  $p = 0.43$ , two-way ANOVA, in E;  $p = 0.013$  in the axons,  $p = 0.016$  in the dendrites, two-way ANOVA.

F. Plot of the run times of NF186-RFP vesicles in neurons transfected with control- (black) or TRIM46-shRNA (grey).

G-H. DIV5 hippocampal neurons co-transfected at DIV1 with a BFP-fill and Kv-Nav (upper panel) or an empty vector (lower panel) and stained for AnkG and TRIM46. The intensity of AnkG and TRIM46 staining at the AIS normalized to neighbouring non-transfected neurons is shown in H. One-way ANOVA with Holm-Sidak's multiple comparison test,  $p = 0.011$  for AnkG,  $p = 0.037$ . At least 17 transfected neurons analyzed per condition, from 2 independent experiments.



In A, scale bars represent 20  $\mu\text{m}$  and 10  $\mu\text{m}$  in the zooms and 10  $\mu\text{m}$  in G. In the kymographs, horizontal bar is 4.44  $\mu\text{m}$  and vertical bar is 4 s.



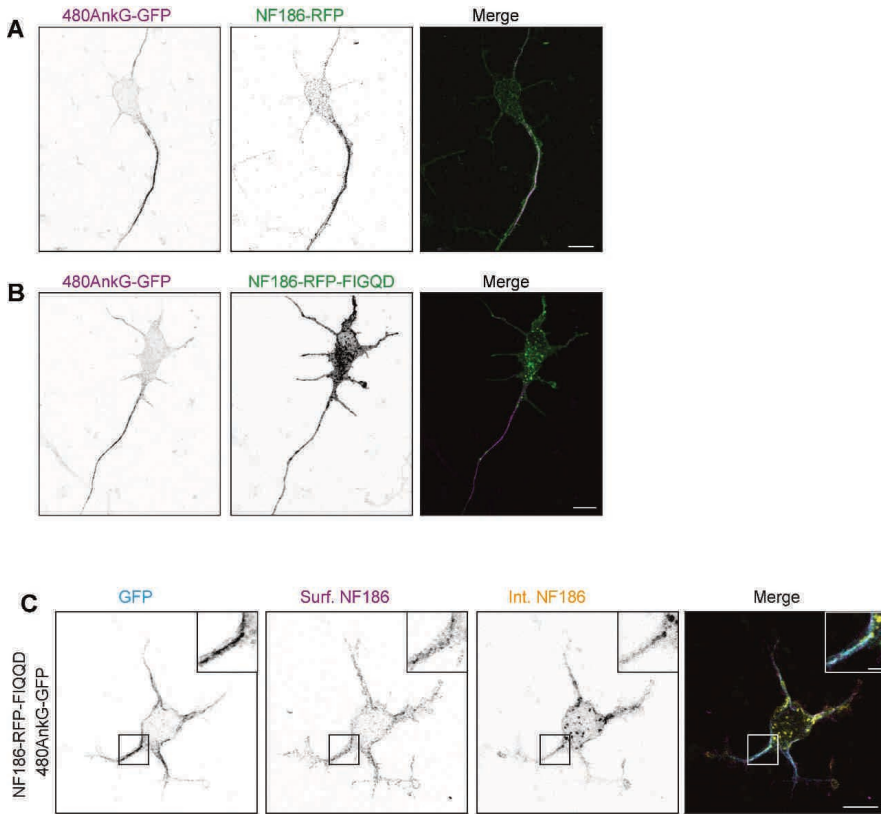


**Figure S7. Related to Figure 7: AnkG allows for stable accumulation of NF186 at the AIS**  
A-B. DIV3 neurons transfected at DIV0 with 480AnkG-GFP and NF186-RFP (A) or NF186-RFP-FIGQD (B).  
C. DIV1 neuron transfected at DIV0 with 480AnkG-GFP and NF186-RFP-FIGQD. Surface NF186 pool is shown in grey, and internalized pool is shown in red.  
In A and B scale bars are 10  $\mu$ m and in C they represent 10  $\mu$ m and 2  $\mu$ m in the zooms.

## Information for supplementary materials available online

### Supplementary Video Legends

**Video S1. 480AnkG Colocalizes with EB3 and Tracks MT Plus-ends, Related to Figure 1:**

Time-lapse movie of a COS-7 cell co-expressing 480AnkG-GFP (magenta) with EB3-RFP (green). The movie consists of 121 frames recorded simultaneously in the two channels with 1 s interval between frames and 100 ms exposure time. Scale bar represents 5  $\mu$ m.

**Video S2. TRIM46 Bundles Parallel MTs and Promotes Rescues of MTs within the Bundle, Related to Figure 5:**

Time-lapse movie of an *in vitro* reconstitution experiment showing a TRIM46 decorated two-MT bundle (arrow) and a single MT (arrowhead) growing from rhodamine-tubulin-labeled GMPCPP seeds in the presence of 15  $\mu$ M tubulin, 20 nM mCherry-EB3 and 20 nM GFP-TRIM46. The movie consists of 301 frames recorded with 2 s interval between frames and 100 ms exposure time. Scale bar represents 5  $\mu$ m.

### Supplementary Table Legend

**Table S1. Mass Spectrometry Analysis of Purified GFP-TRIM46, 480AnkG-GFP, and 480AnkG-NN-GFP with a 10% Cutoff, Related to Figure 5.**

### Key Resources Table

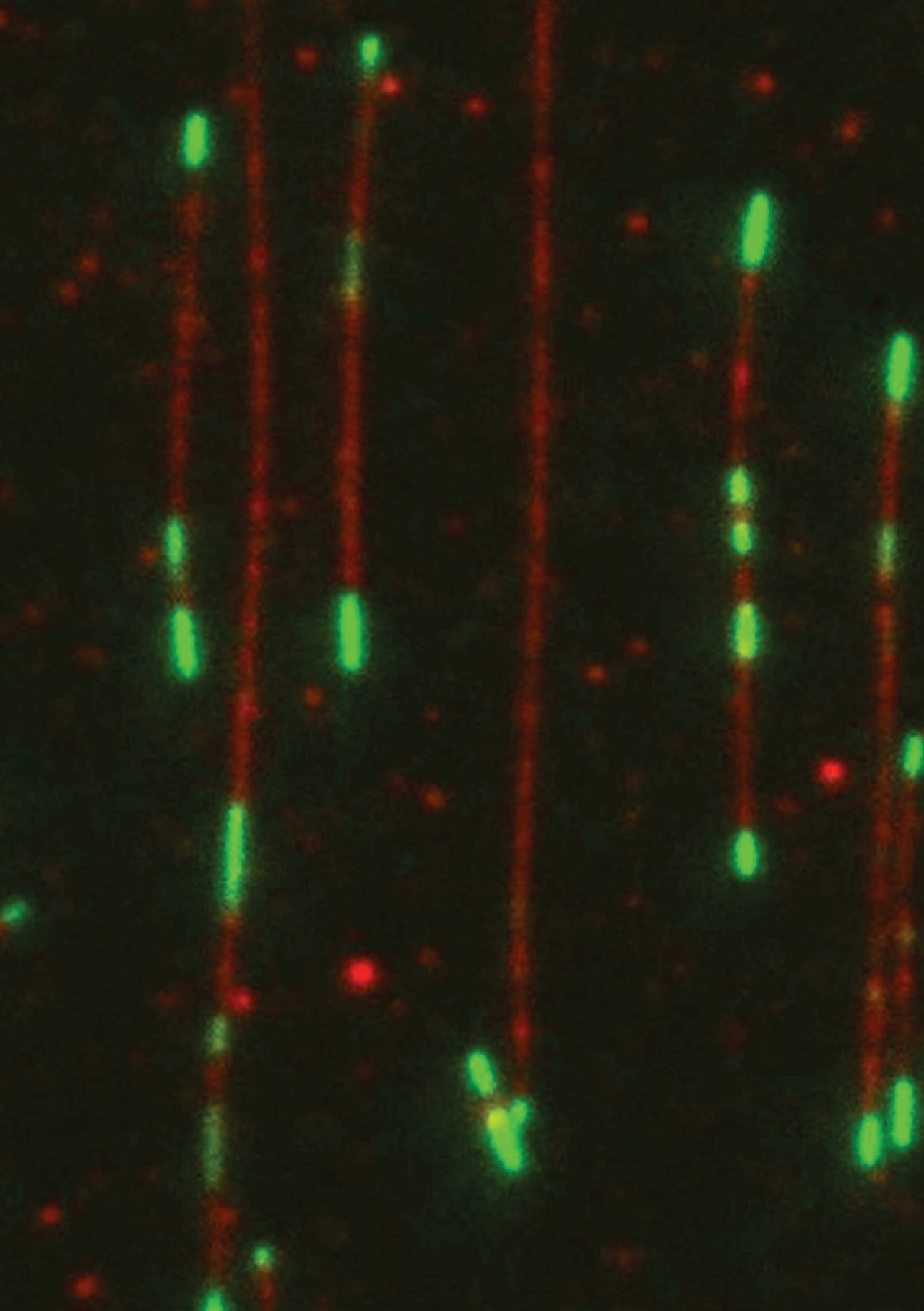
| REAGENT or RESOURCE            | SOURCE                                    | IDENTIFIER                      |
|--------------------------------|---|---------------------------------|
| <b>Antibodies</b>              |   |                                 |
| rabbit anti-EB2                | From A. Akhmanova, Stepanova et al., 2003 | N/A                             |
| mouse anti-AnkG                | Neuromab                                  | Cat# N106/36; RRID: AB_10673030 |
| mouse anti-AnkG, clone N106/20 | Neuromab                                  | Cat# N106/20; RRID: AB_2750699  |
| mouse anti-EB1, clone 5/EB1    | BD Transduction Laboratories              | Cat# 610535; RRID: AB_397892    |
| mouse anti-Rab11, clone47      | BD Transduction Laboratories              | Cat# 610656; RRID: AB_397983    |
| chicken anti-MAP2              | Abcam                                     | Cat# ab5392; RRID: AB_2138153   |
| chicken anti-GFP               | Abcam                                     | Cat# ab13970; RRID: AB_300798   |
| rabbit anti- $\alpha$ -tubulin | Abcam                                     | Cat# ab52866; RRID: AB_869989   |
| rat anti-tyrosinated tubulin   | Abcam                                     | Cat# ab6160; RRID: AB_305328    |
| rabbit anti-GFP                | MBL International                         | Cat# 598S; RRID: AB_591816      |
| mouse anti-GFP, clone 3E6      | Life Technologies                         | Cat# A-11120; RRID: AB_221568   |
| mouse anti- $\alpha$ -tubulin  | Sigma-Aldrich                             | Cat# T6074; RRID: AB_477582     |
| mouse anti-acetylated tubulin  | Sigma-Aldrich                             | Cat# T7451; RRID: AB_609894     |
| mouse anti- $\beta$ -tubulin   | Sigma-Aldrich                             | Cat# T5201; RRID: AB_609915     |
| goat anti-mouse Alexa405       | Life Technologies                         | Cat# A31553; RRID: AB_22160     |
| goat anti-chicken Alexa405     | Life Technologies                         | Cat# ab175675; RRID: AB_2810980 |
| goat anti-rabbit Alexa405      | Life Technologies                         | Cat# A31556; RRID: AB_221605    |
| goat anti-mouse Alexa488       | Life Technologies                         | Cat# A11029; RRID: AB_138404    |
| goat anti-chicken Alexa488     | Life Technologies                         | Cat# A11039; RRID: AB_142924    |
| goat anti-rabbit Alexa488      | Life Technologies                         | Cat# A11034; RRID: AB_2576217   |

| REAGENT or RESOURCE  | SOURCE   | IDENTIFIER                          |
|--|--|-------------------------------------|
| goat anti-mouse Alexa594                                       | Life Technologies                              | Cat# A11032; RRID: AB_141672        |
| goat anti-rabbit Alexa594                                      | Life Technologies                              | Cat# A11037; RRID: AB_2534095       |
| goat anti-mouse Alexa568                                       | Life Technologies                              | Cat# A11031; RRID: AB_14469         |
| goat anti-rabbit Alexa568                                      | Life Technologies                              | Cat# A11036; RRID: AB_143011        |
| goat anti-mouse Alexa647                                       | Life Technologies                              | Cat# A21236; RRID: AB_141725        |
| goat anti-rabbit Alexa647                                      | Life Technologies                              | Cat# A21245; RRID: AB_2535813       |
| goat anti-mouse Atto 647N                                      | Sigma Aldrich                                  | Cat# 50185; RRID: AB_1137661        |
| goat anti-rabbit STAR 580                                      | Abberior                                       | Cat# 2-0012-005-8; RRID: AB_2810981 |
| goat anti-mouse STAR RED                                       | Abberior                                       | Cat# 2-0002-011-2; RRID: AB_2810982 |
| anti-Pan-Neurofascin   | Neuromab                                       | Cat# A12/18; RRID: AB_2282826       |
| rabbit anti-TRIM46   | From C. Hoogenraad, van Beuningen et al., 2015 | N/A                                 |
| rabbit anti-EB3  | From A. Akhmanova, Stepanova et al., 2003      | N/A                                 |
| rabbit anti-IgG  | Agilent  | Cat# Z0412, RRID: AB_2810286        |
| <b>Chemicals, Peptides, and Recombinant Proteins</b>           |  |                                     |
| Vectashield mounting medium                                    | Vectorlabs                                     | Cat# H-1000                         |
| Mix-n-Stain CF640R   | Biotium  | Cat# 92245                          |
| Nocodazole   | Sigma-Aldrich                                  | Cat# M1404; CAS 31430-18-9          |
| Lipofectamine 2000   | Invitrogen                                     | Cat# 1639722                        |
| Fugene6  | Promega  | Cat# E2691                          |
| <b>Critical Commercial Assays</b>                              |  |                                     |
| Rat Neuron Nucleofector kit                                    | Amaxa  | Cat# VVPG-1003                      |
| <b>Deposited Data</b>  |  |                                     |
| Raw mass-spectrometry data                                     | This paper                                     | PXD013685                           |
| <b>Experimental Models: Cell Lines</b>                         |  |                                     |
| Human Bone Osteosarcoma Epithelial (U2OS)                      | ATCC   | CRL-1573                            |
| African Green Monkey SV40-transformed kidneyfibroblast (COS-7) | ATCC   | CRL-1651                            |
| Human embryonic kidney 293 (HEK)                               | ATCC   | HTB-96                              |
| <b>Experimental Models: Organisms/Strains</b>                  |  |                                     |
| Rat (Wistar)   | Janvier  | N/A                                 |
| <b>Recombinant DNA</b>   |  |                                     |
| TRIM46-GFP   | van Beuningen et al., 2015                     | N/A                                 |
| TRIM36-mCherry   | van Beuningen et al., 2015                     | N/A                                 |
| PRC1-mCherry   | van Beuningen et al., 2015                     | N/A                                 |
| 480AnkG-GFP  | Fréal et al., 2016                             | N/A                                 |
| 480AnkG-NN-GFP   | Fréal et al., 2016                             | N/A                                 |
| 480AnkGtail-GFP  | Fréal et al., 2016                             | N/A                                 |
| 270AnkG-GFP  | Fréal et al., 2016                             | N/A                                 |
| myc-Kv-Nav   | Bréchet et al., 2008                           | N/A                                 |
| Rab5-GFP   | Hoogenraad et al., 2010                        | N/A                                 |
| Rab11-GFP  | Hoogenraad et al., 2010                        | N/A                                 |

| REAGENT or RESOURCE        | SOURCE  | IDENTIFIER |
|----------------------------|---|------------|
| Rab6-GFP                   | Schlager et al., 2010                           | N/A        |
| NPY-GFP                    | Schlager et al., 2010                           | N/A        |
| HA-NF186-mRFP-FKBP         | Kuijpers et al., 2016                           | N/A        |
| EB3-RFP                    | Stepanova et al., 2003                          | N/A        |
| mEOS-tubulin               | Cloin et al., 2017                              | N/A        |
| TRIM46-BFP                 | This paper                                      | N/A        |
| pGW1-BFP                   | Kapitein et al., 2010                           | N/A        |
| HA-NF186(FIGQD)-mRFP-FKBP  | This paper                                      | N/A        |
| C70A-480AnkG-GFP           | This paper                                      | N/A        |
| StrepII-480AnkG-GFP        | This paper                                      | N/A        |
| StrepII-480AnkG-mCherry    | This paper                                      | N/A        |
| StrepII-480AnkG-NN-GFP     | This paper                                      | N/A        |
| StrepII-480AnkG-NN-mCherry | This paper                                      | N/A        |
| pTT5-EGFP-N1               | Atherton et al., 2017                           | N/A        |
| pTT5-mCherry-N1            | Atherton et al., 2017                           | N/A        |
| StrepII-GFP-TRIM46         | This paper                                      | N/A        |
| StrepII-GFP-PRC1           | This paper                                      | N/A        |
| StrepII-GFP-C1             | Atherton et al., 2017                           | N/A        |
| 270AnkG+TIP-GFP            | This paper                                      | N/A        |
| MACF18-GFP                 | Honnappa et al., 2009                           | N/A        |
| $\beta$ -tubulin-GFP       | kind gift from Dr. P. Schätzle and Dr. K. Jiang | N/A        |
| shRNA AnkyrinG             | Hedstrom et al., 2007                           | N/A        |
| shRNA TRIM46               | van Beuningen et al., 2015                      | N/A        |
| pSUPER-shRNA               | Brummelkamp et al., 2002                        | N/A        |
| TRIM46-mCherry             | Van Beuningen et al., 2015                      | N/A        |

### Software and Algorithms

|                              |                             |   |
|------------------------------|-----------------------------|---|
| plugin ComDet                | Eugene Katrukha             | <a href="https://github.com/ekatrakha/ComDet">https://github.com/ekatrakha/ComDet</a>                     |
| plugin Pro_Feat_Fit          | Christophe Leterrier        | <a href="https://github.com/cleterrier/Measure_ROIs">https://github.com/cleterrier/Measure_ROIs</a>       |
| Fiji                         | Schindelin, J. et al., 2012 | <a href="https://imagej.net/Fiji">https://imagej.net/Fiji</a>   |
| GraphPad Prism 8             | GraphPad                    | <a href="https://www.graphpad.com/scientific-software/">https://www.graphpad.com/scientific-software/</a> |
| plugin KymoResliceWide v.0.4 | Eugene Katrukha             | <a href="https://github.com/ekatrakha/KymoResliceWide">https://github.com/ekatrakha/KymoResliceWide</a>   |



# 4

## **CLASP Mediates Microtubule Repair by Restricting Lattice Damage and Regulating Tubulin Incorporation**

Amol Aher<sup>1</sup>, Dipti Rai<sup>1#</sup>, Laura Schaedel<sup>2</sup>, Jeremie Gaillard<sup>2</sup>, Karin John<sup>3</sup>, Qingyang Liu<sup>1</sup>, Maarten Altelaar<sup>4</sup>, Laurent Blanchoin<sup>2,5</sup>, Manuel Thery<sup>2,5</sup>, and Anna Akhmanova<sup>1,6,\*</sup>

<sup>1</sup> Cell Biology, Department of Biology, Faculty of Science, Utrecht University, Padualaan 8, 3584 CH Utrecht, the Netherlands

<sup>2</sup> University of Grenoble-Alpes, CEA, CNRS, INRA, Interdisciplinary Research Institute of Grenoble, Laboratoire de Physiologie Cellulaire & Végétale, CytoMorpho Lab, 38054 Grenoble, France

<sup>3</sup> University of Grenoble-Alpes, CNRS, Laboratoire Interdisciplinaire de Physique, 38000 Grenoble, France

<sup>4</sup> Biomolecular Mass Spectrometry and Proteomics, Bijvoet Center for Biomolecular Research, Utrecht Institute for Pharmaceutical Sciences and the Netherlands Proteomics Centre, Utrecht University, Padualaan 8, 3584 CH Utrecht, the Netherlands

<sup>5</sup> Université de Paris, INSERM, CEA, Institut de Recherche Saint Louis, U 976, CytoMorpho Lab, 75010 Paris, France

<sup>6</sup> Lead Contact

# This author has shown that CLASP promotes complete repair of lattice defects present in Taxol-stabilized microtubules.

\* Correspondence: a.akhmanova@uu.nl

**Current Biology. 2020 Jun 8;30(11):2175-2183.e6.;**  
doi: 10.1016/j.cub.2020.03.070.

## Summary

Microtubules play a key role in cell division, motility, and intracellular trafficking. Microtubule lattices are generally regarded as stable structures that undergo turnover through dynamic instability of their ends [1]. However, recent evidence suggests that microtubules also exchange tubulin dimers at the sites of lattice defects, which can be induced by mechanical stress, severing enzymes, or occur spontaneously during polymerization [2, 3, 4, 5, 6]. Tubulin incorporation can restore microtubule integrity; moreover, “islands” of freshly incorporated GTP-tubulin can inhibit microtubule disassembly and promote rescues [3, 4, 6, 7, 8]. Microtubule repair occurs *in vitro* in the presence of tubulin alone [2, 3, 4, 5, 6, 9]. However, in cells, it is likely to be regulated by specific factors, the nature of which is currently unknown. CLASPs are interesting candidates for microtubule repair because they induce microtubule nucleation, stimulate rescue, and suppress catastrophes by stabilizing incomplete growing plus ends with lagging protofilaments and promoting their conversion into complete ones [10, 11, 12, 13, 14, 15, 16, 17]. Here, we used *in vitro* reconstitution assays combined with laser microsurgery and microfluidics to show that CLASP2 $\alpha$  indeed stimulates microtubule lattice repair. CLASP2 $\alpha$  promoted tubulin incorporation into damaged lattice sites, thereby restoring microtubule integrity. Furthermore, it induced the formation of complete tubes from partial protofilament assemblies and inhibited microtubule softening caused by hydrodynamic-flow-induced bending. The catastrophe-suppressing domain of CLASP2 $\alpha$ , TOG2, combined with a microtubule-tethering region, was sufficient to stimulate microtubule repair, suggesting that catastrophe suppression and lattice repair are mechanistically similar. Our results suggest that the cellular machinery controlling microtubule nucleation and growth can also help to maintain microtubule integrity.

## Results and Discussion

### ***CLASP Stalls Depolymerization and Promotes Repair of Microtubule Lattices Damaged by Photoablation***

To investigate whether CLASPs can promote microtubule repair, we modified previously described *in vitro* reconstitution assays with GFP-tagged CLASP2 $\alpha$  purified from HEK293T cells (Figure S1A; Table S1) [12]. Microtubules were grown from GMPCPP-stabilized seeds, visualized by adding fluorescently labeled tubulin and observed by total internal reflection fluorescence (TIRF) microscopy [12, 18]. In this assay, GFP-CLASP2 $\alpha$  (Figure 1A) shows some binding to microtubule lattices and a weak enrichment at growing microtubule tips [12].



To explore the capacity of CLASP to repair damaged microtubules, we performed laser-mediated microsurgery on dynamic microtubules. Laser irradiation at a point along microtubule lattice resulted in local reduction of the tubulin intensity with or without microtubule bending (outcomes I and II), or lattice severing, distinguished by the appearance of two microtubule ends at the irradiated site (outcome III) (Figure 1B). In the presence of tubulin alone, microtubules that bent by more than  $10^\circ$  after damage (outcome I) typically broke (Figures 1B and 1C; Video S1), although in 18% of the cases, microtubules straightened again, suggesting that they were repaired (Figure 1D). These data are in agreement with previous work showing that damaged microtubule lattices can be autonomously repaired by tubulin incorporation [2, 3, 6, 9]. When these experiments were performed in the presence of CLASP2 $\alpha$ , the percentage of successful repair of microtubules bent at an irradiated site by more than  $10^\circ$  increased 3-fold to 62% (Figures 1D and 1G).

Mammalian CLASPs contain three TOG-like domains, TOG1, TOG2, and TOG3, connected by flexible positively charged linkers, and a C-terminal domain (CLIP-ID) that binds to different partners and targets CLASPs to various subcellular locations [17, 19] (Figure 1A). Our previous work has shown that an isolated TOG2 domain has a very low affinity for microtubules and does not bind to free tubulin [12]. However, when TOG2 was fused to the adjacent intrinsically disordered positively charged region (a fusion protein termed TOG2-S, Figure 1A), it could bind to microtubule lattice, show some autonomous enrichment at growing microtubule ends, and suppress catastrophes even in the absence of end-binding (EB) proteins, which normally target CLASPs to growing microtubule plus ends [12]. By performing laser damage experiments in the presence of TOG2-S, we found that it could also promote repair and straightening of microtubules bent after irradiation (Figures 1D, S1A, and S1B; Video S1). Although mass spectrometry analysis of CLASP2 $\alpha$  revealed the presence of some proteins binding to CLASP C terminus, such as CLIP-170 (Table S1), the repair activity observed for TOG2-S, which lacks the partner-binding C-terminal region of CLASP, indicates that the ability to promote microtubule restoration is autonomous to CLASP.

Before irradiation, CLASP2 $\alpha$  weakly labeled entire microtubules, and its fluorescence intensity was the same at the sites that were subsequently repaired and the sites that broke (Figure S1C). However, after irradiation, both CLASP2 $\alpha$  and TOG2-S rapidly bound to the sites of damage (Figures 1E, 1G, S1B, S1D, and S1E), indicating they can autonomously recognize such sites. Over time, the accumulation of CLASP2 $\alpha$  and TOG2-S diminished, whereas tubulin intensity at the irradiated site increased (Figures 1E–1G, S1B, S1D, S1E, and S1G; Video S1). Such an increase was also observed with tubulin alone (Figures 1F and S1F).

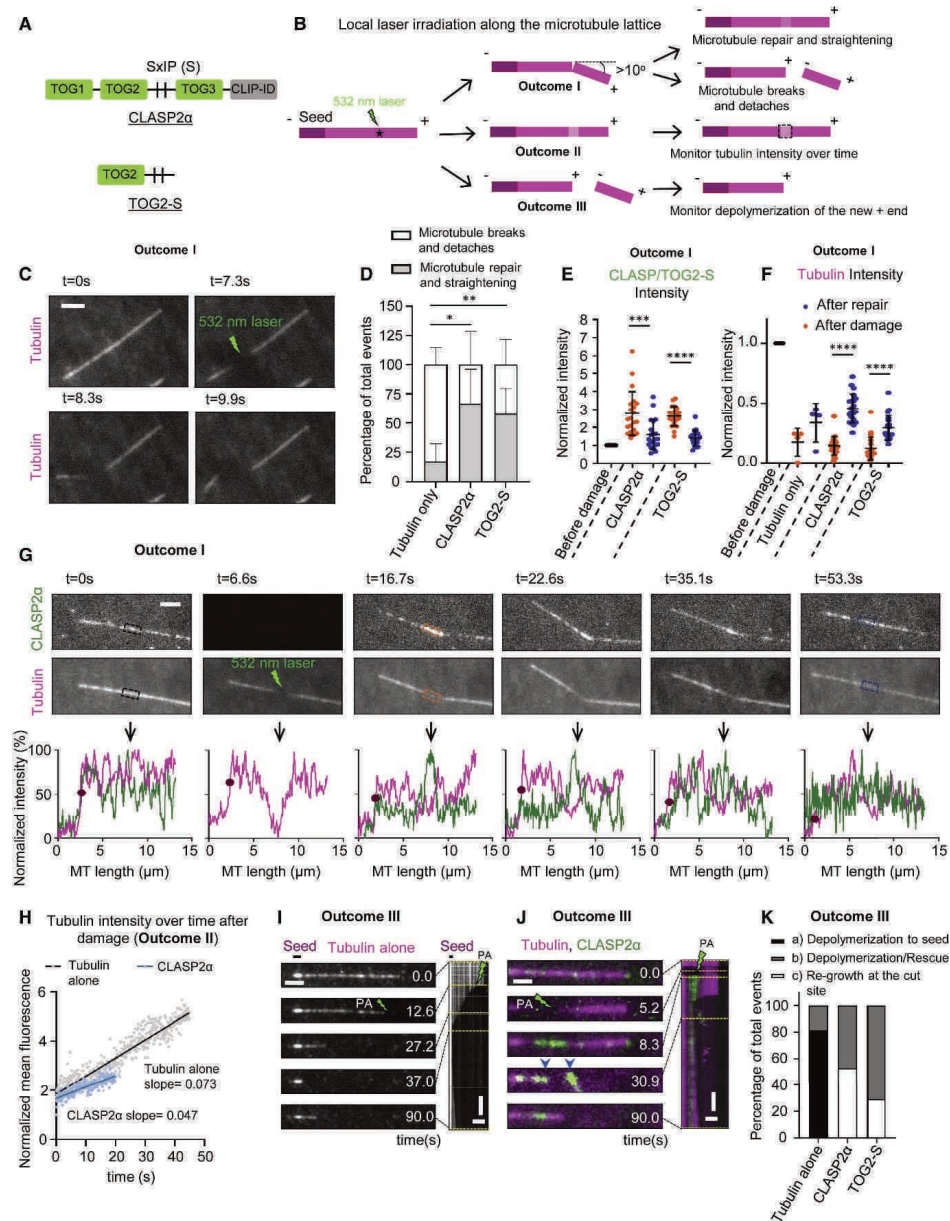


**Figure 1. CLASP Promotes Repair of Microtubule Lattices Damaged by Laser Illumination**

(A) A scheme of full-length CLASP2 $\alpha$  and its TOG2-S fragment. Vertical lines labeled SxIP (Ser-any amino acid-Ile-Pro) represent EB-binding motifs located in the unstructured positively charged region adjacent to the TOG2 domain.

(B) Schematic for an experiment to monitor the possible outcomes of a 532 nm pulsed laser induced damage at a site along the dynamic lattice. (I) Microtubule bending at the site of damage, which can lead to either straightening of the lattice or microtubule breakage. (II) Reduction of the tubulin intensity. (III) Microtubule severing resulting in direct appearance of two microtubule ends.

(C) Stills from a time-lapse video showing photodamage of a dynamic microtubule grown in the presence of Rhodamine-tubulin alone followed by bending and subsequent breakage (outcome I). Scale bar, 2  $\mu\text{m}$ .

(D) Percentage of total events for outcome I resulting in either microtubule breakage or straightening at the point of photodamage in the presence of tubulin alone ( $n = 22$  microtubules analyzed from 4 experiments) or together with either 30 nM GFP-CLASP2 $\alpha$  ( $n = 53$  microtubule analyzed from 6 experiments) or 30 nM GFP-TOG2-S ( $n = 54$  from 8 experiments). Error bars denote SD.

(E and F) Normalized mean intensity at the site of photodamage in case of outcome I for the GFP channel for CLASP2 $\alpha$  and TOG2-S (E) and Rhodamine-tubulin channel in the presence of tubulin alone or together with either CLASP2 $\alpha$  or TOG2-S (F); before damage (black), immediately after damage (orange) and after microtubule straightening (blue). Tubulin alone:  $n = 4$  microtubules, 4 experiments; CLASP2 $\alpha$ :  $n = 21$  microtubules, 4 experiments; TOG2-S:  $n = 20$  microtubules, 6 experiments. Error bars denote SD.

(G) Stills from a time-lapse video showing a dynamic microtubule grown in the presence of Rhodamine-tubulin together with 30 nM GFP-CLASP2 $\alpha$  for outcome I. Normalized intensity profiles along the microtubule for the CLASP (green) and tubulin channel (magenta) at different time points are shown in the bottom panels, with the arrow pointing to the site of photodamage. The purple circle on the plot indicates the end of the microtubule. Scale bars, 2  $\mu\text{m}$ .

(H) Normalized mean tubulin fluorescence intensity over time at the site of local photodamage (outcome II); microtubules were grown in the presence of Rhodamine tubulin alone (gray) ( $n = 35$  microtubules, 2 experiments) or together with 30 nM GFP-CLASP2 $\alpha$  (blue) ( $n = 44$  microtubules, 2 experiments). Straight lines were fitted to the initial increase in tubulin intensity until saturation for the respective mean values yielding slopes as indicated.

(I and J) Stills and the corresponding kymograph of a microtubule grown in the presence of Rhodamine-tubulin alone (I) or together with GFP-CLASP2 $\alpha$  (30 nM) (J) severed with a 532 nm laser as indicated (outcome III). Scale bars: still image, 2  $\mu\text{m}$ ; kymograph, 4  $\mu\text{m}$  (horizontal) and 10 s (vertical). Dotted yellow lines point to the time point of the still in the kymograph.

(K) Percentage of total laser severing events resulting in either immediate microtubule regrowth at the site of photoablation, microtubule depolymerization to the seed or depolymerization followed by rescue along the lattice, in the presence of Rhodamine-tubulin alone or together with either 30 nM GFP-CLASP2 $\alpha$  or 30 nM GFP-TOG2-S. Tubulin alone:  $n = 186$  microtubules, 3 experiments; CLASP2 $\alpha$ :  $n = 36$  microtubules, 3 experiments; TOG2-S:  $n = 48$  microtubules, 8 experiments.

For plots in Figure 1D: \* $p = 0.0091$ , \*\* $p = 0.0381$ , for Figures 1E and 1F, \*\*\*\* $p < 0.0001$ , \*\*\* $p = 0.001$  Mann-Whitney U test. See also Figures S1 and S2, Table S1, and Videos S1 and S2.

However, since repair of bent microtubules in the absence of CLASP2 $\alpha$  or TOG2-S was infrequent, we could not reliably compare tubulin incorporation rates with and without CLASP. To obtain a larger number of measurements, we monitored microtubules that did not bend but displayed reduced tubulin intensity at the site of damage, likely due to a combination of photobleaching and loss of tubulin dimers (Figure 1B, outcome II). We found that both with tubulin alone and in the presence of CLASP2 $\alpha$ , tubulin intensity at the damaged sites first increased linearly after irradiation and then reached a plateau (Figures S1H–S1J). The rate of tubulin incorporation based on the slopes of the linear part of the plot was  $\sim 1.7$ -fold higher for tubulin alone compared to the condition where CLASP2 $\alpha$  was included in the assay (Figure 1H), and the tubulin intensity after repair at the irradiated sites with respect to the intensity immediately after damage increased  $\sim 5.4$ -fold in the case of tubulin alone but only

~1.9-fold in the presence of CLASP2 $\alpha$  (Figures S1H–S1J). Since bent microtubules were restored more often in the presence of CLASP2 $\alpha$  compared to tubulin alone (Figure 1D), this suggests that CLASP2 $\alpha$  most likely promotes rapid repair by inhibiting microtubule disassembly at the irradiated site and thus limits the zone where new tubulin can incorporate. We next tested whether CLASP2 $\alpha$  had a stabilizing effect on microtubule ends generated upon complete microtubule severing (outcome III) (Figure 1B). In agreement with previous work [20], we found that in the presence of tubulin alone, 81% of freshly severed microtubule plus ends depolymerized to the seed, whereas the remaining 19% were rescued along the lattice (Figures 1I–1K; Video S2). In the presence of CLASP2 $\alpha$ , the depolymerization of newly generated plus ends was strongly inhibited: 53% of the microtubules promptly re-grew directly from the ablation site (Figures 1J and 1K; Video S2). The remaining 47% were rescued along the dynamic lattice, in line with the fact that CLASPs act as rescue factors [10, 11, 12, 13, 21] (Figure 1K). TOG2-S fusion was also sufficient to suppress depolymerization of severed plus ends and promoted re-growth at the site of photo-ablation in 29% of the cases, although the protection was less efficient than with full-length CLASP2 $\alpha$  (Figures 1K and S2A). Importantly, in the presence of either CLASP2 $\alpha$  or TOG2-S, none of the ablated microtubules depolymerized to the seed (Figure 1K), and most of these microtubules exhibited only very short depolymerization excursions (<1  $\mu$ m) compared to tubulin alone (Figure S2B). We note that observation of depolymerization events in the presence of CLASP2 $\alpha$  or TOG2-S was not limited by the lengths of the seed-proximal microtubule parts after severing, which were longer than the depolymerization lengths (Figure S2C).

We also tested whether CLASP2 $\alpha$  could protect freshly generated microtubule ends in the absence of tubulin. To test this, we performed local laser ablation of microtubules in the absence of free tubulin, which were capped with GMPCPP-tubulin to prevent their depolymerization (Figure S2D). All freshly generated microtubule ends depolymerized to the seed or the GMPCPP cap in the absence of CLASP2 $\alpha$  but were protected in its presence (Figures S2E–S2H). We conclude that CLASP2 $\alpha$  promotes microtubule repair, and this activity is at least partly dependent on recognition of damaged microtubule lattices and inhibition of their disassembly.

### ***CLASP Converts Partial Protofilament Assemblies into Complete Tubes***

The experiments described above suggest that CLASP promotes formation of complete tubes from microtubules lacking some parts of protofilaments. To further test the effect of CLASP on partial protofilament assemblies, we used a previously described engineered kinesin-5

dimer, which consists of the motor domain and neck linker of *Xenopus* kinesin-5 (Eg5) fused to the motor-proximal coiled coil derived from *Drosophila* kinesin-1 [22].

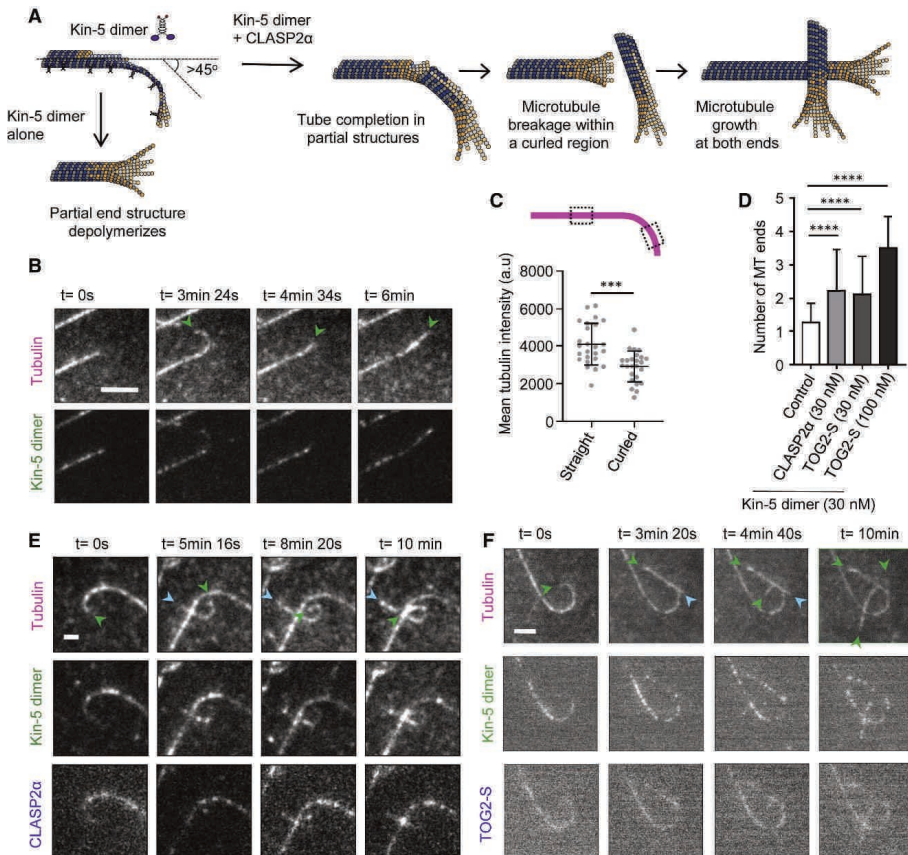


**Figure 2. CLASP Promotes Formation of Complete Microtubules from Partial Protofilament Assemblies**

(A) Cartoon illustrating the changes in tubulin sheet- or ribbon-like structures generated at the plus ends of dynamic microtubules in the presence of 30 nM kinesin-5-GFP dimer (Kin-5 dimer) alone or together with 30 nM GFP-CLASP2α.

(B) Stills from a time-lapse video showing a plus end of a microtubule grown in the presence of Rhodamine-tubulin and 30 nM Kin-5-GFP dimer. Scale bar: 2  $\mu$ m.

(C) Mean tubulin intensity values for the straight and the curled portions of the microtubule lattice as indicated for microtubules grown in the presence of Rhodamine tubulin and 30 nM Kin-5-GFP dimer.  $n = 25$  microtubules from 2 experiments. Error bars denote SD.

(D) Number of newly generated microtubule ends from a single microtubule plus end for microtubules grown in the presence of Rhodamine-tubulin and 30 nM Kin-5-GFP dimer alone ( $n = 38$  microtubule plus ends, 3 experiments) or together with 30 nM TagBFP-CLASP2α ( $n = 95$  microtubule plus ends, 3 experiments), or with 30 nM TagBFP-TOG2-S ( $n = 85$  microtubule plus ends, 3 experiments), or with 100 nM Tag-BFP-TOG2-S ( $n = 26$  microtubule plus ends, 2 experiments). Events where the microtubule plus ends bent by angles over 45° with respect to the lattice were monitored in a 10 min time lapse. Error bars denote SD.

*(E) Stills from a time-lapse video showing the plus end for a microtubule grown in the presence of Rhodamine tubulin, 30 nM Kin-5-GFP dimer, and 30 nM TagBFP-CLASP2 $\alpha$ . Scale bar: 2  $\mu$ m.*

*(F) Stills from a time-lapse video showing a microtubule plus end grown in the presence of Rhodamine-tubulin, 30 nM Kin-5-GFP dimer together with 30 nM TagBFP-TOG2-S. Scale bar: 3  $\mu$ m.*

*For (B), (E), and (F), green arrowheads point to the plus end and blue arrowheads to the minus ends. For all plots, \*\*\*\* $p$  < 0.0001, \*\*\* $p$  = 0.001 and ns, no significant difference with control, Mann-Whitney  $U$  test. See also Video S3.*

---

This engineered kinesin-5 (Kin-5 dimer) was shown to generate long tubulin ribbons and protofilament sheets at microtubule plus ends [22] (Figure 2A), likely by stabilizing specific tubulin conformations and enhancing lateral contacts between tubulin dimers [23]. In the presence of Kin-5 dimer, we observed curled microtubule ends, which displayed a 25% reduction in tubulin intensity compared to the straight parts of the lattice, in line with the idea that the curled regions miss some protofilaments (Figures 2B and 2C). Similar curved microtubule plus-end extensions were also formed when CLASP2 $\alpha$  or TOG2-S were included with the Kin-5 dimer in the assay (Figures 2A, 2E, and 2F; Video S3). However, whereas in the presence of the Kin-5 dimer alone these structures were transient and typically depolymerized, in the presence of CLASP2 $\alpha$  or TOG2-S, curled microtubule ends were converted into multiple straight microtubules (Figures 2D–2F). These data suggest that CLASP2 $\alpha$  and its TOG2-S fragment can promote formation of complete microtubules from protofilament sheets. Since several microtubules could form from a single curled end, these results suggest that CLASP2 $\alpha$  and TOG2-S not only help to repair strongly tapered microtubule ends, as it occurs during catastrophe suppression [12] but also likely promote extension of protofilament bundles from the side, allowing them to close into complete tubes.

### ***CLASP Promotes Complete Repair of Microtubule Lattice Defects***

To generate a substrate in which we could monitor tubulin incorporation into partially damaged microtubule lattices, we prepared Rhodamine-labeled microtubules stabilized with Taxol. Microtubules polymerized in the presence of Taxol are known to exhibit extensive lattice defects [24]; this property has been used, for example, to demonstrate the impact of microtubule defects on kinesin-based transport [25, 26]. Taxol-stabilized microtubules display more structural defects in the lattice when incubated with very low tubulin concentrations [27]. To promote defect formation, we incubated Taxol-stabilized microtubules for 1.5 min in a buffer without Taxol and tubulin (Figure 3A). In these conditions, microtubules gradually lose

tubulin dimers from discrete sites, which can be detected as gaps with a reduced intensity of tubulin signal (Figure 3B; Video S4).

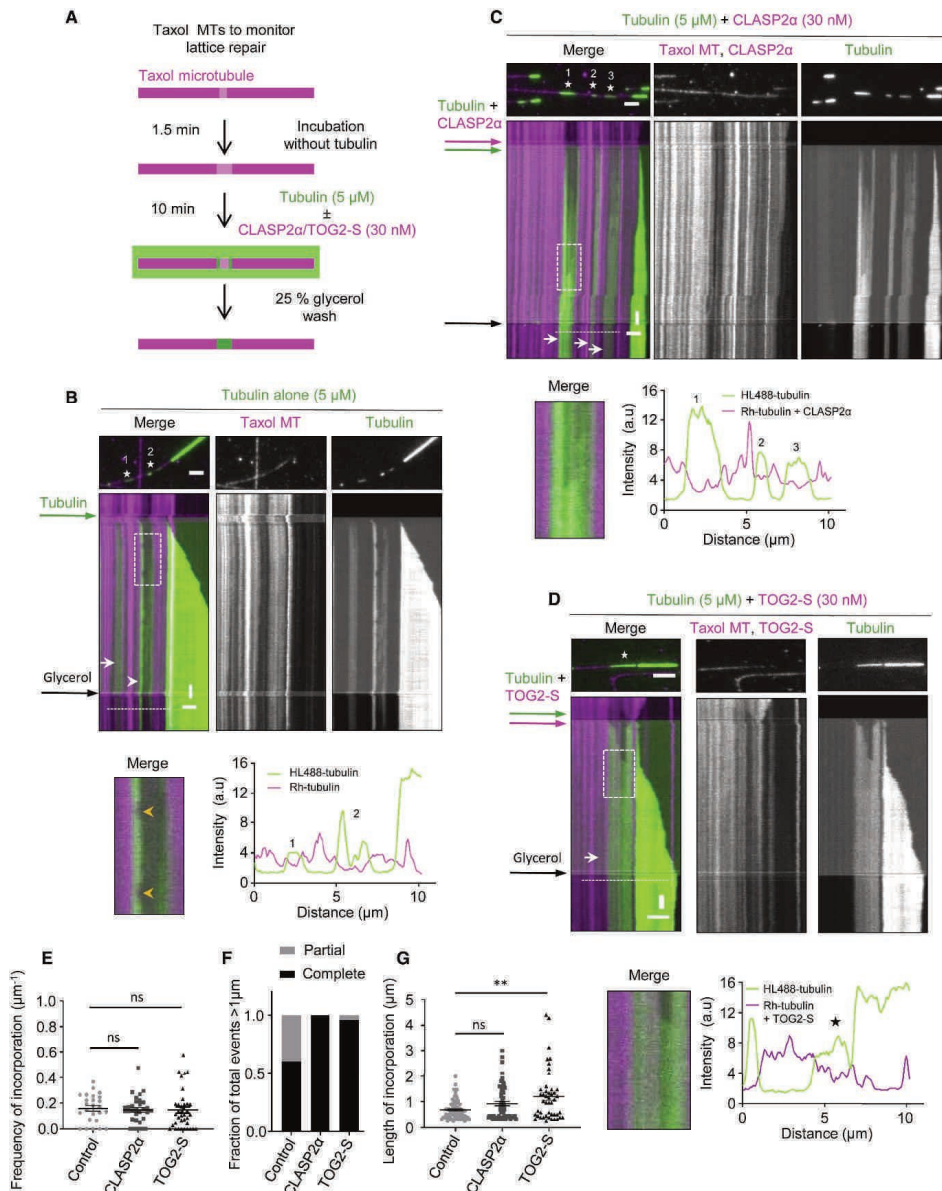


**Figure 3. CLASP Promotes Complete Repair of Damaged Microtubule Lattices**

(A) Schematic for an experiment to monitor tubulin incorporation into damaged microtubule lattices. Microtubules prepared from Rhodamine-tubulin in the presence of Taxol were first incubated without Taxol and tubulin for 1.5 min and subsequently with 5  $\mu$ M HiLyte Fluor-488-labeled tubulin with or without 30 nM mCherry-CLASP2 $\alpha$  or 30 nM mCherry-TOG2-S. After 10 min, the residual free green

tubulin was washed out with the wash buffer supplemented with 25% glycerol to prevent microtubule depolymerization, in order to better visualize incorporation of green tubulin.

(B–D) Microtubule repair in the presence of tubulin alone (B) or together with either 30 nM mCherry-CLASP2 $\alpha$  (C) or 30 nM mCherry-TOG2-S (D). Single frames (top) of time-lapse videos after the final washout and kymographs (bottom) showing green tubulin incorporation sites (numbered asterisks in stills) into Rhodamine-labeled microtubule lattices (magenta). In kymographs, white arrows indicate complete repair and white arrowheads partial repair. Enlarged views of the boxed regions in the kymographs in (B)–(D) showing partial (B) or complete microtubule repair (C and D) in the bottom-left panel for each condition. Yellow arrowheads in (B) (bottom left) indicate events of loss of freshly incorporated tubulin. Intensity profiles along the microtubule for the Rhodamine-labeled microtubule seed channel (magenta) with or without mCherry-CLASP2 $\alpha$ , and for the green tubulin channel are shown in the bottom-right panel for each condition. The numbers indicate incorporation sites specified in stills in (B) and (D). Scale bars: 2  $\mu\text{m}$  (horizontal) and 60 s (vertical). See also Video S4.

(E and G) Frequency of incorporation per unit length per microtubule (E) and the average length of incorporations (G) in the presence of tubulin alone ( $n = 73$ ,  $M = 25$ ,  $L = 459.25 \mu\text{m}$ , 2 experiments), together with 30 nM mCherry-CLASP2 $\alpha$  ( $n = 64$ ,  $M = 31$ ,  $L = 450.74 \mu\text{m}$ , 5 experiments) or 30 nM mCherry-TOG2-S ( $n = 52$ ,  $M = 37$ ,  $L = 418.43 \mu\text{m}$ , 4 experiments), where  $n$ ,  $M$ , and  $L$  are total number of incorporations, total number of microtubules, and total length of microtubules analyzed, respectively. Error bars represent SEM. \*\* $p = 0.0038$  and ns, no significant difference with control, Mann-Whitney U test.

(F) Fraction of total events resulting in either complete or partial repair at the site of tubulin incorporations with the length exceeding 1  $\mu\text{m}$ , in the presence of tubulin alone ( $n = 15$ , 2 experiments), together with either 30 nM mCherry-CLASP2 $\alpha$  ( $n = 22$ , 5 experiments) or 30 nM mCherry-TOG2-S ( $n = 23$ , 4 experiments), where  $n$  is the total number of incorporations longer than 1  $\mu\text{m}$ . See also Video S4.

When 5  $\mu\text{M}$  tubulin with a green (HiLyte Fluor488) fluorescent label was added to such partially “eroded” Rhodamine-labeled microtubules, we observed that green tubulin was incorporated not only at microtubule ends but also into the microtubule lattices where the original tubulin signal was reduced (Figures 3B; Video S4). The addition of CLASP2 $\alpha$  or TOG2-S had no effect on the frequency of tubulin incorporation sites, as they depended on the number of defects induced by Taxol washout and the extent of microtubule erosion (Figures 3C–3E). However, CLASP2 $\alpha$  and TOG2-S increased the percentage of damaged lattice sites that appeared completely “healed” (Figure 3F; Video S4). This was because the polymerization of freshly added tubulin within such sites was continuous, whereas, in the presence of tubulin alone, incorporation was often confined to the edges of the gaps (Figures 3B–3D). As a result, the average length of the analyzed incorporation sites appeared slightly longer in the presence of CLASP2 $\alpha$  or TOG-S, and, in case of TOG2-S, this difference was significant (Figure 3G). Importantly, in this assay, free tubulin concentration was lower than in the assays described above (5  $\mu\text{M}$  versus 15  $\mu\text{M}$  in Figures 1 and 2). This concentration was chosen to allow tubulin incorporation at the ends or the eroded lattice but prevent nucleation of new microtubules, which was observed when CLASP2 $\alpha$  was combined with partially damaged



Taxol-stabilized microtubules at high free tubulin concentration and which complicated the analysis. Altogether, our results indicate that CLASP2 $\alpha$  or its microtubule-tethered TOG2 domain promotes continuous tubulin addition to the ends of partial protofilament assemblies, allowing efficient repair of lattice gaps.

### *Microtubules Exhibit Increased Resistance to Mechanical Stress in the Presence of CLASP*

Finally, we investigated the effect of CLASP on dynamic microtubules damaged in a more natural way, by inducing mechanical stress with a microfluidics setup described previously [2].

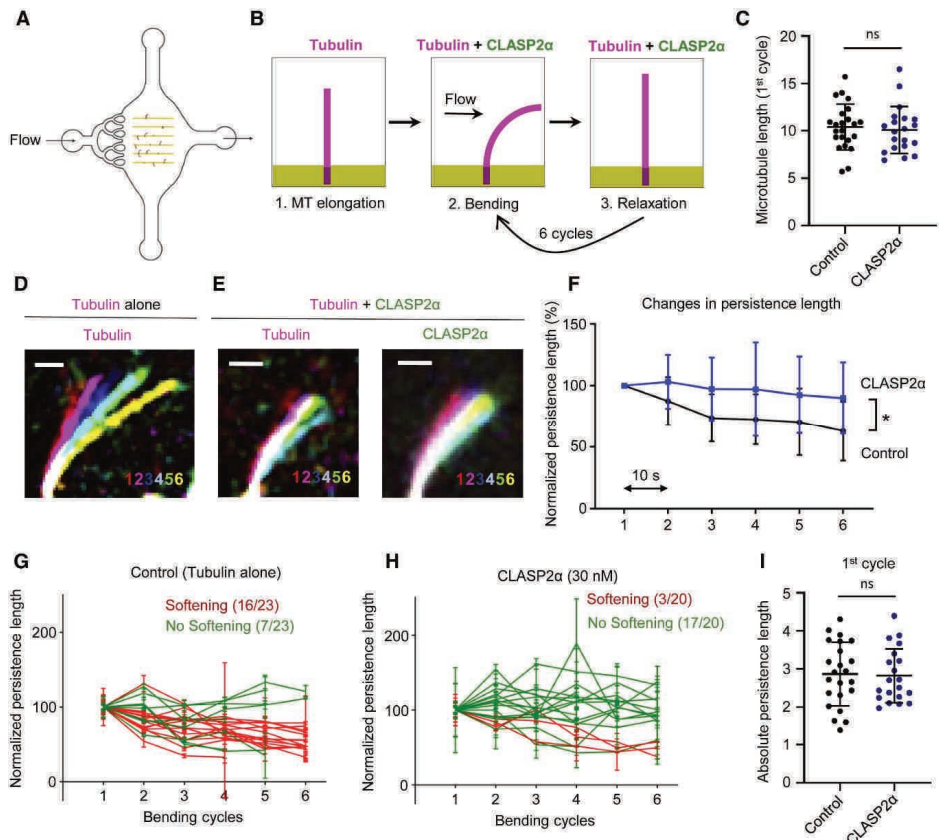


**Figure 4. CLASP2 $\alpha$  Inhibits Microtubule Softening Induced by Hydrodynamic Flow**

(A) Illustration of the microfluidic device used for microtubule bending.

(B) Scheme of the work sequence: 1. Red fluorescent microtubules were grown from seeds grafted on micropatterned lines. 2. Microtubules were bent for 10 s by applying a fluid flow using the same mix as in 1, with or without 30 nM GFP-CLASP2 $\alpha$ . 3. The flow was stopped for 10 s before repeating the bending cycle.

(C) Lengths of microtubules used in the bending experiments in the presence of tubulin alone ( $n = 23$  microtubules) or together with 30 nM GFP-CLASP2 $\alpha$  ( $n = 20$  microtubules). Error bars denote SD.

---

(D and E) Images showing an overlay of maximum bent conformations where every cycle is represented in a different color for the tubulin channel for a microtubule bent in the presence of tubulin alone (D) and for both tubulin and CLASP channels for a microtubule bent in the presence of tubulin together with 30 nM GFP-CLASP2 $\alpha$  (E). Scale bar: 3  $\mu$ m.

(F) Persistence length measured for microtubules bent in the presence (blue curve,  $n = 20$ ) or absence (black curve,  $n = 23$ ) of 30 nM GFP-CLASP2 $\alpha$ . Persistence length was normalized to the value in the first bending cycle for each microtubule. Values represent the average persistence length (mean  $\pm$  SD) of individual measurements shown in Figures 4G and 4H. To test whether microtubules showed softening, a Spearman correlation test for persistence length values over subsequent bending cycles was performed. It revealed significant softening of microtubules in both conditions ( $p = 0.01$  and  $0.08$ , respectively), though it was much less pronounced in the presence of CLASP2 $\alpha$ . A  $t$  test confirmed significant difference between the two curves ( $p = 0.006$ ).

(G and H) Individual persistence length measurements of microtubules bent in the absence (G) and presence (H) of 30 nM GFP-CLASP2 $\alpha$ . Values represent the average of five independent measurements for each bending cycle (mean  $\pm$  SD) and were normalized to the initial value. A Spearman correlation test was performed to test for softening. Red lines indicate microtubules that became significantly softer, and green lines indicate microtubules that did not show significant softening.

(I) Absolute persistence lengths for microtubules bent in the presence of tubulin alone ( $n = 23$  microtubules) or together with 30 nM GFP-CLASP2 $\alpha$  ( $n = 20$  microtubules) after the 1<sup>st</sup> cycle. Error bars denote SD. See also Video S5.

---

In order to study the impact of CLASP on the deformation of microtubules induced by mechanical forces, we applied cycles of hydrodynamic bending stress to microtubules in the absence or presence of CLASP2 $\alpha$ . To this end, we grew dynamic microtubules in the absence of CLASP2 $\alpha$  from GMPCPP and Taxol-stabilized seeds attached to micropatterns inside a microfluidic device (Figure 4A). Microtubules were then bent by an orthogonal fluid flow for 10 s in either the absence or presence of CLASP2 $\alpha$ . The flow was subsequently stopped for 10 s and the bending cycle was repeated (Figure 4B) [28]. Previous work showed that microtubules bend and subsequently straighten after each flow application, but the degree of softening (quantified by monitoring the persistence length of microtubules) increases with each cycle due to the gradual loss of tubulin dimers from the lattice [2]. In the presence of tubulin alone, 70% of the microtubules showed softening after six bending cycles; quantification of the persistence length of the entire microtubule population showed that on average, they became 37% softer (Figures 4C, 4D, 4F, and 4G). In the presence of CLASP2 $\alpha$ , the average drop in the persistence length of microtubules that were of similar length as the control ones (Figure 4C) was much less pronounced (10%), with only 15% of the microtubules showing softening (Figures 4E, 4F, and 4H). This indicates that microtubules exhibit increased resistance to mechanical stress in the presence of CLASP2 $\alpha$ . These data support the idea that CLASP either alters the mechanical properties of microtubules or promotes repair of the damage induced by bending. Since we did not observe any difference in the persistence length

after the first bending cycle (Figure 4I), it is likely that CLASP does not directly alter lattice rigidity but promotes repair of bent lattices.

## Conclusions

Taken together, our data reveal that CLASP2 $\alpha$  is an autonomous microtubule repair factor. Our experiments suggest that CLASP repair activity is a combination of recognition and stabilization of damaged but not yet depolymerizing sites within the microtubule lattice and a more continuous tubulin incorporation at the sites of damage. Since full-length CLASP2 $\alpha$  and its microtubule-tethered TOG2 domain were both active in microtubule repair assays, and, since TOG2 is highly conserved between CLASP1 and CLASP2 and is present in all CLASP isoforms [19, 29], this property is likely shared by all mammalian CLASPs. Furthermore, given that previous work showed that the TOG2-S fusion can suppress catastrophes [12], our data suggest that the mechanism of microtubule repair is similar to that of catastrophe suppression. Our previous work has shown that CLASPs can stabilize a microtubule plus end with an incomplete set of protofilaments, thereby promoting its recovery into a complete tube [12]. Furthermore, CLASPs are essential for microtubule nucleation from the Golgi in cells [30] and reduce the kinetic threshold for templated microtubule nucleation *in vitro* [12]. In the current study, we showed that CLASP2 $\alpha$  promotes formation of complete tubes from tubulin sheets or ribbons generated by kinesin-5 dimer, structures that resemble microtubule nucleation intermediates [23]. All these activities likely depend on the ability of CLASPs to stabilize partial microtubule structures prone to depolymerization, prevent their catastrophic disassembly, and shift the balance toward their continuous polymerization. Given that the microtubule-tethered TOG2 domain, which might be binding between protofilaments [12], was sufficient to promote microtubule lattice repair, this activity might depend on stabilizing lateral contacts between tubulin dimers.

If CLASPs help to repair microtubules rapidly and efficiently, their loss could potentially lead to accumulation of microtubule damage that is repaired slowly. This might explain why CLASP depletion leads to increased guanosine triphosphate (GTP)-tubulin content and EB accumulation along microtubule shafts, a phenotype that could be restored to control levels by the TOG2 domain of CLASP2 [31]. These observations in cells fit well with our observation of lower extent of damage and less extensive tubulin incorporation at irradiated sites in the presence of CLASP. The strong reduction in the density of microtubule networks observed in CLASP-depleted cells could thus be caused not only by reduced microtubule nucleation and plus-end stability as assumed previously but also by the decreased stability of microtubule

lattices, which are repaired less efficiently when CLASPs are absent. An important question for future research is whether and how other components of microtubule polymerization machinery contribute to microtubule repair.

### **Experimental Model and Subject Details**

*E. coli* expression strain BL21 (DE3) was used for recombinant expression and purification of Kin-5-GFP. *E. coli* cells were cultured in standard LB medium supplemented with appropriate antibiotics at 37°C. HEK293T cells were used for expression and purification of CLASP2 $\alpha$  full-length protein and its truncations. CLASP2 $\alpha$  full-length and its truncation constructs were made in modified pEGFP-C1, pmCherry-C1 or pTagBFP-C1 vectors with a StrepII tag as described previously [12]. HEK293T cells were cultured in complete growth medium containing 45% DMEM (Cat# BE12-604F/U1, Lonza), 45% Ham's F10 (Cat# BE12-618F Lonza), and 10% fetal calf serum (Lonza) supplemented with penicillin and streptomycin (Merck) and maintained in an incubator at 5% CO<sub>2</sub> level and 37°C temperature. HEK293T cell lines used were not found in the database of commonly misidentified cell lines, maintained by ICLAC and NCBI BioSample, were not authenticated and were negative for mycoplasma contamination.

### **Method Details**

#### **Protein purification for *in vitro* reconstitutions**

GFP-CLASP2 $\alpha$ , GFP-TOG2-S, mCherry-CLASP2 $\alpha$ , mCherry-TOG2-S, Tag-BFP-CLASP2 $\alpha$  and Tag-BFP-TOG2-S used in the *in vitro* reconstitutions assays were purified from HEK293T cells using the Strep(II)-streptactin affinity purification as described previously (Figure S1A) [12]. Cells were transfected with the Strep-tagged constructs using polyethylenimine (PEI, Polysciences), in a ratio of 3:1 for PEI:DNA. Cells were harvested 2 days after transfection. Cells from a 15 cm dish were lysed in 500  $\mu$ l of lysis buffer (50 mM HEPES, 300 mM NaCl and 0.5% Triton X-100, pH 7.4) supplemented with protease inhibitors (Roche) on ice for 15 minutes. The supernatant obtained from the cell lysate after centrifugation at 21,000  $\times$  g for 20 minutes was incubated with 40  $\mu$ l of StrepTactin Sepharose beads (GE) for 45 minutes. The beads were washed 3 times in the lysis buffer without the protease inhibitors. The protein was eluted with 40  $\mu$ l of elution buffer (50 mM HEPES, 150 mM NaCl, 1 mM MgCl<sub>2</sub>, 1 mM EGTA, 1 mM dithiothreitol (DTT), 2.5 mM d-Desthiobiotin and 0.05% Triton X-100, pH 7.4).

Purified proteins were snap-frozen and stored at  $-80^{\circ}\text{C}$ . Kin-5-GFP was purified from *E. coli* BL-21 as described before (Figure S1A) [22].

### **In vitro microtubule dynamics assays**

Reconstitution of microtubule growth dynamics *in vitro* was performed as described previously [12]. GMPCPP-stabilized microtubule seeds (70% unlabeled tubulin, 18% biotin tubulin and 12% of Rhodamine-tubulin or HiLyte 488 tubulin) were prepared as described before [32]. Briefly, the tubulin mix above was incubated at  $37^{\circ}\text{C}$  for 30 minutes at a total tubulin concentration of  $20\ \mu\text{M}$  with  $1\ \text{mM}$  GMPCPP. Microtubules were pelleted in an Airfuge by centrifugation at  $119,000 \times g$  for 5 minutes. Subsequently, the microtubules were depolymerized by incubation on ice for 20 minutes. A second cycle of polymerization in the presence of  $1\ \text{mM}$  GMPCPP was performed at  $37^{\circ}\text{C}$  for 30 minutes. Microtubule seeds were then pelleted as above and diluted in MRB80 buffer ( $80\ \text{mM}$  piperazine-*N,N*[prime]-bis(2-ethanesulfonic acid (PIPES)), pH 6.8, supplemented with 10% glycerol and snap frozen in liquid nitrogen and stored in a  $-80^{\circ}\text{C}$  freezer until use.

Flow chambers, assembled from plasma-cleaned glass coverslips and microscopic slides were functionalized by sequential incubation with  $0.2\ \text{mg/ml}$  PLL-PEG-biotin (Susos AG, Switzerland) and  $1\ \text{mg/ml}$  NeutrAvidin (Invitrogen) in MRB80 buffer ( $80\ \text{mM}$  piperazine-*N,N*[prime]-bis(2-ethanesulfonic acid (PIPES)), pH 6.8, supplemented with  $4\ \text{mM}$   $\text{MgCl}_2$ , and  $1\ \text{mM}$  EGTA). Microtubule seeds were attached to the coverslip through biotin-NeutrAvidin interactions. Flow chambers were further blocked with  $1\ \text{mg/ml}$   $\kappa$ -casein. The reaction mixture with or without CLASP proteins (MRB80 buffer supplemented with  $14.5\ \mu\text{M}$  porcine brain tubulin,  $0.5\ \mu\text{M}$  Rhodamine-tubulin,  $50\ \text{mM}$  KCl,  $1\ \text{mM}$  guanosine triphosphate (GTP),  $0.5\ \text{mg/ml}$   $\kappa$ -casein, 0.1% methylcellulose, and oxygen scavenger mix ( $50\ \text{mM}$  glucose,  $400\ \mu\text{g/ml}$  glucose oxidase,  $200\ \mu\text{g/ml}$  catalase, and  $4\ \text{mM}$  DTT)) was added to the flow chamber after centrifugation in an Airfuge for 5 minutes at  $119,000 \times g$ . For experiments with the Kin-5-GFP, KCl was excluded from the reaction mixture. The flow chamber was sealed with vacuum grease, and dynamic microtubules were imaged immediately at  $30^{\circ}\text{C}$  using TIRF microscopy. All tubulin products were from Cytoskeleton Inc.

### **TIRF microscopy**

*In vitro* reconstitution assays were imaged on a TIRF microscope setup as described previously [32] or on an iLas2 TIRF setup (see below). In brief, we used an inverted research microscope Nikon Eclipse Ti-E (Nikon) with the perfect focus system (Nikon), equipped with Nikon CFI

Apo TIRF 100x 1.49 N.A. oil objective (Nikon) and controlled with MetaMorph 7.7.5 software (Molecular Devices). The microscope was equipped with TIRF-E motorized TIRF illuminator modified by Roper Scientific France/PICT-IBiSA, Institut Curie. To keep the *in vitro* samples at 30°C, a stage top incubator model INUBG2E-ZILCS (Tokai Hit) was used. For excitation, 491 nm 100 mW Calypso (Cobolt) and 561 nm 100 mW Jive (Cobolt) lasers were used. We used ET-GFP 49002 filter set (Chroma) for imaging of proteins tagged with GFP or ET-mCherry 49008 filter set (Chroma) for imaging of proteins tagged with mCherry. Fluorescence was detected using an EMCCD Evolve 512 camera (Roper Scientific) with the intermediate lens 2.5X (Nikon C mount adaptor 2.5X) or using the CoolSNAP HQ2 CCD camera (Roper Scientific) without an additional lens. In both cases the final magnification was 0.063  $\mu\text{m}/\text{pixel}$ . The iLas2 system (Roper Scientific) is a dual laser illuminator for azimuthal spinning TIRF (or Hilo) illumination and with a custom modification for targeted photomanipulation. This system was installed on Nikon Ti microscope (with the perfect focus system, Nikon), equipped with 150 mW 488 nm laser and 100 mW 561 nm laser, 49002 and 49008 Chroma filter sets, EMCCD Evolve mono FW DELTA 512x512 camera (Roper Scientific) with the intermediate lens 2.5X (Nikon C mount adaptor 2.5X), CCD camera CoolSNAP MYO M-USB-14-AC (Roper Scientific) and controlled with MetaMorph 7.8.8 software (Molecular Device). To keep the *in vitro* samples at 30°C, a stage top incubator model INUBG2E-ZILCS (Tokai Hit) was used. The final resolution using EMCCD camera was 0.065  $\mu\text{m}/\text{pixel}$ , using CCD camera it was 0.045  $\mu\text{m}/\text{pixel}$ .

Both microscopes were equipped with an iLas system (Roper Scientific France/PICT-IBiSA) for FRAP and photoablation. The 532 nm Q-switched pulsed laser (Teem Photonics) was used for photoablation by targeting the laser on the microtubule lattice on the TIRF microscope and next to the lattice to induce damage. For severing or damage, a 20 by 20 pixel box was used for illumination at 10%–15% laser power of the 532 nm pulsed laser with a maximum of 20 Hz at 100% for 100 ms. For severing, the laser was aimed at a point on the microtubule lattice whereas for damage the laser irradiation was performed very close to the microtubule lattice but not directly at the lattice.

### **Intensity quantifications along the lattice at damage site**

For tubulin and CLASP2 $\alpha$ /TOG2-S intensity analysis in Figures 1E and 1F, 6 pixel wide lines were manually drawn at the damage site and the mean intensity values obtained from by Fiji were background subtracted. For both the tubulin and CLASP/TOG2-S intensity analysis, the

mean intensities before damage, after damage and after repair  $I(x)$  were normalized by the mean intensity before damage  $I_{before\,damage}$  yielding mean intensity before damage = 1:

$$I_{norm}(x) = \frac{I(x)}{I_{before\,damage}}$$

For Figures S1C and S1D, the raw intensity values were obtained by manually drawing 10 pixel wide line at the site of damage and the mean value obtained was background subtracted. Similarly, for Figures S1E–S1G, the mean intensity values were recorded at each frame during the time course, background subtracted ( $I_x$ ) and normalized to the mean intensity value before damage to monitor the relative changes in intensity with respect to the intensity before damage:

$$I_{norm}(x) = \frac{I(x)}{I_{before\,damage}} \cdot 100$$

All the intensity profiles were aligned at the point immediately after damage as indicated by the vertical dotted lines and depicted as mean and standard deviation of the normalized intensity at each time point.

For Figures 1H and S1H and S1I, the intensity profiles over time were generated by drawing a 10 pixel wide line at the site of damage to obtain mean intensity values at each time point during acquisition which were subsequently background subtracted ( $I_x$ ). All the intensity profiles were aligned to the time point immediately after damage and normalized to the mean intensity value immediately after damage ( $I_{after\,damage}$ ) (intensity immediately after damage = 1).

$$I_{norm}(x) = \frac{I(x)}{I_{after\,damage}}$$

Mean values and their standard deviation at each time point were then calculated from all the pooled intensity profiles depicted in red in Figures S1H and S1I and the values at 4 time points are plotted in Figure S1J. For the plot in Figure 1H, only the initial linear part of tubulin intensity plots in Figures S1H and S1I were used, for tubulin alone,  $t = 0$  to  $t = 45$  s and for CLASP2 $\alpha$ ,  $t = 0$  to  $t = 20$  s.

### **Intensity analysis for Rhodamine tubulin and CLASP/TOG2-S along a microtubule**

Intensity profiles extraction and alignment of Rh-tubulin and CLASP/TOG2-S (Figures 1G and S1B) were performed using custom written MATLAB routine. First, we obtained microtubule average intensity profile along 6-pixel wide line using Rh-tubulin channel. The

same line was used to get intensity profile in the CLASP2 $\alpha$ /TOG2-S (GFP) channel. After background subtraction each intensity profile  $I(x)$  was normalized

$$I_{norm}(x) = \frac{I(x) - I_{min}}{I_{min_{max}} \cdot 100\%}$$

with respect to the maximum and minimum intensity values along the whole profile. The normalized intensity profiles of different microtubules were aligned so that the plus end tip position was at the origin of the coordinates (Figures 1G and S1B). The plus end position was determined by fitting the Rh-tubulin profile to a Gaussian survival function using equation:

$$I_{norm}(x) = \frac{1}{2} I_{MT} \operatorname{erfc} \left( \frac{x - x_{PF}}{\sqrt{2} \sigma_{PF+PSF}} \right) + I_{BG}$$

where is the complimentary error function,  $I_{MT}$  and  $I_{BG}$  are average intensities of the microtubule and the background,  $x_{PF}$  is the position of plus end tip and  $\sigma_{PF+PSF}$  is the standard deviation of the microtubule tip taper combined with the one for the microscope point spread function.

### Microtubule repair assays with Taxol-stabilized microtubules

Taxol-stabilized microtubules were prepared by polymerizing 29  $\mu$ M porcine brain tubulin containing 13% biotinylated-tubulin and 6% Rhodamine-labeled tubulin in MRB80 buffer supplemented with 2 mM GTP at 37°C for 30 min. Taxol (Sigma-Aldrich) (18  $\mu$ M) was then added to the tubulin-GTP mix and seeds were then sedimented by centrifugation at 16,200  $\times$  g for 15 min at room temperature. Finally, the pellet was resuspended in warm 10  $\mu$ M Taxol solution in MRB80 buffer. Taxol-stabilized microtubules were then wrapped with aluminum foil and stored at room temperature for a maximum of 2 weeks.

For tubulin incorporation experiments, Taxol-stabilized microtubules were immobilized in the flow chamber and were washed immediately with the wash buffer (80 mM PIPES, 4 mM MgCl<sub>2</sub>, 1 mM EGTA, 50 mM KCl, 0.5 mg/ml  $\kappa$ -casein, 0.1% methylcellulose, and oxygen scavenger mix (50 mM glucose, 400  $\mu$ g/ml glucose-oxidase, 200  $\mu$ g/ml catalase, and 4 mM DTT)). Time-lapse movies were immediately started on the TIRF microscope at 30°C at a 2 s time interval with 100 ms exposure time for 25 minutes. During the imaging session, microtubules were incubated in the washing buffer without Taxol and tubulin for 1.5 min to promote lattice defect formation. Subsequently, they were incubated in MRB80 buffer supplemented with 5  $\mu$ M HiLyte Fluor 488-labeled tubulin, 50 mM KCl, 1 mM GTP, 0.5 mg/ml  $\kappa$ -casein, 0.1% methylcellulose, and oxygen scavenger mix (50 mM glucose,



400 µg/ml glucose-oxidase, 200 µg/ml catalase, and 4 mM DTT) with or without 30 nM mCherry-CLASP2α or 30 nM mCherry-TOG2-S for 10 min to promote repair. Finally, the residual free green tubulin was washed out with the wash buffer supplemented with 25% glycerol to prevent microtubule depolymerization and to clearly visualize incorporation of green tubulin into the damaged microtubule lattices. In the analysis, defects longer than 1 µm in size, detectable as gaps in the microtubule, where we can clearly see incorporation at both plus and minus ends of the defect site were considered. Partial repair was defined as an event where we did not see a continuous signal of incorporated tubulin in the green channel along the gap at the repair site after the 25% glycerol washing step.

### **Microtubule repair assays with mechanically damaged microtubules**

#### *Tubulin purification and labeling*

For microtubule bending experiments, tubulin was purified from fresh bovine brain by three cycles of temperature-dependent assembly and disassembly in Brinkley Buffer 80 (BRB80 buffer: 80 mM PIPES, pH 6.8, 1 mM EGTA, 1 mM MgCl<sub>2</sub> plus 1 mM GTP). MAP-free brain tubulin was purified by cation-exchange chromatography (Fractogel EMD SO, 650 M, Merck) in 50 mM PIPES, pH 6.8, supplemented with 1 mM MgCl<sub>2</sub> and 1 mM EGTA. Purified tubulin was obtained after a cycle of polymerization and depolymerization. Fluorescent tubulin (ATTO-565-labeled tubulin) and biotinylated tubulin were prepared as follows: Microtubules were polymerized from brain tubulin at 37°C for 30 min and layered onto cushions of 0.1 M Na-HEPES, pH 8.6, 1 mM MgCl<sub>2</sub>, 1 mM EGTA, 60% v/v glycerol, and sedimented by high-speed centrifugation at 30°C. Then, microtubules were resuspended in 0.1 M Na-HEPES, pH 8.6, 1 mM NHS-ATTO (ATTO Tec), or NHS-Biotin (Pierce) for 10 min at 37°C. The labeling reaction was stopped using 2 volumes of 2x BRB80, containing 100 mM potassium glutamate and 40% v/v glycerol, and then microtubules were sedimented onto cushions of BRB80 supplemented with 60% glycerol. Microtubules were resuspended in cold BRB80. Microtubules were then depolymerized and a second cycle of polymerization and depolymerization was performed before use.

#### *Cover glass micropatterning*

The micropatterning technique was adapted from [28]. Cover glasses were cleaned by successive chemical treatments: 30 min in acetone, 15 min in ethanol (96%), rinsing in ultrapure water, 2 h in Hellmanex III (2% in water, Hellmanex), and rinsing in ultrapure water.

Cover glasses were dried using nitrogen gas flow and incubated for three days in a solution of tri-ethoxy-silane-PEG (30 kDa, PSB-2014, Creative PEGWorks) 1 mg/ml in ethanol (96%) and 0.02% HCl, with gentle agitation at room temperature. Cover glasses were then successively washed in ethanol and ultrapure water, dried with nitrogen gas, and stored at 4°C. Passivated cover glasses were placed into contact with a photomask (Toppan) with a custom-made vacuum-compatible holder and exposed to deep UV (7 mW/cm<sup>2</sup> at 184 nm, Jelight) for 2.5 min. Deep UV exposure through the transparent micropatterns on the photomask created oxidized micropatterned regions on the PEG-coated cover glasses.

#### *Microfluidic circuit fabrication and flow control*

The microfluidic device was fabricated in polydimethylsiloxane (PDMS, Sylgard 184, Dow Corning) using standard photolithography and soft lithography. The master mold was fabricated by patterning 85 µm thick negative photoresist (SU8 3050, Microchem, MA) by photolithography. A positive replica was fabricated by replica molding PDMS against the master. Prior to molding, the master mold was silanized with trichloro(1H,1H,2H,2H-perfluorooctyl)silane (Sigma) for easier lift-off. Four inlet and outlet ports were made in the PDMS device using 0.5 mm soft substrate punches (UniCore 0.5, Ted Pella, Redding, CA). The PDMS device was then brought into contact with a micropatterned cover glass and placed in a custom-made holder that could be fitted on the microscope stage. A transparent plate was fixed on the holder to apply gentle pressure on the chip in order to avoid leaks without the need of permanent bonding to the cover glass. The top plate had four openings for the inlet and outlet tubing. Teflon tubing (Tefzel, inner diameter: 0.03'', outer diameter: 1/16'', Upchurch Scientific) was inserted into the two ports serving as outlets. Tubing with 0.01'' inner and 1/16'' outer diameter was used to connect the inlets via two three-way valves (Omnifit Labware, Cambridge, UK) that could be opened and closed by hand to a computer-controlled microfluidic pump (MFCS-4C, Fluigent, Villejuif, France). Flow inside the chip was controlled using the MFCS-Flex control software (Fluigent). Custom rubber pieces that fit onto the tubing were used to close the open ends of the outlet tubing when needed.

#### *Microtubule growth on micropatterns*

Microtubule seeds were prepared at 10 µM tubulin concentration (30% ATTO-565 or ATTO-488-labeled tubulin and 70% biotinylated tubulin) in BRB80 supplemented with 0.5 mM GMPCPP at 37°C for 1 h. The seeds were incubated with 1 µM Taxotere (Sigma) at room temperature for 30 min and were then sedimented by high speed centrifugation at 30°C and

resuspended in BRB80 supplemented with 0.5 mM GMPCPP and 1  $\mu$ M Taxotere. Seeds were stored in liquid nitrogen and quickly warmed to 37°C before use.

The holder with the chip was fixed on the stage and the chip was perfused with NeutrAvidin (25  $\mu$ g/ml in BRB80, Pierce), then washed with BRB80, passivated for 20 s with PLL-g-PEG (PLL 20K-G35-PEG2K, Jenkam Technology) at 0.1 mg/ml in 10 mM Na-HEPES (pH 7.4), and washed again with BRB80. Microtubule seeds were flown into the chamber at high flow rates perpendicular to the micropatterned lines to ensure proper orientation of the seeds. Unattached seeds were washed out immediately using BRB80 supplemented with 1% BSA. Seeds were elongated with a mixture containing 27  $\mu$ M tubulin (20% labeled) in BRB80 supplemented with 50 mM NaCl, 25 mM NaPi, 1 mM GTP, an oxygen scavenger cocktail (20 mM DTT, 1.2 mg/ml glucose, 8  $\mu$ g/ml catalase and 40  $\mu$ g/ml glucose oxidase), 0.1% BSA and 0.033% methyl cellulose (1500 cp, Sigma). Microtubules were bent by an orthogonal fluid flow either using the same mixture supplemented with 0.02% red fluorescent beads (0.52  $\mu$ m diameter, Thermo Scientific) or supplementing it additionally with 30 nM GFP-CLASP2 $\alpha$ .

### *Imaging*

Microtubules were visualized using an objective-based azimuthal ILAS2 TIRF microscope (Nikon Eclipse Ti, modified by Roper Scientific) and an Evolve 512 camera (Photometrics). The microscope stage was kept at 35°C using a warm stage controller (LINKAM MC60). Excitation was achieved using 491 and 561 nm lasers (Optical Insights). Time-lapse recording was performed using Metamorph software (version 7.7.5, Universal Imaging). Movies were processed to improve the signal/noise ratio (smooth and subtract background functions of ImageJ, version 2.2.0-rc-65 / 1.51 s).

### *Measurement of microtubule persistence length*

The microtubule is described as an inextensible slender filament with length  $L$  and bending rigidity  $\kappa$ , which is bent in two dimensions by the fluid flow. Its elastic energy  $E$  is given by

$$E(\mathbf{r}) = \int_0^L \left\{ \frac{\kappa}{2} \left( \frac{d^2\mathbf{r}}{ds^2} \right)^2 + \frac{\lambda}{2} \left[ \left( \frac{d\mathbf{r}}{ds} \right)^2 - 1 \right] \right\} ds \quad \text{Equation 1}$$

The vector  $\mathbf{r}(s)$  denotes the position of the filament parameterized by the arc length  $s$  and  $\lambda$  denotes a Lagrange multiplier associated with the inextensibility condition  $|\mathbf{dr}/ds| = 1$ . The force exerted on the filament is given by the functional variation of the potential  $E$  with respect to the filament position vector  $\mathbf{r}$

$$\mathbf{F}_B = -\frac{\delta E}{\delta \mathbf{r}} \quad \text{Equation 2}$$

The filament orientation is fixed by the seed orientation at  $s = 0$ , whereas the other end of the filament at  $s = L$  is force-free. The hydrodynamic drag exerted by the fluid flow on a slender filament is given by

$$\mathbf{F}_H = g\mu \left( \mathbf{I} - \frac{1}{2} \frac{d\mathbf{r}}{ds} \otimes \frac{d\mathbf{r}}{ds} \right) \mathbf{v}_b \quad \text{Equation 3}$$

where  $\mathbf{v}_b$  denotes the velocity field measured by the bead displacements,  $\mu$  denotes the viscosity of the fluid and  $g$  denotes a geometrical factor of the order of 1, which depends on the distance of the filament from the surface, the radius of the filament and the distance of the beads from the surface.  $\otimes$  denotes the outer product and  $\mathbf{I}$  is the identity tensor. In mechanical equilibrium

$$\mathbf{F}_B + \mathbf{F}_H = \mathbf{0} \quad \text{Equation 4}$$

which determines the equilibrium shape of the filament subject to the appropriate boundary conditions. The filament rigidity was determined by solving Equations 1, 2, 3, and 4 using the AUTO-07p software package and by minimizing the function

$$\omega^2(\mathbf{k}) = \frac{1}{L} \int_0^L [\mathbf{r}_R(s) - \mathbf{r}(s)]^2 ds \quad \text{Equation 5}$$

where  $\mathbf{r}_R(s)$  denotes the measured position of the filament. The persistence length is then given by  $L_p = \kappa / (k_B T)$ .  $\omega$  is a measure for the distance between the shapes of two microtubules. In the fitting routine for the experimentally measured microtubule shapes,  $\omega$  denotes the distance between the shape of the experimental snake and an inextensible flexible filament subjected to the same flow as the experimental snake. We assumed that the origin of the microtubule was clamped in the direction of the seed. To correct for a measurement error of the microtubule origin, we optimized Equation 5 also for the position of the microtubule origin.

### Mass spectrometry

Purified CLASP2 $\alpha$  was run on SDS-PAGE gel. After in-gel digestion, samples were resuspended in 10% formic acid (FA)/5% DMSO and were analyzed using an Agilent 1290 Infinity (Agilent Technologies) LC connected to an Orbitrap Q-Exactive HF mass spectrometer (Thermo Fisher Scientific). Samples were first trapped (Dr Maisch Reprosil C18, 3  $\mu\text{m}$ , 2 cm x 100  $\mu\text{m}$ ) before being separated on an analytical column (Agilent Poroshell EC-C18, 2.7  $\mu\text{m}$ , 40 cm x 50  $\mu\text{m}$ ), using a gradient of 50 min at a column flow of 150 nL/min. The mass

spectrometer was used in a data-dependent mode, automatically switching between MS and MS/MS. Full scan MS spectra from  $m/z$  375 – 1600 were acquired at a resolution of 60.000 after the accumulation to a target value of 3E6. HCD fragmentation of up to 15 most intense precursor ions was performed at normalized collision energy of 25% after the accumulation to a target value of 1e5. MS2 was acquired at a resolution of 15.000 and dynamic exclusion was enabled. Raw files were processed using Proteome Discoverer 1.4 (version 1.4.0.288, Thermo Fisher Scientific). The database search was performed using Mascot (version 2.4.1, Matrix Science, UK) against the Uniprot human database (version 2.4). Carbamidomethylation of cysteines was set as a fixed modification and oxidation of methionine was set as a variable modification. Trypsin was specified as enzyme and up to two miss cleavages were allowed. Data filtering was performed using percolator, resulting in 1% false discovery rate (FDR). Additional filters were; search engine rank 1 peptides and ion score > 20.

### **Quantification and Statistical Analysis**

Kymographs were generated using the ImageJ plugin KymoResliceWide (<https://github.com/ekatrakha/KymoResliceWide>). MT growth rate was determined from kymographs using an optimized version of the custom-made JAVA plug in for ImageJ as described previously [12]. Number of samples, replicates and error bars have been indicated in the figure legends. Spearman correlation test was performed to test for microtubule softening. All statistical analyses were performed using GraphPad Prism 7 and the details of statistical tests and the resulting p values were included in the figure legends.

### **Data and Code Availability**

ImageJ plugin KymoResliceWide is available online at <https://github.com/ekatrakha/KymoResliceWide>. All data supporting the conclusions of the current study are available from the corresponding author on request.

### **Acknowledgments**

We thank Dr. Kai Jiang, Wuhan University for suggesting experiments with the Kin-5 dimer and Prof. William Hancock, Pennsylvania State University for the kind gift of the Kin-5 dimer construct. This work was supported by the European Research Council Synergy grant 609822 to A. Akhmanova and European Research Council Consolidator grant 771599 to M.T.

### **Author Contributions**

A. Aher, D.R., L.S., M.T., L.B., and A. Akhmanova designed experiments and wrote the paper. A. Aher, D.R., L.S., J.G., K.J., Q.L., and M.A. performed experiments and data analysis, and A. Akhmanova coordinated the project.

**Declaration of Interests**

The authors declare no competing interests.

**Supplemental Information**

Supplemental Information can be found online at <https://doi.org/10.1016/j.cub.2020.03.070>.

## References

1. Desai A., Mitchison T.J. Microtubule polymerization dynamics. *Annu. Rev. Cell Dev. Biol.* 1997;**13**:83–117. [PubMed: 9442869]
2. Schaedel L., John K., Gaillard J., Nachury M.V., Blanchoin L., Théry M. Microtubules self-repair in response to mechanical stress. *Nat. Mater.* 2015;**14**:1156–1163. [PMCID: PMC4620915] [PubMed: 26343914]
3. Aumeier C., Schaedel L., Gaillard J., John K., Blanchoin L., Théry M. Self-repair promotes microtubule rescue. *Nat. Cell Biol.* 2016;**18**:1054–1064. [PMCID: PMC5045721] [PubMed: 27617929]
4. Schaedel L., Triclin S., Chrétien D., Abrieu A., Aumeier C., Gaillard J., Blanchoin L., Théry M., John K. Lattice defects induce microtubule self-renewal. *Nat. Phys.* 2019;**15**:830–838. [PMCID: PMC6924994] [PubMed: 31867047]
5. Aher A., Akhmanova A. Tipping microtubule dynamics, one protofilament at a time. *Curr. Opin. Cell Biol.* 2018;**50**:86–93. [PubMed: 29573640]
6. Vemu A., Szczesna E., Zehr E.A., Spector J.O., Grigorieff N., Deaconescu A.M., Roll-Mecak A. Severing enzymes amplify microtubule arrays through lattice GTP-tubulin incorporation. *Science.* 2018;**361**:eaau1504. [PMCID: PMC6510489] [PubMed: 30139843]
7. Tropini C., Roth E.A., Zanic M., Gardner M.K., Howard J. Islands containing slowly hydrolyzable GTP analogs promote microtubule rescues. *PLoS ONE.* 2012;**7**:e30103. [PMCID: PMC3260198] [PubMed: 22272281]
8. Dimitrov A., Quesnoit M., Moutel S., Cantaloube I., Poüs C., Perez F. Detection of GTP-tubulin conformation in vivo reveals a role for GTP remnants in microtubule rescues. *Science.* 2008;**322**:1353–1356. [PubMed: 18927356]
9. de Forges H., Pilon A., Cantaloube I., Pallandre A., Haghiri-Gosnet A.M., Perez F., Poüs C. Localized Mechanical Stress Promotes Microtubule Rescue. *Curr. Biol.* 2016;**26**:3399–3406. [PubMed: 27916523]
10. Lawrence E.J., Arpag G., Norris S.R., Zanic M. Human CLASP2 specifically regulates microtubule catastrophe and rescue. *Mol. Biol. Cell.* 2018;**29**:1168–1177. [PMCID: PMC5935067] [PubMed: 29540526]
11. Lawrence E.J., Zanic M. Rescuing microtubules from the brink of catastrophe: CLASPs lead the way. *Curr. Opin. Cell Biol.* 2019;**56**:94–101. [PMCID: PMC6370552] [PubMed: 30453184]
12. Aher A., Kok M., Sharma A., Rai A., Olieric N., Rodriguez-Garcia R., Katrukha E.A., Weinert T., Olieric V., Kapitein L.C. CLASP Suppresses Microtubule Catastrophes through a Single TOG Domain. *Dev. Cell.* 2018;**46**:40–58.e8. [PMCID: PMC6035287] [PubMed: 29937387]
13. Al-Bassam J., Kim H., Brouhard G., van Oijen A., Harrison S.C., Chang F. CLASP promotes microtubule rescue by recruiting tubulin dimers to the microtubule. *Dev. Cell.* 2010;**19**:245–258. [PMCID: PMC3156696] [PubMed: 20708587]
14. Moriwaki T., Goshima G. Five factors can reconstitute all three phases of microtubule polymerization dynamics. *J. Cell Biol.* 2016;**215**:357–368. [PMCID: PMC5100292] [PubMed: 27799364]

15. Yu N., Signorile L., Basu S., Ottema S., Lebbink J.H.G., Leslie K., Smal I., Dekkers D., Demmers J., Galjart N. Isolation of Functional Tubulin Dimers and of Tubulin-Associated Proteins from Mammalian Cells. *Curr. Biol.* 2016;**26**:1728–1736. [PubMed: 27291054]
16. Galjart N. CLIPs and CLASPs and cellular dynamics. *Nat. Rev. Mol. Cell Biol.* 2005;**6**:487–498. [PubMed: 15928712]
17. Al-Bassam J., Chang F. Regulation of microtubule dynamics by TOG-domain proteins XMAP215/Dis1 and CLASP. *Trends Cell Biol.* 2011;**21**:604–614. [PMCID: PMC3202638] [PubMed: 21782439]
18. Bieling P., Laan L., Schek H., Munteanu E.L., Sandblad L., Dogterom M., Brunner D., Surrey T. Reconstitution of a microtubule plus-end tracking system in vitro. *Nature.* 2007;**450**:1100–1105. [PubMed: 18059460]
19. Akhmanova A., Hoogenraad C.C., Drabek K., Stepanova T., Dortland B., Verkerk T., Vermeulen W., Burgering B.M., De Zeeuw C.I., Grosveld F., Galjart N. Clasps are CLIP-115 and -170 associating proteins involved in the regional regulation of microtubule dynamics in motile fibroblasts. *Cell.* 2001;**104**:923–935. [PubMed: 11290329]
20. Walker R.A., Inoué S., Salmon E.D. Asymmetric behavior of severed microtubule ends after ultraviolet-microbeam irradiation of individual microtubules in vitro. *J. Cell Biol.* 1989;**108**:931–937. [PMCID: PMC2115382] [PubMed: 2921286]
21. Mimori-Kiyosue Y., Grigoriev I., Lansbergen G., Sasaki H., Matsui C., Severin F., Galjart N., Grosveld F., Vorobjev I., Tsukita S., Akhmanova A. CLASP1 and CLASP2 bind to EB1 and regulate microtubule plus-end dynamics at the cell cortex. *J. Cell Biol.* 2005;**168**:141–153. [PMCID: PMC2171674] [PubMed: 15631994]
22. Chen Y., Hancock W.O. Kinesin-5 is a microtubule polymerase. *Nat. Commun.* 2015;**6**:8160. [PMCID: PMC4600729] [PubMed: 26437877]
23. Chen G.Y., Cleary J.M., Asenjo A.B., Chen Y., Mascaro J.A., Arginteanu D.F.J., Sosa H., Hancock W.O. Kinesin-5 Promotes Microtubule Nucleation and Assembly by Stabilizing a Lattice-Competent Conformation of Tubulin. *Curr. Biol.* 2019;**29**:2259–2269.e4. [PMCID: PMC6684259] [PubMed: 31280993]
24. Arnal I., Wade R.H. How does taxol stabilize microtubules? *Curr. Biol.* 1995;**5**:900–908. [PubMed: 7583148]
25. Gramlich M.W., Conway L., Liang W.H., Labastide J.A., King S.J., Xu J., Ross J.L. Single Molecule Investigation of Kinesin-1 Motility Using Engineered Microtubule Defects. *Sci. Rep.* 2017;**7**:44290. [PMCID: PMC5347089] [PubMed: 28287156]
26. Liang W.H., Li Q., Rifat Faysal K.M., King S.J., Gopinathan A., Xu J. Microtubule Defects Influence Kinesin-Based Transport In Vitro. *Biophys. J.* 2016;**110**:2229–2240. [PMCID: PMC4880806] [PubMed: 27224488]
27. Reid T.A., Coombes C., Gardner M.K. Manipulation and quantification of microtubule lattice integrity. *Biol. Open.* 2017;**6**:1245–1256. [PMCID: PMC5576077] [PubMed: 28663236]
28. Portran D., Schaedel L., Xu Z., Théry M., Nachury M.V. Tubulin acetylation protects long-lived microtubules against mechanical ageing. *Nat. Cell Biol.* 2017;**19**:391–398. [PMCID: PMC5376231] [PubMed: 28250419]



29. Leano J.B., Rogers S.L., Slep K.C. A cryptic TOG domain with a distinct architecture underlies CLASP-dependent bipolar spindle formation. *Structure*. 2013;**21**:939–950. [PMCID: PMC3731388] [PubMed: 23727231]
30. Efimov A., Kharitonov A., Efimova N., Loncarek J., Miller P.M., Andreyeva N., Gleeson P., Galjart N., Maia A.R., McLeod I.X. Asymmetric CLASP-dependent nucleation of noncentrosomal microtubules at the trans-Golgi network. *Dev. Cell*. 2007;**12**:917–930. [PMCID: PMC2705290] [PubMed: 17543864]
31. Grimaldi A.D., Maki T., Fitton B.P., Roth D., Yampolsky D., Davidson M.W., Svitkina T., Straube A., Hayashi I., Kaverina I. CLASPs are required for proper microtubule localization of end-binding proteins. *Dev. Cell*. 2014;**30**:343–352. [PMCID: PMC4133696] [PubMed: 25117684]
32. Mohan R., Katrukha E.A., Doodhi H., Smal I., Meijering E., Kapitein L.C., Steinmetz M.O., Akhmanova A. End-binding proteins sensitize microtubules to the action of microtubule-targeting agents. *Proc. Natl. Acad. Sci. USA*. 2013;**110**:8900–8905. [PMCID: PMC3670352] [PubMed: 23674690]

## Supplementary Figures

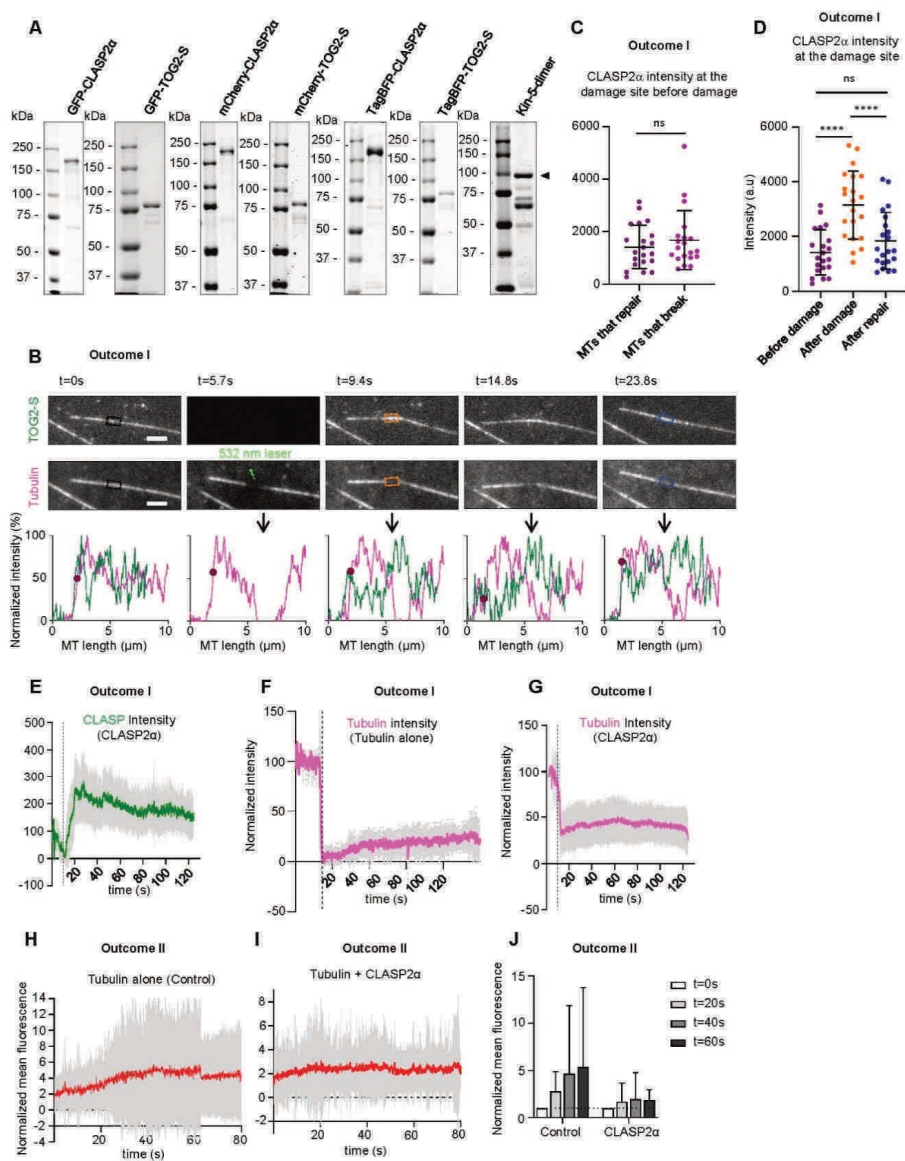


**Figure S1. Characterization of CLASP binding and tubulin incorporation at the sites of microtubule damage, related to Figure 1.**

(A) Proteins purified from HEK293T cells (CLASP2α and TOG2-S constructs) and *E.coli* (Kin-5-dimer) used in this study analyzed by SDS-PAGE.

(B) Stills from a time lapse of a dynamic microtubule grown in the presence of 30 nM GFP-TOG2-S (upper panel) and Rhodamine-tubulin (lower panel) damaged at a point along the lattice as indicated. Intensity profiles along the microtubule for the TOG2-S and tubulin channel at different

time points are shown below, with the arrow pointing to the site of photodamage. The purple circle on the plot indicates the end of the microtubule. Scale bar: 2  $\mu\text{m}$ .

(C) Fluorescence intensity of CLASP2 $\alpha$  at the irradiated site along the lattice before damage for dynamic microtubules grown in the presence of 30 nM GFP-CLASP2 $\alpha$  that were either repaired ( $n=21$  microtubules) or broke ( $n=20$  microtubules). Error bars denote SD.

(D) Fluorescence intensity of CLASP2 $\alpha$  at the photo-damage site along the lattice for dynamic microtubules grown in the presence of 30 nM GFP-CLASP2 $\alpha$  before damage, after damage and after repair. The same, but normalized data are shown in Figure 1E. Error bars denote SD.  $n=21$  microtubules.

(E) Mean intensity of CLASP2 $\alpha$  normalized to the intensity before damage (set at 100) over time at the photodamage site for microtubules that bent to an angle  $>10^\circ$  at the point of photodamage and subsequently straightened (Outcome I).  $n=21$  microtubules.

(F, G) Mean tubulin fluorescence intensity normalized to the intensity before damage (set at 100) over time at the photodamage site for dynamic microtubules grown in the presence of tubulin alone (F) or together with 30 nM GFP-CLASP2 $\alpha$  (G). Only microtubules that bent to an angle  $>10^\circ$  at the point of photodamage and subsequently straightened (Outcome I) are included. All the intensity profiles were aligned at the point immediately after damage as indicated by the vertical dotted lines. Tubulin alone:  $n=4$  microtubules; CLASP2 $\alpha$ :  $n=21$  microtubules.

(H,I) Mean fluorescence intensity at the photodamage site over time normalized to the intensity immediately after damage (set at 1) for microtubules grown in the presence of Rhodamine-tubulin alone (H) ( $n=35$  microtubules from 2 experiments) or together with 30 nM GFP-CLASP2 $\alpha$  (I) ( $n=44$  microtubules from 2 experiments). Red line shows the mean values, grey bars indicate the standard deviation.

(J) Tubulin intensity at the photodamage site after repair with respect to the intensity immediately after damage at the indicated time points for microtubules grown in the presence of Rhodamine-tubulin alone ( $n=35$  microtubules from 2 experiments) or together with 30 nM GFP-CLASP2 $\alpha$  ( $n=44$  microtubules from 2 experiments). Error bars represent SD. For all plots \*\*\*\* $p<0.0001$ , \*\*\* $p=0.001$  and ns=no significant difference with control, Mann Whitney U test. See also Video S1 and S2.

**Figure S2. CLASP protects severed microtubules from depolymerization, related to Figure 1.**

(A) Stills and the corresponding kymograph of a microtubule grown in the presence of Rhodamine-tubulin together with GFP-TOG2-S (30 nM) ablated with a 532 nm laser as indicated. Scale bars: still image, 2  $\mu\text{m}$ ; kymograph, 4  $\mu\text{m}$  (horizontal) and 10 sec (vertical). Dotted yellow lines point to the time point of the still in the kymograph.

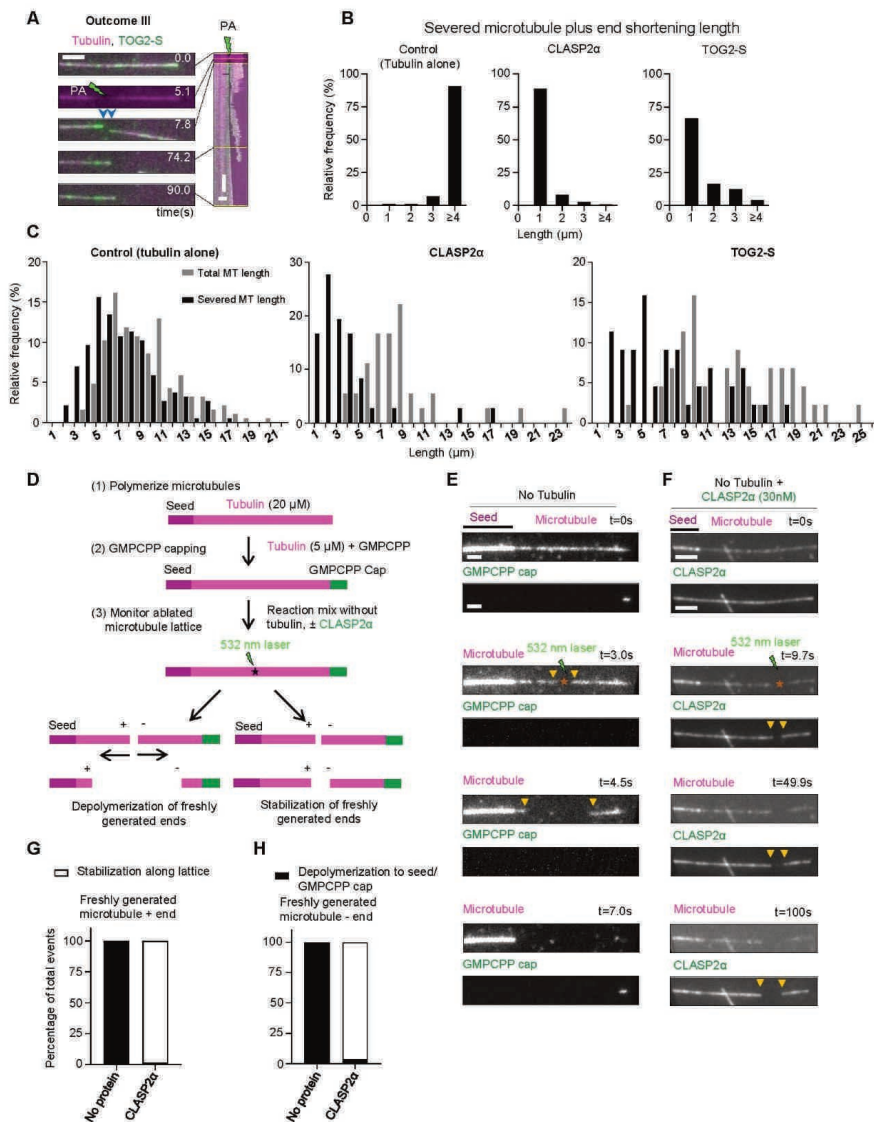
(B) Plots showing the relative frequencies of microtubule plus end shortening lengths after laser-mediated severing of dynamic microtubules grown in the presence of Rhodamine-tubulin alone or together with either 30 nM GFP-CLASP2 $\alpha$  or with 30 nM TOG2-S.  $n=186$  microtubules analyzed from 3 experiments for tubulin alone,  $n=36$  microtubules analyzed from 3 experiments for CLASP2 $\alpha$  and  $n=48$  microtubules analyzed from 8 experiments for TOG2-S.

(C) Plot showing the relative frequencies of total microtubule lengths (grey) and severed microtubule lengths (black) for microtubules grown in the presence of Rhodamine-tubulin alone (left panel) or together with either 30 nM GFP-CLASP2 $\alpha$  (middle panel) or with 30 nM GFP--TOG2-S (right panel).  $n=186$  microtubules analyzed from 3 experiments for tubulin alone,  $n=36$  microtubules analyzed from 3 experiments for CLASP2 $\alpha$  and  $n=48$  microtubules analyzed from 8 experiments for TOG2-S.

(D) Schematic for an experiment to monitor microtubule lattice damage in the absence of tubulin. Microtubules were polymerized in the presence of Rhodamine tubulin followed by capping with GMPCPP. Tubulin was then washed out and microtubules were ablated along the lattice either in the presence of reaction mixture alone or together with 30 nM GFP-CLASP2 $\alpha$ .

(E,F) Stills from a time lapse showing microtubules and GMPCPP cap/ CLASP2 $\alpha$  and GMPCPP cap at different time points. Yellow arrowheads indicate the position of the freshly generated ends upon photoablation. Scale bar: 2  $\mu$ m.

(G,H) Plot showing the outcome for freshly generated plus end (G) and minus end (H) of a microtubule upon laser induced photo-ablation in the presence of reaction mixture without tubulin (no protein) alone ( $n=29$  microtubules from 2 experiments) or together with 30 nM GFP-CLASP2 $\alpha$  ( $n=56$  from 2 experiments).



## Information for supplementary materials available online

### Supplementary Video Legends

#### **Video S1. CLASP Promotes Repair of Microtubule Lattices Damaged by Laser Illumination, Related to Figure 1:**

Microtubule lattice repair at the laser induced damage site in a microtubule grown in the presence of Rhodamine-tubulin alone (upper panel, corresponds to Figure 1C), a microtubule grown in the presence of Rhodamine-tubulin (magenta) and 30 nM GFP-CLASP2 $\alpha$  (green) (middle panel, corresponds to Figure 1G) and a microtubule grown in the presence of Rhodamine-tubulin (magenta) and 30 nM GFP-TOG2-S (green) (lowermost panel, corresponds to Figure 1I). Yellow arrowheads point to the site of laser induced photodamage. Images were acquired using a TIRF microscope in a stream mode at a 100 ms interval. Video is sped up 50 times. Time is shown in seconds.

#### **Video S2. CLASP Prevents Depolymerization of Laser-Severed Microtubules, Related to Figure 1:**

Microtubules were ablated with a laser in the presence of Rhodamine-tubulin alone (upper panel, corresponds to Figure 1I), in the presence of Rhodamine-tubulin (magenta) and 30 nM GFP-CLASP2 $\alpha$  (green) (middle panel, corresponds to Figure 1J) or in the presence of Rhodamine-tubulin (magenta) and 30 nM GFP-TOG2-S (green) (lower panel, corresponds to Figure S2A). Yellow asterisks indicate the site of laser severing and the yellow arrowheads indicate the position of microtubule breakage. Images were acquired using a TIRF microscope in a stream mode at a 100 ms interval. Video is sped up 90 times. Time is shown in seconds.

#### **Video S3. CLASP Promotes Formation of Complete Microtubules from Partial Protofilament Assemblies, Related to Figure 2:**

Microtubules were grown in the presence of Rhodamine-tubulin (magenta) and 30 nM Kin-5-GFP dimer (green) (upper left panel, corresponds to Figure 2B), in the presence of Rhodamine-tubulin (magenta), 30 nM Kin-5-GFP (green) and 30 nM TagBFP-CLASP2 $\alpha$  (blue) (upper right panel, corresponds to Figure 2E), in the presence of Rhodamine-tubulin (magenta), 30 nM Kin-5-GFP (green) and 30 nM TagBFP-TOG2-S (blue) (bottom left panel, corresponds to Figure 2F) or in the presence of Rhodamine-tubulin (magenta), 30 nM Kin-5-GFP (green) and 100 nM TagBFP-TOG2-S (blue) (lower-right panel). Yellow arrowheads indicate the position of microtubule curling induced by the Kinesin-5 dimer. Images were acquired using a TIRF microscope at a 4 s interval. Video is sped up 10 times. Time is shown in seconds.

#### **Video S4. CLASP Promotes Complete Repair of Damaged Microtubule Lattices, Related to Figure 3:**

Taxol-stabilized microtubules (magenta) were initially incubated in a buffer without Taxol and tubulin for 1.5 min and then transferred into a buffer with either 5  $\mu$ M HiLyte 488-labeled tubulin alone (green) (upper panel, corresponds to Figure 3B), 5  $\mu$ M HiLyte 488-labeled tubulin together with 30 nM mCherry-CLASP2 $\alpha$  (middle panel, corresponds to Figure 3C) or 5  $\mu$ M HiLyte 488 labeled tubulin together with 30 nM mCherry-TOG2-S (lower panel, corresponds to Figure 3D) for 10 minutes followed by a 25% glycerol wash. Green tubulin incorporation into the lattice is indicated by numbers for the upper and middle panels and by an asterisk for the lower panel. Images were acquired using a TIRF microscope at a 2 s interval. Video is sped up 75 times. Time is shown in minutes.

#### **Video S5. CLASP2 $\alpha$ Inhibits Microtubule Softening Induced by Hydrodynamic Flow, Related to Figure 4:**

Microtubules (magenta) grown from seeds on micropatterned coverglass bent by orthogonal flow. Microtubules were bent for ten seconds by applying a fluid flow with tubulin alone (left panel, corresponds to Figure 4D) or with 30 nM GFP-CLASP2 $\alpha$  (right panel, corresponds to Figure 4E). The flow was stopped for ten seconds before repeating the bending cycle. This was repeated for 6 cycles.

Scale bar: 3  $\mu$ m Images were acquired using a TIRF microscope at a 0.3 s interval. Video is sped up 17 times. Time is shown in seconds.

### Supplementary Table Legend

**Table S1. Mass Spectrometry Analysis of StrepII-GFP-CLASP2a Purified from HEK293T Cells, Related to Figure 1:**

The hits with more than 10 peptides are listed.

### Key Resources Table

| REAGENT or RESOURCE                                  | SOURCE                | IDENTIFIER                                 |
|--|-----------------------|--|
| <b>Bacterial and Virus Strains</b>                   |                       |  |
| <i>E.coli</i> BL21 (DE3)                             | Agilent               | 200131                                     |
| <b>Chemicals, Peptides, and Recombinant Proteins</b> |                       |  |
| cOmplete™, EDTA-free Protease Inhibitor Cocktail     | Roche                 | Cat# 4693116001                            |
| Tubulin Porcine                                      | Cytoskeleton          | Cat# T240-C                                |
| Tubulin Porcine TRITC                                | Cytoskeleton          | Cat# TL590M                                |
| Tubulin Porcine HiLyte 488™                          | Cytoskeleton          | Cat# TL488M                                |
| Tubulin Porcine HiLyte 647™                          | Cytoskeleton          | Cat# TL670M                                |
| Tubulin Porcine (Biotin)                             | Cytoskeleton          | Cat# T333P                                 |
| GMPCPP   | Jena Biosciences      | Cat# NU-405L                               |
| GTP  | Sigma-Aldrich         | Cat# G8877                                 |
| Glucose oxidase                                      | Sigma-Aldrich         | Cat# G7141                                 |
| Catalase   | Sigma-Aldrich         | Cat# C9322                                 |
| DTT  | Sigma-Aldrich         | Cat# R0861                                 |
| k-casein   | Sigma-Aldrich         | Cat# C0406                                 |
| StrepTactin Sepharose High Performance               | GE Healthcare         | Cat# 28-9355-99                            |
| NeutrAvidin  | Invitrogen            | Cat# A-2666                                |
| Taxol  | Sigma-Aldrich         | Cat# T7402                                 |
| Polyethyleneimine                                    | Polysciences          | Cat# 24765-2                               |
| Methyl cellulose, 4000 cp                            | Sigma-Aldrich         | Cat# M0512                                 |
| d-Desthiobiotin                                      | Sigma-Aldrich         | Cat# D1411                                 |
| Coomassie Brilliant Blue                             | SERVA                 | Cat# 17525.02                              |
| PLL-PEG-biotin                                       | Susos AG, Switzerland | PLL(20)-g[3.5]-PEG(2)/PEG(3.4)-biotin(50%) |

| REAGENT or RESOURCE                                  | SOURCE               | IDENTIFIER                 |
|--|----------------------|----------------------------|
| Tubulin bovine                                       | [4]                  | N/A                        |
| Fractogel EMD SO, 650 M,                             | Merck                | Cat# 116882                |
| NHS-ATTO   | ATTO Tec             | Cat# AD488-35 and AD565-35 |
| NHS-Biotin   | Thermo Scientific    | N/A                        |
| tri-ethoxy-silane-PEG (30 kDa)                       | Creative PEGWorks    | PSB-2014                   |
| Hellmanex III  | HellmaAnalytics      | Cat# 9-307-011-4-507       |
| Taxotere   | Sigma                | Cat# T1912                 |
| SU-8 3050  | Chimie Tech Services | Cat# SU8-3050/0.5          |
| trichloro(1H,1H,2H,2H-perfluorooctyl)silane          | Sigma                | Cat# 448931                |
| StrepII-GFP-CLASP2 $\alpha$ 1-1527 (full length)     | [12]                 | N/A                        |
| StrepII-mCherry-CLASP2 $\alpha$ 1-1527 (full length) | This paper           | N/A                        |
| StrepII-TagBFP-CLASP2 $\alpha$ 1-1527 (full length)  | [12]                 | N/A                        |
| StrepII-GFP-CLASP2 $\alpha$ 295-813 (TOG2-S)         | [12]                 | N/A                        |
| StrepII-mCherry-CLASP2 $\alpha$ 295-813 (TOG2-S)     | This paper           | N/A                        |
| StrepII-TagBFP-CLASP2 $\alpha$ 295-813 (TOG2-S)      | [12]                 | N/A                        |
| Kin-5-GFP  | [22]                 | N/A                        |

#### Experimental Models: Cell Lines

|                |      |           |
|----------------|------|-----------|
| Human: HEK293T | ATCC | CRL-11268 |
|----------------|------|-----------|

#### Recombinant DNA

|  |                             |     |
|--|-----------------------------|-----|
| Kin-5-GFP  | Dr. William O. Hancock [22] | N/A |
| StrepII-GFP-CLASP2 $\alpha$ 1-1527 (full length)     | [12]                        | N/A |
| StrepII-mCherry-CLASP2 $\alpha$ 1-1527 (full length) | This paper                  | N/A |
| StrepII-TagBFP-CLASP2 $\alpha$ 1-1527 (full length)  | [12]                        | N/A |
| StrepII-GFP-CLASP2 $\alpha$ 295-813 (TOG2-S)         | [12]                        | N/A |

| REAGENT or RESOURCE                              | SOURCE     | IDENTIFIER |
|--|------------|------------|
| StrepII-mCherry-CLASP2 $\alpha$ 295-813 (TOG2-S) | This paper | N/A        |
| StrepII-TagBFP-CLASP2 $\alpha$ 295-813 (TOG2-S)  | [12]       | N/A        |

---

**Software and Algorithms**

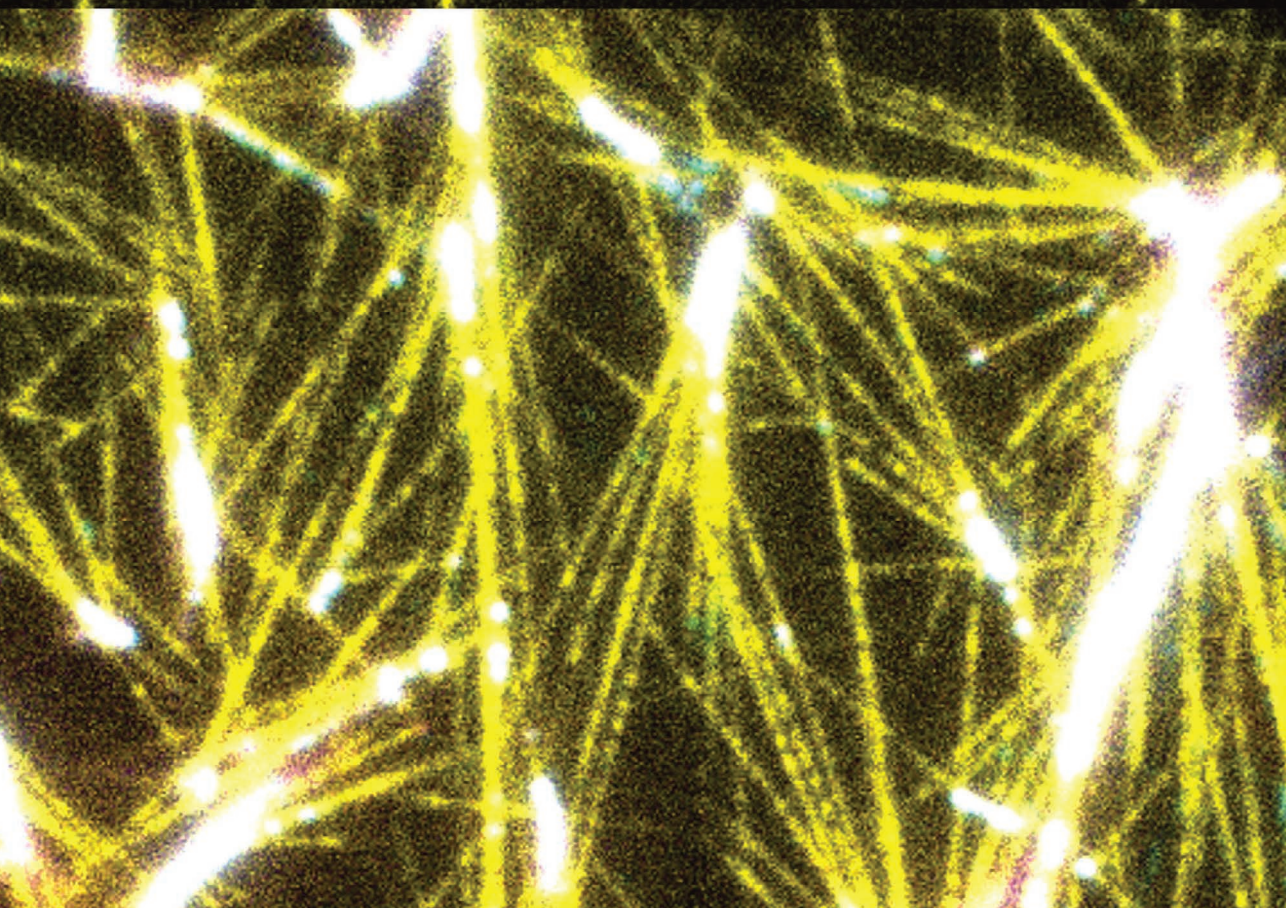
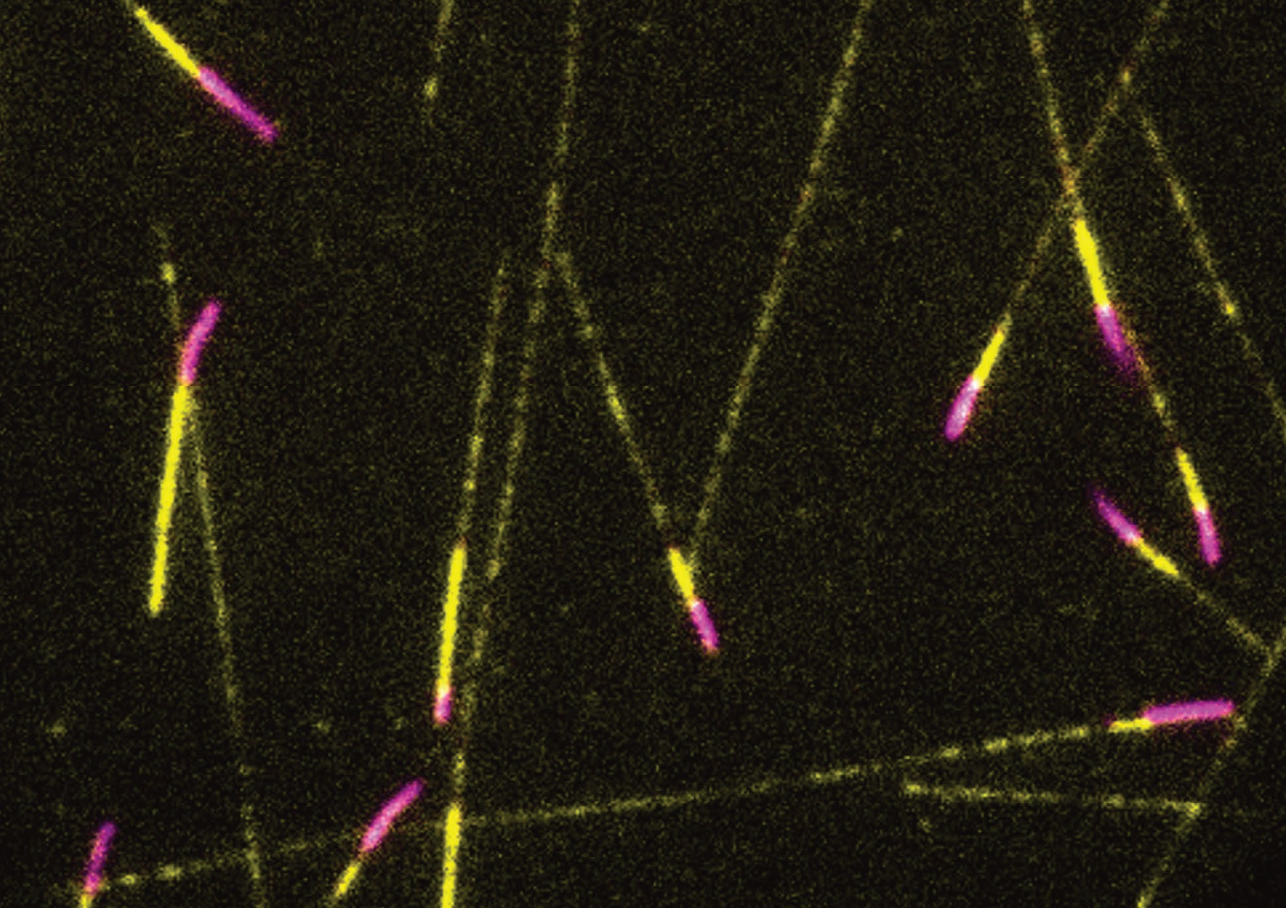

---

|                        |                   |   |
|------------------------|-------------------|---|
| ImageJ                 | NIH               | <a href="https://imagej.nih.gov/ij/">https://imagej.nih.gov/ij/</a>   |
| Metamorph              | Molecular Devices | <a href="https://www.moleculardevices.com/products/cellular-imaging-systems/acquisition-and-analysis-software/metamorph-microscopy">https://www.moleculardevices.com/products/cellular-imaging-systems/acquisition-and-analysis-software/metamorph-microscopy</a> |
| GraphPad Prism         | GraphPad          | <a href="https://www.graphpad.com/scientific-software/prism/">https://www.graphpad.com/scientific-software/prism/</a>   |
| KymoResliceWide plugin | Eugene Katrukha   | <a href="https://github.com/ekatrunkha/KymoResliceWide">https://github.com/ekatrunkha/KymoResliceWide</a>   |

---







# 5

## **In vitro reconstitution of the interplay between CAMSAPs, katanin and WDR47 in regulating microtubule minus-end dynamics**

Dipti Rai<sup>1</sup>, Shasha Hua<sup>1,2,3</sup>, Kelly Stecker<sup>4</sup>, Kai Jiang<sup>1,2,3#</sup> and Anna Akhmanova<sup>1#</sup>

<sup>1</sup> Cell Biology, Department of Biology, Faculty of Science, Utrecht University, Padualaan 8, 3584 CH Utrecht, the Netherlands

<sup>2</sup> The State Key Laboratory Breeding Base of Basic Science of Stomatology (Hubei-MOST) & Key Laboratory of Oral Biomedicine Ministry of Education, School & Hospital of Stomatology, Wuhan University, Wuhan 430071, China

<sup>3</sup> Medical Research Institute, Wuhan University, Wuhan 430071, China

<sup>4</sup> Center for Molecular Medicine, University Medical Center Utrecht, Utrecht, 3584 CX, The Netherlands

<sup>4</sup> Mass Spectrometry and Proteomics, Bijvoet Center for Biomolecular Research, Utrecht Institute for Pharmaceutical Sciences and the Netherlands Proteomics Center, Utrecht University, Padualaan 8, 3584 CH Utrecht, the Netherlands

# Corresponding authors: [jiangkai@whu.edu.cn](mailto:jiangkai@whu.edu.cn); [a.akhmanova@uu.nl](mailto:a.akhmanova@uu.nl)

Manuscript in preparation

### **Abstract**

Microtubules are major constituents of the cytoskeleton controlling numerous aspects of cell physiology. The geometry and density of microtubule networks strongly depend on the factors that control the dynamics of the two microtubule ends, the plus- and the minus-end. Members of CAMSAP/Patronin family are prominent microtubule regulators which specifically stabilize the minus ends of non-centrosomal microtubules in different cellular settings, ranging from apicobasal arrays in epithelial cells and microtubule bundles in neurons to the central pair of microtubules in motile cilia. Previous work in cells suggested that the microtubule-severing enzyme katanin and the WD40 repeat-containing protein WDR47 act as a negative and a positive regulator of CAMSAP-mediated minus-end stabilization, respectively. To get mechanistic insights in these regulatory interactions, we reconstituted in vitro the activity of all three mammalian CAMSAPs in combination with katanin and WDR47. We found that katanin, even when present at a low concentration, can inhibit elongation of CAMSAP-decorated microtubule minus ends, whereas at higher concentrations, it specifically and efficiently severs CAMSAP2/3-decorated microtubule segments. WDR47 is recruited to microtubules decorated by CAMSAPs and inhibits katanin binding and severing. WDR47 also slows down polymerization of the minus ends bound to CAMSAP2 and CAMSAP3 and can potentiate blocking of microtubule minus-end growth in the presence of CAMSAP1. These results provide a biochemical basis for understanding microtubule minus-end regulation by CAMSAPs and their binding partners.

### **Introduction**

Microtubules are one of the major types of cytoskeletal filaments, which serve as rails for rapid intracellular transport, control organelle positioning, cell polarity, motility and chromosome separation during cell division. Therefore, the geometry and density of microtubule arrays are critically important for controlling cell architecture and function (Akhmanova and Kapitein, 2022; Burute and Kapitein, 2019). Microtubules are polarized polymers, with two distinct ends – the slowly growing minus end and rapidly growing plus end (Akhmanova and Steinmetz, 2015; Desai and Mitchison, 1997). While the polymerization of the plus ends is responsible for generation of most of the microtubule mass, the minus ends are often undynamic due to their anchoring at the microtubule-organizing centers (MTOCs) (Sanchez and Feldman, 2017; Vineethakumari and Luders, 2022; Wu and Akhmanova, 2017). Minus ends can be capped by the multisubunit assembly that nucleates microtubules – the  $\gamma$ -tubulin ring complex ( $\gamma$ -TuRC) (Liu et al., 2021b; Thawani and Petry, 2021; Zupa et al., 2021). Free microtubule minus ends

can grow and shrink, and in many animal cell types, they can be decorated and stabilized by the members of CAMSAP/Patronin family proteins (Hendershott and Vale, 2014; Jiang et al., 2014), reviewed in (Akhmanova and Hoogenraad, 2015; Akhmanova and Steinmetz, 2019). In mammals, this family is represented by three members, CAMSAP1, CAMSAP2 and CAMSAP3 (Baines et al., 2009). All three CAMSAPs contain a highly conserved protein domain, CKK, which binds to the groove between two tubulin dimers and shows preference for the region close to the outermost minus end, where the regular microtubule lattice transitions to curved protofilaments (Atherton et al., 2017). Additional domains in CAMSAPs increase microtubule affinity, resulting in two different isoform-specific behaviors: CAMSAP1 tracks growing microtubule minus ends, whereas CAMSAP2 and CAMSAP3 stably decorate microtubule lattice grown from the minus end (Hendershott and Vale, 2014; Jiang et al., 2014). Microtubule stretches decorated by CAMSAP2/3 are very stable and can serve as “seeds” for microtubule re-growth (Jiang et al., 2014), providing a way to generate dense microtubule arrays which are not connected to the microtubule nucleation sites, such as the centrosome. Non-centrosomal microtubules are particularly important in large cells with extensive microtubule networks, such as epithelial cells and neurons, and these are the cell types where CAMSAPs strongly participate in regulating microtubule organization and density by stabilizing and positioning microtubule minus ends (Dong et al., 2017; Khanal et al., 2016; King et al., 2014; Noordstra et al., 2016; Pongrakhananon et al., 2018; Toya et al., 2016; Yau et al., 2014; Zhou et al., 2020).

The stability of CAMSAP-decorated microtubules is their important property, but it also poses a problem – in order to regulate microtubule networks, cells need to have mechanisms to limit and control the number and length of CAMSAP-stabilized microtubule minus ends. Until now, two regulatory mechanisms have been discovered. One involves phosphorylation of CAMSAP2 and CAMSAP3 in mitosis, resulting in their release from microtubules, which prevents CAMSAP2/3-mediated minus end stabilization during mitotic spindle formation (Jiang et al., 2014). The second mechanism operates in interphase and involves the microtubule-severing protein katanin (Jiang et al., 2018; Jiang et al., 2014). Katanin is a member of the ATPases Associated with diverse cellular Activities (AAA+)-type protein superfamily (Lynn et al., 2021). It consists of two subunits: the ATPase-containing subunit p60 and the regulatory subunit p80, bearing a WD40-repeat domain. The interaction between the two katanin subunits is mediated by the N-terminal microtubule-interacting and -trafficking domain of p60 (MIT, or p60N) and the C-terminal domain of p80 (p80C) that together form a large  $\alpha$ -helix bundle, to which CAMSAP2 and CAMSAP3, but not CAMSAP1, bind through

a short helical peptide called katanin-binding helix (KBH, **Fig. 1a**) (Jiang et al., 2018). The interaction between CAMSAP2/3 and katanin limits the length of CAMSAP-decorated microtubule stretches in cells (Jiang et al., 2014), whereas perturbing this interaction by a point mutation in p80 abolishes this effect (Jiang et al., 2018).

Recent work revealed yet another level of complexity in this regulatory mechanism. It was shown that a WD40 repeat-containing protein WDR47 binds to CAMSAPs in the region containing the katanin-binding site (**Fig. 1a**) (Buijs et al., 2021). Importantly, WDR47 plays an essential role in controlling different aspects of brain and neuronal development (Buijs et al., 2021; Chen et al., 2020; Kannan et al., 2017). WDR47 is recruited to microtubules in cells by CAMSAPs and promotes CAMSAP2/3 accumulation on microtubules in neurons (Buijs et al., 2021; Chen et al., 2020). Moreover, overexpression of katanin in neurons causes a loss of CAMSAP2-decorated microtubule stretches, whereas simultaneous expression of WDR47 partially alleviates this phenotype (Buijs et al., 2021). This led to the hypothesis that WDR47 may protect CAMSAP2/3-bound microtubule minus ends from katanin-mediated severing. A related mechanism may operate during the biogenesis of motile cilia, where katanin, CAMSAPs and WDR47 cooperate in generating the central pair of axonemal microtubules (Liu et al., 2021a). Analysis of multiciliated ependymal cells showed that the formation of the axonemal central pair of microtubules requires katanin-mediated microtubule severing, and that the minus ends of these microtubule seeds are stabilized by CAMSAPs, whereas WDR47 promotes efficient formation and proper positioning of these microtubules by concentrating CAMSAPs into the ciliary lumen (Liu et al., 2021a). In chemosensory neurons in *C. elegans*, WDR47 has been shown to affect the movement of intraflagellar transport (IFT) particles, ciliary morphology and function, and thereby, cell-specific ciliogenesis (Song et al., 2022).

Understanding the cooperation between CAMSAPs, katanin and WDR47 is complicated by the fact that mammalian katanin, in addition to having a severing activity, can also decorate and potentially regulate microtubule ends through a heterodimeric complex of its non-enzymatic domains, p60N and p80C (Jiang et al., 2017). To dissect the mechanisms underlying the combined activities of these proteins, we reconstituted their activities *in vitro* on dynamic microtubules. We found that katanin when present at concentrations insufficient for efficient microtubule severing, can inhibit growth of CAMSAP-decorated microtubule minus ends. At a higher concentration, katanin could efficiently cut CAMSAP2/3-decorated microtubule lattices; the resulting microtubule fragments remained stable and elongated, leading to an increase in microtubule number. WDR47, which had no strong microtubule affinity of its own,

was potently recruited to microtubules by all three CAMSAPs. In the presence of CAMSAP1, WDR47 could either track growing minus ends or block their polymerization. In the presence of CAMSAP2 or CAMSAP3, WDR47 decorated CAMSAP-bound microtubule lattices and slowed down their growth from the minus end. WDR47 also inhibited binding of katanin to CAMSAP2/3-decorated microtubules and prevented their severing. These results provide mechanistic insight into microtubule minus end regulation by CAMSAPs, katanin and WDR47.

## Results

### *Katanin-mediated growth inhibition and severing of CAMSAP2/3 decorated microtubules*

Our previous work has shown that the complex of the full length katanin p60 subunit and the C-terminal part of the p80 subunit lacking the WD40 domain (p60/p80C) can sever dynamic microtubules in vitro (Jiang et al., 2017). However, a relatively high concentration (300 nM) was needed for severing, in agreement with the finding that free tubulin inhibits katanin activity (Bailey et al., 2015; Jiang et al., 2017). The p60/p80C complex could induce microtubule severing at much lower concentrations (25 nM) when recruited to microtubules by the binding partner of katanin, ASPM (Jiang et al., 2017). To test whether CAMSAPs can also potentiate katanin-mediated microtubule severing, we have purified fluorescently tagged p60/p80C and different CAMSAP isoforms from HEK293T cells (**Extended data Fig. 1a**), as described previously (Jiang et al., 2017). Initially, we simultaneously added 10 nM p60/p80C and 40 nM CAMSAP3 to the assay where microtubules were grown from GMPCPP-stabilized microtubule seeds and observed using Total Internal Reflection Fluorescence (TIRF) microscopy (Bieling et al., 2007; Jiang et al., 2017). At this low katanin concentration, we observed only very occasional microtubule severing, which led to formation of small microtubule bundles (**Extended data Fig. 1b,c**). We also performed these assays in the absence of ATP and found that in these conditions, instead of microtubule severing, katanin preferentially accumulated at microtubule minus ends and slowed down their growth by ~50% (**Fig. 1b-d**). This effect, which was similar to what we have previously observed for the katanin-ASPM combination (Jiang et al., 2017), thus does not depend on the enzymatic activity of katanin.

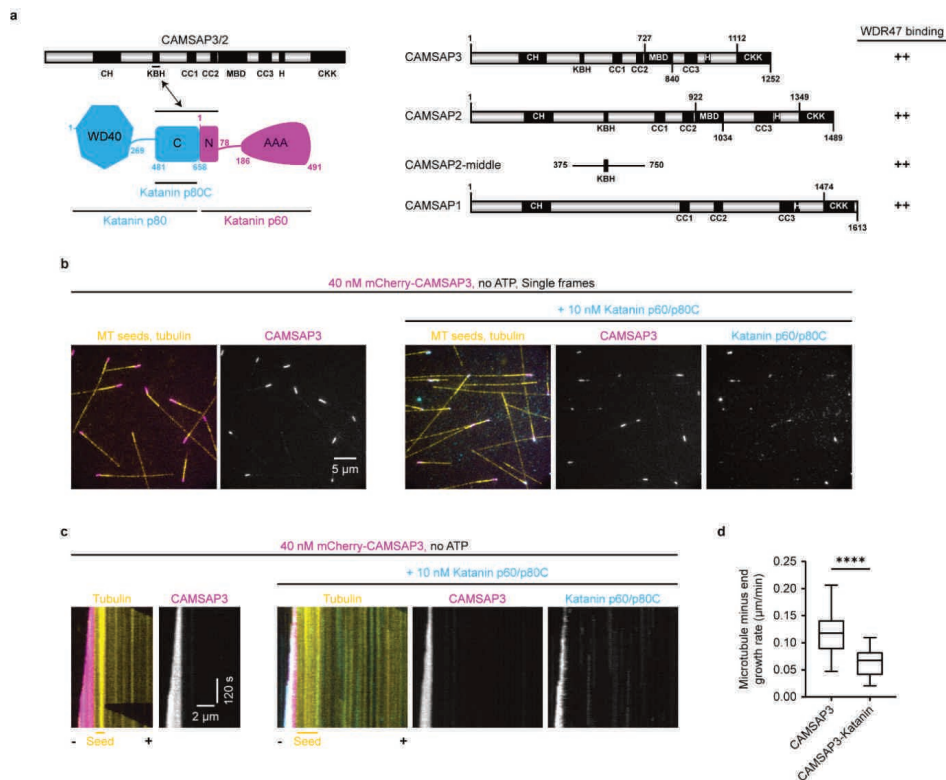


**Figure 1 | Katanin inhibits growth of CAMSAP3-decorated microtubule minus ends.**

**a**, Schematic representation of the domain structure of katanin and CAMSAP proteins and their interaction with WDR47. Indicated domains: AAA, ATPases associated with diverse cellular activities domain of p60; C, conserved C-terminal domain of p80; CC, coiled coil; CH, calponin-homology domain; CKK, CKK domain; H, alpha-helix; KBH, katanin-binding helix; MBD, MT-binding domain; N, N-terminal microtubule-interacting and -trafficking domain of p60; WD40, WD40 repeat domain.

**b**, Single last frames of 10 min time-lapse videos showing control assays (left panel) with microtubules (yellow) and CAMSAP3 (magenta) or with added katanin (cyan, right panel). The assays contain of 40 nM mCherry-CAMSAP3, 15  $\mu$ M tubulin (14.5  $\mu$ M unlabeled porcine tubulin and 0.5  $\mu$ M HiLyte488-tubulin) and no ATP; 10 nM SNAP-AF647 labeled katanin p60/p80C was added in the right panel.

**c**, Representative kymographs from the in vitro reconstitution experiments shown in **b**.

**d**, The box and whisker plot showing quantification of average growth rate of microtubule minus-ends in the presence of 40 nM mCherry-CAMSAP3 and 15  $\mu$ M tubulin with ( $n=35$ ,  $N=35$ ) or without ( $n=33$ ,  $N=33$ ) 10 nM katanin p60/p80C, where  $n$  is the number of growth events and  $N$  is the number of microtubules analyzed from three independent experiments for each condition. The box extends from the 25th to 75th percentiles, while the whiskers extend to the smallest and largest values. The line in the middle of the box is the median. Two-tailed unpaired  $t$ -test was used to test for significance. \*\*\*\* $p < 0.0001$ .



Next, we increased the concentration of p60/p80C complex. In order to be able to observe microtubule severing, we have first incubated microtubule seeds in the presence of tubulin and one of the CAMSAPs, but without katanin, to allow formation of CAMSAP-decorated microtubule segments at growing minus ends, and then substituted the protein mix with the one containing 40 nM p60/p80C (**Fig. 2a**).

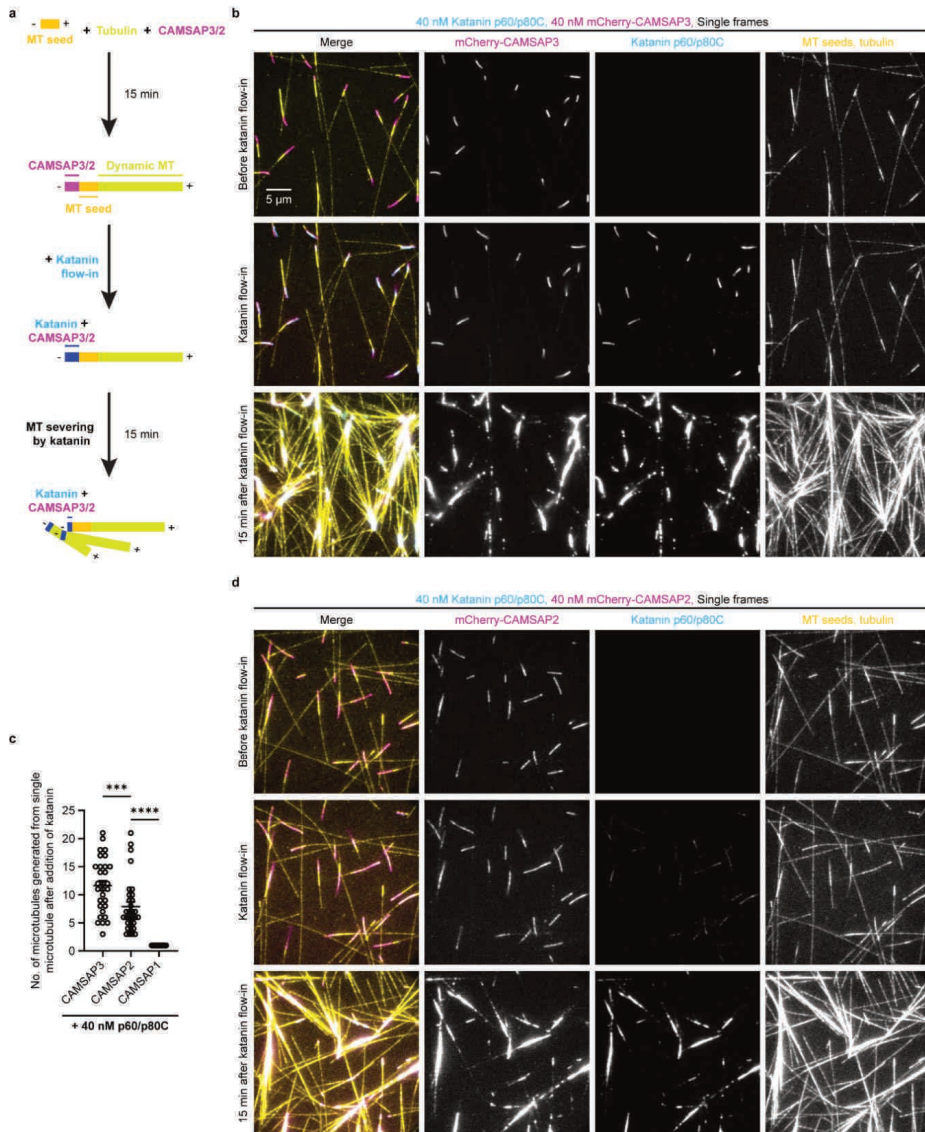


**Figure 2 | Katanin p60/p80C severs and amplifies CAMSAP3 and CAMSAP2-decorated microtubules.**

**a**, Schematic for the *in vitro* reconstitution of microtubule severing.

**b**, Single frames (at indicated steps) from a 20 min time-lapse video showing severing of CAMSAP3-decorated (magenta) microtubules (yellow) by katanin (cyan) after substitution of microtubule polymerization mix (40 nM mCherry-CAMSAP3, 15  $\mu$ M tubulin (14.5  $\mu$ M unlabeled porcine tubulin and 0.5  $\mu$ M HiLyte488-tubulin) and 1 mM ATP) with the microtubule severing mix (the same mix supplemented with 40 nM SNAP-AF647 labeled katanin p60/p80C). Panel **a** depicts the indicated steps: Before katanin flow-in, 10 min after the addition of microtubule polymerization mix (upper panel); Katanin flow-in, immediately after substitution of polymerization mix with severing mix (middle panel); 15 min after katanin flow-in (lower panel).

**c**, Quantification of the number of microtubules generated from a single CAMSAP-decorated microtubule as a result of katanin-mediated severing under the experimental conditions shown in panel **b**, **d** and **Extended data Fig. 1d**.  $n=30$ ,  $N=3$  for CAMSAP3;  $n=31$ ,  $N=3$  for CAMSAP2 and  $n=36$ ,  $N=2$  for CAMSAP1, where  $n$  is the number of single microtubules analyzed and  $N$  is the number of independent experiments. The plot presents mean  $\pm$  s.e.m., and individual data points represent single microtubules analyzed. One-way ANOVA with Tukey's multiple comparisons test was performed to compare the means with each other (\*\*\* $p=0.0007$ ; \*\*\*\* $p < 0.0001$ ).

**d**, Single frames (at indicated steps) from a 20 min time-lapse video showing severing of microtubules (yellow) decorated with 40 nM CAMSAP2 (magenta). Experimental conditions are the same as shown in **b**.

When we added p60/p80C to microtubules preassembled with 10 nM CAMSAP1, a CAMSAP family member that does not contain katanin-binding site (Jiang et al., 2014), 40 nM p60/p80C was insufficient to trigger any severing (**Extended data Fig. 1d**, higher CAMSAP1 concentrations could not be used in the assay because of strong microtubule bundling). However, when we added 40 nM p60/p80C to microtubules decorated with 40 nM CAMSAP3, we observed rapid and specific fragmentation of CAMSAP3-decorated microtubule stretches (**Fig. 2b**). The resulting fragments persisted and initiated growth of new microtubules, leading to the formation of bundled brush-like structures. A similar effect was observed when 40 nM katanin was added to microtubules decorated by CAMSAP2, although the cutting efficiency and the ensuing microtubule amplification were somewhat lower than with CAMSAP3 (**Fig. 2c,d**).

We next purified from HEK293T cells fluorescently tagged full length katanin containing not only the whole p60 subunit but also the complete p80 subunit, including its WD40 domain (**Extended data Fig. 1a**). Analysis of this complex by mass spectrometry revealed no significant contamination with any microtubule-binding proteins (**Extended data Fig. 2a**). This complex was less active than the p60/p80C version, because at 40 nM, it did not sever microtubules decorated with 40 nM CAMSAP3, although it did sever CAMSAP3-bound microtubules when added at a 250 nM concentration (**Fig. 3a,b** and **Extended data Fig. 2b**).

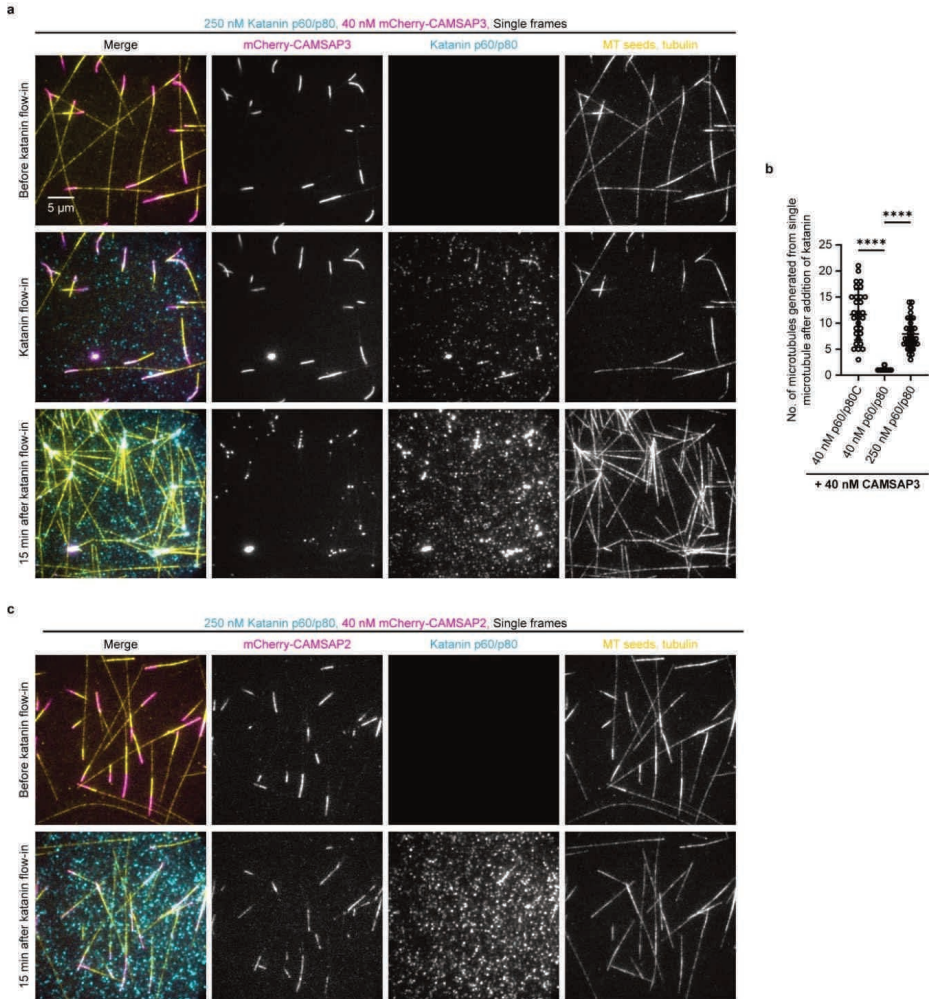


**Figure 3 | Full-length katanin p60/p80 severs and amplifies CAMSAP3-decorated microtubules.**

**a**, Single frames (at indicated steps) from a 20 min time-lapse video showing severing of CAMSAP3-decorated (magenta) microtubule (yellow) minus-ends by 250 nM full-length katanin (cyan). Rest of the experimental conditions are the same as shown in Fig. 2b. The data are also presented in the same way.

**b**, Quantification of the number of microtubules generated from a CAMSAP3-decorated microtubule as a result of katanin-mediated severing under the experimental conditions shown in panel a, Fig. 2b and Extended data Fig. 2b.  $n=30$ ,  $N=3$  for 40 nM p60/p80C;  $n=22$ ,  $N=1$  for 40 nM p60/p80 and  $n=31$ ,  $N=3$  for 250 nM p60/p80, where  $n$  is the number of single microtubules analyzed and  $N$  is the number of independent experiments. The plot presents mean  $\pm$ s.d. and individual data points represent single microtubules analyzed. One-way ANOVA with Šídák's multiple comparisons test was performed for the pairwise

---

*comparison of means. \*\*\*\* $p < 0.0001$ . 40 nM p60/p80C data has been taken from Fig. 2c (CAMSAP3 values) and replotted here for direct comparison.*

*c, Single frames (at indicated steps) from a 20 min time-lapse video showing lack of amplification of microtubules (yellow) decorated with 40 nM mCherry-CAMSAP2 (magenta). Experimental conditions are the same as shown in a.*

---

It should be noted that in these conditions, the actual concentration of katanin in solution could be lower, because we observed significant absorption of katanin on the coverslip surface (**Fig. 3a**). We also combined 250 nM full length katanin with microtubules decorated with 40 or 120 nM CAMSAP2 or with 10 nM CAMSAP1, but observed only mild severing with 120 nM CAMSAP2 and no severing at a lower concentration of CAMSAP2 or with CAMSAP1 (**Fig. 3c** and **Extended data Fig. 2c,d**). This is in line with the observation that CAMSAP2 potentiated p60/p80C-mediated microtubule severing less efficiently than CAMSAP3 (**Fig. 2c**), and CAMSAP1 did not promote microtubule severing at all (**Fig. 2c** and **Extended data Fig. 1d**). The inability of full length katanin to efficiently sever CAMSAP2-bound microtubules could be due to a lower affinity of katanin for CAMSAP2, or a weaker microtubule decoration by CAMSAP2 compared to CAMSAP3 as observed previously (Jiang et al., 2014). We conclude that CAMSAP2-, and particularly CAMSAP3-decorated microtubules can serve as a specific substrate for katanin-mediated microtubule severing.

#### ***WDR47 binds to CAMSAP-decorated minus ends and affects their dynamics***

Next, we used HEK293T cells to purify Twin-Strep- and GFP-tagged WDR47 (**Extended data Fig. 3a,b**). Mass spectrometry-based analysis showed that this WDR47 preparation contained low levels of all three mammalian CAMSAPs, with CAMSAP1 being the most abundant (**Extended data Fig. 3c**). When included in the assay with dynamic microtubules at 15 nM concentration, WDR47 showed very rare cases of microtubule minus-end binding (**Fig. 4 a,b**). However, minus end binding could be observed much more frequently in the presence of 150 nM WDR47 (**Fig. 4 c-e** and **Extended data Fig. 3d**). In such cases, WDR47 could block minus end growth (for a short time or for the whole duration of a 10-minute movie) or track the growing minus end (**Fig. 4c-f** and **Extended data Fig. 3d**). The addition of WDR47 appeared to mildly accelerate the rate of minus-end growth for those microtubules that were not blocked (**Fig. 4g**). Since this effect was observed even at 15 nM WDR47, when only few minus ends were transiently bound by this protein, we do not ascribe to it any significance.

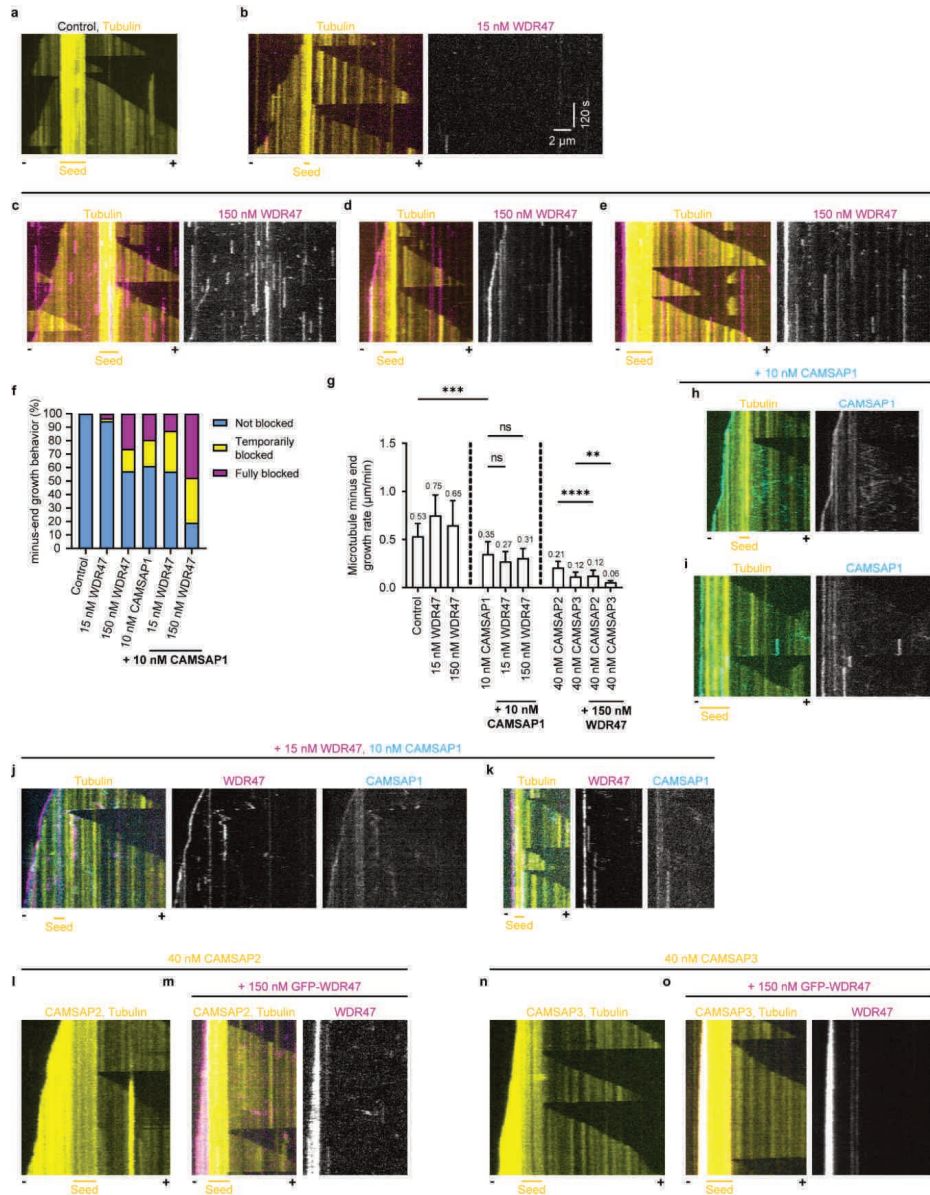


**Figure 4 | WDR47 binds to CAMSAP-decorated microtubule minus ends and affects their dynamics.**

**a-e**, Representative kymographs from *in vitro* reconstitutions of microtubule dynamics in the presence of either 15 µM tubulin alone (**a**), or together with 15 nM GFP-WDR47 (**b**) or 150 nM GFP-WDR47 (**c-e**). **c-e** illustrate 3 different types of minus-end growth behavior: minus-end growth and tracking by WDR47 (**c**); transition from temporarily blocked minus-end outgrowth to growing minus-end (**d**) and completely blocked minus-end of a GMPCPP-stabilized microtubule seed (**e**).

**f**, Quantification of different types of minus-end growth behavior as described for **panels c-e** in the presence of either 15  $\mu\text{M}$  tubulin alone ( $n=19$ ,  $N=1$ ), or together with 15 nM GFP-WDR47 ( $n=38$ ,  $N=3$ ), or 150 nM GFP-WDR47 ( $n=61$ ,  $N=3$ ), or 10 nM CAMSAP1 ( $n=41$ ,  $N=3$ ), or 15 nM GFP-WDR47 and 10 nM CAMSAP1 ( $n=39$ ,  $N=3$ ), or 150 nM GFP-WDR47 and 10 nM CAMSAP1 ( $n=21$ ,  $N=1$ ); where  $n$  is the number of minus ends analyzed and  $N$  is the number of independent experiments analyzed for each condition. Representative kymographs are shown in **a-e**, **h-k** and **Extended data Fig. 3d-f**.

**g**, Quantification of average growth rate of microtubule minus-ends in the presence of either 15  $\mu\text{M}$  tubulin alone ( $n=37$ ,  $N=1$ ), or together with 15 nM GFP-WDR47 ( $n=43$ ,  $N=3$ ), or 150 nM GFP-WDR47 ( $n=46$ ,  $N=3$ ), or 10 nM CAMSAP1 ( $n=33$ ,  $N=3$ ), or 15 nM GFP-WDR47 and 10 nM CAMSAP1 ( $n=34$ ,  $N=3$ ), or 150 nM GFP-WDR47 and 10 nM CAMSAP1 ( $n=8$ ,  $N=1$ ), or 40 nM CAMSAP2 ( $n=45$ ,  $N=3$ ), or 40 nM CAMSAP3 ( $n=33$ ,  $N=3$ ), or 40 nM CAMSAP2 and 150 nM GFP-WDR47 ( $n=35$ ,  $N=3$ ), or 40 nM CAMSAP3 and 150 nM GFP-WDR47 ( $n=35$ ,  $N=3$ ); where  $n$  is the number of growth events analyzed and  $N$  is the number of independent experiments analyzed for each condition. The plot presents mean  $\pm$  s.d. and individual data points represent growth events analyzed. One-way ANOVA with Tukey's multiple comparisons test was performed to compare the means with each other. ns= not significant,  $p>0.05$ ; \* $p<0.05$ ; \*\* $p<0.01$ ; \*\*\* $p<0.001$ ; \*\*\*\* $p<0.0001$ . Representative kymographs are shown in **a-d**, **h, j**, **l-o** and **Extended data Fig. 3d-f**.

**h, i**, Representative kymographs illustrating different microtubule (yellow) minus-end growth behaviors: minus-end tracking by CAMSAP1 (cyan) (**h**) and completely blocked minus-end of a GMPCPP-stabilized microtubule seed (**i**) in the presence of 10 nM mCherry-CAMSAP1 and 15  $\mu\text{M}$  tubulin, as can also be seen in the presence of 150 nM GFP-WDR47 and 15  $\mu\text{M}$  tubulin as shown in panel **c-e**.

**j, k**, Representative kymographs illustrating CAMSAP1 (cyan) colocalization with WDR47 (magenta) and different minus-end growth behavior: minus-end tracking by CAMSAP1 and WDR47 (**j**) and completely blocked minus-end of a GMPCPP-stabilized microtubule seed (**k**) in the presence of 15 nM GFP-WDR47, 10 nM mCherry-CAMSAP1 and 15  $\mu\text{M}$  tubulin, as can also be seen for panels **c-e**, **h** and **i**.

**l-o**, Representative kymographs illustrating WDR47 (magenta) decoration of microtubule (yellow) minus ends: 40 nM mCherry-CAMSAP2 and 15  $\mu\text{M}$  tubulin (**l**) alone or together with 150 nM GFP-WDR47 (**m**); 40 nM mCherry-CAMSAP3 and 15  $\mu\text{M}$  tubulin (**n**) alone or together with 150 nM GFP-WDR47 (**o**). CAMSAPs stretches can be seen as bright yellow signal along minus-end-grown microtubule lattice.

Since minus end binding and tracking are behaviors typical for CAMSAP1, we hypothesized that they were caused by CAMSAP1 contamination in our WDR47 preparations. In agreement with this idea, 10 nM CAMSAP1 alone, which was present at the minus ends of most microtubules, could also block minus-end outgrowth from the seeds or track growing microtubule minus ends; transitions from blocked to growing minus ends were also observed (**Fig. 4f, h, i** and **Extended data Fig. 3e**). To get further support for the idea that WDR47 was targeted to the minus ends by CAMSAP1, we combined 15 nM WDR47 (a concentration at which it did not show any significant minus end binding) with 10 nM CAMSAP1 and observed that the two proteins colocalized on either growing or blocked microtubule minus ends (**Fig.**

**4f,j,k** and **Extended data Fig. 3f**). Similar minus end binding and blocking were observed when 150 nM WDR47 was combined with 10 nM CAMSAP1, but increasing WDR47 concentration in the presence of CAMSAP1 made minus-end blocking more frequent (**Fig. 4f** and **Extended data Fig. 3g**). CAMSAP1 by itself slowed down the growth rate of microtubule minus ends compared to control, and this effect remained unaltered by the addition of WDR47 (**Fig. 4g**).

Finally, we combined WDR47 with CAMSAP2 or CAMSAP3, which both decorate microtubule lattice grown from the minus end, slow down microtubule minus-end polymerization and prevent catastrophes at the minus end (Jiang et al., 2014). When 150 nM WDR47 was added to microtubules in the presence of 40 nM CAMSAP2 or CAMSAP3, it strongly decorated the minus-end-grown part of microtubule and inhibited the rate of minus-end elongation compared to the effects of CAMSAP2 or CAMSAP3 alone (**Fig. 4g, l-o**). No minus-end blocking was observed in these conditions. We conclude that WDR47 can be targeted to microtubules by all three CAMSAPs; it enhances the ability of CAMSAP1 to block minus-end outgrowth and the ability of CAMSAP2 and CAMSAP3 to slow down microtubule minus-end polymerization.

#### ***WDR47 protects CAMSAP2/3-decorated microtubules against katanin-mediated severing***

In the last set of experiments, we examined whether WDR47 can protect CAMSAP2/3-decorated microtubules from katanin-induced fragmentation. Whereas 40 nM p60/p80C could rapidly and efficiently sever microtubules that were decorated by 40 nM CAMSAP2 or CAMSAP3 (**Fig. 2**), very little severing was observed in the assays where microtubules were also decorated by 150 nM WDR47 (**Fig. 5a-c**). Similarly, WDR47 could also potentially inhibit severing of CAMSAP3-bound microtubules by 250 nM full length katanin (**Fig. 5c,d**). A lower concentration of WDR47 (40 nM) was insufficient to inhibit katanin-mediated microtubule severing (**Extended data Fig. 4a**). This difference was likely due to the fact that at 150 nM, WDR47 strongly suppressed the binding of katanin to CAMSAP2/3-decorated microtubules (**Extended data Fig. 4b,c**), whereas at 40 nM WDR47, katanin could still bind to such microtubules (**Extended data Fig. 4a**). Given that the binding sites of WDR47 and katanin on CAMSAP2 and CAMSAP3 overlap (**Extended data Fig. 1a**), the ability of WDR47 to protect CAMSAP2/3-bound microtubules from katanin-mediated fragmentation may be explained by the occlusion of the katanin-binding site on CAMSAP2 and CAMSAP3.

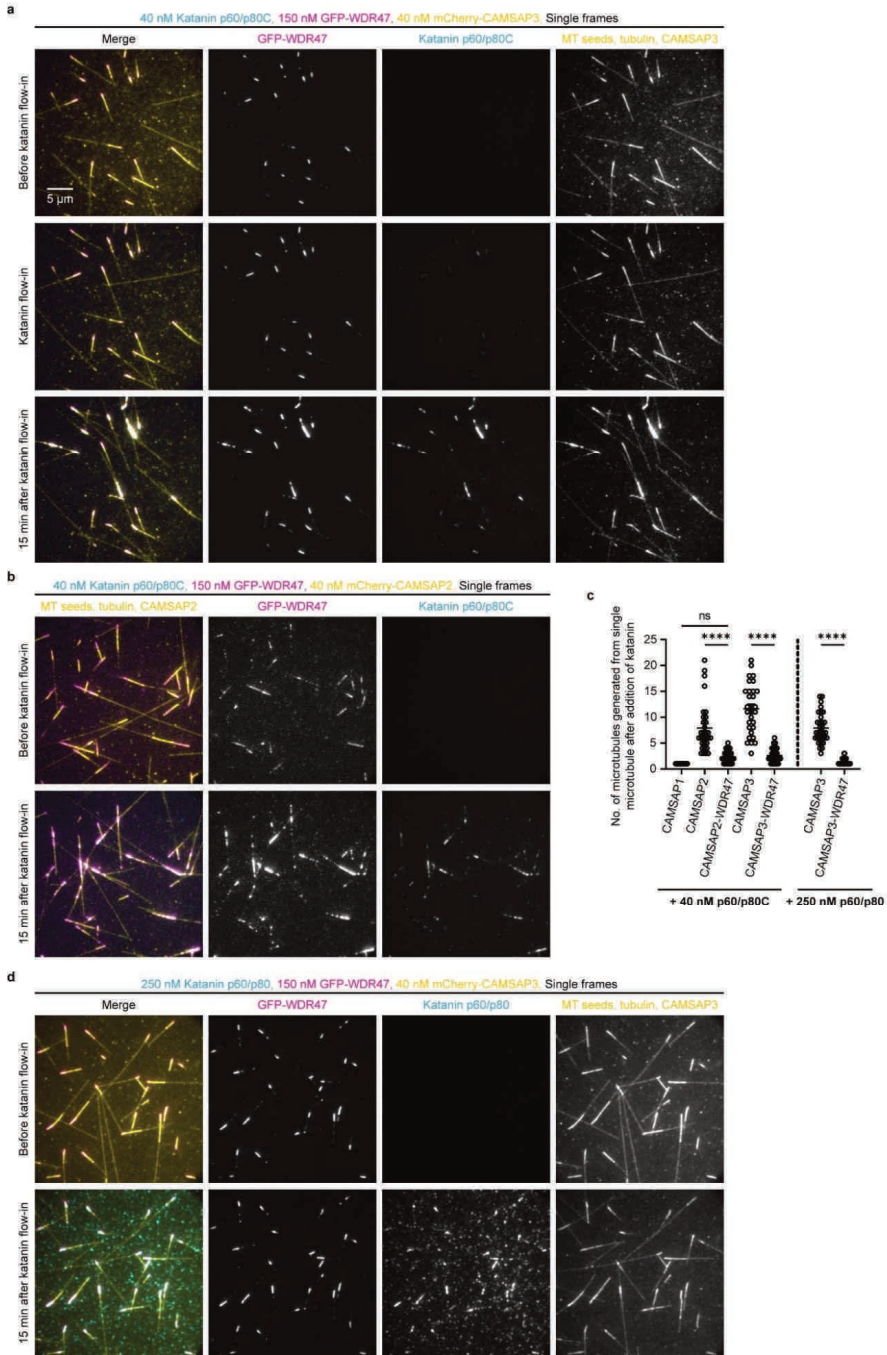


**Figure 5 | WDR47 protects CAMSAP2/3-decorated microtubules against katanin-mediated severing.**



- a**, Single frames (at indicated steps) from a 20 min time-lapse video showing WDR47 (magenta) binding to CAMSAP3-decorated microtubules (yellow) and a strong suppression in microtubule severing and amplification by katanin (cyan) after substitution of microtubule polymerization mix (150 nM GFP-WDR47, 40 nM mCherry-CAMSAP3, 15  $\mu$ M tubulin (14.5  $\mu$ M unlabeled porcine tubulin and 0.5  $\mu$ M rhodamine-tubulin) and 1 mM ATP) with the microtubule severing mix (the same mix as above but supplemented with 40 nM SNAP-AF647 labeled katanin p60/p80C). The data are presented in the same way as in **Fig. 2b**.
- b**, Single frames (at indicated steps) from a 20 min time-lapse video showing lack of amplification of microtubules (yellow) by katanin (cyan) in the presence of WDR47 (magenta) and with 40 nM mCherry-CAMSAP2 in the same experimental conditions as shown in **a**.
- c**, Quantification of the number of microtubules generated from the minus-end of a CAMSAP-decorated microtubule as a result of katanin-mediated severing under the experimental conditions shown in panel **a**, **b**, **d**, **Fig. 2b**, **Fig. 2d**, **Fig. 3a**, **Extended data Fig. 1d** and **Extended data Fig. 4b** and **c**.  $n=36$ ,  $N=2$  for 10 nM CAMSAP1 and 40 nM p60/p80C;  $n=31$ ,  $N=3$  for 40 nM CAMSAP2 and 40 nM p60/p80C;  $n=52$ ,  $N=3$  for 40 nM CAMSAP2, 40 nM p60/p80C and 150 nM WDR47;  $n=30$ ,  $N=3$  for 40 nM CAMSAP3 and 40 nM p60/p80C;  $n=43$ ,  $N=3$  for 40 nM CAMSAP3, 40 nM p60/p80C and 150 nM WDR47;  $n=31$ ,  $N=3$  for 40 nM CAMSAP3 and 250 nM p60/p80;  $n=52$ ,  $N=3$  for 40 nM CAMSAP3, 250 nM p60/p80 and 150 nM WDR47; where  $n$  is the number of single microtubules analyzed and  $N$  is the number of independent experiments. The plot presents mean  $\pm$ s.e.m., and individual data points represent single microtubules analyzed. One-way ANOVA with Tukey's multiple comparisons test was performed to compare the means with each other.  $ns$ = not significant,  $p=0.2675$ ;  $****p < 0.0001$ . Data points without WDR47 have been taken from **Fig. 2c** (CAMSAPs values) and **Fig. 3b** (250 nM p60/p80 value) and replotted here for direct comparison.
- d**, Single frames (at indicated steps) from a 20 min time-lapse video showing lack of amplification of CAMSAP3-decorated microtubule (yellow) minus-ends by 250 nM full length katanin p60/80 (cyan) in the presence of WDR47 (magenta), in the same experimental conditions as shown in **a**.

## Discussion

Microtubule organization and density are controlled by multiple factors with opposing activities, which can either stabilize microtubules or promote their disassembly. Here, we used in vitro reconstitution assays to dissect the regulatory mechanisms controlling the stability of free, non-centrosomal microtubule minus ends. We demonstrated that the microtubule severing enzyme katanin can counteract formation of long stretches of microtubule lattices stabilized by CAMSAP2 and CAMSAP3 in two ways: by inhibiting elongation of their minus ends and by cutting them into pieces. Another partner of CAMSAPs, WDR47, can interfere with katanin binding and prevent microtubule severing. However, similar to katanin, WDR47 also inhibits elongation of microtubule minus ends bound to CAMSAP family members.

Our data indicate that formation CAMSAP-stabilized microtubules depend on the balance between katanin and WDR47. Microtubule regulation by CAMSAP2 and 3 is conceptually simple – they decorate and stabilize microtubule lattices formed through minus-end polymerization (Jiang et al., 2014). The effects of microtubule severing enzymes, such as katanin, are more complex. These enzymes extract tubulin dimers out of microtubule lattice causing their breakage and microtubule loss, but they can also amplify microtubules if the damaged microtubule lattices are repaired to serve as rescue sites (Vemu et al., 2018), or if the pieces of broken microtubules act as templates or microtubule seeds for microtubule re-growth (reviewed in (Kuo and Howard, 2021)). In our *in vitro* assays, a combination of CAMSAP2/3 and katanin powerfully amplified microtubules, an effect that was stronger than previously observed with katanin alone or in combination with another microtubule minus-end-binding protein, ASPM (Jiang et al., 2017). This effect is likely caused by a combination of two factors. First, CAMSAP2 and CAMSAP3 can powerfully stabilize freshly severed microtubules (Jiang et al., 2014). Second, katanin itself can bind and decorate the ends of microtubules it severs, because in addition to the ATPase domain, it also has a positively charged microtubule-binding domain which consists of the heterodimeric complex formed by  $\alpha$ -helices in p60N and p80C and the linker region present in p60 (Jiang et al., 2017).

Importantly, in cells, there is no evidence of strong microtubule amplification caused by the combination of CAMSAPs and katanin. This suggests that additional regulators control the balance between microtubule stabilization and destruction, and that this balance may be shifted towards disassembly rather than amplification of CAMSAP2/3-bound microtubules by katanin. Kinesin-13 family members like MCAK or other microtubule depolymerases (Howard and Hyman, 2007; Walczak et al., 2013) are likely candidates for such negative regulation. Alternatively, the intracellular concentration of active katanin might be insufficient to cause efficient severing of CAMSAP2/3-decorated microtubules, and its ability to limit the length of CAMSAP-bound microtubule stretches might be primarily caused by katanin-mediated inhibition of minus-end assembly (see below). Interestingly, the colocalization of katanin with CAMSAP3 in the pericentrosomal area in epithelial cells has been directly correlated with CAMSAP-mediated microtubule release from the centrosome and implicated in the organization of the non-centrosomal microtubule arrays in these cells (Dong et al., 2017). Therefore, protein module composed of CAMSAPs and katanin can regulate the number, length and the organization of the microtubule minus ends in specific cellular settings.

In the presence of katanin, WDR47 serves as a positive regulator of stability of CAMSAP-bound microtubules. This is in agreement with studies in neurons, where the knockout or

knockdown of WDR47 or increase in katanin activity led to a loss of CAMSAP2/3-decorated microtubules (Buijs et al., 2021; Chen et al., 2020). The finding that WDR47 helps to protect CAMSAP-decorated microtubule stretches is also in agreement with the fact that the loss of WDR47 can be compensated by overexpression of microtubule-binding fragments of CAMSAPs both in neurons and in multiciliated cells (Chen et al., 2020; Liu et al., 2021a).

Another interesting effect that has been uncovered by our in vitro reconstitutions is the cooperative inhibition of microtubule minus-end elongation by all studied factors. In vitro, both microtubule plus- and minus ends can grow, although plus-end polymerization occurs faster. In cells, this difference is typically amplified further: microtubule plus-end growth is accelerated by specific factors such as XMAP215/chTOG (Brouhard et al., 2008; Howard and Hyman, 2007), whereas the minus ends are either capped by  $\gamma$ -TuRC, or their growth is inhibited by different factors. CAMSAP2 and particularly CAMSAP3 slow down tubulin addition to the minus-ends, possibly by affecting their structure (Atherton et al., 2017; Jiang et al., 2014). However, since growth of CAMSAP-decorated minus-ends is processive, one would still expect formation of long stretches of CAMSAP-bound microtubule lattices. One of the reasons why this does not happen might be further inhibition of minus-end growth by WDR47 or katanin. Restricting the length of the minus-end-grown and CAMSAP-decorated microtubule lattices by inhibiting minus-end polymerization would further reduce katanin-mediated severing and amplification because of fewer available cutting sites.

An interesting aspect of such regulation is the interplay between WDR47 and CAMSAP1. CAMSAP1 by itself does not decorate microtubules but rather tracks their minus ends. CAMSAP1 does not interact with katanin but it does strongly bind to WDR47, and together, they can efficiently block microtubule minus-end elongation. In cells, CAMSAP1 can have microtubule-stabilizing effects in glia (Coquand et al., 2021), and its loss in neurons shows phenotypes similar to those of WDR47, such as formation of multiple axons and inhibition of multipolar-bipolar transition during critical neuronal migration (Chen et al., 2020; Zhou et al., 2020). It would be interesting to examine in vitro whether the combination of WDR47 and CAMSAP1 is more potent than CAMSAP1 alone in protecting microtubule minus ends against depolymerization by depolymerases such as MCAK.

To conclude, we have shown that in vitro assays of increasing complexity can be used to dissect the interplay of different regulators in controlling microtubule dynamics and stability. In future, it will be worthwhile to build this complexity even further, by including more proteins or mimicking regulatory effects of protein modifications such as phosphorylation.

## **Materials and methods**

### **DNA constructs**

We used previously described katanin p60/p80C and katanin p60/p80 constructs (Jiang et al., 2017). p80C-SNAP-Twin-Strep and katanin p80-SNAP-Twin-Strep constructs were made by cloning into a modified pTT5 expression vector (Addgene no. 44006) with a C-terminus SNAP-Twin-Strep-tag. GFP-WDR47 construct was described previously (Buijs et al., 2021). Twin-Strep-GFP-WDR47 was made by cloning the full length construct in a modified C1 expression vector with an N-terminus Twin-Strep-GFP-tag. Twin-Strep-mCherry-CAMSAP1, Bio-Tev-mCherry-CAMSAP2 and Bio-Tev-mCherry-CAMSAP3 were made by cloning the previously described full length constructs (Jiang et al., 2014) in modified C1 vectors with either a Twin-Strep-mCherry or Bio-Tev-mCherry tag at the N-terminus. Twin-Strep-tag has been abbreviated as SII-tag in the rest of the chapter.

### **Cell lines and cell culture**

HEK293T cells (from ATCC) were cultured in Dulbecco's Modified Eagle's Medium DMEM/Ham's F10 media (1:1) supplemented with 10% fetal calf serum (FCS) and 1% antibiotics (penicillin and streptomycin) at 37 °C. This cell line was not found in the commonly misidentified cell lines database maintained by the Immunization Coalition of Los Angeles County. The cell lines were routinely checked for mycoplasma contamination using LT07-518 Mycoalert assay. Polyethylenimine (PEI, Polysciences) was used to transfect HEK293T cells with plasmids at 3:1 ratio of PEI:plasmid for StrepTactin- and Streptavidin-affinity based protein purification.

### **Purification of recombinant proteins from HEK293T cells for in vitro reconstitution assays**

Recombinant proteins used in the in vitro reconstitution assays (human GFP-WDR47 and mCherry-CAMSAP1, mouse p60/p80C-SNAP-AF647 and p60/p80-SNAP-AF647) used in the in vitro reconstitution assays were purified using Twin-Strep-tag and Strep-Tactin affinity purification method as described previously (Sharma et al., 2016). In brief, HEK293T cells were transfected with 50 µg of respective constructs per 15 cm dish and harvested 36 hours post-transfection from four 15 cm dishes each. For purification of katanin complex, 30 µg each of both the katanin subunits p60 and p80 constructs were transfected per 15 cm dish. Cells were resuspended and lysed in lysis buffer (50 mM HEPES, 300 mM NaCl, 0.5% Triton-X-100, 1

mM MgCl<sub>2</sub> and 1 mM EGTA (also 1 mM ATP for katanin), pH 7.4) supplemented with EDTA-free protease inhibitor cocktail (Roche). Cell lysates were clarified by centrifugation at 21,000xg for 20 min at 4 °C. The supernatants obtained from the previous step were incubated with equilibrated Strep-Tactin Sepharose beads (28-9355-99, GE Healthcare) for 45 min at 4 °C. Following incubation, beads were washed three times with the wash buffer (50 mM HEPES, 300 mM NaCl and 0.1% Triton-X-100, 1 mM MgCl<sub>2</sub>, 1 mM EGTA and 1 mM DTT (also 1 mM ATP for katanin), pH 7.4) and proteins were eluted for 15 min at 4 °C in elution buffer (50 mM HEPES, 150 mM NaCl (300 mM NaCl and also 1 mM ATP for katanin), 0.05% Triton-X-100, 1 mM MgCl<sub>2</sub>, 1 mM EGTA, 1 mM DTT and 2.5 mM d-Desthiobiotin, pH 7.4). For SNAP-tag labeling of katanin p80C or full-length p80 with Alexa Fluor 647 dye, washed beads were incubated with labeling mix (50 μM Alexa Fluor 647 dye in 50 mM HEPES, 150 mM NaCl and 0.1% Triton-X-100, 1 mM MgCl<sub>2</sub>, 1 mM EGTA, 1 mM ATP and 1 mM DTT, pH 7.4) for 1 hour. Following this incubation, beads were washed five times with wash buffer containing 300 mM NaCl to remove excess dye before elution. After elution, purified katanin was then subjected to buffer exchange using Vivaspin 500 centrifugal concentrator (10 kDa MWCO, Sartorius VS0102) for a final NaCl concentration of 150 mM in eluate.

For GFP-WDR47 purification, following the incubation of the beads with the lysate, beads were additionally washed five times using high salt (1 M NaCl) containing wash buffer (50 mM HEPES, 0.1% Triton-X-100, 1 mM MgCl<sub>2</sub> and 1 mM EGTA, pH 7.4) before washing three times with 300 mM NaCl containing wash buffer.

For purification of human mCherry-CAMSAP2 and mouse mCherry-CAMSAP3, HEK293T cells were transfected with 25 μg of Bio-Tev-mCherry-CAMSAP2 and 25 μg of BirA per 15 cm dish. Cells were harvested 36 hours post-transfection from four 15 cm dishes and resuspended in lysis buffer (50 mM HEPES, 300 mM NaCl, 0.5% Triton-X-100, 1 mM MgCl<sub>2</sub>, 1 mM EGTA and 1 mM DTT, pH 7.4) supplemented with EDTA-free protease inhibitor cocktail (Roche). Cell lysates were incubated with Dynabeads M-280 streptavidin (Invitrogen-11206D) for 1 hour. Beads were washed thrice with lysis buffer without protease inhibitors and thrice with the TEV cleavage buffer (50 mM HEPES, 150 mM NaCl, 0.05% Triton-X-100, 1 mM MgCl<sub>2</sub>, 1 mM EGTA and 1 mM DTT). Proteins were eluted in 50 μl TEV cleavage buffer containing 0.5 μg of glutathione S-transferase-6x-histidine Tobacco etch virus protease site (Sigma-Aldrich) for 2 hr at 4 °C.

Purified proteins were immediately aliquoted, snap-frozen in liquid N<sub>2</sub> and stored at -80 °C. The purity and composition of purified proteins were analyzed by Coomassie-staining of SDS-PAGE gels and mass spectrometry.

**Mass spectrometry**

To assess the quality of purified recombinant proteins that were previously not characterized (GFP-WDR47 and katanin p60/p80-SNAP-AF647), samples were digested using S-TRAP micro filters (ProtiFi) according to the manufacturer's protocol. In brief, 4 µg of protein samples were denatured using 5% SDS buffer, then reduced and alkylated using DTT (20 mM, 10 min, 95 °C) and iodoacetamide (IAA, 40 mM, 30 min). Samples were subjected to acidification and precipitation using a methanol triethylammonium bicarbonate (TEAB) buffer before loading on a S-TRAP column. Trapped proteins were washed with methanol TEAB buffer for four times and then were digested overnight using Trypsin (1 µg, Promega) at 37 °C. Digested peptides were eluted and dried in a vacuum centrifuge before LC-MS analysis.

Reversed phase nLC-MS/MS using an Ultimate 3000 UHPLC coupled to an Orbitrap Q Exactive HF-X mass spectrometer (Thermo Scientific) was used for analysis of samples. Digested peptides were separated over a 50 cm reversed phase column, packed in-house, (Agilent Poroshell EC-C18, 2.7 µm, 50 cm x 75 µm) using a linear gradient with buffer A (0.1% FA) and buffer B (80% acetonitrile, 0.1% FA) ranging from 13-44% B at a flow rate of 300 nL/min over 38 min, followed by a column wash and re-equilibration step. MS data was acquired using a DDA method with the set MS1 scan parameters in profile mode: 60,000 resolution, automatic gain control (AGC) target equal to 3E6, scan range of 375-1600 m/z, maximum injection time of 20 ms. The MS2 scan parameters were set at 15,000 resolution, with an AGC target set to standard, an automatic maximum injection time and an isolation window of 1.4 m/z. Scans were acquired first using a fixed mass of 120 m/z, a mass range of 200-2000 and a normalized collision energy (NCE) of 28. Precursor ions were selected for fragmentation using a 1 s scan cycle, a 10 s dynamic exclusion time and a precursor charge selection filter for ion possessing +2 to +6 charges. The total data acquisition took 55 min.

Raw files were processed using Proteome Discoverer (PD) (version 2.4, Thermo Scientific). A database search was performed using Sequest HT for MS/MS fragment spectra against a human database (UniProt, year 2020) that was modified to include protein sequences from our cloned constructs and a common contaminants database. A fragment mass tolerance of 0.06 Da and precursor mass tolerance of 20 ppm was set for the search parameters. Up to two missed cleavages were allowed by Trypsin digestion. Carbamidomethylation was set as fixed modification and methionine oxidation and protein N-term acetylation was set as variable modifications. Data filtering performed using percolator resulted in 1% FDR for peptide spectrum match (PSM) and a 1% FDR was applied to peptide and protein assemblies. An

additional filter with a minimum Sequest score of 2.0 was set for PSM inclusion. MS1 based quantification was performed using the Precursor Ion Quantifier node with default settings and precursor ion feature matching was enabled using the Feature Mapper node. Common protein contaminants from the results table were filtered out.

## **In vitro reconstitution assays**

### *Preparation of GMPCPP-stabilized microtubule seeds*

Double-cycled GMPCPP-stabilized microtubules used for in vitro assays were prepared as described previously (Mohan et al., 2013). In brief, GMPCPP-stabilized microtubules seeds were prepared in the presence of GMPCPP (Guanylyl-(a,b)-methylene-diphosphonate (Jena Biosciences)) by two rounds of polymerization and a depolymerization cycle. First, a 20  $\mu$ M porcine brain tubulin (Cytoskeleton) mix composed of 70% porcine unlabeled tubulin, 18% biotin tubulin and 12% labeled-tubulin was incubated with 1 mM GMPCPP in MRB80 buffer (pH 6.8, 80 mM K-PIPES, 1 mM EGTA and 4 mM MgCl<sub>2</sub>) for 30 minutes at 37 °C. Polymerization mix was then pelleted by centrifugation in an Airfuge at 119,000xg for 5 min followed by resuspension and depolymerization in MRB80 buffer for 20 min on ice and subsequent polymerization for 30 min in presence of fresh 1 mM GMPCPP at 37 °C. GMPCPP-stabilized microtubule seeds were pelleted, resuspended in MRB80 buffer containing 10% glycerol, aliquoted, snap-frozen in liquid N<sub>2</sub> and stored at -80 °C.

### *In vitro reconstitution of microtubule dynamics*

In vitro reconstitution assays were performed as previously described (Mohan et al., 2013). Flow chamber was assembled using plasma-cleaned glass coverslip (18 x 18 mm coverslips) and microscopic slide attached together using double-sided tape. These chambers were then functionalized by 5 min incubation with 0.2 mg/ml PLL-PEG-biotin (Susos AG, Switzerland) followed by 5 min incubation with 1 mg/ml NeutrAvidin (Invitrogen) in MRB80 buffer. Next, biotinylated-GMPCPP-stabilized microtubule seeds were attached to the coverslip through biotin-NeutrAvidin links by incubating the chamber for 3 min. Non-immobilized seeds were washed away with MRB80 buffer and flow chambers were further incubated with 0.8 mg/ml k-casein to prevent non-specific protein binding. The reaction mix with or without proteins (MRB80 buffer supplemented with 15  $\mu$ M porcine brain tubulin, 80 mM KCl, 1 mM GTP, 0.5 mg/ml k-casein, 0.1% methylcellulose, and oxygen scavenger mix (50 mM glucose, 400 mg/ml glucose-oxidase, 200 mg/ml catalase, and 4 mM DTT)) were added to the flow chambers after

centrifugation in an ultracentrifuge (Beckman Airfuge) for 5 minutes at 119,000xg. Concentrations of the proteins and composition of the reaction mix have been indicated in either figures or figure legends. The flow chambers were then sealed with high-vacuum silicone grease (Dow Corning), and three consecutive 10 min time-lapse videos of 3 different ROIs from the flow chambers were acquired after 2 min incubation (time, t=0) on total internal reflection fluorescence microscope stage at 30 °C. All tubulin products were from Cytoskeleton.

#### *Flow-in assays for microtubule severing*

For flow-in assays, special flow-in chambers were prepared using 24 x 32 mm coverslips attached orthogonally with the slides using double sided tape. Flow chamber was functionalized as mentioned above and GMPCPP-stabilized microtubule seeds were attached to the coverslip through biotin-neutravidin links. Flow chamber was then incubated with 0.8 mg/ml k-casein to prevent non-specific protein binding. Next, a microtubule polymerization mix (15  $\mu$ M tubulin, 80 mM KCl, 1 mM GTP, 1 mM ATP, 0.5 mg/ml k-casein, 0.1% methylcellulose, and oxygen scavenger mix (50 mM glucose, 400 mg/ml glucose-oxidase, 200 mg/ml catalase, and 4 mM DTT) in MRB80 buffer with or without proteins centrifuged in an Airfuge for 5 min at 119,000xg) was added to the chamber and a 10 min time-lapse video was acquired after 2 min incubation (time, t=0) on TIRF microscope stage at 30 °C to monitor the polymerization of microtubule minus-ends. Immediately, another 20 min time-lapse movie was acquired during which the microtubule severing mix (polymerization mix containing katanin) was flowed into the chamber at 5 min after start of this movie.

### **Image acquisition, processing and data analysis**

#### *TIRF microscopy*

In vitro assays were imaged on an iLas2 TIRF microscope setup as described previously (Sharma et al., 2016). Briefly, iLas2 system (Roper Scientific, Evry, France) is a dual laser illuminator for azimuthal spinning TIRF illumination. This system was installed on the Nikon Eclipse Ti-E inverted microscope with a perfect focus system. This microscope was equipped with Nikon Apo TIRF 100x 1.49 N.A. oil objective (Nikon), CCD camera CoolSNAP MYO M- USB-14-AC (Roper Scientific) and EMCCD Evolve mono FW DELTA 512x512 camera (Roper Scientific) with the intermediate lens 2.5X (Nikon C mount adaptor 2.5X), 150 mW 488 nm laser, 100 mW 561 nm laser and 49002 and 49008 Chroma filter sets and controlled



with MetaMorph 7.10.2.240 software (Molecular Devices). The final magnification using Evolve EMCCD camera was 0.064  $\mu\text{m}/\text{pixel}$ . Temperature was maintained at 30 °C to image the in vitro assays using a stage top incubator model INUBG2E-ZILCS (Tokai Hit). Time-lapse images were acquired on Photometrics Evolve 512 EMCCD camera (Roper Scientific) at 3 s time interval with 100 ms exposure time for 10 or 20 minutes.

#### *Microtubule growth dynamics analysis*

Images and movies were processed using Fiji (<https://imagej.net/Fiji>). Kymographs from the in vitro reconstitution assays were generated using the ImageJ plugin KymoResliceWide v.0.4 <https://github.com/ekatruxha/KymoResliceWide>. Microtubule dynamics parameters viz. plus-end growth rate and catastrophe frequency were determined from kymographs using an optimized version of the custom-made JAVA plugin for ImageJ as described previously (Gouveia et al., 2010; Mohan et al., 2013).

#### *Quantification of the number of microtubules generated upon katanin-mediated severing*

Microtubules that were generated after flow-in from katanin-mediated cutting/fragmentation of polymerized minus end lattice (decorated by CAMSAP2/3 or tracked by CAMSAP1) and then subsequent cutting of the minus ends of these newly generated microtubules were counted into the total number of microtubules generated from a parent single microtubule. Microtubules generated as a result of cutting at the polymerized plus end lattice or microtubule crossovers were not considered in this analysis.

#### *Analysis of minus-end growth behaviors*

All the microtubule minus-end growth events were categorized into 3 categories: no blocking- when the minus ends started growing from the start of the movie; temporarily blocked- when minus were blocked for a short time from the beginning of the movie and then transitioned to a growing phase; completely blocked- when minus ends were not growing at all and totally blocked for the entire 10 min duration of the movie.

### **Statistical analysis**

All statistical details of experiments including the definitions, exact values of number of measurements, number of replicates, precision measures and statistical tests performed are mentioned in the figure legends. Data processing and statistical analysis were done in Excel

and GraphPad Prism 9. Significance was defined as: ns = not significant for  $p > 0.05$ , \* $p < 0.05$ , \*\* $p < 0.01$ , \*\*\* $p < 0.001$  and \*\*\*\* $p < 0.0001$ .

**Data availability**

All data that support the conclusions are either available in the manuscript itself or available from the authors on request.

**Code availability**

ImageJ macros used in this study are either available online at <https://github.com/ekatrakha/KymoResliceWide> or from the corresponding authors on request.

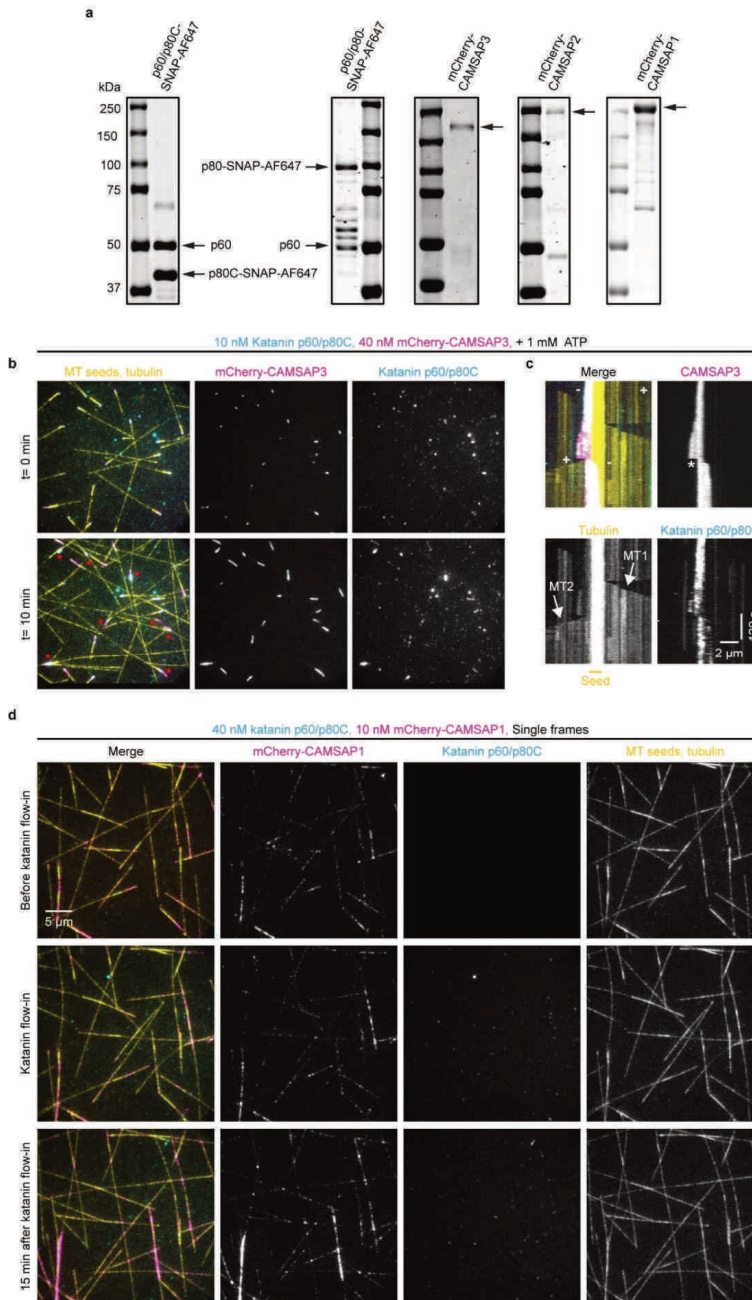
## References

- Akhmanova, A., and C.C. Hoogenraad. 2015. Microtubule Minus-End-Targeting Proteins. *Curr. Biol.* 25:R162-R171.
- Akhmanova, A., and L.C. Kapitein. 2022. Mechanisms of microtubule organization in differentiated animal cells. *Nat Rev Mol Cell Biol.* 23:541-558.
- Akhmanova, A., and M.O. Steinmetz. 2015. Control of microtubule organization and dynamics: two ends in the limelight. *Nat Rev Mol Cell Biol.* 16:711-726.
- Akhmanova, A., and M.O. Steinmetz. 2019. Microtubule minus-end regulation at a glance. *J Cell Sci.* 132.
- Atherton, J., K. Jiang, M.M. Stangier, Y. Luo, S. Hua, K. Houben, J.J.E. van Hooff, A.P. Joseph, G. Scarabelli, B.J. Grant, A.J. Roberts, M. Topf, M.O. Steinmetz, M. Baldus, C.A. Moores, and A. Akhmanova. 2017. A structural model for microtubule minus-end recognition and protection by CAMSAP proteins. *Nature structural & molecular biology.* 24:931-943.
- Bailey, M.E., D.L. Sackett, and J.L. Ross. 2015. Katanin Severing and Binding Microtubules Are Inhibited by Tubulin Carboxy Tails. *Biophys J.* 109:2546-2561.
- Baines, A.J., P.A. Bignone, M.D. King, A.M. Maggs, P.M. Bennett, J.C. Pinder, and G.W. Phillips. 2009. The CKK domain (DUF1781) binds microtubules and defines the CAMSAP/ssp4 family of animal proteins. *Mol Biol Evol.* 26:2005-2014.
- Bieling, P., L. Laan, H. Schek, E.L. Munteanu, L. Sandblad, M. Dogterom, D. Brunner, and T. Surrey. 2007. Reconstitution of a microtubule plus-end tracking system in vitro. *Nature.* 450:1100-1105.
- Brouhard, G.J., J.H. Stear, T.L. Noetzel, J. Al-Bassam, K. Kinoshita, S.C. Harrison, J. Howard, and A.A. Hyman. 2008. XMAP215 is a processive microtubule polymerase. *Cell.* 132:79-88.
- Buijs, R.R., J.J.A. Hummel, M. Burute, X. Pan, Y. Cao, R. Stucchi, M. Altelaar, A. Akhmanova, L.C. Kapitein, and C.C. Hoogenraad. 2021. WDR47 protects neuronal microtubule minus ends from katanin-mediated severing. *Cell reports.* 36:109371.
- Burute, M., and L.C. Kapitein. 2019. Cellular Logistics: Unraveling the Interplay Between Microtubule Organization and Intracellular Transport. *Annu Rev Cell Dev Biol.* 35:29-54.
- Chen, Y., J. Zheng, X. Li, L. Zhu, Z. Shao, X. Yan, and X. Zhu. 2020. Wdr47 Controls Neuronal Polarization through the Camsap Family Microtubule Minus-End-Binding Proteins. *Cell reports.* 31:107526.
- Coquand, L., G.S. Victoria, A. Tata, J.A. Carpentieri, J.B. Brault, F. Guimiot, V. Fraisier, and A.D. Baffet. 2021. CAMSAPs organize an acentrosomal microtubule network from basal varicosities in radial glial cells. *J Cell Biol.* 220:e202003151.
- Desai, A., and T.J. Mitchison. 1997. Microtubule polymerization dynamics. *Annu Rev Cell Dev Biol.* 13:83-117.
- Dong, C., H. Xu, R. Zhang, N. Tanaka, M. Takeichi, and W. Meng. 2017. CAMSAP3 accumulates in the pericentrosomal area and accompanies microtubule release from the centrosome via katanin. *J Cell Sci.* 130:1709-1715.
- Gouveia, S.M., K. Leslie, L.C. Kapitein, R.M. Buey, I. Grigoriev, M. Wagenbach, I. Smal, E. Meijering, C.C. Hoogenraad, L. Wordeman, M.O. Steinmetz, and A. Akhmanova. 2010. In Vitro Reconstitution of the Functional Interplay between MCAK and EB3 at Microtubule Plus Ends. *Current Biology.* 20:1717-1722.
- Hendershott, M.C., and R.D. Vale. 2014. Regulation of microtubule minus-end dynamics by CAMSAPs and Patronin. *Proc Natl Acad Sci U S A.* 111:5860-5865.

- Howard, J., and A.A. Hyman. 2007. Microtubule polymerases and depolymerases. *Curr Opin Cell Biol.* 19:31-35.
- Jiang, K., L. Faltova, S. Hua, G. Capitani, A.E. Prota, C. Landgraf, R. Volkmer, R.A. Kammerer, M.O. Steinmetz, and A. Akhmanova. 2018. Structural Basis of Formation of the Microtubule Minus-End-Regulating CAMSAP-Katanin Complex. *Structure.* 26:375-382 e374.
- Jiang, K., S. Hua, R. Mohan, I. Grigoriev, K.W. Yau, Q. Liu, E.A. Katrukha, A.F. Altelaar, A.J. Heck, C.C. Hoogenraad, and A. Akhmanova. 2014. Microtubule minus-end stabilization by polymerization-driven CAMSAP deposition. *Dev Cell.* 28:295-309.
- Jiang, K., L. Rezabkova, S. Hua, Q. Liu, G. Capitani, A.F.M. Altelaar, A.J.R. Heck, R.A. Kammerer, M.O. Steinmetz, and A. Akhmanova. 2017. Microtubule minus-end regulation at spindle poles by an ASPM-katanin complex. *Nat Cell Biol.* 19:480-492.
- Kannan, M., E. Bayam, C. Wagner, B. Rinaldi, P.F. Kretz, P. Tilly, M. Roos, L. McGillewie, S. Bar, S. Minocha, C. Chevalier, C. Po, P. Sanger Mouse Genetics, J. Chelly, J.L. Mandel, R. Borgatti, A. Piton, C. Kinnear, B. Loos, D.J. Adams, Y. Herault, S.C. Collins, S. Friant, J.D. Godin, and B. Yalcin. 2017. WD40-repeat 47, a microtubule-associated protein, is essential for brain development and autophagy. *Proc Natl Acad Sci U S A.* 114:E9308-E9317.
- Khanal, I., A. Elbediwy, C. Diaz de la Loza Mdel, G.C. Fletcher, and B.J. Thompson. 2016. Shot and Patronin polarise microtubules to direct membrane traffic and biogenesis of microvilli in epithelia. *J Cell Sci.* 129:2651-2659.
- King, M.D., G.W. Phillips, P.A. Bignone, N.V. Hayes, J.C. Pinder, and A.J. Baines. 2014. A conserved sequence in calmodulin regulated spectrin-associated protein 1 links its interaction with spectrin and calmodulin to neurite outgrowth. *J Neurochem.* 128:391-402.
- Kuo, Y.W., and J. Howard. 2021. Cutting, Amplifying, and Aligning Microtubules with Severing Enzymes. *Trends Cell Biol.* 31:50-61.
- Liu, H., J. Zheng, L. Zhu, L. Xie, Y. Chen, Y. Zhang, W. Zhang, Y. Yin, C. Peng, J. Zhou, X. Zhu, and X. Yan. 2021a. Wdr47, Camsaps, and Katanin cooperate to generate ciliary central microtubules. *Nat Commun.* 12:5796.
- Liu, P., M. Wurtz, E. Zupa, S. Pfeffer, and E. Schiebel. 2021b. Microtubule nucleation: The waltz between gamma-tubulin ring complex and associated proteins. *Curr Opin Cell Biol.* 68:124-131.
- Lynn, N.A., E. Martinez, H. Nguyen, and J.Z. Torres. 2021. The Mammalian Family of Katanin Microtubule-Severing Enzymes. *Front Cell Dev Biol.* 9:692040.
- Mohan, R., E.A. Katrukha, H. Doodhi, I. Smal, E. Meijering, L.C. Kapitein, M.O. Steinmetz, and A. Akhmanova. 2013. End-binding proteins sensitize microtubules to the action of microtubule-targeting agents. *Proc Natl Acad Sci U S A.* 110:8900-8905.
- Noordstra, I., Q. Liu, W. Nijenhuis, S. Hua, K. Jiang, M. Baars, S. Remmelzwaal, M. Martin, L.C. Kapitein, and A. Akhmanova. 2016. Control of apico-basal epithelial polarity by the microtubule minus-end-binding protein CAMSAP3 and spectraplaklin ACF7. *J Cell Sci.* 129:4278-4288.
- Pongrakhananon, V., H. Saito, S. Hiver, T. Abe, G. Shioi, W. Meng, and M. Takeichi. 2018. CAMSAP3 maintains neuronal polarity through regulation of microtubule stability. *Proc Natl Acad Sci U S A.* 115:9750-9755.
- Sanchez, A.D., and J.L. Feldman. 2017. Microtubule-organizing centers: from the centrosome to non-centrosomal sites. *Curr Opin Cell Biol.* 44:93-101.
- Sharma, A., A. Aher, N.J. Dynes, D. Frey, E.A. Katrukha, R. Jaussi, I. Grigoriev, M. Croisier, R.A. Kammerer, A. Akhmanova, P. Gonczy, and M.O. Steinmetz. 2016.

- Centriolar CPAP/SAS-4 Imparts Slow Processive Microtubule Growth. *Dev Cell.* 37:362-376.
- Song, C.-X., X.-T. Zeng, W.-X. Zeng, X.-J. Tong, and Q. Li. 2022. WDR47 facilitates cell-specific ciliogenesis by modulating intraflagellar transport. *bioRxiv:2022.2004.2010.487758*.
- Thawani, A., and S. Petry. 2021. Molecular insight into how gamma-TuRC makes microtubules. *J Cell Sci.* 134.
- Toya, M., S. Kobayashi, M. Kawasaki, G. Shioi, M. Kaneko, T. Ishiuchi, K. Misaki, W. Meng, and M. Takeichi. 2016. CAMSAP3 orients the apical-to-basal polarity of microtubule arrays in epithelial cells. *Proc Natl Acad Sci U S A.* 113:332-337.
- Vemu, A., E. Szczesna, E.A. Zehr, J.O. Spector, N. Grigorieff, A.M. Deaconescu, and A. Roll-Mecak. 2018. Severing enzymes amplify microtubule arrays through lattice GTP-tubulin incorporation. *Science.* 361:eaau1504.
- Vineethakumari, C., and J. Luders. 2022. Microtubule Anchoring: Attaching Dynamic Polymers to Cellular Structures. *Front Cell Dev Biol.* 10:867870.
- Walczak, C.E., S. Gayek, and R. Ohi. 2013. Microtubule-depolymerizing kinesins. *Annu Rev Cell Dev Biol.* 29:417-441.
- Wu, J., and A. Akhmanova. 2017. Microtubule-Organizing Centers. *Annu Rev Cell Dev Biol.* 33:51-75.
- Yau, K.W., S.F. van Beuningen, I. Cunha-Ferreira, B.M. Cloin, E.Y. van Battum, L. Will, P. Schatzle, R.P. Tas, J. van Krugten, E.A. Katrukha, K. Jiang, P.S. Wulf, M. Mikhaylova, M. Harterink, R.J. Pasterkamp, A. Akhmanova, L.C. Kapitein, and C.C. Hoogenraad. 2014. Microtubule minus-end binding protein CAMSAP2 controls axon specification and dendrite development. *Neuron.* 82:1058-1073.
- Zhou, Z., H. Xu, Y. Li, M. Yang, R. Zhang, A. Shiraishi, H. Kiyonari, X. Liang, X. Huang, Y. Wang, Q. Xie, S. Liu, R. Chen, L. Bao, W. Guo, Y. Wang, and W. Meng. 2020. CAMSAP1 breaks the homeostatic microtubule network to instruct neuronal polarity. *Proc Natl Acad Sci U S A.* 117:22193-22203.
- Zupa, E., P. Liu, M. Wurtz, E. Schiebel, and S. Pfeffer. 2021. The structure of the gamma-TuRC: a 25-years-old molecular puzzle. *Curr Opin Struct Biol.* 66:15-21.

## Supplementary Figures



*Extended data Figure 1, related to Figure 1 and 2 | Characterization of purified proteins and the effects of katanin-CAMSAP3 combinations.*

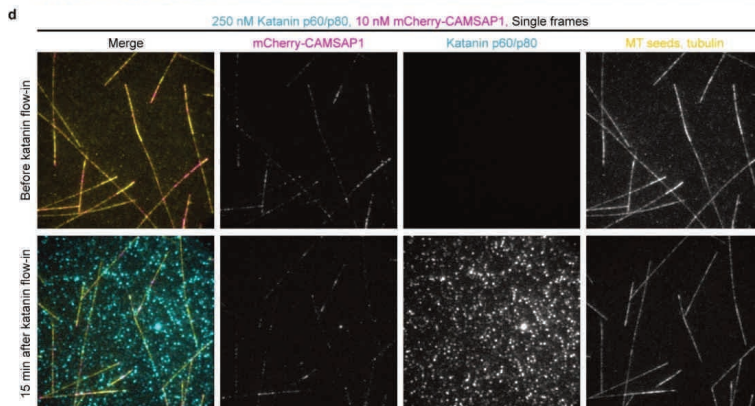
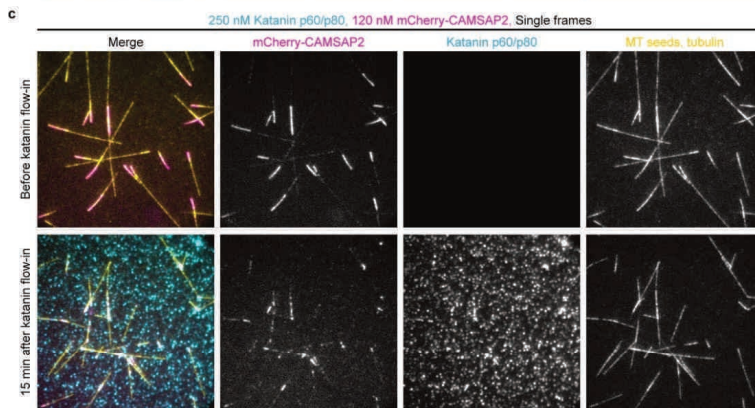
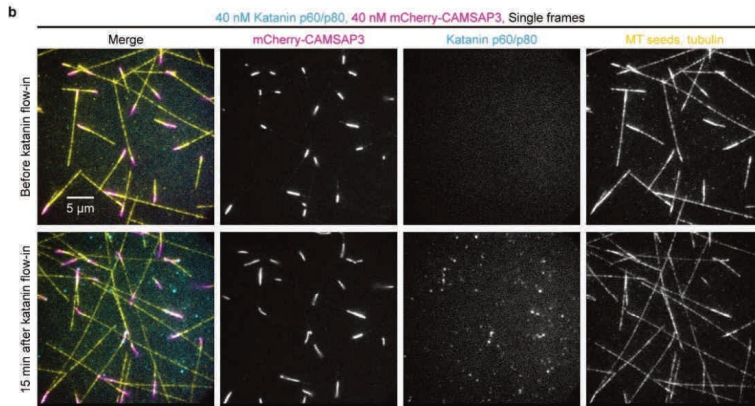
- a**, Coomassie-stained SDS-PAGE gels loaded with purified katanin p60/p80C-SNAP-AF647, katanin p60/p80-SNAP-AF647, mCherry-CAMSAP3 or mCherry-CAMSAP2 or mCherry-CAMSAP1.
- b**, Single last frames of a 10 min time-lapse video showing microtubule severing by katanin (cyan) upon its colocalization to the CAMSAP3-decorated (magenta) microtubule (yellow) minus-ends when 1 mM ATP was added to the assay condition (10 nM SNAP-AF647 labeled katanin p60/p80C, 40 nM mCherry-CAMSAP3, 15  $\mu$ M tubulin (14.5  $\mu$ M unlabeled porcine tubulin and 0.5  $\mu$ M HiLyte488-tubulin) as shown in **Fig. 1b and c (right panels)**. Red asterisks show cutting sites on microtubules.
- c**, Representative kymographs from the in vitro reconstitution experiments shown in **b**. Two white arrows show generation of a 2<sup>nd</sup> microtubule (MT2) upon severing of a pre-existing microtubule (MT1) polymerized from GMPCPP-stabilized seed.
- d**, Single frames (at indicated steps as described for **Fig. 2b**) from a 20 min time-lapse video showing lack of katanin (cyan) localization to CAMSAP1-decorated (magenta) microtubules (yellow) and, thereby, lack of severing by katanin (cyan) after substitution of microtubule polymerization mix (10 nM mCherry-CAMSAP1, 15  $\mu$ M tubulin (14.5  $\mu$ M unlabeled porcine tubulin and 0.5  $\mu$ M HiLyte488-tubulin) and 1 mM ATP) with the microtubule severing mix (the same mix as above but supplemented with 40 nM SNAP-AF647 labeled katanin p60/p80C).

**Extended data Figure 2, related to Figure 3 | Analysis of full-length katanin by mass spectrometry and characterization of effective concentrations of katanin and CAMSAPs for microtubule severing experiments.**

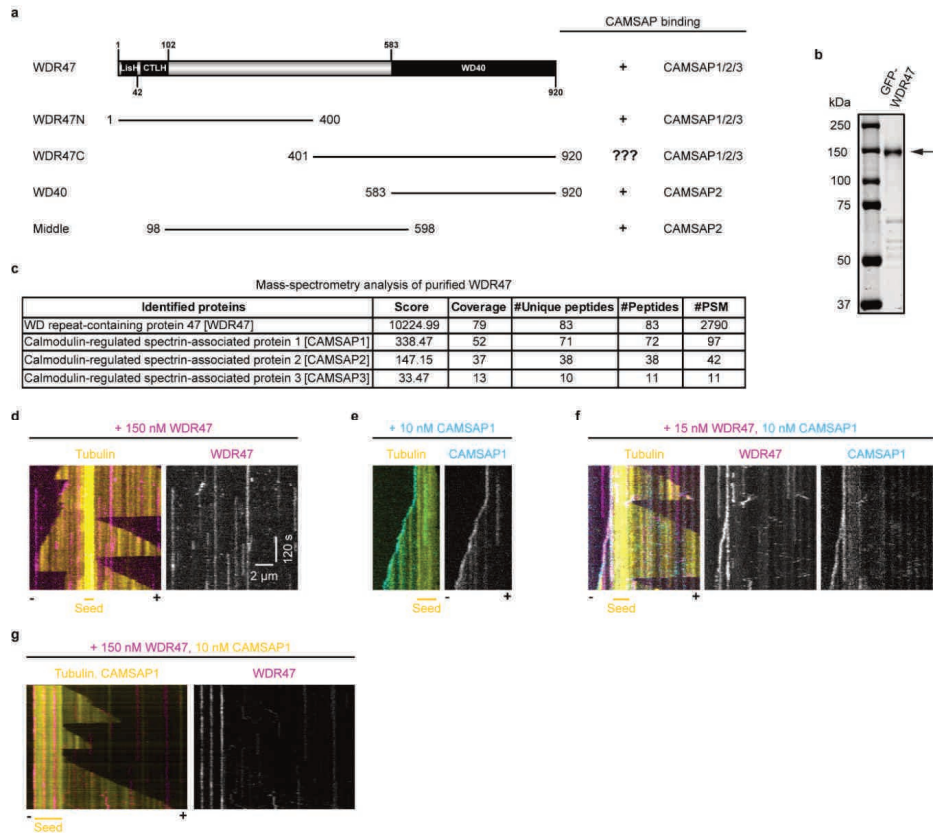
- a**, List of proteins identified by mass spectrometry that were co-purified with katanin p60/p80-SNAP-AF647-SII showing absence of any microtubule associated proteins in top hits. The values in the coverage column are percentages.
- b**, Single frames (at indicated steps as described for **Fig. 2b**) from a 20 min time-lapse video showing lack of any significant katanin (cyan) localization to CAMSAP3-decorated (magenta) microtubules (yellow) and, thereby, lack of severing by katanin p60/p80 (cyan) at lower concentration upon substitution of microtubule polymerization mix (40 nM mCherry-CAMSAP3, 15  $\mu$ M tubulin (14.5  $\mu$ M unlabeled porcine tubulin and 0.5  $\mu$ M HiLyte488-tubulin) and 1 mM ATP) with the microtubule severing mix (the same mix as above but supplemented with 40 nM SNAP-AF647 labeled katanin p60/p80).
- c**, Single frames (at indicated steps) from a 20 min time-lapse video showing very mild severing of CAMSAP2-decorated (magenta) microtubule (yellow) minus-ends by katanin (cyan), when higher concentration of CAMSAP2 (120 nM mCherry-CAMSAP2) was used in the experimental conditions shown in **Fig. 3c**.
- d**, Single frames (at indicated steps) from a 20 min time-lapse video showing lack of katanin p60/p80 (cyan) localization to CAMSAP1-decorated (magenta) microtubules (yellow) and, thereby, lack of severing by katanin (cyan) after substitution of microtubule polymerization mix (10 nM mCherry-CAMSAP1, 15  $\mu$ M tubulin (14.5  $\mu$ M unlabeled porcine tubulin and 0.5  $\mu$ M HiLyte488-tubulin) and 1 mM ATP) with the microtubule severing mix (the same mix as above but supplemented with 250 nM SNAP-AF647 labeled katanin p60/p80).

**a** Mass-spectrometry analysis of purified p60/p80

| Identified proteins   | Score   | Coverage | #Unique peptides | #Peptides | #PSM |
|---|---------|----------|------------------|-----------|------|
| Katanin p80 WD40 repeat-containing subunit B1 [KTNB1_MOUSE] | 2342.53 | 78       | 42               | 42        | 614  |
| Katanin p60 ATPase-containing subunit A1 [KTNA1_MOUSE]      | 2314.29 | 80       | 25               | 44        | 597  |
| Tubulin alpha-1C chain [TUBA1C]                             | 327.31  | 71       | 3                | 24        | 89   |
| Tubulin beta chain [TUBB]                                   | 513.62  | 73       | 5                | 26        | 148  |
| Katanin p60 ATPase-containing subunit A1 [KATNA1]           | 1080.95 | 62       | 11               | 30        | 291  |
| Katanin p60 ATPase-containing subunit A-like 1 [KATNAL1]    | 361.6   | 55       | 17               | 23        | 108  |
| KATNB1-like protein 1 [KATNBL1]                             | 39.23   | 43       | 9                | 9         | 12   |







**Extended data Figure 3, related to Figure 4 | Characterization of purified WDR47 and effects of its binding interaction with CAMSAP1 on microtubule minus-end growth behavior.**

**a**, Schematic representation of the domain structure of WDR47 and a summary of known interactions with CAMSAPs. Indicated domains: CTLH, C-terminal to LisH domain; LisH, lissencephaly-1 homology domain; WD40, WD40 repeat domain.

**b**, Coomassie-stained SDS-PAGE gel loaded with purified GFP-WDR47.

**c**, List of proteins identified by mass spectrometry shows presence of all the three CAMSAPs that were co-purified with GFP-WDR47. The values in the coverage column are percentages.

**d-f**, Representative kymographs illustrating other microtubule (yellow) minus-end growth behaviors: occasional minus-end binding of WDR47 (**d**, magenta); transition from temporarily blocked minus-end to growing minus-end by CAMSAP1 (cyan) binding and tracking (**e**); transition from temporarily blocked minus-end to growing minus-end by CAMSAP1 (cyan) and WDR47 (magenta) and their colocalization (**f**); in the presence of 150 nM GFP-WDR47 (**d**), or 10 nM mCherry-CAMSAP1 (**e**) or 15 nM GFP-WDR47 and 10 nM mCherry-CAMSAP1 (**f**) together with 15  $\mu$ M tubulin from the assays shown in **Fig. 4c-e, h-i** and **j-k** respectively.

*g*, Representative kymographs illustrating a completely blocked microtubule (yellow) minus-end in the presence of 10 nM CAMSAP1 (yellow) and 150 nM GFP-WDR47 (magenta).

---

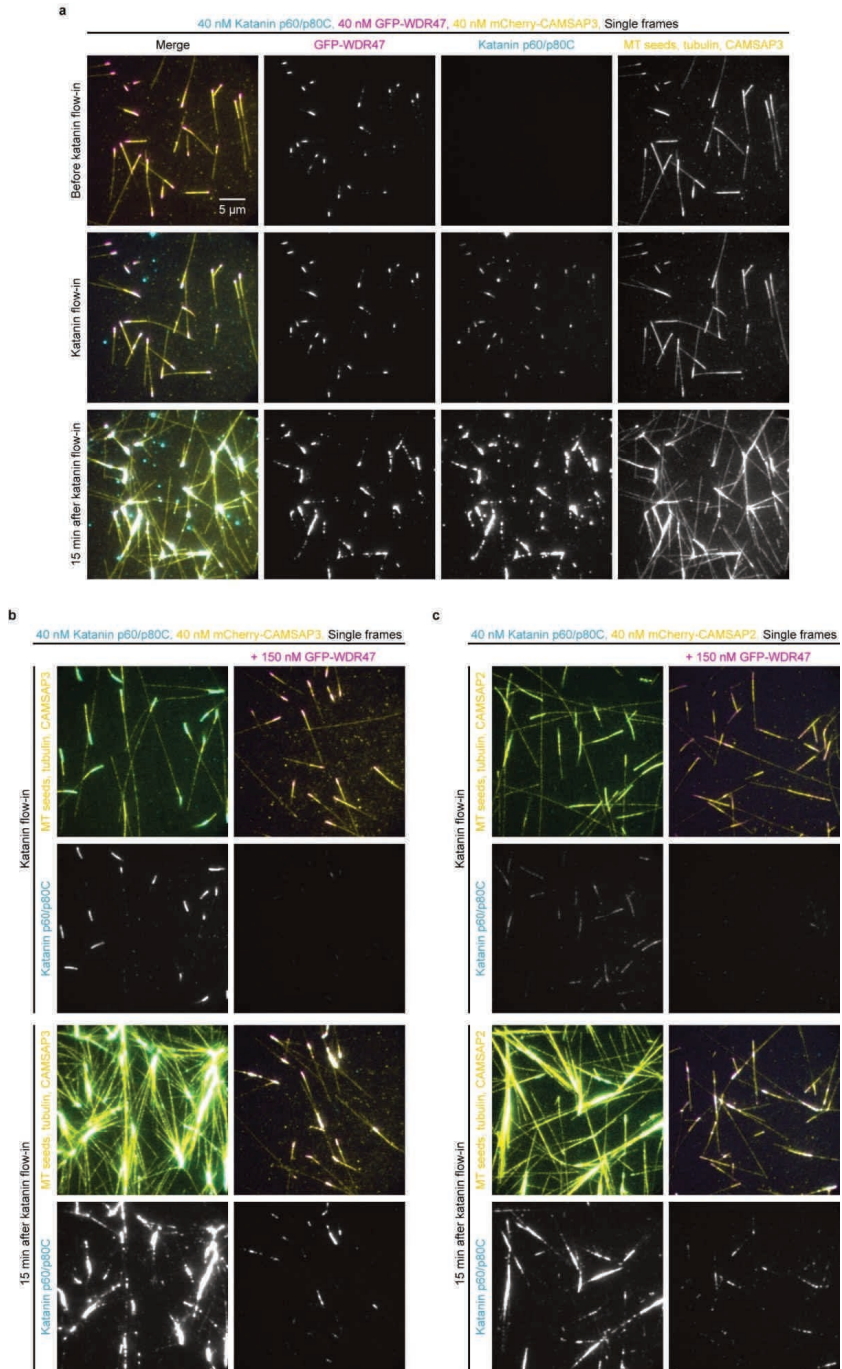
**Extended data Figure 4, related to Figure 5 | WDR47 interferes with the binding of katanin to CAMSAP2/3-decorated microtubule minus-ends.**

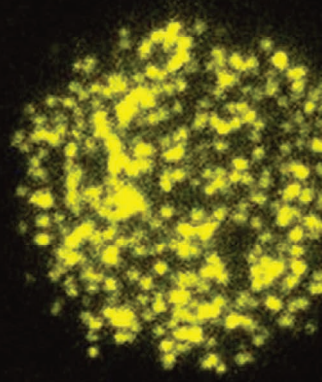
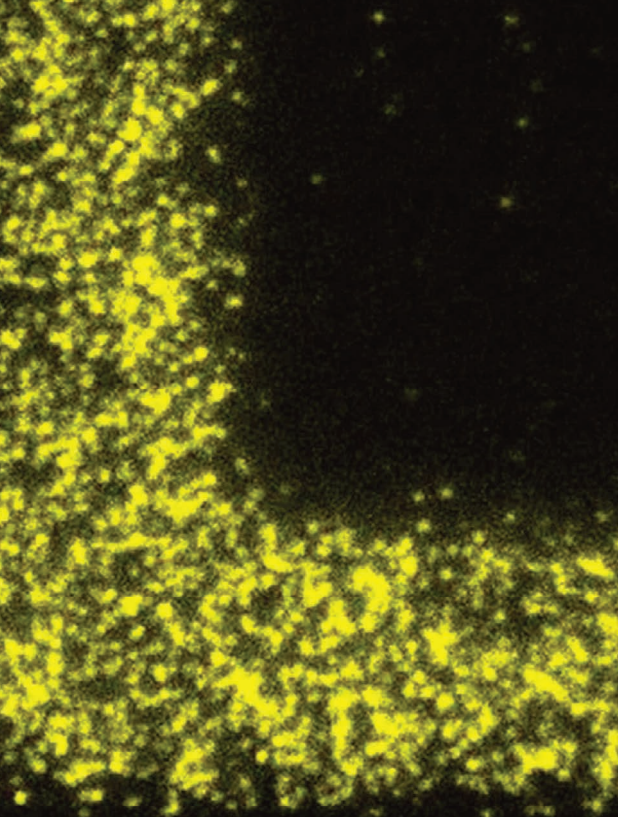
**a**, Single frames (at indicated steps as described for **Fig. 2b**) from a 20 min time-lapse video showing WDR47 (magenta) binding to CAMSAP3-decorated microtubule (yellow) minus-ends, but no strong protection against microtubule severing and amplification by katanin (cyan) upon katanin localization to microtubule minus ends after substitution of microtubule polymerization mix (40 nM GFP-WDR47, 40 nM mCherry-CAMSAP3, 15  $\mu$ M tubulin (14.5  $\mu$ M unlabeled porcine tubulin and 0.5  $\mu$ M rhodamine-tubulin) and 1 mM ATP) with the microtubule severing mix (the same mix as above but supplemented with 40 nM SNAP-AF647 labeled katanin p60/p80C). Intensity scale for katanin channel is same as that of in panels **b** and **c**.

**b,c**, Single frames (at indicated steps) from 20 min time-lapse videos showing suppression of katanin (cyan) binding to CAMSAP2- (**b**) or CAMSAP3-decorated (**c**) microtubule (yellow) minus-ends by WDR47 (magenta, right panels). These images have been reused from **Fig. 2b, d** and **Fig. 5a, b** and scaled to the same intensity level for katanin channel.

Acquisition settings for these assays were kept constant.

Figure continued...

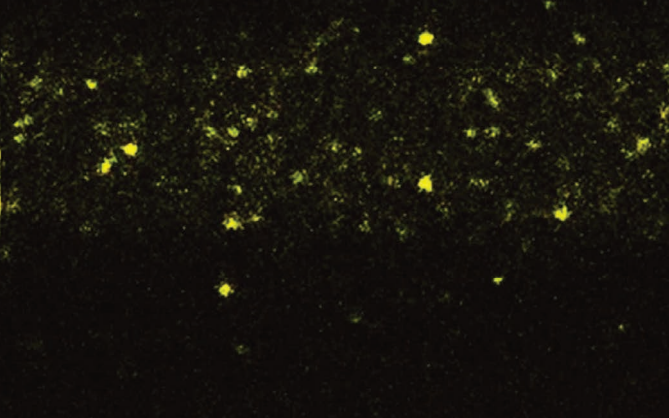
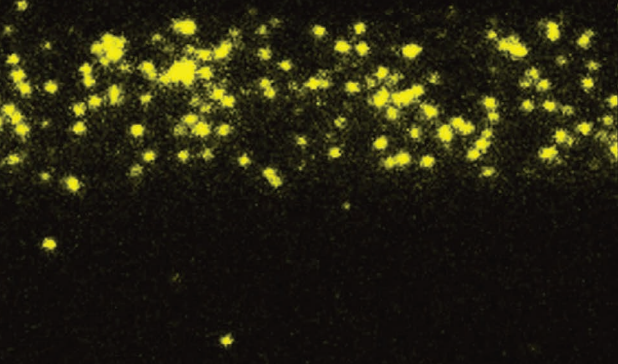




CDK5RAP2 chTOG

GCP3

CLASP2 Ninein



# 6

## General Discussion

Dipti Rai

In this thesis, we used powerful *in vitro* reconstitution assays with purified proteins to study different aspects of the dynamic life of microtubules. With this approach, we can precisely control the concentrations and stoichiometric ratios of tubulin and various regulatory proteins. This would allow us to study the functions of microtubule regulators in conditions that match the physiological setting or deviate from it. Moreover, we can also learn how the individual functions of a regulatory factor can be fine-tuned by its concentration or its dependency on additional factors. We first focused on the origin and growth of a microtubule in **Chapter 2**, and then explored, in **Chapters 3-5**, the different trajectories it follows. In **Chapter 3**, we demonstrated a mechanism for stabilization of microtubules that involves their bundling. In **Chapter 4**, we shed light on microtubule damage, repair and lattice renewal. In **Chapter 5**, we described how microtubule severing and destruction can, paradoxically, amplify microtubule number. In this final chapter, we discuss the advancements we have made over existing knowledge in these research areas.

### **Microtubule nucleation and minus-end regulation**

In cells, microtubules are mainly nucleated from a template called  $\gamma$ -TuRC (Tovey and Conduit, 2018; Liu et al., 2021b; Thawani and Petry, 2021). Recently, native and recombinant  $\gamma$ -TuRCs have been purified from different species ranging from yeast to human in order to perform structural and functional studies (Liu et al., 2020; Wieczorek et al., 2020b; Consolati et al., 2020; Zimmermann et al., 2020; Böhler et al., 2021; Brilot et al., 2021; Würtz et al., 2021, 2022). In Chapter 2, we designed a strategy to purify native  $\gamma$ -TuRCs from HEK293T cells, in which each GCP3 subunit was endogenously tagged with a Twin-Strep-tag and a GFP, for affinity purification and single molecule observations, respectively. This approach provides an advantage compared to other studies, which used either untagged native  $\gamma$ -TuRC purified by exploiting its affinity for the  $\gamma$ -TuNA region of CDK5RAP2 (Wieczorek et al., 2020b) or by using antibodies against  $\gamma$ -TuRC subunits (Liu et al., 2020), or a tagged  $\gamma$ -TuRC, purified by employing a lentivirus-based overexpression construct where not all  $\gamma$ -TuRC species were tagged (Consolati et al., 2020). In our system, we can study each fully assembled  $\gamma$ -TuRCs or even partial subcomplexes and observe nucleation of individual microtubules from a single surface-immobilized  $\gamma$ -TuRC using TIRF microscopy. We reconstituted  $\gamma$ -TuRC-mediated microtubule nucleation *in vitro* to study its regulation. Like others, we confirmed the low nucleation activity of non-activated  $\gamma$ -TuRC and also reported the stimulatory effect of chTOG and CDK5RAP2 on  $\gamma$ -TuRC activity (Choi et al., 2010; Liu et al., 2020; Consolati et al., 2020; Thawani et al., 2020; Wieczorek et al., 2021; Brilot et al., 2021; Würtz et al., 2021). We

additionally showed a strong enhancement of the nucleation efficiency of  $\gamma$ -TuRC by CLASP2. Most importantly, we discovered a new pathway for the generation of microtubule minus-ends that involves a sequential action of  $\gamma$ -TuRC and CAMSAP family proteins. We provide evidence that despite the fact that  $\gamma$ -TuRC caps the minus-end of the microtubule it nucleates, the attachment between microtubule minus end and  $\gamma$ -TuRC is not always perfect. CAMSAPs can still bind to some  $\gamma$ -TuRC-capped minus ends and displace  $\gamma$ -TuRC from these ends while promoting their elongation and stabilization.

We propose that these microtubule minus ends are not fully attached to  $\gamma$ -TuRC and have at least two free protofilaments that are flared at the end, creating a CAMSAP-binding site. It is already known that CAMSAPs bind to an intradimer site between protofilaments at the minus ends (Atherton et al., 2017). Their CKK domain specifically recognizes this unique site between two curved protofilaments with decreased curvature of  $\alpha$ -tubulin. Furthermore, CKK binding induces a protofilament tilt resulting in a right-handed protofilament skew relative to the microtubule helical axis (Atherton et al., 2019). This would lead to further deviation from the straight protofilament conformation at the minus end that would otherwise be necessary for complete attachment to  $\gamma$ -TuRC. CAMSAP2 and CAMSAP3 have also been shown to decorate and stabilize growing minus ends, promote their elongation and inhibit depolymerization, although they slow down minus-end growth rate (Jiang et al., 2014). It was also recently shown that CAMSAP2, which possesses an additional microtubule-binding domain (MBD) in the middle, and CAMSAP3, which contains two additional microtubule-binding regions, the MBD and a helical D2 domain next to the CKK, but not CAMSAP1, which lacks the MBD and D2 regions, prefer binding to expanded microtubule lattices like GMPCPP- and taxol-stabilized microtubules and expand the compact GDP-lattices (Liu and Shima, 2022). In this study, this feature of CAMSAP2/3 to “read” microtubule conformations and “write” structural modifications was compared to that of “reader/writer” MAPs, such as TPX2 and kinesin-1 KIF5C (Nakata et al., 2011; Morikawa et al., 2015; Roostalu et al., 2015; Zhang et al., 2017; Peet et al., 2018; Shima et al., 2018). Given this reading/writing abilities, the binding of CAMSAP2 and CAMSAP3 to the free protofilaments at the minus-ends of  $\gamma$ -TuRC-attached microtubules could promote detachment of the neighboring protofilaments from  $\gamma$ -TuRC. Further binding of CAMSAP2/3 would also stabilize the minus ends and promote their elongation, causing release of microtubules with free and stable minus ends. Subsequently, these modified minus ends with a newly written structural code (i.e., expanded lattice) can recruit molecular motors for their organization and anchoring to a different MTOC.

Coming back to how free protofilament ends are generated at the interface of  $\gamma$ -TuRC and the microtubule minus-end, a recent study could help to address this conundrum. It was shown that partial  $\gamma$ -TuRCs containing 4-5  $\gamma$ -TuSCs and lacking the luminal bridge could nucleate microtubules with the same efficiency as complete  $\gamma$ -TuRCs (Consolati et al., 2020; Thawani et al., 2020; Wieczorek et al., 2021). Since not all  $\gamma$ -tubulins in the ring are required for microtubule nucleation, lateral association of tubulin subunits with the assembling tubulin nucleus on  $\gamma$ -TuRC could lead to the formation of a microtubule with some  $\alpha$ -tubulin subunits at the minus end, which are not attached to  $\gamma$ -tubulin (Mandelkow et al., 1991; McIntosh et al., 2018; Wieczorek et al., 2021; Guyomar et al., 2022). However, the availability of free protofilament minus ends for CAMSAP binding could also be due to the asymmetric structure of  $\gamma$ -TuRC ring that only partially matches microtubule helical pitch and diameter, despite exposing 13  $\gamma$ -tubulin for binding of 13  $\alpha\beta$ -tubulin dimers to make a 13-protofilament microtubule (Liu et al., 2020; Wieczorek et al., 2020b; Consolati et al., 2020; Zimmermann et al., 2020; Böhler et al., 2021; Brilot et al., 2021; Würtz et al., 2021, 2022). This asymmetry could also cause detachment of a few protofilaments in the absence of regulatory factors.

Considering these possibilities, the inhibition of CAMSAP3 binding and microtubule release in the presence of  $\gamma$ -TuRC-activator CDK5RAP2 could be an active regulatory mechanism in cells for stable attachment of microtubule minus-ends to  $\gamma$ -TuRC, and therefore, anchoring to the MTOCs. This hypothesis is further strengthened by our data, where we show that CDK5RAP2 suppresses the capping efficiency of  $\gamma$ -TuRC for 14-protofilament, but not 13-protofilament microtubules. Moreover, recent Cryo-EM structural work has decoded the  $\gamma$ -TuNA-binding site on  $\gamma$ -TuRC (Wieczorek et al., 2020a).  $\gamma$ -TuNA encompasses the conserved helical CM1 domain, which is the minimal CDK5RAP2 domain consistently shown to stimulate  $\gamma$ -TuRC-dependent ectopic cytosolic microtubule nucleation in cells (Choi et al., 2010; Muroyama et al., 2016; Tovey et al., 2021). However, these observations were difficult to reproduce in vitro using purified components (Choi et al., 2010; Liu et al., 2020; Thawani et al., 2020; Rale et al., 2022). These discrepancies have been attributed to the purification method, presence of an auto-inhibitory domain in extended versions of  $\gamma$ -TuNA used or the concentrations of  $\gamma$ -TuNA used for the in vitro reconstitutions. Nevertheless, a clear depiction of binding of  $\gamma$ -TuNA dimer to the MZT2/GCP2-NHD module at position 13 of the 14-spoke-ring hints towards a regulatory mechanism for proper microtubule attachment by controlling  $\gamma$ -TuRC structure (Brilot et al., 2021; Wiecezorek et al., 2020a).

However, we could not detect a structural change in our  $\gamma$ -TuRC reconstructions of negative-stained electron micrographs in the presence of CDK5RAP2. Notably, the densities of terminal



$\gamma$ -TuSC and the luminal bridge were not clearly resolved in our reconstructions. Therefore, we cannot exclude the possibility of conformational changes induced by CDK5RAP2 at these sites. Further studies would be required to find out whether this was due to technical reasons or because the conformational change induced by CK5RAP2 is transient and might occur only upon microtubule nucleation or concerted action of additional factors. A recent study that is in line with the latter idea compared the structure of  $\gamma$ -TuNA-bound human  $\gamma$ -TuRC, purified using its affinity for  $\gamma$ -TuNA, and  $\gamma$ -TuNA-unbound *Xenopus*  $\gamma$ -TuRC (Brilot et al., 2021). This work detected a structural difference in the loose and asymmetric half of the ring at the interface of GCP6 (position 12) and neighboring GCP2 (position 13) of the terminal  $\gamma$ -TuSC. Although this structural change was significant, it was still not enough to completely fit a microtubule, unlike the closed conformation of yeast  $\gamma$ -TuRC. This suggests that similar additional binding sites for  $\gamma$ -TuNA might exist between multiple  $\gamma$ -TuSCs. Alternatively, additional factors or their synergy with microtubule nucleation itself might be required to secure a perfect match; these possibilities will need to be investigated in future.

Alternatively, CDK5RAP2 might improve microtubule attachment to  $\gamma$ -TuRC by allosterically affecting GTP-binding on the  $\gamma$ -tubulin- $\alpha$ -tubulin interface. Whereas lateral interactions between  $\gamma$ -tubulins are not dependent on GTP, the longitudinal contacts with  $\alpha\beta$ -tubulin and their strength have been shown to be dependent on the nucleotide state (Rice et al., 2008; Gombos et al., 2013). CDK5RAP2 was shown to bind to EB1 through its SxIP domain, and therefore track the growing microtubule end (Fong et al., 2009). However, its localization at the plus end strongly depended on its additional dimerization domain next to SxIP-motif (Fong et al., 2017). Therefore, it is possible that CDK5RAP2 SxIP-motif together with its dimerization and CM1 domain can have an additional role in microtubule attachment by affecting the longitudinal contacts between microtubule and  $\gamma$ -tubulin. This would need further investigation by using CDK5RAP2 truncations that lack these regions to dissect if microtubule nucleation and anchoring by the same factor are also distinctly regulated.

Interestingly, monomeric CLASP2 showed strong enhancement of microtubule nucleation from  $\gamma$ -TuRC but had no effect on microtubule anchoring even though it colocalized with  $\gamma$ -TuRC in the absence of free tubulin. This suggests that  $\gamma$ -TuRC activation mechanisms can be different and would depend on the  $\gamma$ -TuRC-activator. The destiny of a microtubule, whether it will stay attached to  $\gamma$ -TuRC or will detach, would depend on the activator or additional microtubule anchoring factors. One such potential factor is ninein, which has been shown to be important for microtubule anchoring, but not nucleation (Mogensen et al., 2000; Abal et al., 2002; Delgehyr et al., 2005; Lechler and Fuchs, 2007; Wang et al., 2015; Goldspink et al.,

2017). In line with this view, in our reconstitutions, ninein suppressed CAMSAP3 binding and microtubule release on its own as well as in the presence of CLASP2 (**Fig. 1a,b**). This suggests that microtubule nucleation and anchoring are distinctly regulated mechanisms.

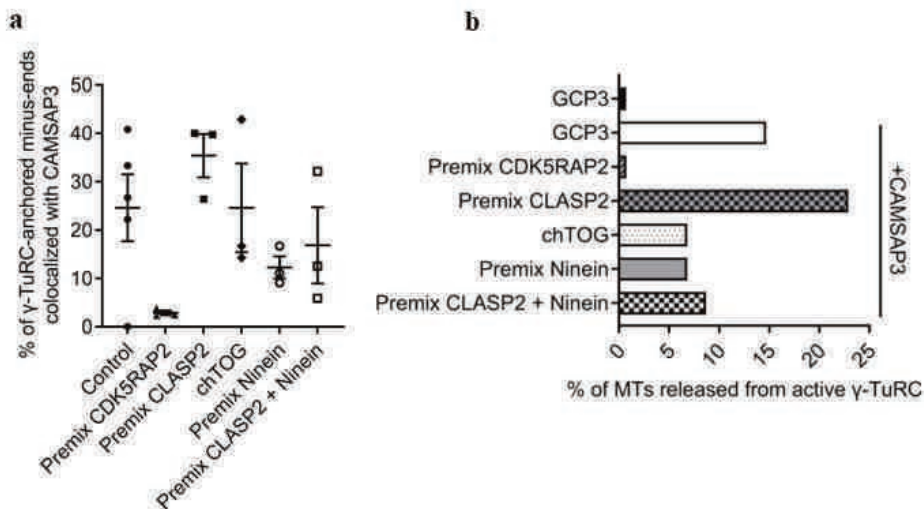


**Figure 1. Ninein suppresses CAMSAP3 binding and microtubule release from  $\gamma$ -TuRC.**

*a*, Colocalization frequency of  $\gamma$ -TuRC-anchored microtubule minus-ends with CAMSAP3, from experiments shown in **Chapter 2, Fig. 3f**.  $n=3$ ,  $m=31$ ,  $l=44$  for premix mCherry-ninein and  $n=3$ ,  $m=27$ ,  $l=69$  for mCherry-CLASP2 + ninein. Individual data points represent single experiments, for which % of  $\gamma$ -TuRC-anchored microtubule minus ends colocalizing with CAMSAP3 were quantified; where  $n$  is the number of independent experiments,  $m$  is the number of fields of view and  $l$  is the total number of active  $\gamma$ -TuRCs analyzed over 10 min duration. The plots present mean  $\pm$  s.e.m.

*b*, Plot showing frequency of microtubule release from active  $\gamma$ -TuRC in the presence of 5 nM SNAPAF647-CAMSAP3 under the experimental conditions shown in **Chapter 2, Fig. 3h**.  $n=44$  for premix mCherry-ninein and  $n=69$  for premix mCherry-CLASP2 + ninein, pooled from three independent experiments; where  $n$  is the number of active  $\gamma$ -TuRCs analyzed.

Also see **Chapter 2, Fig. 3c-h**.

Altogether, our findings call for cryo-EM studies to solve the structure of the  $\gamma$ -TuRC - microtubule minus-end interface. This will help to deduce how CAMSAP-mediated microtubule release is regulated. Furthermore, high resolution Cryo-EM-based structural studies can address several long-standing open questions in the field. What is the role of the 14<sup>th</sup>  $\gamma$ -tubulin in the ring, when microtubules found in most eukaryotic cells are made of 13- protofilaments? Is it to regulate protofilament number? What roles do additional GCP4/5/6 play, and what is the function of unique N-terminal extensions of GCPs and the GCP6-specific insertion in the middle?

Although these additional GCPs show structural and functional similarity to GCP2/3 and share two conserved GRIP1 and GRIP2 domains for their lateral association or binding to  $\gamma$ -tubulin, respectively, their unique sequence features suggest that they can be involved in spatio-temporal regulation of  $\gamma$ -TuRC (Kollman et al., 2011; Farache et al., 2016; Tovey and Conduit, 2018). Consistently, it was shown that the depletion of GCP4/5/6 results in formation of monopolar spindles and reduced  $\gamma$ -tubulin signal at mitotic centrosomes in HeLa cells (Bahtz et al., 2012; Cota et al., 2017). Interestingly, GCP6 depletion showed severe phenotypes like GCP2/3-depletion. Furthermore, the N-terminal  $\alpha$ -helical domains of GCPs (GCP-NHDs) show specific interactions with Mozart1 (MZT1) and MZT2 proteins to form MZT/GCP-NHD modules that have distinct localization within  $\gamma$ -TuRC structure and contribute to various functions (Wieczorek et al., 2020a). For example, MZT2/GCP2-NHD module was shown to interact with CM1 domain of CDK5RAP2, a  $\gamma$ -TuRC activator and tethering factor, which can regulate  $\gamma$ -TuRC structure or recruitment to MTOCs (Choi et al., 2010; Muroyama et al., 2016; Cota et al., 2017; Wieczorek et al., 2020a; Brilot et al., 2021). MZT1 and MZT2 are microproteins, whose role as  $\gamma$ -TuRC-adaptor proteins has been well established (Teixidó-Travesa et al., 2010; Masuda et al., 2013; Lin et al., 2016; Masudaa and Toda, 2016; Cota et al., 2017; Wieczorek et al., 2020a). Additionally, MZT1/GCP3-NHD and MZT1/GCP6-NHD modules were shown to be part of the luminal bridge that is required for  $\gamma$ -TuRC assembly and geometry (Wieczorek et al., 2020a, 2021). These interactions were previously shown to be important for  $\gamma$ -TuRC recruitment to MTOCs (Dhani et al., 2013; Masudaa and Toda, 2016). Similarly, a MZT1/GCP6 module, containing two N-terminal helices of GCP6, was shown to interact with monomeric actin present in the luminal bridge to regulate  $\gamma$ -TuRC geometry and microtubule nucleation (Würtz et al., 2022). Moreover, a  $\gamma$ -TuSC-associated  $\alpha$ -helix of GCP6 at its N-terminus, referred as “GCP6-belt”, was shown to bind to the luminal face of at least two  $\gamma$ -TuSCs and was proposed to stabilize their assembly. Finally, a large segment of GCP6-specific insertion between GRIP1 and GRIP2 domains was shown to be dispensable for  $\gamma$ -TuRC assembly or localization to the centrosome (Haren et al., 2020). Intriguingly, this segment played a role in centriole duplication upon Plk4-dependent phosphorylation (Bahtz et al., 2012). However, a short 100 amino acid sequence at the extreme end of this insertion, composed of multiple small helices, was shown to be important for  $\gamma$ -TuRC assembly and localization to the centrosome (Haren et al., 2020).

Nonetheless, such distinct regulatory mechanisms at multiple levels as described above could make  $\gamma$ -TuRC an excellent anti-cancer drug target, as previously proposed (Tovey and Conduit, 2018). Current anti-cancer drugs, like taxanes or vinca alkaloids, which target microtubules,

are known to cause chemotherapy-induced peripheral neuropathy, in which axonal projections degenerate. Targeting  $\gamma$ -TuRCs in cancer cells would have less dramatic side effects in mature neurons, as these cells employ katanin- and spastin-mediated severing mechanisms to generate microtubules, remodel microtubule network and regulate axonal branch formation once a stable microtubule network has been established (Ahmad et al., 1999; Karabay et al., 2004; Yu et al., 2005, 2008; Conde and Cáceres, 2009). Therefore, loss of axonal projections by  $\gamma$ -TuRC-inhibition might be compensated by regulating the microtubule density in axons by severing activity of katanin and spastin.

### **Microtubule bundling and stabilization**

Given the dynamic instability of free microtubule ends, a requirement of an additional stabilization mechanism becomes inevitable. Furthermore, in densely packed microtubule arrays, such as neuronal axons or mitotic central spindles, it becomes highly important to create minimal space between neighboring microtubules to maximally utilize the microtubule tracks (Conde and Cáceres, 2009). Microtubule bundling is one way to stabilize microtubules by physically crosslinking them (Bodakuntla et al., 2019). In various cellular settings, microtubule networks are often bundled by motors and MAPs. Microtubule bundling proteins typically consist of a dimerization domain and a microtubule-binding domain. Classical MAPs or so-called structural MAPs, such as tau family proteins like tau, MAP2 and MAP4, which bind and stabilize microtubules, can also bundle microtubules (Lewis et al., 1989; Dehmelt and Halpain, 2005). These proteins typically contain a variable projection domain at the N-terminus to regulate spacing between microtubules, multiple conserved tubulin-binding repeats at C-terminus for microtubule binding and a short hydrophobic zipper domain for microtubule bundling (Lewis et al., 1989; Chen et al., 1992). Tau family proteins stabilize microtubules by stabilizing the interdimer as well as intradimer interfaces as they span over three tubulin subunits (Kellogg et al., 2018; Shigematsu et al., 2018).

Another microtubule bundler, PRC1, which orients microtubule in an anti-parallel arrangement (plus ends in opposite direction) at the spindle midzone, can also stabilize microtubules by physically cross-linking them (Subramanian et al., 2010; Walczak and Shaw, 2010; Lee et al., 2015). PRC1 has an N-terminal dimerization domain, a spectrin domain that binds to microtubules and specifies the cross-bridge angle, and a disordered C-terminal domain that forms electrostatic interactions with the neighboring protofilaments (Subramanian et al., 2010; Kellogg et al., 2016). The orientation of the spectrin domain together with the dimerization domain guides the orientation and spacing of microtubules within bundles. Similarly, Cep169,

which was proposed to be a microtubule bundler, accumulates at the distal ends of microtubules and centrosomes, forms homodimers through its N-terminal domain and binds to microtubules through C-terminal domain (Mori et al., 2015).

In Chapter 3, we investigated the underlying mechanism of axon initial segment (AIS) assembly by a microtubule bundling protein, TRIM46, which is specifically localized in the proximal axon and partially overlaps with a scaffold protein, Ankyrin-G (AnkG), in the AIS (van Beuningen et al., 2015; van Beuningen and Hoogenraad, 2016; Freal et al., 2016). TRIM46 is the member of tripartite motif containing (TRIM) protein family of ubiquitin E3 ligases, but no ubiquitin ligase activity has been reported for TRIM46 (Meroni and Diez-Roux, 2005). In neuronal axons, TRIM46 orients microtubules in parallel bundles with plus ends out (van Beuningen et al., 2015). Its ortholog in fly, TRIM9, was also shown to regulate microtubule polarity, together with kinesin-5 and EB1, at branch points in dendrites (Feng et al., 2021). TRIM9 is involved in stabilizing microtubules by suppressing catastrophes of newly generated microtubules that are oriented in parallel fashion along the pre-existing microtubules with the help of kinesin-5. TRIM46 localizes to the proximal axon by its interactions through the N-terminal RING finger and C-terminal COS box domains (van Beuningen et al., 2015). The correct localization of TRIM46 is essential for neuronal polarity and axon specification. We explored the molecular mechanism of its function in Chapter 3 using *in vitro* reconstitutions and cellular assays.

We showed that TRIM46 did not bind to single MTs on its own but got recruited to microtubule bundles that were oriented in a parallel fashion. It had a very mild effect on microtubule plus-end growth rate, but very strongly promoted rescues within microtubule bundles, consequently increasing their length. TRIM46 also stabilized microtubules against nocodazole-induced microtubule disassembly. AnkG could weakly recruit TRIM46 to single microtubules and promote their rescues, while TRIM46 specifically enhanced the enrichment of AnkG on microtubule bundles, suggesting cooperativity between the two proteins. The binding of AnkG to the microtubule plus ends in an EB-dependent manner and its association with membrane protein Neurofascin-186 suggested that AnkG scaffold can recruit TRIM46 bundles into the proximity of the axonal plasma membrane. The recruitment of long and plus-end-out TRIM46-stabilized microtubule bundles to the plasma membrane allowed efficient retrograde transport of endocytosed Neurofascin-186 from distal axons, followed by their stable retention in the AIS by AnkG, which in turn reinforced anchoring of AnkG to the membrane. Therefore, TRIM46 could promote AIS assembly by stabilizing microtubules in cooperation with AnkG.

An important unaddressed question here is how TRIM46 bundles microtubules in a parallel orientation and stabilizes them. The common features of bundling proteins, such as the presence of a microtubule binding domain and a dimerization domain, suggest that they work mainly by cross-linking protofilaments. Such crosslinking could prevent microtubule depolymerization and might promote rescues, thereby stabilizing microtubules. The organization of closely spaced microtubules connected with electron-dense TRIM46 cross-bridges in the AIS suggests that similar mechanisms might exist for TRIM46 as well, although structural domains are very different among PRC1, tau family proteins and TRIM46 (Dehmelt and Halpain, 2005; van Beuningen et al., 2015; Kellogg et al., 2016, 2018; Harterink et al., 2019). Moreover, we also did not see any binding of TRIM46 on single microtubules, but we cannot rule out that it is limited due to saturation of TRIM46 on bundles or, if the binding is very transient, due to the insufficient temporal resolution of our assays. Interestingly, we did see binding of TRIM46 to single microtubules in the presence of AnkG, which is consistent with our model that AnkG and TRIM46 cooperate with each other for microtubule binding. How TRIM46 crosslinks microtubules in a parallel orientation, promotes rescues and stabilizes the lattice is currently unclear. Although microtubule stabilization by TRIM46 might partly be the consequence of rescues, this does not fully explain the inhibition of depolymerization in the stable part of the microtubule lattices within bundles. High resolution Cryo-EM studies would provide insights into the structure of TRIM46 bound to microtubules and reveal the molecular mechanism underlying its activity.

Microtubule bundling by PRC1 plant homolog, MAP65-1 was shown to protect microtubules from katanin-mediated severing by inhibiting katanin binding to microtubule bundles during organization of linear cortical microtubule arrays (Burkart and Dixit, 2019). This protection against katanin was dependent on the cross-linking activity of MAP65-1, and therefore, severing was specifically prevented on microtubule bundles. Similar protective effect was conferred to microtubules by tau in neuronal axons, whereby, tau shielded microtubules from severing by katanin (Qiang et al., 2006; Siahaan et al., 2019). Whether such protective effect against katanin will also be shared by TRIM46 in neuronal axons requires further investigation. Nonetheless, stabilization of microtubule bundles by TRIM46 would increase microtubule lifetime. Therefore, it is tempting to speculate that these long-lived microtubules can accumulate post-translational modification (PTMs) over time and recruit various motor proteins and microtubule regulatory proteins to regulate microtubule density, organization and axonal transport in neurons (Janke and Magiera, 2020). Consistently, it was shown that acetylated microtubules are predominantly bundled (Balabanian et al., 2017; Tas et al., 2017).

The bundling of microtubules, but not tubulin acetylation alone, enhanced kinesin-1 recruitment and run lengths on microtubule bundles (Walter et al., 2012; Balabanian et al., 2017). Furthermore, acetylated microtubule bundles are oriented plus-end out in neuronal axons (Tas et al., 2017). Acetylation has been well-established as a hallmark for long-lived microtubules, therefore, TRIM46 bundles might facilitate axonal entry of kinesin-1 (Tas et al., 2017; Janke and Magiera, 2020).

### **Microtubule damage, repair and lattice renewal**

Once a microtubule is assembled, its maintenance is equally important for carrying out diverse cellular functions. In addition to the dynamic instability of the growing microtubule ends, microtubule disassembly can also be driven by lattice defects and damage accumulated during polymerization or due to shear over time. Motor proteins like kinesin-1, which mainly walk along a single microtubule protofilament, would require continuous microtubule lattices without obstacles for efficient long-range transport as opposed to other motors, such as dynein, kinesin-2 and kinesin-8, which can switch between protofilaments by taking a side-step (Bugiel et al., 2015; Hoepflich et al., 2017; Ferro et al., 2019).

However, microtubule lattices are far from being uniform. Structural heterogeneity within individual microtubules has been known for a long time. Microtubule defects like the occurrence of holes and gaps along the microtubule lattice are commonly observed in cultured cells, *Xenopus* egg extracts and in microtubules polymerized in vitro (Chretien et al., 1992; Kikkawa et al., 1994; Vitre et al., 2008; Atherton et al., 2018; Guyomar et al., 2022). Intrinsic defects in microtubules, observed in these studies, also included changes in protofilament number, holes of one to few tubulin subunits in size, transitions between microtubule lattice types, variation in helix start number or occurrence of multiple seams, at times with an offset of one protofilament, within same microtubule. A study that involved high resolution cryo-electron tomography and careful analysis ascribed these defects to unique lateral interactions between tubulin subunits without longitudinal interactions (Guyomar et al., 2022). Moreover, tubulin dislocations, transitions in protofilament number or microtubule tube closure defects can be induced by increasing the speed of microtubule polymerization or by addition of microtubule stabilizing agents (MSAs), such as taxanes (Vitre et al., 2008; Schaedel et al., 2019; Rai et al., 2019, 2021). High tubulin concentration might promote stable incorporation of tubulin dimers that initially associated only through lateral interactions, by allowing quick addition of more tubulin dimers, and therefore establishing more longitudinal and lateral contacts with new tubulin dimers (Cleary and Hancock, 2021). Furthermore, microtubule

damages can also be created by the compressive forces microtubules experience at the cortex, retrograde actin flow during cell migration, due to microtubule bending and crossings, by microtubule severing enzymes or due to stepping of molecular motors (Waterman-Storer and Salmon, 1997; Kalil and Szebenyi, 2000; Eaton et al., 2002; Schaedel et al., 2015; Aumeier et al., 2016; Vemu et al., 2018; Triclin et al., 2021; Théry and Blanchoin, 2021; Budaitis et al., 2022; Andreu-Carbó et al., 2022). Microtubule defects and damage would eventually lead to microtubule breakage and fragmentation, if not repaired. Microtubule repair can either occur autonomously or can be mediated by MAPs. Microtubules can self-repair by free tubulin incorporation at damage sites (Waterman-Storer and Salmon, 1997; Kalil and Szebenyi, 2000; Aumeier et al., 2016; Triclin et al., 2021; Théry and Blanchoin, 2021; Budaitis et al., 2022; Gazzola et al., 2022). MAPs like EBs, which favor microtubules with 13-protofilament B-lattice structure can promote repair of lattice defects and enrich their favored microtubule lattices (Vitre et al., 2008). However, other MAPs, such as CSPP1 and SSNA1 prevent the depolymerization of damaged microtubule lattice, restrict lattice damage and therefore facilitate self-repair (Lawrence et al., 2021; Berg et al., 2022).

In Chapter 4, we uncovered the role of CLASP2 in microtubule repair and showed evidence for MAP-mediated repair of microtubule damage induced by laser irradiation. We showed that upon inducing photodamage at a site along microtubule lattice, CLASP2 gets recruited rapidly at the irradiated site and prevents lattice disassembly and breakage. Immediate accumulation of CLASP2 at the damage site suggested that it recognizes specific conformation of the lattice generated upon photodamage. Most likely, laser-induced damage exposed the GDP-lattice that transitioned to its intrinsic bent curvature, which CLASP2 might recognize (Aher et al., 2018; Manka and Moores, 2018a; McIntosh et al., 2018; Brouhard and Rice, 2018; Gudimchuk et al., 2020). Upon binding to the damaged site, CLASP2 facilitated tubulin incorporation, promoted complete lattice repair and caused tube closure. After repair, CLASP2 signal was reduced and leveled with its intensity along the rest of the lattice, suggesting that CLASP2 accumulation was specific to tubulin conformation at the damaged site, which was restored to straight conformation upon tube closure. This was also clear in our experiments with an engineered kinesin-5, which alone creates curled partial protofilament assemblies at growing ends that eventually break and depolymerize. CLASP2 converted these partial protofilament structures into complete tubes and prevented their depolymerization after their breakage at curled regions. Moreover, CLASP2 inhibited microtubule softening induced by mechanical stress by preventing damage. We also found that a minimal TOG2-S domain of CLASP2, that suppresses catastrophes and can promote rescues, was sufficient for all these activities of CLASP2. Our



data suggests that the mechanism of microtubule repair by CLASP is similar to that of catastrophe suppression.

Whether CLASP favors a specific lattice type and can prevent accumulation of intrinsic defects during microtubule polymerization, just like EBs, needs to be further investigated. Our finding that CLASP2 prevents depolymerization of new microtubule plus ends generated after laser severing hints that CLASP might expand the GDP-lattice and strengthen lateral contacts. Previous work from our lab has shown that CLASP2 synchronizes protofilament growth and repairs growing plus ends with asynchronously extending protofilament subsets, manifested by the occurrence of a leading and a lagging EB comet (Aher et al., 2018). This further supports the notion that CLASP might strengthen lateral tubulin contacts. However, future work will be needed to understand how CLASP stabilizes the lattice. Previously, CLASP was suggested by Grimaldi et al., 2014 to facilitate GTP hydrolysis by tubulin, because GTP-content along the microtubule shaft was increased in CLASP-depleted cells. However, our work suggests that the high GTP-content in the absence of CLASP in cells could be a consequence of increased microtubule defects, persisting damages and delayed, partial microtubule repair. Altogether, our work establishes that microtubule repair by CLASP might play an additional role in regulating microtubule density in cells, together with its role in microtubule nucleation and catastrophe suppression (Mimori-Kiyosue et al., 2005; Efimov et al., 2007; Miller et al., 2009; Aher et al., 2018).

Interesting outcomes of microtubule lattice repair and GTP-tubulin exchange along the microtubule shaft are the generation of rescue sites and lattice renewal. Freshly incorporated GTP-bound tubulin dimers along the microtubule lattice would serve as rescue sites that can increase microtubule lifetime and thereby stabilize microtubule shafts (Dimitrov et al., 2008; de Forges et al., 2016; Aumeier et al., 2016; Gazzola et al., 2022; Andreu-Carbó et al., 2022). Also, GTP-tubulin dimers newly incorporated into the damaged sites will be non-modified and will replace old tubulin dimers that might have a history of tubulin modification. This would allow the “writer MAPs” to write a new tubulin code at the damage sites, and therefore recruit different factors to reorganize microtubule network according to cellular needs without complete microtubule disassembly (Janke and Magiera, 2020).

### **Microtubule severing and amplification**

Another way to remodel the microtubule network is via microtubule severing and minus-end regulation. In Chapter 5, we demonstrated a way to amplify microtubule number through regulation of minus ends. In cells, microtubule minus ends are usually stabilized and anchored

at MTOCs (Martin and Akhmanova, 2018; Akhmanova and Steinmetz, 2019; Akhmanova and Kapitein, 2022). One such stabilization and anchoring pathway is through regulation of minus ends by CAMSAP/Patronin family members (Akhmanova and Hoogenraad, 2015; Akhmanova and Steinmetz, 2019). CAMSAPs have been previously shown to stabilize the minus ends of non-centrosomal microtubules in different cell types (Akhmanova and Kapitein, 2022). CAMSAPs bind to microtubule minus ends, slow down their growth and prevent catastrophes (Jiang et al., 2014; Hendershott and Vale, 2014). Previously, katanin was shown to interact with CAMSAP2/3, but not CAMSAP1, and regulate the length of CAMSAP-stabilized microtubule stretches in cells (Jiang et al., 2014). Recently, WDR47 was also reported to bind to all three mammalian CAMSAPs and regulate the length of CAMSAP-decorated microtubules in cells (Buijs et al., 2021; Chen et al., 2020). Moreover, CAMSAPs, katanin and WDR47 were shown to cooperate for the formation of axonemal central pair microtubules (Liu et al., 2021a).

We reconstituted the combined effects of the three CAMSAPs, WDR47 and katanin *in vitro* using purified proteins to gain mechanistic insights into their functional interactions. We found that at low concentration, katanin can inhibit elongation of CAMSAP-decorated microtubule minus ends, while at higher concentration, it rapidly severed and amplified CAMSAP2/3-decorated microtubules. WDR47 binds to CAMSAPs and protects CAMSAP-stabilized microtubules from katanin binding and severing. However, it needs to be carefully tested whether WDR47 inhibits only katanin binding or also affects the severing activity of katanin. WDR47 also slowed down the growth rate of the CAMSAP2/3-bound minus ends and potentiated blocking of microtubule minus-end growth in the presence of CAMSAP1. The functional implications of WDR47-CAMSAP1 interaction in cells should be addressed in future. Altogether, we showed that together, CAMSAPs, katanin and WDR47 can regulate the length of stabilized minus ends and microtubule number.

However, the severing outcomes highly depended on the stoichiometries and concentration of the proteins, especially katanin. In the absence of WDR47, a moderate concentration of katanin triggered severing of CAMSAP-stabilized microtubules and caused an increase in microtubule number rather than destruction of microtubules, whereas at a low concentration, katanin mainly regulated the length of CAMSAP-stabilized lattice. The addition of WDR47 shifted the outcome from amplification of microtubule number to controlling the length of stabilized minus ends, thereby fine-tuning the balance between microtubule mass and minus end elongation and stability. The amplification of microtubule number was caused by cutting of CAMSAP-stabilized microtubules, which created many short and stable microtubule templates

that served as microtubule seeds. Therefore, it would be interesting to test whether at a sufficiently high concentration of katanin, there will be a third outcome, i.e., destruction of microtubules (Kuo and Howard, 2021).

Moreover, the presence of stabilizing and destabilizing MAPs, which would control microtubule growth regimes during the severing reaction could also be a determining factor to promote specific outcomes (Kuo et al., 2019). For example, increasing the complexity of these reconstitutions by adding a microtubule depolymerase, like MCAK, might lead to microtubule destruction by counteracting the stabilizing effect of CAMSAPs. In contrast, the addition of a microtubule stabilizer, like CLASP, might further amplify microtubule arrays. Although these ideas need to be further investigated, a recent study shows that this might indeed be the case. In higher plants, in response to blue light, CLASP was shown to be required for driving the reorientation of cortical arrays upon katanin-mediated severing (Lindeboom et al., 2019). Moreover, a fine balance between microtubule cutting, stabilization and minus-end length regulation would be extremely important in cellular settings where the number and location of new microtubules is precisely controlled, such as those of the central pair of microtubules in motile cilia, where exactly two microtubules need to be generated (Liu et al., 2021a). In this study, it was shown that any perturbations, such as overexpression of CAMSAP, loss of WDR47 or altering the level of katanin activity, lead to deviation from the number and location of central microtubules in cilia. Therefore, severing outcomes highly depend on the regulation of katanin localization and activity, and the presence of stabilizing and destabilizing MAPs. We also discuss some interesting consequences of severing in the section below.

### **Resetting the tubulin code**

Apart from regulating polymer mass and minus-end length that are important for remodeling the microtubule organization and density in cells, microtubule severing could be a mechanism to alter the tubulin code by lattice renewal (Sharp and Ross, 2012; McNally and Roll-Mecak, 2018; Roll-Mecak, 2020; Kuo and Howard, 2021; Sarbanes et al., 2022). Tubulin subunits in microtubule lattices generate a “tubulin code” during polymerization or over time, through incorporation of specific tubulin isoforms, or via the actions of “reader/writer” MAPs (Janke and Magiera, 2020). This tubulin code refers to a characteristic feature of the microtubule lattice that governs microtubule interactions with regulatory proteins and various microtubule functions. Regulating the addition of tubulin isoforms during microtubule assembly can control the variation of protofilament numbers in microtubules, which can be observed in different cell

types and organisms (Savage et al., 1989; Raff et al., 1997; Chaaban and Brouhard, 2017; Ti et al., 2018; Chaaban et al., 2018).

In addition to tubulin isotypes, tubulin PTMs can also control microtubule structure, dynamics and interactions with various regulatory proteins, including severing enzymes (Janke and Magiera, 2020). Numerous PTMs are catalyzed by an increasing number of enzymes that introduce tubulin modifications, like acetylation, detyrosination, polyglutamylated, phosphorylation, polyglycylation and polyamination on the C-terminal tails of both  $\alpha$ - or  $\beta$ -tubulin (Magiera and Janke, 2014). These tubulin PTMs play a very important role in regulating microtubule dynamics in neurons, cilia and flagella, and during cell division, and their dysregulation is linked to multiple diseases like ciliopathies, neurological disorders and cancer (Magiera et al., 2018; Roll-Mecak, 2020; Moutin et al., 2021). Moreover, PTMs can be frequently observed on microtubules that are long-lived, such as those in neuronal axons, as high microtubule longevity provides ample opportunity to tubulin modifiers for their actions (Tas et al., 2017; Moutin et al., 2021). PTMs, in turn, can differentially regulate microtubule recruitment of various MAPs, including motor proteins, such as CLIP-170, kinesin-1, kinesin-2, dynein, katanin and spastin (Peris et al., 2006; Kubo et al., 2010; Suryavanshi et al., 2010; Sirajuddin et al., 2014; McKenney et al., 2016; Szczesna et al., 2022).

Coming back to lattice renewal, severing enzymes cut and break microtubules by extracting tubulin dimers from the lattice (Zehr et al., 2020; Sarbanes et al., 2022). If severing is partial, it will generate nanoscale damages on microtubules that would induce self-repair by incorporation of free GTP-tubulin dimers (Vemu et al., 2018). These newly incorporated GTP-tubulin dimers will be in an expanded conformation, while the GDP-tubulin dimers that were removed would be in compact conformation (Zhang et al., 2018; Manka and Moores, 2018b), therefore carrying an intrinsic structural code. In addition, these freshly incorporated tubulin dimers will be mostly unmodified or might have a different modification than the GDP-tubulin dimers that were removed. It was shown previously that katanin gets recruited to polyglutamylated microtubules and severs them efficiently (Valenstein and Roll-Mecak, 2016). A recent study showed that polyglycylation of both  $\alpha$ - and  $\beta$ -tubulin can inhibit katanin binding to microtubules and severing, while the well-studied acetylation of luminal Lys40 in  $\alpha$ -tubulin had no effect on katanin binding or severing (Szczesna et al., 2022). Moreover, the same study also reported that the removal of the terminal tyrosine of  $\alpha$ -tubulin (detyrosination) in the absence of polyglutamylated reduced katanin binding and severing of microtubules. Therefore, old tubulin dimers that are removed by katanin from the lattice are most likely modified, whereas the freshly incorporated ones will be mainly unmodified or with a different

modification, owing to code erasers such as tubulin tyrosine ligase (TTL), carboxypeptidases (CCPs) and HDAC6 (Roll-Mecak, 2020), which act on free tubulin dimers. Thus, the writers of tubulin code can write a new code at damage and repair sites, and MAPs like CLASPs that mediate microtubule repair, as described in Chapter 4, can facilitate lattice renewal.

### **Concluding remarks**

In this thesis, we explored the dynamics and regulation of a microtubule from its minus end to the plus end while passing along the lattice, using complex biochemical *in vitro* reconstitution experiments. We described regulation of microtubule nucleation and growth from  $\gamma$ -TuRC and discovered a novel pathway for generating stable microtubule minus ends that involves an interplay between  $\gamma$ -TuRC and CAMSAPs. We also demonstrated that microtubule bundling by a bundling protein, TRIM46, can provide stability to microtubule lattice. Furthermore, we provide evidence for repair and renewal of damaged microtubule lattices by CLASP2, a microtubule associated protein. We then described how the length of microtubule minus ends and microtubule number can be regulated by a three-protein module, which includes minus-end stabilizing CAMSAP family proteins, a neuronally/ciliary-enriched scaffold protein WDR47 and a microtubule severing enzyme katanin. We additionally discussed how the tubulin code along the lattice can be reset by microtubule damage and repair. Our *in vitro* reconstitution assays helped to dissect the molecular mechanisms underlying the action of these diverse and fascinating microtubule regulators and understand their cellular activities.

---

**References**

- Abal, M., M. Piel, V. Bouckson-Castaing, M. Mogensen, J.B. Sibarita, and M. Bornens. 2002. Microtubule release from the centrosome in migrating cells. *J. Cell Biol.* 159:731–737. doi:10.1083/jcb.200207076.
- Aher, A., M. Kok, A. Sharma, A. Rai, N. Olieric, R. Rodriguez-Garcia, E.A. Katrukha, T. Weinert, V. Olieric, L.C. Kapitein, M.O. Steinmetz, M. Dogterom, and A. Akhmanova. 2018. CLASP Suppresses Microtubule Catastrophes through a Single TOG Domain. *Dev. Cell.* 46:40–58.e8. doi:10.1016/j.devcel.2018.05.032.
- Ahmad, F.J., W. Yu, F.J. McNally, and P.W. Baas. 1999. An Essential Role for Katanin in Severing Microtubules in the Neuron. *J. Cell Biol.* 145:305–315. doi:10.1083/JCB.145.2.305.
- Akhmanova, A., and C.C. Hoogenraad. 2015. Microtubule minus-end-targeting proteins. *Curr. Biol.* 25:R162–R171. doi:10.1016/j.cub.2014.12.027.
- Akhmanova, A., and L.C. Kapitein. 2022. Mechanisms of microtubule organization in differentiated animal cells. *Nat. Rev. Mol. Cell Biol.* 23:541–558. doi:10.1038/s41580-022-00473-y.
- Akhmanova, A., and M.O. Steinmetz. 2019. Microtubule minus-end regulation at a glance. *J. Cell Sci.* 132:1–7. doi:10.1242/JCS.227850.
- Andreu-Carbó, M., S. Fernandes, M.C. Velluz, K. Kruse, and C. Aumeier. 2022. Motor usage imprints microtubule stability along the shaft. *Dev. Cell.* 57:5–18.e8. doi:10.1016/J.DEVCEL.2021.11.019.
- Atherton, J., K. Jiang, M.M. Stangier, Y. Luo, S. Hua, K. Houben, J.J.E. Van Hooff, A.P. Joseph, G. Scarabelli, B.J. Grant, A.J. Roberts, M. Topf, M.O. Steinmetz, M. Baldus, C.A. Moores, and A. Akhmanova. 2017. A structural model for microtubule minus-end recognition and protection by CAMSAP proteins. *Nat. Struct. Mol. Biol.* 24:931–943. doi:10.1038/nsmb.3483.
- Atherton, J., Y. Luo, S. Xiang, C. Yang, A. Rai, K. Jiang, M. Stangier, A. Vemu, A.D. Cook, S. Wang, A. Roll-Mecak, M.O. Steinmetz, A. Akhmanova, M. Baldus, and C.A. Moores. 2019. Structural determinants of microtubule minus end preference in CAMSAP CKK domains. *Nat. Commun.* 10:1–16. doi:10.1038/s41467-019-13247-6.
- Atherton, J., M. Stouffer, F. Francis, and C.A. Moores. 2018. Microtubule architecture in vitro and in cells revealed by cryo-electron tomography research papers. 572–584. doi:10.1107/S2059798318001948.
- Aumeier, C., L. Schaedel, J. Gaillard, K. John, L. Blanchoin, and M. Théry. 2016. Self-repair promotes microtubule rescue. *Nat. Cell Biol.* 18:1054–1064. doi:10.1038/ncb3406.
- Bahtz, R., J. Seidler, M. Arnold, U. Haselmann-Weiss, C. Antony, W.D. Lehmann, and I. Hoffmann. 2012. GCP6 is a substrate of Plk4 and required for centriole duplication. *J. Cell Sci.* 125:486–496. doi:10.1242/JCS.093930.
- Balabanian, L., C.L. Berger, and A.G. Hendricks. 2017. Acetylated Microtubules Are Preferentially Bundled Leading to Enhanced Kinesin-1 Motility. *Biophys. J.* 113:1551–1560. doi:10.1016/j.bpj.2017.08.009.
- Berg, C.M. van den, V.A. Volkov, S. Schnorrenberg, Z. Huang, K.E. Stecker, I. Grigoriev, S.

- Patzke, T. Zimmermann, M. Dogterom, and A. Akhmanova. 2022. CSPP1 stabilizes growing microtubule ends and damaged lattices from the luminal side. *bioRxiv*. 2022.06.23.497320.
- van Beuningen, S.F.B., and C.C. Hoogenraad. 2016. Neuronal polarity: Remodeling microtubule organization. *Curr. Opin. Neurobiol.* 39:1–7. doi:10.1016/j.conb.2016.02.003.
- van Beuningen, S.F.B., L. Will, M. Harterink, A. Chazeau, E.Y. Van Battum, C.P. Frias, M.A.M. Franker, E.A. Katrukha, R. Stucchi, K. Vocking, A.T. Antunes, L. Slenders, S. Doukeridou, P. Sillevs Smitt, A.F.M. Altelaar, J.A. Post, A. Akhmanova, R.J. Pasterkamp, L.C. Kapitein, E. de Graaff, and C.C. Hoogenraad. 2015. TRIM46 Controls Neuronal Polarity and Axon Specification by Driving the Formation of Parallel Microtubule Arrays. *Neuron*. 88:1208–1226. doi:10.1016/j.neuron.2015.11.012.
- Bodakuntla, S., A.S. Jijumon, C. Villablanca, C. Gonzalez-Billault, and C. Janke. 2019. Microtubule-Associated Proteins: Structuring the Cytoskeleton. *Trends Cell Biol.* 29:804–819. doi:10.1016/j.tcb.2019.07.004.
- Böhler, A., B.J.A. Vermeulen, M. Würtz, E. Zupa, S. Pfeffer, and E. Schiebel. 2021. The gamma-tubulin ring complex: Deciphering the molecular organization and assembly mechanism of a major vertebrate microtubule nucleator. *BioEssays*. 43:1–12. doi:10.1002/bies.202100114.
- Brilot, A.F., A.S. Lyon, A. Zelter, S. Viswanath, A. Maxwell, M.J. Maccoss, E.G. Muller, A. Sali, T.N. Davis, and D.A. Agard. 2021. Cml-driven assembly and activation of yeast gamma-tubulin small complex underlies microtubule nucleation. *Elife*. 10:1–35. doi:10.7554/eLife.65168.
- Brouhard, G.J., and L.M. Rice. 2018. Microtubule dynamics: An interplay of biochemistry and mechanics. *Nat. Rev. Mol. Cell Biol.* 19:451–463. doi:10.1038/s41580-018-0009-y.
- Budaitis, B.G., S. Badieyan, Y. Yue, T.L. Blasius, D.N. Reinemann, M.J. Lang, M.A. Cianfrocco, and K.J. Verhey. 2022. A kinesin-1 variant reveals motor-induced microtubule damage in cells. *Curr. Biol.* 32:2416–2429.e6. doi:10.1016/j.cub.2022.04.020.
- Bugiel, M., E. Böhl, and E. Schäffer. 2015. The Kinesin-8 Kip3 Switches Protofilaments in a Sideward Random Walk Asymmetrically Biased by Force. *Biophys. J.* 108:2019. doi:10.1016/J.BPJ.2015.03.022.
- Buijs, R.R., J.J.A. Hummel, M. Burute, X. Pan, Y. Cao, R. Stucchi, M. Altelaar, A. Akhmanova, L.C. Kapitein, and C.C. Hoogenraad. 2021. WDR47 protects neuronal microtubule minus ends from katanin-mediated severing. *Cell Rep.* 36:109371. doi:10.1016/j.celrep.2021.109371.
- Burkart, G.M., and R. Dixit. 2019. Microtubule bundling by MAP65-1 protects against severing by inhibiting the binding of katanin. *Mol. Biol. Cell.* 30:1587–1597. doi:10.1091/MB.C.E18-12-0776/MC-E18-12-0776-S03.MOV.
- Chaaban, S., and G.J. Brouhard. 2017. A microtubule bestiary: structural diversity in tubulin polymers. *Mol. Biol. Cell.* 28:2924–2931. doi:10.1091/mbc.e16-05-0271.
- Chaaban, S., S. Jariwala, C.T. Hsu, S. Redemann, J.M. Kollman, T. Müller-Reichert, D. Sept, K.H. Bui, and G.J. Brouhard. 2018. The Structure and Dynamics of *C. elegans* Tubulin

- Reveals the Mechanistic Basis of Microtubule Growth. *Dev. Cell.* 47:191-204.e8. doi:10.1016/J.DEVCEL.2018.08.023/ATTACHMENT/E12817C3-FA24-4ABA-A188-1E521B65668B/MMC1.PDF.
- Chen, J., Y. Kanai, N.J. Cowan, and N. Hirokawa. 1992. Projection domains of MAP2 and tau determine spacings between microtubules in dendrites and axons. *Nat.* 1992 3606405. 360:674–677. doi:10.1038/360674a0.
- Chen, Y., J. Zheng, X. Li, L. Zhu, Z. Shao, X. Yan, and X. Zhu. 2020. Wdr47 Controls Neuronal Polarization through the Camsap Family Microtubule Minus-End-Binding Proteins. *Cell Rep.* 31. doi:10.1016/j.celrep.2020.107526.
- Choi, Y.K., P. Liu, S.K. Sze, C. Dai, and R.Z. Qi. 2010. CDK5RAP2 stimulates microtubule nucleation by the  $\gamma$ -tubulin ring complex. *J. Cell Biol.* 191:1089–1095. doi:10.1083/JCB.201007030.
- Chretien, D., F. Metoz, F. Verde, E. Karsenti, and R.H. Wade. 1992. Lattice defects in microtubules: Protofilament numbers vary within individual microtubules. *J. Cell Biol.* 117:1031–1040. doi:10.1083/jcb.117.5.1031.
- Cleary, J.M., and W.O. Hancock. 2021. Molecular mechanisms underlying microtubule growth dynamics. *Curr. Biol.* 31:R560–R573. doi:10.1016/J.CUB.2021.02.035.
- Conde, C., and A. Cáceres. 2009. Microtubule assembly, organization and dynamics in axons and dendrites. *Nat. Rev. Neurosci.* 10:319–332. doi:10.1038/nrn2631.
- Consolati, T., J. Locke, J. Roostalu, Z.A. Chen, J. Gannon, J. Asthana, W.M. Lim, F. Martino, M.A. Cvetkovic, J. Rappsilber, A. Costa, and T. Surrey. 2020. Microtubule Nucleation Properties of Single Human  $\gamma$ TuRCs Explained by Their Cryo-EM Structure. *Dev. Cell.* 53:603-617.e8. doi:10.1016/j.devcel.2020.04.019.
- Cota, R.R., N. Teixidó-Travesa, A. Ezquerro, S. Eibes, C. Lacasa, J. Roig, and J. Lüders. 2017. MZT1 regulates microtubule nucleation by linking  $\gamma$ TuRC assembly to adapter-mediated targeting and activation. *J. Cell Sci.* 130:406–419. doi:10.1242/JCS.195321/265286/AM/MZT1-REGULATES-MICROTUBULE-NUCLEATION-BY-LINKING.
- Dehmelt, L., and S. Halpain. 2005. The MAP2/Tau family of microtubule-associated proteins. *Genome Biol.* 6. doi:10.1186/GB-2004-6-1-204.
- Delgehyr, N., J. Sillibourne, and M. Bornens. 2005. Microtubule nucleation and anchoring at the centrosome are independent processes linked by ninein function. 2. doi:10.1242/jcs.02302.
- Dhani, D.K., B.T. Goult, G.M. George, D.T. Rogerson, D.A. Bitton, C.J. Miller, J.W.R. Schwabe, and K. Tanaka. 2013. Mzt1/Tam4, a fission yeast MOZART1 homologue, is an essential component of the  $\gamma$ -tubulin complex and directly interacts with GCP3Alp6. *Mol. Biol. Cell.* 24:3337–3349. doi:10.1091/MBC.E13-05-0253/ASSET/IMAGES/LARGE/3337FIG7.JPEG.
- Dimitrov, A., S. Moutel, I. Cantaloube, and F. Perez. 2008. Detection of GTP-Tubulin conformation in vivo reveals a role for GTP remnants - Supp data. *Science (80-. ).* 4:1353–1357. doi:10.1126/science.
- Eaton, B.A., R.D. Fetter, and G.W. Davis. 2002. Dynactin is necessary for synapse stabilization. *Neuron.* 34:729–741. doi:10.1016/S0896-6273(02)00721-3.



- Efimov, A., A. Kharitonov, N. Efimova, J. Loncarek, P.M. Miller, N. Andreyeva, P. Gleeson, N. Galjart, A.R.R. Maia, I.X. McLeod, J.R. Yates, H. Maiato, A. Khodjakov, A. Akhmanova, and I. Kaverina. 2007. Asymmetric CLASP-Dependent Nucleation of Noncentrosomal Microtubules at the trans-Golgi Network. *Dev. Cell.* 12:917–930. doi:10.1016/j.devcel.2007.04.002.
- Farache, D., A. Jauneau, C. Chemin, M. Chartrain, M.H. Rémy, A. Merdes, and L. Haren. 2016. Functional Analysis of  $\gamma$ -Tubulin Complex Proteins Indicates Specific Lateral Association via Their N-terminal Domains. *J. Biol. Chem.* 291:23112–23125. doi:10.1074/JBC.M116.744862.
- Feng, C., J.M. Cleary, G.O. Kothe, M.C. Stone, A.T. Weiner, J.I. Hertzler, W.O. Hancock, and M.M. Rolls. 2021. Trim9 and Klp61F promote polymerization of new dendritic microtubules along parallel microtubules. *J. Cell Sci.* 134. doi:10.1242/JCS.258437/VIDEO-3.
- Ferro, L.S., S. Can, M.A. Turner, M.M. Elshenawy, and A. Yildiz. 2019. Kinesin and dynein use distinct mechanisms to bypass obstacles. *Elife.* 8. doi:10.7554/ELIFE.48629.
- Fong, K., F.K.C. Au, Y. Jia, S. Yang, L. Zhou, and R.Z. Qi. 2017. Microtubule plus-end tracking of end-binding protein 1 ( EB1 ) is regulated by CDK5 regulatory subunit-associated protein 2. 1:7675–7687. doi:10.1074/jbc.M116.759746.
- Fong, K., S. Hau, Y. Kho, Y. Jia, L. He, and R.Z. Qi. 2009. Interaction of CDK5RAP2 with EB1 to Track Growing Microtubule Tips and to Regulate Microtubule Dynamics. 20:3660–3670. doi:10.1091/mbc.E09.
- de Forges, H., A. Pilon, I. Cantaloube, A. Pallandre, A.M. Haghiri-Gosnet, F. Perez, and C. Poüs. 2016. Localized Mechanical Stress Promotes Microtubule Rescue. *Curr. Biol.* 26:3399–3406. doi:10.1016/j.cub.2016.10.048.
- Freal, A., C. Fassier, B. Le Bras, E. Bullier, S. De Gois, J. Hazan, C.C. Hoogenraad, and F. Couraud. 2016. Cooperative Interactions between 480 kDa Ankyrin-G and EB Proteins Assemble the Axon Initial Segment. *J. Neurosci.* 36:4421–4433. doi:10.1523/JNEUROSCI.3219-15.2016.
- Gazzola, M., A. Schaeffer, B. Vianay, and J. Gaillard. 2022. Microtubules self-repair in living cells.
- Goldspink, D.A., C. Rookyard, B.J. Tyrrell, J. Gadsby, J. Perkins, E.K. Lund, N. Galjart, P. Thomas, T. Wileman, and M.M. Mogensen. 2017. Ninein is essential for apico-basal microtubule formation and CLIP-170 facilitates its redeployment to non-centrosomal microtubule organizing centres. *Open Biol.* 7. doi:10.1098/RSOB.160274.
- Gombos, L., A. Neuner, M. Berynskyy, L.L. Fava, R.C. Wade, C. Sachse, and E. Schiebel. 2013. GTP regulates the microtubule nucleation activity of  $\gamma$ -tubulin. *Nat. Cell Biol.* 2013 1511. 15:1317–1327. doi:10.1038/ncb2863.
- Grimaldi, A.D., T. Maki, B.P. Fitton, D. Roth, D. Yampolsky, M.W. Davidson, T. Svitkina, A. Straube, I. Hayashi, and I. Kaverina. 2014. CLASPs are required for proper microtubule localization of end-binding proteins. *Dev. Cell.* 30:343–352. doi:10.1016/j.devcel.2014.06.026.
- Gudimchuk, N.B., E. V. Ulyanov, E. O’Toole, C.L. Page, D.S. Vinogradov, G. Morgan, G. Li, J.K. Moore, E. Szczesna, A. Roll-Mecak, F.I. Ataullakhanov, and J. Richard

- McIntosh. 2020. Mechanisms of microtubule dynamics and force generation examined with computational modeling and electron cryotomography. *Nat. Commun.* 11:1–15. doi:10.1038/s41467-020-17553-2.
- Guyomar, C., C. Bousquet, S. Ku, J. Heumann, and G. Guilloux. 2022. Changes in seam number and location induce holes within microtubules assembled from porcine brain tubulin and in *Xenopus* egg cytoplasmic.
- Haren, L., D. Farache, L. Emorine, and A. Merdes. 2020. A stable sub-complex between GCP4, GCP5 and GCP6 promotes the assembly of tubulin ring complexes. *J. Cell Sci.* 133. doi:10.1242/jcs.244368.
- Harterink, M., K. Vocking, X. Pan, E.M. Soriano Jerez, L. Slenders, A. Fréal, R.P. Tas, W.J. Van De Wetering, K. Timmer, J. Motshagen, S.F.B. Van Beuningen, L.C. Kapitein, W.J.C. Geerts, J.A. Post, and C.C. Hoogenraad. 2019. Trim46 organizes microtubule fasciculation in the axon initial segment. *J. Neurosci.* 39:4864–4873. doi:10.1523/JNEUROSCI.3105-18.2019.
- Hendershott, M.C., and R.D. Vale. 2014. Regulation of microtubule minus-end dynamics by CAMSAPs and Patronin. *Proc. Natl. Acad. Sci.* 111:5860–5865. doi:10.1073/pnas.1404133111.
- Hoeplich, G.J., K.J. Mickolajczyk, S.R. Nelson, W.O. Hancock, and C.L. Berger. 2017. The Axonal Transport Motor Kinesin-2 Navigates Microtubule Obstacles via Protofilament Switching. *Traffic.* 18:304. doi:10.1111/TRA.12478.
- Janke, C., and M.M. Magiera. 2020. The tubulin code and its role in controlling microtubule properties and functions. *Nat. Rev. Mol. Cell Biol.* 21:307–326. doi:10.1038/s41580-020-0214-3.
- Jiang, K., S. Hua, R. Mohan, I. Grigoriev, K.W. Yau, Q. Liu, E.A. Katrukha, A.F.M. Altelaar, A.J.R. Heck, C.C. Hoogenraad, and A. Akhmanova. 2014. Microtubule Minus-End Stabilization by Polymerization-Driven CAMSAP Deposition. *Dev. Cell.* 28:295–309. doi:10.1016/j.devcel.2014.01.001.
- Kalil, K., and G. Szebenyi. 2000. Common mechanisms underlying growth cone guidance and axon branching. *J. Neurobiol.* 44:145–158. doi:10.1002/1097-4695(200008)44:2<145::AID-NEU5>3.0.CO;2-X.
- Karabay, A., W. Yu, J.M. Solowska, D.H. Baird, and P.W. Baas. 2004. Axonal growth is sensitive to the levels of katanin, a protein that severs microtubules. *J. Neurosci.* 24:5778–5788. doi:10.1523/JNEUROSCI.1382-04.2004.
- Kellogg, E.H., N.M.A. Hejab, S. Poepsel, K.H. Downing, F. DiMaio, and E. Nogales. 2018. Near-atomic model of microtubule-tau interactions. *Science.* 360:1242–1246. doi:10.1126/SCIENCE.AAT1780.
- Kellogg, E.H., S. Howes, S.-C. Ti, E. Ramírez-Aportela, T.M. Kapoor, P. Chacón, and E. Nogales. 2016. Near-atomic cryo-EM structure of PRC1 bound to the microtubule. *Proc. Natl. Acad. Sci.* 113:9430–9439. doi:10.1073/pnas.1609903113.
- Kikkawa, M., T. Ishikawa, T. Nakata, T. Wakabayashi, and N. Hirokawa. 1994. Direct visualization of the microtubule lattice seam both in vitro and in vivo. *J. Cell Biol.* 127:1965–1971. doi:10.1083/jcb.127.6.1965.
- Kollman, J.M., A. Merdes, L. Mourey, and D.A. Agard. 2011. Microtubule nucleation by  $\gamma$ -

- tubulin complexes. *Nat. Rev. Mol. Cell Biol.* 12:709–721. doi:10.1038/NRM3209.
- Kubo, T., H. aki Yanagisawa, T. Yagi, M. Hirono, and R. Kamiya. 2010. Tubulin polyglutamylation regulates axonemal motility by modulating activities of inner-arm dyneins. *Curr. Biol.* 20:441–445. doi:10.1016/J.CUB.2009.12.058.
- Kuo, Y.W., and J. Howard. 2021. Cutting, Amplifying, and Aligning Microtubules with Severing Enzymes. *Trends Cell Biol.* 31:50–61. doi:10.1016/j.tcb.2020.10.004.
- Kuo, Y.W., O. Trottier, and J. Howard. 2019. Predicted Effects of Severing Enzymes on the Length Distribution and Total Mass of Microtubules. *Biophys. J.* 117:2066–2078. doi:10.1016/J.BPJ.2019.10.027.
- Lawrence, E.J., G. Arpag, C. Arnaiz, and M. Zanic. 2021. Ssn1 stabilizes dynamic microtubules and detects microtubule damage. *Elife.* 10. doi:10.7554/ELIFE.67282.
- Lechler, T., and E. Fuchs. 2007. Desmoplakin: An unexpected regulator of microtubule organization in the epidermis. *J. Cell Biol.* 176:147–154. doi:10.1083/JCB.200609109/VIDEO-6.
- Lee, K.Y., B. Esmaeili, B. Zealley, and M. Mishima. 2015. Direct interaction between centralspindlin and PRC1 reinforces mechanical resilience of the central spindle. *Nat. Commun.* 2015 61. 6:1–10. doi:10.1038/ncomms8290.
- Lewis, S.A., I.E. Ivanov, G.H. Lee, and N.J. Cowan. 1989. Organization of microtubules in dendrites and axons is determined by a short hydrophobic zipper in microtubule-associated proteins MAP2 and tau. *Nat.* 1989 3426249. 342:498–505. doi:10.1038/342498a0.
- Lin, T.C., A. Neuner, D. Flemming, P. Liu, T. Chinen, U. Jäkke, R. Arkowitz, and E. Schiebel. 2016. MOZART1 and  $\gamma$ -tubulin complex receptors are both required to turn  $\gamma$ -TuSC into an active microtubule nucleation template. *J. Cell Biol.* 215:823–840. doi:10.1083/JCB.201606092.
- Lindeboom, J.J., M. Nakamura, M. Saltini, A. Hibbel, A. Walia, T. Ketelaar, A.M.C. Emons, J.C. Sedbrook, V. Kirik, B.M. Mulder, and D.W. Ehrhardt. 2019. CLASP stabilization of plus ends created by severing promotes microtubule creation and reorientation. *J. Cell Biol.* 218:190–205. doi:10.1083/JCB.201805047/VIDEO-7.
- Liu, H., and T. Shima. 2022. Preference of CAMSAP3 for microtubules with expanded lattice contributes to stabilization of the minus end. *bioRxiv.* 2022.08.21.504720. doi:10.1101/2022.08.21.504720.
- Liu, H., J. Zheng, L. Zhu, L. Xie, Y. Chen, Y. Zhang, W. Zhang, Y. Yin, C. Peng, J. Zhou, X. Zhu, and X. Yan. 2021a. Wdr47, Camsaps, and Katanin cooperate to generate ciliary central microtubules. *Nat. Commun.* 12:1–15. doi:10.1038/s41467-021-26058-5.
- Liu, P., M. Würtz, E. Zupa, S. Pfeffer, and E. Schiebel. 2021b. Microtubule nucleation: The waltz between  $\gamma$ -tubulin ring complex and associated proteins. *Curr. Opin. Cell Biol.* 68:124–131. doi:10.1016/j.ceb.2020.10.004.
- Liu, P., E. Zupa, A. Neuner, A. Böhrer, J. Loerke, D. Flemming, T. Ruppert, T. Rudack, C. Peter, C. Spahn, O.J. Gruss, S. Pfeffer, and E. Schiebel. 2020. Insights into the assembly and activation of the microtubule nucleator  $\gamma$ -TuRC. *Nature.* 578:467–471. doi:10.1038/s41586-019-1896-6.

- Magiera, M.M., and C. Janke. 2014. Post-translational modifications of tubulin. *Curr. Biol.* 24:R351–R354. doi:10.1016/j.cub.2014.03.032.
- Magiera, M.M., P. Singh, S. Gadadhar, and C. Janke. 2018. Tubulin Posttranslational Modifications and Emerging Links to Human Disease. *Cell.* 173:1323–1327. doi:10.1016/j.cell.2018.05.018.
- Mandelkow, E.M., E. Mandelkow, and R.A. Milligan. 1991. Microtubule dynamics and microtubule caps: A time-resolved cryo-electron microscopy study. *J. Cell Biol.* 114:977–991. doi:10.1083/jcb.114.5.977.
- Manka, S.W., and C.A. Moores. 2018a. The role of tubulin–tubulin lattice contacts in the mechanism of microtubule dynamic instability. *Nat. Struct. Mol. Biol.* 25:1–9. doi:10.1038/s41594-018-0087-8.
- Manka, S.W., and C.A. Moores. 2018b. mechanism of microtubule dynamic instability. 25. doi:10.1038/s41594-018-0087-8.
- Martin, M., and A. Akhmanova. 2018. Coming into Focus: Mechanisms of Microtubule Minus-End Organization. *Trends Cell Biol.* 28:574–588. doi:10.1016/j.tcb.2018.02.011.
- Masuda, H., R. Mori, M. Yukawa, and T. Toda. 2013. Fission yeast MOZART1/Mzt1 is an essential  $\gamma$ -tubulin complex component required for complex recruitment to the microtubule organizing center, but not its assembly. *Mol. Biol. Cell.* 24:2894–2906. doi:10.1091/MBE.E13-05-0235/ASSET/IMAGES/LARGE/2894FIG10.JPEG.
- Masudaa, H., and T. Toda. 2016. Synergistic role of fission yeast Alp16GCP6 and Mzt1MOZART1 in  $\gamma$ -tubulin complex recruitment to mitotic spindle pole bodies and spindle assembly. *Mol. Biol. Cell.* 27:1753–1763. doi:10.1091/MBE.E15-08-0577/ASSET/IMAGES/LARGE/1753FIG8.JPEG.
- McIntosh, J.R., E. O’Toole, G. Morgan, J. Austin, E. Ulyanov, F. Ataullakhanov, and N. Gudimchuk. 2018. Microtubules grow by the addition of bent guanosine triphosphate tubulin to the tips of curved protofilaments. *J. Cell Biol.* 217:2691–2708. doi:10.1083/jcb.201802138.
- McKenney, R.J., W. Huynh, R.D. Vale, and M. Sirajuddin. 2016. Tyrosination of  $\alpha$ -tubulin controls the initiation of processive dynein–dynactin motility. *EMBO J.* 35:1175. doi:10.15252/EMBJ.201593071.
- McNally, F.J., and A. Roll-Mecak. 2018. Microtubule-severing enzymes: From cellular functions to molecular mechanism. *J. Cell Biol.* 217:4057–4069. doi:10.1083/JCB.201612104.
- Meroni, G., and G. Diez-Roux. 2005. TRIM/RBCC, a novel class of “single protein RING finger” E3 ubiquitin ligases. *BioEssays.* 27:1147–1157. doi:10.1002/bies.20304.
- Miller, P.M., A.W. Folkmann, A.R.R. Maia, N. Efimova, A. Efimov, and I. Kaverina. 2009. Golgi-derived CLASP-dependent microtubules control Golgi organization and polarized trafficking in motile cells. *Nat. Cell Biol.* 11:1069–1080. doi:10.1038/ncb1920.
- Mimori-Kiyosue, Y., I. Grigoriev, G. Lansbergen, H. Sasaki, C. Matsui, F. Severin, N. Galjart, F. Grosveld, I. Vorobjev, S. Tsukita, and A. Akhmanova. 2005. CLASP1 and CLASP2 bind to EB1 and regulate microtubule plus-end dynamics at the cell cortex. *J. Cell Biol.* 168:141–153. doi:10.1083/jcb.200405094.

- Mogensen, M.M., A. Malik, M. Piel, V. Bouckson-castaing, and M. Bornens. 2000. Microtubule minus-end anchorage at centrosomal and non-centrosomal sites : the role of ninein. 3023:3013–3023.
- Mori, Y., Y. Inoue, S. Tanaka, S. Doda, S. Yamanaka, and H. Fukuchi. 2015. Cep169 , a Novel Microtubule Plus-End- Tracking Centrosomal Protein , Binds to CDK5RAP2 and Regulates Microtubule Stability. 1:1–13. doi:10.1371/journal.pone.0140968.
- Morikawa, M., H. Yajima, R. Nitta, S. Inoue, T. Ogura, C. Sato, and N. Hirokawa. 2015. X-ray and Cryo-EM structures reveal mutual conformational changes of Kinesin and GTP-state microtubules upon binding. *EMBO J.* 34:1270–1286. doi:10.15252/EMBJ.201490588.
- Moutin, M.J., C. Bosc, L. Peris, and A. Andrieux. 2021. Tubulin post-translational modifications control neuronal development and functions. *Dev. Neurobiol.* 81:253–272. doi:10.1002/dneu.22774.
- Muroyama, A., L. Seldin, and T. Lechler. 2016. Divergent regulation of functionally distinct  $\gamma$ -tubulin complexes during differentiation. *J. Cell Biol.* 213:679–692. doi:10.1083/jcb.201601099.
- Nakata, T., S. Niwa, Y. Okada, F. Perez, and N. Hirokawa. 2011. Preferential binding of a kinesin-1 motor to GTP-tubulin-rich microtubules underlies polarized vesicle transport. *J. Cell Biol.* 194:245. doi:10.1083/JCB.201104034.
- Peet, D.R., N.J. Burroughs, and R.A. Cross. 2018. Kinesin expands and stabilizes the GDP-microtubule lattice. *Nat. Nanotechnol.* 13:386–391. doi:10.1038/S41565-018-0084-4.
- Peris, L., M. Thery, J. Fauré, Y. Saoudi, L. Lafanechère, J.K. Chilton, P. Gordon-Weeks, N. Galjart, M. Bornens, L. Wordeman, J. Wehland, A. Andrieux, and D. Job. 2006. Tubulin tyrosination is a major factor affecting the recruitment of CAP-Gly proteins at microtubule plus ends. *J. Cell Biol.* 174:839–849. doi:10.1083/JCB.200512058/VIDEO-3.
- Qiang, L., W. Yu, A. Andreadis, M. Luo, and P.W. Baas. 2006. Tau Protects Microtubules in the Axon from Severing by Katanin. *J. Neurosci.* 26:3120–3129. doi:10.1523/JNEUROSCI.5392-05.2006.
- Raff, E.C., J.D. Fackenthal, J.A. Hutchens, H.D. Hoyle, and F.R. Turner. 1997. Microtubule architecture specified by a beta-tubulin isoform. *Science.* 275:70–73. doi:10.1126/SCIENCE.275.5296.70.
- Rai, A., T. Liu, S. Glauser, E.A. Katrukha, J. Estévez-Gallego, R. Rodríguez-García, W.S. Fang, J.F. Díaz, M.O. Steinmetz, K.H. Altmann, L.C. Kapitein, C.A. Moores, and A. Akhmanova. 2019. Taxanes convert regions of perturbed microtubule growth into rescue sites. *Nat. Mater.* doi:10.1038/s41563-019-0546-6.
- Rai, A., T. Liu, E.A. Katrukha, J. Estevez-Gallego, S.W. Manka, I. Paterson, J. Fernando Diaz, L.C. Kapitein, C.A. Moores, and A. Akhmanova. 2021. Lattice defects induced by microtubule-stabilizing agents exert a long-range effect on microtubule growth by promoting catastrophes. *Proc. Natl. Acad. Sci. U. S. A.* 118:1–29. doi:10.1073/pnas.2112261118.
- Rale, M., B. Romer, B.P. Mahon, S.M. Travis, and S. Petry. 2022. The conserved centrosomal motif,  $\gamma$ TuNA, forms a dimer that directly activates microtubule nucleation

- by the  $\gamma$ -tubulin ring complex ( $\gamma$ TuRC). 2. 1–47.
- Rice, L.M., E.A. Montabana, and D.A. Agard. 2008. The lattice as allosteric effector: structural studies of alphabeta- and gamma-tubulin clarify the role of GTP in microtubule assembly. *Proc. Natl. Acad. Sci. U. S. A.* 105:5378–5383. doi:10.1073/PNAS.0801155105.
- Roll-Mecak, A. 2020. The Tubulin Code in Microtubule Dynamics and Information Encoding. *Dev. Cell.* 54:7–20. doi:10.1016/j.devcel.2020.06.008.
- Roostalu, J., N.I. Cade, and T. Surrey. 2015. Complementary activities of TPX2 and chTOG constitute an efficient importin-regulated microtubule nucleation module. 17. doi:10.1038/ncb3241.
- Sarbanes, S.L., E.A. Zehr, and A. Roll-Mecak. 2022. Microtubule-severing enzymes. *Curr. Biol.* 32:R992–R997. doi:10.1016/J.CUB.2022.08.046.
- Savage, C., M. Hamelin, J.G. Culotti, A. Coulson, D.G. Albertson, and M. Chalfie. 1989. *mec-7* is a beta-tubulin gene required for the production of 15-protofilament microtubules in *Caenorhabditis elegans*. *Genes Dev.* 3:870–881. doi:10.1101/GAD.3.6.870.
- Schaedel, L., K. John, J. Gaillard, M. V. Nachury, L. Blanchoin, and M. Thery. 2015. Microtubules self-repair in response to mechanical stress. *Nat. Mater.* 14:1156–1163. doi:10.1038/nmat4396.
- Schaedel, L., S. Triclin, D. Chrétien, A. Abrieu, C. Aumeier, J. Gaillard, L. Blanchoin, M. Théry, and K. John. 2019. Lattice defects induce microtubule self-renewal. *Nat. Phys.* 15:830–838. doi:10.1038/s41567-019-0542-4.
- Sharp, D.J., and J.L. Ross. 2012. Microtubule-severing enzymes at the cutting edge. *J. Cell Sci.* 125:2561–2569. doi:10.1242/jcs.101139.
- Shigematsu, H., T. Imasaki, C. Doki, T. Sumi, M. Aoki, T. Uchikubo-Kamo, A. Sakamoto, K. Tokuraku, M. Shirouzu, and R. Nitta. 2018. Structural insight into microtubule stabilization and kinesin inhibition by Tau family MAPs. *J. Cell Biol.* 217:4155–4163. doi:10.1083/JCB.201711182.
- Shima, T., M. Morikawa, J. Kaneshiro, T. Kambara, S. Kamimura, T. Yagi, H. Iwamoto, S. Uemura, H. Shigematsu, M. Shirouzu, T. Ichimura, T.M. Watanabe, R. Nitta, Y. Okada, and N. Hirokawa. 2018. Kinesin-binding-triggered conformation switching of microtubules contributes to polarized transport. *J. Cell Biol.* 217:4164–4183. doi:10.1083/JCB.201711178.
- Siahaan, V., J. Krattenmacher, A.A. Hyman, S. Diez, A. Hernández-Vega, Z. Lansky, and M. Braun. 2019. Kinetically distinct phases of tau on microtubules regulate kinesin motors and severing enzymes. *Nat. Cell Biol.* 21:1086–1092. doi:10.1038/S41556-019-0374-6.
- Sirajuddin, M., L.M. Rice, and R.D. Vale. 2014. Regulation of microtubule motors by tubulin isoforms and post-translational modifications. *Nat. Cell Biol.* 16:335–344. doi:10.1038/ncb2920.
- Subramanian, R., E.M. Wilson-Kubalek, C.P. Arthur, M.J. Bick, E.A. Campbell, S.A. Darst, R.A. Milligan, and T.M. Kapoor. 2010. Insights into antiparallel microtubule crosslinking by PRC1, a conserved nonmotor microtubule binding protein. *Cell.* 142:433–443. doi:10.1016/j.cell.2010.07.012.

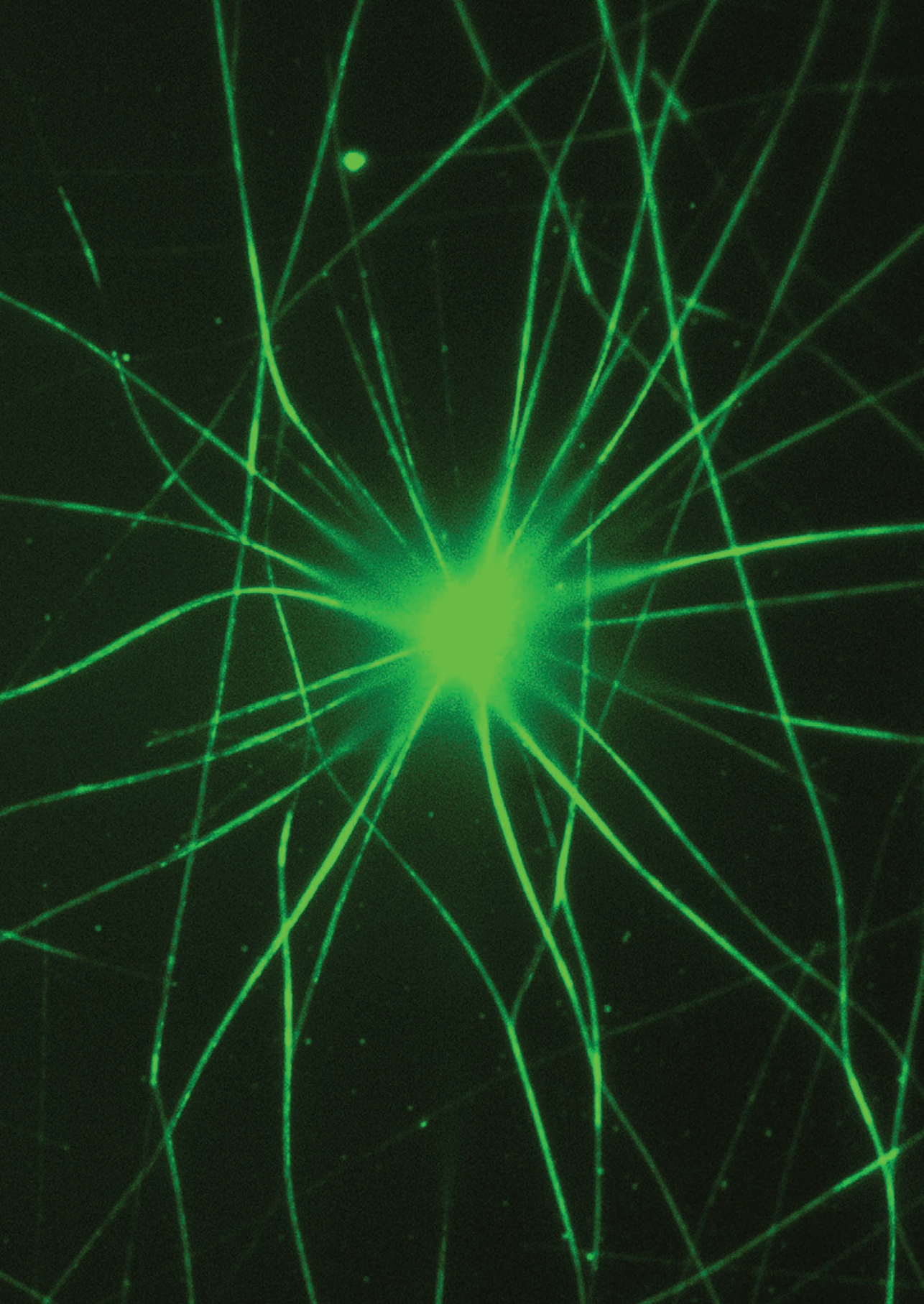
- Suryavanshi, S., B. Eddé, L.A. Fox, S. Guerrero, R. Hard, T. Hennessey, A. Kabi, D. Malison, D. Pennock, W.S. Sale, D. Wloga, and J. Gaertig. 2010. Tubulin Glutamylation Regulates Ciliary Motility by Altering Inner Dynein Arm Activity. *Curr. Biol.* 20:435–440. doi:10.1016/J.CUB.2009.12.062.
- Szczesna, E., E.A. Zehr, S.W. Cummings, A. Szyk, K.K. Mahalingan, Y. Li, and A. Roll-Mecak. 2022. Combinatorial and antagonistic effects of tubulin glutamylation and glycylation on katanin microtubule severing. *Dev. Cell.* 57:2497–2513.e6. doi:10.1016/J.DEVCEL.2022.10.003.
- Tas, R.P., A. Chazeau, B.M.C. Cloin, M.L.A. Lambers, C.C. Hoogenraad, and L.C. Kapitein. 2017. Differentiation between Oppositely Oriented Microtubules Controls Polarized Neuronal Transport. *Neuron.* 96:1264–1271.e5. doi:10.1016/j.neuron.2017.11.018.
- Teixidó-Travesa, N., J. Villén, C. Lacasa, M.T. Bertran, M. Archinti, S.P. Gygi, C. Caelles, J. Roig, and J. Lüders. 2010. The gammaTuRC revisited: a comparative analysis of interphase and mitotic human gammaTuRC redefines the set of core components and identifies the novel subunit GCP8. *Mol. Biol. Cell.* 21:3963–3972. doi:10.1091/MBC.E10-05-0408.
- Thawani, A., and S. Petry. 2021. Molecular insight into how  $\gamma$ -TuRC makes microtubules. *J. Cell Sci.* 134. doi:10.1242/jcs.245464.
- Thawani, A., M.J. Rale, N. Coudray, G. Bhabha, H.A. Stone, J.W. Shaevitz, and S. Petry. 2020. The transition state and regulation of  $\gamma$ -TuRC-mediated microtubule nucleation revealed by single molecule microscopy. *Elife.* 9:1–34. doi:10.7554/ELIFE.54253.
- Théry, M., and L. Blanchoin. 2021. Microtubule self-repair. *Curr. Opin. Cell Biol.* 68:144–154. doi:10.1016/j.ceb.2020.10.012.
- Ti, S.C., G.M. Alushin, and T.M. Kapoor. 2018. Human  $\beta$ -Tubulin Isoforms Can Regulate Microtubule Protofilament Number and Stability. *Dev. Cell.* 47:175–190.e5. doi:10.1016/j.devcel.2018.08.014.
- Tovey, C.A., and P.T. Conduit. 2018. Microtubule nucleation by  $\gamma$ -tubulin complexes and beyond. *Essays Biochem.* 62:765–780. doi:10.1042/EBC20180028.
- Tovey, C.A., C. Tsuji, A. Egerton, F. Bernard, A. Guichet, M. De La Roche, and P.T. Conduit. 2021. Autoinhibition of cnn binding to  $\gamma$ -turcs prevents ectopic microtubule nucleation and cell division defects. *J. Cell Biol.* 220. doi:10.1083/jcb.202010020.
- Triclin, S., D. Inoue, J. Gaillard, Z.M. Htet, M.E. DeSantis, D. Portran, E. Derivery, C. Aumeier, L. Schaedel, K. John, C. Leterrier, S.L. Reck-Peterson, L. Blanchoin, and M. Théry. 2021. Self-repair protects microtubules from destruction by molecular motors. *Nat. Mater.* 20:883–891. doi:10.1038/s41563-020-00905-0.
- Valenstein, M.L., and A. Roll-Mecak. 2016. Graded Control of Microtubule Severing by Tubulin Glutamylation. *Cell.* 164:911–921. doi:10.1016/j.cell.2016.01.019.
- Vemu, A., E. Szczesna, E.A. Zehr, J.O. Spector, N. Grigorieff, A.M. Deaconescu, and A. Roll-Mecak. 2018. Severing enzymes amplify microtubule arrays through lattice GTP-tubulin incorporation. *Science (80-. ).* 361. doi:10.1126/science.aau1504.
- Vitre, B., C. Heichette, C. Garnier, and I. Arnal. 2008. EB1 regulates microtubule dynamics and tubulin sheet closure in vitro. 10. doi:10.1038/ncb1703.

- Walczak, C.E., and S.L. Shaw. 2010. A MAP for bundling microtubules. *Cell*. 142:364–367. doi:10.1016/j.cell.2010.07.023.
- Walter, W.J., V. Beránek, E. Fischermeier, and S. Diez. 2012. Tubulin Acetylation Alone Does Not Affect Kinesin-1 Velocity and Run Length In Vitro. *PLoS One*. 7:e42218. doi:10.1371/JOURNAL.PONE.0042218.
- Wang, S., D. Wu, S. Quintin, R.A. Green, D.K. Cheerambathur, S.D. Ochoa, A. Desai, and K. Oegema. 2015. NOCA-1 functions with  $\gamma$ -tubulin and in parallel to Patronin to assemble non-centrosomal microtubule arrays in *C. elegans*. *Elife*. 4:1–34. doi:10.7554/eLife.08649.
- Waterman-Storer, C.M., and E.D. Salmon. 1997. Actomyosin-based retrograde flow of microtubules in the lamella of migrating epithelial cells influences microtubule dynamic instability and turnover and is associated with microtubule breakage and treadmilling. *J. Cell Biol.* 139:417–434. doi:10.1083/JCB.139.2.417.
- Wieczorek, M., T.L. Huang, L. Urnavicius, K.C. Hsia, and T.M. Kapoor. 2020a. MZT Proteins Form Multi-Faceted Structural Modules in the  $\gamma$ -Tubulin Ring Complex. *Cell Rep.* 31:107791. doi:10.1016/j.celrep.2020.107791.
- Wieczorek, M., S.C. Ti, L. Urnavicius, K.R. Molloy, A. Aher, B.T. Chait, and T.M. Kapoor. 2021. Biochemical reconstitutions reveal principles of human  $\gamma$ -TuRC assembly and function. *J. Cell Biol.* 220. doi:10.1083/JCB.202009146.
- Wieczorek, M., L. Urnavicius, S.C. Ti, K.R. Molloy, B.T. Chait, and T.M. Kapoor. 2020b. Asymmetric Molecular Architecture of the Human  $\gamma$ -Tubulin Ring Complex. *Cell*. 180:165-175.e16. doi:10.1016/j.cell.2019.12.007.
- Würtz, M., A. Böehler, A. Neuner, E. Zupa, L. Rohland, P. Liu, B.J.A. Vermeulen, S. Pfeffer, S. Eustermann, and E. Schiebel. 2021. Reconstitution of the recombinant human  $\gamma$ -tubulin ring complex. *Open Biol.* 11. doi:10.1098/rsob.200325.
- Würtz, M., E. Zupa, E.S. Atorino, A. Neuner, A. Böehler, A.S. Rahadian, B.J.A. Vermeulen, G. Tonon, S. Eustermann, E. Schiebel, and S. Pfeffer. 2022. Modular assembly of the principal microtubule nucleator  $\gamma$ -TuRC. *Nat. Commun.* 13. doi:10.1038/s41467-022-28079-0.
- Yu, W., L. Qiang, J.M. Solowska, A. Karabay, S. Korulu, and P.W. Baas. 2008. The microtubule-severing proteins spastin and katanin participate differently in the formation of axonal branches. *Mol. Biol. Cell*. 19:1485–1498. doi:10.1091/MB.C.E07-09-0878/ASSET/IMAGES/LARGE/ZMK0040884780012.JPEG.
- Yu, W., J.M. Solowska, L. Qiang, A. Karabay, D. Baird, and P.W. Baas. 2005. Regulation of microtubule severing by katanin subunits during neuronal development. *J. Neurosci.* 25:5573–5583. doi:10.1523/JNEUROSCI.0834-05.2005.
- Zehr, E.A., A. Szyk, E. Szczesna, and A. Roll-Mecak. 2020. Katanin Grips the  $\beta$ -Tubulin Tail through an Electropositive Double Spiral to Sever Microtubules. *Dev. Cell*. 52:118-131.e6. doi:10.1016/j.devcel.2019.10.010.
- Zhang, R., B. LaFrance, and E. Nogales. 2018. Separating the effects of nucleotide and EB binding on microtubule structure. *Proc. Natl. Acad. Sci. U. S. A.* 115:E6191–E6200. doi:10.1073/pnas.1802637115.
- Zhang, R., J. Roostalu, T. Surrey, and E. Nogales. 2017. Structural insight into TPX2-



stimulated microtubule assembly. *Elife*. 6. doi:10.7554/ELIFE.30959.

Zimmermann, F., M. Serna, A. Ezquerro, R. Fernandez-Leiro, O. Llorca, and J. Luders. 2020. Assembly of the asymmetric human  $\gamma$ -tubulin ring complex by RUVBL1-RUVBL2 AAA ATPase. *Sci. Adv.* 6:1–20. doi:10.1126/SCIADV.ABE0894.



# **Addendum**

Summary

Nederlandse samenvatting

Curriculum Vitae

List of publications

Acknowledgments

## Summary

Microtubules are one of the major types of cytoskeletal filaments. They are very dynamic polymers made up of  $\alpha\beta$ -tubulin dimers arranged longitudinally in head-to-tail fashion as well as laterally to assemble 13-protofilament hollow cylindrical tubes. The incorporation of GTP-bound  $\alpha\beta$ -tubulin dimers generates a fast growing plus end exposing  $\beta$ -tubulin and a slow growing minus end exposing  $\alpha$ -tubulin. Once incorporated, the GTP bound to  $\beta$ -tubulin undergoes hydrolysis with a delay producing a stable GTP-cap that prevents the microtubule from undergoing depolymerization. In cells, *de novo* assembly of microtubules is controlled by a template called  $\gamma$ -TuRC, which interacts with  $\alpha$ -tubulin. Active  $\gamma$ -TuRCs that can nucleate microtubules are typically anchored at microtubule-organizing centers (MTOCs). Microtubules which are nucleated from  $\gamma$ -TuRC can either remain capped and anchored to the MTOC or be released if they are cut by microtubule severing enzymes like katanin. The release of microtubules from MTOC generates free minus ends, which are then stabilized by minus-end binding proteins called CAMSAPs. However, the plus ends remain very dynamic and undergo transitions from growth to shrinkage, termed “catastrophes”, and the opposite transitions termed “rescues”. Numerous microtubule regulatory proteins act at the plus ends, minus ends and the microtubule shafts connecting the two ends to control the organization and density of cellular microtubule networks (see Chapter 1). In this thesis, we focused on each of these aspects and explored the dynamic life of microtubules by reconstituting these processes *in vitro* using purified proteins.

We first focused on the birth and growth of microtubules and explored their regulation in Chapter 2. We reconstituted microtubule nucleation using purified  $\gamma$ -TuRC and microtubule regulatory proteins and showed that CDK5RAP2, CLASP2 and chTOG promoted microtubule nucleation from  $\gamma$ -TuRC. To our surprise, we discovered that CAMSAPs can bind to  $\gamma$ -TuRC-capped microtubule minus ends and displace  $\gamma$ -TuRC from these ends, generating free and stable microtubule minus ends. Furthermore, we found out that CDK5RAP2, but not CLASP2 or chTOG, can inhibit CAMSAP binding and microtubule release, and CDK5RAP2 does so by improving the fit between  $\gamma$ -TuRC and minus ends of 13-protofilament microtubules. We propose that the destiny of a microtubule depends on the type of the protein complex that activates its nucleation.

In Chapter 3, we shifted our focus from microtubule minus ends to microtubule shaft. We described a mechanism for stabilization of microtubule lattice. We showed that TRIM46, a neuronal microtubule-binding protein, can bundle microtubules in a parallel orientation and

promote microtubule rescues within these bundles. We then established that Ankyrin-G, a scaffold protein, can recruit TRIM46-stabilized microtubule bundles to the axonal membrane in an EB-dependent manner to drive the assembly of the axon initial segment.

In Chapter 4, we uncovered a new role of CLASP2 as a microtubule repair factor participating in microtubule maintenance. We demonstrated that CLASP2, an anti-catastrophe factor, can promote complete repair of microtubule lattices that have been damaged by external factors by restricting lattice damage and inhibiting microtubule depolymerization. We further revealed that CLASP2 facilitates microtubule repair by promoting stable incorporation of free tubulin dimers and tube closure at the damage sites, causing lattice renewal.

Finally, in Chapter 5, we described a three-protein module that can regulate microtubule polymer mass and the length of stabilized minus ends. We showed that katanin, a microtubule severing enzyme, can suppress elongation of CAMSAP3-decorated minus ends at low concentration, while it can cut and amplify CAMSAP2/3-stabilized microtubule minus ends at a higher concentration. WDR47, a WD40 repeat-containing protein, binds to all three CAMSAPs and slows down the growth rate of CAMSAP2/3-decorated minus ends and potentiates the minus-end blocking activity of CAMSAP1. WDR47 can inhibit the binding of katanin to CAMSAP2/3-stabilized minus ends and protect them from severing. The presence of WDR47 shifts the balance from microtubule amplification to minus-end regulation. Together, these three proteins can regulate minus-end dynamics and microtubule number.

To conclude, we have investigated various aspects of the dynamic life of microtubules using complex *in vitro* reconstitution experiments. We obtained mechanistic insights into the regulation of microtubule nucleation, minus-end dynamics, lattice stabilization and maintenance, microtubule number and the interplay between microtubule regulatory proteins. These insights will help to understand how microtubule arrays are organized in cells.

## Nederlandse samenvatting

Microtubuli zijn een van de meest voorkomende onderdelen van het cytoskelet. Het zijn zeer dynamische polymeren, opgebouwd uit  $\alpha\beta$ -tubulinedimeren die door middel van longitudinale en laterale interacties een holle cilindrische buis vormen, bestaande uit 13-protofilamenten. De toevoeging van GTP-gebonden  $\alpha\beta$ -tubulinedimeren aan de microtubulus genereert een snel groeiend plus-uiteinde waar  $\beta$ -tubuline is blootgesteld, en een langzaam groeiend min-uiteinde waar  $\alpha$ -tubuline is blootgesteld. Eenmaal toegevoegd aan de microtubulus wordt de  $\beta$ -tubuline-gebonden GTP gehydrolyseerd met een vertraging, wat resulteert in een stabiele GTP-kap die depolymerisatie van de microtubulus voorkomt. In cellen wordt *de novo* groei van microtubuli bewerkstelligd door een template, genaamd  $\gamma$ -TuRC, die interacteert met  $\alpha$ -tubuline. Actieve  $\gamma$ -TuRCs die microtubuli kunnen initiëren, zijn over het algemeen verankerd aan de structuren die microtubuli organiseren (genaamd ‘microtubule-organizing centers’, of MTOCs). Vanuit  $\gamma$ -TuRC ontstane microtubuli kunnen ofwel gebonden blijven aan  $\gamma$ -TuRC en daarmee verankerd blijven aan een MTOC, of worden vrijgelaten als ze geknipt worden door microtubulus-knipenzymen zoals katanin. Het vrijlaten van MTOC-verankerde microtubuli genereert vrije min-uiteindes, welke vervolgens gestabiliseerd kunnen worden door min-uiteinde-bindende eiwitten genaamd CAMSAPs. De vrije plus-uiteindes blijven echter heel dynamisch en ondergaan zowel transitie van groei naar krimp, genaamd “catastrophes”, als transitie van krimp naar groei, genaamd “rescues”. Vele microtubulus-regulerende eiwitten werken aan het plus-uiteinde, min-uiteinde en de schacht van een microtubulus (die de twee uiteindes verbindt) om zo de algehele organisatie en dichtheid van het cellulaire microtubulus-netwerk te controleren (zie Hoofdstuk 1). In dit proefschrift hebben wij ons geconcentreerd op elk van deze aspecten en onderzochten wij het dynamische leven van microtubuli door deze processen te reconstrueren met gezuiverde eiwitten.

Allereerst hebben wij ons geconcentreerd op de geboorte en groei van microtubuli, en onderzochten wij hun regulatie, in Hoofdstuk 2. We hebben het initiëren van microtubulus-groei gereconstrueerd met gebruik van gezuiverd  $\gamma$ -TuRC en microtubulus-regulerende eiwitten. Hiermee toonden wij aan dat CDK5RAP2, CLASP2 en chTOG de microtubulus-groei vanaf  $\gamma$ -TuRC bevorderden. Tot onze verbazing ontdekten wij dat CAMSAPs aan  $\gamma$ -TuRC-gekapte min-uiteindes kunnen binden en  $\gamma$ -TuRC van deze uiteindes kunnen verdringen, wat vrije en stabiele min-uiteindes genereert. Bovendien ontdekten wij dat CDK5RAP2, in tegenstelling tot CLASP2 of chTOG, CAMSAP-binding en microtubulus-vrijlating kan inhiberen middels het verbeteren van de binding tussen  $\gamma$ -TuRC en min-uiteindes van

microtubuli bestaande uit 13-protofilamenten. Wij stellen voor dat het lot van een microtubulus afhangt van het type eiwitcomplex dat zijn ontstaan activeert.

In Hoofdstuk 3 verlegden wij onze focus van microtubulus min-uiteindes naar de schacht, waarvoor wij een mechanisme van stabilisatie beschreven. We lieten zien dat TRIM46, een neuronaal microtubulus-bindend eiwit, microtubuli kan bundelen in een parallelle oriëntatie en ‘rescues’ binnen deze bundels kan bevorderen. Vervolgens stelden we vast dat Ankyrin-G, een ‘scaffold’ eiwit, TRIM46-gestabiliseerde microtubulus-bundels kan rekruteren naar het axon-membraan met behulp van van EB, om zo de opbouw van het initiële segment van de axon voort te drijven.

In Hoofdstuk 4 bespreken wij een nieuwe rol voor CLASP2 als microtubulus-reparatiefactor. We hebben aangetoond dat CLASP2, een anti-‘catastrophe’ factor, complete reparatie in gang kan zetten van microtubulus-schachten die beschadigd zijn door externe factoren, middels beperking van de beschadiging en het inhiberen van microtubulus-depolymerisatie. Bovendien hebben we aangetoond dat CLASP2 microtubulus-reparatie faciliteert middels het promoten van stabiele incorporatie van vrije tubuline-dimeren en sluiting van de tubulus op de beschadigde locatie, wat het herstel van de schacht teweegbrengt.

Tenslotte beschrijven wij in Hoofdstuk 5 drie eiwitten die de algehele polymeermassa en de lengte van gestabiliseerde microtubulus min-uiteindes kunnen reguleren. We hebben aangetoond dat katanin, een microtubulus-knipenzym, elongatie van CAMSAP2/3-gedecoreerde min-uiteindes kan onderdrukken bij een lage concentratie. Daarentegen kan katanin bij hoge concentratie CAMSAP2/3-gestabiliseerde min-uiteindes knippen en hen daardoor amplificeren. WDR47, een WD40 domein-bevattend eiwit, bindt alle drie de CAMSAPs en vertraagt de groei van CAMSAP2/3-gedecoreerde min-uiteindes. Daarnaast versterkt het de blokkeringsactiviteit van CAMSAP1 op de min-uiteindes. WDR47 kan de binding van katanin aan CAMSAP2/3-gestabiliseerde min-uiteindes inhiberen en deze beschermen tegen knippen. De aanwezigheid van WDR47 verschuift de balans van microtubulus-amplificatie naar regulatie van het min-uiteinde. Samen kunnen deze drie eiwitten de dynamiek van min-uiteindes en de hoeveelheid microtubuli reguleren.

Al met al hebben wij verschillende aspecten van het dynamische leven van microtubuli onderzocht door middel van experimenten met gezuiverde eiwitten. We hebben mechanistische inzichten verkregen betreffende de regulatie van zowel het initiëren van microtubulus-groei, de dynamiek van min-uiteindes, het stabiliseren en onderhouden van de schacht en het samenspel van microtubulus-regulerende eiwitten. Deze inzichten zullen bijdragen aan het begrip van de organisatie van microtubuli in cellen.

## Curriculum Vitae

Dipti Rai was born on September 25<sup>th</sup>, 1990, in Mau, Uttar Pradesh, India. She moved to Varanasi for her secondary education. She obtained her B.Sc. honors degree with distinction and a specialization in zoology from Banaras Hindu University, Varanasi, India in 2014. Inexperienced, but inquisitive towards scientific research, she decided to enter a 3-year master's program (by research) at Tata Institute of Fundamental Research in Mumbai, India and joined Prof. Krishanu Ray's lab. During her master's studies, she investigated the role of kinesin-2 in regulating synapse assembly in the developing central nervous system of *Drosophila* and learnt various microscopy and basic molecular biology techniques. In 2017, after obtaining an M.Sc. degree in Biology with distinction and a research experience of 3 years, she joined the lab of Prof. Anna Akhmanova at Utrecht University, The Netherlands to pursue her PhD. Here, she first started studying the regulation of microtubule dynamics by two axon initial segment proteins and learnt biochemical in vitro reconstitutions. She then worked on understanding the mechanism of microtubule repair by CLASP2. For a major part of her PhD, Dipti focused on studying microtubule nucleation from gamma-tubulin ring complex and its regulation. Additionally, she also explored the regulation of microtubule number and minus-end dynamics in vitro. The results from her research work in PhD are described in this thesis.



---

## List of publications

**CAMSAP-driven microtubule release from  $\gamma$ -TuRC and its regulation by nucleation-promoting factors.**

**Dipti Rai**, Shasha Hua, Jooske L. Monster, Riccardo Stucchi, Kelly Stecker, Yaqian Zhang, Eugene A. Katrukha, Maarten Altelaar, Michal Wieczorek, Kai Jiang, Anna Akhmanova.  
*bioRxiv* 2022.08.03.502613; doi: <https://doi.org/10.1101/2022.08.03.502613>

**Compressive forces stabilise microtubules in living cells.**

Yuhui Li, Ondřej Kučera, Damien Cuvelier, David M. Rutkowski, Mathieu Deygas, **Dipti Rai**, Tonja Pavlovič, Filipe Nunes Vicente, Matthieu Piel, Gregory Giannone, Dimitrios Vavylonis, Anna Akhmanova, Laurent Blanchoin, Manuel Théry  
*bioRxiv* 2022.02.07.479347; doi: <https://doi.org/10.1101/2022.02.07.479347>

**CLASP Mediates Microtubule Repair by Restricting Lattice Damage and Regulating Tubulin Incorporation.**

Amol Aher, **Dipti Rai**, Laura Schaedel, Jeremie Gaillard, Karin John, Qingyang Liu, Maarten Altelaar, Laurent Blanchoin, Manuel Thery, Anna Akhmanova.  
*Curr Biol.* 2020 Jun 8;30(11):2175-2183.e6. doi: [10.1016/j.cub.2020.03.070](https://doi.org/10.1016/j.cub.2020.03.070)

**Feedback-Driven Assembly of the Axon Initial Segment.**

Amélie Fréal, **Dipti Rai**, Roderick P. Tas, Xingxiu Pan, Eugene A. Katrukha, Dieudonnée van de Willige, Riccardo Stucchi, Amol Aher, Chao Yang, A.F. Maarten Altelaar, Karin Vocking, Jan Andries Post, Martin Harterink, Lukas C. Kapitein, Anna Akhmanova, Casper C. Hoogenraad.  
*Neuron.* 2019 Oct 23;104(2):305-321.e8. doi: [10.1016/j.neuron.2019.07.029](https://doi.org/10.1016/j.neuron.2019.07.029)

**A method for estimating relative changes in the synaptic density in *Drosophila* central nervous system.**

**Dipti Rai**, Swagata Dey, Krishanu Ray.  
*BMC Neurosci.* 2018 May 16;19(1):30. doi: [10.1186/s12868-018-0430-3](https://doi.org/10.1186/s12868-018-0430-3)

## Acknowledgments

After almost five years, I have been able to put together a body of research work that could culminate in a fine PhD thesis. Of course, this would not have been feasible without peer support, the companionship of the scientific community to which I belonged and a level of understanding, support and motivation that I received from my family and friends. And this is my opportunity to express my gratitude to all the people who have supported me throughout my PhD journey. So, I cannot keep it short, even if I try.

Undoubtedly, the most crucial role was played by my supervisor **Anna** who provided exceptional guidance and support throughout these years both scientifically and personally. The academic journey can be enjoyable with a terrific PhD advisor, and mine was. I get most of my inspirations from two strong women in my life, you being one of them, Anna. I consider you as my role model because of the academic and non-academic qualities that you possess. I admire your passion and commitment towards science, your scientific integrity and correctness, intellect and memory, rationality, honesty, articulation, tirelessness, dynamic management style and so on. I can keep going but there is no end to this list. Your ability to attract funding is applaudable. You know very well how to keep someone motivated and boost their confidence even in their most difficult times, I have experienced it myself. You acknowledge the hard work in an extremely rewarding way. I cannot thank you enough for the freedom and flexibility that you have given me in my PhD lab life. I have started to practice my talks now and work on my speech to speak slowly because you made me realize its importance in a unique way. There is always something to learn even from your tiniest tales. My writing and graphing skills have improved in response to your feedback, and I believe that I make less mistakes now in stating anything scientifically correct. Sometimes, when I use a wrong English word or at wrong places, you immediately but “indirectly” illuminate me with the correct version in a sentence that makes me laugh and then it gets fixed in my mind almost permanently. I also put efforts now to not use “basically” very frequently in my speech, thanks to you. On a serious note, I have learnt so much from you and am still learning and trying to integrate as many of your above qualities in me. Seeing you awarded with Spinoza prize was a proud moment and I hope that you reach even greater heights in future.

I would like to thank all the members of my thesis assessment committee and doctoral examination committee- **Marileen Dogterom, Elly Hol, Susanne Lens, Sander van den Heuvel, Friedrich Förster, Lukas Kapitein and Martin Harterink** for taking out time to evaluate my thesis and participate in my PhD defense.

**Marileen**, we have interacted significantly during synergy consortium meetings, either in-person at TU, Delft and Utrecht, or virtually on zoom since COVID times. One of the reasons why I like attending the synergy meetings is to learn to think diversly and it has helped me a lot, although those discussions mostly ended up in me doing more experiments. Thanks for your constructive feedback during those meetings. I wish you success towards your goal of creating a synthetic cell. Also, a special thanks to **Vladimir**. I benefited from your questions during synergy meetings and we also ended up collaborating in order to understand the cause or correlation between CAMSAP3 and its preference for distinct microtubule lattices and minus end structure using your Cryo-ET and my in vitro reconstitution techniques. I hope that our results will eventually find a way into a publication. I wish you all the best with your early career and lab at Queen Mary University of London. I would also like to thank other members from Marileen' and **Gijsje Koenderink**'s labs including **Celine, Renu, Reza, Yash, Iliana, Nemo, Ali** and **Eli** for interesting scientific discussions during the synergy meetings and lasts but not the least **Ruben** and **Dieudonné** for carrying Anna lab members to Delft in your cars and having fun and scientific conversations during those road trips and meetings.

**Lukas**, your scientific enthusiasm and energy is contagious, and you are good at selling science. I enjoyed the scientific discussions with you on all my research projects and I appreciate your critical input on those projects. We are also co-authors on **Amelie**'s paper. Thank you for grading the internship reports of all my master students. I was amusingly shocked when you could read and grade the internship report of one of my students within 2 minutes in front of my eyes. You were also part of my PhD supervisory committee along with Sander. I appreciate your time and opinions. Your ability to come up with an alternate interpretation or explanation is commendable. I was happy to attend your inaugural lecture and see you becoming the full professor, and then chair of a new department. I wish you keep climbing the ladder and get awarded the Spinoza prize. **Sander**, thank you for being on my PhD supervisory committee and your honest opinion during that meeting. I remember that you were consistently present in my Monday lunch meeting presentations and have followed my research work. I appreciate your feedback during those meetings. We have crossed each other a lot in corridors of our departments and our short exchange of words during those crossings and Friday borrels were always cheerful. I wish you all the best with your new responsibilities. **Martin**, our common interest in understanding microtubule nucleation and anchoring led to some cool discussions that always included gamma-TuRC, CAMSAPs and Ninein/NOCA-2, not NOCA-1. We also collaborated for biochemical in vitro reconstitutions of microtubules together with different UNC-33/CRMP isoforms, but unfortunately, we did not see any effect

on microtubule dynamics in vitro. Nonetheless, we became co-authors on **Amelie's** paper. I wish you success with your role as an assistant professor and your scientific research.

I had several opportunities for collaboration within the department and outside. I would like to first thank all of them collectively for contributing to my PhD journey. **Amelie**, I started the first project and first collaboration of my PhD with you when you were a post-doc in **Casper's** lab. I am happy that I could contribute to your paper significantly. The length to which the revisions continued still makes me laugh, but I admire your tenacity. It was great to work with you. I wish you good luck with your early scientific career at Vrije Universiteit, Amsterdam.

**Amol**, thank you for teaching me in vitro reconstitutions. You have an aura that instigates people around you for scientific discussions about pioneering and recent literature and work going on in different research groups in the world. I benefited from that and am developing it into a habit. After you left to do a post-doc at Rockefeller, I stopped going to UMC or Educatorium for lunch. That small walk and 20 minutes lunch time was long enough for good discussions. I am happy that I could scientifically contribute to your microtubule repair by CLASP paper. I appreciate it that you still send me links to the papers which are relevant for my research work. Outside the lab as well, you were fun person to hang out with at Indian get-togethers. Your sassy selection of movies for dumb charades was extremely cheeky. You manipulated me to try spare ribs and I tried pig meat for the first time attracting a stare from **Ankit**, thankfully, he promised not to tell my parents. I am happy to see that after a confused phase, you made up your mind to stay in academia. You are a fit for that. Congratulations to you and **Tonja** on your marriage and I wish you both a good career and a happy married life.

**Eugene**, my go-to person for analysis solutions. I would like to thank you for your help with the single molecule GFP-counting analysis and for brainstorming with me on how to address a critical question from the reviewer of my current submission. I hope we will be able to address it one way or another. We will be co-authors on two papers at least. I wish you all the best for your scientific pursuits. I also have another section of acknowledgment for you.

**Michal**, I never expected that I would be collaborating so quickly with you in future when I was reading your Cryo-EM papers on gamma-TuRC structure from your post-doc. You are very efficient, and I hope our paper will get published soon. I wish you the best with your new lab at ETH, Zurich. Speaking of efficient people, **Kelly**, you are one of them. You are an admirably fast and energetic young PI. I enjoyed working with you and **Victor**, and your mass spectrometry and mass photometry data is very useful. I wish you both the very best in your scientific endeavor. **Riccardo**, during my early PhD years, you were the bridge between our department and **Biomolecular Mass Spectrometry & Proteomics (BMSP) group**, especially

**Maarten Altelaar'** and **Albert Heck's** groups at Utrecht University for productive collaborations. You are very helpful, and I enjoyed your company and fun conversations at all the great potluck dinners of our internationals' group at our houses and at lunch tables in the department. I wish you all the best with your new job at Thermo Fisher and a very happy life with **Isabella** and your kid in Switzerland. **Kai**, we overlapped for less than a week and that too when you were visiting Utrecht, while organizing your new lab at Wuhan University, China. I heard a lot of good things about you and **Shasha** in my early days, the amount and quality of research work you have done speaks for you. The stories that Anna has shared about your post-doc life in her lab during the lab meetings or otherwise are inspiring and amusing. I could sense them whenever I looked into your reagent's inventories. I took forward two of your projects after being two years into my PhD. I am happy that I could give a new direction to one of them and that it has started to reach out to journals now. Hopefully, the second one too would take form of a final manuscript before I finish in Anna's lab. Thanks to you and **Shasha** for all the groundwork and I wish you both all the best in your scientific career. I would like to extend my gratitude to **Manuel Thery**, **Joske Monster** and my other collaborators for productive outputs and being co-authors on the publications.

I would also like to thank the faculty- **Ginny**, **Florian**, **Frederik**, **Agathe**, **Harold**, **Corette**, **Sabrina**, **Paul**, **Jan**, **Mike**, **Suzan**, **Saskia**, **Casper** and my colleagues from the departments of Cell biology, Neurobiology, Biophysics and Developmental biology for their input over the years at the work discussions and lunch meetings and their interactions during the social events. **Esther** and **Lena**, you had been cool managing directors of Institute of Biomembranes. Thank you for organizing all the IB talks, conferences and activities for the PhD students of IB graduate school to which I belonged.

**Phebe**, you are the backbone of the department. Without your management and organizational skills, the department would not run. You provide us with a well-stocked and functioning lab, and we can focus on science. Also, you took care of organizing social events in the department, including the Friday borrels. I got to know you better with our conversations that were fun, and I was always surprised by how much you know about Indian food, festivals, movies and culture. I was so pleased to hear that you traveled to Utrecht, on the day when you work from home, just to join the party I organized for my husband at my home. I am happy that you enjoyed my food. Thank you for all these good memories. **Bart**, **Rene** and **Wendy**, thank you for managing the labs, technical support and running the department smoothly. **Ilya**, without you the microscopes would not be functioning properly. Thank you for giving the microscopes demos and helping whenever required. I enjoy your company, we could talk about politics,

wars and different cultures non-stop. I give you an imaginary award for the best costumes and my favorite of them is the hot pink one that you wore at my Halloween party. You have failed to annoy me, and I still don't believe your story that you are a spy in disguise. Thank you for all the gossip. I have missed you on the last few parties that you skipped. But you have kept me cheerful, and I owe you good food for that, that's why I bring snacks to my office. I hope that we will remain friends afterwards. Stay happy and in touch.

Now, I would like to thank the past members of Akhmanova lab who were part of my journey. **Ankit**, the day is still fresh in my memories when you came to receive me at the airport upon my arrival in the Netherlands and welcome me to a new country. You helped me a lot with in vitro reconstitutions and with your suggestions during lab meetings and other times. With you, **Meghna bhabhi** and your beautiful daughters, **Diya** and **Tukku**, it felt like home. I could celebrate Diwali with you and enjoy great Indian dinner that bhabhi used to cook. I am sorry to keep you both hungry because I was late for many lunches due to my sleep schedules on weekends. I am happy that now you have started your career in academia in India. Although the shock with academic bureaucracy at BHU, Varanasi was not new, I am glad that you made the switch to a different University. I wish you all the best with your new lab at Gujarat Biotechnology University. **Ruddi**, you are a nice and funny person. You can run such complex algorithms on your computer but were so scared of vector maps that you would go into hibernation whenever anyone would show them in the lab meetings. I enjoyed the hospitality from you and **Ayliem** on all those potluck dinners on Christmas. I became a "sinner" when I ate beef, despite being a North-Indian Hindu Brahmin, for the first time during those dinners. It was nice to hear that you are enjoying your current job and I wish you, **Ayliem** and your son **Lucas** a happy life. **Chiung-Yi**, you were my first friend in the Netherlands, and I am so glad that we are still close friends. You are one of the kindest, modest and tolerant people I have met, and you do things from the heart. I arrived in the Netherlands just before my birthday (the one I celebrate) and you took me out for dinner at Hofman cafe. That was already a great start to my life in the Netherlands. For a good period of time when TIRF ILAS2 was less occupied, we had an understanding that, by default, afternoon microscope slots on Mondays and Wednesdays were yours, and Tuesdays and Thursdays were mine. That was so relieving. I enjoyed our in-depth discussions on our projects and any reconstitutions problems. Thank you for helping me move apartments two times and build my furniture together with your husband and my good friend **George** (you are in another section below) whom I met because of you. You both are a great couple and a happy family together with **Liam**, your tiger baby. **Cyntha**, we both started our PhD around the same time but we met for the first time directly during the

lab outing before you officially started. You are an exceptionally organized and planned individual and that is what I admire the most about you. I am still shocked that you plan even your holidays one year in advance. What I also admire and am a bit envious of is your ability to remember even little things from general conversations about everyday life. This reflects that you actively listen to a person independent of how petty the information could be. Maybe it's also called being social. These are some qualities I would like to build. Thank you for ordering restriction enzymes timely. I am very thankful to you for helping me with your car to move into one of my apartments, for building my furniture, for explaining the Dutch letter from tax inspector and helping me and reminding me to apply for employments benefits. Thanks for all the extra information on Dutch rules and culture and fun times at various dinners and get-togethers. I hope your holiday together with **Irene** was relaxing and not excessively organized and you are reenergized after all the intense period of paper revision and your defense. I am happy that you finally decided to get married after being influenced by all the marriages happening around. I wish you all the best for your career outside academia and a happy married life with **Irene** in the future. Let's stay in touch! **PJ**, you know how I elaborate your nick name, don't close the book, I won't write it here. You are a very friendly and helpful colleague, and you always have nice suggestions during our scientific discussions. Your fear of a broken -80 °C freezer was hysterical but that turned out to be good for us. Thank you for all the ICT-related help and also your little pranks that made me laugh but also worried sometimes until you revealed the truth. You and **York** together become a mischievous pair, full of jokes and prank ideas. Congratulations again on your marriage to **Rosanna** and new job. I wish you success in all your future endeavors. **York**, if anyone in the lab could compete with Cynthia on organizational skills, it's you. You are very skilled in communication as well. Thanks for ordering lab reagents in a timely manner. Your skillset definitely helped you in landing a job at Thermo Fisher. I am happy that I shared my office with you, **PJ**, **Cyntha** and **Chiung-Yi** and that we traveled to Heidelberg for EMBO microtubule conference by road and could spend some time together outside the lab. I also had the pleasure of attending your wonderful wedding with **Elodie** which was also the first Dutch wedding I attended. Thank you for inviting me and also voting my congratulation card as the best. You both are made for each other, and you look beautiful together. You are already parents to your two Poodles, Ollie and Mephi. I wish you and your family all the best and that it expands further. **Funso**, congratulations on your new job. You are a very kind, calm, helpful and conscientious man. We debated a lot on in vitro reconstitutions and its practice. Besides scientific discussions, we also had a lot of philosophical discussions. You did your PhD from India, so we also had a lot of common

grounds to talk. It was great to meet you. Thanks for all the fun times we shared together and I wish you and your wife a happy life in the Netherlands. **Babet** and **Maud**, you both managed cell culture room very seriously and I am thankful to you for that and our interactions in the lab. **Ivar**, although I overlapped with you significantly, but we mostly interacted through WhatsApp and Facebook as our lab benches and offices were poles apart. You are a happy and cheerful person and that also elevates the mood of people around you. I could see beautiful Australia through your pictures. I wish you all the best in your scientific pursuits and look forward to meeting you in May in Utrecht. **Chao**, thanks for being a good member of the in vitro team, things ran smoothly even when there were so many people doing in vitro at some point. **Kyle**, I would like to thank you for the good times we shared in the department and social gatherings. It was funny that for Halloween during the first COVID wave, we were overdressed and you were underdressed for an American. It was funny to see your reaction because you did not expect us to come to the department in Halloween costumes.

Now, I would like to express my gratitude to the current members of the lab. **Milena**, you are my soulmate in the office. From scientific discussions to very private conversations to gossip to late evening hours especially on Thursdays, we have had it all. We have become friends for life. You are outspoken but also a good listener, that's why I feel free around you and banter about anything. We share so much similarity both scientifically and personally, and I do not want to praise myself (hehe). Your perseverant and resilient nature helps tremendously with your project to deconvolute a clear picture of kinesin-2 functions in shaping ER network, especially because of the interdependency between microtubule, vimentin and ER network. Yet, you have produced spectacular images of all these networks. I am sure you will come up with a scientific model soon after all the brainstorming sessions with Anna. I am very happy that you managed to take out time and engage yourself in so many other activities outside the lab especially bouldering, salsa, Dutch lessons and expat evenings. **Joyce**, you hold a special place in my heart. You are a very composed and polite person and a cool scientist. You do not like the stress of the presentations, but you are good at presenting science. Thanks for taking over the responsibility of lab orders and fulfilling it substantially. In addition to the scientific discussions, I share a similar vibe with you like I share with Milena and I hope that we will remain friends forever. I enjoy yours and **Nemo**'s company immensely. Thank you for organizing social events in the department and hosting me at a lot of parties and game evenings at your place. You both are very hospitable. You are very passionate about sustainability and have turned to full veganism which also benefited me because I never imagined that vegan food can be lip smacking. I wish you all the best with your aikido exam and I hope that you



earn an aikido belt by the end of February. **Saishree**, you joined the lab not so long ago (1.5 years) but in this relatively short time, you have become very dear to me. You quickly made friends and also integrated into the Dutch culture. You are an outspoken feminist, so I really enjoy our conversations beyond in vitro reconstitution of centriolar proteins. We did our masters from the same lab, so you could catch me up on a lot of things happening in TIFR, Mumbai. You are a very creative and sincere person, so I am sure you will do great in future. It's nice that you can equally enjoy the life outside the lab, so you get less time to miss **Srikant**. It's good in the long run. Sometimes, during our conversations, I learnt so many new things from you about life in general that I feel a generation gap (haha). With you, **Milena**, **Joyce** and **Ilya** we have enjoyed so many get-togethers at either Joyce's place or my place. In these few words, I cannot do justice to you four for giving me the emotional and personal support during my difficult times towards the end of 2021 and beginning of 2022, so I will keep it short. I wish you three ladies and **Lola** jolly and sparkling lives.

**Fangrui**, you amaze everyone with your octa knockout cells and your ability to knock out genes successfully. I did my first cloning and first western blot in Anna's lab, and you were the one who taught me these successfully. You also helped my students with your 2x knockdown and gene editing techniques. You were the go-to person to me for molecular biology techniques. We also share a passion for microtubule nucleation and anchoring that led to a lot of in-depth discussions. You have massive amounts of data and every time I look at it, I interpret something new. I would pick you as the most hard-working colleague among our current lab members for the same reason you picked me. I can feel your commitment to science. There had been many Friday afternoon work discussions since my microtubule repair time, where we both could push the meetings to 2 hours that other people had to squeeze their work updates in next half an hour and still, we would finish when the borrels were over. Ruddi used to leave halfway or fall asleep seeing your number of slides (>30). I enjoyed those days a lot because those discussions together with Anna's wisdom were super interesting. It was so fortunate for me that you could train Yinlong with your technical skills. In addition to science, we shared a passion for warm and spicy food. Thank you for the silk scarf that you brought for me from China as a wedding gift. I am very thankful to you for all your help, and I wish you all the best in figuring out your research interest and a post-doc lab. Also, my best wishes for your second baby on the way. **Boris**, we hardly joined the same lab meeting, but we did get time in the lab to talk about scientific and non-scientific things. We used to hang out more outside the lab with our internationals group. It was initially difficult to start a conversation with you, but we eventually got along and shared some good ones. Thank you for the snacks

that you brought from Israel. I gain momentum whenever you play your psychedelic playlist in the lab, and I like it. Hopefully, we will be able to teach each other some of our traditional cuisines before we drift apart like we promised. I wish you good luck with the final rounds of job interviews outside academia. **Emma**, I admire your abilities to work on collaborative projects not just between Anna and Lukas labs but also with UMC. And you still manage to organize IB PhD talks, retreats and activities and also lab activities. Thank you for all of that. I wish you all the best with the expansion of basal bodies in human airway ciliated epithelial cells, you already got success. **Hugo**, Same goes with you. You were first an exceptional master student in Anna's lab and then collaborative PhD student in Anna' and Lukas' lab. You are highly motivated and efficient that also gave you a great publication record, well within your PhD contract. You collaborated with Paul Tillberg's expansion microscopy group at Janelia and enhanced the resolution from 4- to 10-fold. Your TREx microscopy images are wonderful. I am impressed with you. I wish you good luck with your PhD defense (soon) and migration in venture capital funds and I am sure you will live a very wealthy life. **Lilian**, you are an enthusiastic person. Thank you for taking over the CLASP KO project from me, those CLASPs knockout cells are spectacular, where you can count number of microtubules on fingers. I would have been so restless if the world could not see them. Your expansion microscopy data will eventually build a nice scientific model. I look forward to that. Your effort with Joyce and Jey for sustainable labs is commendable. **Harriet**, I am impressed with the in vitro reconstitutions you have done with combining so many ciliary tip proteins in your timescale in the lab. I enjoyed the times we shared in the department as well as outside. Let's see how slow your microtubules can grow with your ciliary tip module proteins and their web. All the best! **Yinlong**, you learnt cellular work from Fangrui and you liked it so much that you decided to work in vivo rather than in vitro. But that turned out to be so useful for me as you could produce data for the rebuttal of my paper that strengthened our model and addressed one of the reviewer concerns by providing cellular relevance. Thank you for your help. I wish you all the best in your future endeavor. **Matheus**, you are a happy guy with always a smiling face that lifts up mood. I wish you success with your remaining short period in Anna's lab and wish you all the best with finishing your PhD in Brazil.

**Robin**, the latest PhD addition but not latest Anna lab addition. You were an excellent master student of mine and we both learnt a lot together. I already shared my good thoughts for you in the laudation I gave during your master's graduation ceremony. Your cum laude master's degree justified your efforts. Thank you for giving the opto-CLASP project a new direction when you showed us those CLASP-depleted cells with only a few microtubules remaining.

They made us so curious that we sidelined the idea of photo-inactivable CLASP for good. I am sure with your ability to tackle experimental challenges; you will also develop a paradigm to study the high-resolution structures of our in vitro microtubule samples using Cryo-EM. I look forward to reading your future publications. **Misko**, you were another excellent master student of mine. You continued CLASP project from where Robin left. With you, we learnt together how low microtubules can go in CLASP-depleted cells and the numbers were spectacular in your centriole and CLASP-depleted cells. You also worked on further determining the underlying mechanism and produced data that helped us to understand the role (or not) of other microtubule associated proteins and effect of CLASP-depletion on centrosomal proteins. We also completely dumped the idea of opto-CLASP in your presence because of the repeated issues of protein aggregation and cell line heterogeneity and this was a good call. Your scientific enthusiasm and hard work are commendable. You decided to stay in the department, and I wish you success with continuing your PhD in Frederik's lab. I would like to thank my other master students **Jelle** and **Guus**, whom I co-supervised with Amol, who struggled the most with the ambitious optogenetic CLASP project. I would also like to thank my bachelor students **Remy**, **Nina**, **Joris** and **Iris**, whom I co-supervised with Chiung-Yi in 2018, and **Beert** and **Max**, whom I supervised online during COVID times in 2020 when I was stuck in India for additional two and half months after my holiday. Collectively, my students have helped me in improving my supervision skills and the experience taught me to have a dynamic supervision style for individual students. So, thanks to all of you. I wish you all a bright future.

Now, I would like to thank my colleagues and friends in the department. **Josiah**, the English guy, we bonded over various get-togethers that mainly involved food, games and drinks. Thank you for the fun times we shared. Junior **Anna**, I am happy that you found a place where you can get privacy and mental peace. Thank you for the food you brought from India or made for dinners at my place. I wish you success with your PhD.

Our department has been a super interactive and collaborative one, scientifically and otherwise. We could approach anyone for discussions and get help with equipment and lab reagents. The borrels and lab outings made our department very sociable. So, I would like to thank all those colleagues with whom I overlapped either in the past or at present and associated one way or another especially- PhDs: **Malina**, **Klara**, **Daphne**, **Manon**, **Robbelien**, **Katerina**, **Xingxiu**, **Yujie**, **Carlijn**, **Robin**, **Liu**, **Marijn**, **Sara**, **Lisa**, **Jelmer**, **Lotte**, **Ate**, **Wouter**, **Jian**, **Feline**, **Sybren**, **Jessica**, **Nicky**, **Dennis**, **Vida**, **Thomanai**, **Anne**, **Roderick**, **Cátia**, **Giel**, **Derk**, **Nazmiye**, **Mai Dan**, **Ha**, **Chun Hei**; and post-docs: **Mithila**, **Desiree**, **Eitan**, **Jey**, **Wilco**, **Anna**, **Yolanda**, **Arthur**, **Marvin**, **Bart**, **Max**, **Niels**, **Eliana**, **Inês** and **Sofia**.

I want to take a pause here, and then thank my other internationals group with whom it felt like home- **Mithila, Eugene, Desirée, Chiung-Yi, George, Ruddi, Aylien, Eitan, Zlil, Boris**. I already mentioned some of you above, but I want to emphasize that you meant a lot to me throughout my PhD journey. I cannot do justice to the gratitude I owe you guys in these limited pages of my PhD thesis, but I am certain that you all know how I feel for you. We travelled to Ukraine together for E&D's wedding. We have bonded over many lunches, Christmas dinners (at Ruddi's place), picnics, barbecues, game evenings, house warmings, birthdays, weddings, E&D bachelor and bachelorette party, babies (Teo, Liam, Asia), parties and occasional drinks that I did not miss home. Thank you for all of that and I wish you all a very cheerful and healthy life. **Eitan**, we share a positive and happy aura and a passion for food that has grown immensely in me. I wish you could have stayed a bit longer in the Netherlands. I admire that you are a very responsible person as well as a citizen, it was very clear when you traveled to Israel just for voting because you wanted right leaders. I wish you, **Zlil** and your baby girl **Asia** a very sparkling and happy life in Israel. **George**, you enjoy my food so much that I like cooking for you and **Chiung-Yi**, just to see your contented reaction. But it was not always pleasant, one time your stomach was hurting because I was a little late to warn you about Indian pickles (that still makes me laugh). I owe you a lot for all the times you have picked me up in your car for all those get-togethers and parties. **Desirée**, you kept our group together by making "The misanthropy club" on WhatsApp (hehe). I feel pampered around you, **Eugene, Ruddi, Aylien** and **Mithila**. I enjoyed the boat trip, silly dares (in the bus and streets), the burlesque lesson and the company of your friends at your bachelorette party. **Mithila**, you have always been there for me since the beginning of my PhD. You were also the link to the Indian community. In addition to the immense personal support, you also gave me academic support. You discussed my projects in-depth and always had good points and questions. You taught me micropatterning and helped me to prepare photomask for Anna's lab, which I kept with you in Lukas lab. We talk about life in general and share great laughter together, but at the same time I also respect your take on life. I am super happy that even though you started your job recently at Catalyze, Amsterdam, you took out time to be my paranymp and stand by my side also on my PhD defense day. I wish you a lot of strength and success in learning the funding and business side of academia and a happy, peaceful and stable life in the Netherlands.

The other community that kept me lively was the Indian community in Utrecht. A lot of us have dispersed now since COVID, but I especially want to thank **Aridaman** and **Sakshi** for your hospitality. You hosted us for a lot of potlucks where we played games or discussed a lot about academic life, life as an expat in UMC or life in general. I wish you both all the best for

the new chapter of your life in Massachusetts. If I end up as a post-doc in the USA, then I am sure we will be seeing each other there. Otherwise, somewhere in India on our holidays.

**Krishanu** and **Swagata**, you were my supervisor and mentor in M.Sc. and built the foundation of my research skills. I learnt a lot from both of you. Congratulations Krishanu on your new role as the Director of NBRC, Manesar. I know you will also be able to manage your lab well at TIFR. Swagata, you will be my friend forever. I wish you reach the heights you deserve in your scientific career and wish you a lot of success in running your lab at NBRC.

I also want to thank **Anasuya**, **Sweta** and **Samya**. We started our masters in the same batch in TIFR, India, but were also not very far from each other in our PhDs at University of Tübingen, Germany, KU Leuven, Belgium, LMB Cambridge, UK, and me at Utrecht University. We (except Samya and his visa issues) managed to plan last-minute Christmas trips to countries in Europe every year until COVID. Although not everyone could join each year, we remained connected through video calls on weekends. We kept each other motivated and strong. I am so happy that you all have defended your PhD already now and I will soon join the club.

I also want to thank my friends from bachelor studies- **Kanchan**, **Ankita** and **Nivedita** for checking up on me regularly, for emotional support through all those video calls on weekends and for being physically present on my wedding (for which you were waiting since bachelors) in India last year during the tail of third COVID wave.

I also want to thank first my extended family I made last year, my in-laws, for their support and understanding in the past one year.

Now, I will try but I don't think I can put my gratitude and love into words for my sister, **Deepika**. You are that other strong woman out of the two in my life from whom I derive inspirations. You are ambitious, committed, tireless, efficient, tenacious, tolerant and yet family oriented. You have been defeated but only to grow stronger. I wish I can be half the person you are. You have been an indispensable support system and my go-to person whenever I go through rough phases in my life. Thank you! I also want to thank **Bhavna**, my sister-in-law, **Nitin**, my brother and **Sudhir**, my brother-in-law for the emotional and personal support I received. You all believe in me so much that I have no room for disappointments.

**Mummy** and **Daddy**, whatever I do starts with you and ends with you. Thank you for your sacrifices and raising and supporting strong independent daughters and daughter-in-law.

**Utkarsh**, you are my world! After 10 years, it was made official last year at our wedding. Our relationship was tested at all levels by a long distance of 8.5 years, and we passed! Thank you!

- Dipti





